WILEY-VCH

Oliver Zerbe and Simon Jurt

Applied NMR Spectroscopy for Chemists and Life Scientists

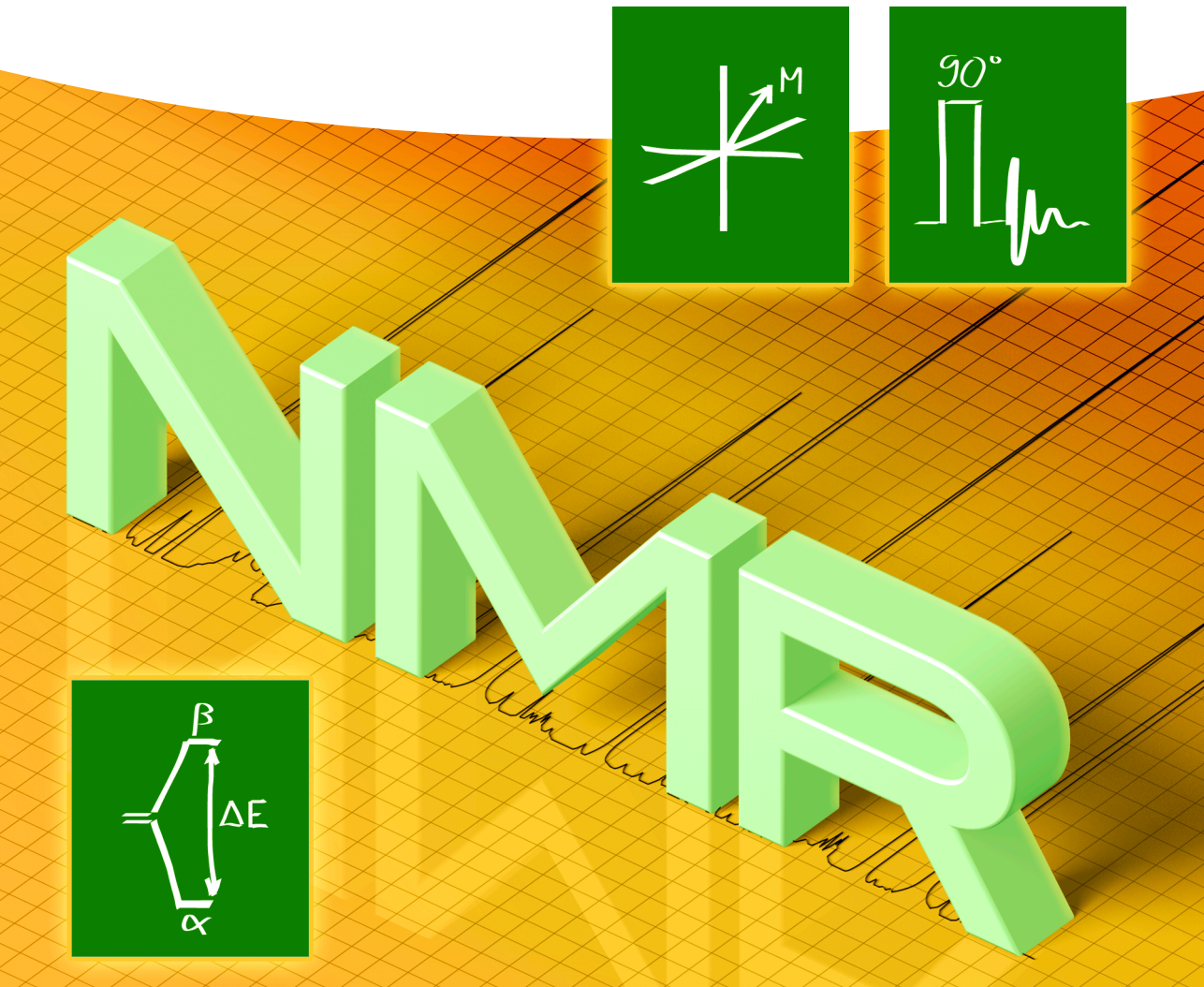

Oliver Zerbe and Simon Jurt

Applied NMR Spectroscopy for Chemists and Life Scientists

Related Titles

Gauglitz, G., Vo-Dinh, T., Moore, D. S. (eds.)

Handbook of Spectroscopy

2014
Second, completely revised and enlarged edition, ISBN: 978-3-527-32150-6

Findeisen, M., Berger, S.

50 and More Essential NMR Experiments
A Detailed Guide

2014
Print ISBN: 978-3-527-33483-4

Günther, H.

NMR Spectroscopy
Basic Principles, Concepts and Applications in Chemistry

2013
Third Edition, Print ISBN: 978-3-527-33000-3; also available in electronic formats

Pregosin, P.S.

NMR in Organometallic Chemistry

2012
Print ISBN: 978-3-527-33013-3

Friebolin, H.

Basic One- and Two-Dimensional NMR Spectroscopy

2011
Fifth Edition, Print ISBN: 978-3-527-32782-9

Berger, S., Sicker, D.

Classics in Spectroscopy
Isolation and Structure Elucidation of Natural Products

2009
Print ISBN: 978-3-527-32516-0

Oliver Zerbe and Simon Jurt

Applied NMR Spectroscopy for Chemists and Life Scientists

WILEY-VCH
Verlag GmbH & Co. KGaA

Authors

Prof. Dr. Oliver Zerbe
University Zürich
Institute of Organic Chemistry
Winterthurstrasse 190
8057 Zürich
Switzerland

Simon Jurt
University Zürich
Institute of Organic Chemistry
Winterthurstrasse 190
8057 Zürich
Switzerland

All books published by Wiley-VCH are carefully produced. Nevertheless, authors, editors, and publisher do not warrant the information contained in these books, including this book, to be free of errors. Readers are advised to keep in mind that statements, data, illustrations, procedural details or other items may inadvertently be inaccurate.

Library of Congress Card No.:
applied for

British Library Cataloguing-in-Publication Data:
A catalogue record for this book is available from the British Library.

Bibliographic information published by the Deutsche Nationalbibliothek
The Deutsche Nationalbibliothek lists this publication in the Deutsche Nationalbibliografie; detailed bibliographic data are available on the Internet at http://dnb.d-nb.de.

© 2014 WILEY-VCH Verlag GmbH & Co. KGaA, Boschstr. 12, 69469 Weinheim, Germany

All rights reserved (including those of translation into other languages). No part of this book may be reproduced in any form – by photoprinting, microfilm, or any other means – nor transmitted or translated into a machine language without written permission from the publishers. Registered names, trademarks, etc. used in this book, even when not specifically marked as such, are not to be considered unprotected by law.

Cover Design Formgeber, Mannheim
Typesetting le-tex publishing services GmbH, Leipzig, Germany
Printing and Binding betz-Druck GmbH, Darmstadt, Germany

Hardcover ISBN 978-3-527-32775-1
Softcover ISBN 978-3-527-32774-4
ePDF ISBN 978-3-527-67785-6
ePub ISBN 978-3-527-67783-2
Mobi ISBN 978-3-527-67784-9

Printed on acid-free paper

Contents

Preface *XV*

1 Introduction to NMR Spectroscopy *1*
1.1 Our First 1D Spectrum *1*
1.2 Some Nomenclature: Chemical Shifts, Line Widths, and Scalar Couplings *2*
1.3 Interpretation of Spectra: A Simple Example *5*
1.4 Two-Dimensional NMR Spectroscopy: An Introduction *9*

Part One Basics of Solution NMR *11*

2 Basics of 1D NMR Spectroscopy *13*
2.1 The Principles of NMR Spectroscopy *13*
2.2 The Chemical Shift *16*
2.3 Scalar Couplings *17*
2.4 Relaxation and the Nuclear Overhauser Effect *20*
2.5 Practical Aspects *23*
2.5.1 Sample Preparation *23*
2.5.2 Referencing *25*
2.5.3 Sensitivity and Accumulation of Spectra *27*
2.5.4 Temperature Calibration *29*
2.6 Problems *30*
Further Reading *31*

3 ^{1}H NMR *33*
3.1 General Aspects *33*
3.2 Chemical Shifts *34*
3.2.1 Influence of Electronegativity of Substituents *35*
3.2.2 Anisotropy Effects *35*
3.2.3 Other Factors Affecting Chemical Shifts: Solvent, Temperature, pH, and Hydrogen Bonding *37*

3.2.4 Shift Reagents *37*
3.3 Spin Systems, Symmetry, and Chemical or Magnetic Equivalence *39*
3.3.1 Homotopic, Enantiotopic, and Diastereotopic Protons *42*
3.3.2 Determination of Enantiomeric Purity *43*
3.4 Scalar Coupling *44*
3.4.1 First-Order Spectra *45*
3.4.2 Higher-Order Spectra and Chemical Shift Separation *47*
3.4.3 Higher-Order Spectra and Magnetic Equivalence *49*
3.5 ^{1}H–^{1}H Coupling Constants *50*
3.5.1 Geminal Couplings *50*
3.5.2 Vicinal Couplings *50*
3.5.3 Long-Range Couplings *52*
3.5.4 ^{1}H Couplings to Other Nuclei *52*
3.6 Problems *54*
Further Reading *55*

4 NMR of ^{13}C and Heteronuclei *57*
4.1 Properties of Heteronuclei *57*
4.2 Indirect Detection of Spin-1/2 Nuclei *59*
4.3 ^{13}C NMR Spectroscopy *59*
4.3.1 The ^{13}C Chemical Shift *60*
4.3.2 X,^{13}C Scalar Couplings *64*
4.3.3 Longitudinal Relaxation of ^{13}C Nuclei *68*
4.3.4 Recording ^{13}C NMR Spectra *68*
4.4 NMR of Other Main Group Elements *70*
4.4.1 Main Group Nuclei with $I = 1/2$ *71*
4.4.2 Main Group Nuclei with $I > 1/2$ *75*
4.5 NMR Experiments with Transition Metal Nuclei *78*
4.5.1 Technical Aspects of Inverse Experiments with $I = 1/2$ Metal Nuclei *79*
4.5.2 Experiments with Spin $I > 1/2$ Transition Metal Nuclei *81*
4.6 Problems *82*
Further Reading *84*

Part Two Theory of NMR Spectroscopy *85*

5 Nuclear Magnetism – A Microscopic View *87*
5.1 The Origin of Magnetism *87*
5.2 Spin – An Intrinsic Property of Many Particles *88*
5.3 Experimental Evidence for the Quantization of the Dipole Moment: The Stern–Gerlach Experiment *93*
5.4 The Nuclear Spin and Its Magnetic Dipole Moment *94*
5.5 Nuclear Dipole Moments in a Homogeneous Magnetic Field: The Zeeman Effect *96*

5.5.1 Spin Precession *98*
5.6 Problems *103*

6 Magnetization – A Macroscopic View *105*
6.1 The Macroscopic Magnetization *105*
6.2 Magnetization at Thermal Equilibrium *106*
6.3 Transverse Magnetization and Coherences *108*
6.4 Time Evolution of Magnetization *109*
6.4.1 The Bloch Equations *110*
6.4.2 Longitudinal and Transverse Relaxation *112*
6.5 The Rotating Frame of Reference *115*
6.6 RF Pulses *117*
6.6.1 Decomposition of the RF Field *118*
6.6.2 Magnetic Fields in the Rotating Frame *119*
6.6.3 The Bloch Equations in the Rotating Frame *120*
6.6.4 Rotation of On-Resonant and Off-Resonant Magnetization under the Influence of Pulses *121*
6.7 Problems *122*

7 Chemical Shift and Scalar and Dipolar Couplings *125*
7.1 Chemical Shielding *125*
7.1.1 The Contributions to Shielding *127*
7.1.2 The Chemical Shifts of Paramagnetic Compounds *131*
7.1.3 The Shielding Tensor *132*
7.2 The Spin–Spin Coupling *133*
7.2.1 Scalar Coupling *134*
7.2.2 Quadrupolar Coupling *140*
7.2.3 Dipolar Coupling *141*
7.3 Problems *144*
Further Reading *145*

8 A Formal Description of NMR Experiments: The Product Operator Formalism *147*
8.1 Description of Events by Product Operators *148*
8.2 Classification of Spin Terms Used in the POF *149*
8.3 Coherence Transfer Steps *151*
8.4 An Example Calculation for a Simple 1D Experiment *152*
Further Reading *153*

9 A Brief Introduction into the Quantum-Mechanical Concepts of NMR *155*
9.1 Wave Functions, Operators, and Probabilities *155*
9.1.1 Eigenstates and Superposition States *156*
9.1.2 Observables of Quantum-Mechanical Systems and Their Measured Quantities *157*

9.2 Mathematical Tools in the Quantum Description of NMR *158*
9.2.1 Vector Spaces, Bra's, Ket's, and Matrices *158*
9.2.2 Dirac's Bra–Ket Notation *159*
9.2.3 Matrix Representation of State Vectors *160*
9.2.4 Rotations between State Vectors can be Accomplished with Tensors *161*
9.2.5 Projection Operators *162*
9.2.6 Operators in the Bra–Ket Notation *163*
9.2.7 Matrix Representations of Operators *165*
9.3 The Spin Space of Single Noninteracting Spins *166*
9.3.1 Expectation Values of the Spin-Components *168*
9.4 Hamiltonian and Time Evolution *169*
9.5 Free Precession *169*
9.6 Representation of Spin Ensembles – The Density Matrix Formalism *171*
9.6.1 Density Matrix at Thermal Equilibrium *173*
9.6.2 Time Evolution of the Density Operator *173*
9.7 Spin Systems *175*
9.7.1 Scalar Coupling *176*

Part Three Technical Aspects of NMR *179*

10 The Components of an NMR Spectrometer *181*
10.1 The Magnet *181*
10.1.1 Field Homogeneity *182*
10.1.2 Safety Notes *183*
10.2 Shim System and Shimming *184*
10.2.1 The Shims *184*
10.2.2 Manual Shimming *185*
10.2.3 Automatic Shimming *186*
10.2.4 Using Shim Files *187*
10.2.5 Sample Spinning *187*
10.3 The Electronics *187*
10.3.1 The RF Section *188*
10.3.2 The Receiver Section *189*
10.3.3 Other Electronics *189*
10.4 The Probehead *189*
10.4.1 Tuning and Matching *190*
10.4.2 Inner and Outer Coils *191*
10.4.3 Cryogenically Cooled Probes *191*
10.5 The Lock System *192*
10.5.1 The ^{2}H Lock *192*
10.5.2 Activating the Lock *193*
10.5.3 Lock Parameters *194*

10.6 Problems *194*
Further Reading *194*

11 Acquisition and Processing *195*
11.1 The Time Domain Signal *197*
11.2 Fourier Transform *199*
11.2.1 Fourier Transform of Damped Oscillations *199*
11.2.2 Intensity, Integral, and Line Width *200*
11.2.3 Phases of Signals *201*
11.2.4 Truncation *202*
11.2.5 Handling Multiple Frequencies *202*
11.2.6 Discrete Fourier Transform *203*
11.2.7 Sampling Rate and Aliasing *204*
11.2.8 How Fourier Transformation Works *205*
11.3 Technical Details of Data Acquisition *209*
11.3.1 Detection of the FID *209*
11.3.2 Simultaneous and Sequential Sampling *210*
11.3.3 Digitizer Resolution *213*
11.3.4 Receiver Gain *214*
11.3.5 Analog and Digital Filters *215*
11.3.6 Spectral Resolution *216*
11.4 Data Processing *217*
11.4.1 Digital Resolution and Zero Filling *217*
11.4.2 Linear Prediction *219*
11.4.3 Pretreatment of the FID: Window Multiplication *220*
11.4.4 Phase Correction *227*
11.4.5 Magnitude Mode and Power Spectra *229*
11.4.6 Baseline Correction *230*
11.5 Problems *231*
Further Reading *232*

12 Experimental Techniques *233*
12.1 RF Pulses *233*
12.1.1 General Considerations *234*
12.1.2 Hard Pulses *235*
12.1.3 Soft Pulses *236*
12.1.4 Band-Selective RF Pulses *237*
12.1.5 Adiabatic RF Pulses *238*
12.1.6 Composite Pulses *240*
12.1.7 Technical Considerations *241*
12.1.8 Sources and Consequences of Pulse Imperfections *243*
12.1.9 RF Pulse Calibration *244*
12.1.10 Transmitter Pulse Calibration *245*
12.1.11 Decoupler Pulse Calibration (^{13}C and ^{15}N) *246*
12.2 Pulsed Field Gradients *247*

12.2.1 Field Gradients *247*
12.2.2 Using Gradient Pulses *248*
12.2.3 Technical Aspects *250*
12.3 Phase Cycling *251*
12.3.1 The Meaning of Phase Cycling *251*
12.4 Decoupling *255*
12.4.1 How Decoupling Works *255*
12.4.2 Composite Pulse Decoupling *256*
12.5 Isotropic Mixing *257*
12.6 Solvent Suppression *257*
12.6.1 Presaturation *258*
12.6.2 Water Suppression through Gradient-Tailored Excitation *259*
12.6.3 Excitation Sculpting *260*
12.6.4 WET *260*
12.6.5 One-Dimensional NOESY with Presaturation *260*
12.6.6 Other Methods *261*
12.7 Basic 1D Experiments *262*
12.8 Measuring Relaxation Times *262*
12.8.1 Measuring T1 Relaxation – The Inversion-Recovery Experiment *262*
12.8.2 Measuring T2 Relaxation – The Spin Echo *263*
12.9 The INEPT Experiment *266*
12.10 The DEPT Experiment *268*
12.11 Problems *270*

13 The Art of Pulse Experiments *271*
13.1 Introduction *271*
13.2 Our Toolbox: Pulses, Delays, and Pulsed Field Gradients *272*
13.3 The Excitation Block *273*
13.3.1 A Simple 90° Pulse Experiment *273*
13.3.2 The Effects of 180° Pulses *273*
13.3.3 Handling of Solvent Signals *274*
13.3.4 A Polarization Transfer Sequence *275*
13.4 The Mixing Period *277*
13.5 Simple Homonuclear 2D Sequences *278*
13.6 Heteronuclear 2D Correlation Experiments *279*
13.7 Experiments for Measuring Relaxation Times *281*
13.8 Triple-Resonance NMR Experiments *283*
13.9 Experimental Details *284*
13.9.1 Selecting the Proper Coherence Pathway: Phase Cycles *284*
13.9.2 Pulsed Field Gradients *286*
13.9.3 *N*-Dimensional NMR and Sensitivity Enhancement Schemes *288*
13.10 Problems *289*
Further Reading *289*

Part Four Important Phenomena and Methods in Modern NMR *291*

14 Relaxation *293*
14.1 Introduction *293*
14.2 Relaxation: The Macroscopic Picture *293*
14.3 The Microscopic Picture: Relaxation Mechanisms *294*
14.3.1 Dipole–Dipole Relaxation *295*
14.3.2 Chemical Shift Anisotropy *297*
14.3.3 Scalar Relaxation *298*
14.3.4 Quadrupolar Relaxation *298*
14.3.5 Spin–Spin Rotation Relaxation *299*
14.3.6 Paramagnetic Relaxation *299*
14.4 Relaxation and Motion *299*
14.4.1 A Mathematical Description of Motion: The Spectral Density Function *300*
14.4.2 NMR Transitions That Can Be Used for Relaxation *302*
14.4.3 The Mechanisms of T1 and T2 Relaxation *303*
14.4.4 Transition Probabilities *304*
14.4.5 Measuring Relaxation Rates *306*
14.5 Measuring ^{15}N Relaxation to Determine Protein Dynamics *306*
14.5.1 The Lipari–Szabo Formalism *307*
14.6 Measurement of Relaxation Dispersion *310*
14.7 Problems *313*

15 The Nuclear Overhauser Effect *315*
15.1 Introduction *315*
15.1.1 Steady-State and Transient NOEs *318*
15.2 The Formal Description of the NOE: The Solomon Equations *318*
15.2.1 Different Regimes and the Sign of the NOE: Extreme Narrowing and Spin Diffusion *320*
15.2.2 The Steady-State NOE *321*
15.2.3 The Transient NOE *324*
15.2.4 The Kinetics of the NOE *324*
15.2.5 The 2D NOESY Experiment *325*
15.2.6 The Rotating-Frame NOE *327*
15.2.7 The Heteronuclear NOE and the HOESY Experiment *329*
15.3 Applications of the NOE in Stereochemical Analysis *330*
15.4 Practical Tips for Measuring NOEs *332*
15.5 Problems *333*
Further Reading *334*

16 Chemical and Conformational Exchange *335*
16.1 Two-Site Exchange *335*
16.1.1 Fast Exchange *338*
16.1.2 Slow Exchange *340*

16.1.3 Intermediate Exchange *340*
16.1.4 Examples *342*
16.2 Experimental Determination of the Rate Constants *344*
16.3 Determination of the Activation Energy by Variable-Temperature NMR Experiments *346*
16.4 Problems *348*
Further Reading *349*

17 Two-Dimensional NMR Spectroscopy *351*
17.1 Introduction *351*
17.2 The Appearance of 2D Spectra *352*
17.3 Two-Dimensional NMR Spectroscopy: How Does It Work? *354*
17.4 Types of 2D NMR Experiments *357*
17.4.1 The COSY Experiment *358*
17.4.2 The TOCSY Experiment *359*
17.4.3 The NOESY Experiment *362*
17.4.4 HSQC and HMQC Experiments *364*
17.4.5 The HMBC Experiment *365*
17.4.6 The HSQC-TOCSY Experiment *366*
17.4.7 The INADEQUATE Experiment *367*
17.4.8 *J*-Resolved NMR Experiments *368*
17.5 Three-Dimensional NMR Spectroscopy *370*
17.6 Practical Aspects of Measuring 2D Spectra *370*
17.6.1 Frequency Discrimination in the Indirect Dimension: Quadrature Detection *370*
17.6.2 Folding in 2D Spectra *376*
17.6.3 Resolution in the Two Frequency Domains *377*
17.6.4 Sensitivity of 2D NMR Experiments *378*
17.6.5 Setting Up 2D Experiments *379*
17.6.6 Processing 2D Spectra *380*
17.7 Problems *381*

18 Solid-State NMR Experiments *383*
18.1 Introduction *383*
18.2 The Chemical Shift in the Solid State *384*
18.3 Dipolar Couplings in the Solid State *386*
18.4 Removing CSA and Dipolar Couplings: Magic-Angle Spinning *387*
18.5 Reintroducing Dipolar Couplings under MAS Conditions *388*
18.5.1 An Alternative to Rotor-Synchronized RF Pulses: Rotational Resonance *390*
18.6 Polarization Transfer in the Solid State: Cross-Polarization *391*
18.7 Technical Aspects of Solid-State NMR Experiments *393*
18.8 Problems *394*
Further Reading *394*

19 Detection of Intermolecular Interactions *395*
19.1 Introduction *395*
19.2 Chemical Shift Perturbation *397*
19.3 Methods Based on Changes in Transverse Relaxation (Ligand-Observe Methods) *398*
19.4 Methods Based on Changes in Cross-Relaxation (NOEs) (Ligand-Observe or Target-Observe Methods) *400*
19.5 Methods Based on Changes in Diffusion Rates (Ligand-Observe Methods) *403*
19.6 Comparison of Methods *404*
19.7 Problems *405*
Further Reading *406*

Part Five Structure Determination of Natural Products by NMR *407*

20 Carbohydrates *419*
20.1 The Chemical Nature of Carbohydrates *419*
20.1.1 Conformations of Monosaccharides *422*
20.2 NMR Spectroscopy of Carbohydrates *423*
20.2.1 Chemical Shift Ranges *423*
20.2.2 Systematic Identification by NMR Spectroscopy *424*
20.2.3 Practical Tips: The Choice of Solvent *429*
20.3 Quick Identification *430*
20.4 A Worked Example: Sucrose *430*
Further Reading *437*

21 Steroids *439*
21.1 Introduction *439*
21.1.1 The Chemical Nature *440*
21.1.2 Proton NMR Spectra of Steroids *441*
21.1.3 Carbon Chemical Shifts *443*
21.1.4 Assignment Strategies *444*
21.1.5 Identification of the Stereochemistry *447*
21.2 A Worked Example: Prednisone *449*
Further Reading *456*

22 Peptides and Proteins *457*
22.1 Introduction *457*
22.2 The Structure of Peptides and Proteins *458*
22.3 NMR of Peptides and Proteins *461*
22.3.1 ^{1}H NMR *461*
22.3.2 ^{13}C NMR *464*
22.3.3 ^{15}N NMR *467*
22.4 Assignment of Peptide and Protein Resonances *469*

22.4.1 Peptides *470*
22.4.2 Proteins *473*
22.5 A Worked Example: The Pentapeptide TP5 *476*
Further Reading *480*

23 Nucleic Acids *481*
23.1 Introduction *481*
23.2 The Structure of DNA and RNA *482*
23.3 NMR of DNA and RNA *486*
23.3.1 ^{1}H NMR *486*
23.3.2 ^{13}C NMR *489*
23.3.3 ^{15}N NMR *490*
23.3.4 ^{31}P NMR *490*
23.4 Assignment of DNA and RNA Resonances *492*
23.4.1 Unlabeled DNA/RNA *492*
23.4.2 Labeled DNA/RNA *496*
Further Reading *498*

Appendix *499*
A.1 The Magnetic *H* and *B* Fields *499*
A.2 Magnetic Dipole Moment and Magnetization *500*
A.3 Scalars, Vectors, and Tensors *501*
A.3.1 Properties of Matrices *504*

Solutions *507*

Index *525*

Preface

NMR spectroscopy has developed very successfully from its early beginnings in the 1940s, at which time it was mainly subject to research in the labs of a few physicists, to its present frequent use by a broad community. Widespread use of NMR started in the 1960s when instruments moved into the laboratories of chemists to support analytics of synthesized products. The progress of modern chemistry only became possible with the advent of powerful analytical instrumental methods, with NMR spectroscopy playing a very pivotal role amongst them. To understand the importance of NMR, we only need to look back on natural product synthesis prior to the advent of NMR, where all intermediates had to be compared to known compounds through chemical transformations. Today, NMR is not only used by chemists, but also by researchers working in material science, structural biologists, the pharmaceutical industry, in product quality control as well as in many more fields of application.

Considering the importance of NMR in many branches of chemistry basic NMR knowledge is traditionally taught in the chemistry curriculum, and this is often done in combination with other spectroscopic techniques such as IR, UV, or MS. The content of these courses primarily aims at providing the student with practical skills of how to elucidate the structure of small (usually organic) molecules from simple spectra, mostly 1D and simple 2D spectra. Accordingly, the necessary empirical knowledge for example typical chemical shifts for important compound classes are taught, whereas the physicochemical background on the nature of the chemical shifts is less frequently explained. A reader interested in these topics is faced with a plethora of very good NMR books. However, these books generally aim at a readership with more advanced knowledge in physical chemistry and quantum mechanics, and as a result the reader may have difficulty understanding the presented topics.

NMR has rapidly moved into adjacent branches of science and today it is not only chemists that come into contact with NMR. Modern molecular biology makes heavy use of NMR to understand the structure and dynamics of biological macromolecules such as proteins, nucleic acids, or oligosaccharides. Today, some of the top Bio-NMR groups are hosted in the biological sector. NMR is also being increasingly applied in pharmaceutical sciences, both in the academic as well as in the industrial environment. Physicists also use NMR, often solid-state techniques, to

probe for properties of materials; and last but not least NMR experiments are performed in industrial labs worldwide.

We have written this book as an introduction to NMR for scientists in the abovementioned fields. A guiding principle of the book is to introduce a topic first in very simple terms, and then to reexamine the topic at more elevated levels of theory. Thereby we hope to provide the reader with a source of knowledge that bridges the gap to the more advanced NMR books. We feel that the taught content and level of theoretical detail should be sufficient for a chemistry student at all levels, including those undertaking a PhD thesis unless the thesis topic is directly related to NMR. Of course, the reader is strongly encouraged to consult more advanced NMR textbooks, since we cannot cover all theoretical details in this book.

Twenty years ago samples were usually handed over to an NMR department and the spectroscopist would have returned processed and often also interpreted spectra. Since that time the situation has changed significantly to one where all these steps are performed by the students themselves. At the University of Zurich students are taught how to record their own NMR spectra, and they have hands-on experience of the spectrometers from the second year of their studies onwards. The stability of modern NMR spectrometer equipment and software has enabled nonexpert users to use NMR and easily perform more advanced 2D or even 3D NMR experiments. We feel, however, that it is important that the technical aspects of NMR are properly understood. The first steps in setting up an experiment are usually locking, shimming, probehead tuning etc., and although these steps are now often done automatically by the spectrometer we feel that it is unsatisfactory if users do not properly understand the actual meaning of these steps. Also of tremendous importance is correct spectra processing, and again, this is currently mostly done by the students themselves.

The book begins with a short basic introduction to solution NMR for the novice and explains the meaning of chemical shift and scalar couplings whilst also demonstrating how a small organic compound is readily identified from simple 1D spectra. The basics of NMR are then covered in the next part of the book with the second chapter reexamining the basic topics in more detail while also describing practical aspects of sample preparation, referencing etc. The third chapter provides an in-depth account of proton NMR spectroscopy, containing much of the empirical knowledge required for proton spectra interpretation. Following on from this we provide a similar account for ^{13}C and other X nuclei.

The second part of the book then presents the theory of NMR at a more advanced level, from single spins to macroscopic magnetization. It also describes the origin of the chemical shift and scalar couplings, and introduces the product operator formalism which is currently the most common technique to describe NMR experiments. This part finishes with a brief introduction to the quantum-mechanical description of NMR, and whilst this may prove too advanced for the novice reader, we considered it important for those readers that would like to consult the primary literature on NMR. The chapter introduces the meaning of many technical terms used in the field and may help in bridging the gap to the more advanced NMR books. Should students feel that they can successfully read the classical NMR liter-

ature after having read our book then we would certainly be very happy. Particularly in this last chapter we have excluded a lot of material for which the interested reader is referred to the more advanced NMR books or the original literature.

The third part of the book is devoted to the technical aspects of NMR, providing an overview of the instrument, spectra processing methods, and going into detail on spectra acquisition. Important experiments are described as well as features of pulses, gradients etc. For readers looking for more detail on the NMR experiments we have also added a chapter on the architecture of pulse programs.

The fourth part is devoted to special topics in NMR. It introduces important topics such as relaxation, the nuclear Overhauser effect, exchange phenomena, two-dimensional NMR, solid-state NMR, and the detection of intermolecular interactions by NMR (often referred to as screening in industry).

A good understanding of basic theory and the available set of experiments is certainly required, however the prime goal of NMR is still to correctly elucidate the chemical structure of a compound and this requires solid knowledge of empirical rules and an overview of the available NMR methods and experiments. Often the set of experiments that are most helpful for a particular task depend on the class of compound, and will be different, for example, for a peptide compared to an alkaloid. In this regard we present in the fifth part of the book a few important classes of natural products (carbohydrates, steroids, peptides, and nucleic acids). Each chapter begins with a brief summary of important chemical and structural features of the molecules concerned, provides summaries of typical chemical shifts, and suggests suitable strategies to most efficiently assign compounds from that class. Finally, an interpretation of a representative example from the class in question is provided on the basis of 1D and 2D spectra. PDF files of all spectra for enlargement are available under www.chem.uzh.ch/static/nmrbook. We will also publish corrections under this link.

This book was written with the invaluable help of many friends, who provided advice on the content of chapters and helpful criticism on how the material is presented. Any remaining errors are entirely our fault. We are particularly thankful to Stefan Berger, Sebastian Benz, Marcel Blommers, Fred Damberger, Marc-Olivier Ebert, Matthias Ernst, Thomas Fox, Gerd Gemmecker, Roland Hany, Erhard Haupt, Jan Helbing, Bernhard Jaun, Henning Jacob Jessen, Silke Johannsen, Ishan Calis, Wiktor Kozminski, Andrea Mazzanti, Frank Löhr, Detlef Moskau, Kerstin Möhle, David Neuhaus, Bernhard Pfeiffer, Daniel Rentsch, Alfred Ross, Markus Vöhler, Reto Walser, and Gerhard Wider. Nadja Bross helped with the preparation of the figures, measuring spectra, and critical reading of the chapters. Finally, we would like to thank our families for their patience.

Zurich, August 2013 *Simon Jurt and Oliver Zerbe*

1
Introduction to NMR Spectroscopy

Tremendous progress has been made in NMR spectroscopy with the introduction of multidimensional NMR spectroscopy and pulse Fourier transform NMR spectroscopy. For a deeper understanding of the experiment, a little knowledge of quantum physics is required. We will summarize the physical foundations of NMR spectroscopy in more detail in the following chapter. In this chapter, we will introduce the novice reader to the field of NMR spectroscopy in a simple way like we ourselves were introduced to it a long time ago. We will show some simple 1D spectra, and briefly describe what kind of information we can extract from these. For the moment we will assume that the spectra have been recorded by "someone," and we will skip the technical aspects. Later in the book we will discuss all aspects of NMR spectroscopy – experimental, technical, and theoretical – to make you an NMR expert, who can run your own spectra and interpret them skillfully. You should then also have obtained the necessary knowledge for troubleshooting problems during data acquisition. Throughout the book we will introduce you to a subject first in a simple way, and then extend the discussion to more specialized topics and provide a more rigorous explanation.

1.1
Our First 1D Spectrum

Let us jump right into cold water and have a first glimpse at the spectrum of a simple organic compound. As an example we will choose an aromatic compound that is a natural product but produced synthetically on a large scale, called vanillin. So, let us have a first look at the proton spectrum (Figure 1.1).

We notice a number of signals at various places. The signals seem to be of different intensity. If we look a bit more closely, we recognize that lines are split into multiplets (see the expansion). Below the spectrum we find a scale which roughly runs from 0 to 10 ppm. The signals indicated by an arrow belong to the solvent (the signal at 2.5 ppm is from residual dimethyl sulfoxide and the signal at 0 ppm is from the tetramethylsilane standard used for referencing). Otherwise we can count six signals, corresponding to six different types of protons in vanillin. The

Applied NMR Spectroscopy for Chemists and Life Scientists, First Edition. Oliver Zerbe and Simon Jurt.
©2014 WILEY-VCH Verlag GmbH & Co. KGaA. Published 2014 by WILEY-VCH Verlag GmbH & Co. KGaA.

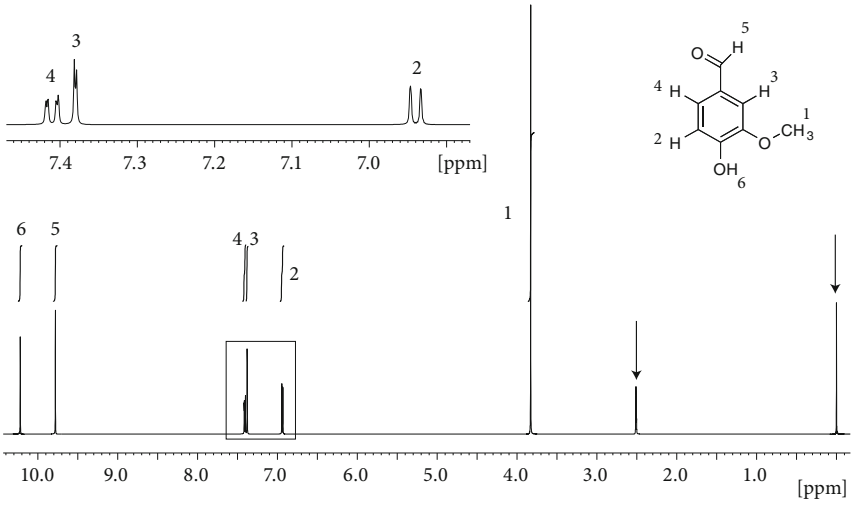

Figure 1.1 Proton NMR spectrum of a simple organic compound. The two arrows point to the standard for referencing (the tetramethylsilane signals) and the solvent line (the dimethyl sulfoxide signal). Integral traces are depicted above the signals. The expansion shows the aromatic protons.

region from 6.9 to 7.5 ppm is expanded in the top panel. To start, let us learn a bit of nomenclature first

1.2
Some Nomenclature: Chemical Shifts, Line Widths, and Scalar Couplings

The phenomenon that the resonance frequency of a nucleus depends on the chemical environment is called *chemical shift*.[1)] The chemical shift is largely determined by the electron density around the nucleus. For practical reasons the chemical shift is given in parts per million relative to a standard. Chemical shifts, in general, are an invaluable source of information for the interpretation of spectra. In principle, they can be computed fairly precisely nowadays using quantum mechanical methods such as density functional theory. What makes chemical shifts really useful is that they are influenced by the presence of functional groups, double bonds, aromatic ring systems, and so on. This has led to elaborate tables of chemical shifts empirically derived from databases. You will find many of these tables in our chapters on proton and heteronuclear NMR, or in textbooks dedicated to that purpose. As a chemist, however, you will need to "memorize" some basic values. If you are

1) The chemical shift was discovered in 1950 by W.G. Proctor and F.C. Yu when they measured the magnetic moment of different types of nuclei. To their surprise they observed two distinct ^{14}N lines for a solution of NH_4NO_3. The same observation was made almost simultaneously by W.C. Dickinson in the case of ^{19}F nuclei.

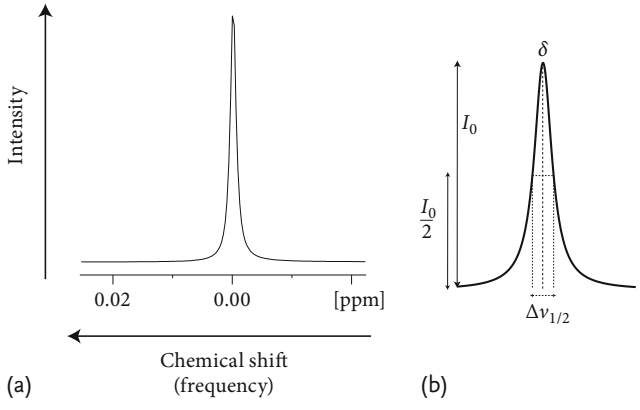

Figure 1.2 (a) A single resonance line. The frequency scale runs from the right to the left. A line with typical Lorentzian shape is depicted in (b).

working on a certain class of compounds, you will become an expert on chemical shifts for these molecules.

Let us now look more closely at a single line (Figure 1.2).

The line has a certain shape, a *Lorentzian* lineform. The signal is symmetric, and the highest intensity denotes the chemical shift position δ. The *line width* of the signal usually refers to the width at half height. Increasing values of chemical shift or frequency are plotted to the left for traditional reasons (note this is different from how it is usually done in physics or mathematics). Although the signals occur at certain frequencies, the frequency scale itself is not drawn, because it depends on the strength of the magnet. Instead, the values are presented in parts per million, which is the difference in frequency from a standard normalized by the frequency of the standard (do not worry, we will see how this scale is derived in more detail later).

Often signals are split into a number of lines (Figure 1.3), sometimes as many as nine or even more. These splittings are called *scalar couplings*, and originate from an interaction of the corresponding proton with neighboring protons, either on the same carbon or on the adjacent carbon(s) or heteroatom.

The center of the multiplet corresponds to the chemical shift δ of that signal. The separation of adjacent lines is called the *scalar coupling constant*, often abbreviated as J. Depending on whether the neighboring carbons are separated by rotatable bonds or whether the bond is sterically fixed, the number of lines due to scalar coupling is $N + 1$ (free rotation about the C–C bond) or 2^N (defined dihedral angle), where N denotes the number of neighboring protons. J is independent of the magnetic field strength and is specified in hertz. The individual lines often have different intensities (see Figure 1.3). Shown on the right of Figure 1.3 is a singlet, a doublet, a triplet, and a quartet. In the case of the quartet, the line intensities are 1 : 3 : 3 : 1. Since the number of lines follows simple rules, it helps us to establish the environment of the proton.

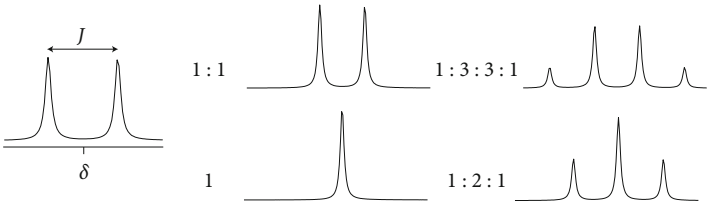

Figure 1.3 Scalar *J* couplings. Typical multiplet patterns for doublets, triplets and quartets are shown.

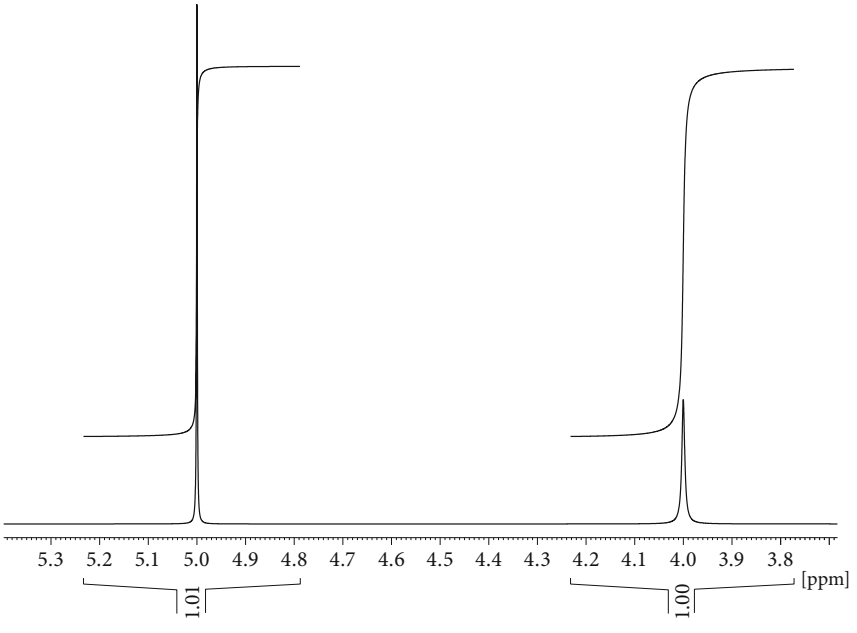

Figure 1.4 The effect of variable line widths. Two lines of very different intensity but the same integral are shown.

The intensity of the signals can be determined by integrating the spectra, and the *integrals* will tell us whether a certain signal is due to one, two, three, or more protons (Figure 1.4).

Integrals can be drawn as integral trails (usually directly on top of the signal) or their value can be plotted below the signal. Figure 1.4 displays two signals of identical integral but very different line width, with the signal at the lower frequency (the one on the right) being less intense. The line width has diagnostic value that is often underappreciated. Some lines become broader than others because the lifetime of the proton in a certain environment is short, a phenomenon due to either chemical or conformational exchange.

Spectra often also contain lines that do not belong to the molecule under study; some of them are referred to as *artifacts*. Such signals can belong to the solvent. In

Fourier transform NMR spectroscopy deuterated solvents are mandatory, but the degree of deuteration is never 100% and residual signal from the nondeuterated form is present. Another signal that is almost always present in proton spectra is the signal due to water, either from residual water in the solvent or because the compound has not been dried completely. Thirdly, a standard is often added for calibrating spectra. In most organic solvents tetramethylsilane is used because the signal usually occurs at one end of the spectrum and does not overlap with the signals of interest. Two-dimensional spectra contain other artifacts that are due to incomplete removal of unwanted coherence pathways, and we will deal with them later.

1.3
Interpretation of Spectra: A Simple Example

To get used to interpreting spectra, and to illustrate the strength of NMR spectroscopy, let us try to elucidate the structure of a small organic molecule. Its ^{1}H spectrum is shown in Figure 1.5.

The spectrum displays a number of signals, and the particular location of the signals, the chemical shift, already tells us a lot about the chemical nature of this molecule. For example, the signals at 7 ppm appear in a range that is typical for aromatic protons. Or, the signal around 3.6 ppm is most likely from a proton in the vicinity of some heteroatom. The signals around 1 ppm are most likely from methyl protons, which is also supported by the integral values of 3 and 6, respectively. Even

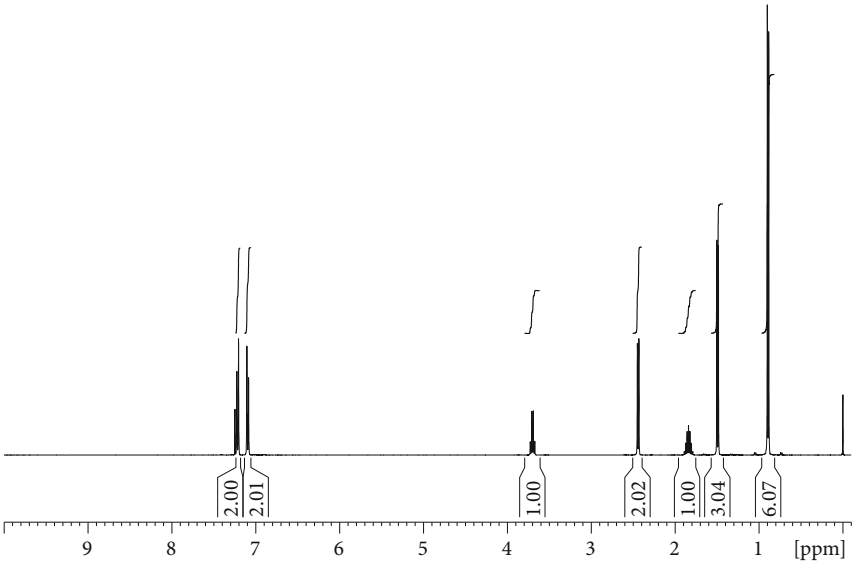

Figure 1.5 Proton NMR spectrum of ibuprofen.

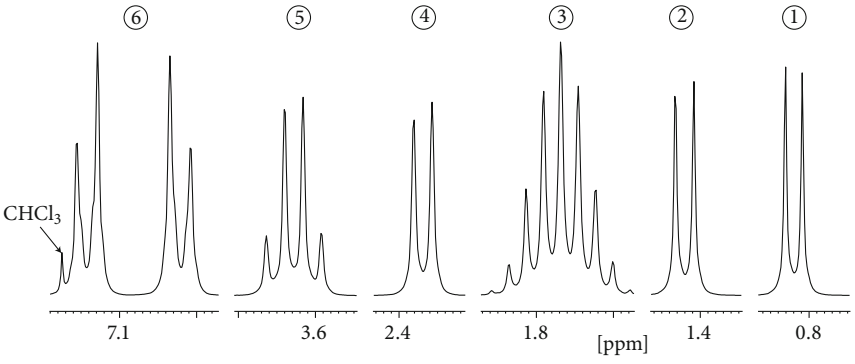

Figure 1.6 Expansions of the proton NMR spectrum revealing the multiplet fine structure of the signals.

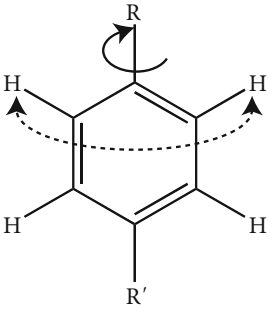

Figure 1.7 Our first fragment. Due to the symmetry of a para distributed benzene only two signals are observed for the four protons.

more helpful is the fine structure of the signals. To see that, let us zoom in a bit on the spectrum (Figure 1.6).

Most of the signals display the usual $(N + 1)$ multiplet pattern expected for protons in freely rotatable chains. The signal group labeled with *6* in Figure 1.6 consists of two doublets, which however, for reasons which will be explained in Section 3.4.2, are somewhat skewed. So let us begin building up the molecule.

We start with the signal group *6* in the range from 7–7.2 ppm. As mentioned before, this is the range typically observed for aromatic protons. The integral of these signals corresponds to 4. Although we do not know much about the chemical nature of the aromatic ring, we assume that it does not contain a heteroatom for the moment, and therefore is most likely derived from benzene. Four aromatic protons (instead of six) therefore indicates that the compound is a *disubstituted* benzene. The next question is whether the π system is 1,2-, 1,3-, or 1,4-disubstituted. In our case it is easy to determine this. We see only two peaks (two doublets). Since we have four aromatic protons, this is only possible if the substitution is such that two protons each become identical because of symmetry (see Figure 1.7). The aromatic ring therefore must be para disubstituted.

We will now try to identify the structure of the two substituents. Let us start with signal *1* at 0.8 ppm. It corresponds to six protons, likely two methyl groups. The

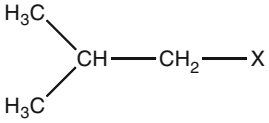

Figure 1.8 Our second fragment, an isobutyl group.

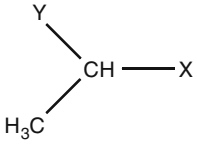

Figure 1.9 Our third fragment.

signal is due to either two distinct methyl groups at quaternary carbons (hence two singlets) or two identical methyl groups bound to a common carbon possessing *one* additional proton (hence two doublets with identical chemical shift). The latter case corresponds to an isopropyl group, for which we expect at least a septet ($6 + 1$ lines) for the CH proton. We say "at least" because the isopropyl group is connected to the remainder of the molecule, and other couplings may be due to the protons from the connecting carbon. In addition, the signal must integrate for *one* proton.

Indeed, if we look very carefully, we see that signal *3* at 1.8 ppm is split into nine lines (the outer lines are fairly weak and can easily escape our attention). This greatly supports the presence of an isopropyl group. Nine lines corresponds to eight protons on neighboring carbons. Since we have identified six already, the isopropyl group must be connected to a methylene (CH_2) group. The methylene signal must display an integral equal to 2, and the only signal that is left with such an integral is the one at 2.4 ppm (*4*). Since this signal is a doublet, and one of the connected carbons is a CH (from the isopropyl group), there cannot be any other CH carbons attached. Maybe this isobutyl fragment (Figure 1.8) is directly linked to the aromatic ring, a guess that must be verified later.

So far we have "explained" the presence of signals *1*, *3*, *4*, and *6*, and there remain two more signals *(2* and *5*). Obviously signal *2*, which integrates for three protons, corresponds to a methyl group. Again, the doublet nature tells us that the methyl group is connected to a CH carbon. That proton signal must have at least four lines and an integral of 1, establishing the quartet *5* at 3.6 ppm as the neighbor. Since the signal has a multiplicity of four, no other CH is connected to that carbon.

If we again assume that this is the other fragment (Figure 1.9) linked to the aromatic ring, we are however missing one substituent, because one carbon has so far only three neighbors. The chemical shift of the proton at that carbon is 3.6 ppm, fairly low and indicating that a heteroatom is close. The full spectrum in addition displays a very broad signal around 10 ppm (we do not see it in Figure 1.5 because it is too broad), possibly from a hydroxyl proton. However, it could also be from a carboxyl group, and we will not be able to distinguish the two possibilities on the basis of the proton NMR spectrum. To resolve this ambiguity, let us have a look at the ^{13}C spectrum (Figure 1.10).

The signal at 180 ppm is due to a carboxyl group. The four signals in the range 125–142 ppm are due to the aromatic ring (two carbons each correspond to one sig-

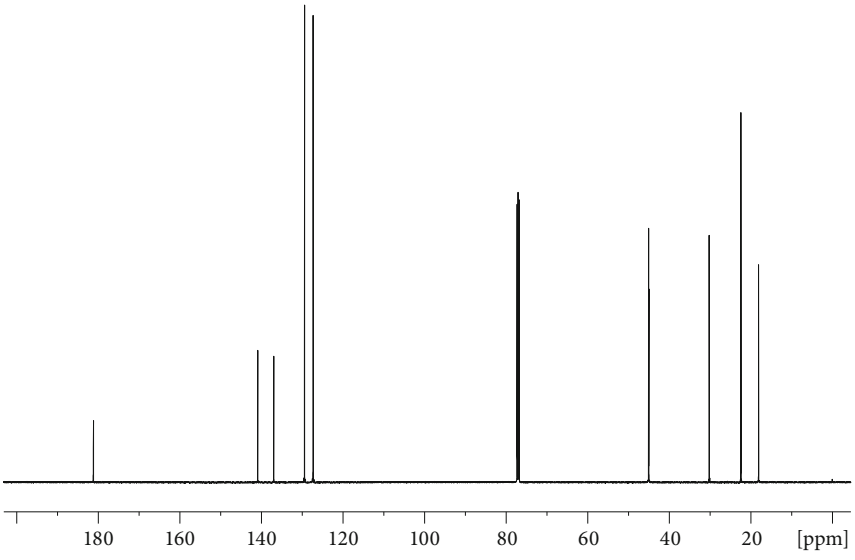

Figure 1.10 The ^{13}C NMR spectrum of ibuprofen.

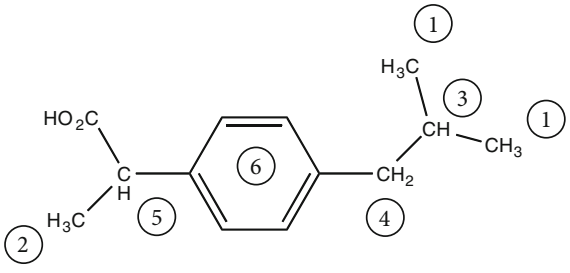

Figure 1.11 The molecular structure of ibuprofen and assignments of the proton signals.

nal due to the symmetry of the para-disubstituted ring). The signal around 77 ppm is from the chloroform solvent, and the four lines are from the other five carbons (the two isopropyl methyl carbons give rise to one signal). The missing fragment is therefore a carboxyl group and the structure of the compound is therefore unambiguously established as 2-[4-(2-methylpropyl)phenyl]propanoic acid (Figure 1.11), also known as ibuprofen, a painkiller that is produced on a multiton scale worldwide.

Of course, this is a very simple case, without any signal overlap. Moreover, the information on couplings and integrals always made the assignments unambiguous, and this is mostly not the case. However, we will see later that with the help of modern methods, in particular 2D NMR spectroscopy, fairly complicated molecules can still be identified unambiguously. However, we need to learn a few things before then so that we can exploit the power of NMR methods fully.

1.4
Two-Dimensional NMR Spectroscopy: An Introduction

The success of modern Fourier transform NMR spectroscopy is intimately linked to the development of multidimensional NMR spectroscopy. Protein structure determination by solution NMR spectroscopy or the elucidation of the structure of complex natural products is impossible without resorting to such methods. In the example of ibuprofen described above, the assignment was only possible in a straightforward fashion using 1D spectra, because at each point only a single resonance could be connected that had the right number of couplings and the correct integral. As soon as the molecules become larger, many ambiguous cases will arise, so further connectivities become unclear. The power of 2D shift-correlation spectroscopy is that the correct correlations can be directly extracted from the spectrum.

Two-dimensional spectra contain two frequency dimensions, and usually these correspond to chemical shifts. In the case of homonuclear spectra (the two frequency axes belong to the same type of nucleus, e.g., two proton frequencies), a diagonal runs through the 2D map, where the frequencies are the same in both dimensions. The really interesting information, however, resides in the off-diagonal, the so-called *cross peaks*. These peaks correspond to different chemical shifts and directly connect coupled nuclei. The exact type of experiment will determine which type of couplings (scalar or dipolar) have been used to establish the correlation. The

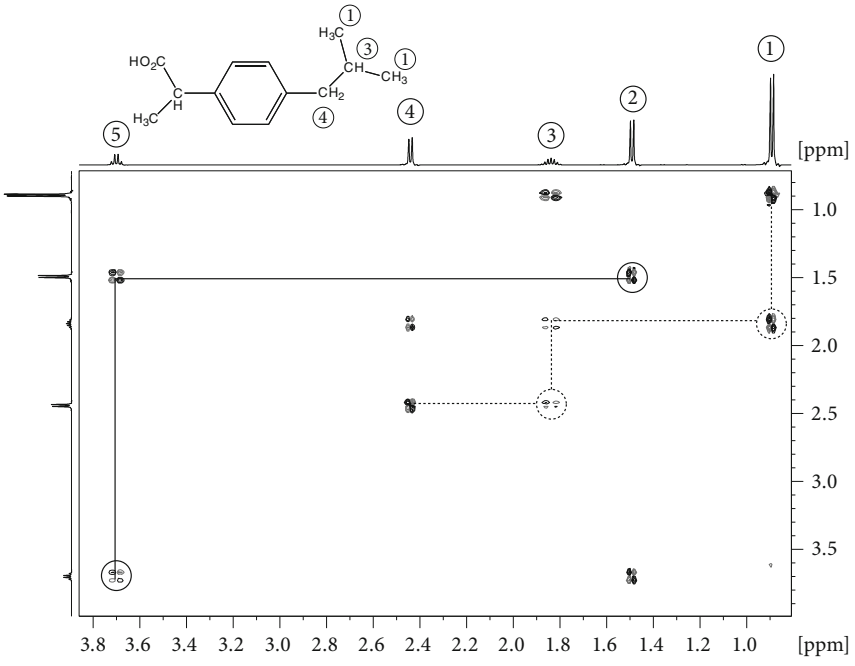

Figure 1.12 Two-dimensional correlation spectroscopy (COSY) spectrum of ibuprofen.

2D spectra are 3D objects, with two frequency dimensions, and the third dimension corresponding to the intensity of the signals. Usually, 2D spectra are displayed in the form of *contour plots*, quite similar to topographic maps, in which different heights (mountains) are indicated by contour lines that connect places of similar height. One of the simplest 2D experiment is the *COSY* experiment, a shift–shift correlation experiment in which correlations occur through scalar (usually vicinal) couplings. In the COSY spectrum in Figure 1.12 we have traced through correlations of the substituents in ibuprofen; the cross peaks are encircled, and the path for the isopropyl fragment is shown by dotted lines.

Part One
Basics of Solution NMR

2
Basics of 1D NMR Spectroscopy

2.1
The Principles of NMR Spectroscopy

It is one of the postulates of quantum physics that certain particles such as electrons or protons posses a property called spin giving rise to two different energy levels when brought into a magnetic field. This postulate, which formally emerged from mathematical equations, was called *nuclear spin* (I). The nuclear spin gives rise to a small *magnetic dipole moment*. The relationship between intrinsic magnetic moment and nuclear spin is given by the *gyromagnetic ratio* γ, a characteristic constant for each type of nucleus. Spins occur in multiples of 1/2 ($I = 1/2, 1, 3/2, \ldots$). However, the most frequently observed nuclei in NMR spectroscopy all have spin 1/2. The relevant properties of some selected nuclei are given in Table 2.1. Importantly, ^{12}C has zero spin and thus we can only observe the much less abundant ^{13}C isotope.

Classical physics predicts that a dipole moment orients itself in a magnetic field such that the energy becomes smallest, but apart from that, it can assume any ori-

Table 2.1 NMR-relevant properties of the most important nuclei.

Isotope[a)]	Spin quantum number I	Natural abundance (%)	γ (10^7 rad s^{-1} T^{-1})	Receptivity (relative to ^{13}C) at Nat. Abund.	NMR frequency (^{1}H = 100 MHz) (MHz)
$^{1}_{1}$H	1/2	99.99	26.7522	5870	100
$^{2}_{1}$H	1	0.01	4.1066	0.006	15.35
$^{13}_{6}$C	1/2	1.1	6.7283	1	25.15
$^{15}_{7}$N	1/2	0.36	−2.7126	0.02	10.14
$^{19}_{9}$F	1/2	100	25.1623	4890	94.09
$^{31}_{15}$P	1/2	100	10.8394	391	40.48

a) For more complete tables, see Chapter 4.

Applied NMR Spectroscopy for Chemists and Life Scientists, First Edition. Oliver Zerbe and Simon Jurt.
©2014 WILEY-VCH Verlag GmbH & Co. KGaA. Published 2014 by WILEY-VCH Verlag GmbH & Co. KGaA.

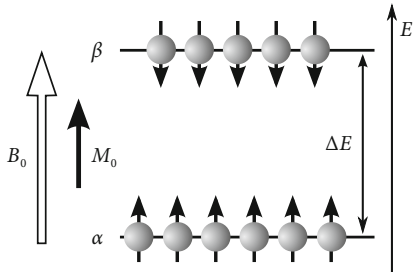

Figure 2.1 Spin alignment in the external magnetic field. The z component of a spin-1/2 particle can be aligned with or against the external magnetic field B_0. A parallel alignment of the microscopic dipole moments is energetically favorable, resulting in an slight excess of parallel aligned dipole moments and hence gives rise to a net magnetic moment M along the z axis.

entation. In contrast, in quantum physics, only two basic or principal orientations are possible for nuclear spins with spin $I = 1/2$: the magnetic moment can align with or against the direction of the magnetic field. Or more precisely, the z component of the magnetic moment can align with or against the direction of the magnetic field (assuming the magnetic field is along z). This gives rise to two separate energy levels, with the smaller energy for a parallel alignment, and we measure the transition between these (Figure 2.1). The associated spin states with a positive or negative orientation for the z component of the spin, the so-called eigenstates[1)], are called the α state and the β state.

The α and β states are filled according to the *Boltzmann distribution*

$$\frac{N(\beta)}{N(\alpha)} = \exp\left(\frac{-\Delta E}{kT}\right) \tag{2.1}$$

resulting in a slight excess of α states (the lower energy state for nuclei with $\gamma > 0$), giving rise to a macroscopic magnetic moment, the so-called net magnetization. Since the external magnetic field by definition points in the $+z$ direction, magnetization in thermal equilibrium is aligned with the z axis.

When the magnetic moment from the spin does not coalign with the magnetic field (the spin is not in an eigenstate[1)]), it starts to rotate about the axis of the

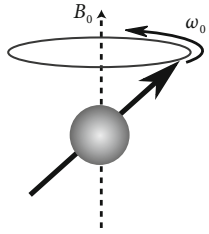

Figure 2.2 Spin precession. The magnetic moment of an individual spin precesses about the axis of the external field B_0 with a frequency ω_0 called the Larmor frequency.

1) The technical terms used in the quantum-mechanical treatment of spins, and their meaning will be explained in detail in Chapter 9.

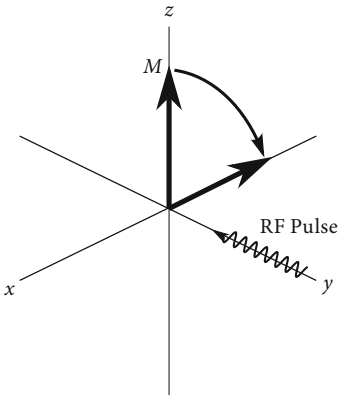

Figure 2.3 Radio frequency (RF) pulses. By applying an RF field, we can rotate the magnetization into the *xy* plane.

magnetic field, like a spinning top (Figure 2.2). This motion is called *precession*, its frequency, the precession or *Larmor frequency* ω_0 (rad/s), is the property that we measure in NMR spectroscopy:

$$\omega_0 = -\gamma B_0 \tag{2.2}$$

A closer look at the properties of a spin ensemble reveals that we cannot detect a signal without perturbing the system through the transient application of a radio frequency (RF) field, a so-called RF pulse. When, for example, a 90° pulse is applied to proton spins at thermal equilibrium, the magnetization is rotated into the *xy* plane as depicted in Figure 2.3.

Precession of the magnetization in the *xy* plane induces an oscillating signal in a detection coil, the so-called *free induction decay* (FID). Thereby, the frequency of the signal is directly proportional to the spin precession frequency.

In Figure 2.4c we see an analogy from electrical engineering. Therein, a current is induced in a coil when the latter is rotated in a magnetic field, the working principle of a power generator. In the case of the NMR experiment, the coil is not rotated

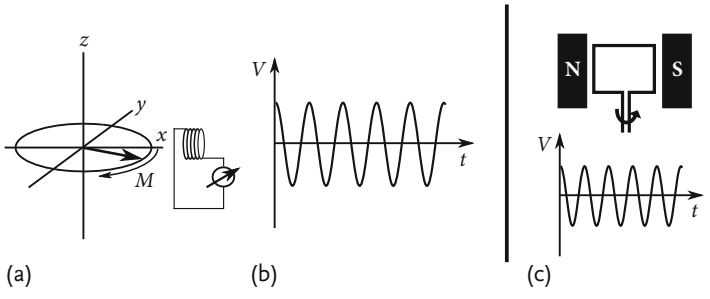

Figure 2.4 Induction of a signal voltage in the receiver coil. The rotating macroscopic magnetization results in a fluctuating field in the receiver coil (a), giving rise to an alternating voltage (b). This is similar to a coil rotated in a static field (c), the principle of a generator.

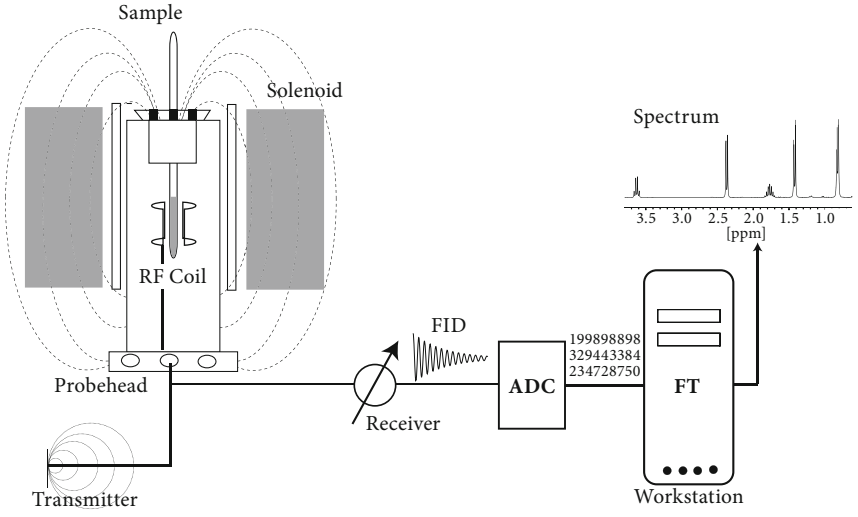

Figure 2.5 Schematic setup of the NMR experiment. ADC – analog-to-digital converter, FID – free induction decay, FT – Fourier transformation.

but rather the magnetic field, expressed in terms of magnetization, rotates relative to the coil, but otherwise the result is the same: an alternating voltage is induced whose frequency is proportional to the rotation frequency of either the magnetization (Figure 2.4a) or the coil (Figure 2.4c). The signal recorded is then converted to a spectrum through a mathematical operation called Fourier transformation.

So, what does the experimental setup look like? The setup is depicted in Figure 2.5 (note that the components are not drawn to the correct scale). In solution NMR spectroscopy the substance (powder or liquid) is dissolved in a solvent. A small glass tube is filled with solution, and transferred into a fairly strong magnet. Inside the magnet the sample is placed within RF coils which are used both for pulsing as well as for receiving the signal. The current from the coil is then fed into the receiver, and is converted into numbers by the analog-to-digital converter to give what we call the FID. The FID, composed of intensity/time pairs, is then subsequently converted into intensity/frequency pairs using the Fourier transform by a computer, ultimately resulting in the spectrum. The spectrometer also contains an RF transmitting system (the transmitter), which is required to produce the RF pulses, and all those components are, of course, also controlled by the computer.

2.2 The Chemical Shift

The chemical shift is related to the electron density around the nucleus, and is of much analytical value. The fact that signals are observed in a certain chemical shift range is often a good indication that a certain functional group is present, and

the information gathered often allows one to directly recognize that the molecule belongs to a certain class of compounds.

In general, the more functionalized molecules are, the better the *signal dispersion* (the spectral range covered by the signals) is. This is particularly true for those molecules that have many electron-withdrawing groups or aromatic moieties. The typical range of signals in proton spectra is 10 ppm, although often hydrogen-bonded hydroxyl and NH protons are observed at very high values (e.g., 14 ppm). In contrast, much overlap is observed in pure hydrocarbon compounds. In such cases, ^{13}C NMR spectra are particularly valuable. Carbon chemical shifts are also easier to predict, and signal overlap in ^{13}C NMR spectra is rare. The typical chemical shift range is from 0 to 220 ppm.

The chemical shift is related to the resonance frequency of a particular nucleus. Since the frequency itself is proportional to the strength of the magnetic field, the chemical shift is usually given relative to a standard, and normalized with respect to the frequency of that standard. As a result, chemical shifts from various instruments or laboratories can be compared, and are characteristic for a certain nucleus in a specific compound in a particular solvent. The chemical shift of a nucleus x is defined as

$$\delta(x) = \frac{\omega_x - \omega_{\text{ref}}}{\omega_{\text{ref}}} \times 10^6 \tag{2.3}$$

in which ω_{ref} is the frequency of the standard (e.g., tetramethylsilane, TMS). Since the normalized values are very small they are multiplied by 10^6 and presented in parts per million. Chemical shifts of protons mainly depend on the so-called *diamagnetic contribution* (see Chapter 7 for a more thorough discussion on this topic), which depends on the electron density around the nucleus. Other contributions are due to local anisotropies as well as steric effects. The electron cloud decreases the magnitude of the static field at the locus of the spin, the nucleus. This phenomenon is referred to as the *shielding effect*, and the decreased effective magnetic field at the site of the nucleus is responsible for a decrease in resonance frequency.

To indicate whether a certain effect shifts the resonance frequency to lower or higher ppm values, the terms *upfield* and *downfield* are often used. An upfield shift means that the resonance frequency is shifted to lower ppm values, whereas a downfield shift indicates that the resonance frequency is shifted to higher ppm values (Figure 2.6). The expressions "downfield" and "upfield" originate from the days of continuous wave NMR spectroscopy, where the frequency was kept constant while the magnetic field was swept, and they can be a bit confusing to newcomers. Nevertheless, they are used very often, also in this book.

2.3 Scalar Couplings

Spins feel the presence of neighboring spins, and therefore signals are often split into many components. While this may seem to be a nuisance, it is of enormous di-

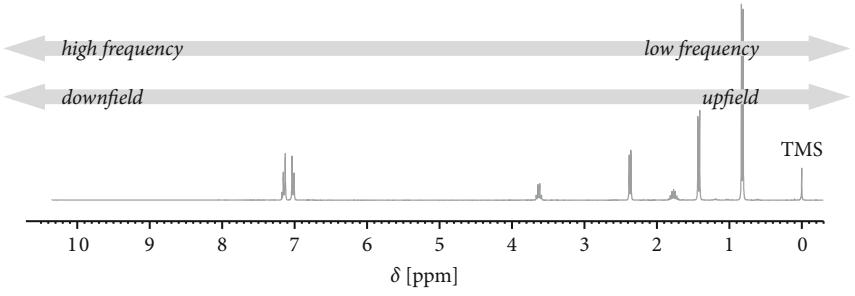

Figure 2.6 Chemical shift scale. The chemical shift is usually specified in parts per million. Similar to the shift scale, the absolute frequencies run from the right to the left. Signals appearing to the left in the spectrum are often denoted as downfield shifted, whereas signals appearing to the right are called upfield shifted.

agnostic value because it reports on the number of neighboring nuclei. As depicted in Figure 2.7, for a particular spin S it makes a difference if another spin I separated by a few bonds (usually fewer than four) is in the α state or the β state. Scalar couplings are transmitted via electrons, and therefore depend on the number of intervening bonds. The interaction with a sufficiently close spin-1/2 nucleus splits a line into two, resulting in a doublet. The separation of the two lines is called the *scalar coupling constant*, represented by the symbol J and specified in hertz. A superscript indicates the number of intervening bonds, and most of the observed proton couplings are of the ^3J type. ^3J couplings are called *vicinal* couplings and ^2J couplings are called *geminal* couplings. Couplings can only be observed between spins that are not magnetically equivalent (see Section 3.3), and hence geminal couplings are often not observed. Couplings between like spins (same isotope) are called *homonuclear couplings*, and those between different types of isotopes are called *heteronuclear couplings*.

Importantly, scalar couplings are independent of the strength of the external magnetic field. A 10 Hz coupling remains a 10 Hz coupling regardless of whether the spectrum is measured with a 300 MHz or a 900 MHz spectrometer. This fact can be used to distinguish whether a signal is split into two lines due to scalar coupling or whether the two lines represent signals with different chemical shifts. An additional important point to realize is that scalar couplings are mutual: the line splitting (in hertz) due to scalar coupling between nucleus A and nucleus B will be the same no matter whether the splitting is measured on nucleus A or nucleus B. Furthermore, coupling constants can be positive or negative. When a parallel orientation of the spin states gives a positive contribution to the total energy, the coupling constant is (by definition) positive. If the opposite applies, the coupling constant is negative. While interesting from a theoretical point of view, and important when simulating higher-order spectra, the absolute signs of coupling constants are usually of minor practical importance. The mechanism of scalar coupling will be treated in much more detail in Chapter 7.

As we will see later, the magnitude of the ^3J coupling depends on the dihedral angle, a relationship that became famous as the *Karplus relation*. Let us consider a

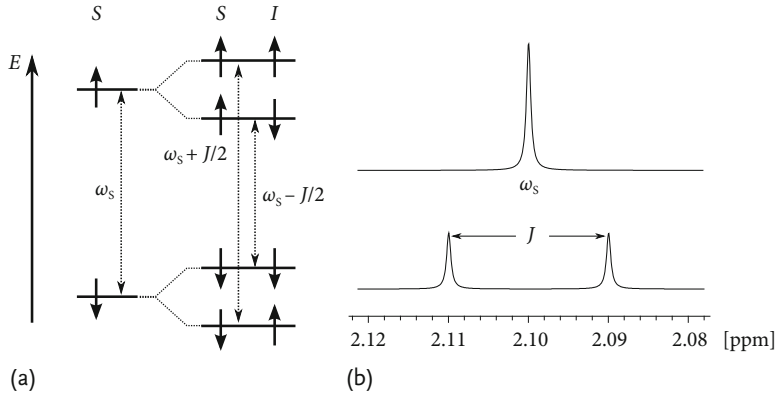

Figure 2.7 Line splitting due to scalar coupling. The energy levels of the *S* spin are, depending on the orientation of the *I* spin, split into two distinct levels (a). Observable single-quantum transitions of spin *S* are indicated by dashed arrows. Accordingly, the single line we would observe in the absence of any coupling is split into two components separated by the coupling constant *J* (b).

CH proton H_a with a neighboring methylene group. The two CH_2 protons H_b and H_c (see Figure 2.8) may split the line of H_a with coupling constants with the same magnitude (Figure 2.8b) or with coupling constants with very different magnitudes (Figure 2.8a). If the central C–C bond is not free to rotate, as is generally the case for cyclic compounds, the two ^3J couplings can be very different. In case of open-

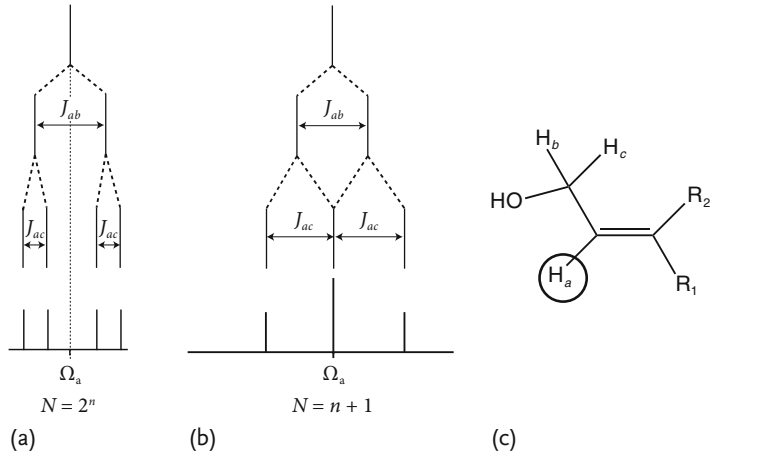

Figure 2.8 Line splitting due to scalar coupling. Coupling patterns are depicted for a proton *a* which couples to two other protons *b* and *c* (c). When the coupling between protons *a* and *b* is different from the coupling between protons *a* and *c* ($J_{ab} \neq J_{ac}$), the resonance line of proton *a* is split into four lines (a). When J_{ab} and J_{ac} are the same, two lines will overlap and the line is split into a triplet (b). Depending on whether the couplings to *n* neighboring nuclei are different or the same, the number of observed lines *N* is $N = 2^n$ or $N = n + 1$, respectively.

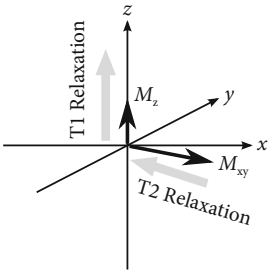

Figure 2.9 Relaxation. T1 relaxation brings longitudinal magnetization back to equilibrium z magnetization. T2 relaxation results in a decay of transverse magnetization.

chain molecules, there will be rapid rotation about the central C–C bond, and as a result of this rotation, the ^3J couplings are often averaged to a single value, usually about 7 Hz. In the latter case, the central line is due to overlap of two lines, and hence we will observe a triplet with 1 : 2 : 1 intensity. For different couplings a doublet of doublets occurs. However, as we will see later, rotation alone is not a sufficient condition for the observation of a single coupling constant.

2.4 Relaxation and the Nuclear Overhauser Effect

In an NMR experiment, spins are excited by RF pulses. As a result, the population of α and β states is changed from thermal equilibrium, and also some state of *phase coherence* is achieved. *Relaxation* is a process that drives the spin ensemble back to thermal equilibrium. Mechanistically it originates from *local* fluctuating *magnetic fields*, and we will discuss that in much more detail in Chapter 14. For the moment we simply state that in contrast to optical spectroscopy, in NMR spectroscopy relaxation is comparably slow (on the order of seconds), mostly leaving ample time to manipulate spins and measure their frequencies precisely.

There are two different relaxation processes that are mechanistically linked to some extent (Figure 2.9). *Longitudinal* or *T1 relaxation* reestablishes the Boltzmann distribution of α and β states. It acts solely on the longitudinal component of magnetization, and brings z magnetization in itself back to thermal equilibrium, that is, to point in the $+z$ direction (according to the excess of α states in thermal equilibrium). *Transverse* or *T2 relaxation* describes the decay of transverse magnetization (or speaking in more general terms the loss of phase coherence), and thereby reduces the signal that is induced in the receiver coil directly. The analogy to a pendulum is depicted in Figure 2.10.

Excursus 2.1: Relaxation – an analogy to the damped oscillator

The fate of a signal that originates from a single resonance can be compared to the amplitude of a pendulum that has been displaced at time $t = 0$, and then swings back and forth (see Figure 2.10). The oscillation of the pendulum

occurs at a certain frequency, and the frequency does not change over time. However, damping due to friction results in a reduction of the amplitude of the oscillation Δx, and eventually the signal has completely decayed. The process follows an exponential curve, and the time constant of the exponential is called the *relaxation time*.

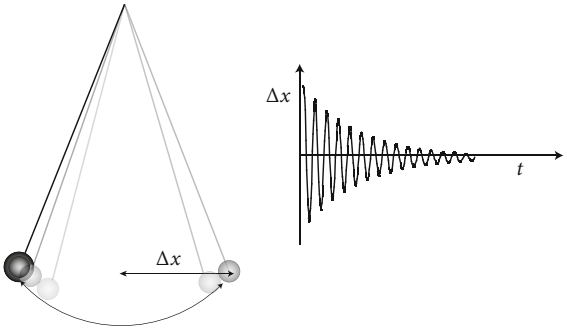

Figure 2.10 A mechanical analogy of spin relaxation. A pendulum swings back and forth. Monitoring the elongation Δx over time records a damped cosine.

But how do we experience the two relaxation mechanisms in our life as a spectroscopist? NMR spectra are usually obtained by repeating the experiment many times. Thereby the signal is coherently added and the signal-to-noise ratio is accordingly increased. However, between successive scans we need to wait for a specific amount of time to allow z magnetization to recover; this, brought into the xy plane during the succeeding scan, again gives rise to detectable magnetization. If we do not wait long enough, the magnetization becomes progressively saturated. Therefore, the so-called *relaxation or interscan delay* is inserted prior to the NMR experiment, which needs to be adjusted to the T1 values of the spins under study.

Transverse relaxation determines how fast our signal actually decays and thereby influences the line width. Molecules with short T2 display broad lines. T2 relaxation typically increases with slower rotational diffusion of the molecules. Therefore, T2 relaxation times typically become shorter with larger molecular size, lower temperature, and higher viscosity. To give an example, T2 values for some proton resonances in large proteins can be as short as 10 ms. Sampling the signal for 1 s does not make much sense if the signal has already decayed after 10 ms, and therefore we need to adjust the acquisition time to T2. Moreover, T2 relaxation times also largely influence what type of manipulations we can perform with the spin system because we cannot manipulate magnetization that has already decayed completely. To summarize, T2 relaxation determines the acquisition time and hence the possible resolution in spectra as well as the type of pulse experiments that we can perform on the system and T1 relaxation determines how long we have to wait before the next scan. In Figure 2.11 we demonstrate how T1 and T2 effects become visible in carbon or proton spectra.

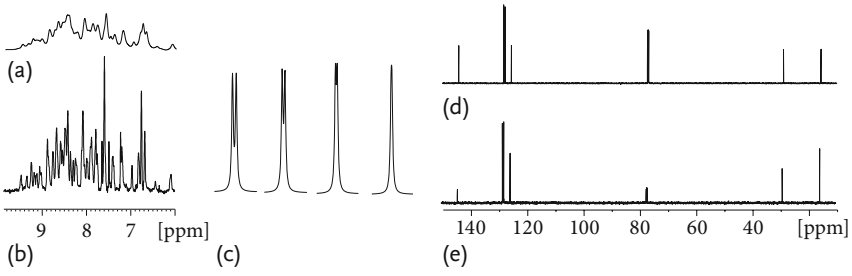

Figure 2.11 Relaxation effects in spectra. (a,b) proton spectra of a protein at two different temperatures, high (b) and low (a). (c) highlights how increasing line widths affect resolution for a 2 Hz coupling, and whether we can recognize such small scalar couplings. (d,e) demonstrate the effect of vastly different T1 times in ^{13}C NMR spectra. Slowly relaxing nuclei, for example, the one at 145 ppm, display less intense peaks because the relaxation delay was not sufficiently long. The spectrum in (d) was recorded with a so-called inverse-gated sequence and very long relaxation delay.

In Figure 2.11a,b an expansion of the proton spectra of a protein measured at two different temperatures is shown. The concomitant increase in line widths to an extent that individual signals cannot be recognized in Figure 2.11a is obvious. This is a pure T2 effect that originates from slower molecule tumbling at lower temperature. Broader lines also have an impact on how well scalar couplings can be recognized on signals. This is depicted in Figure 2.11c, where signals are shown that have a coupling of 2 Hz, but different line widths. Obviously the larger the line width, the more difficult it is to recognize the coupling – up to the point where it appears to be a singlet. The carbon spectrum Figure 2.11d,e demonstrates the effect of rapid pulsing. The signal at 145 ppm has far too low intensity in the spectrum shown in the lower trace. This corresponds to a quaternary carbon that has a long T1 relaxation time, relaxing more slowly, and hence recovery of z magnetization is much reduced when pulsing is too fast. This is a pure T1 effect. The spectrum in Figure 2.11d was recorded with a much longer relaxation delay. The two large signals at approximately 130 ppm each correspond to two equivalent carbons. T1 effects are more prominent in ^{13}C NMR spectra than in ^{1}H spectra because the T1 relaxation times vary greatly for carbon nuclei (between 1 s and more than 1 min!), largely depending on the distance to the closest proton. In contrast, proton T1 times are more uniform.

T1 relaxation is also responsible for a phenomena known as the *nuclear Overhauser effect* (NOE), which we will describe in more detail in Chapter 15. In short, longitudinal relaxation causes disturbances to the α/β populations of other nuclei in close proximity (usually less than 5 Å). Depending on whether the NOE is positive or negative, this results in an increase or decrease of the respective magnetization. The effect is due to dipolar interactions and rapidly decreases for larger distances.

The homonuclear ^{1}H–^{1}H NOE is often used to establish stereochemistry in molecules, or to determine the structure of biomolecules such as proteins, nucleic acids, or oligosaccharides in solution, and will be the subject of many succeeding

chapters. Heteronuclear ^{1}H–X NOEs, on the other hand, are often used for signal enhancement in X-detected (e.g., ^{13}C) experiments (Chapter 4 and Section 12.4).

2.5 Practical Aspects

2.5.1 Sample Preparation

Samples for NMR experiments should have a suitable concentration. For proton NMR spectroscopy, usually a few milligrams of an organic compound is sufficient. Using too highly concentrated samples is not recommended since this can degrade the quality of ^{1}H spectra. For ^{13}C spectroscopy, the concentrations must be higher, tens of milligrams if available. Very high concentrations are required for certain experiments, such as the INADEQUATE.

The choice of solvent is largely determined by the solubility of the compound. Some solvents display a weak lock signal (see Section 10.5), such as chloroform. D_2O has a strong temperature dependence of the lock signal. NOE spectroscopy (NOESY) spectra recorded in these two solvents are therefore more likely to display artifacts from instabilities. The residual solvent line should also not directly overlap with signals of interest. Some solvents contain impurities that may act as a catalyst in sample degradation. Chloroform often contains a trace of acid that can decompose acid-labile samples. Another, often neglected, aspect is the very different prices of solvents. Chloroform is the cheapest of the deuterated solvents, while deuterated tetrahydrofuran, for example, is very expensive. We refrain from presenting prices here because they change so quickly, but it is advisable to compare them from time to time. Another important aspect when choosing the solvent is the melting point or boiling point, particularly when variable-temperature NMR experiments are planned. Many of us have run into the problem that deuterated dimethyl sulfoxide (DMSO) solidifies at 18.5 °C. For some solvents the boiling point is so low that the solvent will evaporate during long measuring times, resulting in serious shim problems (decrease the homogeneity of the magnetic field). Some solvents can be used over large temperature ranges, and these are described in Chapter 16. Finally, some solvents can be easily removed (e.g., chloroform), while removal of others (e.g., DMSO) is difficult. Basic properties of solvents are summarized in Table 2.2.

Most probeheads nowadays are made for 5 mm tubes. When samples are spun (Figure 2.12), the quality of the tubes becomes an issue, and expensive tubes are required. We feel that with the present shim systems, spinning is usually not required for good line shapes, and should not be used for 2D NMR experiments in general. As a consequence, we usually buy the cheapest tubes, even for expensive samples. In 5 mm tubes the volumes should be between 500 and 600 µl, depending on the vendor and type of probehead. It is good practice to always use, for example, 500 µl for the samples, because shimming can then be done quickly starting from

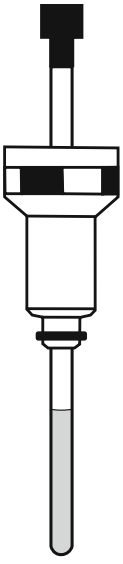

Figure 2.12 Sample tube in a spinner.

previously determined settings. If you are using less than 450 µl, the shim can often not be adjusted properly any longer. If your samples are mass limited, but not solubility limited, special glass tubes in which the volume is mostly restricted to the active volume of the NMR coil can be used. A well-known example of these are the so-called Shigemi tubes. In these 200–230 µl instead of 500 µl can be used. Alternatively, you can use 3 mm tubes. We have used them in 5 mm probes, with special spinners for 3 mm. Tubes with smaller diameter not only contain less solvent and hence require less of the substance but it is also possible to perform measurements at high salt concentrations in these tubes. However, use of 3 mm tubes in 5 mm probes is not optimal because the filling factor is poor and hence the sensitivity lower. If you often perform experiments on very low sample quantities, it may be a good idea to buy a 3 mm or even a 1 mm probe.

Samples should be clear solutions. Any insoluble particles must be removed by filtration or centrifugation. We have often seen particles from the chromatography columns in NMR samples. If insoluble material is contained in the sample, the spectra may still be good, but often they are deteriorated. A particular problem is paramagnetic impurities because they will broaden the lines considerably! And finally, carefully clean the tubes, and make sure you do not use, for example, plasticware (e.g., plastic tips for the pipet) when adding certain solvents. Chloroform, for example, may extract softeners from plastics. There is nothing more annoying than spending much effort on purifying your compound and then introducing softeners into the sample in this way. Clean your glass tubes from the outside with a soft tissue to remove anything spilled over the tube or grease from your fingertips. On high-field instruments you can see grease from your fingertips in spectra of very dilute samples!

2.5.2 Referencing

Referencing of NMR spectra is a very important although often overlooked point. This is particularly important when data are deposited in databases, or when compounds are to be identified from chemical shifts using databases or programs for chemical shift predictions. Unfortunately it is very difficult for others to detect if spectra have not been calibrated correctly, and hence if the reported chemical shifts deviate from the true values.

In principle two different methods are used for referencing: *Direct referencing* refers to calibrating the spectra in respect to a *genuine* signal of known chemical shift, by adding a reference compound (Figure 2.13) to the sample or by using the residual solvent signal. We distinguish between primary and secondary reference substances. The primary reference substances by definition have a chemical shift of zero. The chemical shifts of the secondary reference substances have been determined relative to the primary standards in separate experiments and can be found in data sheets. Ideally the chemical shift of the standard should be affected by changes in temperature or pH only very little, should resonate in a spectral range that is largely devoid of other signals to avoid overlap, and finally, the standard should not interact with the solute or solvent. Direct referencing is by far the most commonly used method for small-molecule NMR spectroscopy. The classic primary standard for proton and carbon NMR spectroscopy is TMS. The TMS signal is located at the low-frequency end of the spectrum (on the right side), and its frequency is set to 0 ppm both in carbon NMR spectra and in proton NMR spectra.

TMS Tetramethylsilane

^{1}H: δ = 0 ppm
^{13}C: δ = 0 ppm

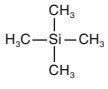

DSS 2,2-Dimethyl-2-silapentane-5-sulfonic acid sodium salt

^{1}H: δ = 0 ppm

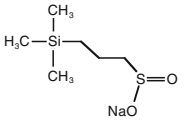

Cyclosilane

^{1}H: δ = 0.327 ppm

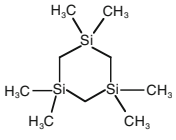

TSP 3-(Trimethylsilyl)-propionic acid sodium salt

^{1}H: δ = 0 ppm
^{13}C: δ = 1.7 ppm

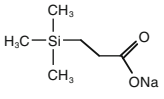

Dioxane

^{1}H: δ = 3.75 ppm
^{13}C: δ = 67.4 ppm

Figure 2.13 Frequently used reference compounds with their chemical shifts.

TMS is apolar and hence applicable with chloroform and most other organic solvents. In aqueous solution and sometimes also in methanol a trimethylsilyl derivative of a salt such as 3-(trimethylsilyl)propionic acid sodium salt or 2,2-dimethyl-2-silapentane-5-sulfonic acid sodium salt can be used. Instead of using internal standards as described above, it can be necessary to use external standards. For that purpose the standard substance is put into a small capillary (capillaries usually used for determining melting points are convenient). The sealed capillary can then be placed directly in the NMR tube. In this way the reference compound does not come into contact with the sample; however, this is a cruder way of referencing spectra. Quite often, the signal of the residual nondeuterated solvent is used for referencing, and this has the advantage that no other compound needs to be added (which may be hard to remove afterward). If you do this, it is very important that you report the chemical shift which you used for that signal. For example, for the residual chloroform signal you find a number of chemical shifts. In BioNMR spectroscopy, proton spectra are often referenced to the water line. The water signal is highly temperature dependent and its chemical shift can be calculated (at pH 5.5) according to

$$\delta(\mathrm{H_2O}) = 7.83 - \frac{T\,(\text{in K})}{96.9} \quad (\text{ppm}) \tag{2.4}$$

The precision in the chemical shift therefore additionally is related to how precise the measuring temperature is known. Please realize that the temperature on the spectrometer display can easily be wrong by a few degrees, and that you need to calibrate the temperature once using a dedicated sample for that purpose (see Section 2.5.4).

In *indirect referencing* the frequency of the zero chemical shift position is calculated using Ξ values. The values denote ratios of absolute frequencies at the 0 ppm position of X nuclei and the absolute frequency of the ^{1}H signal of TMS when measured with the same magnetic field strength and are given in percentages as

$$\Xi_\mathrm{X} \equiv \frac{\nu_\mathrm{X}}{\nu_\mathrm{H}} \cdot 100 \tag{2.5}$$

Accordingly, the frequencies of 0 ppm of X spectra can be calculated from the actually measured ^{1}H frequency of TMS. For example, let us assume that you have calibrated the proton chemical shift scale from the TMS signal, and thus obtained the frequency of 0 ppm. The frequency of 0 ppm of the ^{15}N chemical shift scale can then be computed according to

$$\nu_\mathrm{N} = \nu_\mathrm{H} \frac{\Xi_\mathrm{N}}{100} \tag{2.6}$$

Indirect referencing is convenient and recommended by IUPAC. In particular, you can also calculate approximate spectrometer frequencies for nuclei that you have not measured so far. We are convinced that the precision is sufficient for most applications. Correct referencing is very important! Do not forget to state in

publications what method and standard you used for the chemical shift scale, and at what pH and temperature the measurement was taken.

In Table 2.2 we list the proton and ^{13}C chemical shifts of the most commonly used solvents.

2.5.3 Sensitivity and Accumulation of Spectra

Compared with other spectroscopic methods such as IR and UV spectroscopy, NMR spectroscopy is rather insensitive. Therefore, the sample must be relatively concentrated to record spectra with an acceptable *signal-to-noise ratio* within a reasonable measuring time (some milligrams for ^{1}H NMR spectra of medium-sized molecules). The sensitivity largely depends on the gyromagnetic ratio and the natural abundance of the isotope (see Table 2.1). The equilibrium magnetization M_{eq} of spin-1/2 nuclei is proportional to $\gamma^2 B_0$. Brought into the xy plane by an RF pulse, this magnetization is capable of inducing a voltage in the receiver coil that is proportional to dM_x/dt and therefore proportional to the Larmor frequency $\omega_0 = -\gamma B_0$. Thus, the induced signal is proportional to $\gamma^3 B_0^2$. For nuclei with quantum number $I > 1/2$, there is an additional factor $\frac{4}{3} I(I+1)$ which must be taken into account. From a single-scan ^{1}H NMR spectrum we can expect approximately 6000 times more signal than from the corresponding ^{13}C NMR spectrum. Dramatic differences in sensitivity for different isotopes at their natural abundance make some nuclei very hard to detect, for example, ^{15}N and some metal nuclei with very low frequencies.

In addition to the signal of interest there will also be noise in the spectra, and the sources of noise are manifold. The main origin is usually the small fluctuating voltage induced by thermal (Brownian) motion of the electrons in electronic components prior to the analog-to-digital converter such as the RF coil, RF cables, and amplifier, the so-called thermal noise. The extent to which a signal can be distinguished from noise critically depends on the signal-to-noise ratio S/N, where S stands for the signal height and N for the average noise level. Considering the fact that the noise of the tuned circuit increases as the square root of the observed frequency ($\sqrt{\gamma B_0}$), the signal-to-noise ratio is described approximately by

$$\frac{S}{N} \propto \gamma^{5/2} B_0^{3/2} \tag{2.7}$$

The signal-to-noise ratio can be improved by adding up a number of n FIDs. While the signal S of a resonance in every FID will be the same and therefore coherently add up, the noise fluctuates around zero and will only increase by a factor $\sqrt{n}$. The signal-to-noise ratio of m added spectra compared with that of k added spectra is given by

$$\left[\frac{S}{N}\right]_m = \sqrt{n}\left[\frac{S}{N}\right]_k \tag{2.8}$$

Table 2.2 Properties of solvents most commonly used for NMR measurements. Adapted from Budavari S. *et al.* (1989) *The Merck Index, an Encyclopedia of Chemicals, Drugs, and Biologicals*, 11th edn, Merck Co, Inc., Rahway.

Solvent	$\delta(^1H)$ (ppm) (multiplicity)	$\delta(^{13}C)$ (ppm) (multiplicity)	$\delta(H_2O)$ (HOD) (ppm)	Melting point (°C)	Boiling point (°C)
Acetic acid	11.65	178.99 (1)	11.5	16.7	118
	2.04	20.0 (7)			
Acetone	2.05	206.68 (1)	2.8	−94	56.5
		29.92 (7)			
Acetonitrile	1.94	118.69 (1)	2.1	−45	81.6
		1.39 (7)			
Benzene	7.16	128.39 (3)	0.4	5.5	80.1
Chloroform	7.24	77.23 (3)	1.5	−63.5	61–62
D_2O	4.8 at 25 °C	–	4.8 at 25 °C	3.81	101.42
Dimethylformamide	8.03 (1)	163.15 (3)	3.5	−61	153
	2.92 (5)	34.89 (7)			
	2.75 (5)	29.76 (7)			
Dimethyl sulfoxide	2.50 (5)	39.51 (7)	3.3	18.45	189
Ethanol	5.19 (1)	56.96 (5)	5.3	−114.1	78.5
	3.56 (1)	17.31 (7)			
	1.11 (m)				
Methanol	4.78 (1)	49.15 (7)	4.9	−97.8	64.7
	3.31 (5)				
Methylene chloride	5.32 (3)	54.00 (5)	1.5	−95	39.75
Pyridine	8.74 (1)	150.35 (3)	5.0	−42	115–116
	7.58 (1)	135.91 (3)			
	7.22 (1)	123.87 (3)			
Tetrahydrofuran	3.58 (1)	67.57 (5)	2.4–2.5	−108.5	66
	1.73 (1)	25.37 (5)			
Toluene	7.09 (m)	137.86 (1)	0.4	−95	110.6
	7.00 (1)	129.24 (3)			
	6.98 (5)	128.33 (3)			
	2.09 (5)	125.49 (3)			
		20.4 (7)			
Trifluoroacetic acid	11.50 (1)	164.2 (4)	11.5	−15.4	72.4
		116.6 (4)			
Trifluoroethanol	3.88 (4 × 3)	126.3 (4)	5.0	−43.3	75
		61.5 (4 × 5)			

with $n = m/k$. As a consequence, doubling the number of scans will increase the signal-to-noise ratio by a factor of 1.41 (and not by a factor of 2). To increase the signal-to-noise ratio by a factor of 2, the number of scans must be increased by a factor of 4. In other words, to get the same signal-to-noise level with a sample 10 times less concentrated, the number of scans must be 100 times greater. Thus, low sample concentrations and/or nuclei with inherent low sensitivity can easily result in prohibitively long measuring times.

Accumulation of spectra requires that we allow the z magnetization to recover between successive scans. Therefore a delay, the so-called interscan or relaxation delay, is inserted between successive scans. This delay should usually be about one to five times the T1 relaxation time constant. When the delay is too short, for example, when we pulse too fast, only little z magnetization will be accessible and therefore only little signal will add up with each successive scan. Moreover, the signal intensities will strongly depend on the particular T1 values.

In order to optimize signal strength, often only part of the z magnetization is tipped into the xy plane by using pulse angles less than 90° (e.g., 30°), the so-called *Ernst angle*, which maximizes the signals within a given experiment time. This employs the fact that the increase of xy magnetization follows a sine dependency, whereas the reduction of z magnetization follows a cosine dependency on the flip angle.

2.5.4 Temperature Calibration

Many chemical shifts are sensitive to the exact temperature. A particularly prominent example is the position of the hydroxyl protons of water, which experiences a drift of approximately 0.1 ppm over 10 °C. When chemical shifts are reported in the literature, it matters a lot that the specified measuring temperature is correct. In most NMR probeheads, the temperature is measured using a temperature sensor below the RF coils. The temperature on the spectrometer display unfortunately usually does not report the correct temperature, and the actual sample temperature can easily be off by 5 °C. Therefore, it is important to calibrate the temperature from time to time. An often used sample for this purpose contains 1% CH_3OH in Methanol-d_4. The hydroxyl proton shift experiences a large temperature dependence, while the methyl proton shift does not change significantly. The difference in chemical shift between the hydroxyl and methyl protons therefore changes with temperature, from which the exact temperature can be calculated according to

$$T = A\Delta\delta + B \quad \begin{array}{l} \text{for } \Delta\delta \text{ from 1.4965 to 1.76: } A = -114.83;\ B = 471.85 \\ \text{for } \Delta\delta \text{ from 1.76 to 2.08: } A = -125;\ B = 490 \\ \text{for } \Delta\delta \text{ from 2.08 to 2.43: } A = -140;\ B = 521.33 \end{array} \tag{2.9}$$

The methanol sample allows temperature calibration in the range from 180 to 300 K. For higher temperatures, a sample of 80% ethylene glycol in DMSO can be

used. For that sample the actual sample temperature is then calculated from the shift difference between the hydroxyl and methylene protons according to

$$T = -108.33\Delta\delta + 460.41 \tag{2.10}$$

Some experiments, for example, TOCSY and ^{13}C broadband decoupling experiments, deliver a lot of RF power to the probe and result in significant sample heating. In this case the temperature display does not indicate the correct sample temperature even if it has been calibrated!

2.6 Problems

2.1. Show the energy level diagram for a spin 1/2 nucleus with a negative gyromagnetic ratio when (a) no external magnetic field is present, (b) the external magnetic field is applied along z and (c) the external magnetic field is applied along x. Indicate the spin components and the magnetic dipole moments μ of the spins by arrows.

2.2. In which direction is thermal equilibrium magnetization aligned to for (a) nuclei with a positive gyromagnetic ratio and (b) nuclei with a negative gyromagnetic ratio when the external magnetic field points along the z axis?

2.3. Why does the nuclear magnetic moment not just align with the external magnetic field B_0 but instead precesses about the axis of the B_0-field? Is there a classical analogue to that phenomenon?

2.4. Which component of the magnetization is measured during acquisition of the FID?

2.5. How do we create transverse magnetization?

2.6. The exact resonance frequency of the same type of nuclei (e.g., ^1H) may vary within a molecule. Under which term is this phenomenon known and what is the reason for it?

2.7. Two resonance lines are separated by 0.03 ppm on a 300-MHz spectrometer and by 0.01 ppm on a 900-MHz spectrometer. Are these two lines due to two separate signals (two nuclei with different chemical shifts) or due to a single resonance signal split into a doublet due to scalar spin–spin coupling?

2.8. Denote the two processes that describe the return of magnetization to thermal equilibrium.

2.9. Suppose you have isolated two isomers of an organic molecule; 15 mg of isomer A and 5 mg of isomer B. How many more scans do you need to measure isomer B in order to obtain NMR spectra with a comparable signal-to-noise ratio?

Further Reading

Claridge, T. (2008) *High-Resolution NMR Techniques in Organic Chemistry*, 2nd edn, Tetrahedron Organic Chemistry.

Günther, H. (1995) *NMR Spectroscopy: Basic Principles, Concepts, and Applications in Chemistry*, 2nd edn, John Wiley & Sons, Ltd.

Fiebolin, H. (2011) *Basic One- and Two-Dimensional NMR Spectroscopy*, Wiley-VCH Verlag GmbH.

3
^{1}H NMR

From Chapter 1 we have already acquired some basic knowledge of proton and carbon spectra and have learned what kind of information we can extract from them. We have seen that chemical shifts, multiplet patterns, intensities, and line widths provide valuable information which allows us to assess whether our synthesis was successful or not, or to elucidate the structure of unknown compounds.

In this chapter we will examine the proton chemical shift and scalar couplings in more depth. In particular, we will introduce some useful empirical rules for chemical shifts and coupling constants that are a prerequisite for successful interpretation of spectra. At the same time we will see that the type of solvent, the measuring temperature, or the magnetic field strength may have a tremendous impact on the appearance of a spectrum. But first, let us have a look at some general aspects of ^{1}H NMR spectroscopy.

3.1
General Aspects

Proton NMR spectroscopy is very sensitive compared with NMR spectroscopy using other nuclei, such as ^{13}C and ^{15}N. A few milligrams of substance is usually enough to obtain good-quality routine spectra of small to medium-sized organic molecules. As mentioned before, using too concentrated samples is not recommended since this can heavily degrade the quality of spectra and can result in line broadening due to shimming problems, increased viscosity (increased T2 relaxation), or radiation damping effects (see Section 6.4.2.2).

The choice of the solvent is determined by facts that were largely discussed in Section 2.5.1. In the case of proton NMR spectroscopy, we need to consider exchange with solvent protons/deuterons as well. Whether exchangeable protons such as hydroxyl or amine protons can be observed in spectra largely depends on whether protic solvents such as methanol or water or aprotic solvents such as dimethyl sulfoxide (DMSO), acetone, and chloroform are used. OH and NH protons will usually be missing in protic solvents because of exchange by deuterium from the solvent. Also acidic impurities in $CDCl_3$ often cause acid-catalyzed proton exchange such that signals of labile protons will be missing or severely broadened

Applied NMR Spectroscopy for Chemists and Life Scientists, First Edition. Oliver Zerbe and Simon Jurt.
©2014 WILEY-VCH Verlag GmbH & Co. KGaA. Published 2014 by WILEY-VCH Verlag GmbH & Co. KGaA.

and may additionally trigger sample decomposition for acid-labile compounds. In contrast, polar *aprotic* solvents such as DMSO and acetone slow down exchange such that OH or NH signals and even their couplings can often be observed in these solvents.

3.2 Chemical Shifts

Proton chemical shifts are typically in the range between 0 and 10 ppm. Figure 3.1 gives an overview of the expected shifts of some important functional groups. The most important contribution to the chemical shift of protons is of diamagnetic nature. As will be described in more detail in Chapter 7, diamagnetic effects tend to decrease the effective magnetic field at the locus of a nucleus. In particular, the chemical shifts of protons are influenced by the electronegativity of neighboring substituents, magnetic anisotropy effects, steric effects, and solvent effects.

In general it is very complicated to compute exact chemical shifts of protons from first principles. It needs a lot of expertise to interpret chemical shifts, but you will find a plethora of shift charts on the Web or in dedicated books. Using empirical rules is usually sufficiently precise.

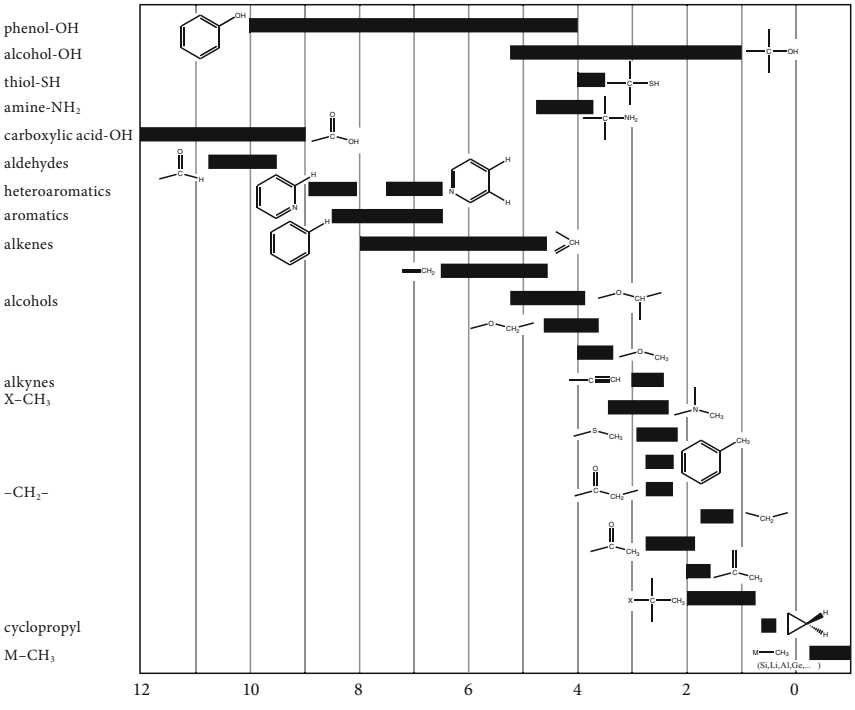

Figure 3.1 Typical chemical shift ranges (in ppm) for protons in some selected chemical groups.

Table 3.1 Effect of halogen substitution on the ^{1}H chemical shifts (ppm) of methane.

X	CH_3X	CH_2X_2	CHX_3
F	4.27	5.45	6.49
Cl	3.06	5.30	7.24
Br	2.69	4.94	6.83
I	2.15	3.90	4.91

3.2.1
Influence of Electronegativity of Substituents

Put into simple terms, the electron cloud surrounding a nucleus shields the nucleus from the external magnetic field, and thereby lowers the field compared with the field at a "naked" nucleus and thereby reduces the resonance frequency. Since the electron density at the site of a proton depends on the electronegativity of neighboring substituents, different resonance frequencies will be observed for various groups of protons within a molecule. In general, electronegative substituents tend to reduce electron density at the proton, and therefore deshield the proton, giving rise to higher chemical shifts.

When discussing chemical shifts, one must note that these are usually referenced against a standard; in proton NMR spectroscopy this is often tetramethylsilane (TMS). Silicon has a low electronegativity (even when compared with carbon) and therefore the protons in TMS are relatively strongly shielded from the external field. Because of that, most protons of organic compounds resonate at a higher frequency than those of TMS and therefore appear on the left side of the TMS signal (remember for historical reasons the frequency scale in NMR spectra runs from the right to the left).

The influence of electronegativity on the chemical shift is nicely illustrated by the series of halogenated methyl derivatives given in Table 3.1. The stronger the electron-pulling effect of the halogen substituent(s), the less shielded the protons are.

3.2.2
Anisotropy Effects

Anisotropy is a frequently encountered term in NMR spectroscopy, and refers to the spatially nonisotropic nature of a given quantity. In the context of anisotropy effects discussed herein, it means that some functional groups can give rise to a local magnetic moment which, depending on the spatial relationship between the proton and the functional group, can strongly shield or deshield the proton. Such effects are particularly pronounced in the vicinity of π electrons, and can provide spatial information.

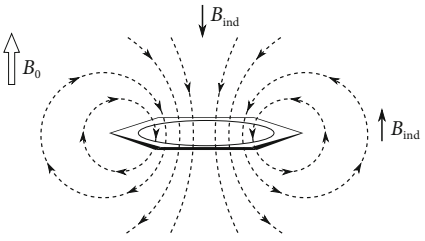

Figure 3.2 Ring current effect of benzene.

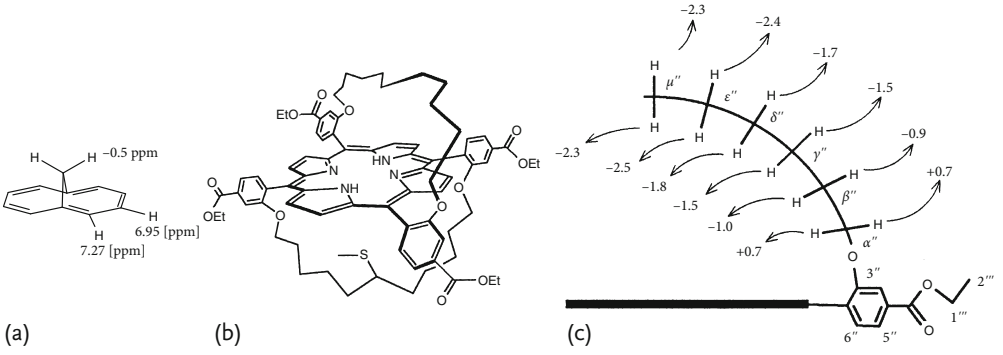

Figure 3.3 Anisotropy effects. The magnetic anisotropy of 1,6-methano[10]annulene (a) considerably reduces the chemical shift of the protons above the aromatic ring system. The porphyrin derivative depicted in (b) contains an aliphatic chain that runs across the porphyrin system. Depending on the location of the methylene protons their chemical shift is between −2.3 and +0.7 ppm (c). (Reproduced with permission from S. Matile, PhD thesis University of Zurich 1994).

The effect is easy to understand for a benzene ring: whenever the ring is perpendicular to the external magnetic field B_0, a ring current is induced. From school physics we know that a current circulating in a loop gives rise to a magnetic field. In the case of benzene, the electrons circulate in such a way that the field produced *counteracts* the B_0 field above or below the ring (hence it is a *diamagnetic* effect). As a result, the induced magnetic field B_{ind} reduces the strength of the magnetic field above and below the plane of the benzene ring, whereas it increases the magnetic field in the periphery of the ring. As a consequence, protons located above the ring exhibit an upfield shift, whereas protons located in the periphery exhibit a downfield shift (Figure 3.2). It is worth noting that in liquid-state NMR spectroscopy (due to fast molecular tumbling) such anisotropy effects will be averaged to a single value.

Two examples of shift effects due to magnetic anisotropy in aromatic systems are shown in Figure 3.3.

Other functional groups showing similar π-electron-induced effects are alkenes, alkynes, and carbonyls (see Figure 3.4). In particular, the upfield shift observed for protons in alkyne groups (2–3 ppm) can be explained by the magnetic anisotropy of triple bonds.

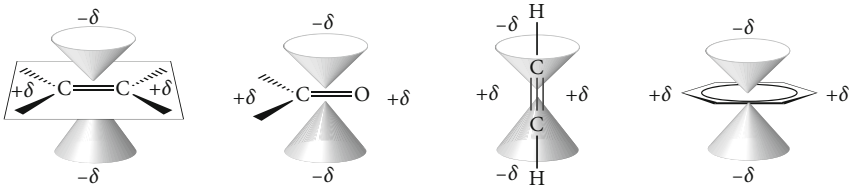

Figure 3.4 Anisotropy cones. The magnetic field is weakened above and below the cones and increased outside the cones. This results in a reduction or increase of the chemical shift as indicated by $-\delta$ and $+\delta$, respectively.

3.2.3
Other Factors Affecting Chemical Shifts: Solvent, Temperature, pH, and Hydrogen Bonding

Chemical shifts also depend to some extent on the solvent. Especially aromatic solvents such as benzene and toluene can alter chemical shifts by up to 0.8 ppm. Thus, when reporting chemical shifts, one should always specify the solvent. Changing the solvent can be useful in the case of signal overlap, and we will see how helpful this can be when measuring proton spectra of steroids in Section 21.1.2.

Chemical shifts may also depend on the sample concentration. If a compound is prone to self-association, the spectrum will undergo characteristic changes when concentrations are changed. If you suspect that your sample aggregates, then it is often a good idea to dilute it and remeasure the spectrum. If it changes, then self-association takes place. Of course, it is important to not change the solvent system (buffer?) during dilution.

Changing the pH will change the appearance of the spectrum. This effect can be rather dramatic if ionizable groups (e.g., carboxyl groups) are present, and if the pH change takes place near the pK_a.

The temperature has a major influence on the lifetime of solvent–solute complexes, and in particular on the stability of hydrogen bonds formed with the solvent. As we will see in Chapter 16, the temperature dependence of chemical shifts can be used to study conformational exchange by NMR spectroscopy. Temperature effects are usually more pronounced in proton spectra than in carbon spectra.

3.2.4
Shift Reagents

Proton spectra of certain compound classes display low signal dispersion, with those from steroids being one prominent example (see Chapter 21). The problem of resonance overlap was even severer in the past when no high-field instruments (on the basis of present standards) were available. One way to improve signal dispersion is the use of *shift reagents*. As discussed in more detail in Section 7.1.2, paramagnetic compounds influence the chemical shift via the *Fermi contact interaction* and via the *pseudocontact shift*. The former effect is limited to the immediate

vicinity of the paramagnetic center, and is therefore only intramolecular. The pseudocontact shift depends on r^{-3} and therefore can also be intermolecular. Certain paramagnetic metals shift resonances in a distance-dependent but also orientation-dependent manner. The trick is to find suitable metals for which the paramagnetic effect is not too large (to not result in complete bleaching of all signals within a certain sphere) or too small (little effects). Lanthanide ions are most suitable, and europium, ytterbium, or praseodymium ions are often used. Shift reagents, hence, are mostly metal chelators coordinating to lanthanides.

The influence of a shift reagent is depicted in Figure 3.5 for increasing amounts of the shift reagent Eu(fod)$_3$ added to cholestan-3β-ol. We observe a better dispersion of the proton spectrum at a higher concentration of the shift reagent. The change in resonance frequency is different for the signals – some shift a lot and others do not shift much. For example, the signal at 3.55 ppm shifts by about 1 ppm, whereas the signal at 5.35 ppm does not change its frequency. This is caused by the preferential coordination of the lanthanide ion to the 3-OH group. In general we observe an increase in line width with increasing concentration. When a shift reagent is added, a good compromise must be found between the required frequency shifts and the increase in line width. In Section 3.3.2 we will learn about chiral shift reagents that can be used to separate enantiotopic protons.

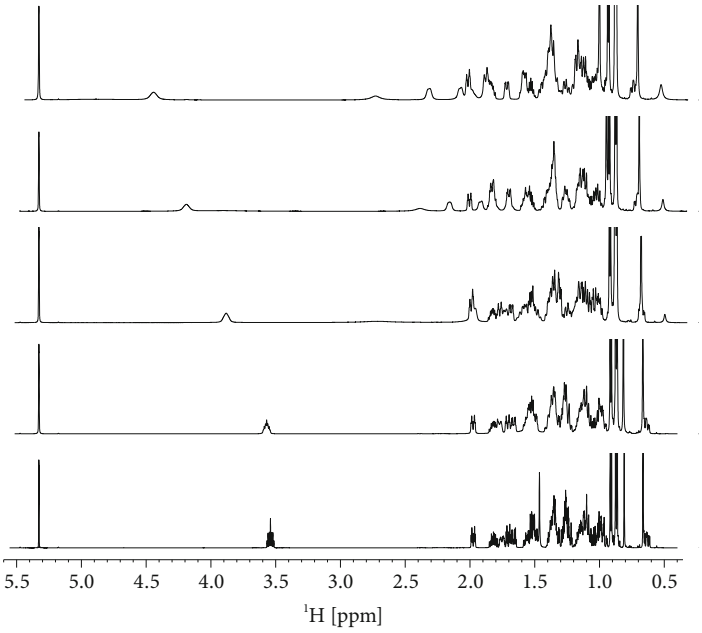

Figure 3.5 Effects from a shift reagent. The 600 MHz proton NMR spectra of cholestan-3β-ol in the absence (bottom trace) and presence of increasing amounts of the shift reagent Eu(fod)$_3$ (fod – 1,1,1,2,2,3,3,7,7,7-decafluoro-4,6-heptanedionato ligand).

3.3
Spin Systems, Symmetry, and Chemical or Magnetic Equivalence

We would like to introduce some fundamental nomenclature of spin systems at this point. A *spin system* is a uninterrupted chain of scalarly coupled nuclei. Protons belonging to the same spin system need not all mutually couple with each other, but it must be possible to draw a connecting path that includes only scalarly coupled nuclei. That in particular often excludes the presence of quaternary carbons or other non-proton-bearing atoms in the chain. Spin systems are usually designated using a letter code.

Nuclei with the same chemical shift are called *isochronous*. These are nuclei either that through symmetry elements such as rotation axes or mirror planes can be transformed into each other or that have the same chemical shift just by chance. Those related by symmetry are called *chemically equivalent*. Symmetry of molecules reduces the number of signals in NMR spectra and therefore often allows us to recognize substitution patterns simply from the number of signals in the spectra. An example is disubstituted aromatic molecules (Figure 3.6). If both substituents are different, only the para-disubstituted aromatic compound contains an element of symmetry. Accordingly, such compounds are easily recognized by the presence of two doublets in the aromatic region, each of them coding for two protons.

Importantly, scalar couplings between chemically equivalent or isochronous nuclei cannot be observed. Chemically equivalent nuclei are labeled with the same letter of the alphabet, whereas for chemically nonequivalent nuclei different letters of the alphabet are used. The separation of the letters in the alphabet reflects the difference in the chemical shift. A two-spin system in which the two protons resonate at 2.0 and 4.5 ppm is called an AX system, while a system in which the two protons resonate at 2.0 and 2.01 ppm is called an AB system. As we will see in a moment, AX and AB systems display differences in the appearance of multiplet patterns. The number of chemically equivalent nuclei is specified by subscripts, for example, A_3X for CH_3OH. *Magnetically equivalent* nuclei are chemically equivalent, but in addition have *identical* scalar coupling constants with *all* other spins. Spin systems with chemically equivalent but magnetically nonequivalent nuclei

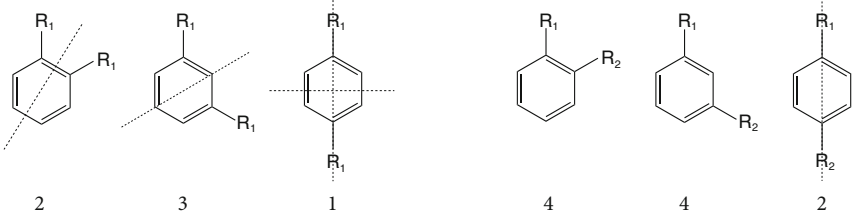

Figure 3.6 Symmetry and the number of signals. The number of signals in the proton spectra of disubstituted aromatic compound are shown below the structures for the case when both substitutents are identical (a) and when they are different (b). Symmetry axes are indicated by dashed lines.

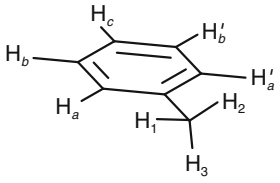

Figure 3.7 The spin system of toluene.

will always give rise to higher-order spectra (Section 3.4.2). The presence of chemically equivalent but magnetically nonequivalent nuclei is indicated by a dash. Let us have a closer look at chemical and magnetic equivalence by considering some examples.

To explain these concepts we will discuss them in the context of toluene (Figure 3.7). Obviously, this molecule has a symmetry axis. Therefore, both protons in the ortho position and both protons in the meta position have the same chemical environment, and thus are chemically equivalent. Hence, the five aromatic protons in total give rise to three resonance signals – one for the ortho protons, one for the meta protons, and one for the proton in the para position.

Are the protons also magnetically equivalent? To answer this question let us look at the two protons in the ortho position (H_a and $H_{a'}$). H_a has a ^3J coupling to proton H_b, whereas $H_{a'}$ has a ^5J coupling to H_b. Therefore, these protons are magnetically nonequivalent. The same applies for the meta protons. Thus, the five aromatic protons build an AA′BB′C system. Now let us look at the protons of the methyl group. If no rotation occurs about the C–C bond and the structure looks exactly like that depicted in Figure 3.7, only two of the three methyl protons would be equivalent (H_1 and H_2). However, because at ambient temperature the methyl group rotates rapidly, the chemical shifts of the three protons will average to a single value, and the methyl protons are therefore chemically equivalent. However, as we will see in the next example, rotation by itself is not a sufficient condition for chemical equivalence.

Figure 3.8 shows the Newman projections for the three rotamers of an ethyl derivative that has a stereogenic center at the distant carbon. For each of the three rotamers there is no symmetry operation which relates protons H_a and H_b; therefore, H_a and H_b in all three rotamers are chemically nonequivalent. Furthermore, also a rotation about the C–C axis does not result in two identical spatial relations for the two protons. Consequently, even in the case of rapid rotation about the C–C axis, protons H_a and H_b will be chemically nonequivalent, and thus will give rise to two separate signals in the spectrum. Such protons are called *diastereotopic*. The two protons will likely have very similar but not necessarily identical chemical shifts. If the proton at the stereogenic center at the back has a very different chemical shift, this is an ABX system. In the case of slow or no rotation, we would observe six signals for the two diastereotopic protons whose intensity represents the relative populations of the three rotamers. The terms “slow” and “fast” will become much clearer in Chapter 16 when we discuss effects of exchange.

Now let us see what happens if we replace group Y in Figure 3.8 by another group X. The corresponding rotamers are shown in Figure 3.9. In rotamer I the two pro-

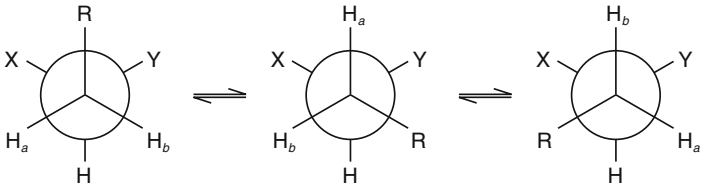

Figure 3.8 Different rotamers about a C*–CH_2–R moiety, in which C* denotes a chiral center.

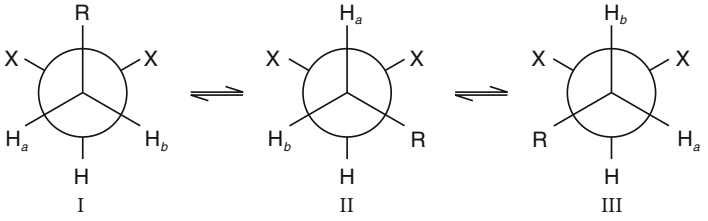

Figure 3.9 Different rotamers about a C*–CH_2–R moiety, in which C* denotes a nonchiral center.

tons are equivalent. In rotamers II and III the protons are nonequivalent. However, these two rotamers behave like enantiomers, and proton H_b in rotamer III will have the same shift as proton H_a in rotamer II. Thus, if the molecule rapidly rotates about the C–C axis, the chemical shifts of H_a and H_b will average to a single value, and the two protons are therefore chemically equivalent. A similar consideration reveals that also the coupling of H_a and H_b to the third proton H will be averaged. Thus, in this case the three protons form an A_2X system.

Other well-known examples of magnetic equivalence or nonequivalence are 1,1-difluoroethylene and 1,1-difluoroallene (Figure 3.10). Both molecules have a symmetry axis and therefore the protons as well as the fluorines in both molecules are chemically equivalent. However, in 1,1-difluoroethylene the H proton has a cis coupling to F, whereas H′ has a trans coupling to F. Therefore, the nuclei are magnetically nonequivalent. In contrast, in 1,1-difluoroallene both protons share the same orientation relative to a given fluorine substituent, and are therefore magnetically equivalent.

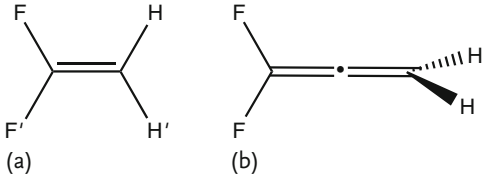

Figure 3.10 Magnetically nonequivalent protons of 1,1-difluoroethylene (a) and magnetic equivalent protons of 1,1-difluoroallene (b).

3.3.1
Homotopic, Enantiotopic, and Diastereotopic Protons

As we have seen above, sometimes a single signal for the two protons of a methylene group is observed and sometimes the chemical shifts of the two methylene protons are different. The same applies for the two methyl groups of isopropyl fragments. The reason is that the two X groups within a $–CX_2R–$ fragment may be homotopic, enantiotopic, or diastereotopic.

In order to test which of the three possibilities is correct for the group in question, each X is replaced by a new test group T as shown in Figure 3.11. If the two new forms are identical molecules, the groups are *homotopic*. Homotopic protons are chemically equivalent and will only result in a single signal. If the substitution creates a pair of enantiomers, the two groups are *enantiotopic*. Such groups will give a single signal in a nonchiral environment but may be resolved into two separate signals using chiral solvents or chiral shift reagents (see Section 3.3.2). When the two new forms are diastereomers, the groups are called *diastereotopic*. As we saw in the previous section, this is usually the case when a stereogenic center is present in the molecule. Diastereotopic groups are chemically nonequivalent and hence can give rise to two signals, but may by chance be isochronous. Whether one or two signals are observed is most often related to the distance from the stereogenic center.

Sometimes classification can be quite tricky. A classic example is acetaldehyde diethyl acetal: although the molecule has no stereogenic center, the methylene protons are diastereotopic. As shown in Figure 3.12 the substitution of one of the methylene protons by a test group T creates a chiral center at the acetal carbon. Consequently A and B are diastereomers.

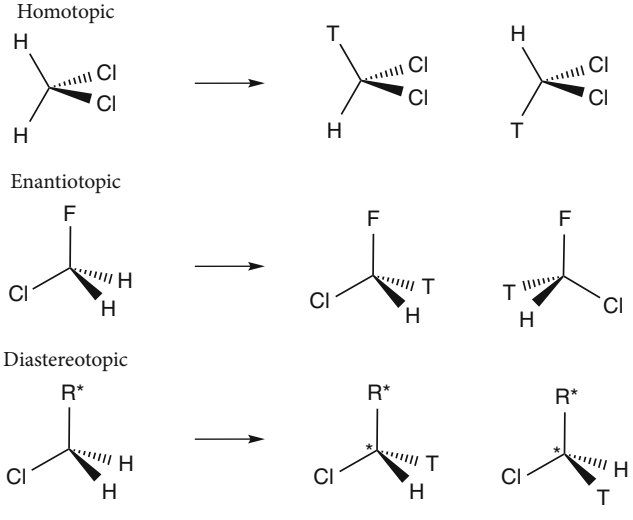

Figure 3.11 Examples of homotopic, enantiotopic, and diastereotopic methylene protons. R* has a stereogenic center.

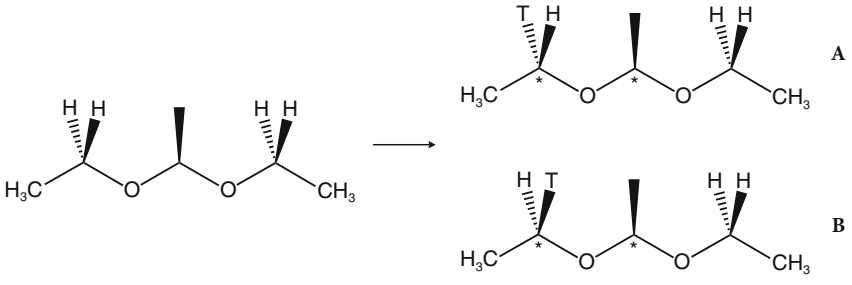

Figure 3.12 The two methylene protons of diethyl acetal are diastereotopic.

3.3.2 Determination of Enantiomeric Purity

The determination of enantiomeric purity is very important nowadays. Traditionally, this is achieved by measuring the angle of rotation for polarized light. However, for this method the corresponding value for the pure enantiomer must be known a priori. NMR spectroscopy allows one to determine the enantiomeric purity from first principles, but you need to be very careful when making such claims.

As described above, diastereotopic protons may give rise to two different signals. Similarly, diasteromeric molecules have a priori different NMR spectra. Enantiomers, on the other hand, have identical NMR spectra unless they are in a chiral environment. (In the case of the polarimeter, the chiral environment is the plane-polarized light.)

In principle, two different ways exists to provide such a chiral environment for NMR measurements: The most obvious but usually least practical method is to use a chiral solvent. The issue here is that although it may not be too complicated to make such a chiral solvent, it needs to be perdeuterated to be useful in NMR spectroscopy. The method more often applied is to form a diastereomeric compound by derivatization with a chiral compound, preferably with a single enantiomer of it. A famous example of a chemical derivative is *Mosher's reagent*, which in addition also allows one to determine the absolute configuration. Mosher's reagent (α-methoxy-α-trifluoromethylphenylacetic acid (MTPA) chloride; see Figure 3.13a) is a chiral acyl chloride derivative that can be coupled to hydroxyl groups of secondary alcohols. The interesting feature of the reagent is that it contains an aromatic ring as a substituent, which, via its ring-current effect, will shift resonances in spatial proximity *in a predictable fashion* depending on their position relative to the aromatic ring.

The alcohol is derivatized as both the (*R*)-MTPA and the (*S*)-MTPA ester. The chemical shifts of protons on the adjacent carbon are noted, and their difference is computed as $\Delta\delta^{RS} = \delta(R) - \delta(S)$. For all protons on one side of the stereogenic center $\Delta\delta^{RS} < 0$ and for all protons on the other side $\Delta\delta^{RS} > 0$. The protons on the sides adjacent to the stereogenic center can then be placed as shown in Figure 3.13c.

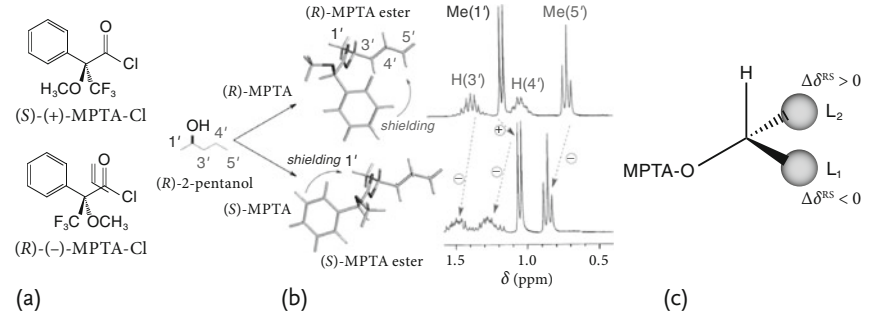

Figure 3.13 Mosher's reagent (α-methoxy-α-trifluoromethylphenylacetic acid (MTPA) chloride). The two forms of the MTPA reagents are depicted in (a). Spectra for the derivatization of (*R*)-2-pentanol are shown in (b). The placement of protons on the sides adjacent to the stereogenic center is shown in (c). Modified with permission from Seco *et al.* (2012) *Chem. Rev.*, **112**, 603–4641.

Another set of reagents are the so-called *chiral shift reagents*. They form noncovalent, often transient, diastereomeric complexes with the compound of interest. One representative of this class is what became known as *Pirkle's reagent* (1-anthracen-9-yl-2,2,2-trifluoroethanol). Pirkle's reagent is a chiral alcohol (see Figure 3.14), and other compounds belonging to this class are depicted in Figure 3.14. Other chiral shift reagents belong to the class of the so-called *lanthanide shift reagents* that are complexes of chiral ligands with lanthanide ions. We heard about shift reagents in Section 3.2.4. In contrast to simple shift reagents, the signals due to the *S* and *R* forms are shifted by *chiral* shift reagents differently and therefore they separate. Chiral ligands are mostly camphor derivatives (see Figure 3.14). Lanthanide shift reagents result in line broadening – adding too much will significantly deteriorate the spectra. Only a fraction of a small spatula tip is usually sufficient. Start by adding only small quantities, and if the effect is too small (signals not yet separated) add (a little!) more. While lanthanide shift reagents increase line widths, no such behavior occurs with Pirkle's reagent or the other aromatic compounds depicted in Figure 3.14.

3.4 Scalar Coupling

In Section 2.3 we briefly discussed that resonance lines are often split into multiplets due to scalar coupling. When the coupling occurs between like spins (same isotope), we call them *homonuclear couplings*, and when the coupling occurs between unlike spins (different isotopes), we call them *heteronuclear couplings*. With the high proton density of organic molecules it is clear that homonuclear couplings make a very important contribution to the spectrum. Therefore, in the following we will focus on the homonuclear ^{1}H–^{1}H couplings. Some aspects of heteronuclear ^{1}H couplings will then be discussed at the end of this section.

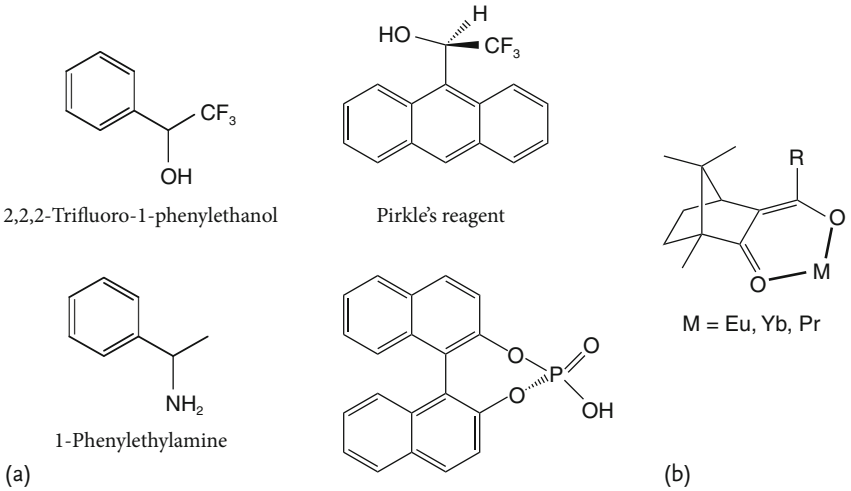

Figure 3.14 Chiral shift reagents. (a) The four compounds form diastereomeric complexes with the compound of interest via weak hydrophobic interactions. (b) The chiral lanthanide shift reagent, a camphor derivative, interacts with potential ligand groups in the molecule of interest via short-lived coordination.

3.4.1 First-Order Spectra

To understand the multiplet patterns we need to know some basic rules. First of all, couplings between spins that possess identical chemical shifts are not observable. This includes all those protons that either are chemically equivalent or possess identical chemical shifts just by chance and hence are isochronous (this is rare). A clear definition of equivalence was presented in Section 3.3.1. A typical example of equivalent protons is methyl protons. Because the three protons are equivalent, you will never observe a coupling amongst the three protons of a methyl group but you will always recognize it as a single line – a singlet. A second rule is that when a proton couples to a group of equivalent spins, they will share a single coupling constant J provided that the C–C bonds to neighboring carbons are *freely rotatable*. So, for example, the couplings between the methine proton and all methyl protons within a $CH–CH_3$ fragment will be the same and characterized by a single coupling constant ^3J. An empirical rule is that ^3J couplings between protons connected by freely rotatable bonds are usually very similar and about 7 Hz (in the absence of electronegative substituents).

So let us look at a proton that couples to n equivalent neighbor protons by a single coupling constant J. Each proton causes a line splitting of the resonance line. As shown in Figure 3.15, the first neighbor splits the resonance line into a doublet. Each of these doublet components is then split again into two lines by a second neighbor proton. Because the coupling constants are the same, the inner lines will overlap. Thus, we obtain a triplet with intensities in the ratio 1 : 2 : 1. Similar rules

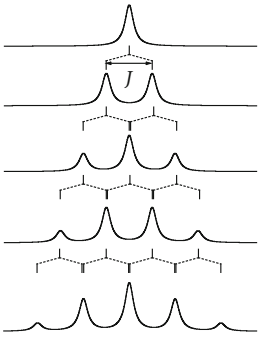

n		
0	Singlet (s)	1
1	Doublet (d)	1 1
2	Triplet (t)	1 2 1
3	Quartet (q)	1 3 3 1
4	Quintet	1 4 6 4 1
5	Sextet	1 5 10 10 5 1
6	Septet	1 6 15 20 15 6 1
7	Octet	1 7 21 35 35 21 7 1
8	Nonet	1 8 28 56 70 56 28 8 1

Figure 3.15 Multiplet patterns for a spin equally coupling to a number of n adjacent spins. On the left side the systematic construction of the multiplets is shown. The intensities of the individual lines can be deduced from Pascal's triangle depicted on the right.

apply to the construction of a quartet with intensities in the ratio 1 : 3 : 3 : 1. Coupling to further protons will split the signal into quintets (five lines), sextets (six lines), septets (seven lines), and so on. Thus, in general, for a proton coupling to n adjacent protons with the same magnitude, we observe a multiplet consisting of $n + 1$ lines. The intensities of the individual lines are given by the binomial coefficients which are readily obtained from *Pascal's triangle* (Figure 3.15).

An example for a sextet is the methylene protons at position 2 of a propyl fragment disregarding possible further couplings. An example for a nonet is the methine proton of a isobutyl fragment. The intensity ratio between the center and the outer components of a nonet is 70 : 1! Whether such weak lines are detected or not largely depends on the signal-to-noise ratio of the spectrum and whether you expand the spectrum vertically sufficiently when you look at the signal.

Often rotations about bonds are hindered or even completely absent (e.g., in cyclic systems). In such cases the coupling constants between adjacent protons often shows large variations due to the different dihedral angles (Section 3.5.2). Furthermore, geminal or small long-range coupling may be observed. Thus, we will likely encounter situations where multiplets can be described no longer using a single coupling constant but rather by a number of different coupling constants. This can result in quite complicated multiplet patterns. The construction of these multiplets can be done in an analogous fashion. Consider, for example, a proton with 14 Hz coupling to a single proton X and an additional 4 Hz coupling to a group of three equivalent protons M. In the multiplet construction we will start with the largest coupling. As shown in Figure 3.16a, proton X causes a 14 Hz line splitting to form a doublet. Each doublet line is then further split by the three equivalent M protons into a quartet with 4 Hz coupling. Thus, in total we obtain a doublet of quartets. Some further examples are depicted in Figure 3.16b. Obviously, it can be difficult to correctly identify the multiplicities. Fortunately, powerful software tools help a lot in analyzing multiplet patterns.

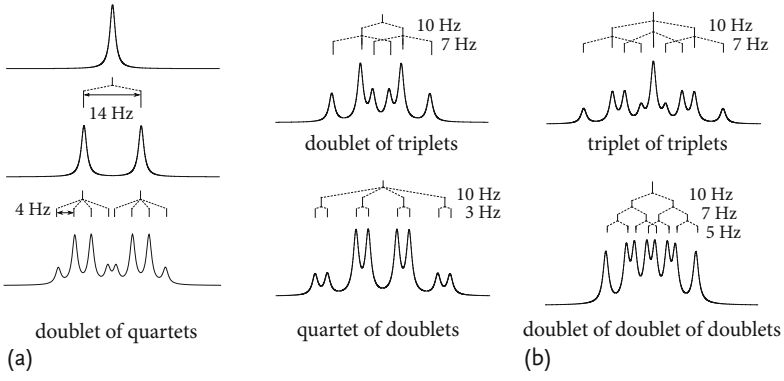

Figure 3.16 Multiplets of multiplets. The construction of a doublet of triplets (a) and some further examples (b). Depending on the multiplicities and the coupling constants, the multiplets may look quite complicated.

3.4.2
Higher-Order Spectra and Chemical Shift Separation

When chemical shift differences and coupling constants are similar in size, higher-order effects occur. Such effects leads to a distortion of the intensities in multiplets, sometimes to an extent that the nature of the underlying spin systems cannot be recognized anymore without much experience. The effect of higher-order spectra is depicted in Figure 3.17.

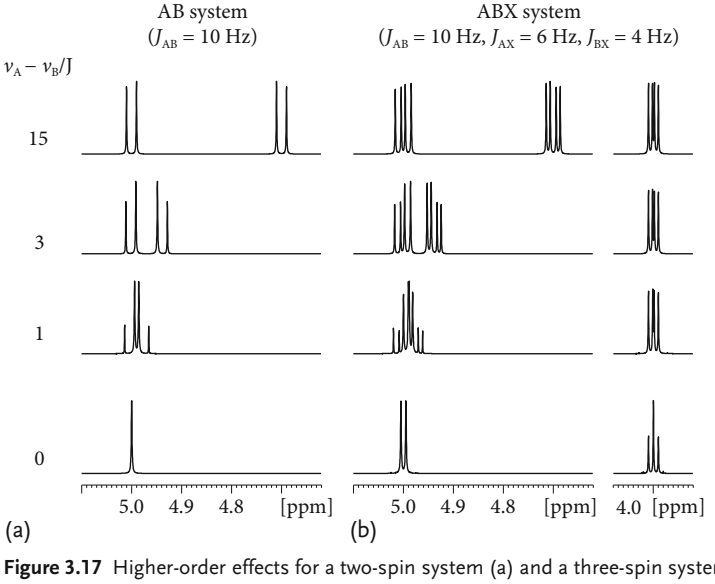

Figure 3.17 Higher-order effects for a two-spin system (a) and a three-spin system (b).

Higher-order effects become apparent in spectra when the chemical shift difference in hertz becomes smaller than 10 times the mutual coupling:

$$\left|\frac{\Delta\delta_{AB}(\text{Hz})}{J_{AB}}\right| \lesssim 10 \tag{3.1}$$

In such systems the intensity of lines does not follow the "normal" rules, and even more lines than usual may be encountered. Let us look at the spectra in Figure 3.17a, which show a two-spin system. In the top spectrum the nuclei have a relatively large shift difference and the doublet components show the expected 1 : 1 ratio of intensities. When the shift separation becomes smaller, the intensities become distorted, with enhanced intensities for the inner lines and attenuated intensities for the outer lines. This resembles the appearance of a roof, and therefore is referred to as the "roof effect." It is taken to the extreme in the third spectrum, where the outer lines are hardly visible. In the fourth spectrum, where the chemical shift difference is zero, the inner doublet lines completely overlap, and the intensity of the outer lines is zero, leaving a singlet. This is the reason why couplings for isochronous nuclei (nuclei with identical chemical shift) cannot be observed directly. The spectra in Figure 3.17b are for a three-spin system, in which the X part is shown separately. The doublet of doublets structure of signals is clearly visible in the top spectrum. However, from the third spectrum, it would be extremely hard to draw a conclusion about the nature of the spin system from the signal on the left. It is therefore of prime importance to recognize the presence of higher-order effects in spectra immediately. Since the chemical shift difference (in hertz) depends on

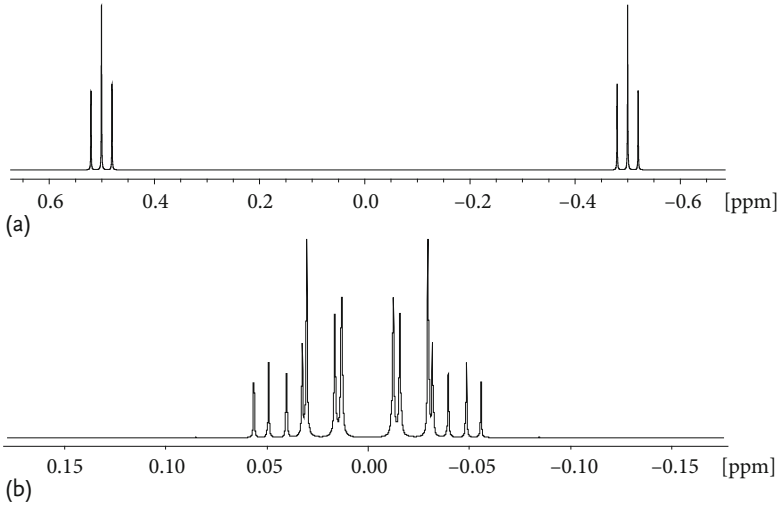

Figure 3.18 Higher-order effect of an A_2B_2 spin system. Simulated spectra for the case when the shift difference is much larger than the coupling constant ($\Delta\delta_{AB}/J_{AB} = 50$) (a) and when the shift difference is small ($\Delta\delta_{AB}/J_{AB} = 3$) (b).

the field strength, higher-order effects in spectra are more likely to occur at lower field, for instance, in proton spectra acquired with an old 60 MHz spectrometer. At the higher fields that are usually used nowadays (300 MHz and higher) such effects are observed less frequently, and accordingly the spectra are simpler to analyze. For example, if we have a 0.15 ppm chemical shift difference between two protons, with a 600 MHz spectrometer this corresponds to $0.15 \times 600 = 90$ Hz, which is more than 10 times the usual 7 Hz coupling.

Higher-order effects can only be understood in quantum mechanical terms and rigorous quantum mechanical calculations must be used to analyze such spectra. How complicated higher-order spectra may appear is illustrated in Figure 3.18.

3.4.3
Higher-Order Spectra and Magnetic Equivalence

A spin system with magnetically equivalent spins will always result in higher-order spectra. A good example is given by thiophene (Figure 3.19).

This molecule has an axis of symmetry, and hence H_A and $H_{A'}$ are chemically equivalent. However they are magnetically nonequivalent because the coupling of H_A to H_X is different from the coupling of $H_{A'}$ to H_X. Thus, the four protons of thiophene form an AA′XX′ spin system. Such systems always result in higher-order spectra, no matter how large the chemical shift separation is (see Figure 3.20).

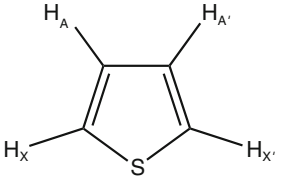

Figure 3.19 The symmetric pairs of protons in thiophene are chemically equivalent; however they are magnetically nonequivalent and thus form an AA′XX′ system.

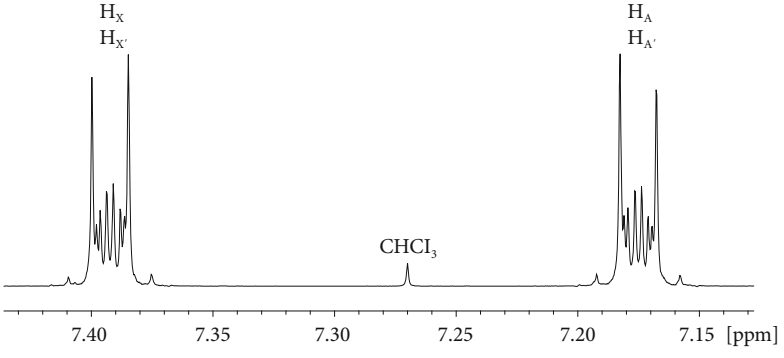

Figure 3.20 Proton NMR spectrum of thiophene in chloroform (400 MHz).

3.5
^{1}H–^{1}H Coupling Constants

Apart from the large ^1J proton–proton coupling constant of 276 Hz observed for molecular hydrogen (H_2),[1] the proton–proton couplings observed in ^{1}H spectra are usually within the range of 0–30 Hz with the order $^2J > {}^3J > {}^4J$. As mentioned in Section 2.3, coupling constants can be positive or negative. However, since we can normally only extract absolute values from spectra, we do not care much about that. For completeness, we mention that $^2J_{HH}$ couplings are mostly negative, while $^3J_{HH}$ couplings are always positive.

3.5.1
Geminal Couplings

Geminal (^2J) couplings between methylene protons of saturated systems are usually in the range of 10–15 Hz. An exception is cyclopropane derivatives, where substantially smaller geminal couplings of 2–5 Hz are observed. In general there is a strong correlation between the magnitude of geminal couplings and the H–C–H bond angle (see Figure 3.21). The larger the bond angle, the smaller the coupling constant. This can be understood on the basis of the fact that the s-orbital content and hence the hybridization influences the magnitude of the coupling. CH moieties that are sp^3 hybidized have bond angles close to 109°, whereas for sp^2 hydridization the value is 120°. Geminal couplings of terminal double bonds are relatively small (0–3 Hz).

As stated above, couplings can only be observed between chemically nonequivalent protons, and therefore the chemical shifts of the two protons bound to the same carbon atom must be different in order to observe a geminal coupling (compare Section 3.3.1).

3.5.2
Vicinal Couplings

Vicinal (^3J) couplings are by far the most frequently observed couplings in ^{1}H spectra. For saturated systems their magnitude is closely related to the dihedral

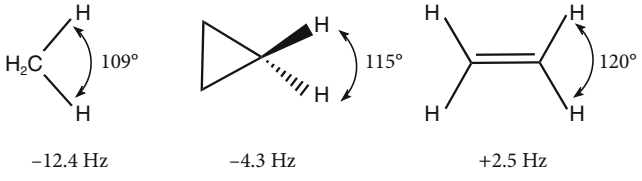

Figure 3.21 Dependence of the geminal ^{1}H couplings on the H–C–H bond angle.

1) The scalar coupling in H_2 cannot be determined directly, but is calculated from the coupling in ^{1}H–^{3}H.

H–C–C–H angle ϕ, a relation described by the famous *Karplus relationship*:

$$^3J(\phi) = A\cos^2(\phi) + B\cos(\phi) + C \tag{3.2}$$

Here A, B, and C are semiempirical coefficients that depend on the particular CH–CH moiety (substituents, presence of heteroatoms, etc.). A variety of similar relations have been established for vicinal couplings to heteronuclei as well. Figure 3.22 shows the Karplus curve that applies for ethane derivatives. The important feature to remember is that for parallel or antiparallel arrangements of the carbon–proton bond vectors the coupling is large, whereas for orthogonal arrangements the coupling is small.

When there is free rotation about the C–C bond, the coupling constants will usually average to a single value of about 7 Hz. This is the reason why the vicinal couplings in open chains are often very similar and the familiar $n + 1$ multiplets are obtained. However, in the absence of free rotation as in cyclic systems, or when rotation is sterically hindered, the Karplus relationship may allow one to derive the relative configuration at a neighboring center, as shown in Figure 3.23.

Similarly, ^3J coupling constants can be used to determine configurations at double bonds, where the trans configuration usually gives rise to much larger couplings than the cis configuration (Figure 3.23b). Electronegative substituents de-

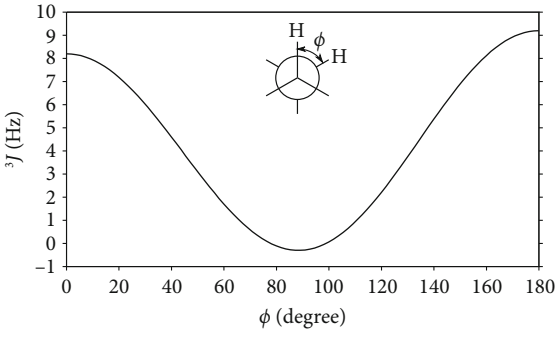

Figure 3.22 Karplus curve describing the vicinal coupling as a function of dihedral angle ϕ for ethane derivatives.

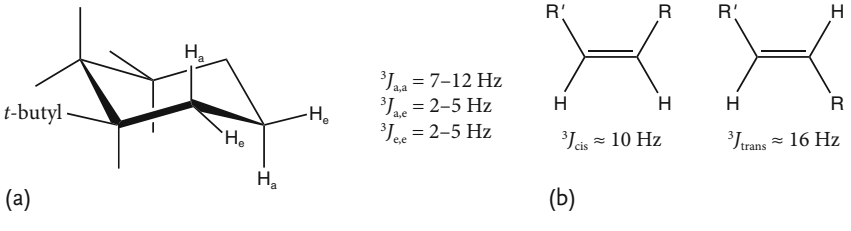

Figure 3.23 Vicinal coupling in rigid systems. ^3J couplings between axial–axial protons are usually larger than for axial–equatorial or equatorial–equatorial configurations (a). Similarly, trans couplings in double bonds are usually larger than cis couplings (b).

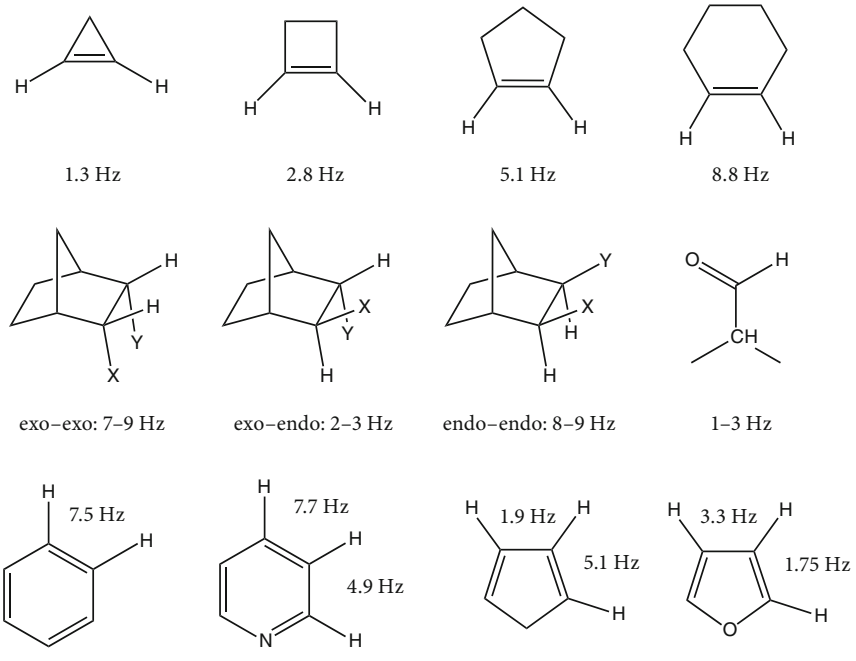

Figure 3.24 Some examples of ^{3}J couplings.

crease both the cis and the trans couplings (e.g., for fluoroethylene, $^{3}J_{cis} = 4.7$ Hz, $^{3}J_{trans} = 12.8$ Hz).

Vicinal couplings in aromatic systems are usually around 6–8 Hz. Some further examples of vicinal couplings are displayed in Figure 3.24.

3.5.3 Long-Range Couplings

Proton couplings over more than three bonds are usually very small and therefore rarely observed. Important exceptions are the allylic or homoallylic couplings as well as sterically fixed conformations where the intervening bonds describe a zigzag or "W." In addition, increased long-range couplings are observed when more than one coupling pathway is available as is often the case in bicyclic systems. Some examples of ^{4}J and ^{5}J couplings are shown in Figure 3.25.

3.5.4 ^{1}H Couplings to Other Nuclei

Couplings to ^{13}C Coupling constants for one-bond (^{1}J) couplings between ^{1}H and ^{13}C range from about 130 Hz for aliphatic groups and about 160 Hz for aromatic or vinylic groups to 250 Hz and more for alkynic or halognated carbons (e.g., 249 Hz for acetyelene, 239 Hz for CHF_3, and 267 Hz for formyl fluoride). The coupling

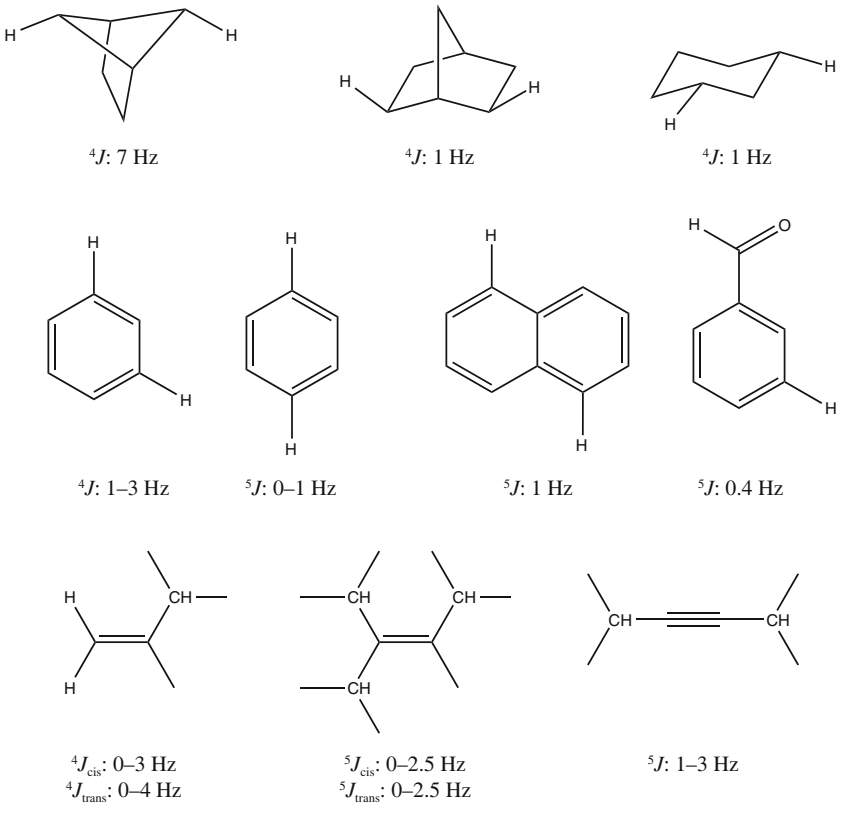

Figure 3.25 Examples for long-range couplings.

constant increases with increasing s character of the carbon. Since the natural abundance of ^{13}C is only about 1%, the carbon couplings in a proton NMR spectrum are only noticeable as small satellite signals to the left and right of the main signal. The magnitude of the geminal $^{2}J_{CH}$ coupling depends strongly on the system and usually assumes values in the range from 0 to 20 Hz (triple bonds, approximately 50 Hz). Vicinal $^{3}J_{CH}$ coupling constants assume values in the range from 0–16 Hz and are strongly influenced by the dihedral angle, the C–C bond length, and the electronegativity of the substituents. Long-range couplings over more than three bonds are usually very small. An exception is conjugated π systems, where $^{4}J_{CH}$ and sometimes even $^{5}J_{CH}$ couplings can be observed.

Couplings to ^{19}F Geminal $^{2}J_{FH}$ couplings are usually in the range of 40–80 Hz. The coupling constant increases with increasing number of fluorine substituents (CH_3F, 46 Hz; CH_2F_2, 50 Hz; CHF_3, 80 Hz). The geminal couplings in vinylic systems are relatively large (about 80 Hz). Vicinal $^{3}J_{FH}$ couplings are usually in the range of 0–30 Hz. Similar to the case of $^{3}J_{HH}$ couplings, they show a strong dependence on the dihedral angle or whether the coupling in olefinic systems is cis or

trans (trans > cis; e.g., $^{3}J_{FH}^{trans} = 52$ Hz, $^{3}J_{FH}^{trans}$=20 Hz in fluoroethylene). Small ^{4}J and ^{5}J F–H couplings can be observed sometimes (0–6 Hz).

Couplings to ^{31}P One-bond ^{1}H–^{31}P couplings are about 200 Hz in phosphanes (e.g., 192 Hz in dimethyl phosphane) but can have values up to 700 Hz in phosphite derivatives (e.g., 710 Hz in dimethyl phosphite). The values for ^{2}J and ^{3}J couplings are much smaller and are usually in the range of 10–30 Hz.

Couplings to ^{2}H Since the electronic structure of deuterium and proton bonds is almost identical, the ^{2}H couplings are also about six times smaller than the corresponding ^{1}H couplings due to the about six times smaller magnetic moment of deuterium. Because deuterium has spin 1, three possible values for the spin z component (1, 0, −1) exist and therefore the deuterium coupling causes a threefold line splitting with an intensity ratio of 1 : 1 : 1. Deuterium couplings are often observed for the solvent residual ^{1}H signals. For example, the residual ^{1}H line of deuterated methyl groups (CHD_2) is split into a quintet.

3.6 Problems

3.1. The following spectra represent the aromatic signals of disubstituted benzene derivatives. Which spectrum belongs to the ortho-, meta- and para-disubstituted aromatic rings?

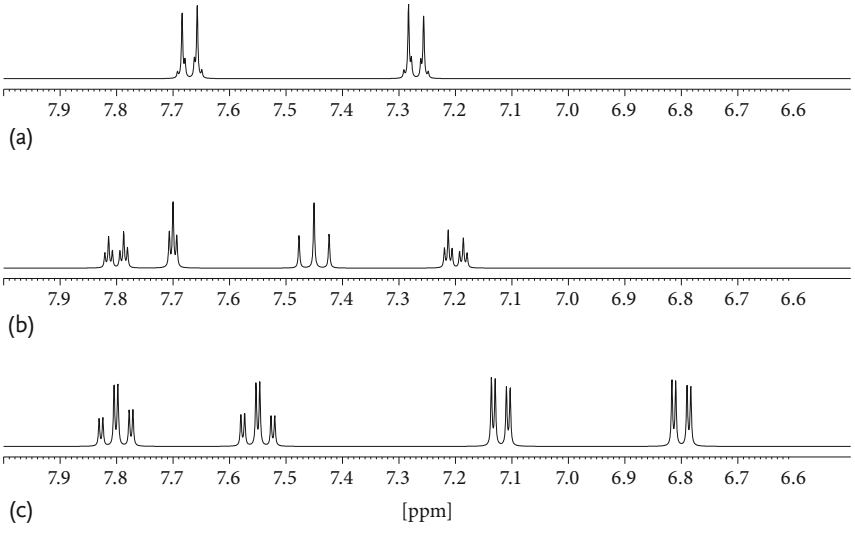

3.2. Some line intensities within the multiplets shown in Exercise 3.1 seems to be skewed. What term is used to refer to this effect and when does this effect start to occur?

3.3. The multiplets shown in spectrum (a) of Exercise 3.1 are not just two simple doublets as further line components can be seen. What is the reason for this? Which term is used to describe such spectra? What is the nomenclature of the spin system?

3.4. Draw the multiplet patterns of the following spin systems: A_2X_3, AMX_2 (J_{AM}: 10 Hz; J_{AX}: 7 Hz; J_{MX}: 5 Hz). Give the relative line intensities within the multiplets.

3.5. List the spin systems for the following molecules (use the ABX, AA′M … nomenclature)

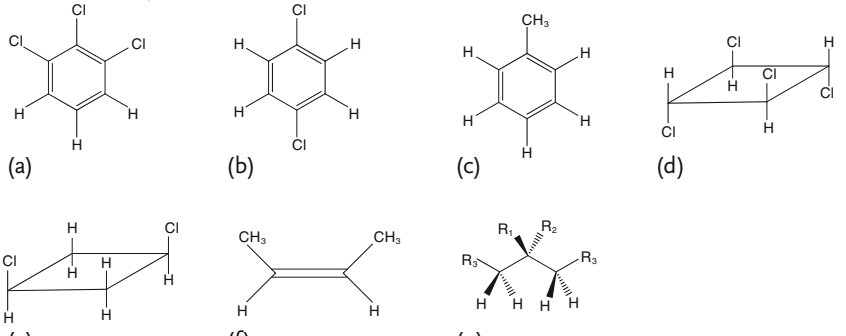

3.6. Using which methods is it possible to distinguish between enantiotopic protons. What is the underlaying principle of these methods?

Further Reading

Hesse, M., Meier, H., and Zeeh, B. (2007) *Spectroscopic Methods in Organic Chemistry*, 2nd edn, Thieme.

Pretsch, E., Bühlmann, P., and Badertscher, M. (2009) *Structure Determination of Organic Compounds: Tables of Spectral Data*, 4th edn, Springer.

4
NMR of ^{13}C and Heteronuclei

4.1
Properties of Heteronuclei

Of course, NMR is not limited to the ^{1}H nucleus, and a lot of the other elements of the periodic table are NMR-active. As we will see, however, the ^{1}H nucleus has the most favorable properties because of its high natural abundance (99.9%), its large γ associated with a high frequency, and the fact that the spin I is 1/2. ^{19}F and ^{31}P have similar properties and are very favorable nuclei.

The NMR-active nuclei can be sorted into five classes depending on their spectroscopic properties. These are presented in Table 4.1.

Nuclei from group Ia have perfect NMR properties. Class Ib members also display favorable relaxation properties and their natural abundance is high enough for direct detection. The nuclei from group Ic require isotope enrichment for direct detection. The members of group II display favorable relaxation line widths, but their low γ results in a low frequency, often outside the frequency range of standard probeheads. In addition, the longitudinal relaxation times T1 are very long, and hence long relaxation delays are necessary, resulting in long measuring times even if the number of scans is moderate.

For all nuclei with spin $> 1/2$ only direct detection is usually possible unless the ligand field is highly symmetric. An exception is the members of group IIIa. Due to their small quadrupole moment Q, they essentially behave like spin-1/2 nuclei, with line widths smaller than 10 Hz (often 0.5 Hz or less), allowing one often to extract scalar couplings. The members of group IIIb can be directly detected and they still display comparably narrow lines. Members of group IV display much broader lines, and for nonsymmetric environments, the line widths are often in the kilohertz range. Figure 4.1 displays a comparison of ^{59}Co spectra for symmetric and asymmetric complexes.

Finally, we present an overview of the resonance frequencies of the NMR-active nuclei (Figure 4.2).

For the direct detection of low-γ nuclei, high sample quantities are usually required (at least tens of milligrams). In the case of insufficient sample solubility,

Applied NMR Spectroscopy for Chemists and Life Scientists, First Edition. Oliver Zerbe and Simon Jurt.
©2014 WILEY-VCH Verlag GmbH & Co. KGaA. Published 2014 by WILEY-VCH Verlag GmbH & Co. KGaA.

Table 4.1 Classes of NMR-active isotopes.

Class	NMR properties	Representatives	Abundance	Observation
Ia	$I = 1/2$	^{1}H, ^{19}F, ^{31}P	100%	Direct detection
Ib	Medium–large γ Short T1	^{13}C, ^{29}Si, ^{77}Se, ^{111}Cd, ^{113}Cd, ^{117}Sn, ^{119}Sn, ^{125}Te, ^{129}Xe, ^{195}Pt ^{199}Hg, ^{203}Tl, ^{205}Tl, ^{207}Pb	1–99%	Direct detection and indirect methods
Ic		^{3}H	< 1%	Enrichment required
II	$I = 1/2$ Small γ Long T1	^{89}Y, ^{103}Rh ^{57}Fe, ^{107}Ag, ^{109}Ag, ^{183}W, ^{187}Os ^{15}N	100% < 100% < 1%	Direct detection at high field, indirect methods, and special probes
IIIa	$I \geqq 1$	^{2}H, ^{6}Li, ^{133}Cs		Direct detection, 2D experiment possible
IIIb	Small Q Long T1	^{91}Zr, ^{95}Mo, ^{99}Ru ^{51}V, ^{53}Cr		Couplings often resolved
IV	$I \geqq 1$ Medium Q Short T1	^{7}Li, ^{39}K, ^{11}B, ^{14}N, ^{17}O, ^{33}S, ^{35}Cl, ^{51}V ^{55}Mn, ^{59}Co, ^{61}Ni, ^{101}Ru, ^{105}Pd		Direct detection
V	$I \geqq 1$ Large Q Very short T1	Br, I, etc.		Not accessible for liquid NMR spectroscopy

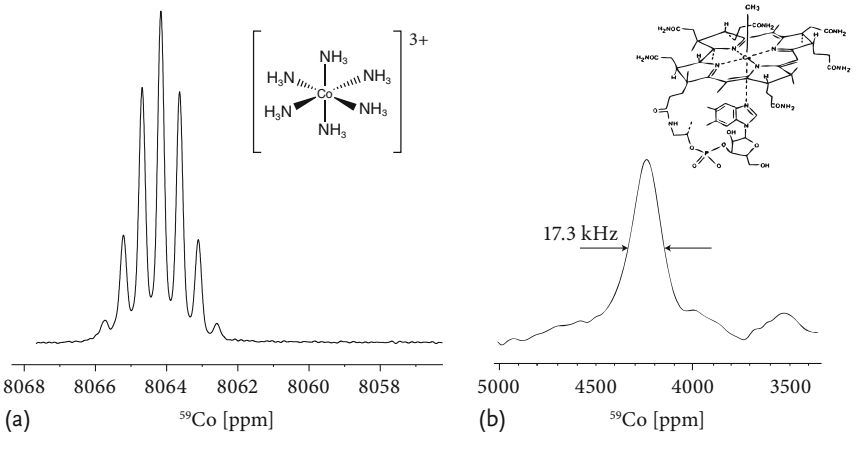

Figure 4.1 ^{59}Co NMR spectra of $Co[^{15}NH_3]_6$ (a) and a vitamin B_{12} derivative (b). The splittings in the spectrum in (a) are due to scalar coupling with ^{15}N.

probes with enlarged diameter (e.g., 10 mm) have to be used. Quantification of the signal is difficult, and there are no reliable integrals.

For historical reasons we will devote an entire section to ^{13}C NMR spectroscopy. We will then quickly list the major features of $I = 1/2$ and $I > 1/2$ main group elements followed by a similar description for the transition metals.

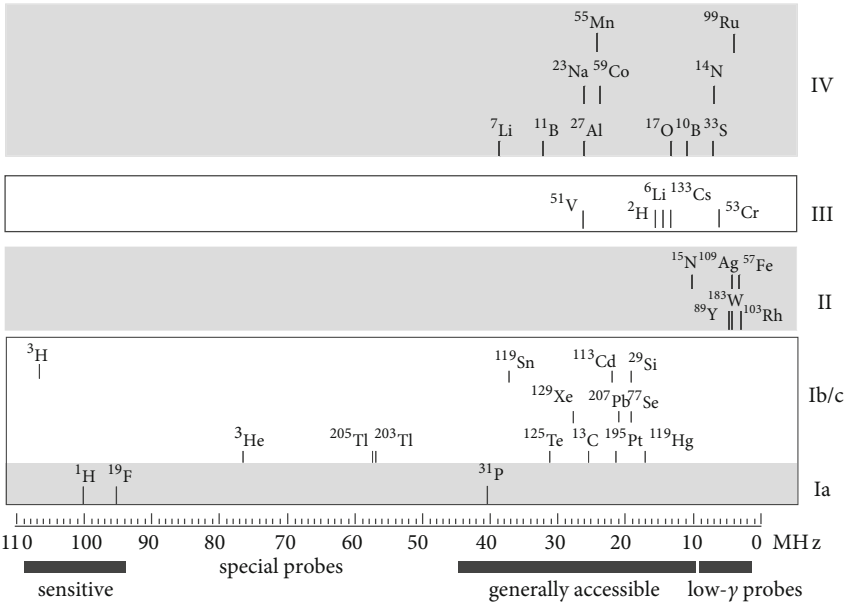

Figure 4.2 Graphical overview of NMR frequencies of nuclei from groups I–IV normalized to a proton frequency of 100 MHz.

4.2
Indirect Detection of Spin-1/2 Nuclei

The sensitivity of NMR experiments is related to the gyromagnetic ratio of the excited and detected spins ($S/N \propto \gamma_{ex}\gamma_{det}^{3/2}$). Due to the very low γ of most metal nuclei, direct detection is very insensitive. In contrast, polarization-transfer experiments may allow, in particular for low-γ nuclei with high natural abundance of the spin-1/2 isotope, detection of the metal chemical shifts at comparably low concentrations. The sensitivity gains from the various polarization-transfer techniques are compared for some nuclei in Figure 4.3.

An inverse $^{1}H,^{187}Os$ correlation experiment will boost the sensitivity by a factor of roughly 12 000. If the inverse experiment takes 1 h, direct detection would take 1.5 years! We would like to add that indirect detection methods such as the heteronuclear single-quantum coherence (HSQC) experiment can also be used to *correlate* two sensitive nuclei (e.g., ^{1}H with ^{19}F or ^{31}P).

4.3
^{13}C NMR Spectroscopy

^{13}C NMR spectroscopy plays a very important role in structure elucidation. For many compounds, in particular those with little proton density, carbon chemical

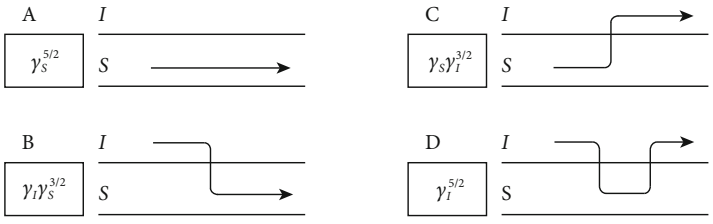

	^{13}C	^{15}N	^{57}Fe	^{103}Rh	^{183}W	^{187}Os
A (NOE)	2.99	–3.93	16.4	–16.8	12.9	22.6
B (INEPT)	3.98	9.86	30.8	31.6	23.7	43.2
C (reversed INEPT)	7.93	31.0	171	178	115	284
D (2-PT; HSQC)	31.5	305	5263	5610	2737	12264

Figure 4.3 Comparison of the sensitivity of various ways to detect nuclei. NOE nuclear Overhauser effect, INEPT insensitive nuclei enhancement by polarization transfer, 2-PT double polarization transfer, HSQC – heteronuclear single-quantum coherence.

shifts and correlations along the carbon skeleton are crucial for identification of the compound. As we will see, carbon chemical shifts are much less influenced by effects of the solvent, pH, or temperature, and are therefore suitable as entries in databases for compound identification. Of course, the low natural abundance of about 1% causes sensitivity problems. However, with the advent of double-polarization-transfer experiments such as HSQC and HMBC experiments, carbon chemical shifts can be recorded on quantities of 1 mg in less than a few hours. Nowadays, it is expected that carbon spectra have been fully assigned and support the structure proposed.

Carbon chemical shifts and the scalar couplings follow simple rules, which will be described in the following.

4.3.1 The ^{13}C Chemical Shift

The ^{13}C chemical shift scale runs from approximately 0 to 220 ppm. Due to the low abundance of ^{13}C nuclei, the occurrence of $^{13}C,^{13}C$ isotopomers is extremely unlikely, and hence $^{13}C,^{13}C$ couplings will not be visible in the spectra. But of course scalar couplings to protons or any other NMR-active nucleus present such as ^{31}P or ^{19}F are visible. As we will see later, ^{13}C spectra are usually recorded such that they are broadband proton decoupled and the signals are therefore almost always singlets. The singlet appearance in combination with the large chemical shift range of more than 200 ppm results in excellent signal separation and very little reso-

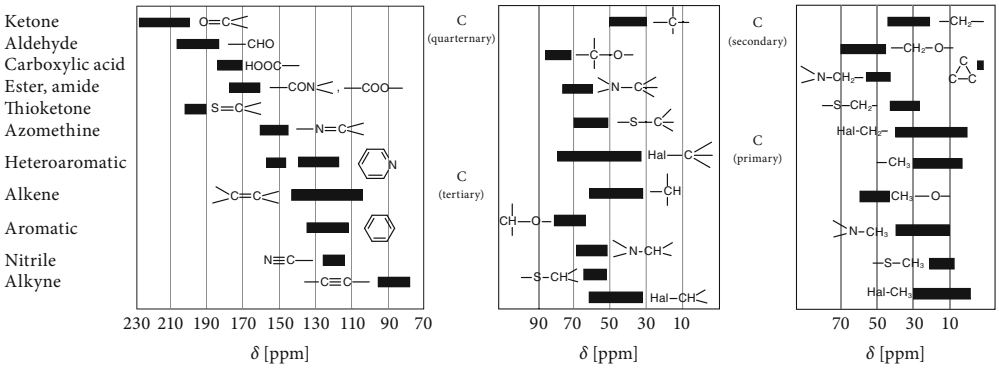

Figure 4.4 Summary of ^{13}C chemical shifts. Chemical shifts are reported relative to tetramethylsilane at 0 ppm. Adpated from Mason (see Further Reading).

nance overlap. The ^{13}C chemical shifts of the most common chemical entities are summarized in Figure 4.4.

As with most other heavy atoms the chemical shift is mainly governed by the paramagnetic contribution:

$$\sigma_N^{para} = \frac{(\mu_0 \mu_B^2)}{2\pi \Delta E \langle r^3 \rangle_{2p}} [Q_{NN} + \Sigma Q_{NB}] \tag{4.1}$$

To summarize, the shift depends on the mean excitation energy ΔE and the charge density and bond order characterized by the values of Q_{NN} and Q_{NB}. Accordingly, the paramagnetic contribution σ_N^{para} depends on the availability of low-lying excited electronic states. A low value of ΔE causes deshielding. An interesting correlation between ΔE in UV spectra and δ_C has been observed, supporting this view. Q_{NB} measures the relative importance of σ versus π bond character and is nonzero only if both σ and π bonds exist between atoms N and B.

Increasing substitution of saturated carbon atoms changes the $\sigma \rightarrow \sigma^*$ transition, and more heavily substituted carbon atoms resonate at lower field. In unsaturated systems the excited π^* states are much lower, explaining why unsaturated ^{13}C nuclei are less shielded. The distance term $\langle r^{-3} \rangle_{2p}$ displays a large dependence on the nuclear charge at nucleus N. An increase of electron density at nucleus N will expand the 2p orbital.

Hybridization The hybridization is the dominant factor for the ^{13}C chemical shift since it will influence both ΔE and r. The general trend is $\sigma(sp^3) > \sigma(sp) > \sigma(sp^2)$, similar to what has been observed in proton NMR.

Inductive effects For substituted carbon positions the chemical shift is related to the electronegativity of the substituent. This effect shows a clear trend at the α position. The effect is due to a decrease in electron density at the 2p orbitals. As can be seen from Table 4.2, this is only true for the α position.

Table 4.2 Effects of substituents on ^{13}C chemical shifts (ppm).

Electronegativity	Substituent X	C atom $CH_2(\alpha)$	$CH_2(\beta)$	$CH_2(\gamma)$
2.1	H	0	0	0
2.5	CH_3	+9	+10	−2
2.5	SH	+11	+12	−6
3.0	NH_2	+29	+11	−5
3.0	Cl	+31	+11	−4
4.0	F	+68	+9	−4

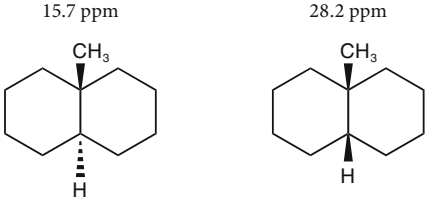

(a) *trans*-9-methyldecaline (b) *cis*-9-methyldecaline

Figure 4.5 Chemical shifts for *trans*-9-methyldecalin (a) and *cis*-9-methyldecalin (b).

Steric effects ^{13}C chemical shifts are very sensitive to stereochemistry. Steric corrections to the shift are due to repulsive forces between atoms close in space that cause distortions of the electron distributions. A steric perturbation of a C–H bond results in a motion of electrons toward the carbon center, causing shielding of the carbon. The effect is most dramatic when the two proton-bearing carbon bonds are in a γ-gauche relative orientation. An example for the steric effect is presented in Figure 4.5.

Electric field effects Local electric fields, for example, from proximate ionized groups, polarize carbon bonds and thereby change the electron density at the ^{13}C site. The effect depends on both the strength of the electric field and its gradient $\partial E/\partial r$. For α carbons the effect is smaller than for β carbons. Protonation of ionizable groups usually results in upfield shifts of about 0.5–4 ppm for the α carbons and β carbons, and less than 1 ppm for $C_{\gamma/\delta}$.

Hyperconjugation effects First-row heteroatoms X cause characteristic upfield shifts of −2 to −6 ppm upon replacement of H by X if they are antiperiplanar to the observed ^{13}C nucleus. The effect has been explained by an interaction of the lone pair electron of X with the C_α–C_β bond (Figure 4.6). As a result, an increase in electron density occurs at C_γ. The effect is strongest for N, O, or F.

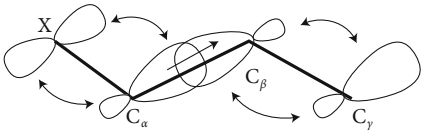

Figure 4.6 Hyperconjugation effects. The lone pair of the X atom polarizes the C_α–C_β bond, which in turn affects the electron density at C_γ.

Mesomeric effects Mesomeric effects are well known in organic chemistry. Classic examples are redistribution of lone-pair electron density from, for example, NH_2 subsitutents into aromatic π systems and the reduction of aromatic π-electron density by electron-withdrawing groups such as $-NO_2$ (see Figure 4.7). Accordingly, substituents with lone pairs shield the ortho and para carbons, and electron-withdrawing substituents deshield these carbons. In fact, because of other effects (e.g, steric interactions) the effects on the ortho carbons are small, whereas the effects on the para positions are significant. Another example is the carbonyl moiety. In one of the mesomeric forms a negative partial charge is on the oxygen and a positive partial charge is on the carbonyl carbon, which explains the low-field shift for such carbon resonances (for a ketone about 210 ppm). The carbonyl frequency is decreased in esters and amides (approximately 170 ppm) and in carbonyls conjugated to double bonds (see Figure 4.7).

Neighbor anisotropy effects Similarly to proton NMR, local anisotropy effects such as ring currents will affect the ^{13}C resonances. However, the effect is less dramatic than for proton chemical shifts (less than 1 ppm).

Heavy atom effects A heavier halogen atom such as iodine results in an upfield shift at the C_α position. The substituent effect for iodine at the C_α position is -6 ppm, whereas it is $+68$ ppm for fluorine. The heavy atom effect has been explained in terms of increased diamagnetic shielding due to the presence by a large number of electrons from the heavy atom. While for fluorine the inductive effect

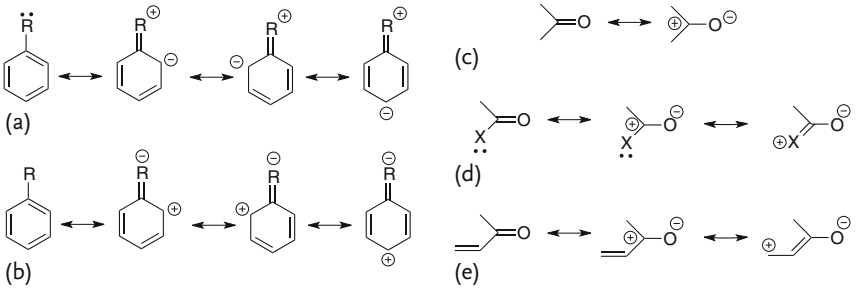

Figure 4.7 Mesomeric effects. Electron-donating (a) and electron-withdrawing (b) substituents alter electron densities at ortho and para positions. Similarly, the carbonyl carbon bears a partial positive charge (c). This may be compensated if atoms with lone pairs are attached (e.g., O in esters or N in amides) (d), or in conjugated carbonyls (e).

Table 4.3 Steric correction factors.

Observed C	Highest substituent at neighboring C			
	CH_3	CH_2	CH	$C_{quaternary}$
Primary	0	0	−1.1	−3.4
Secondary	0	0	−2.5	−6.0
Tertiary	0	−3.7	−8.5	−10.0
Quaternary	−1.5	−8.0	−10.0	−12.5

clearly dominates, for iodine this is obviously overcompensated by the heavy atom effect.

Increment systems Substituting a CH moiety with an CX moiety will change the resonance frequencies at the C_α, C_β, C_γ, and C_δ positions in a highly predictable manner. The magnitude and sign of the change of the chemical shift depends on the substituent and the position, and has been tabulated for most substituents. These increment systems can then be used to predict the chemical shift to a precision of a few parts per million. The predicted ^{13}C chemical shift is

$$\delta_i = B + \sum A_k n_k + \sum S_{i\alpha} \tag{4.2}$$

in which B is the so-called basis value and A_k is the substituent increment of the kth atom summed over all α, β, γ, and δ positions, and $S_{i\alpha}$ are steric or electronic correction factors. The substituent increments for carbon atoms are $A_\alpha = 9.1$ ppm, $A_\beta = 9.4$ ppm, $A_\gamma = -2.5$ ppm, and $A_\delta = 0.3$ ppm. The basis values B are −2.3 ppm for open-chain alkanes, 123.3 ppm for olefinic carbons, and 128.5 ppm for benzene derivatives. The steric correction factors are given in Table 4.3.

As an example we will calculate the predicted ^{13}C chemical shifts of 2,2-dimethylpentane and compare them with the experimental data (Table 4.4).

The deviations from the measured values are very modest, and the prediction gives you a good indication of whether the structure proposed is reasonable or not. Nowadays these somewhat tedious calculations are done by computer programs, and often you only need to sketch the chemical structure. Tables also exist in the literature to estimate changes when substituting a hydrogen atom with a certain group (e.g., CH → C–OH).

4.3.2 X,^{13}C Scalar Couplings

4.3.2.1 ^{13}C,^{1}H Couplings

^1J(C,H) coupling constants Scalar couplings are transmitted via Fermi-contact interaction, which requires electrons to have nonvanishing probability at the nucleus (see Section 7.2.1). Therefore, hybridization (percentage of s orbitals!) strongly influences the ^1J(C,H) coupling constants. As a rule of thumb, the scalar coupling

Table 4.4 Prediction of ^{13}C chemical shifts (ppm) of 2,2-dimethylpentane.

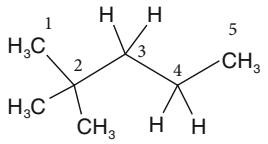

^{13}C no.	Basis	α	β	γ	δ	Steric correction	Predicted	Measured
1	−2.3	9.1	3 × 9.4	−2.5	0.3	−3.4	29.4	29.5
2	−2.3	4 × 9.1	9.4	−2.5	–	−8.0	33.0	30.6
3	−2.3	2 × 9.1	4 × 9.4	–	–	−6.0	47.5	47.3
4	−2.3	2 × 9.1	9.4	3 × (−2.5)	–	0	17.8	18.1
5	−2.3	9.1	9.4	−2.5	3 × 0.3	0	14.6	15.1

constant can be estimated by multiplying the s-orbital percentage by 500 (e.g., for sp^3, $0.25 \times 500 = 125$ Hz). Another factor contributing to the magnitude of the scalar couplings is inductive effects from substituents. A few examples are depicted in Figure 4.8.

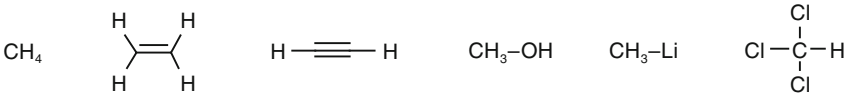

Figure 4.8 $^1J(^{13}C,^1H)$ coupling constants (Hz) for selected examples.

^2J(C,H) coupling constants (geminal couplings) The magnitude of the geminal coupling constants depends strongly on the system and usually has values in the range from 0–20 Hz (triple bonds, approximately 50 Hz). The magnitude of the geminal coupling constant therefore reveals little structural information.

^3J(C,H) coupling constants (vicinal couplings) The magnitude of the vicinal coupling constants assumes values in the range from 0–16 Hz. It is strongly influenced by the dihedral angle (similar to the proton–proton couplings), the C–C bond length, the bond angle, and the electronegativity of the substituents. The dependence of the vicinal coupling on the magnitude of the dihedral angle involved is exploited in NMR spectroscopy of carbohydrates, proteins, and nucleic acids. The three-bond C,H coupling follows a Karplus-type relationship as depicted in Figure 4.9 that has been parameterized as

$$^3J(\mathrm{C,H}) = 3.6\cos^2\theta - 1.0\cos\theta + 4.3 \qquad (4.3)$$

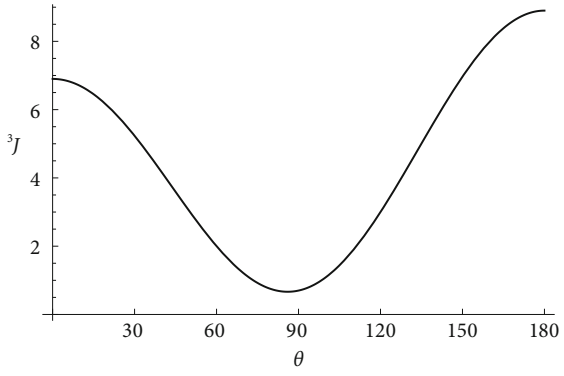

Figure 4.9 Dependence of the ^3J(C,H) coupling on the dihedral angle θ.

^{3+n}J(C,H) coupling constants (long-range couplings) Coupling constants between proton and carbon nuclei separated by more than three bonds are usually very small. However, in conjugated π systems, the values are a little larger, so these couplings can be observed. Long-range couplings are not really important for structure elucidation. It is important to note that the magnitude of the scalar couplings is often not sufficient to distinguish two-bond and three-bond C,H scalar couplings.

Two-bond, three-bond, and long-range C,H scalar couplings are extensively exploited in HMBC experiments (see Section 17.4.5).

4.3.2.2 $^{13}C,^{13}C$ Couplings

Homonuclear ^{13}C couplings cannot usually be observed because of the low natural abundance of ^{13}C (1.1%). The so-called satellite lines are 200 times smaller than the center lines. Carbon–carbon couplings are of course observable in isotopically enriched molecules; this fact is exploited in protein NMR spectroscopy. The magnitude of the ^1J(C,C) coupling constant depends on the hybridization of the nuclei involved. Substituent effects are largely limited to the couplings of the attached carbon (see Figure 4.10). One-bond C–C couplings are used for magnetization transfer in the INADEQUATE (see Section 17.4.7).

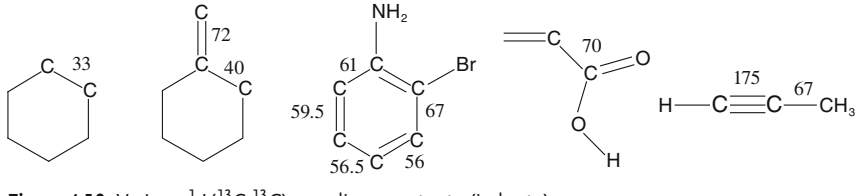

Figure 4.10 Various ^1J($^{13}C,^{13}C$) coupling constants (in hertz).

4.3.2.3 $^{13}C,^{31}P$ Couplings

Since phosphorus exists in the form of a single stable isotope with spin 1/2 , $^{13}C,^{31}P$ couplings will appear as doublets in proton-decoupled carbon spectra. The magnitudes of the one-bond $^{13}C,^{31}P$ couplings vary dramatically, with values observed in the range between −53 and +476 Hz. Interestingly, $^{1}J(^{13}C,^{31}P)$ coupling constants may also take values around 0 Hz (Figure 4.11), which is the range for geminal or vicinal couplings. As a consequence, couplings cannot be easily used to determine by how many bonds the carbon and phosphorus nuclei are separated.

$(H_3C–CH_2–CH_2–CH_2)_3P$ $CH_3–P(O)–(O–CH_2–CH_3)_2$

$^{1}J_{C,P} = -11$
$^{2}J_{C,P} = +12$
$^{3}J_{C,P} = +13$
$^{4}J_{C,P} = 0$

$^{1}J_{C,P} = 143$
$^{2}J_{C,P} = -5.9$
$^{3}J_{C,P} = +5.9$

Figure 4.11 Various $^{n}J(^{13}C,^{31}P)$ coupling constants (in hertz).

4.3.2.4 $^{13}C,^{19}F$ Couplings

Like phosphorus, fluorine exists in the form of a single stable isotope and therefore gives rise to line splittings in carbon spectra similar to ^{31}P. The magnitude of the coupling decreases with increasing number of separating bonds. $^{13}C,^{19}F$ coupling constants are relatively large (160–400 Hz; Figure 4.12). In aliphatic systems, $^{13}C,^{19}F$ couplings may not be observed over four bonds, but in conjugated π systems couplings over up to eight bonds have been found.

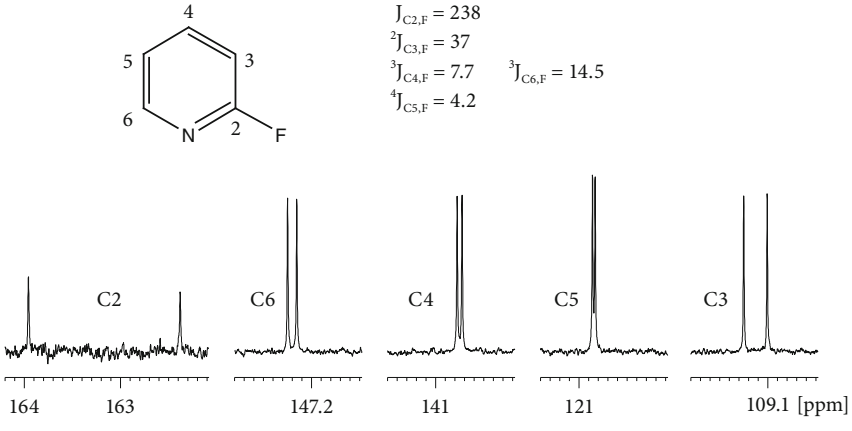

Figure 4.12 Various $^{n}J(^{13}C,^{19}F)$ coupling constants (in hertz) in 2-fluoropyridine.

4.3.3
Longitudinal Relaxation of ^{13}C Nuclei

Longitudinal (T1) relaxation of ^{13}C nuclei is mainly governed by two mechanisms: dipolar relaxation and relaxation by chemical shift anisotropy (CSA) (see Sections 14.3.1 and 14.3.2). Dipolar relaxation is the predominant mechanisms for all sp^3-hybridized carbons. Its efficiency depends on how far away the next dipolar partner spin is. If there are protons directly attached to the carbon, dipolar relaxation will be efficient. Quaternary carbons cannot use this source; other protons are much further away (e.g., 2.5 Å instead of 1.1 Å, remember that dipolar relaxation is proportional to r^{-6}!). Carbon nuclei that are part of double bonds (sp^2 hybridized) can relax via CSA, and this mechanism, although usually less efficient than dipolar relaxation, becomes faster at higher field (its efficiency is proportional to B^2). The T1 values of carbon therefore span a considerable range, from a few seconds to minutes as indicated in Figure 4.13.

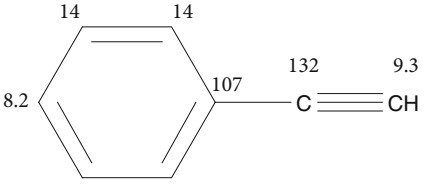

Figure 4.13 T1 relaxation times of phenylacetylene.

The non-proton-bearing carbon of the triple bond in the aromatic compound relaxes very slowly, since the next proton is quite far away. As we will see shortly, the experiment repetition rate for ^{13}C NMR spectra is set to such short values that quaternary carbons do not fully relax. They will remain in a semisaturated state during the experiment, and hence the signal intensity from them is much smaller!

Carbon nuclei bound to a quadrupolar nucleus will usually relax rather quickly and may be significantly broadened because of that.

4.3.4
Recording ^{13}C NMR Spectra

A single one-pulse carbon NMR experiment will result in carbon NMR spectra in which all signals are split into multiplets by the rather large ^1J and the smaller ^nJ couplings with the protons. Homonuclear C,C couplings are absent for compounds at natural ^{13}C abundance. But the splitting due to the proton couplings will unnecessarily complicate the spectra. Therefore, carbon NMR spectra are usually broadband proton decoupled (Section 12.4). However, splittings with other NMR-active heteronuclei can be present (e.g., from ^{19}F or ^{31}P). The information on the multiplicity (the number of attached protons) can be easily read from the DEPT spectra (Section 12.10) if required.

^{13}C NMR spectra will always contain considerable amount of noise because the signal is so weak. An important feature of these spectra is that because of the vastly different T1 relaxation times the signal intensities cannot be interpreted in a quantitative fashion any longer. Apart from the T1 effect, another contribution comes from the heteronuclear nuclear Overhauser effect (NOE). Decoupling the protons results in the population levels of the protons being perturbed, and they will cross-relax via carbon to go back to the equilibrium states (see Chapter 15). The heteronuclear NOE between a proton and a carbon is positive, so it will increase the signal intensity, and the gain can be up to 100%. Protonated carbons display stronger signals because they have more efficient T1 relaxation *and* they receive a heteronuclear NOE.

Still there is a method to measure carbon NMR spectra in which signals are related to their occurrence. The experiment is called an "*inverse-gated*" ^{13}C experiment. Therein the decoupler is turned off during the relaxation delay, and is only switched on during data acquisition. Apart from that, the relaxation delay must be chosen to be long enough to avoid effects from T1, and as a compromise we typically use 60 s instead of the normally used 5 s. That means that an experiment with the same number of scans will take 12 times as long, and the signal boost from the NOE is missing. To cut a long story short, you need a lot of sample to run inverse-gated experiments, but sometimes they can be very helpful. Normal

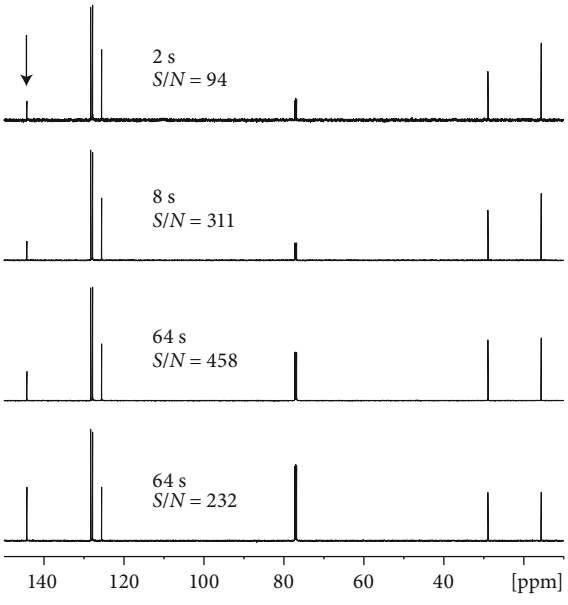

Figure 4.14 Proton-decoupled ^{13}C NMR spectra of ethylbenzene. For each spectrum the relaxation delay used is indicated, as is the signal-to-noise ratio (S/N) of the quaternary carbon (indicated by an arrow). The spectrum at the bottom is from the inverse-gated experiment. The same number of scans was used for all spectra. The signal around 77 ppm is from the solvent $CDCl_3$.

^{13}C NMR spectra of ethylbenzene recorded with various relaxation delays are compared with the spectrum from an inverse-gated experiment in Figure 4.14.

The signal intensities are comparable only in the inverse-gated experiment. Because of the symmetry of the *p*-ethylbenzene, the signals at 128 ppm code for two carbons each. With increasing relaxation delay, the intensity of the quaternary carbon increases. The difference in the two spectra recorded with a relaxation delay of 64 s is that the heteronuclear NOE is missing in the inverse-gated experiment.

4.4 NMR of Other Main Group Elements

NMR spectroscopy is often immediately associated with proton or carbon NMR. However, there are many other often neglected nuclei from the periodic table of elements for which reasonable spectra can be recorded. Often NMR spectra of these help us understand the structure or reactivity of compounds, and therefore the importance of measuring these nuclei extends far beyond the simple accumulation of chemical shifts.

Tables 4.5 and 4.6 summarize the NMR-related properties of nuclei from main group elements. Nuclei with $I > 1/2$ posses a quadrupolar nucleus, and lines are usually broad due to the efficient quadrupolar relaxation in the absence of high symmetry of the ligand field. However, when the quadrupole moment is small as for ^{2}H, for example, very reasonable spectra may still be recorded. Some heteroatoms are so important in chemistry or biology that they have also been frequently studied by NMR experiments. These are boron, (silicon), nitrogen, phos-

Table 4.5 NMR properties of spin-1/2 main group elements. Adapted from Harris (1986) *Nuclear Magnetic Resonance (A Physicochemical view)*, Longman.

Nucleus	Abundance (%)	$\gamma/10^7$ (rad T^{-1} s^{-1})	Ξ (MHz)	Receptivity (relative to ^{13}C)	Standard
^{1}H	99.95	26.752	100.000 000	5670	Me_4Si
^{13}C	1.11	6.728	25.145 004	1.0	Me_4Si
^{15}N	0.37	−2.712	10.136 783	0.022	CH_3NO_2
^{19}F	100	25.181	94.094 003	4730	$CFCl_3$
^{29}Si	4.70	−5.319	19.867 184	20	Me_4Si
^{31}P	100	10.841	40.480 737	377	H_3PO_4
^{77}Se	7.6	5.12	19.071 523	3	Me_2Se
^{119}Sn	8.58	−10.021	37.290 662	25.6	Me_4Sn
^{125}Te	6.99	−8.498	31.549 802	12.7	Me_2Te
^{129}Xe	26.44	−7.441	27.81	32.3	$XeOF_4$
^{205}Tl	70.50	15.589	57.633 833	791	$TlNO_3$
^{207}Pb	22.6	5.540	20.920 597	11.4	Me_4Pb

phorous, (oxygen), and fluorine. They will be described separately, and we will provide a short overview of the remaining nuclei and refer the interested reader to special monographs on the topic that also contain extensive chemical shift tables.

In Section 2.5.2 we described that referencing can be performed directly to a standard of known chemical shift, or indirectly via the Ξ value, which relates the proton chemical shift scale to the scale of the nucleus of interest. Indirect referencing is preferable because it circumvents problems with different conditions for making the reference sample. However, since both methods are widely used, we describe both the Ξ value and the standard.

4.4.1
Main Group Nuclei with $I = 1/2$

4.4.1.1 ^{3}H NMR

Tritium is the NMR isotope with the highest frequency, and special probes are required. Because tritium is a beta emitter, safety when conducting such measurements is an issue, and they can only be performed in specialized laboratories. However, the effects from the radioactive decay do not affect the environment greatly unless the glass tube breaks. The sensitivity depends on the enrichment. In principle, tritium at 100% abundance is even more sensitive than protons, but for practical and safety reasons enrichment is never that high. The chemical shifts are highly similar to the proton chemical shifts – substituting a proton with tritium will give rise to a signal at more or less the same chemical shift.

4.4.1.2 ^{15}N NMR

Nitrogen is an important element in nature. It is found in biomolecules (proteins and nucleic acids) as well as in heterocycles of natural products. Nitrogen-containing ligands are also frequently encountered in catalysts. The low natural abundance of ^{15}N requires large sample quantities, and measurements are additionally hampered by the long T1 times of this nucleus (often in the range of minutes!). When detection of ^{15}N is performed directly, because of the negative γ of ^{15}N the heteronuclear NOE can be negative, so in unfavorable cases the signal may completely disappear. In those case one should use inverse-gated decoupling techniques.

But in general the method of choice is indirect detection via an ^{15}N,^{1}H correlation experiment (HSQC or heteronuclear multiple-quantum correlation, HMQC). For directly bonded protons the coupling is large (90–100 Hz). Even if this is not the case, a long-range coupling can often be found for the coherence transfer, provided that the proton lines are reasonably sharp. ^{15}N,^{1}H correlation experiments are the most frequently performed experiments in BioNMR spectroscopy.

Two different scales exist in ^{15}N NMR spectroscopy, the ammonia and the nitromethane scale. The ammonia scale is used by the BioNMR community, and the nitromethane scale is used in organic chemistry. The ^{14}N and ^{15}N chemical shifts are interchangeable. Because nitrogen-containing moieties are often involved

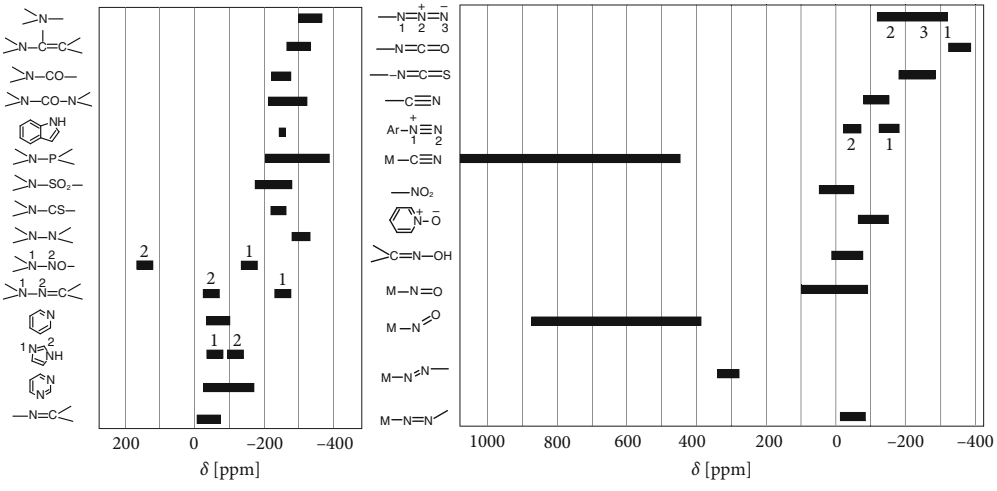

Figure 4.15 ^{15}N chemical shift ranges (referenced to the $MeNO_2$ scale). Adapted with permission from Berger *et al.* (1997) *NMR Spectroscopy of the Non-Metallic Elements*, John Wiley & Sons, Ltd.

in the formation of hydrogen bonds, the chemical shifts strongly depend on pH, temperature, concentration, counterion, and so on. The ^{15}N chemical shift scale mainly runs from −400 to +800 ppm. Large values of shielding are observed for singly bonded nitrogen, and the most deshielded nitrogens are part of N=X double bonds. The literature is full of ^{15}N chemical shift tables. Substituent patterns exist like for carbon spectra, and good correlations with electron density and Hammett-like substituent parameters have been observed. Many metal-coordinating ligands coordinate via nitrogen, and coordination shifts occur upon complexation. Chemical shift ranges for important nitrogen-containing compound classes are summarized in Figure 4.15.

One-bond ^{15}N–^{1}H scalar couplings are large (in the range of 90 Hz), but may vary considerably with substituents. Long-range ^{15}N–^{1}H scalar couplings may still be up to 10 Hz and are useful for HMBC-type experiments.

4.4.1.3 ^{19}F NMR

Fluorine is rarely present in natural products. Introducing ^{19}F therefore has the advantage that no disturbing background signals are observed. Drugs frequently contain fluorine. The ^{19}F nucleus has almost 100% abundance, a high frequency, and is therefore very sensitive. A technical problem unfortunately is that the ^{19}F frequency is outside the normal range, and you need a dedicated probehead for it. On lower-frequency instruments the proton channel can often be tuned for ^{19}F; however, then you cannot decouple it from protons. Many QNP probes (probes that can be tuned to four different frequencies) have ^{19}F capabilities.

The ^{19}F chemical shift scale runs from approximately −400 to +800 ppm. The ^{19}F chemical shifts are usually referenced relative to $CFCl_3$ (Figure 4.16). Due to

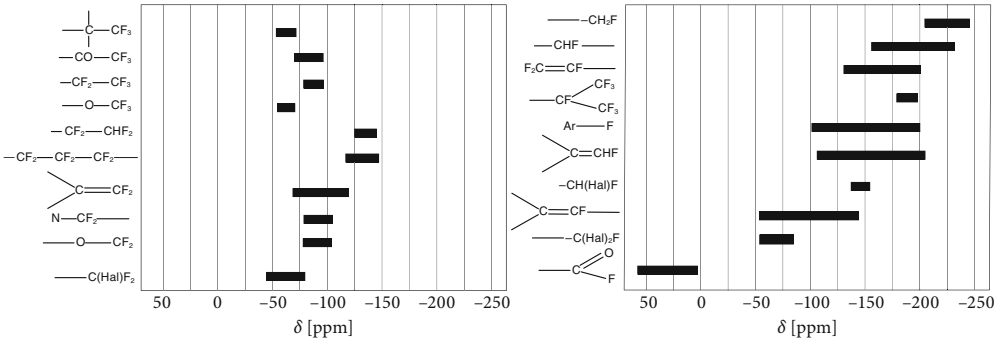

Figure 4.16 Overview of ^{19}F chemical shifts, referenced relative to $CFCl_3$. Adapted with permission from Berger *et al.* (1997) *NMR Spectroscopy of the Non-Metallic Elements*, John Wiley & Sons, Ltd.

the presence of two major chlorine isotopes, the ^{19}F signal displays three major lines, of which the center one is set to 0 ppm. Shifts are correlated to the electron density at the fluorine site. The chemical shift is sensitive to the charge: ^{19}F shielding decreases from neutral molecules to the anion, and decreases from the neutral molecule to the cation as well. The ^{19}F chemical shift is highly sensitive to the environment. In the pharmaceutical industry NMR-based assays have been established that detect binding of ^{19}F-containing drugs to proteins by changes in the ^{19}F chemical shift.

The one-bond scalar couplings involving ^{19}F can be very large, as large as 4000 Hz, depending on the type of the bonded atom. For fluorinated compounds long-range couplings can be observed in ^{13}C NMR spectra over many bonds, up to ^{5}J.

4.4.1.4 ^{29}Si NMR

Organosilicon chemistry has stirred interest in this nucleus. ^{29}Si is slightly more sensitive than ^{13}C. The chemical shift scale runs from −200 to +100 ppm. The shifts are determined by the paramagnetic contribution, and extensive tables can be found. The one-bond scalar couplings to a proton depend on the s character of the atomic orbitals of the Si–H bonds. Due to the negative γ of ^{29}Si, the heteronuclear NOE can be used to monitor flexibility (similar to its use in ^{15}N NMR spectroscopy). Sometimes, the ^{29}Si chemical shift is recorded indirectly via ^{1}H.

4.4.1.5 ^{31}P NMR

^{31}P NMR is frequently measured. Phosphorous is contained in nucleic acids, as well as in many ligands in organometallic systems. ^{31}P is sensitive because of its relatively high frequency and 100% natural abundance. ^{31}P relaxes via CSA, and the optimal instrument for direct detection is a 400 MHz spectrometer. Direct detection of ^{31}P is usually the method of choice. The presence of phosphorous in organic compounds will be indirectly revealed by the presence of scalar couplings in the ^{13}C NMR spectra.

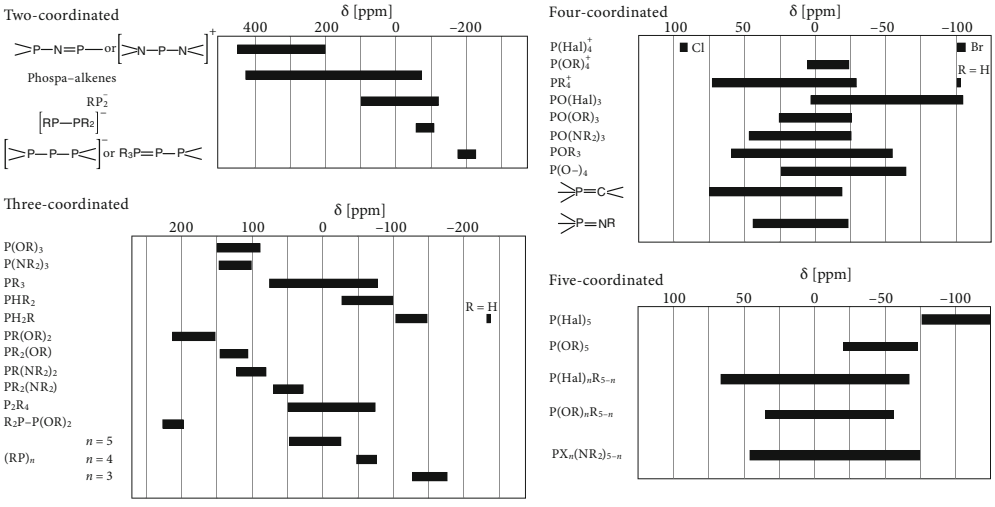

Figure 4.17 Overview of ^{31}P chemical shifts. Compound classes are divided according to the coordination number of ^{31}P. Shifts are referenced to 85% phosphoric acid. Adapted with permission from Mason (1987) *Multinuclear NMR*, Plenum Press.

The ^{31}P chemical shifts cover a wide range, from approximately −400 to +600 ppm. The shift seems to largely depend on the number and type of directly bonded atoms, and much less on the charge or structure. This is indicated in Figure 4.17. Extensive tables for ^{31}P chemical shifts can be found in the literature.

Upon complexation of ^{31}P to a metal, the ^{31}P chemical shift can change dramatically, by more than 100 ppm. Usually the change is proportional to the chemical shift of the uncomplexed species.

Direct (^1J) P–P couplings can be as large as a few hundred hertz. ^{31}P–^{199}Hg scalar couplings of 12 kHz have been measured! ^{31}P–^{13}C coupling may also be large, tens of hertz. In aromatic systems, scalar couplings to ^1H or ^{13}C can propagate over many bonds, and can be fairly large even for long-range couplings. Couplings to ^{31}P can be very confusing in ^{13}C NMR spectra when they are not recognized as such!

4.4.1.6 ^{77}Se NMR

Recording ^{77}Se NMR spectra at natural abundance is difficult, but spectroscopy of enriched samples is sensitive. The chemical shift range is between −900 and +2400 ppm, and the shifts show a strong temperature- and solvent dependence. T1 times are often long (up to 30 s).

4.4.1.7 ^{119}Sn NMR

In principle, three spin-1/2 isotopes of Sn exist: ^{115}Sn, ^{117}Sn, and ^{119}Sn. The latter has the highest abundance and highest frequency, and is therefore used the most. The ^{119}Sn chemical shift covers the range between −2500 and +3000 ppm. Besides direct measurements, also ^{119}Sn,^1H and ^{119}Sn,^{119}Sn correlation experiments have been reported.

4.4.2
Main Group Nuclei with $I > 1/2$

Table 4.6 summarizes the NMR properties of nuclei of main group elements with $I > 1/2$. Unfortunately, some of the chemically most important atoms do not posses suitable NMR properties, and therefore Cl, Br, I, and S are all rarely investigated by NMR. With the exception of ^{6}Li and ^{133}Cs, all alkali and alkaline earth metals have appreciable quadrupole moments and are therefore experimentally not easily accessible. Although some work has been done in this area, we refer the interested reader to specialized literature (e.g., the book by Mason given in the Further Reading section). All group 13 elements except for Tl are quadrupolar nuclei.

Table 4.6 NMR properties of $I > 1/2$ nuclei of main group elements. Adapted from Harris (1986) *Nuclear Magnetic Resonance (A Physicochemical view)*, Longman.

Nucleus	Spin	Abundance (%)	$\gamma/10^7$ (rad T^{-1} s^{-1})	Ξ (MHz)	Quadrupole moment (10^{28} C m^2)	Sensitivity (relative to ^{13}C)	Standard
^{2}H	1	0.02	4.107	15.351	0.0028	0.0082	$CDCl_3$
^{6}Li	1	7.42	3.937	14.717	−0.0008	3.58	LiCl
^{7}Li	3/2	92.58	10.398	38.866	−0.04	1540	LiCl
^{10}B	6/2	19.58	2.875	10.746	0.085	22.3	BF_3
^{11}B	3/2	80.42	8.584	32.089	0.041	752	BF_3
^{14}N	1	99.63	1.934	7.228	0.01	5.69	CH_3NO_2 NH_3
^{17}O	5/2	0.037	−3.628	13.561	−0.026	0.0611	D_2O
^{23}Na	3/2	100	7.080	26.466	0.10	526	NaCl
^{25}Mg	5/2	10.13	−1.639	6.126	0.22	1.54	$MgCl_2$
^{27}Al	5/2	100	6.976	26.077	0.15	1170	$Al(NO_3)_3$
^{33}S	3/2	0.76	2.055	7.681	−0.055	0.0977	$(NH_4)_2SO_4$ Cs_2SO_4
^{35}Cl	3/2	75.53	2.624	9.809	−0.10	20.2	NaCl
^{37}Cl	3/2	24.47	2.184	8.165	−0.079	3.78	NaCl
^{39}K	3/2	93.1	1.250	4.672	0.049	2.69	KCl
^{43}Ca	7/2	0.145	−1.803	6.738	−0.049	0.0492	$CaCl_2$
^{71}Ga	3/2	39.6	8.173	30.551	0.12	320	$Ga(NO_3)_3$
^{73}Ge	9/2	7.76	−0.936	3.498	−0.18	0.622	$(CH_3)_4Ge$
^{75}As	3/2	100	4.595	17.18	0.29	144	$NaAsF_6$
^{79}Br	3/2	50.54	6.723	25.130	0.37	228	NaBr
^{81}Br	3/2	49.46	7.247	27.089	0.31	279	NaBr
^{127}I	5/2	100	5.382	20.117	−0.79	539	KI
^{133}Cs	7/2	100	3.528	13.187	−0.003	273	$CsNO_3$
^{209}Bi	9/2	100	4.342	16.23	−0.38	801	$Bi(NO_3)_3$

Nevertheless, the quadrupole moment of ^{27}Al is low enough such that in favorable cases reasonable spectra can be recorded, and its sensitivity is also comparably high. Most group 14 elements have a spin-1/2 isotope (except for ^{77}Ge, which is difficult to handle). Group 15 elements with exception of ^{31}P and ^{15}N are quadrupolar nuclei, on which (except for ^{14}N) very little work has been done so far. Similarly, the group 16 elements Se and Te are rarely measured. In the following we describe a few nuclei for which more extensive NMR data have been published.

4.4.2.1 ^{2}H NMR

The deuterium nucleus has spin $I = 1$; however, the quadrupole moment is fairly small, so reasonably narrow lines are still obtained. When a single site in a molecule is replaced by deuterium, the corresponding H,D coupling is scaled by 1/6.5 ($\gamma(^2H)/\gamma(^1H)$). In combination with the increased line widths, that means that scalar couplings are usually not resolved. Still, the relaxation times are still reasonably long (T1 times in the range of seconds to milliseconds). The deuterium chemical shift scale is interchangeable with the proton chemical shift scale. This means that the deuterium shift in parts per million will be approximately the same as the proton chemical shift. In contrast, replacing hydrogen by deuterium causes isotope shifts for the NMR signals of neighboring nuclei such as ^{1}H, ^{13}C, and ^{15}N.

The low natural abundance of deuterium results in very long data acquisition times. This situation dramatically changes when isotope enrichment is used, and for 100% deuterated sites 1D spectra can be accumulated within a few minutes. A particularly interesting field for application is studies of reaction mechanisms, which often involve the use of deuterated reagents and the incorporation of deuterium at specific sites. Provided that the proton spectrum has been assigned, measurement of the deuterium spectrum will immediately reveal the site of deuterium incorporation.

4.4.2.2 ^{6}Li and ^{7}Li NMR

^{7}Li is much more abundant than the ^{6}Li. Due to the very small quadrupole moment for ^{6}Li, the lines are extremely narrow, and hence this nucleus is a bit similar to ^{13}C (but the frequency is much lower). ^{7}Li is easily observed at natural abundance. Also here, the quadrupole moment is small, so line widths are often less than 10 Hz. The chemical shift range runs approximately from -9 to $+3$ ppm. Because of its favorable properties, a number of 2D experiments have been done for ^{6}Li, for example, ^{1}H,^{6}Li correlations, ^{6}Li,^{6}Li exchange spectroscopy (EXSY), ^{6}Li,^{6}Li correlation spectroscopy (COSY), and ^{1}H,^{6}Li heteronuclear Overhauser effect spectroscopy (HOESY) experiments. A technical point to note is that since the ^{6}Li and ^{2}H frequencies are so similar, you have to make sure that no ^{2}H stop filters remove the signal from ^{6}Li!

4.4.2.3 ^{10}B and ^{11}B NMR

The two boron isotopes are both quadrupolar nuclei. Because of its higher natural abundance, smaller quadrupole moment, and higher NMR frequency, ^{11}B is the preferred isotope. The sensitivity of ^{11}B NMR spectroscopy is comparably high, allowing one to measure milligram quantities of substance. T1 values are often in the millisecond range and therefore allow rapid pulsing. Depending on the symmetry of the compound, the line widths may be between a few hertz in the most favorable cases and several hundred hertz. The chemical shift scale runs approximately from −100 to +100 ppm. It can be roughly distinguished into four-coordinate sp^3 species (−128 to +20 ppm) and three-coordinate sp^2 species (−8 to +92 ppm). Substituent effects are significant, but are largely tabulated and understood. One-bond scalar couplings to a proton depend on the substituents, but are mostly larger than 100 Hz. The $^1J(^{11}B,^{11}B)$ couplings are between 0 and 20 Hz

While compounds containing a single boron site are simple, the ^{11}B NMR spectra of the polycyclic boranes and carboranes can be very complicated. In favorable cases ^{11}B,^{11}B COSY spectra can be used to assign the signals. Boron NMR is not magic, and can be very useful to determine the structure (and possibly also the dynamics) of organic compounds containing boron. Be aware that standard NMR tubes are made of borosilicate glass, giving rise to a broad background signal. This can be avoided by using Quartz tubes.

4.4.2.4 ^{14}N NMR

^{14}N relaxation is governed by quadrupolar relaxation. Sufficiently narrow lines are only obtained if the symmetry or the mobility or both are high. Due to the short T1 times, pulsing can be done rapidly, but the lines may be too broad to be meaningful. ^{14}N and ^{15}N scales are interchangeable, and because of the importance of nitrogen in natural products, extensive literature on chemical shifts exists. Despite the fact that the ^{14}N isotope is highly abundant (99.7 %), it is not very suitable for NMR spectroscopy because of its broad lines and ^{15}N is therefore the preferred isotope. For chemical shift trends, see Figure 4.15.

4.4.2.5 ^{17}O NMR

Both its low natural abundance and the large quadrupole moment result in unfavorable properties of the ^{17}O nucleus. But because oxygen plays such a prominent role in organic compounds ^{17}O NMR experiments have been performed quite frequently. Line widths are in the range between 20 and 300 Hz. For sensitivity reasons, enrichment with ^{17}O is recommended if possible. Sometimes mechanistic studies are performed, for example, in the presence of $H_2{}^{17}O$, to investigate whether oxygen is picked up from the solvent or transferred intramolecularly.

The ^{17}O chemical shift scale covers more than 2500 ppm, and the shifts are very sensitive to structural changes.

4.5
NMR Experiments with Transition Metal Nuclei

Metal nuclei are of much interest to chemists and biochemists. They form the chemically important units in many catalysts, and they can stabilize protein or RNA structures or form catalytic centers. As mentioned in Section 7.1.1.2, a correlation between chemical reactivity and chemical shifts is often observed since both depend on the gap between the highest occupied molecular orbital (HOMO) and the lowest unoccupied molecular orbital (LUMO) (see Figure 4.18)

Despite the interest in metal chemical shifts, they are often not easily accessible. Their direct measurement is hampered by the often very low frequency. This results in inherently low sensitivity, because for direct detection the signal is related to $\gamma^{5/2}$. Another problem, related to inefficient dipolar coupling with these low values of γ, is the very long T1 relaxation times. They determine how rapidly you can repeat an experiment, and these are often in the minute range for metal nuclei! A further problem is acoustic ringing, which results in severe baseline distortions, but pulse sequences have been developed to deal with that. Often probeheads display background signals from components which contain the element measured. And last not least, not every NMR probe is tunable to those low frequencies! It is therefore not so surprising that the number of studies of metal NMR is comparably low compared with, for example, the number of studies of ^{13}C or ^{31}P NMR.

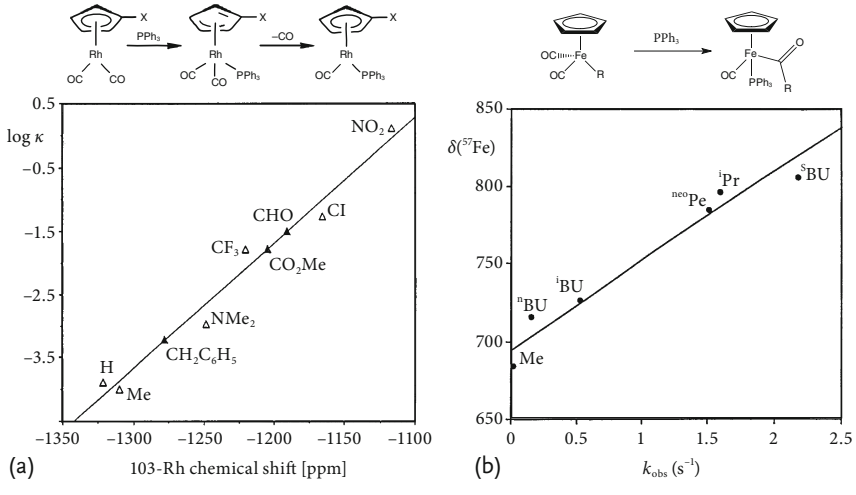

Figure 4.18 Correlation of the ^{103}Rh chemical shifts of substituted (X)CpRh(CO)$_2$ complexes (Cp is cyclopentadiene) with the rate constants of the carbonyl displacement reaction with PPh_3 (a) and the CO insertion rate and the ^{57}Fe chemical shift (b). Reproduced with permission from von Philipsborn (1999) *Chem. Soc. Rev.*, **28**, 95–105.

4.5.1
Technical Aspects of Inverse Experiments with $I = 1/2$ Metal Nuclei

For sensitivity reasons it is much more preferable to use a scalar coupling to a high-frequency nucleus for detection in one of the HSQC- or HMQC-type experiments. In the case of metal hydrides the metal–proton coupling can be used, but often a long-range coupling to a proton is still large enough for reasonable transfer efficiencies in an HMBC-type experiment. The line width must be at least comparable to the coupling used, otherwise the transfer is too inefficient. That is sometimes a problem for labile complexes with broad proton lines. Many complexes possess phosphorous ligands, and hence ^{31}P–X correlations can be measured to indirectly obtain the chemical shift of the X nucleus. In that case a triple-resonance probe with an inner coil tunable to ^{31}P (and ^{1}H) and the outer coil broadband tunable (down to ^{103}Rh) is preferable. Such a probe is unfortunately usually not standard equipment, and you need to go to an NMR center specialized in doing such experiments, or buy one.

From the standpoint of sensitivity, $I = 1/2$ metals with high natural abundances such as ^{103}Rh result in good correlation spectra, irrespective of the absolute frequency of the nucleus. Recording [^{103}Rh,^{1}H] HMQC spectra is likely the only way to obtain chemical shifts at realistic concentrations for Rh. In practice, there are a couple of problems, such as (i) the chemical shift range is unknown, (ii) the pulse length of the 90° pulse is unknown, and (iii) the scalar coupling is unknown. Therefore, in such experiments a little tinkering is necessary before the proper conditions are found. Let us start with the pulse lengths. If possible a highly concentrated standard can be used, which may allow calibration with few pulses. The required relaxation delay may be very long due to the long T1 times. The approximate frequency can be calculated from the proton frequency (see the discussion of indirect referencing in Section 2.5.2). But some nuclei have very broad ranges (more than 10 000 ppm), and therefore the expected chemical shift may be unclear. For that reason we recommend using HMQC-type sequences, which due to the absence of 180° pulses still work over very large ranges. Record an HMQC spectrum with a very large spectral width in the indirect dimension. If you obtain a signal, move the offset of the X-channel a bit to see whether the signal is folded or not. If it remains at the same position, then decrease the spectral width and record the spectrum with more scans over a narrower spectral width to obtain good resolution and hence little uncertainty in the chemical shift. If you do not know the coupling, use a short duration of the delay (e.g., for a 50 Hz coupling) and then increase the delay to obtain maximum signal. This can be done on the first increment, and does not require the recording of a full experiment in each case. Often you can also see the splitting due to the X nucleus in the proton (or ^{31}P) spectrum.

It all sounds complicated but after a little training you will be able to measure good spectra, if your compound has suitable properties. In Figure 4.19 we display [^{119}Ag,^{1}H] and [^{57}Fe,^{31}P] HMQC spectra. They have all been recorded in a few hours. Direct detection of these nuclei would not have been possible at the used concentrations.

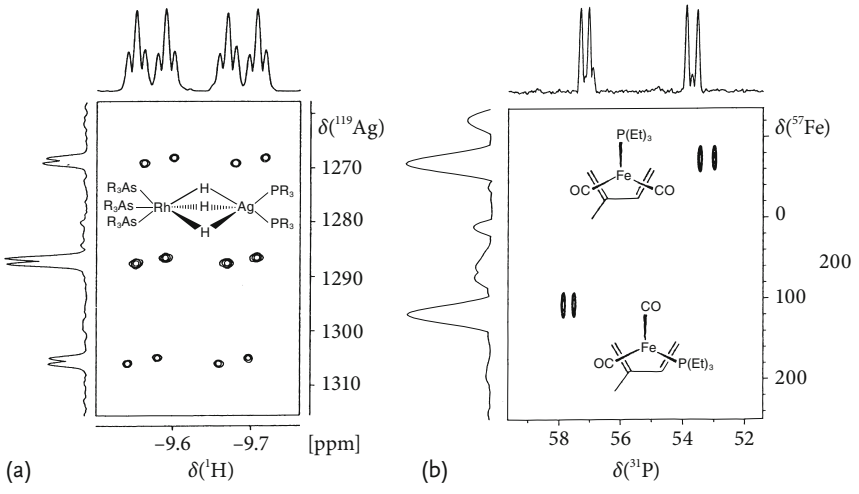

Figure 4.19 Examples of inverse-detection experiments for silver (a) and iron (b) complexes. Reproduced with permission from Nanz (1993) PhD thesis, Zurich.

Finally, we would like to make one more remark. If you want to record the pulse lengths or tune the probe for a so-far unknown nucleus, start from the values of a nucleus with a similar γ that you have measured before. For example, the frequency of ^{113}Cd is similar to that of ^{13}C. Therefore, start tuning and matching of the probe from the settings for ^{13}C. Similarly, the 90° ^{113}Cd pulse has a length similar to that for ^{13}C.

Table 4.7 summarizes the NMR properties of spin-1/2 transition metal nuclei.

Finally, we would like to make a few remarks about some nuclei that have been looked at more frequently. Some of the transition metal nuclei posses comparably high frequencies, for example, ^{113}Cd, ^{119}Sn, ^{199}Hg, ^{195}Pt, and ^{205}Tl. ^{199}Hg and ^{113}Cd have similar NMR properties, but need to be enriched due to their low natural abundance. ^{113}Cd has been used a lot in BioNMR experiments to replace the NMR-silent Zn or Ca nuclei (the radii of Cd^{2+}, Zn^{2+}, and Ca^{2+} are similar). The chemical shift range is large and sensitive to the coordination geometry and type of coordinating atom. The ^{205}Tl nucleus has favorable NMR properties. But on most probeheads the frequency is in the blind region, and the probe cannot be tuned to it (like for ^{19}F). ^{195}Pt has quite favorable NMR properties. It can be measured directly or via indirect detection. It is important because of the presence of Pt in catalysis and medicinal chemistry. The ^{195}Pt chemical shift is very temperature sensitive (this is the case with many transition metal nuclei).

^{57}Fe and ^{109}Ag are both important in chemistry, but their low frequencies results in very long T1 times. Therefore, they are best detected via ^{1}H or ^{31}P if possible. ^{109}Ag is much more abundant than ^{57}Fe. ^{89}Y and ^{103}Rh are both spin-1/2 nuclei, but because of their low frequency they can only be measured indirectly, and the same is true for most other nuclei in Table 4.7.

Table 4.7 Properties of NMR-active spin-1/2 metal nuclei. Adapted from Harris (1986) *Nuclear Magnetic Resonance (A Physicochemical view)*, Longman.

Nucleus	Abundance (%)	$\gamma/10^7$ (rad s^{-1} T^{-1})	Ξ (MHz)	Sensitivity (relative to ^{13}C)	Reference
^{57}Fe	2.2	0.866	3.238	0.0042	$Fe(CO)_5$
^{77}Se	7.6	5.12	19.071 523	3.0	$SeMe_2$
^{89}Y	100	−1.316	4.917	0.68	$Y^{3+}(aq)$
^{103}Rh	100	−0.846	3.172 310	0.18	$Rh(acac)_3$
^{109}Ag	48.2	−1.250	4.653 623	0.28	$Ag^{+}(aq)$
^{113}Cd	12.3	−5.955	22.193 173	7.7	$Cd(ClO_4)_2$
^{119}Sn	8.6	−10.021	37.290 662	26	$SnMe_4$
^{125}Te	7.0	−8.498	31.549 802	13	$TeMe_4$
^{171}Yb	14.3	4.712	17.61	4.5	$Yb(Cp^*)_2(THF)_2$
^{183}W	14.4	1.120	4.161 733	0.061	Na_2WO_4
^{187}Os	1.6	0.616	2.282 343	0.0011	OsO_4
^{195}Pt	33.8	5.768	21.414 376	19	$Na_2[PtCl_6]$
^{199}Hg	16.8	4.815	17.910 841	5.6	$Hg(ClO_4)_2$
^{205}Tl	70.5	15.589	57.633 833	791	$Tl^{+}(aq)$
^{207}Pb	22.6	5.540	20.920 597	11	$PbMe_4$

Note: Cp* – 1,2,3,4,5-pentamethylcyclopentadiene, acac – acetylacetonate, THF – tetrahydrofuran

4.5.2
Experiments with Spin $I > 1/2$ Transition Metal Nuclei

Depending on the quadrupole moment the line widths of signals from quadrupolar metals can be very large, often tens of kilohertz! This, of course, severely limits the precision with which chemical shifts can be determined, and excludes the use of 2D NMR spectroscopy. When the signal line width is in the range of the spectral width, phasing becomes very challenging! This problem may be enhanced by the acoustic ringing effect. As described before, the line widths for quadrupolar nuclei are related to the symmetry of the ligand field, and for highly symmetric complexes reasonably sharp signals may still be obtained. This is demonstrated in Figure 4.1, depicting ^{59}Co spectra of both a highly symmetric and an asymmetric cobalt complex.

Large quadrupolar couplings result in short T1 times, sometimes allowing the experiment to be repeated very rapidly, often with a relaxation delay of a few milliseconds, so even broad lines may be recorded within reasonable measuring times. To measure such spectra, start with the largest spectral width that you can use. It helps if you switch off oversampling, because then the spectral width can be larger (often 100 000 Hz), depending on the speed of the digitizer. If you see a signal, shift the offset, for example, by 1000 Hz. If the signal remains at the same position, it is

Table 4.8 NMR properties of transition metal nuclei with $I > 1/2$. Adapted from Harris (1986) *Nuclear Magnetic Resonance (A Physicochemical view)*, Longman.

Nucleus	Spin	$\gamma/10^7$ (rad T^{-1} s^{-1})	Abundance (%)	Quadrupole moment (10^{28} C m^2)	Ξ (MHz)	Receptivity (relative to ^{13}C)	Standard
^{51}V	7/2	7.045	99.76	−0.05	26.336	2170	$VOCl_3$
^{53}Cr	3/2	−1.512	9.55	0.038	5.651	0.489	K_2CrO_4
^{55}Mn	5/2	6.608	100	0.11	24.70	997	$KMnO_4$
^{59}Co	7/2	6.317	100	0.38	23.61	1570	$K_3[Co(CN)_6]$
^{61}Ni	3/2	−2.394	1.19	0.16	8.949	0.231	$Ni(CO)_4$
^{91}Zr	5/2	−2.496	11.23	−0.21	9.3298	6.04	$Zr(Cp)_2Cl_2$
^{95}Mo	5/2	1.750	15.72	0.11	6.542	2.92	Na_2MoO_4
^{99}Ru	5/2	−1.234	12.72	0.076	4.614	0.827	$K_4[Ru(CN)_6]$

not folded. Only then can you trust what you see. Otherwise, you may pick up some background from the probe which is unrelated to the nucleus of interest. To check for possible background signal, run the experiment with and without the sample in the magnet.

Table 4.8 lists properties of a selection of metal nuclei with $I > 1/2$.

In general, the chemical shift ranges of transition metal nuclei can be very large (e.g., more than 13 000 ppm for ^{59}Co). The ^{51}V nucleus is rather sensitive, and also possess a comparably small Q, and is therefore the most suitable nucleus within this selection. Many ^{51}V chemical shifts are tabulated for coordination compounds of vanadium or for vanadates. The high receptivity of the ^{59}Co nucleus partially compensates for the broad lines due to efficient quadrupolar relaxation. Moreover, the short T1 times allow rapid pulsing. The medium-sized Q and the high receptivity of ^{55}Mn also permit direct detection of that nucleus, but the line widths can easily have values of tens of kilohertz. Again, we recommend the interested reader consult the literature, and the corresponding chapters in the book by Mason provide a good introduction (see Further Reading).

4.6 Problems

4.1. Describe the following isotopes with respect to their suitability for NMR measurements and their sensitivity (low to high): ^{3}H, ^{2}H, ^{16}O, ^{14}N, ^{57}Fe, ^{29}Si, ^{28}Si, ^{10}B, ^{32}S, ^{31}P.

4.2. Give the number of signals in the ^{13}C spectra of the following aromatic compounds:

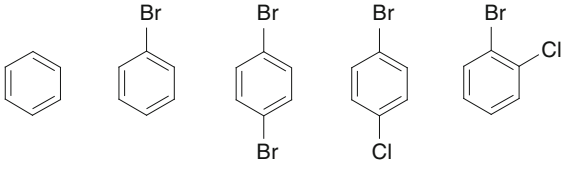

4.3. Similarly, calculate the number of signals in the ^{13}C spectra for the following compounds:

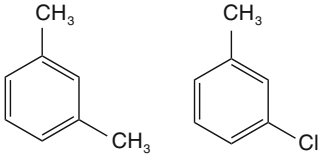

$H_3C–F$ $D_3C–OH$

4.4. Assign the following chemical shifts to the highlighted C atoms: 55.5/108.2/120.8/126.5/174.4 ppm

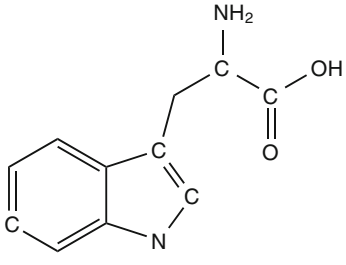

4.5. Similarly assign the following chemical shifts to the C-Atoms highlighted in the structures: 0/15.0/20.5/32.9/59.1/73.4/96.0/162.3/198.4 ppm.

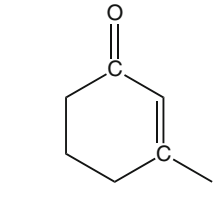

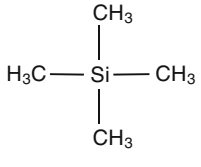

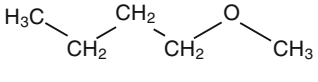

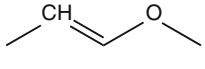

Further Reading

Mason, J. (1987) *Multinuclear NMR*, Plenum Press.

Berger, S., Braun, S., and Kalinowski, H.-O. (1997) *NMR Spectroscopy of the Non-Metallic Elements*, John Wiley & Sons, Ltd.

Pregosin, P.S. (2012) *NMR in Organometallic Chemistry*, Wiley-VCH Verlag GmbH.

Kalinowski, H.-O., Berger, S., and Braun, S. (1988) *Carbon-13 NMR Spectroscopy*, John Wiley & Sons, Ltd.

von Philipsborn, W. (1999) Probing organometallic structure and reactivity by transition metal NMR spectroscopy. *Chem. Soc. Rev.*, **28**, 95–105.

Nanz, D. (1993) Indirekte Detektion in der NMR Spektroskopie metallorganischer Systeme, PhD thesis, Zurich.

Wehrli, F.W. and Wirthlin, T. (1983) *Interpretation of Carbon-13 NMR Spectra*, John Wiley & Sons, Ltd.

Part Two
Theory of NMR Spectroscopy

In this part we describe the theory behind the NMR experiments in more depth. To begin with, let us recapitulate some of the basic facts we introduced in previous chapters. We have learned that a magnetic field induces a *macroscopic* magnetic moment in the sample. This dipole moment can be understood in terms of *microscopic* magnetic moments that stem from individual nuclei. These magnetic moments are weakly aligned in the presence of a magnetic field, and in turn are related to the nuclear spin. Furthermore, we have learned that we can rotate the macroscopic magnetic moment, also called magnetization, into a plane orthogonal to the external magnetic field by applying RF pulses. Once magnetization is in the transverse plane, it starts to precess about the axis of the magnetic field with a particular frequency that is influenced by the gyromagnetic ratio γ, the chemical environment (the chemical shift δ), and interactions with neighboring nuclear spins (scalar coupling).

While this picture is sufficient for a basic understanding of the principle of pulsed NMR spectroscopy as required for the interpretation of simple 1D NMR spectra, it fails to explain the more complicated techniques that will be presented in Part Five. For example, the magnetization flow (coherence transfer) in multidimensional correlation spectroscopy can only be followed when theoretical tools describing individual spins are available. Once we have developed a more detailed picture of what an individual spin really is, we will extend our description to large collections of spins, the spin ensemble.

The concept of spin can only be properly described in quantum mechanical terms. As we neither assume nor expect that the reader has profound knowledge of quantum mechanics, and because an accurate introduction to the field of quantum mechanics is clearly beyond the scope of this book, we largely refrain from a detailed mathematical treatment. Instead, we try to present a pictorial view whenever possible referring to analogues of classical physics, and use a vector representation. For readers interested in the formal quantum mechanical description, we introduce the basic concepts briefly in Chapter 9, however without claim of completeness.

At the start of this part we will briefly look at magnetism as a general property of matter. We will then turn from the macroscopic level to the microscopic view and look at the spin and the related magnetic moment considering only a single nucleus. For simplicity we will initially disregard any spin–spin interaction, and

only describe the interaction with the external magnetic field. Subsequently, we will look at nuclear magnetism at a macroscopic level, as present in a large collection of identical spins, again disregarding possible interactions among the spins. Apart from the collective motion in the static field, we will examine the action of RF pulses. Then we will turn to the fundamental concepts of chemical shift, as well as scalar and dipolar coupling between spins. As we will see later, these couplings form the basic interactions through which magnetization is shuffled between different nuclei in multipulse and multidimensional NMR experiments. Finally, we will introduce the so-called product operator formalism by which it becomes possible to describe an NMR experiment in much detail in a simple and elegant way, however without a detailed derivation of the formalism.

5
Nuclear Magnetism – A Microscopic View

5.1
The Origin of Magnetism

Magnetism describes how materials respond to a magnetic field. Since all materials interact with magnetic fields, magnetism is a general property of materials. However, only a few materials (e.g., iron, cobalt, and nickel) posses the most distinct form of magnetism that is encountered in daily life. Such materials are called ferromagnetic, a property that most of us intuitively associate with magnetism. They are the materials from which permanent magnets are made. Most materials and substances, however, do not possess permanent magnetism, but a magnetic moment can be *induced* in them:

$$M = \chi H \tag{5.1}$$

in which M is the magnetization (the magnetic dipole moment per unit volume), χ the magnetic susceptibility (a dimensionless, material-specific constant), and H the applied magnetic field strength. Note that in NMR the magnetic field is described by the magnetic field or magnetic flux density denoted by the symbol B. For a short discussion on the difference between the H field and the B field, see Appendix A.1. Materials with $\chi > 0$ are called *paramagnetic*, and those with $\chi < 0$ are called *diamagnetic*. The magnetic susceptibility determines the way an object interacts with a magnetic field (Figure 5.1). Paramagnetic materials tend to increase the field strength within the object, diamagnetic substances will decrease it.

If we now look at the origin of magnetism we realize that the magnetism of materials is due to microscopic dipole moments (see also Appendix A.2) stemming from the electron's orbital angular momentum, the electron spin, and the nuclear spin (Figure 5.2). All three sources have in common that they rely on the basic fact that a moving charge gives rise to a magnetic field. In the case of the electron's angular momentum, the effect can be understood using classical physics in analogy to the magnetic field produced by the current of a conducting loop.

The magnetism due to the spin is a bit more difficult to understand. The idea of a spinning charge proves to be too simple. For example, the uncharged neutron

Applied NMR Spectroscopy for Chemists and Life Scientists, First Edition. Oliver Zerbe and Simon Jurt.
©2014 WILEY-VCH Verlag GmbH & Co. KGaA. Published 2014 by WILEY-VCH Verlag GmbH & Co. KGaA.

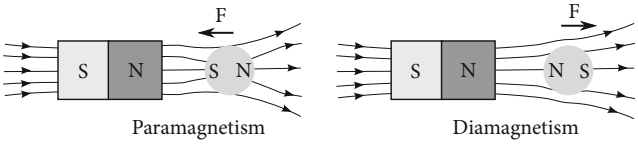

Figure 5.1 Paramagnetism versus diamagnetism. In paramagnetic objects a magnetic moment is induced parallel to the direction of the applied field. The object is attracted by the magnet. In diamagnetic objects the induced magnetic moment opposes the direction of the applied field. Such an object experiences a repulsive force.

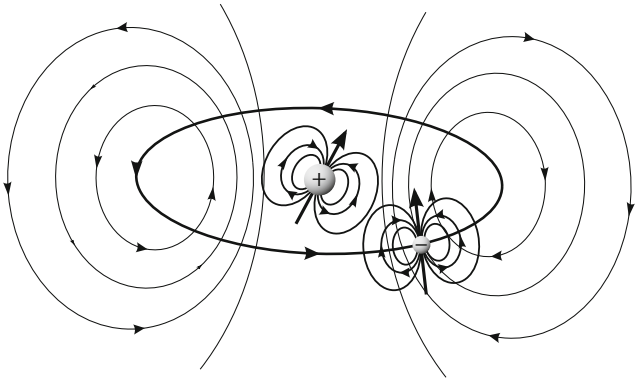

Figure 5.2 Origin of magnetism. Magnetic fields due to the orbital motion of the electron, the electron spin, and the nuclear spin.

also possesses a magnetic moment, which can only be explained by considering the neutron's substructure. However, we leave this question to physicists and will not go into that topic in more depth.

About 95% of the magnetism of ferromagnetic materials is due to the electron spin. The remaining 5% is due to the electron's orbital momentum and the nuclear spin, whereby the contribution of the nuclear spin is very much smaller than that of the electron's orbital momentum and thus is often considered to be negligible. Nevertheless, it is this small induced magnetism that gives rise to the NMR phenomenon and to which we will give our attention in the following sections. But before we do that, let us have a closer look at the property of spin.

5.2
Spin – An Intrinsic Property of Many Particles

Physicists realized early on that a correct description of atomic absorption spectra required an additional variable for the electrons. In 1924 Wolfgang Pauli attributed an additional quantum number to the electron to provide the basis for the exclusion principle. To explain this additional degree of freedom for the electron, in 1925 George E. Uhlenbeck and Samuel A. Goudsmit proposed the concept of an electron

spin. Such a spin could account for the two possible senses of rotation that an electron could posses when rotating about its own axis, so to say that it has two values for its angular momentum. However, attempts to incorporate this as solutions to the wave functions in a quantum mechanical description proved to be impossible. A breakthrough was achieved in 1928 when Paul A.M. Dirac demonstrated that spin is a result of the relativistic treatment of electrons, and that it presents an intrinsic property like the mass or the charge of a particle.

Excursus 5.1: A Historical Review of Spin

The Einstein–de Haas experiment (1915) was intended to prove Ampere's idea (1820) that magnetism is caused by molecular currents. The idea behind the experiment is that when magnetism is really caused by orbiting electrons, as a consequence of conservation of angular momentum, an iron rod should start to rotate when magnetization (the rotational sense of the electrons) is inverted by means of an external magnetic field. The experiment showed that this is indeed the case, and also quantitatively provided almost the correct predicted value of $2m_e/e$. However, more precise measurements carried out soon thereafter provided values that were only half as large. For some time (until the discovery of the electron spin by Uhlenbeck and Goudsmit in 1925) this was called the "gyromagnetic anomaly."

The discovery of the spin by Uhlenbeck and Goudsmit was motivated by the observation of a fine splitting in atomic spectra when the atoms were exposed to a magnetic field, called the anomalous Zeeman effect. In contrast to the "normal" Zeeman effect, which was understood in terms of a spatial quantization of the electron's orbital magnetic moment, the anomalous Zeeman effect could not be explained at that time. Proof of this spatial quantization of atomic magnetic moments was the ultimate goal of the Stern–Gerlach experiment (1921). Ironically, the magnetic moment of silver atoms which Stern and Gerlach used in their experiment is not due to the orbital angular momentum of electrons but due to the electron spin, as became evident with the discovery of the electron spin (and the Schrödinger model (1926)).

In order to explain qualitatively the anomalous Zeeman effect, Uhlenbeck and Goudsmit postulated the presence of electron spin in a short article in *Naturwissenschaften* in 1925, as well as in a *Nature* article entitled "Spinning electrons and the structure of spectra." It is worth mentioning that they wished to withdraw the former article after they received serious criticism from Hendrik A. Lorentz, whom they had asked to comment on the paper, but "fortunately for them" it was too late. It is also worth noting that they made explicit reference to an article by Arthur H. Compton (1921) in which the concept of electron spin had already been proposed, however without attracting much attention. Finally, in this context it is also important to mention the 20-year-old Ralph Kronig, who presented the idea of a spinning electron to Wolfgang Pauli and Niels Bohr just about 1 year before the seminal article of Uhlenbeck and Goudsmit. Pauli and

Bohr, however, strongly dismissed the idea because of a discrepancy by a factor of 2 that occurred in the calculation of the fine structure of atomic hydrogen spectra, and because with the electron being treated as a classical sphere, the electron would have to rotate with a velocity much faster than that of light, and thus Kronig finally abandoned his idea of a spinning electron.

Of course, this criticism also applies to the article of Uhlenbeck and Goudsmit, and likely was the reason why they wanted to withdraw it. This problem was resolved by Llewellyn H. Thomas, who in 1926 showed that the factor-of-2 discrepancy disappears when relativistic effects are taken into account. Finally, in 1928 Paul A.M. Dirac presented the relativistic wave function for the electron, in which the spin and its properties appear quite "naturally."

To conclude, the Einstein–de Haas effect it due to the electron spin. For us, as nonphysicists, it is quite remarkable to note that the decision as to whether the effect is caused by an orbiting electron or by a "spinning" charge only depends on a factor of 2! It is also quite surprising that although we are permanently told by physicists that there is *no* classical analogue of spin in the real world, in essence the Einstein–de Haas experiment demonstrates that the spin must be related to something we would call ordinary angular momentum.

However, spin is not an exclusive property of electrons and is also found for protons and neutrons. In fact, spin is a fundamental, nonvariable, and characteristic property of basic particles (see Table 5.1). It is specified by the spin quantum number s, which may adopt values of $N/2$, with $N = 0, 1, 2, 3, \ldots$ In the case of the electron, s is $1/2$.

Similar to the classical spin angular momentum, the spin is a vector quantity. The Stern–Gerlach experiment that is described below, however, demonstrates that only *discrete* values of the spin components can be observed. For a particle possessing spin quantum number s, there are $2s + 1$ possible values (at a distance of $\hbar$) for its components (s_x, s_y, s_z), according to the series

$$-s\hbar, -s\hbar + \hbar, -s\hbar + 2\hbar, \ldots, s\hbar$$

with $\hbar$ denoting the Planck constant h (6.626×10^{-34} J s) divided by 2π. Thus, in the case of a spin-1/2 particle, the z component of the spin can adopt the values

Table 5.1 Spin of some basic particles.

Particle	Charge e	Spin s
Electron	-1	1/2
Quark	$+2/3$ or $-1/3$	1/2
Proton	$+1$	1/2
Neutron	0	1/2
Photon	0	1

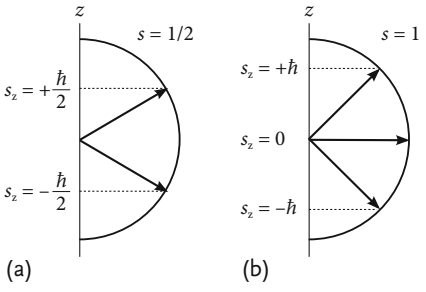

Figure 5.3 Spatial quantization of spin angular momentum for a spin-1/2 particle (a) and a spin-1 particle (b).

$\pm\frac{\hbar}{2}$, whereas for a spin-1 particle the z component can adopt the values $\pm\hbar$ and zero as depicted in Figure 5.3.

Furthermore, the components of the spin angular momentum obey the so-called uncertainty principle.[1)] This means, knowing one component of the spin precisely, we cannot specify the other components. In other words, it is impossible to precisely specify more than one component of the spin simultaneously.

Moreover, theoretical considerations show that the total spin angular momentum S ($S = \sqrt{s_x^2 + s_y^2 + s_z^2}$) is equal to $\hbar\sqrt{s(s+1)}$, a value that surprisingly is always larger than the maximum observable spin component $\hbar s$, which results in the often heard statement "the spin is never fully aligned to any axis."

Although the spin cannot be described by any rotation in a classical sense, its properties display strong similarity to those of a classical angular momentum. In the analogous classical rotor, a rotating sphere of mass m, depicted in Figure 5.4a, is characterized by its angular momentum $\boldsymbol{L}$ along the axis of rotation. For comparison, a spin-1/2 particle with $s_z = \hbar/2$ is shown by the vector model in Figure 5.4b. Therein the vector of total spin angular momentum $\boldsymbol{S}$ is located on the surface of a cone. The cone's central axis corresponds to the direction, in which the spin component is assumed to be known (here the z axis). Thus, the projection of $\boldsymbol{S}$ onto that axis yields the known component of the spin (here $s_z = \hbar/2$). The uncertainty of the residual (here transverse) spin components is indicated by the cone. The residual component of the total spin must be somewhere in the xy plane, but we do not (cannot) know where. If we, for example, measured the x component, the state would collapse and the cone would rotate by 90° to the $+x$ axis or $-x$ axis depending on whether $+\hbar/2$ or $-\hbar/2$ is obtained for s_x.

The similarities but also important differences between properties of spins and classical rotors are summarized in Table 5.2.

1) The uncertainty in spin angular momentum is not a result of inappropriate experimental technique. It follows directly from fundamental rules of quantum mechanics, a fact that was difficult to accept even for many great scientists (e.g., Albert Einstein), who made great efforts to overcome the uncertainty by searching for additional, so-called "hidden" variables – however without success.

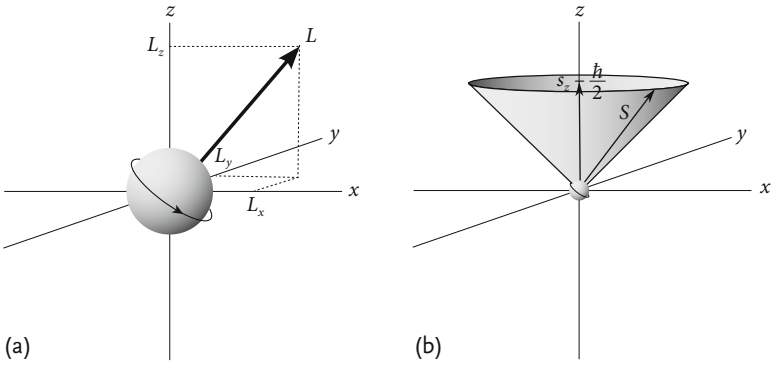

Figure 5.4 Comparison of a classical angular momentum $\boldsymbol{L}$ (a) and a nonclassical spin angular momentum $\boldsymbol{S}$ of a spin-1/2 particle in a state with $s_z = +\frac{1}{2}\hbar$ (b).

Table 5.2 Comparison of important properties of classical rotors and the angular momentum of spins.

	Angular momentum – classical rotor	**Angular momentum – spin**
Magnitude	L: Depending on the rotation frequency, the angular momentum can adopt *any* value. The angular momentum is larger for higher angular frequencies.	S: The total spin angular momentum is an absolute quantity with the value $\hbar\sqrt{s(s+1)}$. It depends on the spin quantum number s of a specific particle and cannot be changed.
Components	L_x, L_y, L_z: The angular momentum can be decomposed into its components L_x, L_y, and L_z. The magnitude of these can be defined in absolute terms.	s_x, s_y, s_z: The components of spins can only adopt discrete values of $-s\hbar$ to $+s\hbar$ in integer increments of $\hbar$. The magnitudes of these cannot be determined independently. They follow the uncertainty principle.
Rotating the coordinate system	The coordinate system can always be chosen such that the total angular momentum is aligned along a unique axis.	Irrespective of the choice of the coordinate system, the total angular momentum does not coalign with a unique axis. Therefore, it is not because of an improper choice of the coordinate system that the measured spin will always adopt values smaller than the total spin.

The spin itself is a quantity that is difficult to measure experimentally. Qualitatively it is confirmed by the Einstein–de Haas effect, which shows that the electron spin is indeed related to a kind of angular momentum. Much more experimentally accessible is the magnetic dipole moment, which is closely related to the spin. The magnetic dipole moment is the property on which the NMR phenomenon relies, and which was examined by Otto Stern and Walter Gerlach in their famous experiment – now known as the Stern–Gerlach experiment

5.3
Experimental Evidence for the Quantization of the Dipole Moment: The Stern–Gerlach Experiment

If particles have intrinsic magnetism it should be possible to influence a particle beam by the presence of a magnetic field. This was demonstrated in the famous Stern–Gerlach experiment. The idea behind this experiment is that a particle with a magnetic dipole moment ($\boldsymbol{\mu}$) placed in an inhomogeneous magnetic field experiences a force (F) that is proportional to the field gradient ($\boldsymbol{B}_{\text{grad}}$) and the dipole component in the direction of the gradient ($\mu || B_{\text{grad}}$) (Figure 5.5).

A beam of particles with random orientations of their dipole moments should be diffracted in a continuous band of directions when passing through a inhomogeneous magnetic field. Although this experiment was done originally in 1922 by Stern and Gerlach with silver atoms, it was later also performed with protons.

The protons are displaced by the magnetic field gradient by equal amounts in two opposite directions along z (Figure 5.6a). From that we can conclude that the z component of the proton's magnetic dipole moment can only adopt two discrete values of same magnitude but opposite direction. Of course, the same applies for the y component. Although the experiment actually determines magnetic dipole moments, we will use the proportionality of the dipole moment and spin and refer to the "spin" with the symbol I.

Now we can examine what happens if we place additional magnets in the beam paths as illustrated in Figure 5.6b. For example, if we put a second magnet in the upper path with exactly the same orientation as the first magnet, all protons will be displaced by the same amount, and again in the $+z$ direction. From that we can conclude if we know the spin component of a proton in one direction in space, a measurement of the spin component in that direction will always provide the known component. In contrast, if the second magnet is placed orthogonal to the first one, the beam is again split into two components of equal intensity. Furthermore, if we place a third magnet whose poles are along z in one of these latter two paths, we will observe an equal splitting into two components along z. This means if we know the spin component of a proton according to one direction in space, a measurement of the spin component *orthogonal to that direction* will provide the values $\pm\frac{1}{2}\hbar$ with equal probabilities. For example, if we know the proton

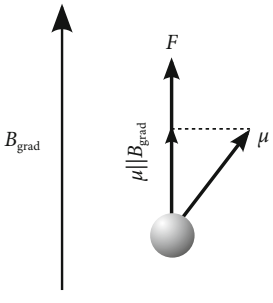

Figure 5.5 Force acting on a magnetic dipole moment in an inhomogeneous magnetic field.

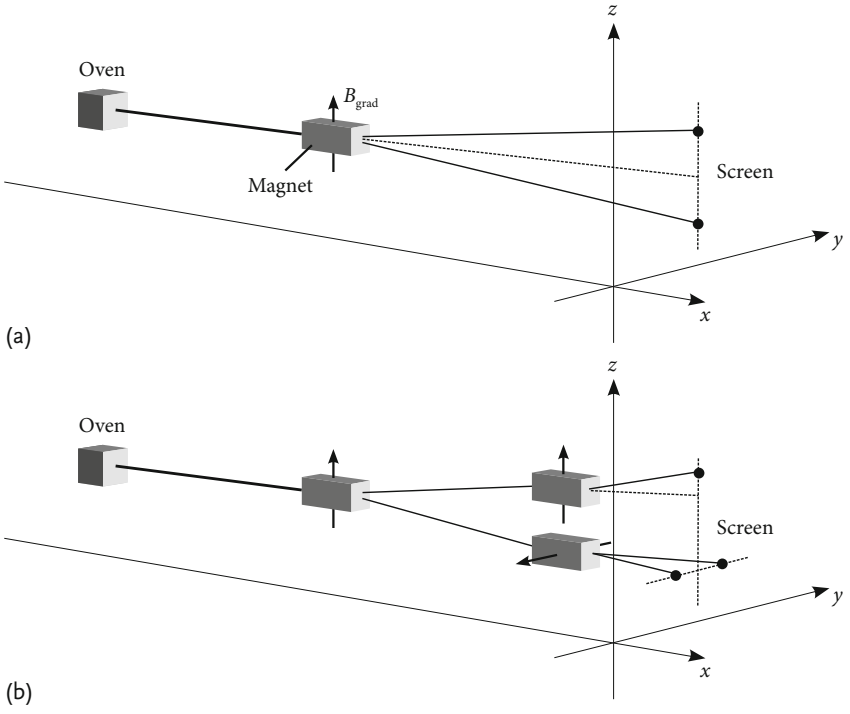

Figure 5.6 The Stern–Gerlach experiment. Diffraction of a beam of protons in an inhomogeneous magnetic field.

has $I_z = -\frac{1}{2}\hbar$, a measurement of I_y will result in 50% of cases in a value of $+\frac{1}{2}\hbar$ and in 50% of cases in a value of $-\frac{1}{2}\hbar$. Moreover, by measuring an orthogonal component (here I_y), we lose the information about the former known component (here I_z). This experiment thereby confirms our statement above that spin can only be known in one direction precisely. The (small) world of quantum physics can sometimes be rather confusing.

5.4
The Nuclear Spin and Its Magnetic Dipole Moment

Most elements have stable isotopes with nuclei that possess spin. In the case of nuclear spin, the symbol I is used instead of s. Similarly, the *nuclear spin quantum number* I may adopt any positive integer multiple of $\frac{1}{2}$, thus

$$I = \frac{1}{2}N \quad \text{with} \quad N = 0, 1, 2, 3, \ldots \tag{5.2}$$

and the spin component that can be observed for a nucleus with spin I is given by the series

$$-I\hbar, -I\hbar + \hbar, -I\hbar + 2\hbar, \ldots, I\hbar \tag{5.3}$$

The nuclear states associated with these possible values of the spin components are specified by the *magnetic quantum number m*. According to the series (5.3), we can distinguish $2I + 1$ basic spin states for any component. Of particular interest are the spin components along the z axis, associated with the quantum number m_z. This is because the coordinate system is chosen such that the external static magnetic field is per definition aligned with the z axis. We have

$$m_z = -I, -I + 1, -I + 2, \ldots, I \tag{5.4}$$

It is impossible to predict the spin quantum number I of a nucleus. However, the following rules indicate which values of I are possible for a certain isotope:

- Nuclei with an odd mass will have a half-integer value for the spin ($I = 1/2, 3/2, 5/2, \ldots$).
- Nuclei with an even mass will have an integer spin number ($I = 0, 1, 2, 3, \ldots$).
- If the nucleus is composed of both an even number of protons and an even number of neutrons, the spin is zero ($I = 0$). A famous example is the ^{12}C isotope (six protons, six neutrons).
- If the number of protons and neutrons are both odd, the nucleus will have an integer spin ($I = 1, 2, 3, \ldots$) (e.g., ^{2}H (a proton and a neutron) has spin 1).

As we saw in Chapter 2 the most important nuclei in NMR spectroscopy (^{1}H, ^{13}C, ^{15}N, ^{31}P, and ^{19}F) all posses spin 1/2 (see Table 5.3). Therefore, we will briefly summarize the properties of spin-1/2 nuclei:

- Spin quantum number: $I = 1/2$
- Spin components: $-\frac{1}{2}\hbar$ and $+\frac{1}{2}\hbar$ (e.g., $I_z = \pm\frac{1}{2}\hbar$)
- Magnetic quantum number: $m_z = \pm\frac{1}{2}$.

The spin states associated with $m_z = +\frac{1}{2}$ are called the α state and the ones associated with $m_z = -\frac{1}{2}$ are called the β state.

The *magnetic dipole moment* μ of a nucleus is related to the spin by

$$\boldsymbol{\mu} = \gamma \boldsymbol{I} \tag{5.5}$$

Therein γ is the *gyromagnetic ratio*, an isotope-specific constant (see Table 5.3), and can adopt positive or negative values, corresponding to a parallel or an antiparallel alignment of the magnetic dipole moment with the spin. Since the spin is quantized, the magnetic moment is also quantized. The component of the dipole moment along an axis can assume values of $\gamma\hbar m$. For the magnetic moment along the z axis, we find, for example,

$$\mu_z = \gamma\hbar m_z \tag{5.6}$$

Table 5.3 NMR-relevant properties of the most important nuclei.

Isotope	Spin I	Natural abundance (%)	γ (10^7 rad s^{-1} T^{-1})	Sensitivity (relative to ^{13}C)	NMR frequency (MHz) (^{1}H = 100 MHz)
$^{1}_{1}$H	1/2	99.99	26.752 220 5	5870	100
$^{2}_{1}$H	1	0.01	4.106 629 14	0.006	15.350 609
$^{10}_{5}$B	3	19.9	2.874 679 52	23	10.743 658
$^{11}_{5}$B	3/2	80.1	8.584 707	777	32.083 974
$^{12}_{6}$C	0	98.9	–	–	–
$^{13}_{6}$C	1/2	1.1	6.728 286	1.0	25.145 020
$^{14}_{7}$N	1	99.64	1.933 779 8	5.9	7.226 317
$^{15}_{7}$N	1/2	0.36	−2.712 618 8	0.02	10.136 767
$^{16}_{8}$O	0	99.76	–	–	–
$^{17}_{8}$O	5/2	0.04	−3.628 06	0.07	13.556 457
$^{19}_{9}$F	1/2	100	25.162 33	4890	94.094 011
$^{29}_{14}$Si	1/2	4.69	−5.319 03	2.2	19.867 187
$^{31}_{15}$P	1/2	100	10.8394	391	40.480 742

Thus, for a spin-1/2 nucleus, there are two possible values for its dipole moment along z. In the absence of an external magnetic field, these two orientations are energetically equivalent. However, when an external field along z is applied, the two orientations of the dipole moment become energetically split. This is called the *Zeeman effect*.

5.5 Nuclear Dipole Moments in a Homogeneous Magnetic Field: The Zeeman Effect

In an NMR experiment the nuclei are placed in a very strong homogeneous external magnetic field $\boldsymbol{B}$. As mentioned above, by definition it points in the direction of the z axis. Therefore, the x component and the y component of the external field are both zero, and $\boldsymbol{B}$ has a z component solely. The external field is usually denoted as $\boldsymbol{B}_0$ and its strength (which equals the z component) is given in units of tesla (T):

$$\boldsymbol{B}_0 \equiv \begin{pmatrix} 0 \\ 0 \\ B_0 \end{pmatrix} \tag{5.7}$$

In classical physics the potential energy of a magnetic dipole $\boldsymbol{\mu}$ in a magnetic field $\boldsymbol{B}$ is given by the scalar product (see Excursus 5.2):

$$E = -\boldsymbol{B} \cdot \boldsymbol{\mu} \tag{5.8}$$

If the magnetic field has only a z component, the energy is simply

$$E = -B_z \mu_z \tag{5.9}$$

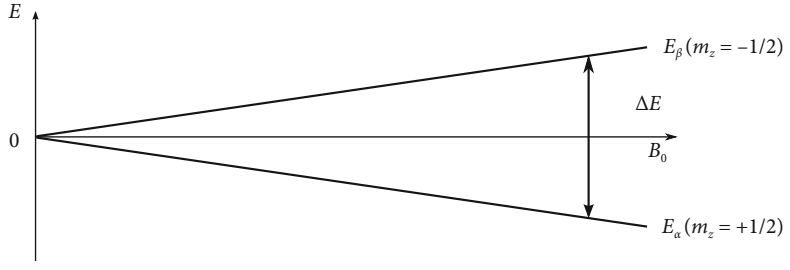

Figure 5.7 Zeeman splitting. Dependence of the energies of the α and β states of spin-1/2 nuclei on the magnetic field strength B_0 along the z axis.

If we substitute (5.6) for the magnetic moment of the spin, the energy of the spin states in the magnetic field B_0 becomes

$$E = -\gamma \hbar m_z B_0 \tag{5.10}$$

Accordingly, spin states characterized by a different magnetic quantum number m_z become energetically separated in the presence of an external field (see Figure 5.7), while they are degenerate in the absence of an external field. The discrimination in energy of spin states in a magnetic field is called the Zeeman effect. In the case of a spin-1/2 nucleus, two discrete energy levels, one for the α state and one for the β state, are observed. They are

$$E_\alpha = -\gamma \hbar \frac{1}{2} B_0 \tag{5.11}$$

$$E_\beta = +\gamma \hbar \frac{1}{2} B_0 \tag{5.12}$$

and for the energy difference $\Delta E = E_\beta - E_\alpha$, we obtain

$$\Delta E = \gamma \hbar B_0 \tag{5.13}$$

In a very simplified picture of NMR, transitions between states of different energy can be observed by absorption and emission of radiation of energy corresponding to $\Delta E = h\nu$. Therefore, using (5.13) and the relation $\Delta E = h\nu$, for the spectral frequency of a nucleus we obtain

$$\nu_0 = \frac{|\gamma| B_0}{2\pi} \tag{5.14}$$

This is the frequency for "naked" nuclei that are not influenced by their surrounding electrons and do not interact with each other. The influence of chemical shift and spin–spin coupling results in effective magnetic fields (B_{eff}) that are slightly different from B_0. We will see later how such additional contributions are taken into account.

While such an energy level approach is sufficient to explain the spectral frequencies, it is too simplistic to describe the more sophisticated NMR techniques. To understand how the spins are manipulated in these experiments, we need to introduce the concept of *spin precession*.

Excursus 5.2: Energy of a Magnetic Dipole Moment in a Magnetic Field

For a microscopic magnetic moment in a homogeneous magnetic field the situation is similar to that of a compass needle in Earth's magnetic field.

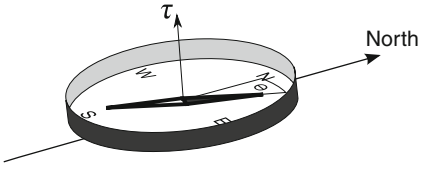

The needle experiences a force to coalign with the magnetic field, resulting in a torque τ that acts on the needle. The torque is related to the magnetic moment $\boldsymbol{\mu}$ and the strength of the magnetic field $\boldsymbol{B}$ by the vector product $\boldsymbol{\tau} = \boldsymbol{\mu} \times \boldsymbol{B}$ or in magnitude by

$$\tau = B\mu \sin(\theta) \tag{5.15}$$

with θ being the angle between vectors $\boldsymbol{\mu}$ and $\boldsymbol{B}$. If the two vectors coalign ($\theta = 0°$ or $180°$), the torque is zero, whereas if the two vectors are perpendicular ($\theta = 90°$), the torque is a maximum. The energy required to rotate the needle (dipole) from a position given by θ_1 to one given by θ_2 corresponds to the integral of (5.15) in the range (θ_1, θ_2). Solving the integral, we find the difference in energy between the two configurations is

$$\Delta E = B\mu(-\cos(\theta_2) + \cos(\theta_1))$$

The potential energy with respect to an orientation orthogonal to the magnetic field ($\theta_1 = 90°$) is then given by $-B\mu \cos(\theta_2)$, which is equivalent to the scalar product $-\boldsymbol{B}\cdot\boldsymbol{\mu}$. Thus, for the potential energy of a magnetic dipole in a magnetic field, we find

$$E = -\boldsymbol{B} \cdot \boldsymbol{\mu}$$

5.5.1 Spin Precession

The concept of spin precession is closely related to a classical physics phenomenon that is well known to us from our daily life – the precessional motion of a spinning

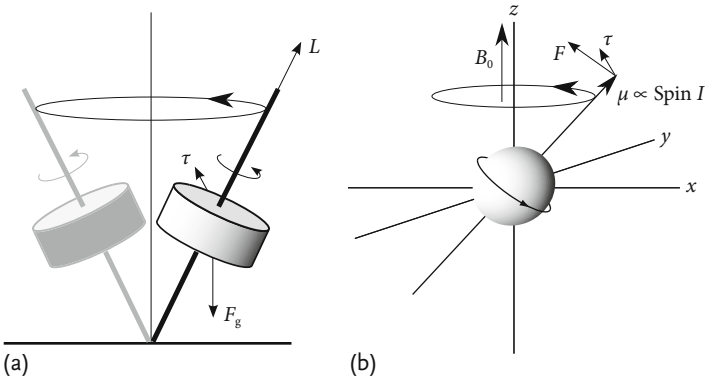

Figure 5.8 Comparison of the precessional motion of a spinning top (a) and a magnetic dipole in a magnetic field (b).

top. To briefly remind you, a spinning top as shown in Figure 5.8a has an angular momentum (L) along the rotational axis. The gravitational field exerts a force (F_g) on the spinning top, giving rise to a torque (τ) that results in a rotation along the surface of a cone, known as *precession*. Similarly, as shown in Figure 5.8b, for the case of the nuclear spin, the spin angular momentum interacts with the torque arising from the interaction of the magnetic field (B_0) with the magnetic moment (μ) of the spins, resulting in precession of the spin. This precession is known as *Larmor precession*, and its derivation from classical physics laws is outlined in Excursus 5.3.

In essence, the Larmor precession causes a fluctuation of the nuclear dipole moment in the xy plane. Its frequency in terms of angular velocity (rad/s) is given by

$$\omega_0 = -\gamma B_0 \tag{5.16}$$

Dividing by 2π gives the frequency in hertz (s^{-1}), the so-called resonance frequency

$$\nu_0 = \frac{|\gamma| B_0}{2\pi} \tag{5.17}$$

It is the resonance or basic frequency of a specific isotope at a given field strength. Note the equivalence of (5.14) and (5.17). Equation 5.16 is fundamental for NMR. It states simply that the precession frequency is related to the strength of the field – stronger magnets result in higher resonance frequencies. Moreover, it states that the frequency is isotope specific – nuclei from the same isotope are expected to yield the same frequency. However, as we have seen before, we have to take the surrounding electrons into account, a phenomenon known as the chemical shift.

Using a right-handed Cartesian coordinate system (Figure 5.9), which has become customary when describing NMR experiments, we can deduce the sense of rotation from the right-hand rule.

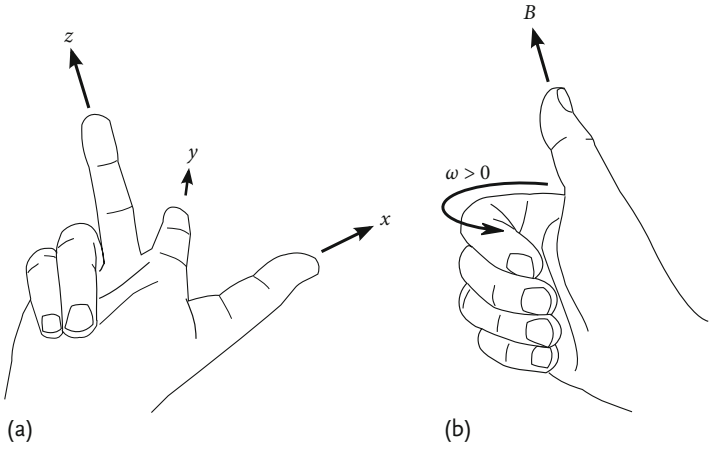

Figure 5.9 The right-handed coordinate system and the sense of rotation. As shown, the order of the axes (a) can be deduced from the thumb, the forefinger, and the middle finger of the right hand. The sense of rotation (b) can be deduced from the fingers of the right hand.

The rule states that when the thumb of the right hand points in the direction of the magnetic field ($\boldsymbol{B}$), the fingers point in the direction of rotation for positive values of ω. However, since the real sense of rotation in NMR spectroscopy is only of importance in rare cases, for simplicity we will assume that spin precession inherently follows the right-hand fingers, regardless of the particular sign of γ. Note, the spectrometer software takes different signs of the frequency corresponding to different signs of γ into account, and converts them such that resonance frequencies are always positive.

Excursus 5.3: Derivation of the Spin Precession from Classical Physics

From classical mechanics we know that the time evolution of angular momentum $\boldsymbol{L}$ is related to the torque $\boldsymbol{\tau}$ by

$$\frac{\mathrm{d}\boldsymbol{L}}{\mathrm{d}t} = \boldsymbol{\tau} \tag{5.18}$$

In the case of a magnetic dipole moment $\boldsymbol{\mu}$ in a magnetic field $\boldsymbol{B}$, the torque is given by the vector product

$$\boldsymbol{\tau} = \boldsymbol{\mu} \times \boldsymbol{B} \tag{5.19}$$

Combining both equations and replacing the classical angular momentum $\boldsymbol{L}$ by the spin angular momentum $\boldsymbol{I}$, we obtain

$$\frac{\mathrm{d}\boldsymbol{I}}{\mathrm{d}t} = \boldsymbol{\mu} \times \boldsymbol{B} = \gamma\, \boldsymbol{I} \times \boldsymbol{B} \tag{5.20}$$

Thus, the evolution of $\boldsymbol{I}$ is described by a system of three coupled differential equations. In particular, when replacing the arbitrary magnetic field $\boldsymbol{B}$ by the

external static field $\boldsymbol{B}_0$ we obtain

$$\frac{\mathrm{d}\boldsymbol{I}}{\mathrm{d}t} = \gamma \begin{pmatrix} I_x \\ I_y \\ I_z \end{pmatrix} \times \begin{pmatrix} 0 \\ 0 \\ B_0 \end{pmatrix} = \gamma \begin{pmatrix} I_y B_0 \\ -I_x B_0 \\ 0 \end{pmatrix}$$

which gives rise to the coupled differential equations

$$\frac{\mathrm{d}I_x}{\mathrm{d}t} = -\omega_0 I_y \tag{5.21}$$

$$\frac{\mathrm{d}I_y}{\mathrm{d}t} = \omega_0 I_x \tag{5.22}$$

$$\frac{\mathrm{d}I_z}{\mathrm{d}t} = 0 \tag{5.23}$$

in which we used $\omega_0 = -\gamma B_0$. The general solution of these equations describes a vector precessing about the z axis. For example, if we assume that the spin component in the xy plane $\langle I_{xy} \rangle$ is initially aligned to the x axis ($\boldsymbol{I}_{(0)} = (\langle I_{xy} \rangle, 0, \langle I_z \rangle)$), we obtain the particular solution

$$\boldsymbol{I}_{(t)} = \begin{pmatrix} \langle I_{xy} \rangle \cos(\omega_0 t) \\ \langle I_{xy} \rangle \sin(\omega_0 t) \\ \langle I_z \rangle \end{pmatrix} \tag{5.24}$$

Thus, in the classical interpretation of NMR, spins (1/2) are depicted as rotating spheres precessing about the B_0 field whereby only two fixed orientations for its z component are allowed.

Excursus 5.4: Mathematical Description of Rotations

In NMR, rotations are described by trigonometric functions. This is depicted in Figure 5.10. The y component of a rotating vector is plotted against the time that the vector needs for the rotation. It is easily seen that the points can be connected by a sine function. If we do the same for the x component, we will obtain a cosine.

Depending on the vector position at $t = 0$, the components are no longer described by pure sine and cosine functions, but a phase angle ϕ must be taken into account. For a vector $\boldsymbol{V}$ rotating with angular velocity ω and making an angle ϕ with the x axis at $t = 0$, the vector's orientation as a function of time is given by

$$\boldsymbol{V}(t) = \boldsymbol{e}_x V \cos(\omega t + \phi) + \boldsymbol{e}_y V \sin(\omega t + \phi) \tag{5.25}$$

with V the norm of the vector ($V = |\boldsymbol{V}|$), and $\boldsymbol{e}_x$ and $\boldsymbol{e}_y$ the unit vectors along the x axis and the y axis, respectively.

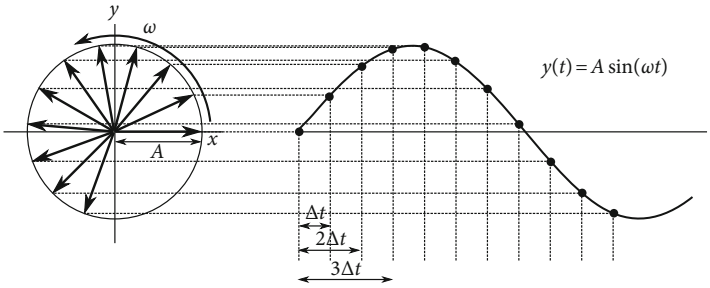

Figure 5.10 A sine wave formed by a rotating vector. Plotting the y position of a vector that rotates with constant angular velocity ω against time results in a sine function.

Rotating vectors can be described in a very straightforward way by using complex numbers. A complex number $z = a + \mathrm{i}b$ has a real part a and an imaginary part b (with a and b real numbers), and i is the symbol for the imaginary unit $\sqrt{-1}$. Complex numbers are usually represented as points in the complex plane, as shown in Figure 5.11. Thereby one axis represents the real part, and the other the imaginary part of the complex number. A point z in the complex plane can then be specified either directly by its rectangular Cartesian coordinates (a, b) or in terms of its polar coordinates (r, φ). With $a = r\cos(\varphi)$ and $b = r\sin(\varphi)$ the complex number is

$$z = r\cos(\varphi) + \mathrm{i}r\sin(\varphi) \tag{5.26}$$

It can be shown that this expression is equivalent to the complex exponential

$$z = r\mathrm{e}^{\mathrm{i}\varphi} \tag{5.27}$$

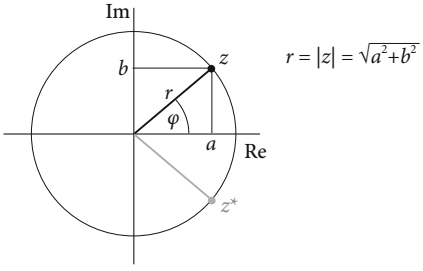

Figure 5.11 The plane of complex numbers.

If we compare (5.25) and (5.26) it becomes clear that a rotating vector can be described as a complex number evolving along a circle in the complex plane.

For that we relabel the x axis with Re and the y axis with Im. Using (5.27), we can then write

$$\boldsymbol{V}(t) \equiv V\mathrm{e}^{\mathrm{i}(\omega t+\phi)} \tag{5.28}$$

It is useful to define the complex conjugate z^* of a complex number z, which is kept by mirroring the point z along the real axis, such that

$$z = a + \mathrm{i}b = r(\cos(\varphi) + \mathrm{i}\sin(\varphi)) = r\mathrm{e}^{\mathrm{i}\varphi} \tag{5.29}$$

$$z^* = a - \mathrm{i}b = r(\cos(\varphi) - \mathrm{i}\sin(\varphi)) = r\mathrm{e}^{-\mathrm{i}\varphi} \tag{5.30}$$

With this the real and imaginary parts are obtained as

$$\mathrm{Re}(z) = \frac{1}{2}(z + z^*) \tag{5.31}$$

$$\mathrm{Im}(z) = \frac{1}{2\mathrm{i}}(z - z^*) \tag{5.32}$$

and in addition for the squared norm we have

$$|z|^2 = z^* z \tag{5.33}$$

As we will see, in NMR experiments we are ultimately often able to measure only one component of the rotating "vector." For example, if it is the x component, with (5.31) we have

$$V_x(t) = V\frac{1}{2}[\mathrm{e}^{\mathrm{i}(\omega t+\phi)} + \mathrm{e}^{-\mathrm{i}(\omega t+\phi)}] \tag{5.34}$$

which clearly demonstrates that an oscillation along a single axis can be represented in terms of two counter-rotating vectors. A fact which we will make use of later in this book.

5.6 Problems

5.1. What is the property a nucleus must have so that it can be observed by NMR?

5.2. Is a nucleus composed of 20 protons and 20 neutrons an NMR-active nucleus? What do you think?

5.3. How many Zeeman energy levels are there for a spin 3/2 nucleus?

5.4. Is nuclear magnetism a paramagnetic or a diamagnetic effect? Does it depend on the sign of the gyromagnetic ratio γ?

5.5. A nucleus with a gyromagnetic ratio of 16×10^7 rad s^{-1} T^{-1} has a resonance frequency of 400 MHz at a certain magnetic field strength. (a) What is the resonance frequency of a nucleus with a gyromagnetic ratio of 8×10^7 rad s^{-1} T^{-1} at that magnetic field strength? And what resonance frequencies do you expect if you decrease the magnetic field by a factor of two?

6
Magnetization – A Macroscopic View

In Chapter 5 we looked at single spins placed in a magnetic field. In NMR spectroscopy, however, we do not (even cannot) measure individual spins; instead, we measure a rather large number of spins simultaneously. In fact, the number of spins must be extremely large to obtain a signal of sufficient strength. Accordingly, in our NMR experiment we always measure the average sum of a large number of individual nuclear dipole moments, the so-called *magnetization*. While at a first glance this may seem to make the story more difficult, in some respects the opposite is true. Because for large quantities statistics becomes applicable, the uncertainty in the spin angular momentum is removed to some extent. Moreover, the macroscopic property of spins, the magnetization, is much simpler to describe than the magnetic moment of an individual spin. As we will see, in the case of noninteracting spins, to which we will limit our description in this chapter, the macroscopic property behaves like classical objects.

At the beginning of this chapter we will introduce general aspects of net magnetization. We will look at the x, y, and z components of magnetization at thermal equilibrium. To describe the x and y components of magnetization we need to introduce the concept of coherence. The time evolution of magnetization can then be deduced by considering the results from Section 6.4. For a complete description we also need to introduce the topic of relaxation. Finally, we will understand how we can manipulate magnetization by applying an oscillating radio frequency (RF) field orthogonal to the direction of the main field, the so-called B_1 field, usually referred to as RF pulses.

6.1
The Macroscopic Magnetization

Suppose we look at a large number of N equivalent nuclei with spin 1/2 that are of the same isotope and have a unique resonance or precession frequency. Such a large collection of equivalent spins is called a *spin ensemble*. We may envisage the spin ensemble as a large collection of spin vectors as shown in Figure 6.1, each representing a magnetic dipole moment of different orientation but the same magnitude. Adding up all the magnetic moments results in the macroscopic vector

Applied NMR Spectroscopy for Chemists and Life Scientists, First Edition. Oliver Zerbe and Simon Jurt.
©2014 WILEY-VCH Verlag GmbH & Co. KGaA. Published 2014 by WILEY-VCH Verlag GmbH & Co. KGaA.

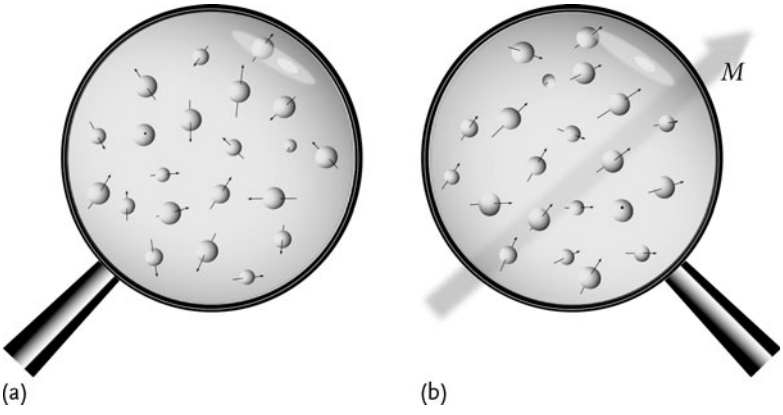

Figure 6.1 Magnetization due to alignment of nuclear magnetic moments. For a collection of spins with random orientation for their magnetic moments, there is zero net magnetization (a). In contrast, when the magnetic moments are weakly aligned, their vector sum accounts for observable net magnetization M (b).

quantity $\boldsymbol{M}$, called *magnetization*. Thus, magnetization corresponds to the vector sum of all individual dipole moments.

$$\boldsymbol{M} = \sum_i \boldsymbol{\mu}_i \tag{6.1}$$

The z component of $\boldsymbol{M}$ is referred to as *longitudinal magnetization,* whereas the component in the xy plane is often referred to as *transverse magnetization*.

Clearly, if and how much magnetization is obtained from a spin ensemble depends on how strongly the spins are aligned, and on the particular magnitude of each individual magnetic moment, that is, γ of the nuclei in question. In the absence of an external magnetic field there is no alignment in any direction. In contrast, in the presence of an external magnetic field the spins will become weakly aligned, resulting in observable magnetization. To what extent the spins are aligned in a magnetic field is the subject of the next section.

6.2 Magnetization at Thermal Equilibrium

As outlined in Section 5.5, the energy of spin states characterized by different magnetic quantum numbers m_z is split in the presence of an external magnetic field. This is called the *Zeeman effect*. According to statistical thermodynamics, populations of states with different energy are disparate, and are described by the Boltzmann distribution:

$$\frac{N_\beta}{N_\alpha} = \mathrm{e}^{-\Delta E/(kT)} \tag{6.2}$$

in which k is the Boltzmann constant ($k = 1.381 \times 10^{-23}$ J/K), T the absolute temperature of the sample in kelvins, and ΔE the energy difference between the α state and the β state ($\Delta E = E_\beta - E_\alpha = \hbar\gamma B_0$). Because ΔE is very small (much smaller than kT), the exponential function can be approximated by the first two terms of its power series ($\exp(-x) \approx 1 - x$), and we obtain

$$\frac{N_\beta}{N_\alpha} \approx 1 - \frac{\hbar\gamma B_0}{kT} \tag{6.3}$$

which is also known as the "high-temperature approximation." From that the population difference $\Delta N = N_\alpha - N_\beta$ is easily computed. Using $N_\alpha = 0.5(N + \Delta N)$, $N_\beta = 0.5(N - \Delta N)$, and $(N - \Delta N)/(N + \Delta N) \approx 1 - 2\Delta N/N$ for small values of ΔN, we obtain for the population difference

$$\Delta N \approx N\frac{\hbar\gamma B_0}{2kT} \tag{6.4}$$

This difference is very small. To give you an impression, for ^{1}H nuclei at 293 K in a field of 14.09 T (equivalent to approximately 600 MHz), the relative difference $\Delta N/N$ is only 0.000 05. That means if 10 000 spins occupy the β state, 10 001 spins are in the energetically favorable α state, and it is only the one spin in excess that will give rise to the observed signal. Nevertheless, it is this small difference which accounts for the equilibrium magnetization. The equilibrium magnetization is computed from the number of dipole moments in excess (pointing in the $+z$ direction) times the spin's individual dipole moment along z. In other words, we need to multiply (6.4) by $\frac{1}{2}\hbar\gamma$. By doing so, we obtain for the thermal equilibrium magnetization M_{eq} of spin-1/2 nuclei

$$M_{eq} = N\frac{\gamma^2\hbar^2 B_0}{4k_B T} \tag{6.5}$$

The important point to note here is that the equilibrium magnetization depends quadratically on the gyromagnetic ratio of an isotope. As a consequence, magnetization from ^{13}C nuclei, for which γ is around four times smaller than for ^{1}H, will be smaller by a factor of 16 compared with that from ^{1}H nuclei. Therefore, much less signal must be expected for those nuclei with a low γ. As we have already seen in Section 2.5.3, the intensity of the NMR signal depends once more on γB_0.

Because B_0 has zero component in the xy plane, the xy components of the spins are not associated with changes in energy and therefore the spins have no preference to orient themselves in the xy plane. Accordingly, no spin alignment and thus no net magnetization is observed in the xy plane at thermal equilibrium and therefore we have solely z magnetization or longitudinal magnetization at thermal equilibrium. To observe any transverse magnetization we must tip the longitudinal magnetization into the transverse plane. As we will see in more detail in Section 6.6, this can be achieved by application of an RF pulse.

6.3 Transverse Magnetization and Coherences

Transverse magnetization is much more difficult to understand than longitudinal magnetization. While z magnetization is characterized by population differences of α and β states, transverse magnetization is characterized by a specific phase relationship between the α and β states, called *coherence*. This can be only understood by a rigorous quantum mechanical treatment of the spin. The following considerations should highlight the problem.

The Stern–Gerlach experiment demonstrated that a measurement of the z component of spin-1/2 nuclei invariably gives two distinct values, which we attribute to the α state and the β state. From that we might conclude that a spin when exposed to a magnetic field is *either* in the α state or the β state. This is a convenient picture to explain the NMR spectrum in terms of transitions or to explain the equilibrium z magnetization as we have seen before. However, the picture of a spin ensemble represented by spins in pure α and β states is not appropriate any longer when discussing transverse magnetization. According to the Stern–Gerlach experiment, the expectation values of the x and y components for a particle beam comprising spins in pure α or β states are zero in both cases. Thus, for a spin ensemble composed of pure α and β states we cannot expect any transverse component and hence any net magnetization in the xy plane.

In fact, transverse spin components are described as *linear combinations* of α and β states, by using the concept of *superposition*: $\psi = a\alpha + b\beta$. In essence, it can be shown that any spin state for which the orientation of its spin angular momentum is assumed to be "known" along a specific direction (e.g., along the x axis) can be represented by such a superposition state. In that respect, the "pure" α and β states for which the spin is known along the z axis must be considered as particular cases (with a or b equal to zero) of this more general concept of spin states. But, in general, a spin does not need to be in either the α state or the β state, but can adopt a "mixture" of both. This is described in more detail in Chapter 9.

The magnetic dipole moment depends on the orientation of the spin, and thus transverse magnetization must be characterized by a certain amount of spin alignment in the xy plane. While in thermal equilibrium no correlation of phases exists, through the action of RF pulses a certain degree of correlation of phases is achieved, so immediately after the pulse (and before transverse magnetization dephases due to T2 relaxation again) phases are not statistically distributed any longer; however, a quite small preference for a certain phase exists. This is referred as to *phase coherence* (Figure 6.2). This must not be confused with the coherent motion of isochronous spins. Although isochronous spins precess at the same frequency, their phases do not need to be correlated.

In the case of isolated, noninteracting nuclei, the phase coherence is directly related to observable magnetization. This particular form of coherence is called single-quantum coherence. However, as we will see in Section 7.2.1.5, other coherences exist which are not directly observable. These coherences specify a specific correlation in the spin alignment of scalarly coupled spins, and are called multiple-

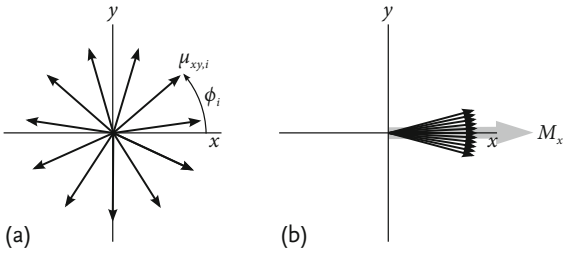

Figure 6.2 Phase coherence. When the *xy* components of the spins are uniformly distributed in the *xy* plane, their transverse magnetic dipole moments mutually cancel (a). In contrast, when the phases (ϕ_i) of the spins are similar, the vector addition results in net transverse magnetization *M* (b).

quantum coherences. As an example, let us look at two scalarly coupled spins *S* and *I*. Through clever application of pulses we may create a state in which some of the spins are correlated in a way that at some point in time both spins point simultaneously in the positive or negative *x* direction. Although the spins are specifically aligned in the transverse plane, there is no net magnetization, neither for spin *I* nor for spin *S*. However, as we will see later, such multiple-quantum coherences can be converted into observable single-quantum coherences.

The concept of coherences is very important for the description of multidimensional experiments. The macroscopic property magnetization is obtained from the spin ensemble using statistical methods. While individual spins display the odd behavior of quantum objects, when computing the macroscopic properties from a very large ensemble of spins, we find that the magnetization calculated in such a way behaves very much like a classical physical object. In thermal equilibrium, magnetization corresponds to a vector pointing along the *z* axis, and we can easily rotate that vector by 90° to create transverse magnetization. For most of the time it will be sufficient to look at magnetization and not at individual spins, with the prominent exception of relaxation-related matters. Moreover, we wish to limit our description at the moment to the principal features of *macroscopic* magnetization without taking interactions between different spins into account. So let us look at how the magnetization of noninteracting spins evolves in time.

6.4
Time Evolution of Magnetization

In the previous two sections we described the macroscopic magnetic moment by introducing the concept of magnetization, a vector quantity that represents the degree of spin polarization (alignment) within an ensemble (Figure 6.3). In this section we will see how the magnetization vector evolves in time and thereby derive an analytical description of the signal that we record in our receiver coil. If we disregard any spin–spin interactions, the time evolution of magnetization is fully characterized by a system of three differential equations, known as the *Bloch*

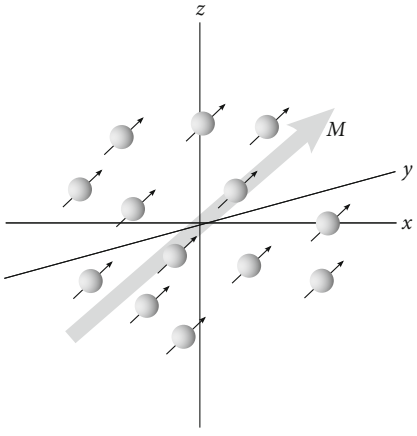

Figure 6.3 Representation of magnetization by spatial alignment of individual spins.

equations. These equations allow a detailed description of the evolution of x, y, or z magnetization in the presence of an external magnetic field, and they also take into account damping of the signal due to relaxation.

6.4.1 The Bloch Equations

The *Bloch equations* form a set of coupled differential equations describing the motion of the magnetization vector. They were introduced phenomenologically in 1946 by Felix Bloch, one of the great contributors in the early days of NMR studies and a Nobel laureate. Basically, they consist of two terms, one that describes the interaction of magnetization $\boldsymbol{M}$ with the magnetic field $\boldsymbol{B}$, and the other that accounts for relaxation. In a compact form, the Bloch equations are given by

$$\frac{\mathrm{d}\boldsymbol{M}(t)}{\mathrm{d}t} = \gamma\, \boldsymbol{M}(t) \times \boldsymbol{B}(t) - R(\boldsymbol{M}(t) - \boldsymbol{M}_{\mathrm{eq}}) \quad \text{with}$$
$$R = \begin{pmatrix} \mathrm{T2}^{-1} & 0 & 0 \\ 0 & \mathrm{T2}^{-1} & 0 \\ 0 & 0 & \mathrm{T1}^{-1} \end{pmatrix} \tag{6.6}$$

R is the relaxation matrix. Note the similarity of (5.20), which describes the interaction of an individual spin with the magnetic field, and (6.6). Knowing the initial magnetization $\boldsymbol{M}(0)$, the magnetic field $\boldsymbol{B}(t)$, and the relaxation matrix, we can compute the magnetization at any later time $\boldsymbol{M}(t)$ by integrating (6.6). The Bloch equations are very useful to compute the impact of RF pulses. However, at the moment we will look at the free precession only, in which the magnetic field is given by the external static field B_0, thus $\boldsymbol{B}(t) = (0, 0, B_0)$. In that case the Bloch equation becomes

$$\frac{\mathrm{d}M_x(t)}{\mathrm{d}t} = \gamma\, M_y(t)\, B_0 - \frac{M_x(t)}{\mathrm{T2}} \tag{6.7}$$

$$\frac{\mathrm{d}M_y(t)}{\mathrm{d}t} = -\gamma\, M_x(t)\, B_0 - \frac{M_y(t)}{\mathrm{T2}} \tag{6.8}$$

$$\frac{\mathrm{d}M_z(t)}{\mathrm{d}t} = -\frac{M_z(t) - M_{\mathrm{eq}}}{\mathrm{T1}} \tag{6.9}$$

With use of $\omega_0 = -\gamma\, B_0$, the solutions are

$$M_x(t) = (M_x(0)\cos(\omega_0 t) - M_y(0)\sin(\omega_0 t))\mathrm{e}^{-\frac{t}{\mathrm{T2}}} \tag{6.10}$$

$$M_y(t) = (M_y(0)\cos(\omega_0 t) + M_x(0)\sin(\omega_0 t))\mathrm{e}^{-\frac{t}{\mathrm{T2}}} \tag{6.11}$$

$$M_z(t) = (M_z(0) - M_{\mathrm{eq}})\mathrm{e}^{-\frac{t}{\mathrm{T1}}} + M_{\mathrm{eq}} \tag{6.12}$$

The first two equations describe damped harmonic oscillations, while the third equation describes the asymptotic return of z magnetization to equilibrium. Together they define a vector that precess about the z axis, and it simultaneously rotates toward the z axis and simultaneously changes its length due to relaxation. The trajectory for pure initial x magnetization is shown in Figure 6.4. With $\mathrm{T2} \leq \mathrm{T1}$ the magnetization vector can never become larger than in thermal equilibrium. In the limiting case of $\mathrm{T2} = \mathrm{T1}$, the tip of the magnetization vector moves along the surface of a cone.

Herein we have calculated the time evolution in the conventional laboratory frame. However, as we will see in a moment, in NMR it is much more convenient to describe the evolution of magnetization in a frame that rotates at a frequency close to the spin's Larmor frequency. But first let us have a closer look at the phenomenon of relaxation.

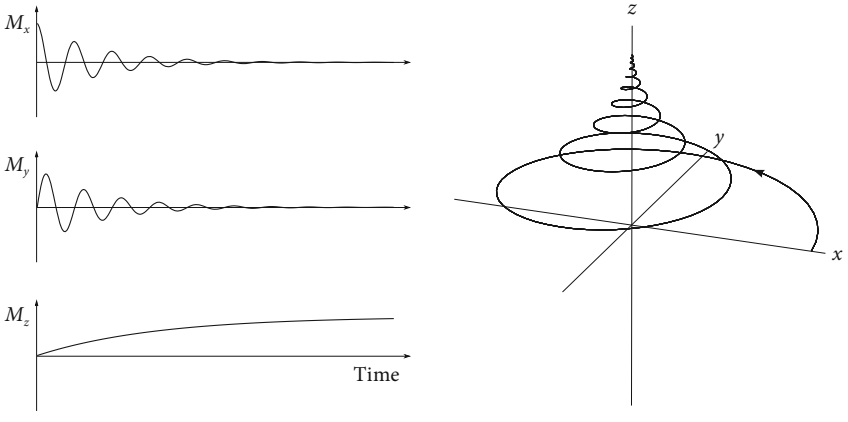

Figure 6.4 Time course of the magnetization for free precession. (a) The amount of x, y, and z magnetization in the course of free precession. (b) The trajectory of the magnetization vector in the laboratory frame. The precession frequency is chosen to be much smaller than it is at common field strengths, where we normally would observe many millions of oscillations. The relaxation times were chosen such that $\frac{\mathrm{T1}}{\mathrm{T2}} = 2$.

6.4.2 Longitudinal and Transverse Relaxation

Perturbation of a system from its thermal equilibrium results in a process known as relaxation. Relaxation drives the system back to equilibrium. Relaxation is the result of random changes in the orientation of the individual spins. There are different mechanisms that trigger this reorientation, and they are discussed in more detail in Chapter 14. In general, two relaxation processes are distinguished: one process is responsible for the return of z magnetization (longitudinal magnetization) to thermal equilibrium and is referred to as *spin–lattice, longitudinal,* or *T1 relaxation*; the second process causes magnetization in the xy plane, the transverse magnetization, to decay to zero, and is called *spin–spin, transverse,* or *T2 relaxation.*

6.4.2.1 Longitudinal Relaxation

In a large ensemble of spins such as that represented in Section 6.1 at any time some spins flip from the α state to the β state or vice versa by exchange of energy with the environment of the spins, the so-called lattice. Accordingly, this process is also referred to as spin–lattice relaxation. How often these spin flips or transitions occur is given by the transition probabilities $W_{\alpha\beta}$ and $W_{\beta\alpha}$ (see Figure 6.5a). Importantly, transitions from the energetically higher state to the lower state are a bit more likely to occur than transitions the other way round ($W_{\beta\alpha} > W_{\alpha\beta}$), resulting in a higher population of the α states in thermal equilibrium (assuming $\gamma > 0$).

Qualitatively, longitudinal relaxation is a first-order process that is proportional to the extent that longitudinal magnetization deviates from equilibrium z magne-

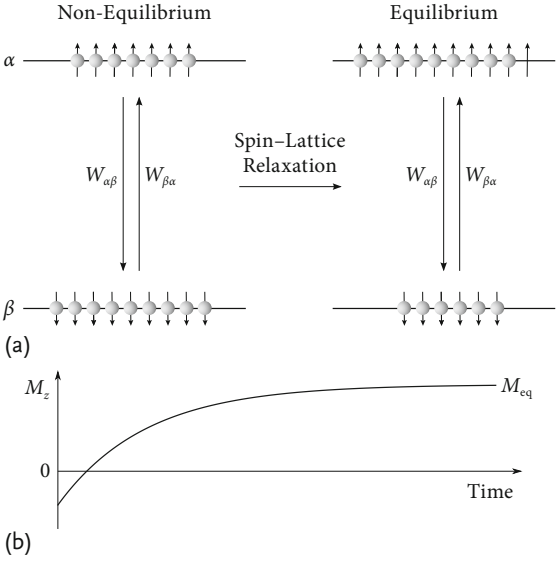

Figure 6.5 Longitudinal relaxation. Spin flips cause a return to thermal equilibrium (a). As shown in (b), the amount of z magnetization thereby follows an asymptotic exponential growth.

tization ($M_z - M_{eq}$):

$$\frac{dM_z}{dt} = -\frac{1}{T1}(M_z - M_{eq}) \tag{6.13}$$

T1 denotes the longitudinal relaxation time constant, which can be replaced by the rate constant R_1 ($R_1 = T1^{-1}$). This rate constant is related to the transition probabilities by $R_1 = W_{\alpha\beta} + W_{\beta\alpha}$.[1] If we denote z magnetization at time zero by $M_z(0)$, (6.13) integrates to

$$M_z(t) = (M_z(0) - M_{eq})e^{-\frac{t}{T1}} + M_{eq} \tag{6.14}$$

Thus, relaxation of longitudinal magnetization is described by an asymptotic exponential growth as shown in Figure 6.5b. The T1 relaxation time constants differ from site to site within a molecule, and can be measured by the so-called inversion-recovery experiment as described in Section 12.8. For medium-sized organic molecules in solution, they are on the order of seconds in the case of protons, but can assume values of some tens of seconds for carbon nuclei.

6.4.2.2 **Transverse Relaxation**

Transverse relaxation describes the decay of xy magnetization as a result of loss of phase coherence among the spins. The main contribution to this loss of coherence is due to dipolar interactions with nearby spins, hence the name spin–spin relaxation. We may envisage this process as the randomization of previously correlated phases as a consequence of spin flips in the xy plane (disregarding spin precession for a moment). For example, let us assume that we initially have pure x magnetization. As depicted in Figure 6.6a, we can then represent the spin ensemble by some spins pointing along the $+x$ axis and some spins pointing along the $-x$ axis. If we denote their numbers by N_x and N_{-x}, respectively, x magnetization then corresponds to the difference $\Delta N = N_x - N_{-x}$. The important difference from longitudinal relaxation is, that in contrast to α and β states, the two spins states (parallel and antiparallel to the x axis) have the same energy, and both "spin flips" ($x \rightarrow -x$ and $-x \rightarrow x$) are equally probable, denoted by W.[2] As a consequence, the difference in the number of spins N_x and N_{-x} continually decreases until it becomes zero at thermal equilibrium, where the number of spins N_x and N_{-x} must be the same according to $N_x W = N_{-x} W$ at equilibrium.

In essence it follows that transverse relaxation is a first-order kinetic process. Denoting the amount of magnetization in the xy plane by M_{xy} ($M_{xy} = \sqrt{M_x^2 + M_y^2}$), we find that transverse relaxation obeys the differential equation

$$\frac{dM_{xy}}{dt} = -\frac{1}{T2} M_{xy} \tag{6.15}$$

1) Sometimes in the literature the assumption is made that both transition probabilities ($\alpha \rightarrow \beta$ and $\beta \rightarrow \alpha$) are the same, for which R_1 is then given by $2W$.

2) We will see in Chapter 14 that mechanisms other than spin flips contribute to T2 relaxation as well. These become dominant for large molecules.

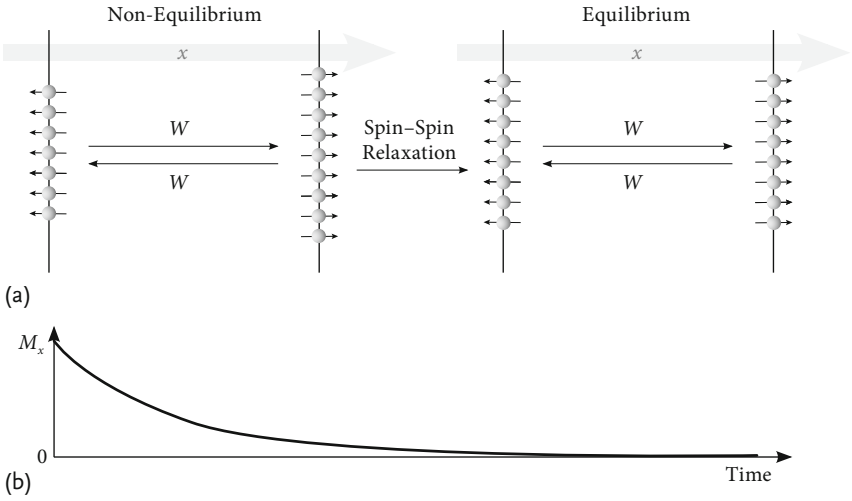

Figure 6.6 Transverse relaxation. (a) Random reorientation of the transverse components of the spins causes a loss of transverse magnetization. For simplicity, this is illustrated by considering the *x* components of the spins only and suppression of the precessional motion of the spins. As shown in (b), the amount of transverse magnetization follows an exponential decay.

where T2 is the transverse relaxation time constant, which is the reciprocal value of the rate constant R_2 ($R_2 = 2W$). With the initial value of xy magnetization $M_{xy}(0)$, (6.15) integrates to

$$M_{xy}(t) = M_{xy}(0)\mathrm{e}^{-\frac{t}{\mathrm{T2}}} \tag{6.16}$$

This equation describes the exponential decay of transverse magnetization as shown in Figure 6.6b.

While for small and medium-sized molecules the T2 values are similar to the corresponding T1 values, for macromolecules they are in general much smaller and can be a few milliseconds (see Figure 14.9). From relaxation theory it follows that T2 $\leq$ T1.

As described in Section 2.4, transverse relaxation determines the line width of the signal in the spectrum. However, it is important to realize that random "spin flips" are not the only contribution to the decay of the signal. Another important source of dephasing of transverse magnetization is the B_0 inhomogeneity. The observed line with of the signal is therefore often much larger than one would expect from spin–spin relaxation alone. The contribution of B_0 inhomogeneities to the actual line width is referred to as *inhomogeneous broadening* and is usually taken into account by specifying the effective transverse relaxation time constant T2*

$$\frac{1}{\mathrm{T2}^*} = \frac{1}{\mathrm{T2}_{\mathrm{homog.}}} + \frac{1}{\mathrm{T2}_{\mathrm{inhomog.}}} \tag{6.17}$$

where $\mathrm{T2}_{\mathrm{homog.}}$ refers to the homogeneous broadening of the signals (T2 relaxation in a perfect homogeneous B_0 field). It is worth noting that there is a fundamental

difference in the mechanism leading to homogenous or inhomogeneous broadening. In contrast to the dephasing of magnetization due to random spin flips (T2 relaxation), the dephasing due to field inhomogeneities can be removed with a so-called spin-echo element that is part of experiments to measure T2 relaxation (see Section 12.8.2).

An additional source of line broadening is due to *radiation damping*. Thereby the voltage induced in the RF coil due to the precession of a strong resonance (e.g., the ^{1}H line of only partially deuterated solvents) acts as a very weak (selective) RF pulse (Section 6.6). It rotates the magnetization of the corresponding resonance toward the positive z axis. Through that process the magnetization in the xy plane rapidly decreases. Similarly to fast T2 decay the line width of the corresponding resonance line is strongly increased. As the induced RF field is very weak, the effect is selective to the strong resonance itself and only resonances very close to it. Depending on the sensitivity (the Q) of the probehead in use, radiation damping can result in line widths of several hundred hertz.

6.5 The Rotating Frame of Reference

So far we have only looked at spins characterized by a single precession frequency. Of course, for an accurate description of NMR experiments we need to take into account the variation in precession frequencies due to the chemical shift phenomenon. While at common field strengths the values of Larmor precession in absolute terms are very large (on the order of hundreds of megahertz for ^{1}H), the maximum difference in frequency between signals within a spectrum, known as the signal dispersion, due to the chemical shift is usually some kilohertz at most. Nevertheless, these "small" frequency differences primarily determine the appearance of a spectrum. As the Zeeman contribution is common to all like spins, it is reasonable to remove that part and only retain the "interesting" small contribution that accounts for the chemical shift. This can be accomplished by specifying the resonance frequencies with respect to a reference frequency ω_{ref}, which is mostly chosen to be the center frequency of the observed spectral range (see Figure 6.7).

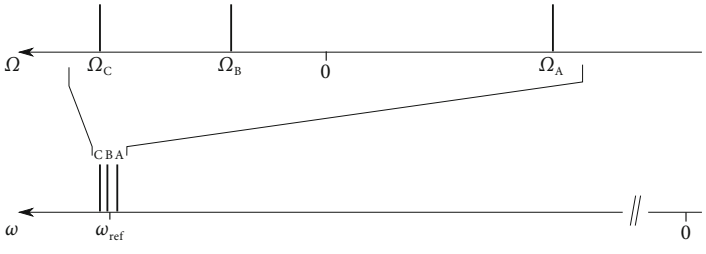

Figure 6.7 Changing the frequency scale. The lower panel shows three resonances using the absolute frequency scale. The relative scale shown in the upper panel uses the frequency offset relative to a reference frequency ω_{ref}.

That means that for a nucleus at site i with an absolute precession frequency ω_i, the frequency relative to the center frequency ω_{ref}, the so-called offset frequency Ω_i, is given by

$$\Omega_i = \omega_i - \omega_{\text{ref}} \tag{6.18}$$

Physically this corresponds to introducing a new coordinate frame that rotates around the z axis with angular velocity ω_{ref}, the so-called *rotating frame of reference*. As shown in Figure 6.8, a vector that precesses at velocity ω in the static laboratory frame is seen by an observer in the rotating frame with a lower frequency ($\Omega = \omega - \omega_{\text{ref}}$), and if we choose $\omega_{\text{ref}} = \omega$, the vector is even static.

As shown in Figure 6.9, the external magnetic field B_0 is modulated in strength in the rotating frame. The offset frequency of a resonance can be seen as the consequence of a residual field B_0', according to $\Omega = -\gamma B_0'$. For example, if the offset frequency is zero, the magnetization vector does not precess and thus the spins seem to experience no external field ($B_0' = 0$). Alternatively, if the rotating frame

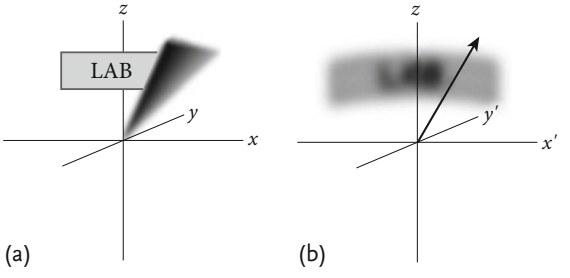

Figure 6.8 The rotating frame of reference. A vector precesses about the z axis as seen in the static laboratory frame (a). If the coordinate system is rotated around the z axis at same rate as the vector, the observer in the rotating frame will perceive the vector as static (b).

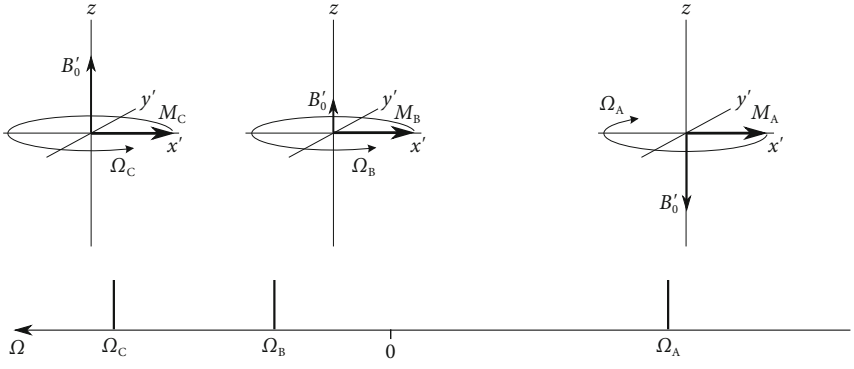

Figure 6.9 Apparent external field B_0' in the rotating frame of reference. In the rotating frame of reference a residual field along z accounts for the offset of a resonance. The smaller the offset, the smaller the magnitude of the residual field. The direction of B_0' depends on the sign of the offset frequency.

rotates faster than a magnetization vector does ($\omega_{\mathrm{ref}} > \omega_i$), then the vector rotates in the opposite direction ($\Omega_i < 0$) and hence the field experienced is negative. While this seems to introduce another unnecessary complication, we will see in the next section that it makes the calculations much easier, particularly in the presence of an additional RF field.

6.6 RF Pulses

As we saw in Section 6.1 thermal equilibrium *transverse* magnetization is zero. To create transverse magnetization we need to apply an additional RF field. Usually, this additional field is applied for a short time only, and therefore the term "pulse" is used in this context. RF pulses form the backbone of all NMR experiments. Through their use it is possible to manipulate magnetization in the course of an experiment in the desired way to form what we commonly call a "pulse sequence." But how does the pulse work?

Obviously, the additional field must be capable of rotating magnetization. As we have seen before, magnetization precesses about the direction of a magnetic field vector. Thus, to tip magnetization from the z position toward the xy plane we need to apply an additional magnetic field *orthogonal* to the B_0 field. Let us for the moment assume that this additional field is static and applied along the x axis or the y axis (we will see later that this is not the case). In order to understand what happens when both fields are present at the same time, we need to perform a vector addition of the two fields and let the magnetization rotate about the resulting axis. If we do that we will quickly realize that the orthogonal field (which for technical reasons can only be produced by a small coil) is many orders of magnitude weaker than the B_0 field. As a consequence, the resulting field will more or less exactly point in the direction of the B_0 field and not perpendicular to it. As we will see in the next section, the trick is to apply the orthogonal magnetic field not as a static field, but as an oscillatory field – quite small in amplitude and of frequency similar to the precession frequency of the spins. This oscillatory field is denoted as the RF or B_1 field, and it is produced by a very small coil enclosing the sample, the so-called RF coil.

In the following we will try to explain in more detail how the RF field rotates the magnetization into the transverse plane. For that purpose it is convenient to decompose the RF field into two components and then shift our point of observation from the static laboratory frame to the rotating frame of reference. Finally, we will adapt the Bloch equations for the presence of the B_0 and B_1 fields in a rotating frame and describe off-resonance effects.

6.6.1 Decomposition of the RF Field

As depicted in Figure 6.10, during an RF pulse the alternating current in the RF coil produces an oscillating magnetic field (B_{RF}) across the coil. The RF field is orthogonal to the main field B_0 and many orders of magnitude weaker.

In the same way as we can decompose plane-polarized light into two circularly polarized components that rotate in opposite sense, we can decompose the RF field into two components (see Figure 6.11) of the same length ($B_{RF}/2$) that rotate in opposite directions, one with $+\omega_{RF}$ and the other with $-\omega_{RF}$ (see also Excursus 5.4). One of these two components, namely, the one with $+\omega_{RF}$, rotates in the same sense as the spin precesses (for positive values of γ).

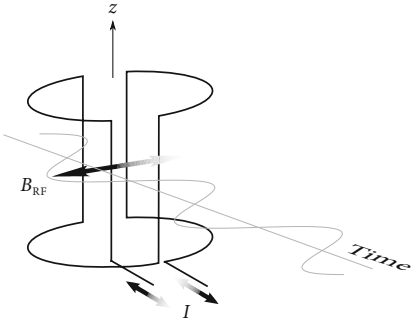

Figure 6.10 Origin of the radio frequency (RF) field. The alternating flow of current gives rise to an oscillating magnetic field within the RF coil.

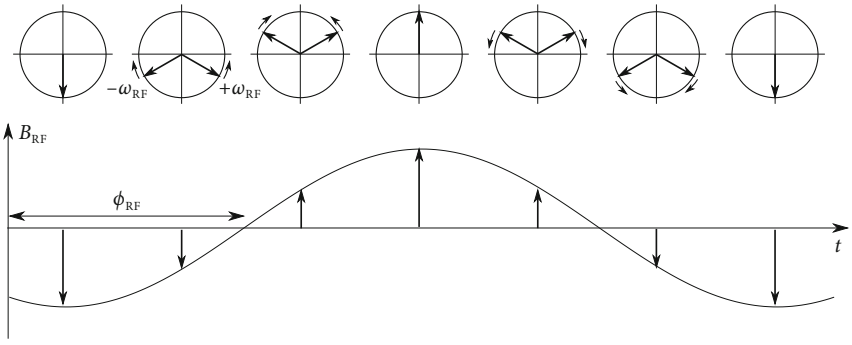

Figure 6.11 Decomposition of the RF field. A sinusoidal field as shown in the lower trace is equivalent to the vector sum of two counter-rotating components.

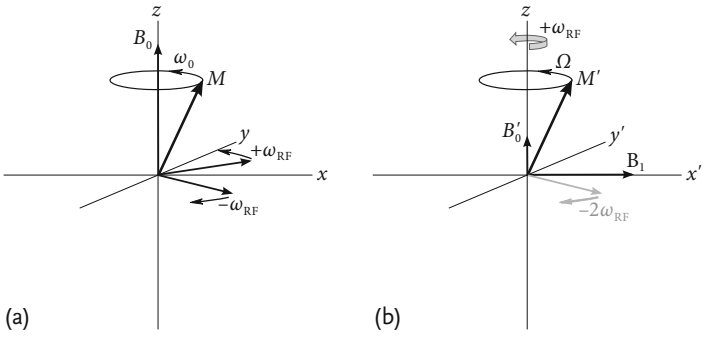

Figure 6.12 Relevant quantities in the static frame and in the rotating frame. Magnetization vector, RF field components, and B_0 field with respect to the static frame (a) and the rotating frame of reference (b). The off-resonant component of the RF field (shown in gray) can usually be disregarded.

6.6.2 Magnetic Fields in the Rotating Frame

To be able to calculate the rotation of magnetization under the influence of the B_0 and RF fields, it is best to switch to a properly chosen rotating frame. Let us assume we move into the rotating frame of reference that rotates exactly at $+\omega_{RF}$. In such a frame one of the two B_1 field components is static, while the other rotates with $-2\omega_{RF}$ (Figure 6.12).

We call the static component the on-resonant component or just the B_1 field and the other the off-resonant component of the RF field. The crucial point is that we can disregard the off-resonant component, which rotates in the opposite sense to the magnetization.

What is the strength of the field along the z axis, B_0', in such a frame? We discussed this in Section 6.5, and will only remind you that if the precession frequency of the spin is exactly the same as ω_{RF}, Ω_i' is zero and hence so is the apparent field B_z'. To summarize, when the spin of interest is exactly on-resonant, in a frame rotating about z with a frequency of ω_{RF} no field is present in the z direction, and the B_1 field in the transverse plane is *static*. Since we are now left with a single static field, its effect is easy to predict, and is analogous to the spin precession about B_0 (see Section 5.5.1). Note that the phase of the RF pulse will determine the direction of the B_1 field in the transverse plane.

In the laboratory frame, the magnetization vector rotates about two axes, about the z axis and about an axis in the xy plane. The rotation about z corresponds to the precession at the Larmor frequency. The rotation about the transverse axis is due to the pulse, and is often referred to as *nutation*. The nutation frequency is many orders of magnitude smaller than the Larmor frequency. Because so many rotations are present in the system, we show rotation axes and rotation frequencies as experienced in the laboratory frame separately in Figure 6.13.

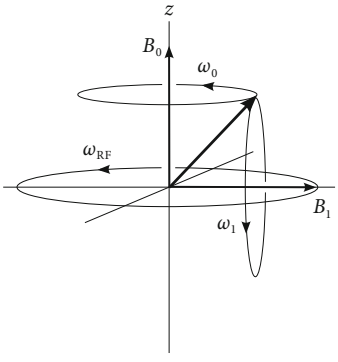

Figure 6.13 The orientation and the strengths of magnetic fields. A magnetization vector M precesses about the axis of the static field at the Larmor frequency ω_0. The B_1 field rotates about the z axis at a frequency ω_{RF}, which ideally is close to ω_0. Due to the pulse, the magnetization is rotated about an orthogonal axis at a frequency of ω_1. ω_0 and ω_{RF} are on the order of megahertz, while ω_1 is usually on the order of kilohertz at maximum.

6.6.3 The Bloch Equations in the Rotating Frame

By introducing the rotating coordinate system, and by disregarding the off-resonant RF component, we can compute the action of RF pulses by modified Bloch equations relatively easily. To do that, we need to substitute B_0 with the effective field along z in that frame, B_0', and assume that B_1 is static, and those are the only fields of relevance. If we assume the B_1 field is along x and disregard the effects of relaxation, the Bloch equations in the rotating frame of reference then become

$$\frac{\mathrm{d}\boldsymbol{M}}{\mathrm{d}t} = \gamma \begin{pmatrix} M_x \\ M_y \\ M_z \end{pmatrix} \times \begin{pmatrix} B_1 \\ 0 \\ B_0' \end{pmatrix} = \gamma \begin{pmatrix} M_y B_0' \\ M_z B_1 - M_x B_0' \\ -M_y B_1 \end{pmatrix} . \tag{6.19}$$

When the spins are exactly on-resonant ($B_0' = 0$), this simplifies to

$$\frac{\mathrm{d}\boldsymbol{M}}{\mathrm{d}t} = \gamma \begin{pmatrix} 0 \\ M_z B_1 \\ -M_y B_1 \end{pmatrix} \tag{6.20}$$

which has the solution

$$\boldsymbol{M}(t) = \begin{pmatrix} M_x(0) \\ M_y(0)\cos(\omega_1 t) - M_z(0)\sin(\omega_1 t) \\ M_z(0)\cos(\omega_1 t) + M_y(0)\sin(\omega_1 t) \end{pmatrix} \tag{6.21}$$

with $\omega_1 = -\gamma B_1$. Equation 6.21 describes a vector rotating about the x axis. Similarly, it can be shown that when the B_1 field points along the y axis, the magnetization rotates about the y axis, or more generally, the magnetization will rotate about the direction of the B_1 field. Thus, if the RF pulse is exactly on-resonant, and

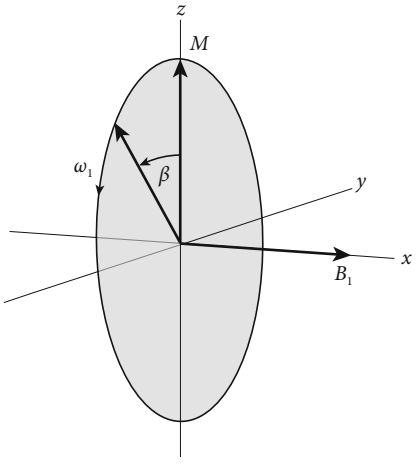

Figure 6.14 Nutation of magnetization during an RF pulse in the rotating frame. Initial z magnetization, exactly on-resonant to the RF field, will rotate in a plane orthogonal to the B_1 field. As it has become standard to describe NMR in the rotating frame of reference, the dashes next to the labels, which are usually used to indicate the rotating frame, have been omitted here.

starting with equilibrium z magnetization, the magnetization will rotate in a plane orthogonal to B_1 as shown in Figure 6.14. Of course, all this is with regard to the rotating frame.

6.6.4 Rotation of On-Resonant and Off-Resonant Magnetization under the Influence of Pulses

In the previous sections we demonstrated that by transformation into a properly chosen rotating coordinate system for an on-resonant spin, only a single field, the transverse B_1 field, is present. In such a frame, rotation of magnetization occurs as depicted in Figure 6.14. This presentation is much easier to understand than trajectories of pulses in laboratory frames, and therefore we find this representation a lot in the NMR literature. However, we need to keep in mind under what circumstances this presentation is valid.

The angular frequency of rotation, the *nutation* frequency, is related to the RF field strength by

$$\omega_1 = -\gamma B_1 \tag{6.22}$$

As in the case of Larmor precession, the sense of nutation depends on the sign of the gyromagnetic ratio γ of the nucleus. For simplicity, we will again assume that γ and hence the nutation is positive, and thus follows the right-hand rule (hence an x pulse will rotate magnetization toward the $-y$ axis). The flip angle β obtained

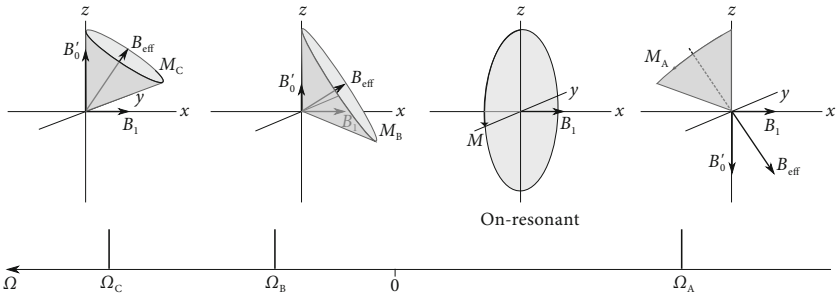

Figure 6.15 RF offset. The course of z magnetization (e.g., thermal equilibrium magnetization) for some particular offset frequencies in comparison with a 90° on-resonant pulse.

for a pulse of duration t_p is then given by

$$\beta = |\gamma| B_1 t_p \tag{6.23}$$

Most important are 90° and 180° pulses (often the phase is specified by a subscript, for example a 90°_x pulse).

The case in which magnetization is not on-resonant ($B_0' \neq 0$) is mathematically more demanding in the rotating frame. Instead of looking at a single field along a transverse axis, the B_1 field, we now have to consider the vector sum of two fields (B_0' and B_1) to yield the effective field B_{eff}'. B_{eff}' then presents a static field and, as in the case of free precession, the spin simply precesses about the direction of that field. With increasing RF offset, the offset frequency (Ω) of the spin will increase, and hence B_0' will become larger. As a consequence, the axis of rotation (the B_{eff} field) is increasingly tilted toward the z axis. This is qualitatively shown in Figure 6.15. The magnetization vector for such resonances evolves along the surface of a cone about the effective field.

The very important point to be noted here is that depending the offset of the resonance, only part of the magnetization is transferred into the transverse plane. As we will see later, this nonuniform transformation of the magnetization by RF pulses results in spectral artifacts, the so-called off-resonance effects.

6.7 Problems

6.1. In thermal equilibrium the population difference between the α and β spin states is governed by the Boltzmann distribution. Using the high-temperature approximation, how is the population difference related to the gyromagnetic ratio and the magnetic field strength?

6.2. What does it mean to the amount of observable magnetization if the gyromagnetic ratios of two nuclei differ by a factor of two?

6.3. What is the difference between populations and coherences?

6.4. Time evolution of magnetization is fully characterized by the Bloch equations. Is this true?

6.5. Group the following terms together: T2 relaxation; longitudinal relaxation; spin-lattice relaxation; T1 relaxation; transverse relaxation; spin–spin relaxation.

6.6. How is the shape of the FID related to the relaxation time constant T2 in the case of short T2s? And how does that influence the signal in the spectrum?

6.7. Does the line width of a signal directly reflect the transverse relaxation time T2?

6.8. An important concept in the description of NMR is the rotating frame of reference. In particular the action of RF pulses is best described in a rotating frame of reference. To which frequency is the reference frequency therefore usually related to?

6.9. What is the result of a 90° pulse when applied to thermal equilibrium magnetization that is exactly on-resonant? And what happens when the magnetization is not exactly on-resonant?

7
Chemical Shift and Scalar and Dipolar Couplings

As described in Chapter 2, the precession frequency depends on the exact strength of the magnetic field experienced by the nucleus, and for an isolated "naked" nucleus it would be $\omega_0 = -\gamma B_0$. However, in molecules the nuclei are surrounded by electrons and other nuclei, and we need to take their interactions with the nucleus of interest into account if we want to understand the phenomena of chemical shift, direct (dipolar) spin–spin couplings, and indirect (scalar) spin–spin couplings.

All these interactions have in common that they alter the effective magnetic field at the site of a nucleus, and hence the precession frequency. To perceive how a spin evolves under the influence of nearby electrons and other nuclear magnetic moments, we need to consider the local fields produced by them. Unfortunately this is not very simple. Since the spin is a quantum mechanical quantity, the magnetic field produced by it must be treated in quantum mechanical terms. It is in general not possible to describe spin evolution under spin–spin couplings using the classical equations of motion analogous to the Bloch equations, and vector representations are only of limited use.

In fact, the time-dependent Schrödinger equation must be employed to predict how the spins evolve, and this requires knowledge of the Hamiltonian, the energy operator of the system. A short introduction to this topic can be found in Chapter 9. The Hamiltonians are usually found by describing the interactions in terms of classical physics, and then replacing the nonclassical quantities (here the dipole moment $\boldsymbol{\mu}$) by the corresponding operators (here the spin operators I_x, I_y, and I_z). An example will be presented in Section 14.3.1.

As a detailed quantum mechanical treatment is beyond the scope of this book, we will not manipulate Hamiltonians here, but will rather describe the interactions qualitatively. However, we will have a closer look at the origin of these interactions, and how they influence the appearance of the spectra.

7.1
Chemical Shielding

As described in Chapter 2, the origin of chemical shift is the varying electronic environment of the nuclei. Figure 7.1a displays a bare nucleus in a homogeneous ex-

Applied NMR Spectroscopy for Chemists and Life Scientists, First Edition. Oliver Zerbe and Simon Jurt.
©2014 WILEY-VCH Verlag GmbH & Co. KGaA. Published 2014 by WILEY-VCH Verlag GmbH & Co. KGaA.

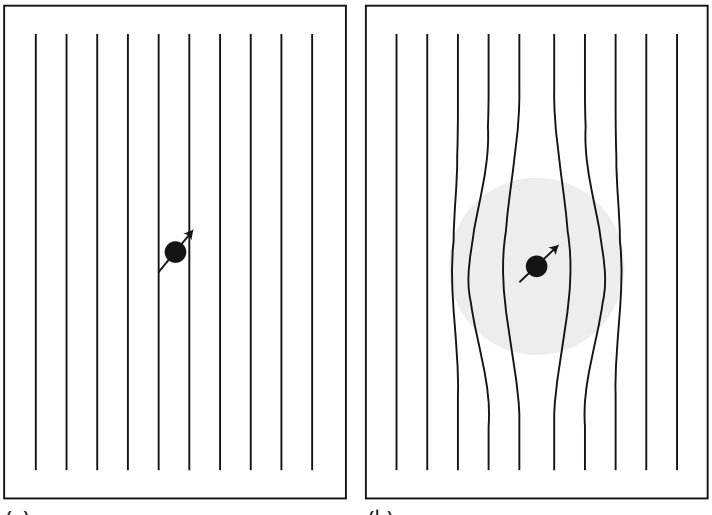

Figure 7.1 NMR-active nucleus in a magnetic field in the absence (a) or presence (b) of shielding electrons. The strength of the field is proportional to the separation of the field lines.

ternal magnetic field indicated by equidistant vertical field lines. According to (2.2) the nucleus will precess proportional to the field strength B_0 with frequency ω_0. In Figure 7.1b the more realistic situation is shown, where the nucleus is surrounded by (s) electrons. The electron cloud has the effect of *shielding* the nucleus to some extent from the external field. Therefore, the effective local field at the site of the nucleus is somewhat weaker, and accordingly the precession frequency of the nucleus is lower. Because the electron distribution differs in molecules from site to site, the shielding and thus the resonance frequencies change for the various sites.

The shielding is usually specified by the symbol σ. In liquid-state NMR the shielding is characterized by a single constant, the isotropic shielding constant σ_{iso}. Its values are normally in the parts per million range, and indicate by what fraction the external field is reduced because of the shielding (for positive σ). In view of (2.2), the resonance frequency becomes

$$\omega_{\mathrm{iso}} = -\gamma\,(1 - \sigma_{\mathrm{iso}})\,B_0 \tag{7.1}$$

When reporting chemical shifts the difference from a standard normalized to the field is reported (see (2.3)). In contrast to shielding in solution, in solid-state NMR, shielding must be described by a tensor. We will have a look at that at the end of this section. First let us look at the different contributions to shielding.

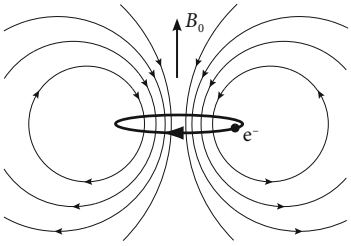

Figure 7.2 Diamagnetic contribution to the chemical shift from the motion of electrons.

7.1.1 The Contributions to Shielding

There are several mechanism that contribute to chemical shielding:

$$\sigma = \sigma_{\text{dia}} + \sigma_{\text{para}} + \sigma_{\text{m}} + \sigma_{\text{rc}} + \sigma_{\text{ef}} + \sigma_{\text{solv}} \tag{7.2}$$

Here σ_{dia} is the *diamagnetic* contribution, σ_{para} the *paramagnetic* contribution, σ_{m} the *neighbor anisotropy effect*, σ_{rc} the *ring-current* contribution, σ_{ef} the *electric field effect*, and σ_{solv} the *solvent effect*. Depending on which nucleus we are interested in, for example, ^{1}H or ^{13}C, and the particular environment, their relative magnitudes can be very different. In the following we describe all these effects in more detail.

7.1.1.1 The Diamagnetic Term

The *diamagnetic effect* of shielding can be understood by the circular motion of the electrons as illustrated in Figure 7.2. The static magnetic field B_0 causes the electrons to precess about the axis of the magnetic field. Thereby, a current is generated that itself induces a magnetic field. The direction of the induced field is opposed to that of the static field and acts to decrease the strength of the latter.

This effect is called the *Lamb shift*. It can be calculated as

$$\sigma_{\text{iso}} = \frac{\mu_0 e^2}{3m_{\text{e}}} \int r\rho(r)\mathrm{d}r \tag{7.3}$$

in which $\rho(r)$ is the electron density, r the distance of the electron from the nucleus, e the charge, and m_{e} the mass of the electron. One important statement of this so-called *Biot–Savart law* is that it is the electron density *at large distances from the nucleus* that is of primary importance for the counteracting field. The diamagnetic shielding describes the behavior of spherically distributed electrons such as electrons from the s orbital of protons, and computationally it primarily depends on the ground-state electronic properties. It is the dominant term for proton shifts but is less important for heavier nuclei. In addition, the diamagnetic (shielding) contribution tends to be similar for nuclei of one isotope except protons, and in all cases other than protons is negligible in size.

7.1.1.2 The Paramagnetic Term

In addition to a diamagnetic contribution there may also be a *paramagnetic (deshielding) contribution* to the chemical shift which accounts for the nonspherical

electron distribution and becomes more important for heavier nuclei such as ^{13}C, ^{15}N, ^{31}P, and metal nuclei, while the diamagnetic contribution dominates for ^{1}H. Quantum mechanically speaking, the paramagnetic term may be calculated by finding the way by which the electron wave functions are modified by the magnetic field. Such a modification of the wave function takes place because the properties of exited states (contributions from low-lying unoccupied orbitals, mostly but not exclusively, the lowest unoccupied molecular orbital, LUMO) are mixed into ground-state wave functions (especially the highest occupied molecular orbital, HOMO) through the presence of the static field. The paramagnetic term requires a nonspherical electron distribution (a nonvanishing angular momentum) and can hence only be applied to nuclei that have non-s-orbital electrons. Furthermore, the excited states must be connected to the ground state by magnetic-dipole-allowed transitions. In these transitions, the electronic charge seems to rotate in going from one orbital to another (e.g., from $p_x \rightarrow p_y$, two orbitals in which the principal directions of electron density are orthogonal).

The paramagnetic term is dominant for all nuclei other than protons. It may be large when the nucleus in question is surrounded by an asymmetric distribution of p and d electrons, or if low-lying excited states of the correct symmetry are present. The paramagnetic term results in an induced field that is parallel to the static field and therefore leads to *deshielding*, which means higher resonance frequencies. The shift range due to the paramagnetic contribution is much larger than that for the diamagnetic shift. This is obvious from the huge shift ranges (e.g., several thousand parts per million for ^{57}Fe compared with approximately 15 ppm for ^{1}H).

The calculation of the paramagnetic shift is rather involved and requires exact knowledge of the excited-state wave functions. For ^{13}C it can be approximated by

$$\sigma_{\text{para}} = \frac{\mu_0 \mu_B^2}{2\pi \Delta E r^{-3}} [Q_i + \Sigma Q_j] \tag{7.4}$$

In this formula, ΔE is the energy difference between the HOMO and the LUMO, r is the radius of the 2p orbital (which is related to the atomic number and the position in the periodic table) and the Q describe electron densities and bond orders. Very low lying ground-state wave functions are usually paired with rather high lying excited state wave functions such that the resulting energy separation is comparably large. Since the paramagnetic shift is inversely proportional to the energy gap, the shift is large when the gap is small. Reactivities of compounds are often related to HOMO/LUMO energy separations and chemical shifts have therefore been successfully used to screen for reactive compounds.

7.1.1.3 **Chemical Shift Anisotropy**

The distribution of the electrons about the nucleus is usually nonspherical. The magnitude of the shielding therefore depends on the relative orientation of the nucleus with respect to the static field. For a more thorough discussion of this, see Section 7.1.3. For sp^3 carbons the nuclei are tetrahedrally coordinated and the electron distribution is almost invariant under rotation. For sp^2 carbons such as

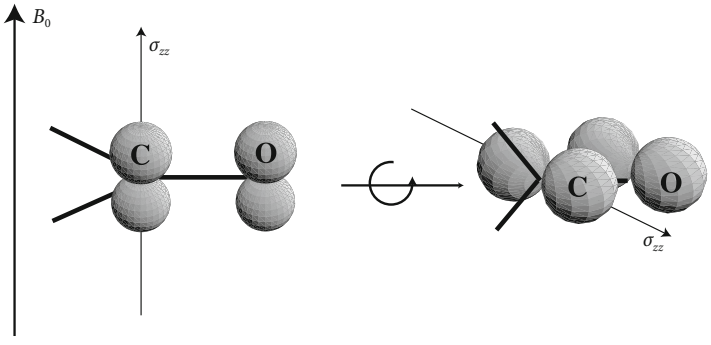

Figure 7.3 Chemical shift anisotropy. Two different orientations are shown for a carbonyl moiety: the orientation on the left corresponds to the largest shielding (lowest frequency) for the carbonyl ^{13}C nucleus.

aromatic or carbonyl nuclei the shielding highly depends on the orientation of the bond relative to the static field.

Figure 7.3 highlights the dependence of the shielding of the carbonyl carbon nucleus on the orientation of its zz axis with respect to the external field. The zz axis is usually taken as the axis with the largest shielding, and in the case of the carbonyl carbon it coincides with the direction of the p_z orbital. Another example of a nucleus with large chemical shift anisotropy (CSA) is the ^{15}N nucleus in compounds of the type R_3N. Here, the orientation of the lone pair at the nitrogen defines the direction of the largest shielding. Since the molecule rotates quickly in solution, the chemical shift observed is an average over the shifts corresponding to the different orientations, the so-called isotropic chemical shift. However, when rotation is hindered, as is the case in the solid state, the line is significantly broadened. In liquids this effect contributes to relaxation, and is the major relaxation mechanism for nonprotonated carbons. CSA values can be measured from solid-state NMR. The value of the chemical shift for the isotropic case can be taken as one-third of the trace: $\sigma_{\text{iso}} = \frac{1}{3}(\sigma_{xx} + \sigma_{yy} + \sigma_{zz})$.

7.1.1.4 The Neighbor Anisotropy Effect and the Ring-Current Effect

Some types of neighboring bonds create an additional magnetic field which is anisotropic in space. An example is a triple bond. The π electrons of the triple bond form an electron cloud that extends around the bond axis in the form of a tube. The magnetic field forces the electrons to rotate about the bond axis, creating a magnetic field whose direction is along the bond axis and which again counteracts the static field. A similar counteracting field is formed in the π cloud of aromatic systems. Such anisotropies can dramatically change the appearance of proton spectra. They usually dramatically increase the dispersion of proton spectra. However, in order to give substantial effects, the protons that are influenced must be sterically fixed relative to the anisotropic group. This is, for example, the case for folded proteins that do adopt a unique structure. The observed shifts can be either shielding or deshielding depending on the exact position of the proton.

These effects can be dramatic. Aliphatic protons that are fixed in space *above the plane* of an aromatic ring can be shifted to values below 0 ppm, and those *in the plane* can be shifted to values higher than 10 ppm. A number of examples are presented in Section 3.2.2.

In a single or triple bond the magnetic susceptibility is similar in the two directions orthogonal to the bond, and the CSA can be computed as

$$\Delta\sigma = \frac{1}{3r^3}\left[(\chi_{\parallel} - \chi_{\perp})(1 - 3\cos^2(\theta))\right]\frac{1}{4\pi} \tag{7.5}$$

where θ is the angle with respect to the bond axis, r the distance to the center, and χ the magnetic susceptibilities parallel and perpendicular to the bond axis. As can be seen from the formula, the effect depends strongly on the distance and orientation. Anisotropy effects play a particularly large role in proton NMR, and they are described in more detail in Section 3.2.2.

7.1.1.5 The Electric Field Effect

Strongly polar groups create intramolecular electric fields. This has the effect of distorting the electron density in the rest of the molecule and will hence influence the chemical shifts. It can act to increase or decrease the chemical shifts of adjacent nuclei.

7.1.1.6 Hydrogen Bonds

Hydrogen bonds decrease the electron density at the proton site involved and hence lead to a high-frequency shift. The effect is especially pronounced for symmetric hydrogen bonds (those in which the distance from the proton to both acceptors is equal). Protons that are hydrogen bonded are often recognized from their chemical shift. Their shift is less temperature, concentration, and solvent dependent. Protons that are part of hydrogen bonds exchange much more slowly with labile solvent deuterons and can therefore be differentiated from others. This is used in protein NMR experiments to identify β sheets or α helices that display extended hydrogen-bond networks.

7.1.1.7 The Solvent Effect

It is very important to realize that different solvents may have different effects on the chemical shifts, and this effect is particularly pronounced in proton NMR spectra. Quite often overlapping signals can be resolved when the solvent is changed. Benzene and acetone are examples of solvents that cause large changes in chemical shifts, and they may completely change the appearance of a spectrum that has been acquired in chloroform.

The polar solvent effect is basically an electric field effect. Polar solvents will induce a reaction field if polar groups are present in the solute. The reaction field will reshuffle electrons in the solute. The effect is such that it reinforces the already present effect from inductive groups and hence can be both shielding and deshielding. This effect is negligible for isotropic molecules such as tetramethylsilane, which is therefore often chosen as a standard for reference.

Other solvents with strong anisotropy also lead to dramatic changes in the spectra. A classic example is benzene. The effect is especially strong when benzene selectively complexes parts of the molecule due to the ring-current effect from the benzene ring. Such selective effects may be the case when not all parts of the molecule can be accessed by the solvent, and motional effects due to the rapid reorientation of benzene are not completely averaged out due to the disklike shape of the benzene molecule. Often comparison of spectra recorded in benzene (low-frequency shifts) and acetone (high frequency shifts) is helpful for molecules with complicated spectra.

7.1.2 The Chemical Shifts of Paramagnetic Compounds

Paramagnetic compounds have unpaired electrons. When paramagnetic impurities are contained in the sample, the lines are usually considerably broadened for solvent-accessible protons. The distance-dependent relaxation effect is often used for structural purposes. However, the chemical shift can also be influenced. One of the types of mechanisms leading to a change in resonance frequency is due to the *Fermi contact* term. The contact shift is given by an additional magnetic field generated at the nucleus by the electron magnetic moment located at the nucleus itself. We will learn more about the Fermi contact interaction when we have a closer look at scalar coupling. Suffice to say for the moment that for the Fermi contact, electron density at the nucleus is important, and hence occupation of s-type orbitals (note the p orbitals have zero electron density at the nucleus). The shift due to the contact term is

$$\Delta\sigma = -2\pi\alpha_N \frac{g\mu_B S(S+1)}{3\gamma_I KT} \tag{7.6}$$

in which g is the electronic g factor, and α_N is the electron–nuclear spin coupling constant (the other constants have their usual meaning). The direction of the shift depends on the sign of α_N. We should note that if $g = g_e$, the contact shift is isotropic (independent of orientation). If g is different from g_e and anisotropic, then the contact shift is also anisotropic. To be spread about onto neighboring atoms, spin density must be delocalized. The shift due to the direct Fermi contact is very large (it can be 50 ppm or more) but usually locally limited.

The second type of interaction is the dipolar interaction between the nucleus and the electron, and is referred to as the *pseudocontact shift*. Under certain circumstances the pseudocontact shift can be expressed as

$$\Delta\sigma = \mu_B^2 S(S+1)\left(g\parallel^2 - g_\perp^2\right)\frac{(1-3\cos^2\theta)}{9kTr^3} \tag{7.7}$$

where r is the distance of the paramagnetic center to the nucleus and θ is the angle between $\boldsymbol{r}$ and the symmetry axis of the g factor. The pseudocontact shift can be an intermolecular effect. Since its interaction depends on the r^3, it can reach much further than the direct contact term (up to 20 Å), but the shifts are usually smaller.

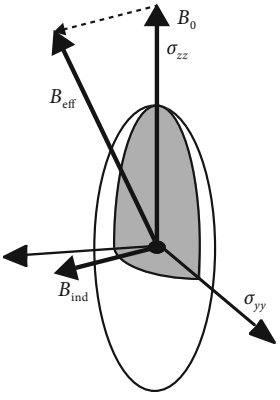

Figure 7.4 Definition of the shielding tensor. The shielding tensor maps the vector representing the *static* field B_0 onto the principal components of the shielding tensor, giving rise to the induced field B_{ind}, which together with B_0 results in the *effective* field B_{eff}.

So-called shift reagents contain a suitable metal complexed to a ligand to yield a system that is soluble in the solvent used. These paramagnetic reagents serve to disperse proton NMR spectra. Thereby, a 2 ppm shift range for aliphatic protons can be dispersed over 6 ppm after addition of the shift reagent, thereby reducing spectral overlap at the expense of line broadening.

7.1.3 The Shielding Tensor

To describe the effect of shielding in more general terms we need to look at the changes of the external field B_0. Generally one has to consider a small induced magnetic field B_{ind}, produced on a particular nuclear site when the molecule is exposed to a magnetic field. Together with B_0 this will result in a effective field B_{eff} to which the spin precession frequency is related.

Depending on the symmetry of the electron density, the direction and magnitude of the effective field, B_{eff}, and hence the chemical shift may depend on the orientation of the molecule in the static field. This behavior is called *chemical shift anisotropy* (CSA). In general, the shielding must therefore be related by a tensor, the so-called *shielding tensor* $\boldsymbol{\sigma}$:

$$\boldsymbol{B}_{\text{eff}} = -\boldsymbol{\sigma}\boldsymbol{B}_0 + \boldsymbol{B}_0 \tag{7.8}$$

The term $-\boldsymbol{\sigma}\boldsymbol{B}_0$ is often also denoted as the *induced field* $\boldsymbol{B}_{\text{ind}}$. The vector addition of this induced field and the static field yields the field that is effective at the nucleus.

The shielding tensor $\boldsymbol{\sigma}$ is a second-rank tensor that can be described by a 3×3 matrix. It rotates the vector describing the external field into another vector that describes the *induced* field (Figure 7.4):

$$\boldsymbol{B}_{\text{ind}} = \begin{bmatrix} \sigma_{xx} & \sigma_{xy} & \sigma_{xz} \\ \sigma_{yx} & \sigma_{yy} & \sigma_{yz} \\ \sigma_{zx} & \sigma_{zy} & \sigma_{zz} \end{bmatrix} \begin{bmatrix} 0 \\ 0 \\ B_0 \end{bmatrix} \tag{7.9}$$

The elements of the shielding tensor depend on the particular orientation of the molecule. Often it is more convenient to represent the shielding tensor in its *principal axis system* (PAS). In the frame of the principal axis system, the shielding tensor consists of three diagonal elements, the so-called principal components, with $\sigma_{xx} \leq \sigma_{yy} \leq \sigma_{zz}$, and all off-diagonal elements are zero.

However, in liquid-state NMR experiments, because of rapid tumbling anisotropic contributions to the chemical shift are usually averaged out and we observe for a particular nucleus a narrow single line in the spectrum at its isotropic chemical shift δ_{iso}. The *isotropic chemical shielding* σ_{iso} is the average of these three diagonal elements and this is the quantity we measure in solution NMR experiments:

$$\sigma_{\text{iso}} = \frac{1}{3}(\sigma_{xx} + \sigma_{yy} + \sigma_{zz}) \tag{7.10}$$

In the solid state, because of the lack of rotational motion, other components of the shielding tensor are observed, resulting in characteristic powder patterns. These are described in more detail in Chapter 18, and examples are depicted in Figure 18.2. For example, the *anisotropy* $\Delta\sigma$ characterizes the deviation from cubic symmetry,

$$\Delta\sigma = \sigma_{zz} - \frac{1}{2}(\sigma_{xx} + \sigma_{yy}) = \frac{3}{2}(\sigma_{zz} - \sigma_{\text{iso}}) \tag{7.11}$$

(this accounts for the distortion of an octahedron when you pull on two opposite edges along the z coordinate), and the *asymmetry* is defined as

$$\eta = \frac{\sigma_{xx} - \sigma_{yy}}{\sigma_{zz} - \sigma_{\text{iso}}} = \frac{3(\sigma_{xx} - \sigma_{yy})}{2\Delta\sigma} \tag{7.12}$$

The term $\sigma_{xx} - \sigma_{yy}$ is also called the *rhombicity* of the tensor, and in that context defines the difference in shielding in the x and y directions. The *axiality* denotes the difference of the shielding in the z direction from the average shielding in the transverse plane. The direction of the largest shielding by definition is along z!

The type of distortions from octahedral symmetry described above are schematically depicted in Figure 7.5.

7.2 The Spin–Spin Coupling

In NMR spectroscopy the term "spin–spin coupling" denotes the interaction between nuclear spins. There are two different ways in which spins can interact with each other: a nucleus can sense the dipolar field of another nuclear dipole either directly through space or indirectly mediated via the intervening electrons. These two possibilities are called "direct dipole–dipole coupling" and "dipolar coupling" in the first case and "indirect dipole–dipole coupling," "scalar spin–spin coupling," and "J coupling" in the second case. Throughout this book we will use the term

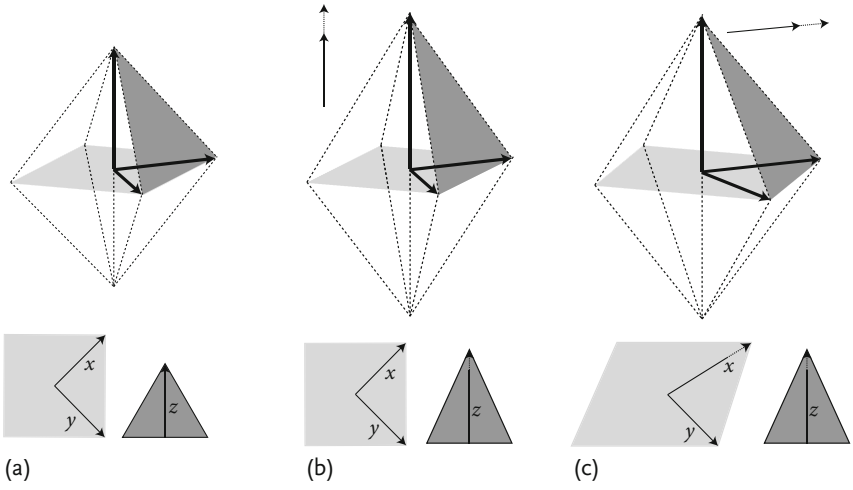

Figure 7.5 Distortions of a tensor from perfect octahedral symmetry. (a) A perfect octahedron, which corresponds to a tensor in which the values of the principal axis are the same. (b) The change when the value of the *z* component is increased. (c) An additional increase of the *x* component. The plane spanned by the *x* and *y* components changes from a square to a rhombus (see the bottom panels in (a)–(c)). The thin arrows indicate the direction of distortion (elongation).

"dipolar coupling" for the direct interaction and "scalar coupling" for the indirect, electron-mediated, interaction.

The strength of the dipolar interaction is proportional to the separation distance $\frac{1}{r^3}$. The contributions from dipolar coupling cannot usually be observed in an isotropic (liquid) phase. This is because the dipolar coupling depends on the orientation of the connecting vector to the static field. This orientation rapidly changes in solution due to molecular tumbling, and the dipolar coupling therefore averages to zero. However, it can be observed in the solid state or in liquid crystals. The scalar coupling in contrast leads to a splitting of resonance lines. The effect is mediated via the electrons and its magnitude therefore rapidly decreases when the number of intervening bonds increases and becomes very small if there are more than three, with a few exceptions.

7.2.1 Scalar Coupling

As the name suggests, scalar spin–spin coupling depends on the scalar product of two spins I and S ($\boldsymbol{\mu}_I \cdot \boldsymbol{\mu}_S$). The energy of interaction is described by the coupling tensor $\boldsymbol{J}$. However, as is the case for the shielding tensor, in solution the scalar coupling is usually averaged to a single value, the scalar coupling constant J. The scalar coupling constant is usually given the symbol ${}^{n}J$, in which n denotes the number of intervening bonds.

When the shift difference of the two spins is much larger than J, we only need to consider the spin components collinear to the B_0 field (I_z and S_z). We then say

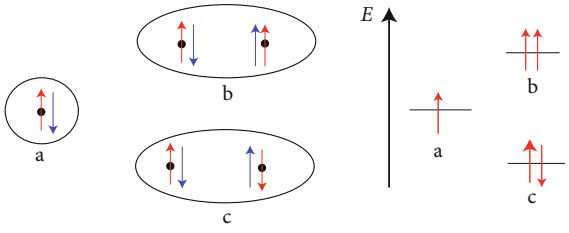

Figure 7.6 Energy levels for an isolated spin a and a pair of scalarly coupled spins b and c. Fermi contact between an electron spin and a nuclear spin that are parallel as for b is energetically unfavorable.

the coupling is "weak." In contrast, when the shift difference is small with respect to J, no such approximation can be made and we need to take into account all three terms of the scalar product. In that case the coupling is denoted as "strong" and it gives rise to much more complicated signal patterns than in the case of weak couplings, and higher-order effects start to occur (see Section 3.4.2). Since the precession frequencies of unlike spins are always very different, heteronuclear couplings are always "weak."

The basic mechanism that propagates the coupling is the *Fermi contact* interaction (Figure 7.6). This effect describes the coupling between the nuclear spin and the electron spin. Electrons that occupy an orbital that has a nonvanishing electron density at the nucleus (such as s electrons) have the electron spin antiparallel to the nuclear spin (Hund's rule). If the atom is bonded to another atom, then the two s orbitals of the separate atoms form a σ orbital, which is occupied by two electrons with antiparallel spin (Pauli principle). The second nuclear spin can now have its spin parallel or antiparallel to the spin of the second electron depending on whether it is in the α state or the β state. The antiparallel alignment is energetically favorable for nuclei with positive γ and hence lowers the corresponding energy level.

The magnitude of the coupling constant can be calculated as

$$J = \left(\frac{2\mu_0 g_e \mu_B}{3}\right)^2 \gamma_A \gamma_B \Psi_A^2(0)\, \Psi_B^2(0)\, c_A^2 c_B^2 \left(\frac{1}{\Delta T}\right) \tag{7.13}$$

where γ_A and γ_B are the gyromagnetic ratios of the nuclei involved, $\Psi_A^2(0)$ is the electron density at the site of nucleus A, and c_A is the coefficient of the contribution of the atomic orbital of nucleus A to the σ molecular orbital. ΔT is the *triplet excitation energy*, which is a measure of the energy required to promote an electron from the singlet to the triplet spin state (parallel alignment).

Figure 7.7 highlights the situation for a one-bond coupling, and the propagating electrons are the s electrons that share a common σ orbital. For couplings to heavier elements, other contributions such as paramagnetic spin–orbit and spin–dipolar terms have to be taken into account as well, and hence (7.13) is no longer valid.

The *one-bond coupling* constant usually has a positive sign. The s character of orbitals depends heavily on the hybridization of the nuclei involved. This is very

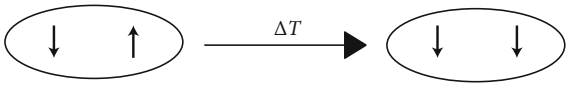

Figure 7.7 Definition of the triplet energy.

clear from the $^1J(^1H,^{13}C)$ coupling constants which can be roughly estimated as 140 Hz (sp^3), 160 Hz (sp^2), and 250 Hz (sp) (see also Section 4.3.2.1). The sp orbital has the highest content of s character and hence results in the largest coupling. The coupling also depends on the gyromagnetic ratios of the nuclei involved. When hydrogen is substituted with deuterium, the corresponding coupling to another proton is approximately scaled by the factor $\frac{\gamma_D}{\gamma_H} = \frac{2}{13}$. Therefore, for comparisons the couplings are sometimes reported in the form of the *reduced couplings*, which are defined as

$$\kappa_{ik} = \frac{J_{ik}}{h} \frac{2\pi}{\gamma_i} \frac{2\pi}{\gamma_k} \tag{7.14}$$

7.2.1.1 ^2J Couplings

The situation for *two-bond scalar (or geminal) couplings* is schematically shown in Figure 7.8. Again, the lowest energy for coupling of the electron spin with the nuclei with positive γ is for the antiparallel arrangement. Within the σ orbital the two electrons are antiparallel (Pauli principle). For the intervening atom *X* the two localized electrons must be *parallel* (Hund's rule), and then the other electron occupying the second σ orbital has antiparallel spin again. Compared with the one-bond coupling the sign of the two-bond scalar coupling is reversed (negative). In principle, for every extra atom in the chain, the sign of the coupling should alternate. This is strictly only true when pathways along localized σ orbitals are considered. When, however, an sp^2-hybridized carbon is part of the system, the two-bond coupling is positive (e.g., for formaldehyde). Accordingly, the two-bond couplings in the case of $^1H,^1H$ couplings largely depend on the hybridization of the carbon nucleus involved. But things are unfortunately more complicated, and there are many contributions to the two-bond coupling, some of which mutually cancel. Therefore, the two-bond scalar couplings are often smaller than the three-bond couplings.

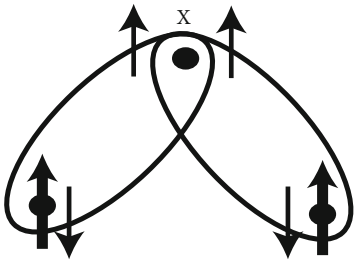

Figure 7.8 ^2J scalar couplings. The pathway for transmission of scalar couplings is depicted for localized σ bonds. According to Hund's rule the electrons at the intervening center X are parallel.

7.2.1.2 ^3J Couplings

The *three-bond couplings* (vicinal couplings) display a characteristic dependence on the dihedral angle involved (Figure 7.9). The relationship has become known as the *Karplus relationship*, and the analytical expression is

$$^3J = A + B\cos\phi + C\cos^2\phi \tag{7.15}$$

Accordingly, the scalar coupling is large for the synperiplanar or antiperiplanar arrangements of coupled nuclei, and is smallest when they are orthogonal. The relationship is valid for $^3J(^1H,^1H)$, $^3J(^1H,^{13}H)$, $^3J(^{13}C,^{13}C)$, or even proton couplings to metal nuclei. Values of the constants *A*, *B*, and *C* have been determined for those cases. The relationship is extensively exploited in stereochemical analysis, in particular when the bonds involved are not free to rotate (for applications, see Sections 3.5.2 and 4.3.2.1).

This angular dependence occurs because the dihedral angle determines the degree of overlap of the molecular orbitals (Figure 7.10). The larger the overlap, the better information on spin polarization is propagated through the chain of bonds, and thereby the better is the efficiency of transfer. This is important because the coupling must be propagated along the σ orbitals.

The overlap of the two σ orbitals is minimal when the dihedral angle is 90°. The Karplus curve is symmetric about 180°, which also defines the maximum value of the ^3J coupling. Further effects on the vicinal couplings are (i) electronegative substituents that decrease ^3J because they reduce electron density, (ii) increasing H–C–C bond angles decrease ^3J because this is accompanied by reduced s character, and (iii) increasing C–C bond lengths that also decrease ^3J values.

In cases where double bonds are part of the coupling pathway, we also need to consider participation of π electrons. At first sight it is difficult to understand how spin polarization from s electrons can influence polarization of π electrons, considering that the π orbitals have a node in the direction of the σ orbital. Without providing a detailed explanation, we simply state here that the electron from the

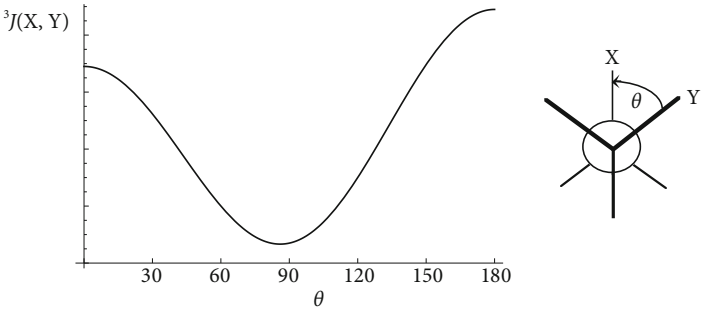

Figure 7.9 Angular dependence of the ^3J couplings. Karplus curve for ^3J scalar couplings for two nuclei X and Y. The curve is symmetric about 180°, and only the first part is shown.

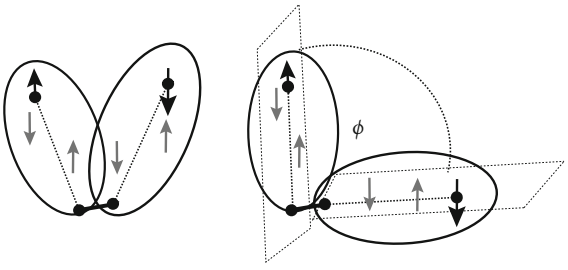

Figure 7.10 Orbital overlap for two molecular orbitals in a H–C–C–H fragment. The overlap of the two C–H σ orbitals depends on the dihedral angle ϕ. The central bond is depicted in bold, and the C–H bonds are indicated by dotted lines.

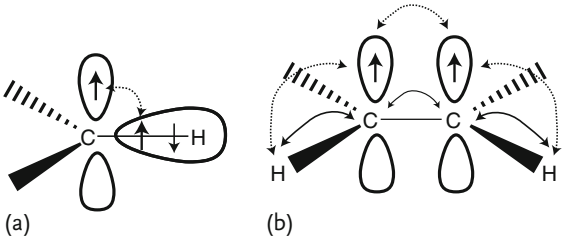

Figure 7.11 Polarization of electrons in σ and π orbitals. (a) A π electron polarizes the electron from the adjacent σ orbital such that its spin state is parallel (arrow with dotted line). (b) In the case of the ^3J pathway involving a double bond, the coupling is propagated via the σ electrons (arrows with solid lines) *and* via the π electrons (arrows with dotted lines). For conjugated π systems transfer via π electrons becomes dominant.

π orbital polarizes the σ electron that is closest to the common atom such that its spin state is *parallel* (see Figure 7.11).

7.2.1.3 ^nJ Long-Range Scalar Couplings

Long-range couplings (^4J, ^5J) are rarely observed. For saturated systems they require the atoms to be coplanar and in a zigzag (W) conformation. Two pathways contribute (see Figure 7.12). In one pathway, depicted in Figure 7.12a, overlap of vicinal orbitals results in spin correlation, and therefore the spins on the pathway alternate in sign. The second pathway (Figure 7.12b) consists of a spin correlation in geminal orbitals, as discussed in the case of the two-bond couplings, which is then propagated via a vicinal interaction. Note that the sign for both pathways is opposite.

Relatively far reaching scalar couplings are observed in π systems. In principle, π electrons cannot propagate scalar couplings, because π orbitals have nodes at the position of the nuclei. Therefore, spin correlation between σ and π electrons is required (see Figure 7.11). As a rule of thumb ^3J couplings of protons are dominated by the σ mechanism, while for ^4J and ^5J transfer through both the σ and the π electrons contributes. Couplings between vicinal double-bond protons (C**H**=C**H**) are positive, allylic (^4J, C**H**–CH=C**H**) couplings are negative, and ho-

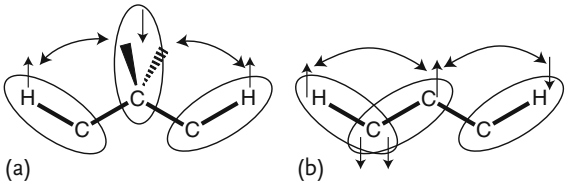

Figure 7.12 Mechanism of ^4J couplings. Two pathways contribute, one with two spin correlations via vicinal interactions (a), and one with a geminal and a vicinal interaction (b).

moallylic couplings (C**H**–C=C–C**H**) are again positive. Since π-electron systems are highly delocalized, in extended π systems scalar couplings can be propagated over many bonds. The orientation of the double bond in ^4J couplings is not important, for example, cisoid and transoid couplings are of similar magnitude. For more examples of long-range scalar couplings involving protons, see Section 3.5.3.

7.2.1.4 The Energy Level Diagram of an *IS* Spin System

Which resonance line in a pair of doublets from two mutually coupled spins belongs to which transition depends on the signs of J and γ. For a homonuclear case, the energy levels for a two-spin IS system are depicted in Figure 7.13a.

If we define the first spin as spin I and the second spin as spin S an $\alpha\beta$ level corresponds to the state where spin I is in the α state and spin S is in the β state. Then the $\alpha\alpha \rightarrow \alpha\beta$ transition changes the spin state of the S spin. Depending on whether γ of the observed nucleus and the coupling are positive or negative, the transitions belong to different lines in the spectrum as indicated in Figure 7.13b.[1)]

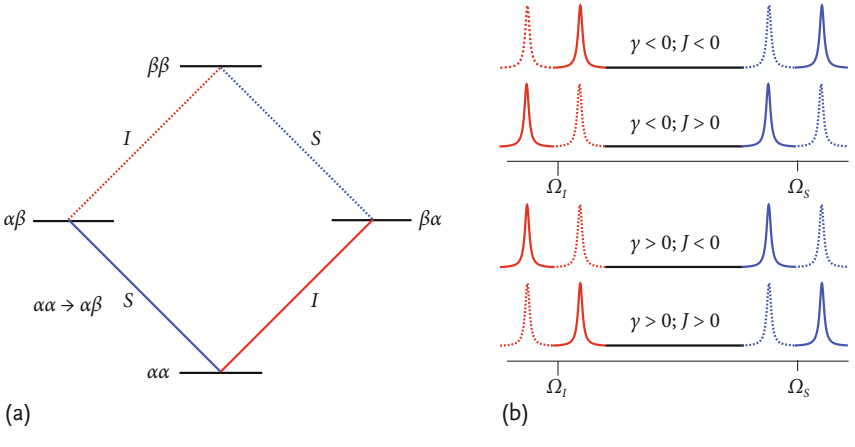

Figure 7.13 Energy level diagram for a scalarly coupled two-spin system (a), the corresponding 1D spectra depending on the sign of J and γ (b).

1) For a thorough discussion on this matter, see the wonderful book by Levitt (Spin Dynamics).

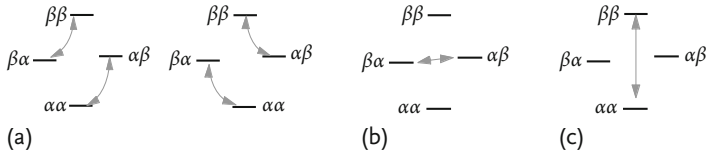

Figure 7.14 Single-quantum (a), zero-quantum (b), and double-quantum (c) transitions for a two-spin system.

7.2.1.5 NMR Transitions in a Scalarly Coupled Two-Spin System

For two coupled spins I and S, the transitions that may occur are at the single-quantum, double-quantum, and zero-quantum frequencies (Figure 7.14). Single-quantum transitions correspond to single-spin flips, whereas zero-quantum and double-quantum transitions correspond to simultaneous two-spin flips. Double-quantum transitions involve simultaneous spin flips in the same direction ($\alpha_I\alpha_S \rightarrow \beta_I\beta_S$ or vice versa), while zero-quantum transitions involve spin flips in the opposite direction ($\alpha_I\beta_S \rightarrow \beta_I\alpha_S$ or vice versa). The frequencies for single-quantum transitions correspond to the Larmor frequencies of the I or S spin (ω_I or ω_S). The frequency of the zero-quantum transitions correspond to the difference between the Larmor frequencies ($\omega_I - \omega_S$), and the double-quantum transitions correspond to the sum frequency ($\omega_I + \omega_S$). The maximum quantum number that can be formed depends on the number of coupled spins; for example, three coupled spins can form triple-quantum coherences at most.

Multiple-quantum coherences are not directly observable, but can be converted into single-quantum coherences. Nevertheless, the frequencies of multiple-quantum coherences may, for example, be measured in the indirect dimensions of 2D experiments. A famous experiment that records double-quantum frequencies, for example, is the INADEQUATE experiment (see Section 17.4.7), and another one the double-quantum-filtered (DQF) COSY experiment. In the DQF-COSY experiment, singlets (most importantly those from solvent signals) are suppressed.

7.2.2 Quadrupolar Coupling

The charge distribution of spin-1/2 nuclei is perfectly symmetric, and hence these nuclei behave like point charges. In contrast all nuclei with $I > 1/2$ posses an ellipsoidal charge distribution. As a consequence they have an electric *quadrupole moment* Q. Accordingly, the energy of these nuclei depends on their orientation in an *electrical* field (Figure 7.15).

Whereas the magnetic dipole moment of the spins *directly* interacts with the external magnetic field, the electric quadrupole moment interacts with the local electric field *gradient*. The electrical field at the nuclei is determined by the substituents (or ligands). When a quadrupolar nucleus is placed in a magnetic field, the energy levels of the nuclear spin additionally depend on the electric field gradient.

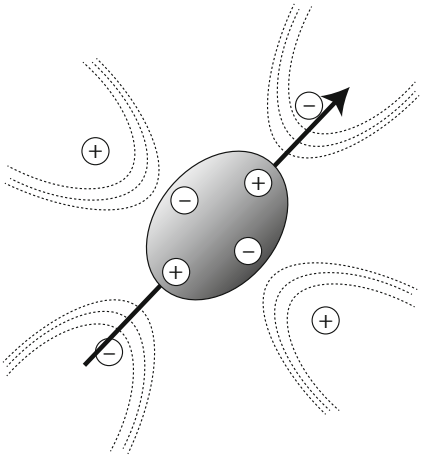

Figure 7.15 Quadrupolar nuclei in an electric field. The nuclear quadrupole moment orients itself in an electric field gradient. The electric field gradient is shown by the dotted lines.

In the liquid state, molecular motions change the local electric field gradient, and thereby induce transitions between the different magnetic states, giving rise to *quadrupolar relaxation* (see also Section 14.3.4). Depending on the magnitude of the quadrupole moment Q, this type of relaxation is very efficient and may results in extremely small values of T1. The *nuclear quadrupole coupling constant* is very large, and depends on the symmetry of the ligand field. For an ^{14}N nucleus ($I = 1$), the nuclear quadrupole coupling constant is a few kilohertz in the highly symmetric $^{14}NH_4^+$ ion, but is in the range of megahertz in asymmetric environments (e.g., about 9 MHz in NHF_2). The presence of a *neighboring* quadrupolar nucleus also has consequences for the relaxation properties of scalarly coupled spin-1/2 nuclei. Due to the rapid T1 relaxation of the quadrupolar nucleus, the scalar coupling to an attached spin-1/2 nucleus is modulated, resulting in increased relaxation of the $I = 1/2$ nucleus. This phenomenon is called *scalar relaxation of the second kind* (see Section 14.3.3). An example is the relaxation of a ^{13}CO site in a metal carbonyl compound in which the metal nucleus has $I > 1/2$. An example for organic compounds is the line widths of ^{13}C in R–C≡N (nitrile) groups.

7.2.3
Dipolar Coupling

The small magnetic moments of nuclear spins give rise to dipolar fields that act like tiny magnets. Nuclei in close proximity will sense these local fields produced by other spins and the spins will interact with each other. This interaction is called *dipolar coupling*. Since, in contrast to scalar coupling, the interactions take place directly through space, they are also called *direct spin–spin couplings*.

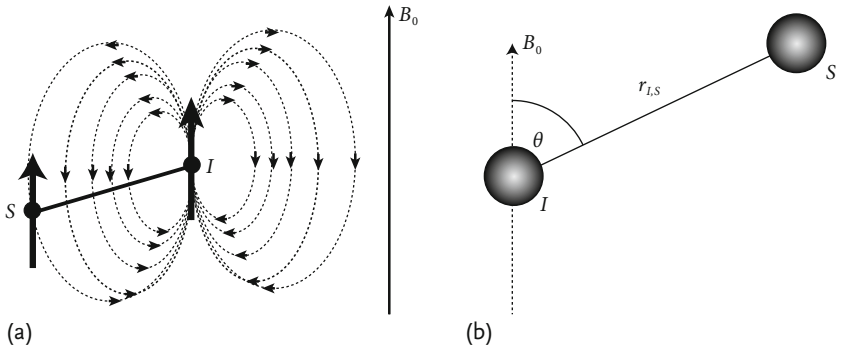

Figure 7.16 Mechanism of dipolar coupling. The dipolar field of spin *I* alters the magnetic field perceived by spin *S* (a). The strength depends on the distance $r_{I,S}$ and the orientation of the connecting vector with respect to the magnetic field as described by the angle θ (b).

The dipolar coupling constant d of two nuclei I and S separated by an internuclear distance r is

$$d_{IS} = -\frac{\mu_0 \gamma_I \gamma_S \hbar}{4\pi} \cdot \frac{1}{r_{IS}^3} \tag{7.16}$$

The magnitude of the dipolar coupling constant depends on the distance between the two dipolar-coupled spins and their respective gyromagnetic ratios. Therefore, a proton–proton dipolar coupling is much stronger than a ^{1}H–^{15}N dipolar coupling at similar distances. Since dipolar interactions are important sources of relaxation, proton relaxation times are mostly related to proton densities.

Dipolar couplings are quite strong, usually on the order of several kilohertz. But why do we not notice them in solution NMR spectra? Again, as for CSA, the reason is related to the rapid tumbling in solution. As depicted in Figure 7.16a, the dipolar field is not spherically symmetric, and the dipolar coupling depends on the relative position of the nuclei. As the molecule rotates, the dipolar coupling changes. A more detailed calculation shows that the coupling is effectively averaged to zero in the case of isotropic reorientation of molecules, and hence dipolar couplings cannot be observed in solution. Isotropic reorientation means that the molecule rotates about all possible axes with similar probability.

However, when the molecules do not freely rotate, as is the case in the solid state, dipolar couplings become visible. Since molecules are arbitrarily oriented in a powder, dipolar couplings will give rise to line widths of several kilohertz, and thus dipolar couplings dramatically increase the line widths and reduce the resolution. A more detailed mathematical treatment on the spatial dependency of dipolar couplings can be found in Excursus 7.1. As we will see in Chapter 18, fortunately the dipolar couplings can be effectively reduced by rapid spinning of the sample about a certain angle known as the magic angle.

Finally, we wish to mention that dipolar interactions are often the most effective source of relaxation (see Sections 2.4 and 14.3.1) and, related to that, are also responsible for the nuclear Overhauser effect (NOE) (Chapter 15). Because the NOE

arises from the *mutual* interaction of spins, the NOE is related to the *square* of the dipolar field, and the strength therefore depends on r^{-6}.

Equation 7.16 shows that the strength of the dipolar field depends on the distance to the dipole. In Excursus 7.1 we demonstrate how the coupling depends on the angle θ that the connecting vector makes with the external field. Finally, it also depends on terms denoting the state of the spins, and these are also manipulated in (primarily solid-state) NMR experiments.

Excursus 7.1: Spatial Dependence of Dipolar Couplings

The magnetic field produced by a magnetic point dipole $\boldsymbol{\mu}_I$ as a function of the spatial position is

$$\boldsymbol{B}_\mathrm{d} = \frac{\mu_0}{4\pi} \frac{3(\boldsymbol{\mu}_I \cdot \boldsymbol{r})\boldsymbol{r} - \boldsymbol{\mu}_I r^2}{r^5} \tag{7.17}$$

where $\boldsymbol{r}$ is the vector describing the spatial position relative to the dipole and r is the distance to the dipole ($r = |\boldsymbol{r}|$) (Figure 7.17a).

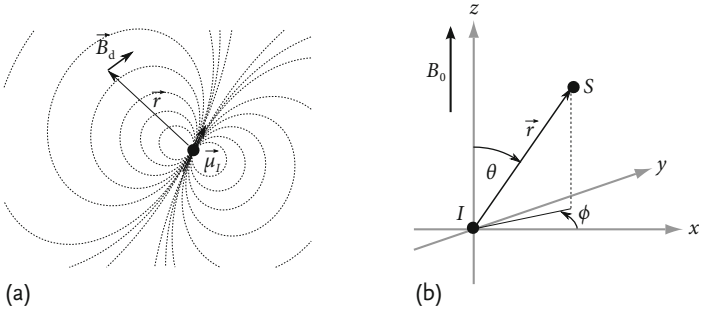

Figure 7.17 Dipole field (a) and definition of the angles θ and ϕ (b).

Thus, a nucleus S at position $\boldsymbol{r}$ experiences a magnetic field $\boldsymbol{B}_\mathrm{d}$ originating from another nucleus I as described by (7.17). The energy of a dipole in a magnetic field is $E = -\boldsymbol{B} \cdot \boldsymbol{\mu}$. Thus, the energy of the dipole $\boldsymbol{\mu}_S$ in the dipolar field $\boldsymbol{B}_\mathrm{d}$ of nucleus I is

$$E_\mathrm{dd} = -\frac{\mu_0}{4\pi} \frac{3(\boldsymbol{\mu}_I \cdot \boldsymbol{r})(\boldsymbol{\mu}_S \cdot \boldsymbol{r}) - \boldsymbol{\mu}_I \cdot \boldsymbol{\mu}_S r^2}{r^5} \tag{7.18}$$

Expressing vector $\boldsymbol{r}$ in polar coordinates,

$$\boldsymbol{r} = r \begin{pmatrix} \sin(\theta)\cos(\phi) \\ \sin(\theta)\sin(\phi) \\ \cos(\theta) \end{pmatrix} = r\hat{r}(\theta, \phi) \tag{7.19}$$

with $\hat{r}(\theta, \phi)$ denoting the unit vector along $\boldsymbol{r}$ (see Figure 7.17b), and the magnetic moments in terms of spin operators expressed as

$$\boldsymbol{\mu} = \gamma \hbar I = \gamma \hbar \begin{pmatrix} I_x \\ I_y \\ I_z \end{pmatrix} \tag{7.20}$$

we obtain

$$E_{\mathrm{dd}} = -\frac{\mu_0 \gamma_I \gamma_S \hbar^2}{4\pi r^3} [3(I \cdot \hat{r}(\theta, \phi))(S \cdot \hat{r}(\theta, \phi)) - I \cdot S] \tag{7.21}$$

For convenience, the energy is usually expressed in terms of angular velocity (rad/s) in NMR experiments (according to $E = h\nu = \hbar\omega$). Thus, if we divide (7.21) by $\hbar$, the prefactor becomes the dipolar coupling constant d (see (7.16)). Because the interaction with the external magnetic field is much stronger than the dipole–dipole interaction ($\omega_0 \gg \omega_{\mathrm{dd}}$), some terms of the scalar products in (7.21) may be dropped and the dipolar coupling simplifies to

$$E'_{\mathrm{dd}} = \frac{1}{2} d(3\cos^2(\theta) - 1)(3 I_z S_z - I \cdot S) \tag{7.22}$$

for the homonuclear case ($\gamma_I = \gamma_S$), or to

$$E'_{\mathrm{dd}} = d(3\cos^2(\theta) - 1) I_z S_z \tag{7.23}$$

for the heteronuclear case ($\gamma_I \neq \gamma_S$), with $E' = E/\hbar$.

7.3 Problems

7.1. What are the relative resonance frequencies of two nuclei A and B when nucleus A is more shielded from the external magnetic field than nucleus B?

7.2. A nucleus is chemically shielded from the external field by 200 ppm on a 600-MHz spectrometer. What is the shielding of that nucleus on a 300-MHz spectrometer?

7.3. The one-bond ^{1}H–^{13}C coupling constants are positive ($\sim$ 140 Hz for aliphatic carbons) whereas the amide one-bond ^{1}H–^{15}N coupling constants are negative ($\sim$ −90 Hz). Explain the difference in the sign of the coupling constants assuming the coupling is entirely governed by the Fermi-contact interaction. (Hint: the energy contribution due to scalar interaction of a heteronuclear two-spin system IS is expressed by $J I_z S_z$, where I_z and S_z are the spin z components of the nuclei.)

7.4. The direct dipole–dipole couplings can be as large as several kHz. Why do we usually not observe them in liquid-state NMR?

7.5. As mentioned in 7.4, we usually do not observe line splittings due to direct dipole–dipole couplings in liquid-state NMR, whereas the line splitting due to the scalar coupling is observed. Please explain this.

7.6. Does the quadrupolar coupling describe an interaction of the nuclear spin with the magnetic or with the electric field? And what is the problem with quadrupole nuclei?

Further Reading

Harris, R.K. (1986) *Nuclear Magnetic Resonance Spectroscopy*, Longman.

Levit, M.H. (2008) *Spin Dynamics*, 2nd edn, John Wiley & Sons, Ltd.

Keeler, J. (2010) *Understanding NMR Spectroscopy*, 2nd edn, John Wiley & Sons, Ltd.

Günther, H. (1995) *NMR Spectroscopy: Basic Principles, Concepts, and Applications in Chemistry*, 2nd edn, John Wiley & Sons, Ltd.

8
A Formal Description of NMR Experiments: The Product Operator Formalism

We have made use of the vector model to visualize the NMR phenomenon so far. While these pictures are comparatively easy to understand, they are of very limited value when trying to understand the trickery involved in modern NMR experiments. We will now introduce a formalism, referred to as the *product operator formalism* (POF), to describe the outcome and coherence flow in complicated sequences. Only with this formalism will you be able to understand coherence transfer – the ultimate step in any 2D shift correlation experiment. Do not skip this section just because it contains some formulas and theory. In fact, the POF can be used as a cooking recipe without fully understanding the quantum mechanical foundations of the latter. It simply uses some trigonometric functions. The mathematics involved is indeed very simple – the most challenging aspect is not to get lost in the manifold of terms that may be formed, and to recognize which of these terms contribute to the signal and which do not. We promise that with a little practice you can use the POF and become an NMR guru.

The POF uses a few principles. Firstly, almost everything in NMR can be visualized as a rotation. Precession of transverse magnetization giving rise to chemical shifts is a rotation. Pulses rotate magnetization. Scalar spin–spin coupling can be visualized as a rotation. Secondly, the interactions mentioned above can be computed in sequential order as products. Pulses must be computed at the time points when they occur in the experiment, but it does not matter whether we compute the effects from chemical shift or scalar coupling first, the result is the same. The effects from relaxation are usually disregarded in those calculations (but can be easily introduced at any time). The POF is a versatile tool. It will help us a lot in understanding NMR experiments. We must also mention an important limit: the POF breaks down in cases of strong coupling. The alternative is to use the density formalism (which the real NMR gurus use), and this is what you should really do if you believe life without linear algebra is worthless.

In the following we will describe how the effects from chemical shift, scalar coupling, and RF pulses are described in the POF. In Excursus 5.4 we learned that when we monitor the x component of a rotating vector versus time we obtain an oscillating sine or cosine function (or a mixture of both). In the POF formalism we

Applied NMR Spectroscopy for Chemists and Life Scientists, First Edition. Oliver Zerbe and Simon Jurt.
©2014 WILEY-VCH Verlag GmbH & Co. KGaA. Published 2014 by WILEY-VCH Verlag GmbH & Co. KGaA.

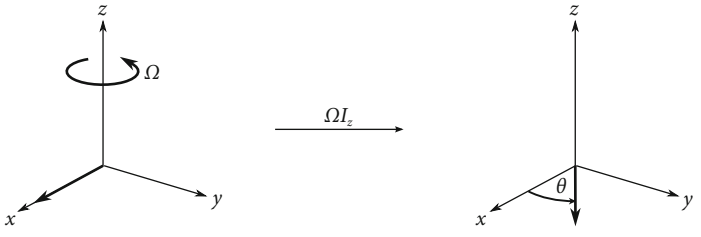

Figure 8.1 Description of rotations: rotation about the z axis with a frequency Ω rotates magnetization aligned along the x axis by an angle θ.

denote rotations as depicted in Figure 8.1 by the following equation:

$$I_x \xrightarrow{\Omega I_z} I_x \cos(\Omega t) + I_y \sin(\Omega t) \tag{8.1}$$

The initial magnetization vector points in the x direction. The spin is labeled as I, and hence this state is called I_x. On top of the arrow we denote the axis of rotation (the z axis). Since in our case I-spin magnetization is rotated about the z axis, we write I_z, and the frequency of rotation is Ω. On the right-hand side of the arrow you will find two terms – the initial state, associated with the cosine, and the state into which the initial state evolves following a 90° rotation, associated with the sine. The argument of the trigonometric functions is the frequency with which this interaction evolves in time multiplied by the time elapsed. It is always the same: the initial state is multiplied by the cosine, and the state due to a 90° rotation is multiplied by the sine. This is easy to remember since the cosine of 0° is 1, and the sine of 0° is 0. Note that after a certain time the cosine term becomes -1, and hence magnetization is then aligned along the $-x$ axis.

The sign convention for rotations is that applying a field along the y axis will result in a rotation in a *clockwise* sense. To follow the rotation due to a pulse applied along the y axis, look down the y axis from the coordinate origin and rotate clockwise, for example, from z to $+x$. You can also use the right-hand rule to follow the rotation: point the thumb of your right hand in the direction of the x axis. The fingers will indicate the direction of rotation (see Section 5.5.1).

8.1 Description of Events by Product Operators

The required rotations for *pulses* about the x axis are

$$I_z \xrightarrow{\beta I_x} I_z \cos(\beta) - I_y \sin(\beta) \tag{8.2}$$

with β denoting the flip angle.

Analogously, for *chemical shift evolution* we need

$$I_x \xrightarrow{\Omega I_z} I_x \cos(\Omega t) + I_y \sin(\Omega t) \tag{8.3}$$

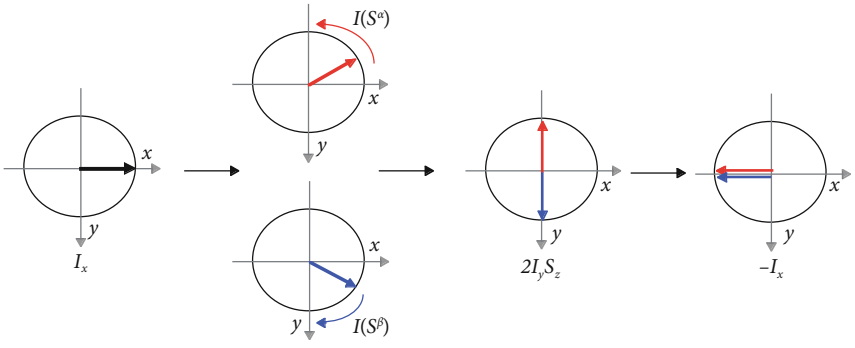

Figure 8.2 Evolution due to scalar coupling.

with Ω as the chemical shift offset.

In the case of *scalar couplings*, things are a bit more complicated. The formal description is

$$I_x \xrightarrow{\pi J I_z S_z} I_x \cos(\pi J t) + 2 I_y S_z \sin(\pi J t) \tag{8.4}$$

Magnetization oscillates between in-phase and antiphase terms. In this case it is not so obvious why the term I_x evolves into $2 I_y S_z$. We know the result from scalar coupling in the spectrum — a line becomes split by the scalar coupling into two lines separated by J. Accordingly, we can look at this as two magnetization vectors that evolve at different frequencies. If we look at this in a frame that rotates with the center frequency of the resonance, then the frequency of one component is positive, and that of the other component is negative. Hence, the vectors describing the magnetization rotate in opposite directions, and they are associated with the S spin, to which they couple. One component is associated with S_α, and the other is associated with S_β. After a 90° rotation they are pointing in opposite directions, a state referred to as antiphase.

This state is denoted as $2 I_y S_z$. Why? As described in Figure 8.2, the blue vector points in the y direction, and hence its state is $I_y S_\beta$. The other component (the red vector in Figure 8.2) is pointing along $-y$ and hence its state is $-I_y S_\alpha$. The sum of both is $I_y S_\beta - I_y S_\alpha = I_y(S_\beta - S_\alpha) = 2 I_y S_z$. (We make use of the fact that the difference in the population of the α and β states is $2 S_z$).

8.2 Classification of Spin Terms Used in the POF

Now we have introduced all the tools that we need to follow the coherence flow in an NMR experiment. However, we need to understand the physical meaning of a number of terms:

- I_z: longitudinal I-spin magnetization. This refers to the Boltzmann thermal equilibrium distribution of z magnetization. Applying a 180° pulse to the ther-

mal equilibrium state will produce $-I_z$. Longitudinal magnetization (or z magnetization) does not give rise to a signal in the receiver coil. It is an incoherent state (there is no phase relationship among the spins). This is usually the state from which the NMR experiment starts provided that the relaxation delay was chosen to be long enough.

- I_x and I_y: transverse x magnetization and y magnetization. This is the *only* term that will give rise to a signal in the receiver coil directly. Note that this has a *single transverse term*.
- $I_x S_z$: antiphase I-spin magnetization (or I-spin magnetization antiphase with respect to S). This term is not directly observable but will through scalar coupling evolve into in-phase I-spin magnetization. Some experiments produce such a state at the start of data acquisition (e.g., the DQF-COSY experiment). In this case the signal at the beginning of the free induction decay is zero and will increase with time.
- $I_x S_y$: two-spin coherence (mixture of zero-quantum and double-quantum coherence), often also called multiple-quantum coherence. This spin state does not give rise to a signal in the receiver coil. However, multiple-quantum coherences can be observed in the indirect dimension of 2D experiments.
- $I_z S_z$: longitudinal two-spin order. This state contains no transverse operators and hence does not give rise to a signal.

What does the signal look like? Obviously, the center of the signal will be at frequency Ω_I. This is the frequency difference from the carrier frequency and not the absolute frequency. For a brief discussion on this topic, see Section 6.5. Because of a scalar coupling, the resonance line can be split into two lines (a doublet). For in-phase couplings associated with the cosine modulation of the coupling, the two lines will have equal sign. For so-called antiphase couplings (the sine-modulated term) the two lines will have opposite sign. Cross peaks in COSY spectra display active and passive couplings (see Chapter 17). The corresponding stick spectra are displayed in Figure 8.3.

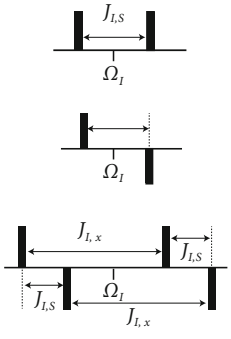

$I_x \cos(\pi J_{I,S} t)\cos(\Omega_I t)$

$2I_y S_z \sin(\pi J_{I,S} t)\cos(\Omega_I t)$

$2I_y S_z \sin(\pi J_{I,S} t)\cos(\pi J_{I,x} t)\cos(\Omega_I t)$

Figure 8.3 Stick spectra for a number of different signals. The corresponding product operator formalism terms are displayed on the right.

Excursus 8.1: Evolution of Multiple-Quantum Terms

Product operators such as $I_x S_y$, for example, operators that contain more than one transverse operator, denote *multiple-quantum coherences*. In particular, $I_x S_y$ represents a mixture of *zero-quantum and double-quantum coherences*. The zero-quantum terms correspond to so-called *flip–flop transitions* (one spin flips from the α state to the β state, while the other flips from the β state to the α state). The double-quantum transitions are synchronous flips ($\alpha\alpha$ to $\beta\beta$ or $\beta\beta$ to $\alpha\alpha$). Since they exhibit transverse coherences, they do evolve chemical shift. For two spins I and S with single-quantum frequencies Ω_I and Ω_S, the double-quantum terms evolve at $\Omega_I + \Omega_S$, while the zero-quantum terms evolve at $\Omega_I - \Omega_S$:

$$D\,Q_x \rightarrow \cos[(\Omega_I + \Omega_S)t] \cdot D\,Q_x + \sin[(\Omega_I + \Omega_S)t] \cdot D\,Q_y \tag{8.5}$$

and

$$Z\,Q_x \rightarrow \cos[(\Omega_I - \Omega_S)t] \cdot Z\,Q_x + \sin[(\Omega_I - \Omega_S)t] \cdot Z\,Q_y \tag{8.6}$$

Without further proof we tabulate the terms for pure double-quantum and zero-quantum coherences in Table 8.1.

Another property of multiple-quantum coherences is worth mentioning. In muitiple-quantum coherences of the type $I_{x,y} S_{x,y}$[1)] no scalar coupling evolves between the I and S spins. However, both I and S may evolve scalar couplings with other spins that are not part of the multiple-quantum coherence (if they couple to those).

Table 8.1 Operators for pure zero-quantum and double-quantum coherences.

Operator	Definition	Operator	Definition
DQ_x	$I_x S_x - I_y S_y$	ZQ_x	$I_x S_x + I_y S_y$
DQ_y	$I_x S_y + I_y S_x$	ZQ_y	$I_y S_x - I_x S_y$

8.3 Coherence Transfer Steps

Many NMR experiments (in fact almost all 2D experiments) transfer magnetization from one spin to another. For coherent transfers (transfers across the scalar cou-

1) $I_{x,y}$ denotes that both I_x and I_y may be chosen.

pling) the important initial event is that antiphase magnetization has been formed. The antiphase term is then transferred from *I*-spin to *S*-spin transverse magnetization

$$2I_x S_z \rightarrow -2I_z S_x \tag{8.7}$$

The term on the left of the equation evolves at the chemical shift of the *I* spin, whereas the term on the right evolves at the chemical shift of the *S* spin. This transfer can be achieved through application of 90° pulse(s). In the homonuclear case (both *I* and *S* are of the same type, e.g., both are protons), a single 90° *y* pulse is sufficient, whereas in the heteronuclear case two separate 90° pulses, one on each channel, are needed.

An example of incoherent transfer occurs in the nuclear Overhauser effect spectroscopy (NOESY) experiment in the mixing time

$$-I_z \rightarrow \pm S_z \tag{8.8}$$

The sign of S_z depends on the sign of the nuclear Overhauser effect (see Chapter 15).

8.4 An Example Calculation for a Simple 1D Experiment

As a simple example we now describe a simple 1D single-pulse experiment using the POF. The 1D experiment consists of a simple 90° pulse immediately followed by data acquisition. Accordingly, we start from equilibrium *z* magnetization and calculate the effect from the 90° pulse applied along the *y* axis:

$$I_z \rightarrow I_x \tag{8.9}$$

As a result, transverse *I*-spin magnetization is formed that can evolve at the chemical shift of the *I* spin:

$$I_x \rightarrow I_x \cos(\Omega_I t) + I_y \sin(\Omega_I t) \tag{8.10}$$

If the *I* spin is coupled to another spin, it will also evolve the scalar coupling, which we will compute separately for each term on the right-hand side of (8.10):

$$\begin{aligned} &I_x \cos(\Omega_I t) + I_y \sin(\Omega_I t) \rightarrow \\ &\quad I_x \cos(\Omega_I t)\cos(\pi J t) + 2I_y S_z \cos(\Omega_I t)\sin(\pi J t) \\ &\quad + I_y \sin(\Omega_I t)\cos(\pi J t) - 2I_x S_z \sin(\Omega_I t)\sin(\pi J t) \end{aligned} \tag{8.11}$$

This is a very simple example. In Chapter 17 you will find a more complicated (but also more insightful) description of the 2D COSY experiment using the POF. The art of using the POF is to not keep all terms that are close to zero, but to reduce

the number of terms (remember that each interaction doubles the total number of terms). For example, the insensitive nuclei enhancement by polarization transfer (INEPT) sequence transfers proton magnetization to a heteronucleus across the one-bond coupling. The delay during which the one-bond coupling evolves can in the case of C,H or N,H couplings be almost exactly tuned to the coupling, and the sine term is close to 1 and the cosine term close to 0, so the cosine term can be dropped. Similarly, chemical shift is refocused during that period, and therefore also the sine term for the chemical shift evolution can be dropped. If you do not pay attention to this, the number of terms in your calculations will quickly explode.

Further Reading

Levit, M.H. (2008) *Spin Dynamics*, 2nd edn, John Wiley & Sons, Ltd.

Keeler, J. (2010) *Understanding NMR Spectroscopy*, 2nd edn, John Wiley & Sons, Ltd.

Freeman, R. (1988) *Nuclear Magnetic Resonance*, John Wiley & Sons, Ltd.

Kessler, H., Gehrke, M., and Griesinger, C. (1988) Two-dimensional NMR-spectroscopy: Background and overview of the experiments. *Angew. Chem. Int. Ed. Engl.*, **27**, 490–536.

Sörensen, O.W., Eich, G.W., Levitt, M.H., Bodenhausen, G., and Ernst, R.R. (1983) Product operator formalism for the description of NMR pulse experiments. *Prog. Nucl. Magn. Reson. Spectrosc.*, **16**, 163–192.

9
A Brief Introduction into the Quantum-Mechanical Concepts of NMR

In this section we will introduce the concepts required for a better understanding of the quantum mechanical tools used in NMR. We assume that the reader already has heard of quantum mechanics (QM) in introductory courses. You might have already heard that quantum mechanics enables us to calculate the energy levels for the electron in a hydrogen atom or those of a harmonic oscillator. It is quite possible that you are only reluctantly reminded of those topics as it requires solving differential equations and facing Hermite polynomials – likely not a favorite topic for many chemists and biologists. There is good news for those readers: the math required for a *formal* quantum mechanical description of the spin and the NMR experiment is much simpler and essentially limited to basic linear algebra.

In the first section we will briefly remind the reader of the fundamental concepts of QM, comprising a concise discussion of the central concept of wave functions and operators and the mathematical structures behind these. Thereafter, we will introduce the abstract formulation of quantum mechanics required for the formal description of a single spin, and then introduce statistical methods to treat the large ensembles of spins that are manipulated and measured in NMR experiments.

9.1
Wave Functions, Operators, and Probabilities

In quantum mechanics the dynamics of a particle (in our case the spin) are described by a *wave function* or *state function* ψ, and its measurable quantities (e.g., z or x components of the spin) are associated by *operators* that act on the wave function. Thus, one can say that the state of the quantum system is *fully* characterized by the state function ψ. The operators are mathematical "recipes" that allow us to extract the values of the measurable quantities from the wave function. Quantities that we can measure are also called observables. For example, $\hat{I}_x$ is the operator of an observable, the x component of the spin.

In more general terms, assume there is an observable quantity A associated with the wave function by the operator $\hat{A}$. When the result of the action of $\hat{A}$ on a wave

Applied NMR Spectroscopy for Chemists and Life Scientists, First Edition. Oliver Zerbe and Simon Jurt.
©2014 WILEY-VCH Verlag GmbH & Co. KGaA. Published 2014 by WILEY-VCH Verlag GmbH & Co. KGaA.

function φ is just the product of the same wave function multiplied by a constant λ

$$\hat{A}\varphi = \lambda\varphi \tag{9.1}$$

then φ is called an *eigenfunction* or *eigenstate* and λ an *eigenvalue* of operator $\hat{A}$ (eigen is the German word for characteristic). If we have a particle at some point in time in a state that is described by the eigenfunction φ, then a measurement of the observable A at that time will *always* yield the value λ.

9.1.1 Eigenstates and Superposition States

Usually, more than one eigenfunction exists for a particular operator. In the case of the z component of spin-1/2, expressed by the operator $\hat{I}_z$, the Stern–Gerlach experiment has shown the existence of *two* eigenstates φ_α and φ_β, and measuring these will result in values of $-1/2\hbar$ and $+1/2\hbar$ as the corresponding eigenvalues (see Section 5.3).

But not only can the system be in two different eigenstates, it can also be in a mixture of two or more eigenstates. To account for the (co)existence of these different eigenstates we can formulate the general form of the wave function ψ as a *linear combination* of a set of basis functions

$$\psi = c_1\varphi_1 + c_2\varphi_2 + \cdots + c_n\varphi_n \tag{9.2}$$

in which the various φ_i are the basis functions of the system, and c_i the coefficients that describe how much they contribute to the wave function. The basis functions are *orthogonal* (the formal definition of orthogonality is $\int \varphi_1^*\varphi_2 \mathrm{d}\tau = 0$), and as a consequence of that none of them can be obtained by a linear combination of any of the others (they are said to be linearly independent). Furthermore, by multiplying the basis functions by appropriate factors, we can ensure that these functions are also normalized such that $\int \varphi_i^*\varphi_i = 1$. The set of functions $\varphi_1, \varphi_2, \ldots, \varphi_n$ comprises a *complete set* of *orthonormal* basis functions, with which *any possible state* of the system can be described.

For an isolated spin-1/2 the basis comprises just *two* eigenfunctions, and there are no further states we need to consider. If we call the operator that is associated with the z component of the spin $\hat{I}_z$ we postulate

$$\begin{aligned}\hat{I}_z\varphi_\alpha &= +\frac{1}{2}\varphi_\alpha \\ \hat{I}_z\varphi_\beta &= -\frac{1}{2}\varphi_\beta\end{aligned} \tag{9.3}$$

and hence the state for an isolated single spin-1/2 is presented by

$$\psi = a\varphi_\alpha + b\varphi_\beta \tag{9.4}$$

It is an important feature of a quantum-mechanical system that it does not need to be entirely in one of the eigenstates, but can occupy a mixture of both (the coefficients "a" and "b" in the expansion of ψ can both be nonzero). Such a state is

called a *superposition state*. It is not true that a spin must be *either* in the α *or* β state.

9.1.2 Observables of Quantum-Mechanical Systems and Their Measured Quantities

When a quantum-mechanical system is described by a superposition of eigenstates of an operator $\hat{A}$ it is impossible to predict which eigenvalues of A we will observe. We can only specify the probability $P(\lambda_i)$ with which a certain value λ_i will be measured, and the probability is related to the coefficients of the expansion by

$$P(\lambda_i) = |c_i|^2 = c_i^* c_i \tag{9.5}$$

Because in any case one of all the possible eigenvalues will be observed, the sum of the individual probabilities must be equal to one

$$\sum_i P(\lambda_i) = \sum_i c_i^* c_i = 1$$

This is true when ψ is normalized such that

$$\int \psi^* \psi = 1$$

We can verify that claim by explicitly writing down the expansions

$$\begin{aligned}\int \psi^* \psi &= \int (c_1^* \varphi_1^* + c_2^* \varphi_2^*)(c_1 \varphi_1 + c_2 \varphi_2) \\ &= c_1^* c_1 \int \varphi_1^* \varphi_1 + c_1^* c_2 \int \varphi_1^* \varphi_2 + c_2^* c_1 \int \varphi_2^* \varphi_1 + c_2^* c_2 \int \varphi_2^* \varphi_2\end{aligned}$$

Since terms like $\int \varphi_1^* \varphi_2$ vanish due to the orthogonality of the basis functions, and because the basis functions are normalized ($\int \varphi^* \varphi = 1$) all that remains is

$$\int \psi^* \psi' = c_1^* c_1 + c_2^* c_2 \tag{9.6}$$

The product $c_1^* c_1$ presents the probability of finding the system in the state φ_1. Since the right-hand side of equation (9.6) sums over all possible states, it must equal 1.

By knowing the probabilities by which the individual eigenvalues appear, we can calculate the *expectation* (or mean) *value* when a property associated with an operator $\hat{A}$ is obtained from a number of *repeated* measurements of *identical* quantum systems all described by the same state function ψ. In general, the expectation value of an observable A corresponds to the probability-weighted sum of eigenvalues λ_i

$$\langle A \rangle = \sum_i P(\lambda_i) \lambda_i \tag{9.7}$$

for which we can write

$$\langle A \rangle = \int \psi^* \hat{A} \psi \tag{9.8}$$

We can prove (9.8) by explicitly writing down the different terms

$$\int \psi^* \hat{A} \psi = \int (c_1^* \varphi_1^* + c_2^* \varphi_2^* + c_3^* \varphi_3^* + \ldots) \hat{A} (c_1 \varphi_1 + c_2 \varphi_2 + c_3 \varphi_3 + \ldots)$$

which can be rewritten as

$$\begin{aligned} \int \psi^* \hat{A} \psi &= \int (c_1^* \varphi_1^* + c_2^* \varphi_2^* + c_3^* \varphi_3^* + \ldots) \\ &\quad \times (c_1 \lambda_1 \varphi_1 + c_2 \lambda_2 \varphi_2 + c_3 \lambda_3 \varphi_3 + \ldots) \\ &= c_1^* c_1 \lambda_1 \int \varphi_1^* \varphi_1 + c_2^* c_2 \lambda_2 \int \varphi_2^* \varphi_2 + c_3^* c_3 \lambda_3 \int \varphi_3^* \varphi_3 \\ &= c_1^* c_1 \lambda_1 + c_2^* c_2 \lambda_2 + c_3^* c_3 \lambda_3 + \ldots \\ &= P(\lambda_1) \lambda_1 + P(\lambda_2) \lambda_2 + P(\lambda_3) \lambda_3 + \ldots \end{aligned}$$

Note that all terms that contain integrals with orthogonal basis functions such as $\int \varphi_1^* \varphi_2$ are dropped in the second line and all terms like $\int \varphi_1^* \varphi_1$ that are equal to one due to the fact that the basis functions are normalized are dropped in the third line.

9.2 Mathematical Tools in the Quantum Description of NMR

We have learnt before that any wave function can be decomposed into the basis components as long as these form a complete basis. We know for example that any vector in three-dimensional space can be expressed in the form of its cartesian coordinates, which are the projections of the vector onto the x, y, and z axis. In analogy, we need to develop a formalism to describe quantum-mechanical states as well as transitions between these states.

9.2.1 Vector Spaces, Bra's, Ket's, and Matrices

A central mathematical structure behind the quantum mechanics used for the spins is that the coefficients of the N orthonormal basis functions in the expansion of the wave function are treated as coordinates of a vector in N-dimensional vector space, a so-called *Hilbert space*. In this context ψ is called a *state vector* and its elements are given by the coefficients of the expansion (the coefficients we obtain when ψ is expressed in terms of its base states φ_i).

The integral $\int \psi^* \psi'$ is a measure of how much two different wave functions ψ and ψ' have in common, the degree of *interference*. If we write out this integral for

the two wave functions $\psi = c_1\varphi_1 + c_2\varphi_2$ and $\psi' = c_1'\varphi_1 + c_2'\varphi_2$ we obtain

$$\int \psi^* \psi' = c_1^* c_1' + c_2^* c_2' \tag{9.9}$$

Here we have skipped the individual steps in the calculation because we have done this already to derive (9.6).

This product very much reminds us of the *scalar product* of two vectors $\boldsymbol{A}$ and $\boldsymbol{B}$ in Euclidian space

$$\begin{aligned}\boldsymbol{A} \cdot \boldsymbol{B} &= (x_a \boldsymbol{e}_x + y_a \boldsymbol{e}_y + z_a \boldsymbol{e}_z) \cdot (x_b \boldsymbol{e}_x + y_b \boldsymbol{e}_y + z_b \boldsymbol{e}_z) \\ &= x_a x_b \boldsymbol{e}_x + y_a y_b \boldsymbol{e}_y + z_a z_b \boldsymbol{e}_z\end{aligned}$$

Therefore, the integral $\int \psi^* \psi'$ corresponds to the scalar product of two state functions.

9.2.1.1 Transformation Between Basis Sets

The state function ψ depicted in Figure 9.1 denotes a vector that points into the plane spanned by the two basis functions (or basis vectors) φ_1 and φ_2, and the coefficients c_1 and c_2 are derived from the projection of this state function onto the basis vectors. As demonstrated in Figure 9.2 we can easily also choose another set of orthogonal basis states to define the same vector ψ. The state function in that (rotated) basis can be expressed as $\psi = c_1'\varphi_1' + c_2'\varphi_2'$. We can also rotate the coordinate system such that the vector ψ is coaligned with one of the axes of the basis functions, so that the state becomes an eigenstate in that basis. While our state vector ψ is in eigenstate when the basis is chosen as depicted in Figure 9.2b it is in a superposition state in the presentation in Figure 9.2a! Whether a system is in an eigenstate or superposition state therefore depends on the presentation and hence the choice of basis vectors.

9.2.2 Dirac's Bra–Ket Notation

Paul A.M. Dirac, one of the early major contributors to the field of quantum mechanics, introduced a very simple notation. Therein a state vector ψ is represented

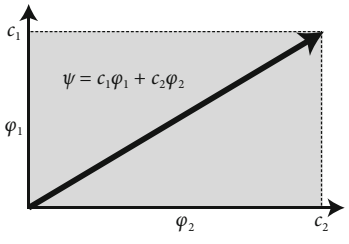

Figure 9.1 Graphical representation of the state $\psi = c_1\varphi_1 + c_2\varphi_2$ in two-dimensional Hilbert space.

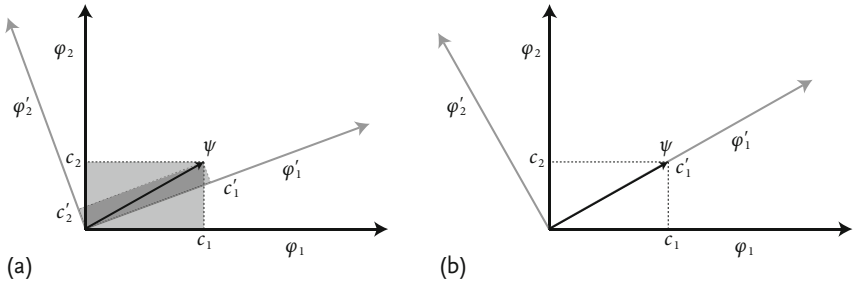

Figure 9.2 (a) A rotation of the coordinate system results in a new representation of the state vector with a different set of basis vectors. (b) The rotation depicted on the right transforms the state vector ψ into a basis such that it becomes the eigenbasis.

by the *ket* $|\psi\rangle$, and its complex conjugate ψ^* by the *bra* $\langle\psi|$. The scalar product is then given by the *bra–ket* $\langle\psi|\psi\rangle$, where we use the central "|" to indicate that we are calculating the *scalar* product. Thus, we have for example

$$\psi \equiv |\psi\rangle \tag{9.10}$$

$$\psi^* \equiv \langle\psi| \tag{9.11}$$

$$\int \psi_1^* \psi_2 \equiv \langle\psi_1|\psi_2\rangle \tag{9.12}$$

For a spin-1/2, the α and β state form a *complete orthonormal* base. The orthonormality is expressed by the scalar products

$$\begin{aligned} \langle\alpha|\alpha\rangle &= \langle\beta|\beta\rangle = 1 \\ \langle\alpha|\beta\rangle &= \langle\beta|\alpha\rangle = 0 \end{aligned} \tag{9.13}$$

and *all possible states* can be described by

$$|\psi\rangle = a|\alpha\rangle + b|\beta\rangle \tag{9.14}$$

9.2.3 Matrix Representation of State Vectors

Manipulations of the vectors described above are dramatically simplified by the use of matrix algebra. In the matrix formulation the components of the basis vectors are conveniently noted as column vectors. For example, each of the base states $|\alpha\rangle$ and $|\beta\rangle$ is represented by a column vector

$$|\alpha\rangle \equiv \begin{bmatrix} 1 \\ 0 \end{bmatrix} \quad |\beta\rangle \equiv \begin{bmatrix} 0 \\ 1 \end{bmatrix} \tag{9.15}$$

and the corresponding bra's are represented by row vectors

$$\langle\alpha| \equiv \begin{bmatrix} 1 & 0 \end{bmatrix} \quad \langle\beta| \equiv \begin{bmatrix} 0 & 1 \end{bmatrix} \tag{9.16}$$

The scalar product $\langle\alpha|\alpha\rangle$ then takes the form

$$\langle\alpha|\alpha\rangle \equiv \begin{bmatrix}1 & 0\end{bmatrix}\begin{bmatrix}1\\0\end{bmatrix} = 1 \tag{9.17}$$

(for a reminder on matrix algebra see Appendix A.3.1). Similarly, for the scalar products $\langle\beta|\beta\rangle$, $\langle\alpha|\beta\rangle$, and $\langle\beta|\alpha\rangle$ we obtain

$$\begin{aligned}&\langle\beta|\beta\rangle \equiv \begin{bmatrix}0 & 1\end{bmatrix}\begin{bmatrix}0\\1\end{bmatrix} = 1\,; \quad \langle\alpha|\beta\rangle \equiv \begin{bmatrix}1 & 0\end{bmatrix}\begin{bmatrix}0\\1\end{bmatrix} = 0\,;\\ &\langle\beta|\alpha\rangle \equiv \begin{bmatrix}0 & 1\end{bmatrix}\begin{bmatrix}1\\0\end{bmatrix} = 0\end{aligned} \tag{9.18}$$

reflecting the orthonormality of the basis functions. For any arbitrary state $|\psi\rangle$ we can then write

$$|\psi\rangle = a|\alpha\rangle + b|\beta\rangle = a\begin{bmatrix}1\\0\end{bmatrix} + b\begin{bmatrix}0\\1\end{bmatrix} = \begin{bmatrix}a\\b\end{bmatrix}$$

and

$$\langle\psi| = \begin{bmatrix}a^* & b^*\end{bmatrix}$$

For the scalar product we obtain

$$\langle\psi|\psi\rangle = \begin{bmatrix}a^* & b^*\end{bmatrix}\begin{bmatrix}a\\b\end{bmatrix} = a^*a + b^*b$$

9.2.4
Rotations between State Vectors can be Accomplished with Tensors

In NMR the spin states evolve under the influence (Hamiltonians) of RF-pulses, free precession, and spin–spin interactions (see Chapter 7). Thereby, an initial state ψ_i is transformed into a final state ψ_f. This transformation corresponds to a rotation of the state vector in Hilbert space (Figure 9.3). A suitable object to transform a vector A into another vector B is known as a *tensor* or a *rotation matrix*. If we define the initial state of the spin as

$$|\psi_i\rangle = a_i|\alpha\rangle + b_i|\beta\rangle$$

and the final state by

$$|\psi_f\rangle = a_f|\alpha\rangle + b_f|\beta\rangle$$

then we can now define a matrix $\hat{R}$ that transforms ψ_i into ψ_f:

$$|\psi_f\rangle = \hat{R}|\psi_i\rangle \tag{9.19}$$

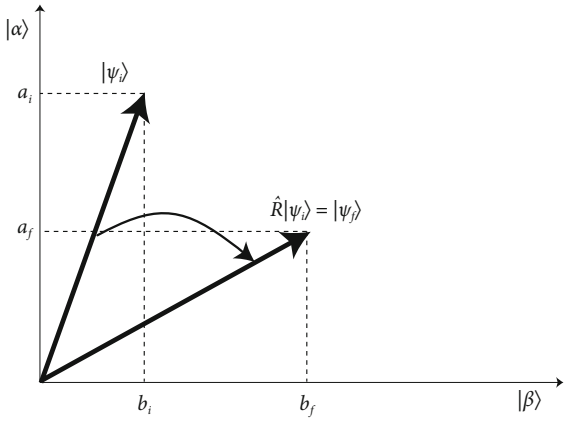

Figure 9.3 *Rotation of vectors*: multiplication of a vector $|\psi_i\rangle$ by a rotation matrix $\hat{R}$ results in the rotation of the vector yielding a new vector with different coefficients in the expansion of the wave function.

Since the initial and final states are both normalized, these transformations are rotations that do not change the length of the vectors (so-called *unitary transformations*) and the operator $\hat{R}$ is a rotation matrix.

To mathematically express the transformation we multiply the initial state, given by a column vector, with the rotation matrix to obtain another column vector, representing the final state:

$$\begin{bmatrix} a_f \\ b_f \end{bmatrix} = \begin{bmatrix} a_{11} & a_{12} \\ a_{21} & a_{22} \end{bmatrix} \begin{bmatrix} a_i \\ b_i \end{bmatrix}$$

Thus, any linear transformation of a state $|\psi_i\rangle$ into another state $|\psi_f\rangle$ can be achieved through multiplication by an $N \times N$ square matrix, with N being the dimension of the Hilbert space (e.g., the number of basis states). As will be described later on, any operator can be represented as a matrix. Alternatively, we can state that the rotation matrix is the matrix representation of an operator, the rotation operator. Rotation operators play an important role in quantum mechanics. They can be used to transform one particular state into another one or (more often) to change the basis.

9.2.5
Projection Operators

In Section 9.2.1 we have seen that the product of a row vector with a column vector results in a number (a scalar). If we multiply them in the opposite order we end up with a matrix:

$$|\psi_1\rangle\langle\psi_2| = \begin{bmatrix} a_1^* \\ b_1^* \end{bmatrix} \begin{bmatrix} a_2 & b_2 \end{bmatrix} = \begin{bmatrix} a_1^* a_2 & a_1^* b_2 \\ b_1^* a_2 & b_1^* b_2 \end{bmatrix} \tag{9.20}$$

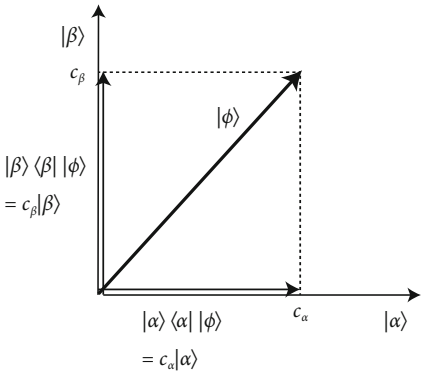

Figure 9.4 *Projection vectors*: multiplying a vector $|\phi\rangle$ with the projection operators $|\alpha\rangle\langle\alpha|$ and $|\beta\rangle\langle\beta|$ results in vectors defined by the corresponding projections onto the two individual orthogonal axes.

Such a matrix can be an operator. The operator $|\psi_1\rangle\langle\psi_2|$ maps ψ_2 onto ψ_1, and therefore these operators are called *projection operators*. To understand its meaning let us apply the operator $|\psi_1\rangle\langle\psi_1|$ to some function $|f\rangle$

$$|\psi_1\rangle\langle\psi_1||f\rangle = |\psi_1\rangle\langle\psi_1|f\rangle = |\psi_1\rangle n$$

Here n denotes a scalar (a number), that presents the projection of $|f\rangle$ onto $|\psi_1\rangle$.

Lets look at one example. Assume we have a state $|\psi\rangle$ presented in the base $\{\varphi_1,\varphi_2\}$ but we like to present the state in the base $\{\alpha,\beta\}$ as $|\psi\rangle = a|\alpha\rangle + b|\beta\rangle$. The problem now consists of finding the expansion coefficients a and b. These coefficients are extracted by calculating the scalar products $\langle\alpha|\psi\rangle$ (for a) and $\langle\beta|\psi\rangle$ (for b), respectively. As depicted in Figure 9.4, the product $\langle\alpha|\psi\rangle$ projects the vector $|\psi\rangle$ onto the $|\alpha\rangle$ axis and $\langle\beta|\psi\rangle$ projects the vector $|\psi\rangle$ onto the $|\beta\rangle$ axis. Finally, to end up with a state vector, we need to multiply the coefficients with the corresponding base vectors, resulting in the expressions $|\alpha\rangle\langle\alpha||\psi\rangle$ and $|\beta\rangle\langle\beta||\psi\rangle$, with the projection operators $|\alpha\rangle\langle\alpha|$ and $|\beta\rangle\langle\beta|$.

The usefulness of projection operators stems from the fact that they help to calculate the coefficients in the expansion of an arbitrary vector in a particular basis.

9.2.6
Operators in the Bra–Ket Notation

In this section we will show that the spin operators can be expressed in terms of ket's and bra's. Starting from a general state for a spin-1/2 particle $|\psi\rangle = a|\alpha\rangle + b|\beta\rangle$ we use the property of projection operators that multiplying the state $|\psi\rangle$ with a projection operator such as$|\alpha\rangle\langle\alpha|$ will project the vector $|\psi\rangle$ onto the $|\alpha\rangle$ axis, resulting in $a|\alpha\rangle$ (see above). We can therefore rewrite

$$|\psi\rangle = a|\alpha\rangle + b|\beta\rangle = |\alpha\rangle\langle\alpha||\psi\rangle + |\beta\rangle\langle\beta||\psi\rangle$$

Upon rearrangement we obtain

$$|\psi\rangle = (|\alpha\rangle\langle\alpha| + |\beta\rangle\langle\beta|)|\psi\rangle$$

It follows that the expression in parentheses must correspond to unity. In fact, it represents the identity operator **1**.

$$\mathbf{1} = |\alpha\rangle\langle\alpha| + |\beta\rangle\langle\beta| \tag{9.21}$$

As the identity operator doesn't alter a state vector, we can always put it in front. Using that trick we can express the other spin operators in terms of bra's and ket's. All we need to do is to calculate the product of these with the unity operator. For example, in the case of I_z we obtain

$$I_z\mathbf{1} = I_z(|\alpha\rangle\langle\alpha| + |\beta\rangle\langle\beta|)$$

Using the relations defined in (9.3) we can rewrite this as

$$\begin{aligned} I_z\mathbf{1} &= \frac{1}{2}|\alpha\rangle\langle\alpha| - \frac{1}{2}|\beta\rangle\langle\beta| \\ &= \frac{1}{2}(|\alpha\rangle\langle\alpha| - |\beta\rangle\langle\beta|) \end{aligned} \tag{9.22}$$

For completeness we will introduce *laddering* and *polarization* operators here as well. These important projection operators are frequently used in NMR, and their use will be shown in more detail in Section 9.3.

The *rising operator* is defined as

$$I_+|\alpha\rangle = 0 \quad I_+|\beta\rangle = |\alpha\rangle \tag{9.23}$$

and the *lowering operator* as

$$I_-|\beta\rangle = 0 \quad I_-|\alpha\rangle = |\beta\rangle \tag{9.24}$$

The bra–ket representations of these operators are computed as

$$I_+(|\alpha\rangle\langle\alpha| + |\beta\rangle\langle\beta|) = |\alpha\rangle\langle\beta| \tag{9.25}$$

$$I_-(|\alpha\rangle\langle\alpha| + |\beta\rangle\langle\beta|) = |\beta\rangle\langle\alpha| \tag{9.26}$$

Finally, we introduce the *polarization operators* as

$$I_\alpha = |\alpha\rangle\langle\alpha| \tag{9.27}$$

$$I_\beta = |\beta\rangle\langle\beta| \tag{9.28}$$

9.2.7
Matrix Representations of Operators

When computing manipulations of state vectors in matrix format we must also use matrix representations for the operators. The matrix elements of an operator can be computed as

$$A_{nm} = \langle n|\hat{A}|m\rangle \tag{9.29}$$

where n and m are the basis states of the state function that describe the system. For example, the matrix representation for the z component of the spin can be computed by substituting the general operator $\hat{A}$ with $\hat{I}_z$. The element in the upper left corner (A_{11}) of the matrix for example is calculated as

$$\langle\alpha|\hat{I}_z|\alpha\rangle = \langle\alpha|\frac{1}{2}|\alpha\rangle = \frac{1}{2}\langle\alpha|\alpha\rangle = \frac{1}{2}$$

After calculating all elements we obtain

$$\begin{pmatrix} \langle\alpha|\hat{I}_z|\alpha\rangle & \langle\alpha|\hat{I}_z|\beta\rangle \\ \langle\beta|\hat{I}_z|\alpha\rangle & \langle\beta|\hat{I}_z|\beta\rangle \end{pmatrix} = \begin{pmatrix} \frac{1}{2} & 0 \\ 0 & -\frac{1}{2} \end{pmatrix}$$

An analogous calculation yields the matrices for I_x and I_y and the identity operator 1. Collectively, these four matrices are known as the *Pauli spin matrices*:

$$I_z = \frac{1}{2}\begin{pmatrix} 1 & 0 \\ 0 & -1 \end{pmatrix}; \qquad I_x = \frac{1}{2}\begin{pmatrix} 0 & 1 \\ 1 & 0 \end{pmatrix};$$
$$I_y = \frac{1}{2}\begin{pmatrix} 0 & \mathrm{i} \\ \mathrm{i} & 0 \end{pmatrix}; \qquad 1 = \begin{pmatrix} 1 & 0 \\ 0 & 1 \end{pmatrix} \tag{9.30}$$

Note that they describe the x, y, and z components of a single spin in the basis of α- (or spin($\uparrow$)) and β- (or spin($\downarrow$)) states.

Mathematically $\langle\alpha|\hat{I}_z|\beta\rangle$ corresponds to $\int \psi_\alpha^* \hat{I}_z \psi_\beta \mathrm{d}\tau$, in which integration is carried out over all relevant variables. Let us look at Figure 9.5 to understand what this operation physically means.

The operation $\hat{A}|\varphi_1\rangle$ manipulates the vector $|\varphi_1\rangle$ in such a way that it potentially changes both its orientation and length, producing a new vector. The second step is

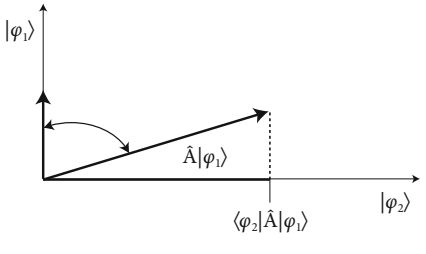

Figure 9.5 Graphical presentation of the operation $\langle\varphi_2|\hat{A}|\varphi_1\rangle$.

forming the scalar product, that corresponds to projecting $\hat{A}|\varphi_1\rangle$ onto the $|\varphi_2\rangle$ axis. Loosely speaking we can state that $\langle n|\hat{A}|m\rangle$ extracts the "A character" that is common to both states n and m. Note that the orientation of the resulting vector $\hat{A}|\varphi_1\rangle$ only changes if $|\varphi_1\rangle$ is not an eigenstate of $\hat{A}$. For example, $|\beta\rangle$ is an eigenstate of $\hat{I}_z$. Accordingly, $\hat{I}_z|\beta\rangle$ will still be orthogonal to $|\alpha\rangle$ and hence the scalar product is zero ($\langle\alpha|\hat{I}_z|\beta\rangle = 0$). Since $|\alpha\rangle$ is not an eigenstate of I_x, the state $|\alpha\rangle$ is rotated by the operator $\hat{I}_x$ and the scalar product $\langle\alpha|\hat{I}_x|\beta\rangle$ (the matrix element $I_{x,12}$) no longer is zero.

9.3 The Spin Space of Single Noninteracting Spins

In Section 9.1.1 we saw how the operators for the z component of spin are defined in the z-basis (see (9.3)). With the completeness of the base $\{|\alpha\rangle, |\beta\rangle\}$, it must be possible to also express x and y components of spins in terms of α and β states. The eigenstate of $\hat{I}_x$ with eigenvalue $m_x = +1/2$ must fulfill the equation $\hat{I}_x|\psi\rangle = +1/2|\psi\rangle$ with $|\psi\rangle$ being a linear combination of the form $a|\alpha\rangle + b|\beta\rangle$. Unfortunately, we cannot solve this equation because we do not know how the operator $\hat{I}_x$ acts on the α and β states yet. However, it can be demonstrated that we can express the operators $\hat{I}_x$ and $\hat{I}_y$ as linear combinations of the raising and lowering operators $\hat{I}_+$ and $\hat{I}_-$[1)]

$$\hat{I}_x = \frac{1}{2}(\hat{I}_+ + \hat{I}_-) \quad \hat{I}_y = -\frac{\mathrm{i}}{2}(\hat{I}_+ - \hat{I}_-) \tag{9.31}$$

from which, using the definitions of the laddering operators ((9.23) and (9.24)) we can calculate the operator definitions of I_x and I_y in bra–ket notation as

$$\hat{I}_x = \frac{1}{2}(\hat{I}_+ + \hat{I}_-) = \frac{1}{2}(|\alpha\rangle\langle\beta| + |\beta\rangle\langle\alpha|) \tag{9.32}$$

$$\hat{I}_y = \frac{1}{2}(\hat{I}_+ - \hat{I}_-) = -\frac{\mathrm{i}}{2}(|\alpha\rangle\langle\beta| - |\beta\rangle\langle\alpha|) \tag{9.33}$$

If we solve the eigenvalue equation for $\hat{I}_x$ we obtain

$$\begin{aligned} \hat{I}_x|\psi\rangle &= +\frac{1}{2}|\psi\rangle \\ \frac{1}{2}(\hat{I}_+ + \hat{I}_-)(a|\alpha\rangle + b|\beta\rangle) &= \frac{1}{2}(a|\alpha\rangle + b|\beta\rangle) \\ \frac{1}{2}(a|\beta\rangle + b|\alpha\rangle) &= \frac{1}{2}(a|\alpha\rangle + b|\beta\rangle) \end{aligned} \tag{9.34}$$

1) These relations can be derived from the commutation properties of the spin, assuming that they obey the same rules as those found for the orbital angular momentum. For a thorough discussion on that topic see J.W. Hennel and J. Klinowski, Fundamentals of Nuclear Magnetic Resonance, Longman Scientific & Technical, 1993, p. 20–25.

which is true for $a = b$. If in addition we require the state to be normalized ($\langle\psi|\psi\rangle = 1$), we have the additional requirement $|a|^2 + |b|^2 = 1$, and we obtain the general solution $a = b = 1/(\sqrt{2})\exp(i\varphi)$. The ambiguity regarding the phase factor $\exp(i\varphi)$ illustrates the fact, that we can multiply a state $|\psi\rangle$ with an arbitrary phase factor $\exp(i\varphi)$ without changing the physical meaning of the state. If we arbitrarily chose $\varphi = 0$, the eigenstate of $\hat{I}_x$ with eigenvalue $m_x = +1/2$ is

$$\left|m_x, +\frac{1}{2}\right\rangle = \frac{1}{\sqrt{2}}|\alpha\rangle + \frac{1}{\sqrt{2}}|\beta\rangle \tag{9.35}$$

Similarly we can find the eigenstates with $m_x = -1/2$ and $m_y = \pm 1/2$. They are summarized in Excursus 9.1 below.

Excursus 9.1: Eigenstates of Spin Operators $\hat{I}_x$, $\hat{I}_y$ and $\hat{I}_z$ Expressed in the Eigenbase of $\hat{I}_z$

$$\begin{aligned}
\left|m_z, +\frac{1}{2}\right\rangle &= |\alpha\rangle \\
\left|m_z, -\frac{1}{2}\right\rangle &= |\beta\rangle \\
\left|m_x, +\frac{1}{2}\right\rangle &= \frac{1}{\sqrt{2}}|\alpha\rangle + \frac{1}{\sqrt{2}}|\beta\rangle \\
\left|m_x, -\frac{1}{2}\right\rangle &= \frac{1}{\sqrt{2}}|\alpha\rangle - \frac{1}{\sqrt{2}}|\beta\rangle \\
\left|m_y, +\frac{1}{2}\right\rangle &= \frac{1}{\sqrt{2}}|\alpha\rangle + \frac{i}{\sqrt{2}}|\beta\rangle \\
\left|m_y, -\frac{1}{2}\right\rangle &= \frac{1}{\sqrt{2}}|\alpha\rangle - \frac{i}{\sqrt{2}}|\beta\rangle
\end{aligned} \tag{9.36}$$

These equations are expressed in the z representation, that uses a base in which $|\alpha\rangle$ and $|\beta\rangle$ form the basis vectors. These two eigenvectors correspond to spin states in which the spins are entirely up or down (parallel or antiparallel to the magnetic field, that is along z). Surprisingly, we can obtain states along any direction in space, for example along x, upon superimposing these two states, that means by adding vectors along $+z$ and $-z$. This is only possible because we do not add these vectors in an ordinary geometrical sense.

But how do we easily find out which superposition corresponds to a particular orientation of the spin vector? A convenient tool for that purpose is to represent the spins as vectors on a sphere.

Therein the spin vector corresponds to a vector of unity length that is directed to one particular point of the surface of a sphere (see Figure 9.6). The north pole corresponds to the $|\alpha\rangle$ state and the south pole to the $|\beta\rangle$ state. In general, the spin

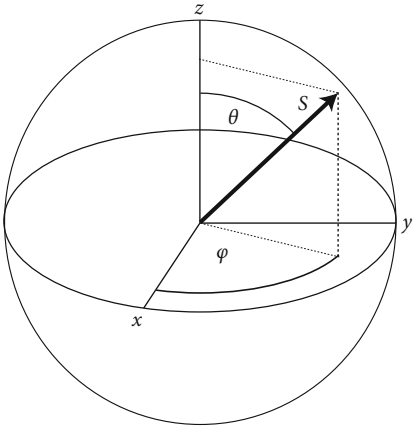

Figure 9.6 Orientation of a single spin in polar coordinates.

vector $|S\rangle$ as specified in polar coordinates is

$$|S\rangle = \cos\left(\frac{\theta}{2}\right)|\alpha\rangle + \sin\left(\frac{\theta}{2}\right)\mathrm{e}^{\mathrm{i}\varphi}|\beta\rangle \tag{9.37}$$

To compute the coefficients for the $|\alpha\rangle$ and $|\beta\rangle$ state for a given direction of the spin vector we simply need to evaluate the trigonometric expressions in (9.37).

9.3.1
Expectation Values of the Spin-Components

We saw in Section 9.1.2 that the expectation value of an observable A takes the form $\langle A\rangle = \langle\psi|A|\psi\rangle$. For the general case defined as $|\psi\rangle = a|\alpha\rangle + b|\beta\rangle$, the expectation value for the spins z component is

$$\begin{aligned}
\langle I_z\rangle &= \langle\psi|\hat{I}_z|\psi\rangle \\
&= (\langle\alpha|a^* + \langle\beta|b^*)\hat{I}_z(a|\alpha\rangle + b|\beta\rangle) \\
&= (\langle\alpha|a^* + \langle\beta|b^*)\left(a\frac{1}{2}|\alpha\rangle - b\frac{1}{2}|\beta\rangle\right) \\
&= a^*a\frac{1}{2}\langle\alpha|\alpha\rangle - a^*b\frac{1}{2}\langle\alpha|\beta\rangle + b^*a\frac{1}{2}\langle\beta|\alpha\rangle - b^*b\frac{1}{2}\langle\beta|\beta\rangle \\
&= \frac{1}{2}(a^*a - b^*b)
\end{aligned}$$

Similarly, for the expectation value of the x and y components we find

$$\langle I_x\rangle = \langle\psi|\hat{I}_x|\psi\rangle = \langle\psi|\frac{1}{2}(\hat{I}_+ + \hat{I}_-)|\psi\rangle = \frac{1}{2}(a^*b + b^*a)$$

$$\langle I_y\rangle = -\frac{\mathrm{i}}{2}\left(a^*b - b^*a\right)$$

As we will make use of these relations in further sections, we summarize them in Excursus 9.2.

Excursus 9.2: Expectation Values of Spin Operators $\hat{I}_x$, $\hat{I}_y$, $\hat{I}_z$ and the Identity Operator 1 for an Arbitrary Spin State $|\psi\rangle = a|\alpha\rangle + b|\beta\rangle$

$$\begin{aligned}\langle I_x\rangle &= \frac{1}{2}(a^* b + b^* a)\\ \langle I_y\rangle &= -\frac{\mathrm{i}}{2}(a^* b - b^* a)\\ \langle I_z\rangle &= \frac{1}{2}(a^* a - b^* b)\\ \langle \mathbf{1}\rangle &= a^* a + b^* b = 1\end{aligned} \tag{9.38}$$

9.4 Hamiltonian and Time Evolution

NMR experiments create states that change in time and everything considered so far would be more or less useless if we would not be able to describe their time evolution. The time evolution of a quantum system is governed by the *time-dependent Schrödinger equation*

$$\mathrm{i}\hbar\frac{\partial}{\partial t}|\psi\rangle = H|\psi\rangle \tag{9.39}$$

where H is the Hamilton operator describing the energy of the system. When the state vector $|\psi\rangle$ is given as a superposition of eigenstates $|\psi_i\rangle$ of a time-independent Hamiltonian H, thus $|\psi_{(0)}\rangle = a_1|\varphi_1\rangle + a_2|\varphi_2\rangle + \ldots$ with $H|\varphi_i\rangle = \omega_i|\varphi_i\rangle$, the Schrödinger equation becomes

$$\begin{aligned}\mathrm{i}\frac{\partial}{\partial t}|\psi_{(t)}\rangle &= H|\psi_{(t)}\rangle\\ &= \omega_1 a_1(t)|\varphi_1\rangle + \omega_2 a_2(t)|\varphi_2\rangle + \ldots\end{aligned}$$

which has the general solution

$$|\psi_{(t)}\rangle = a_1\mathrm{e}^{-\mathrm{i}\omega_1 t}|\varphi_1\rangle + a_2\mathrm{e}^{-\mathrm{i}\omega_2 t}|\varphi_2\rangle + \ldots \tag{9.40}$$

9.5 Free Precession

We have seen that we are able to predict how the system evolves in time provided we know the Hamiltonian. But how do we find the correct Hamiltonian? According to the general rules of quantum mechanics, the Hamiltonian operator is obtained by

formulating the energy of a system first classically, and then replacing the dynamical quantities of the particle by the corresponding quantum mechanical operators. Starting from (5.8)

$$E = -\boldsymbol{\mu} \cdot \boldsymbol{B}$$

and replacing the classical magnetic moment $\boldsymbol{\mu}$ by the quantum mechanical magnetic moment of the nuclear spin we obtain

$$H = -\gamma \, \boldsymbol{I} \cdot \boldsymbol{B} \tag{9.41}$$

If we chose our coordinate system in such a way that the magnetic field coincides with the z axis, such that the x and y components are both zero, we then obtain for the so-called Zeeman Hamiltonian characterizing a spin in the external B_0-field

$$\begin{aligned} H_Z &= -\gamma \, B_0 \hat{I}_z \\ &= \omega_0 \hat{I}_z \end{aligned} \tag{9.42}$$

(remember, herein $\hat{I}_z$ is the reduced spin operator related to the magnetic quantum number m_z as described in Section 9.3).

With the $|\alpha\rangle$ and $|\beta\rangle$ states being eigenstates of H_Z with the eigenvalues $+\omega_0/2$ and $-\omega_0/2$ respectively, the time evolution of an arbitrary spin state $|\psi_{(0)}\rangle = a_0|\alpha\rangle + b_0|\beta\rangle$ using (9.40) is

$$|\psi_{(t)}\rangle = a_0 \mathrm{e}^{-\mathrm{i}\frac{\omega_0}{2}t}|\alpha\rangle + b_0 \mathrm{e}^{\mathrm{i}\frac{\omega_0}{2}t}|\beta\rangle \tag{9.43}$$

If we calculate the expectation values of the spin components, using (9.38), we obtain for the x component

$$\begin{aligned} \langle I_x \rangle_{(t)} &= \frac{1}{2}\left(a^*_{(t)} b_{(t)} + b^*_{(t)} a_{(t)}\right) \\ &= \frac{1}{2}\left(a_0^* b_0 \mathrm{e}^{\mathrm{i}\omega_0 t} + b_0^* a_0 \mathrm{e}^{-\mathrm{i}\omega_0 t}\right) \\ &= \frac{1}{2} a_0^* b_0 [\cos(\omega_0 t) + \mathrm{i}\sin(\omega_0 t)] + \frac{1}{2} b_0^* a_0 [\cos(\omega_0 t) - \mathrm{i}\sin(\omega_0 t)] \\ &= \frac{1}{2}\left(a_0^* b_0 + b_0^* a_0\right)\cos(\omega_0 t) + \frac{\mathrm{i}}{2}\left(a_0^* b_0 - b_0^* a_0\right)\sin(\omega_0 t) \\ &= \langle I_x \rangle_{(0)} \cos(\omega_0 t) - \langle I_y \rangle_{(0)} \sin(\omega_0 t) \end{aligned}$$

Proceeding in a similar way for the expectation values of the y and z component, we obtain

$$\begin{aligned} \langle I_y \rangle_{(t)} &= \langle I_y \rangle_{(0)} \cos(\omega_0 t) + \langle I_x \rangle_{(0)} \sin(\omega_0 t) \\ \langle I_z \rangle_{(t)} &= \langle I_z \rangle_{(0)} \end{aligned}$$

Apparently, the expectation values describe a vector whose x and y components rotate in the xy plane while the z component remains constant. We could also analyze (9.43) using the spin function (9.37). We then have

$$|\psi_{(\theta,\phi,t)}\rangle = \cos\left(\frac{\theta}{2}\right)\mathrm{e}^{-\mathrm{i}\frac{\omega_0}{2}t}|\alpha\rangle + \sin\left(\frac{\theta}{2}\right)\mathrm{e}^{-\mathrm{i}\phi}\mathrm{e}^{\mathrm{i}\frac{\omega_0}{2}t}|\beta\rangle \tag{9.44}$$

Using the fact that a state vector can be multiplied with an arbitrary phase factor, we can multiply it by $e^{i\frac{\omega_0}{2}t}$ to obtain

$$\begin{aligned}|\psi_{(\theta,\phi,t)}\rangle &= \cos\left(\frac{\theta}{2}\right)|\alpha\rangle + \sin\left(\frac{\theta}{2}\right)e^{-i\phi}e^{i\omega_0 t}|\beta\rangle \\ &= \cos\left(\frac{\theta}{2}\right)|\alpha\rangle + \sin\left(\frac{\theta}{2}\right)e^{-i(\phi-\omega_0 t)}|\beta\rangle\end{aligned}$$

In view of Figure 9.6 and using $\phi' = \phi - \omega_0 t$ that means that the spin precesses about the z axis.

9.6 Representation of Spin Ensembles – The Density Matrix Formalism

So far we have only considered single spins. In Section 9.2.1 we have shown that a single spin can be represented in a vector space, and the state of the spin in such a representation is denoted by the direction of the vector. In NMR, however, we always measure a large numbers of spins simultaneously and the spins represent a statistical mixture of states. In this section we will see how to treat such an *ensemble* of spins.

Suppose we have many spins the state of which is represented by one vector each. Now, all vectors may point exactly in the same direction (this would refer to the case where the coefficients of the α and β states, the basis states, are exactly the same for all spins). Such a case is called a *pure state*. In the more general case where the vectors do not point in the same direction this is called a *mixed state*. Note that pure states may be superposition states, and the requirement for a pure state is only that all spins in the ensemble are represented by the *same* state function.

Let us look at a spin ensemble consisting of two spins – one in the α state and one in the β state. We can visualize these two spins in terms of two spin vectors, one pointing into the positive and the other into the negative z direction. Clearly, if we add the components of the spins, there is no net spin component. We may now ask the question, whether it is possible to describe the spins in terms of a single averaged state vector? Unfortunately the answer is no. As soon as we express the spins as an averaged state vector of the form $\alpha + \beta$, the resultant state would have a nonzero spin component in the xy plane (see (9.35)). Thus, we cannot specify the state of a spin ensemble in terms of an averaged state vector. The problem is, that the observables of the spin are related to the *products* of the coefficients of the expansion, and therefore we need to evaluate these products before averaging. As described in the following, this is achieved by representing the ensemble not by an averaged state vector, but by an averaged operator, the so-called *density operator*. But other than the operators we have introduced so far, this operator does not denote a physical observable nor does it serve as a rotation operator but rather presents the (usually mixed) state of the system.

The idea is that every state $|\psi\rangle$ can be represented as a projection operator $|\psi\rangle\langle\psi|$ (for a formal definition of these see Section 9.2.5). If this operator acts

on a state $|\psi\rangle$ the resultant state is just again the same state $|\psi\rangle$, according to $(|\psi\rangle\langle\psi|)|\psi\rangle = |\psi\rangle\langle\psi|\psi\rangle = |\psi\rangle$. For all other states $|\psi'\rangle$ the resultant state is $\lambda|\psi\rangle$ with $\lambda = \langle\psi|\psi'\rangle$ which, unless $|\psi'\rangle = |\psi\rangle$, is always smaller than one.

Starting from the definition of the projection vector $|\psi\rangle\langle\psi| = a|\alpha\rangle + b|\beta\rangle$ and using the relations summarized in (9.38), we can write the projection operator as an appropriately weighted sum of the three linearly independent Pauli matrices plus the identity matrix (9.30)

$$\begin{aligned}|\psi\rangle\langle\psi| &= 2\langle I_x\rangle I_x + 2\langle I_y\rangle I_y + 2\langle I_z\rangle I_z + \frac{1}{2}\mathbf{1} \\ &= 2\langle I_x\rangle \begin{bmatrix} 0 & 1 \\ 1 & 0 \end{bmatrix} + 2\langle I_y\rangle \begin{bmatrix} 0 & \mathrm{i} \\ \mathrm{i} & 0 \end{bmatrix} + 2\langle I_z\rangle \begin{bmatrix} 1 & 0 \\ 0 & -1 \end{bmatrix} + \frac{1}{2}\begin{bmatrix} 1 & 0 \\ 0 & 1 \end{bmatrix}\end{aligned} \tag{9.45}$$

in which $\langle I_x\rangle$ denotes the expectation value of the x component of the spin. Thereby, the state of the spin can be decomposed into contributions of x, y, and z components. Each spin of the ensemble can be represented that way. The important property of such a presentation is that we can now add all the states and take their average. The resulting operator is called the *density operator* σ, and its matrix representation is called the *density matrix*

$$\begin{aligned}\sigma &= \frac{1}{N}\sum_i |\psi_i\rangle\langle\psi_i| \\ &= \overline{|\psi\rangle\langle\psi|} = \begin{bmatrix} \overline{a^*a} & \overline{b^*a} \\ \overline{a^*b} & \overline{b^*b} \end{bmatrix} = 2\overline{\langle I_x\rangle} I_x + 2\overline{\langle I_y\rangle} I_y + 2\overline{\langle I_z\rangle} I_z + \frac{1}{2}\mathbf{1}\end{aligned} \tag{9.46}$$

Therein the bar indicates the *ensemble average*. When the number of spins is large, as is always the case in NMR, the ensemble averaged expectation values match the macroscopically observable quantities (e.g., the x, y, or z magnetization). The products of the coefficients that form the elements of the density matrix have a special meaning: the diagonal elements of the density matrix represents populations of states whereas the off-diagonal elements represent coherences. The density matrix is thus a comprehensive representation of the entire state of the *ensemble* of spins. If we are interested in computing the effect of pulses or the evolution of the spin ensemble we need to use the density matrix.

Often we are interested in extracting information on one particular observable out of this matrix. This can be achieved in the following way:

$$\overline{\langle A\rangle} = \mathrm{Tr}\{\sigma\hat{A}\} \tag{9.47}$$

in which Tr denotes the *trace*, the sum of all diagonal elements of the resulting matrix.

9.6.1
Density Matrix at Thermal Equilibrium

At thermal equilibrium the populations of the density matrix are filled according to the Boltzmann distribution

$$\frac{N_i}{N} = Z^{-1} \exp\left(-\frac{E_i}{k_B T}\right)$$

with Z being the partition function defined as

$$Z = \sum_i \exp\left(-\frac{E_i}{k_B T}\right)$$

With $|E_i|/(k_B T) \ll 1$, we can approximate the exponentials by the first two terms of its power series ($\exp(-x) \approx 1-x$). With this and noting that $\sum E_i = 0$, we obtain the approximation

$$\frac{N_i}{N} = \frac{1 - \frac{E_i}{k_B T}}{d} \tag{9.48}$$

with d denoting the dimensionality of the Hilbert space. In principle we can now directly use (9.48) to calculate the populations $c_i^* c_i$ of the density matrix, or, noting that $E_i = \langle \varphi_i | \hbar H | \varphi_i \rangle$, we can express (9.48) as an operator, known as the density operator at thermal equilibrium σ_{eq}

$$\sigma_{eq} = \frac{\mathbf{1} - \frac{\hbar H}{k_B T}}{\mathrm{Tr}\,[\mathbf{1}]}$$

where we have used the fact that the dimensionality of the Hilbert space just corresponds to the trace of the identity matrix (the sum of the diagonal elements). As the absolute values usually are not of interest, and because the identity operator just presents a constant term (see below), the density operator is often simply written as

$$\sigma_{eq} = -H$$

For example, for an ensemble of noninteracting spins we have the equilibrium density operator

$$\sigma_{eq} = -\omega_0 I_z = \gamma B_0 I_z \tag{9.49}$$

This result is not further surprising in that it parallels (9.46) considering that at thermal equilibrium we have only z magnetization.

9.6.2
Time Evolution of the Density Operator

To see how the density operator evolves in time, we need to calculate how the individual projection operators that contribute to the density operator evolve in time.

For that we compute the time derivative of the projection operator $|\psi\rangle\langle\psi|$

$$\frac{\partial(|\psi\rangle\langle\psi|)}{\partial t} = \frac{\partial|\psi\rangle}{\partial t}\langle\psi| + |\psi\rangle\frac{\partial\langle\psi|}{\partial t} \tag{9.50}$$

and substitute the time derivatives, using the Schrödinger equation (9.39) by

$$\frac{\partial}{\partial t}|\psi\rangle = -\mathrm{i}H|\psi\rangle \tag{9.51}$$

and

$$\frac{\partial\langle\psi|}{\partial t} = \left(\frac{\partial}{\partial t}|\psi\rangle\right)^* = \langle\psi|H\mathrm{i} \tag{9.52}$$

to obtain

$$\frac{\partial\left(|\psi\rangle\langle\psi|\right)}{\partial t} = -\mathrm{i}H|\psi\rangle\langle\psi| + |\psi\rangle\langle\psi|H\mathrm{i} \tag{9.53}$$

The time evolution of the ensemble is obtained from the ensemble average of (9.53):

$$\frac{\partial\left(\overline{|\psi\rangle\langle\psi|}\right)}{\partial t} = -\mathrm{i}(H\overline{|\psi\rangle\langle\psi|} - \overline{|\psi\rangle\langle\psi|}H) \tag{9.54}$$

With $\overline{|\psi\rangle\langle\psi|} = \sigma$, the time evolution of the density operator is governed by the differential equation

$$\boxed{\begin{aligned}\frac{\partial\sigma}{\partial t} &= -\mathrm{i}(H\sigma - \sigma H)\\ &= -\mathrm{i}[H,\sigma]\end{aligned}} \tag{9.55}$$

where $[H,\sigma]$ is the shorthand notation for the commutator of operator H and σ, $[H,\sigma] = H\sigma - \sigma H$. Equation 9.55 is known as the *Liouville–von Neumann equation*. This is the master equation of NMR that allows us to compute the time evolution of the density operator under a specific Hamiltonian. We add here important commutators that allow us to compute chemical shift evolution and the effects from scalar or dipolar coupling:

$$\begin{aligned}[I_z, I_x] &= \mathrm{i}I_y\\ [I_y, I_z] &= \mathrm{i}I_x\\ [I_x, I_y] &= \mathrm{i}I_z\\ [I_z, S_z] &= 0\\ [I_x, I_z S_z] &= \mathrm{i}I_y S_z\\ [I_z, I_z S_z] &= 0\end{aligned} \tag{9.56}$$

To give an example, let us have a look at the time evolution of a spin ensemble under free precession, $H = \omega_0 I_z$. Let us assume that at a certain point in time

the ensemble is described by the density operator $\sigma = a\,I_x + b\,I_y + c\,I_z + 1/2\mathbf{1}$. Inserting the expression into (9.55) we obtain

$$\begin{aligned}\frac{\partial\sigma}{\partial t} &= -\mathrm{i}\left[\omega_0 I_z, a\,I_x + b\,I_y + c\,I_z + \frac{1}{2}\mathbf{1}\right] \\ &= -\mathrm{i}\omega_0 a[I_z, I_x] - \mathrm{i}\omega_0 b[I_z, I_y] - \mathrm{i}\omega_0 c[I_z, I_z] - \mathrm{i}\omega_0\frac{1}{2}[I_z, \mathbf{1}] \qquad (9.57)\end{aligned}$$

As we see, the evolution of the spin ensemble ultimately is governed by the commutation rules of the spin operators. Considering that $[I_z, I_z]$ and $[I_z, \mathbf{1}]$ are both zero and using $[I_z, I_x] = \mathrm{i}\,I_y$, $[I_z, I_y] = -\mathrm{i}\,I_x$, Eq. (9.57) then becomes

$$\frac{\partial\sigma}{\partial t} = \omega_0 a\,I_y - \omega_0 b\,I_x$$

This means that the I_x component of the density operator successively transforms into I_y while the I_y component transforms into $-I_x$, both with a rate constant given by ω_0. This describes just the characteristic cyclic transformation of the components of a vector precessing with angular velocity ω_0 in the xy plane. Formally, we can express this by

$$\begin{aligned}I_x &\xrightarrow{\omega_0 I_z} I_x\cos(\omega_0 t) + I_y\sin(\omega_0 t) \\ I_y &\xrightarrow{\omega_0 I_z} I_y\cos(\omega_0 t) - I_x\sin(\omega_0 t) \\ I_z &\xrightarrow{\omega_0 I_z} I_z\end{aligned}$$

This is just what we learned about shift evolution from the product operator formalism (POF) presented in Chapter 8.

As you may have already noted, very similar to the description of state vectors in Hilbert space, the density operator itself can be considered as a vector, just of another vector space, known as the Liouville space, that can be decomposed into the cartesian spin operators. The evolution of the density operator can then be considered as a rotation of a vector from state σ_1 to state σ_2

$$\begin{pmatrix}\sigma_2\end{pmatrix} = \begin{bmatrix}\boldsymbol{R}\end{bmatrix}\begin{pmatrix}\sigma_1\end{pmatrix}$$

Thereby the rotation matrix $\boldsymbol{R}$ is the matrix representation of the super operator $\hat{\hat{R}}$. The Liouville space often serves as a starting point in the more advanced description of NMR.

9.7 Spin Systems

Interacting spins are described in the product base of the individual spins. For two interacting spins I and S these are the products states $|\alpha_I\alpha_S\rangle$, $|\alpha_I\beta_S\rangle$, $|\beta_I\alpha_S\rangle$ and

$|\beta_I\beta_S\rangle$:

$$|\psi\rangle = c_1|\alpha_I\alpha_S\rangle + c_2|\alpha_I\beta_S\rangle + c_3|\beta_I\alpha_S\rangle + c_4|\beta_I\beta_S\rangle \tag{9.58}$$

The four states form a complete orthonormal base. As the spins are nonequivalent and thus distinguishable, their spin components can be measured separately and are described in terms of the three cartesian spin operators of spin I (I_x, I_y, I_z) and the three cartesian spin operators of spin S (S_x, S_y, S_z). The I operators act exclusively on spin I and the S operators on spin S. For example, we have $I_z|\alpha\beta\rangle = 1/2|\alpha\beta\rangle$ or $S_z|\alpha\beta\rangle = -1/2|\alpha\beta\rangle$. Note that the product states are still eigenstates of the operators I_z and S_z. Moreover, they are also eigenstates of the products of operators I_z and S_z, for example $I_z S_z|\alpha\beta\rangle = -1/4|\alpha\beta\rangle$.

To obtain the matrix representations for a two spin IS system we need to form the outer product (see Appendix A.3.1) of the corresponding two column representations of the individual states (see (9.15)):

$$|\alpha\alpha\rangle_{IS} = |\alpha\rangle_I|\alpha\rangle_S = \begin{bmatrix}1\\0\end{bmatrix}_I \otimes \begin{bmatrix}1\\0\end{bmatrix}_S = \begin{bmatrix}1\\0\\0\\0\end{bmatrix} \tag{9.59}$$

The operator for I_z in such a basis is obtained by forming the outer product of the Pauli spin matrix presentations of I_z and the unity matrix:

$$I_z = I_z\mathbf{1} = \frac{1}{2}\begin{bmatrix}1 & 0\\0 & -1\end{bmatrix} \otimes \begin{bmatrix}1 & 0\\0 & 1\end{bmatrix} = \frac{1}{2}\begin{bmatrix}1 & 0 & 0 & 0\\0 & 1 & 0 & 0\\0 & 0 & -1 & 0\\0 & 0 & 0 & -1\end{bmatrix} \tag{9.60}$$

9.7.1 Scalar Coupling

The interaction energy of scalar coupling is described by the scalar product $J\boldsymbol{\mu}_I \cdot \boldsymbol{\mu}_S$. The quantum-mechanical formulation is obtained by replacing the classical dipole moments $\boldsymbol{\mu}$ by the magnetic moment of the spins I and S as

$$H_J = 2\pi J\, I \cdot S = 2\pi J(I_x S_x + I_y S_y + I_z S_z) \tag{9.61}$$

Together with the Hamiltonians describing the Zeeman interaction of the spins with the external magnetic field (9.42), the full Hamiltonian of the two-spin system is

$$\begin{aligned} H_{IS} &= H_{Z,I} + H_{Z,S} + H_{J,IS} \\ &= \omega_I I_z + \omega_S S_z + 2\pi J(I_x S_x + I_y S_y + I_z S_z) \end{aligned} \tag{9.62}$$

Unfortunately, the base states $|\alpha\alpha\rangle$, $|\alpha\beta\rangle$, $|\beta\alpha\rangle$, and $|\beta\beta\rangle$ are not eigenstates of the Hamiltonian. This complicates the calculation of the time evolution of the

spins during an NMR experiment. In an analytical approach we would need to find the eigenstates of (9.62) by forming appropriate linear combinations of the base states. However, the effects of RF pulses also need to be recast in terms of these new eigenstates, and the computations would provide little insight into the spin physics.

Fortunately, it can be shown that when the difference in the precession frequencies of the spins is much larger than the scalar coupling constant (the so-called weak-coupling case, $|\omega_I - \omega_S| \gg |2\pi J|$), we can just drop the terms $I_x S_x$ and $I_y S_y$ from the Hamiltonian. We can rationalize this by saying that when the spins precess at very different rates, the scalar interaction of the spins x and y components rapidly oscillates and hence effectively average to zero provided the scalar interaction is comparably weak and we only need to take into account the scalar interaction between the spins z components that does not alter during the spins precession. This is known as the *secular approximation* or the *weak coupling approximation*. In that case the Hamiltonian becomes

$$H_{IS,\text{weak}} = \omega_I I_z + \omega_S S_z + 2\pi J I_z S_z \tag{9.63}$$

This approximation is always valid for I and S belonging to different isotopes. In contrast, when the shift difference of homonuclear spin systems and the magnitude of the coupling constant becomes comparable in size we are obliged to use the nontruncated Hamiltonian (9.62) which results in the much more complicated higher-order spectra.

In contrast to the Hamiltonian describing strong coupling (9.62), the base states $|\alpha\alpha\rangle$, $|\alpha\beta\rangle$, $|\beta\alpha\rangle$, and $|\beta\beta\rangle$ are eigenstates of the Hamiltonian H_{weak} (9.63). The corresponding eigenvalues are

$$\begin{aligned}
|\alpha\alpha\rangle &: E_1 = \frac{1}{2}\omega_I + \frac{1}{2}\omega_S + \frac{1}{2}\pi J \\
|\alpha\beta\rangle &: E_2 = \frac{1}{2}\omega_I - \frac{1}{2}\omega_S - \frac{1}{2}\pi J \\
|\beta\alpha\rangle &: E_3 = -\frac{1}{2}\omega_I + \frac{1}{2}\omega_S - \frac{1}{2}\pi J \\
|\beta\beta\rangle &: E_4 = -\frac{1}{2}\omega_I - \frac{1}{2}\omega_S + \frac{1}{2}\pi J
\end{aligned} \tag{9.64}$$

The two single quantum transitions affecting spin I for example are $|\beta\alpha\rangle \rightarrow |\alpha\alpha\rangle$ with $\Delta E = \omega_I + \pi J$ and $|\beta\beta\rangle \rightarrow |\alpha\beta\rangle$ with $\Delta E = \omega_I - \pi J$, the two doublet components of spin I, separated by $2\pi J$ (rad/s).

Maybe you have already wondered why we are only able to detect the single quantum transitions. To answer this question consider for example the superposition state $|\psi\rangle = 1/2(|\alpha\alpha\rangle + |\alpha\beta\rangle + |\beta\alpha\rangle + |\beta\beta\rangle)$. Under the Hamiltonian of chemical shift and scalar coupling the time evolution of the state using (9.64) is

$$|\psi_{(t)}\rangle = \frac{1}{2}\left(\mathrm{e}^{-\mathrm{i}E_1 t}|\alpha\alpha\rangle + \mathrm{e}^{-\mathrm{i}E_2 t}|\alpha\beta\rangle + \mathrm{e}^{-\mathrm{i}E_3 t}|\beta\alpha\rangle + \mathrm{e}^{-\mathrm{i}E_4 t}|\beta\beta\rangle\right) \tag{9.65}$$

Assume we have a detector that continuously detects the x component of spin I. We then calculate the expectation value of I_x

$$\begin{aligned}
\langle I_x\rangle_{(t)} &= \langle\psi_{(t)}|\, I_x|\psi_{(t)}\rangle \\
&= \frac{1}{2}\left(\langle\alpha\alpha|e^{iE_1t} + \langle\alpha\beta|e^{iE_2t} + \langle\beta\alpha|e^{iE_3t} + \langle\beta\beta|e^{iE_4t}\right)\frac{1}{2}\left(I_+ + I_-\right) \\
&\quad\times\frac{1}{2}\left(e^{-iE_1t}|\alpha\alpha\rangle + e^{-iE_2t}|\alpha\beta\rangle + e^{-iE_3t}|\beta\alpha\rangle + e^{-iE_4t}|\beta\beta\rangle\right) \\
&= \frac{1}{8}\left(\langle\alpha\alpha|e^{iE_1t} + \langle\alpha\beta|e^{iE_2t} + \langle\beta\alpha|e^{iE_3t} + \langle\beta\beta|e^{iE_4t}\right) \\
&\quad\times\left(e^{-iE_1t}|\beta\alpha\rangle + e^{-iE_2t}|\beta\beta\rangle + e^{-iE_3t}|\alpha\alpha\rangle + e^{-iE_4t}|\alpha\beta\rangle\right) \\
&= \frac{1}{8}\left(e^{i(E_1-E_3)t} + e^{i(E_2-E_4)t} + e^{i(E_3-E_1)t} + e^{i(E_4-E_2)t}\right) \\
&= \frac{1}{4}\cos[(\omega_I + \pi J)t] + \frac{1}{4}\cos[(\omega_I - \pi J)t]
\end{aligned}$$

In the third line we made extensive use of the fact that the basis states are orthogonal and hence all scalar products vanish with the exception of those formed between the same states. As you can see, the detector (I_x) only "links" the states that differ by $\Delta m_z(I) = \pm 1$. As a consequence we can only measure single-quantum transitions associated with the corresponding frequencies $E_1 \leftrightarrow E_3$ and $E_2 \leftrightarrow E_4$. Similarly we can show that the detection of S_x yields the transitions $E_1 \leftrightarrow E_2$ and $E_3 \leftrightarrow E_4$.

Part Three
Technical Aspects of NMR

In the early days of NMR, acquisition of NMR spectra and data processing used to be a daunting task that required expertise by someone well trained in this field. Measurements were often governed by troubleshooting of technical problems. Data processing required extensive computing knowledge, not to mention hardware and software issues in this part as well. Nowadays, instruments are mostly stable, largely due to the much-improved electronics, and almost every aspect of the measurement is computer controlled. In addition, we have learned to live with computers, and software has become much more user-friendly.

As a result of these improvements, NMR measurements can be conducted after a short period of training. Setting up sophisticated experiments often only requires a basic instrument setup and the loading of a predefined parameter set for that experiment. Such parameters will also provide reasonable settings for data processing. Nevertheless, we feel that it is deeply unsatisfying if you only use the NMR instrument as a black box. You will realise that as soon as something does not work as you have planned, or when you want to try something new. In this part we would like to provide some background on the instrumental aspects, show you how to process your data, and introduce a few simple but important 1D NMR experiments. Finally, we want to introduce you to basic concepts of pulse programs. Once you have read all this you will understand the logic behind the basic spectrometer setup, and maybe you can modify your experiments a bit, or you will at least know the meaning of the most important parameters in your NMR experiment.

10
The Components of an NMR Spectrometer

Figure 10.1 shows typical components of a modern routine NMR spectrometer. The most impressive piece of equipment is the *magnet*, which produces the B_0 field. Other parts are the *console*, where most of the electronics reside, a *preamplifier*, a cooling unit for regulation of the sample temperature, and a *workstation* to control the spectrometer and for data processing. The magnet is equipped with a *shim system*, a tube coaxial to the vertical axis of the magnet, which is needed to improve field homogeneity. The *probehead* is inserted from the bottom into the magnet and plugged into the lower part of the shim system. Depending on the applications, different probes can be used.

To insert and remove samples, an airflow (the lift) is activated which smoothly transports the sample to the upper part of the magnet bore. For measurements, the sample is inserted from the top, and lowered by reducing the lift air such that the sample is placed in the center of the field. The sample temperature is adjusted with a gas that is blown into the probe. For this purpose the variable-temperature gas (air or nitrogen of around −5°C) from the *cooler* is heated in the probehead to the desired temperature and passed along the sample tube. For low-temperature measurements well below 0 °C, the gas of a liquid nitrogen evaporator or exchanger is usually used.

10.1
The Magnet

The strong magnetic main (or B_0) field is provided by a *superconducting magnet* as depicted in Figure 10.2. The main (or B_0) coil is placed in a liquid helium bath (at about 2–4 K) so that the electrical resistance of the coil wire is zero. Nowadays field strengths reach about 22 T (corresponding to an ^{1}H frequency of 1 GHz) and are about 440 000 times the strength of the magnetic field of Earth (about 0.5 G). As the solenoid is superconducting, no external current source is necessary and the magnet must usually be charged only once at the time of installation. To reduce the loss of expensive helium, the helium dewar is surrounded by liquid nitrogen. Both liquid helium and liquid nitrogen must be added at regular time intervals

Applied NMR Spectroscopy for Chemists and Life Scientists, First Edition. Oliver Zerbe and Simon Jurt.
©2014 WILEY-VCH Verlag GmbH & Co. KGaA. Published 2014 by WILEY-VCH Verlag GmbH & Co. KGaA.

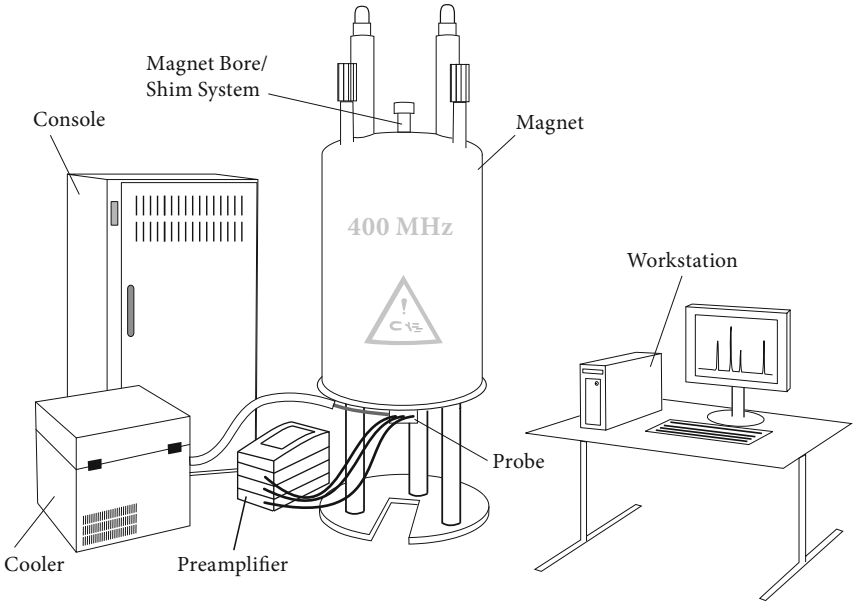

Figure 10.1 Components of an NMR spectrometer. The most important pieces of hardware are the magnet, the console, and the probe.

(normally on the order of several months for liquid helium and several weeks in the case of liquid nitrogen).

Although the magnet is superconducting, the field slowly drifts. The field drift is normally on the order of some parts per billion per hour. While this seems to be negligible on an absolute scale, it becomes severe when good spectral resolution (up to fractions of a hertz) should be obtained from measurements that potentially last days. For example, a field drift of 4 ppb/h for a 500 MHz magnet corresponds to a change in ^{1}H frequency of 2 Hz/h. Without compensating for this, the signals of (long-term) 1D spectra would become considerably broadened and those of multidimensional spectra badly distorted. As we will see in Section 10.5, the field drift is compensated by the *lock system*.

Furthermore, to prevent disturbances most magnets are fitted with pneumatic vibration-damping legs.

10.1.1 Field Homogeneity

From the example given above it is also clear that for high-resolution spectra the magnetic field within the sample volume must be extremely homogeneous. Preferably field deviations should be less than 1 ppb across the measuring volume (the so-called active volume). Such good homogeneity is only possible when the field produced by the main coil is corrected with additional coils, the shim coils or just

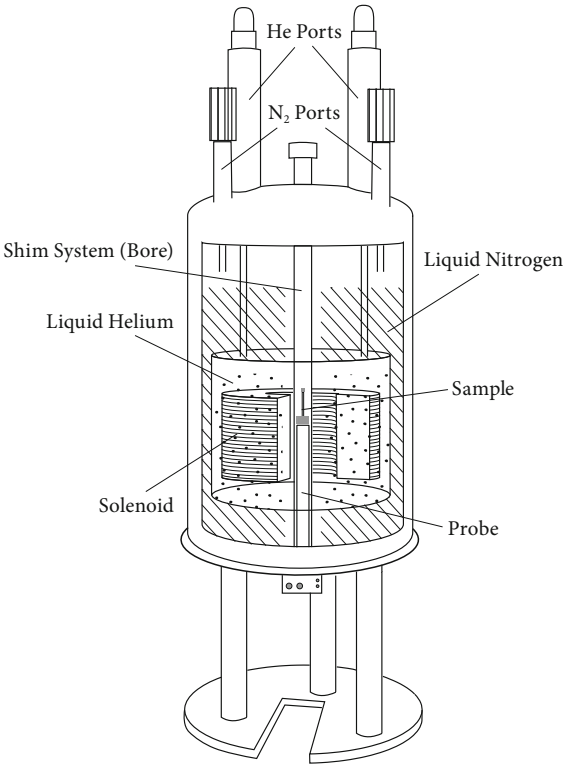

Figure 10.2 Schematic layout with cross-sectional view of a superconducting NMR magnet.

shims. Basically there are two types of shims, cryoshims and room temperature (RT) shims. The cryoshims are used for a rough field optimization and as the term "cryo" indicates these are superconducting coils located in the liquid helium bath. They are adjusted during installation of the magnet by the service engineer, and they help to reduce the ^{1}H line width to about 100 Hz. The RT shims are located in the shim system within the magnet bore. As will be explained in more detail in the next section, they are used for locally fine tuning the magnetic field.

10.1.2 Safety Notes

The magnetic field strength of an NMR magnet denotes the field at the center of the magnet. Outside the magnet the field decreases rapidly, and most modern NMR magnets are actively shielded. This is achieved by additional coils wrapped around the main coil generating a counteracting field so that the outward field (the *stray field*) is strongly attenuated. For shielded magnets the radial 5 G line nowadays is often located within the magnet dewar. Nevertheless, the magnetic field below the magnet may be quite strong, strong enough to alter watches or erase information

from credit cards, and therefore you should also never carry magnetizable objects such as iron tools close to the magnet. People who have heart pacemakers are not allowed to approach the magnets. In addition, care must be taken that the helium level never falls below a critical value. Otherwise the coil could warm up, and lose superconductivity, generating a large amount of heat, resulting in the complete boil off of all liquid helium. This is called a quench, an impressive but also very expensive event. A quench may also occur just by chance because of coil defects. In any case it is advisable to leave the room as quickly as possible if a magnet quenches. However, there is no reason to panic, since helium is not toxic, and it will take some time until oxygen is displaced from the room. Finally, we wish to remind you that liquid gases should always be handled with care and safety goggles and protective gloves should be worn. Liquid gases can result in very severe burns otherwise.

10.2
Shim System and Shimming

We mentioned in the last section that we cannot expect narrow line widths unless the magnetic field within the sample volume is highly homogeneous. Because the field homogeneity depends on the geometry of the sample tube, the solvent, the filling height, and the temperature, the field must be corrected whenever a new sample is inserted into the magnet or when the sample temperature is changed. The procedure is called shimming and is done by adjusting the current in the RT shim coils.

10.2.1
The Shims

The basic idea behind the shims is to produce a local field that when added to the static field results in a very homogeneous field. The RT shim coils are located on the shim bore, a tube that runs though the magnet, such that they surround the sample. The shim coils are not coils in the classic sense, they are rather conductor paths on tapes. Each of them is designed to produce a specific spatial field profile, called the shim function. Basically these profiles correspond to the spherical harmonics. The profiles of the on-axis shims correspond to functions of the form $B_{(z)} = z^n$. In the case of $n=1$, this is a linear function, and hence the correction field increases linearly in the z direction. Similarly, the z^4 shim corresponds to a parabolic profile that rises more steeply than for z^2. Depending on the current supplied, the amplitude of these functions changes. The number of shims depends on the particular hardware, but is often found to be around 20. Generally, the higher the B_0 field is, the more shims are needed.

Two sets of shims exist, on-axis and off-axis shims. The first ones produce correction fields that are symmetric around the z axis, the long axis of the sample, and hence are used to correct for field inhomogeneities along the z axis. Off-axis shims

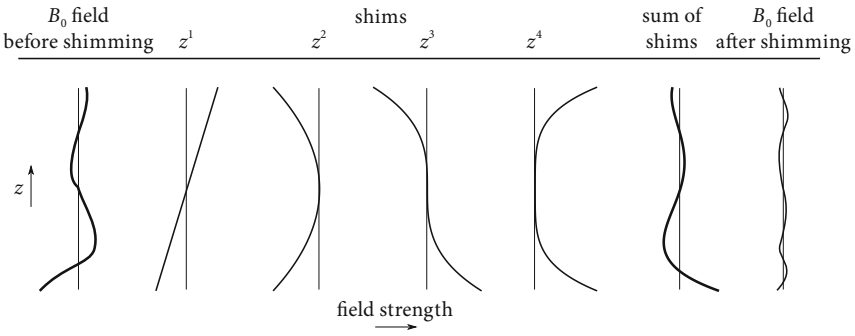

Figure 10.3 Shim function of the z^1–z^4 shims. When the amplitudes of these functions are correctly set, they add up to a field that will compensate for inhomogeneities in the B_0 field.

correct for field inhomogeneities along the x and y axes. If all shim currents are properly adjusted, the shims will generate a field of inhomogeneity similar to that of the uncorrected B_0 field but of opposite sign. Addition to the main field results in a very uniform field strength across the active volume. The compensating effect when using the z^1–z^4 shims is illustrated in Figure 10.3. The art of shimming is to find the shim currents that generate the appropriate correction field. Because the shims depend on each other, this is not a simple task, and shimming in general must be performed in an iterative fashion. There are different methods and strategies for shimming. The shims can be adjusted either manually or by automatic procedures, using criteria such as the amplitude of the lock signal (the lock level), the shape of the envelope of the free induction decay, or by direct inspection of the shapes of the spectral lines.

10.2.2 Manual Shimming

For manual shimming it is most common to initially use the lock level as the criterion. The more homogeneous the field is, the narrower and hence more intense the resonance signal becomes, and thus the lock level increases as the shim currents are changed in the proper direction. If you cannot observe an increase in the lock level anymore, we suggest you record a simple ^{1}H spectrum with a few scans and inspect the line shapes to decide whether the field homogeneity is already fine or needs further improvement. Usually the signal of the reference substance (e.g., the tetramethylsilane signal) or the residual ^{1}H signal of the solvent line is used for that purpose. Because the line shape is influenced by the different shims in a very specific way, knowledge of such rules enables the experienced spectroscopist to further improve the field homogeneity even when the lock level indicates no further improvement is possible. Some of these rules are depicted in Figure 10.4. Depending on the operator's expertise and the performance of the spectrometer, manual shimming can be quite time consuming. Fortunately modern spectrometer offer tools for automatic shimming.

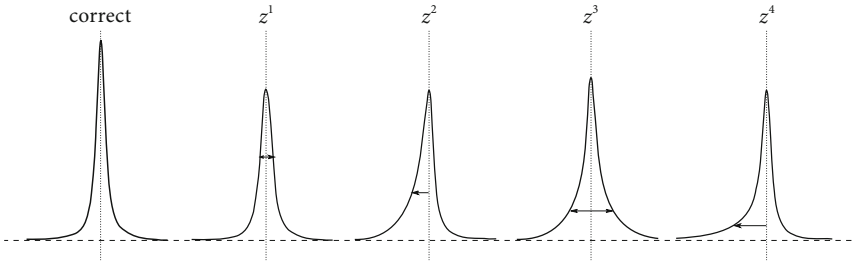

Figure 10.4 Influence of shims on the line shape. Poor line shapes due to misadjustment of the on-axis shims compared with perfectly adjusted shims (leftmost signal). The shims affect the line shape in a specific way. The general rules are as follows: the higher the order of the misadjusted shim, the lower the part of the signal that becomes affected; misadjustment of shims with an odd order results in symmetric line broadening, whereas misadjusted of shims with an even order results in asymmetric line shapes. The asymmetry also indicates in which direction the corresponding shim value must be changed.

10.2.3 Automatic Shimming

The simplest although probably not most efficient method for automatic shimming is to let the software do what the operator normally does by manual shimming, that is, to successively change the shim values while observing the lock level. A number of different optimization protocols have been developed (e.g., the simplex method) by which the shims are changed in different order and step sizes. A smooth variant of automatic shimming is often applied during long-term experiments, for example, to compensate for solvent evaporation or changes in field homogeneity due to cryogen boil off. A much more efficient method is *gradient shimming*. As discussed in Section 12.2, application of a field gradient results in spatial encoding of frequencies. If there is one dominant line in the spectrum (e.g., the water line in aqueous samples or the deuterium line from the solvent), this will result in a continuous band of frequencies, with the lowest and highest frequency signals resulting from spins at both ends of the sample. As discussed in Section 12.2.2, a gradient-echo experiment results in a profile in which the field inhomogeneity adds to the phase of the signal. This phase change can be locally resolved through the spatially dependent gradient encoding/decoding and allows one to improve the shim in a predictive and iterative fashion. The important feature here is that the frequencies in the resulting spectrum are related to the position of the spins in the sample, and hence the strength of the field is probed with spatial resolution in the z direction. Any deviations can be corrected for in the proper way since the response of the field to the different shims is known. This sounds complicated but this procedure is very simple to perform and works almost perfectly! To be able to perform gradient shimming the probe must be capable of generating pulsed field gradients of course.

10.2.4
Using Shim Files

The geometry of the particular probehead used has by far the most dominant effect on the field homogeneity, and shimming a sample when a probe is inserted into a magnet for the first time can be quite tricky. Usually this task is performed by an expert and the shim values determined in this way are written to a file. The first step in shimming is usually to read in the standard shim values of the particular probe used. However, it is then almost always necessary to optimize the shims of lowest order (e.g., z^1–z^4 and x, xz, y, yz). As the main field tends to drift, the field profile will also change and therefore the standard values should be adjusted from time to time by shimming a standard (the so-called line shape) sample. Adjusting field homogeneity is more difficult with higher fields, and also more complicated with wide-bore magnets or samples with a large diameter. Off-axis shims depend much less on the sample, and only need to be touched when very good homogeneity is desired. The z^1 and z^2 shims always need to be adjusted, and on all spectrometers. Higher-order shims, for example, z^4, to a large extent depend on the filling height of the sample. If you always use, for example, 500 µl of solvent, then you do not need to make large adjustments to z^4.

10.2.5
Sample Spinning

The influence of field inhomogeneities in the xy plane can be averaged out by spinning the sample about its long axis. The drawback of sample spinning is spinning sidebands that are located to the left and right of the main signal at a distances that correspond to the particular spinning rate and a multiple of it (usually 20 Hz). These are due to a modulation of the resonance signal when passing compartments of different field strength. Moreover, when bad NMR tubes (imperfect symmetric tubes) are used, rotation is nonuniform, which introduces time-dependent changes in tuning and matching that lead to severe spinning sidebands. Therefore, sample spinning is usually not recommended during multidimensional experiments, and it is strictly forbidden for experiments that require solvent suppression or use signal subtraction schemes such as NOE experiments.

10.3
The Electronics

A modern NMR spectrometer consists of many different electronic devices. Most of them are situated in a cabinet, the so-called console. Although the particular design and configuration of the electronics depends on the particular manufacturer and spectrometer type (generation), they have much of the basic architecture in common. Electronics are rapidly developing, we will not go into too much technical detail here but will rather give a rough overview of the most important components.

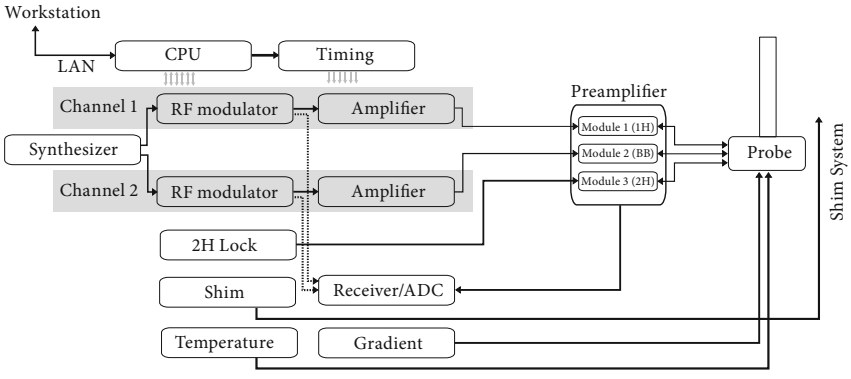

Figure 10.5 Schematic representation of the commonest parts of the spectrometer electronics and the wiring. ADC analog-to-digital converter, BB broadband.

The working principle of an NMR spectrometer is schematically shown in Figure 10.5. The workstation communicates via a network interface with the spectrometer CPU. The CPU in turn nowadays communicates with all other units. As most events in the course of an experiment must take place in a highly synchronous way and for very precise durations of time (on the order of nanoseconds), there is a central timing unit that precisely coordinates the different events (e.g., RF pulses, gradient pulses, acquisition).

10.3.1 The RF Section

The RF section of a spectrometer usually consists of several channels. For each type of nucleus to which RF pulses are applied during the experiment an individual RF channel is required. For example, for the basic ^{1}H-decoupled ^{13}C experiment, two RF channels are required, one set to the ^{13}C frequency used for the ^{13}C excitation pulses, and the other set to the ^{1}H frequency for ^{1}H decoupling. The channel assigned to the nuclei which we wish to observe during collection of the free induction decay is called the *observe channel* (in our example it is the ^{13}C channel). The other channel(s), used for spin decoupling (here the ^{1}H channel) but in some experiments also for application of excitation pulses, is often called the decoupler channel(s).

Usually there is a dedicated ^{1}H channel and one or several broadband channels. The amplifiers of the broadband channels are capable of generating RF pulses over a wide range of resonance frequencies (see Figure 10.6). In addition, because more powerful pulses are required to excite low-γ nuclei, these amplifiers are usually stronger than the ^{1}H amplifier. Although the electronics are broadband, some frequencies, for example, those of ^{19}F, ^{205}Tl, or ^{3}He, are outside the normal range for which the X coils of probeheads can be tuned, and therefore require special probes.

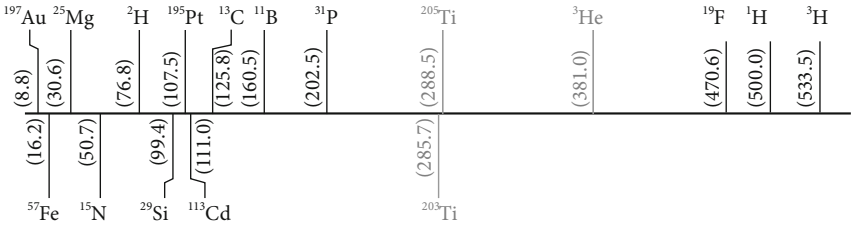

Figure 10.6 Spread of resonance frequencies of some selected nuclei. The numbers in parentheses denotes the particular resonance frequencies (MHz) at a field strength of 11.75 T (500 MHz spectrometer frequency).

A piece of quartz with a precisely oscillating signal (e.g., 10 MHz) serves as the master clock to time all events on the spectrometer. This signal is also used to generate the RF pulses of desired frequency, phase, and amplitude in the RF generator (usually by direct digital synthesis). Whenever an RF pulse is required, this signal is fed via an amplifier and a preamplifier into the probe.

10.3.2 The Receiver Section

During acquisition, the response of the sample is picked up by the RF coil of the observe channel and then fed via the preamplifier to the receiver. The preamplifier is usually located close to the probe to boost the tiny signal so that it is easier to distinguish it from the thermal noise introduced in the cables afterward. As we will see in Section 11.3.1, in the receiver the signal is multiplied by the carrier frequency of the observe channel, thereby essentially subtracting the carrier frequency. As a consequence, the signal is now in the audio range.

10.3.3 Other Electronics

As already mentioned and explained further in Section 10.5, the lock channel is required to operate the magnet at a constant field. Furthermore, the console houses the shim board that supplies the shim currents, a temperature control unit, and a gradient unit to generate the pulsed field gradients (see Chapter 12.2).

10.4 The Probehead

A conventional probehead (or "probe" for short) as shown in Figure 10.7 typically contains two RF coils. These are small (usually saddle-shaped) coils enclosing the sample tube. When the RF transmitter signal is delivered to the coil, an oscillating magnetic field (the RF field) is produced across the coil, which excites all those

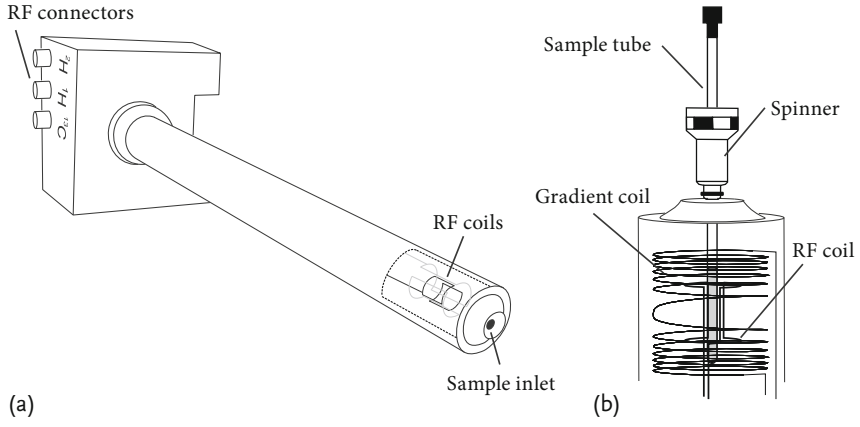

Figure 10.7 Typical design of a liquid-state NMR probehead. (a) The probe with its RF connectors and RF coils. (b) The upper part of the probe where the sample is placed. Most probes are fitted with gradient coils allowing one to apply field gradients.

spins that have resonance frequencies close to the transmitter (carrier) frequency. Similarly, the oscillating magnetic field of excited spins induces an alternating voltage in the coil that is recorded by the receiver. Thus, depending on whether the spectrometer is in the transmitting or the receiving mode the RF coil is part of either a transmitter or a receiver circuit. In both cases we have a resonant circuit and (similar to a radio receiver) the circuit must be properly tuned to meet the resonance condition in the frequency range of interest, and matched to an impedance of 50 Ω. This is called tuning and matching the probe.

10.4.1 Tuning and Matching

Tuning and matching of the RF circuits is achieved by adjusting two variable capacitors within the probe (see Figure 10.8). Mismatching and mistuning results in less effective RF power transmission, and a lower quality factor Q of the coil requires longer pulses and results in lower sensitivity. Placing a sample in the coil changes its inductive resistance, and hence the probe should be tuned and matched whenever the sample or the temperature is changed. In practice, the probe is usually tuned and matched by adjusting the capacitors to minimize the amount of reflected RF power. Because the two capacitors are not independent of each other, tuning and matching must be performed in an iterative fashion.

An RF coil cannot usually be tuned over the whole frequency range of NMR-active isotopes (see Figure 10.6) but the RF circuits are designed to be tunable either for one or a few nuclei only or for nuclei within a specific frequency range (e.g., ^{15}N to ^{31}P), a so-called broadband coil. The selective coils are often double tuned to two resonance frequency simultaneously (e.g., ^{13}C and ^{15}N). Similarly, the ^{1}H coil is often double tuned to the ^{2}H frequency.

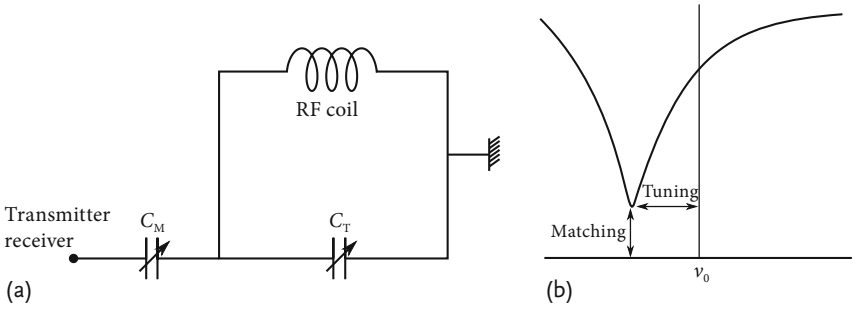

Figure 10.8 Tuning and matching of the RF circuit. Tuning and matching is achieved by adjusting the variable capacitors C_T and C_M within the probe's RF circuit (a). (b) A so-called *wobbling curve*. During wobbling the carrier is quickly swept through a few megahertz around the carrier frequency. The dip in the curve corresponds to the frequency that is absorbed best. For perfect tuning and matching, the dip is in the center (tuning) and reaches the baseline (matching).

10.4.2
Inner and Outer Coils

The RF coils are positioned concentrically around the sample tube (see Figure 10.7). The inner coil is more sensitive and delivers shorter pulses. It is therefore reasonable to use the inner coil for detection of the low-sensitivity heteronuclei and use the outer coil for detection or decoupling of the much more sensitive ^{1}H nuclei. This is the traditional arrangement used in the early days of NMR spectroscopy. However, for ^{1}H-detected correlation spectroscopy (so-called inverse experiments) with improved sensitivity it is advantageous to have ^{1}H on the inner coil and in turn place the heteronuclei on the outer coil. Probes with such a configuration are called inverse probes.

Nowadays, most probes are equipped with gradient coils, at least with a *z*-gradient coil. These coils are used to temporarily destroy the B_0 homogeneity and are located in the upper part of the probe close to the RF coils (see Figure 10.7b). As we will see later, pulsed field gradients are used during many NMR experiments, and they are also required for the very useful gradient shimming.

For conventional RT probes, the sample temperature can usually be adjusted over a relatively wide range of temperature (e.g., usually from −150 to 150 °C for conventional RT probes).

10.4.3
Cryogenically Cooled Probes

Cryogenically cooled probes offer improved sensitivity (about four times) compared with conventional RT probes. This is achieved by cooling the RF coil with cold helium gas to a temperature of about 20 K while the sample is kept around RT. In this way the thermal noise generated by the probe coils is considerably reduced. For further reduction of thermal noise, the preamplifier, which then becomes an

integral part of the probe, is usually cooled to about 80 K. To supply the cold helium gas, a number of additional instruments are necessary. Most systems compress the helium from the probes again, and a special gas expansion unit exploits the Joule–Thomson effect to cool the gas again (like a refrigerator).

10.5 The Lock System

Stability of the magnetic field is a prerequisite to obtain high-resolution spectra, especially during long-term measurements. If the B_0 field is unstable, the signal frequency will differ from scan to scan, resulting in considerable line broadening. In addition, improper regulation of the lock circuit results in dramatically increased levels of t1 noise in multidimensional spectra, a particular nuisance in NOESY spectra. As mentioned in Section 10.1, one source of field instability is the inherent field drift of the NMR magnet itself. Additional, external sources of field disturbances, for example, strong electric motors or moving massive magnetic objects (e.g., elevators), may be present. To correct for such disturbances and to maintain a constant field, the field-frequency lock system is used.

10.5.1 The ^{2}H Lock

The lock system continuously observes a reference signal to correct for field drifts. Usually the deuterium signal of the solvent is used for that purpose. The ^{2}H frequency is normally far outside the frequency range of interest, and thus its observation does not interfere with the NMR experiment. In cases where deuterium is the nucleus of interest (^{2}H NMR), optionally an ^{19}F lock can be used if the required hardware is used (this is not standard even on modern spectrometers). In the following we describe the ^{2}H lock exclusively, albeit the principles are essentially the same for the ^{2}H and the ^{19}F lock.

The ^{2}H lock circuit continuously measures the deuterium line of the solvent. If the solvent exhibits several deuterium lines, the most intense signal is usually observed. A change in the magnetic field will cause a frequency shift to the ^{2}H signal. This shift is recognized by the lock system and immediately corrected for by delivering a suitable current to an additional coil located on the shim system, known as the Z_0 or H_0 coil (see Figure 10.9). Thus, the lock system is a feedback circuit which generates corrections to the main magnetic field B_0 such that the resonance frequency of the deuterium line, and consequently also the resonance frequencies of all other signals, remain constant.

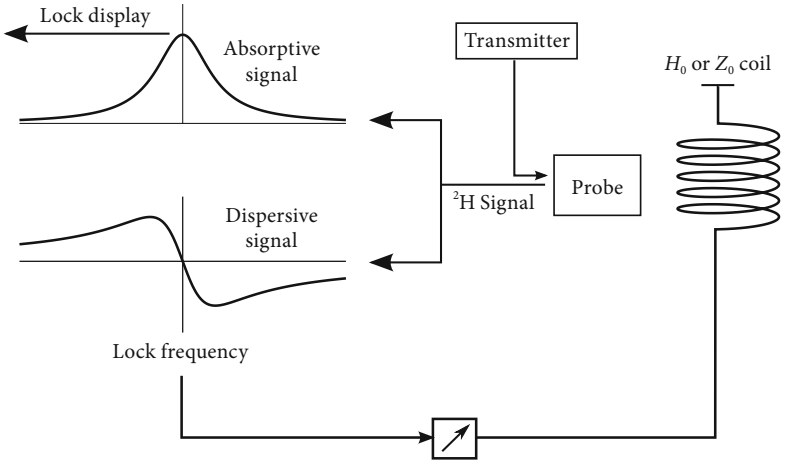

Figure 10.9 Principle of the ^{2}H field-frequency lock circuit. Any variation in the magnetic field strength causes a frequency alteration in the ^{2}H reference signal. This is most effectively recognized from the dispersive signal. Depending on the frequency drift, a current is supplied to the Z_0 coil, generating a compensating magnetic field, so that the ^{2}H frequency, and consequently also all other resonance frequencies, remain constant.

10.5.2 Activating the Lock

Usually the lock system has to be activated once the sample has been placed in the magnet. After the type of solvent has been specified, the chemical shift of the deuterium line is read out from a list and its nominal resonance frequency is calculated according to the basic spectrometer ^{1}H frequency. During the lock-in process, the field is adjusted to match this frequency. By this process the lock system not only ensures stability of the magnetic field during the experiment, but also that the field is virtually always exactly the same. Once the system has locked-in, the intensity of the lock signal at the particular ^{2}H frequency is continuously measured. Strictly speaking, the lock signal consists of two signals: an absorptive and a dispersive signal (see Sections 11.2 and 11.3.1). The intensity of the absorptive signal is usually shown by the lock line that can be used for shimming. For field correction the dispersive contribution of the lock signal is used because it is more sensitive to fluctuations and directly reveals in which direction the field must be corrected (see Figure 10.9). As long as the deuterium line is exactly on-resonant, the amplitude of the signal is zero. As soon as the field changes, the ^{2}H line is off-resonant and the amplitude of the lock signal becomes positive or negative. The feedback loop immediately increases or decreases the current of the Z_0 (H_0) coil accordingly.

10.5.3
Lock Parameters

For optimal operation of the frequency-lock circuit, some parameters need to be adjusted. Although a suitable set of lock parameters are usually read in during the lock-in process, it can be necessary to adjust them manually. The lock power (power of the ^{2}H transmitter) should be sufficiently high to obtain a reasonable sensitivity (signal-to-noise ratio) of the lock signal, but must be below the level at which saturation effects start to occur (this can be easily recognized by an unstable lock signal). The lock phase is adjusted to result in pure absorptive and dispersive parts of the signal (maximum intensity of the lock line). Misadjustment of the lock phase results in much less effective field regulation. Moreover, the behavior of the lock line during shimming is erratic. The lock gain (the gain of the lock receiver) is usually adjusted so that the lock signal is strong enough. By this the dynamic range of the analog-to-digital converter is reasonably utilized without causing overflow. Furthermore, there are some additional parameters by which the responsiveness of the feedback loop can be adjusted. Generally, the lower the signal-to-noise ratio of the lock signal, the slower the lock circuit should react. The choice of the responsiveness parameter depends also on the solvent.

10.6
Problems

10.1. What is the general purpose of the shim system?

10.2. What is the purpose of sample spinning in liquid-state NMR?

10.3. RF coils are an integral part of (a) the RF amplifiers, (b) the probehead, or (c) the shim system?

10.4. The signal-to-noise ratio of a proton spectrum is rather poor although the sample concentration is reasonable high. What could be the reason for the "attenuated" resonance signals?

10.5. The deuterium lock circuit is used to compensate (a) for magnetic field instabilities or (b) instabilities in the sample temperature?

10.6. How do room-temperature instabilities influence spectrometer performance?

Further Reading

Levit, M.H. (2008) *Spin Dynamics*, 2nd edn, John Wiley & Sons, Ltd, Chapter 4.

Berger, S. and Braun, S. (2004) *200 and More NMR Experiments*, Wiley-VCH Verlag GmbH.

11
Acquisition and Processing

Data acquisition and processing plays an extraordinarily important role in NMR spectroscopy. To understand why NMR spectroscopy is different in many aspects from other forms of spectroscopy, we will review the differences from other spectroscopic techniques.

Generally speaking, spectroscopy examines the interaction of radiation with matter. In many spectroscopic methods this is done by measuring the absorption (or emission) of radiation while the frequency of the radiation (the wavelength) is continuously varied. The result is the familiar absorption (or emission) spectra in which the intensity of absorption or emission is plotted versus frequency. A similar approach was also used in the early days of NMR spectroscopy when the intensity of transverse magnetization was continuously measured while either the transmitter frequency or more commonly the magnetic field was slowly varied in the so-called continuous wave method. Each time the resonance condition was fulfilled, a certain amount of equilibrium z magnetization was transferred into the xy plane and thereby induced a signal in the receiver coil, directly resulting in a signal in the spectrum. However, such an approach is highly inefficient since the field must be swept very slowly, and it is much more effective to measure the response of all nuclear spins at once after all spins have been excited simultaneously by a strong RF pulse, and then to extract the spectrum by a Fourier transformation, the so-called Fourier transform NMR method. In other words, we make use of the well-known Fellgett or multiplex advantage.

It is clear that this presents a fundamental difference compared with many other spectroscopic methods since the spectrum is obtained in a much less direct manner. This is schematically depicted in Figure 11.1.[1)]

The fact that the response of all excited spins is recorded *simultaneously* has important consequences: intensities and frequencies of signals must be derived from the time evolution of the transverse magnetization and hence the time dependence of the magnetization must be captured in much detail. The signal itself is called the *time domain signal* or *free induction decay* (FID). The FID, possibly a superposition of many hundred frequencies, includes all spectral information but unfortunately

1) Fourier transform versions of IR spectroscopy and mass spectrometry are also known; however, they are less widely used.

Applied NMR Spectroscopy for Chemists and Life Scientists, First Edition. Oliver Zerbe and Simon Jurt.
©2014 WILEY-VCH Verlag GmbH & Co. KGaA. Published 2014 by WILEY-VCH Verlag GmbH & Co. KGaA.

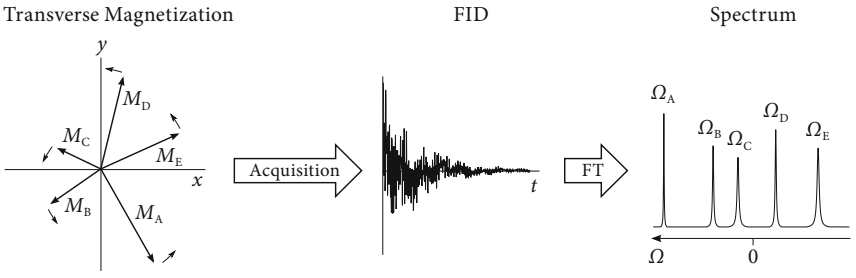

Figure 11.1 The Fourier transform NMR method. Magnetization vectors precessing in the transverse plane induce a signal in the receiver coil which is detected as the free induction decay (FID) and then converted into the spectrum through a Fourier transformation (FT).

we cannot identify the frequencies contained easily. Therefore, the spectral information must be extracted in a second step via a Fourier transformation. Thereby the time domain data are transformed into the *frequency domain* or simply the *spectrum*. Since the Fourier transform is accomplished by a computer, the time domain signal must be presented in a digitized form as discrete time/intensity pairs (see Figure 11.2).

The discrete Fourier transform has important properties that influence the rate at which we will sample the signal and the resolution that we can obtain from the spectra. Figure 11.2 gives you a first glimpse at what the signal looks like for the case of a single resonance line.

As we can see, the FID is given by a number of N discrete points, always separated by the same amount of time, the so-called *dwell time* (Δt). The total acquisition time (T_{aq}) corresponds to the total number of recorded data points (N), the time domain data points, multiplied by the dwell time:

$$T_{aq} = \Delta t \cdot N \tag{11.1}$$

The *spectral width* (SW in the following equation), the width of the spectrum expressed in units of hertz, is controlled by setting the dwell time:

$$\mathrm{SW} = \frac{1}{\Delta t} \tag{11.2}$$

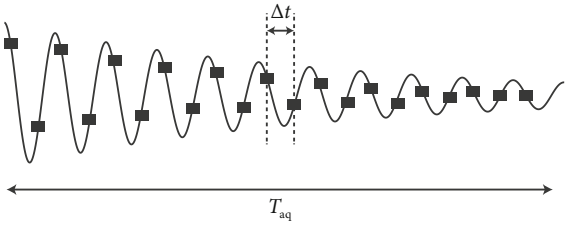

Figure 11.2 The time domain signal. The FID is sampled as discrete points always separated by the same amount of time, the dwell time.

The carrier frequency, that is, the frequency of the transmitter on the observe channel, will determine the center of the acquired spectrum. Hereby, we have briefly introduced the parameters by which we can determine the center of the spectrum, the width of the spectrum, and its resolution. As we will describe below, setting up experiments and processing spectra has many more aspects, and we will look at all of these in much more detail. However, before we discuss the details of data acquisition, we will introduce the Fourier transform, because its properties have a big impact on how we record data.

In what follows we will first introduce the mathematical expressions to describe the time domain signal. For the sake of simplicity we will initially assume that the signal has been recorded as a continuous signal instead of a discrete signal. We will subsequently introduce the Fourier transform that allows us to derive simple analytical expressions for the relation between the signal and the resulting spectral line. Once we understand how the Fourier transform converts continuous functions, we will be ready to take the next step and learn about the *discrete Fourier transform* (DFT), which is used by the computers to convert the FID into the spectrum. We will then describe some important acquisition parameters in more detail (e.g., the spectral width, sampling rate, number of sampling points, acquisition time). We will then see how the FID is really recorded in NMR experiments to distinguish positive and negative frequencies, the so-called *quadrature detection*, and turn our attention to other technical aspects of data acquisition. Finally, we will see how we can improve the quality of the spectrum through multiplication of the FID by tailored functions, called *apodization*, and by *zero filling* or *linear prediction*.

11.1 The Time Domain Signal

All we measure in NMR experiments is the evolution of transverse magnetization. Transverse magnetization can be represented in terms of rotating vectors. Thus, to get an idea of how we can describe the time domain signal mathematically, we have to consider vectors in the xy plane, basically rotating at frequencies on the order of megahertz. However, as we will see in more detail in Section 11.3.1, the magnetization is measured relative to the carrier frequency that corresponds to the center frequency of the spectral window. Thus, we measure frequency differences from the carrier frequency, or, speaking in commoner terms, we measure frequency *offsets*. To denote these offsets we use the Greek letter Ω (see Figure 11.1). Because it is much more convenient to operate with angular frequencies, we usually assume Ω is given in units of radians per second.

So let us look at a vector in the xy plane as shown in Figure 11.3. The coordinates of the vector are given by its angle α and the length (or norm) M_0. Alternatively, we can present its x and y components as the projections onto the x and y axes. Using basic trigonometry, we obtain $\boldsymbol{M} = (M_x, M_y) = (M_0 \cos(\alpha), M_0 \sin(\alpha))$.

As we will understand later, it is much more convenient to represent vectors using complex numbers. Taking the x component to be the real quantity and the y

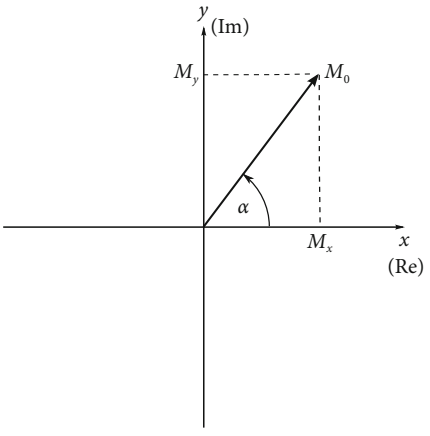

Figure 11.3 Magnetization vector in the *xy* plane. Usually the vector is described in the complex plane.

component to be the imaginary quantity, we can describe the vector by $M_0(\cos(\alpha) + \mathrm{i}\sin(\alpha))$, or using Euler's formula express it in polar form as $M_0 \exp(\mathrm{i}\alpha)$. If we assume the vector rotates with constant angular velocity Ω_A, the angle α is given as $\alpha = \Omega_\mathrm{A} t + \phi$, in which ϕ is the angle at time zero. If we use polar coordinates the rotating vector is simply described by

$$\boldsymbol{M}(t) = M_0 \mathrm{e}^{\mathrm{i}(\Omega_\mathrm{A} t + \phi)} \tag{11.3}$$

The term $\mathrm{e}^{\mathrm{i}(\Omega_\mathrm{A} t + \phi)}$ is commonly called the *phase*. As described in Section 2.4 *xy* magnetization decays exponentially to zero due to relaxation, and we take account of that by inserting a damping factor $\exp(-R_2 t)$, in which R_2 is the transverse relaxation rate constant related to transverse relaxation time T2 by $R_2 = \mathrm{T2}^{-1}$. Thus, we have

$$\boldsymbol{M}(t) = M_0 \mathrm{e}^{-R_2 t} \mathrm{e}^{\mathrm{i}(\Omega_\mathrm{A} t + \phi)} \tag{11.4}$$

The signal usually represents a superposition of a number of such functions related to signals at different frequency, which all have their own sets of parameters (M_0, R_2, Ω_A, ϕ). In reality the signal consists of discrete data points, but for simplicity let us look at a single continuous function and assume that the detector continuously records the *x* and *y* components of the vector. Thus, the recorded signal is proportional to $\boldsymbol{M}(t)$, and in complex notation it is given by

$$s(t) = s_0 \mathrm{e}^{-R_2 t} \mathrm{e}^{\mathrm{i}(\Omega_\mathrm{A} t + \phi)} \tag{11.5}$$

where s_0 is proportional to the amount of transverse magnetization at time zero. For the general case in which the FID consists of several resonances, we obtain

$$s(t) = \sum_n s_{0_n} \mathrm{e}^{-R_{2,n} t} \mathrm{e}^{\mathrm{i}(\Omega_n t + \phi_n)} \tag{11.6}$$

11.2
Fourier Transform

The Fourier transform is a mathematical operation that transforms time domain data into frequency domain data and thereby relates two functions $f(t)$ and $F(\Omega)$ by

$$F(\Omega) = \int_{-\infty}^{\infty} f(t) e^{-i\Omega t} dt \tag{11.7}$$

$$f(t) = \frac{1}{2\pi} \int_{-\infty}^{\infty} F(\Omega) e^{i\Omega t} d\Omega \tag{11.8}$$

Equation 11.8 is known as the inverse Fourier transform. We call $F(\Omega)$ the Fourier transform of $f(t)$. Fourier transformation has many applications in mathematics, physics, and engineering, and the variables t and Ω may have different meanings. In our case they are clearly related to time and frequency, and $f(t)$ is the time domain signal and $F(\Omega)$ the frequency domain signal or simply the spectrum.

11.2.1
Fourier Transform of Damped Oscillations

Substituting (11.5) for $f(t)$ into (11.7) and assuming for the moment that ϕ is zero, we obtain

$$\begin{aligned} S(\Omega) &= \int_{0}^{\infty} s_0 e^{-R_2 t} e^{i(\Omega_A - \Omega)t} dt \\ &= \mathrm{Abs}(\Omega) + i\,\mathrm{Dsp}(\Omega) \end{aligned} \tag{11.9}$$

with

$$\mathrm{Abs}(\Omega) = s_0 \frac{R_2}{R_2^2 + (\Omega_A - \Omega)^2} \tag{11.10}$$

and

$$\mathrm{Dsp}(\Omega) = s_0 \frac{(\Omega_A - \Omega)}{R_2^2 + (\Omega_A - \Omega)^2} \tag{11.11}$$

The time domain signal is only known for $t \geq 0$ and the lower limit of the integral has therefore been replaced by zero. Equation 11.9 shows that the spectrum consists of a real and an imaginary part. The real and imaginary parts are described by the pure absorptive and dispersive Lorentzian curves given in (11.10) and (11.11) and which are depicted in Figure 11.4. For the general case in which ϕ is different from zero, the spectrum presents a mixture of absorptive and dispersive Lorentzians that we will describe later. Let us have a closer look at the properties of the absorptive Lorentzian now.

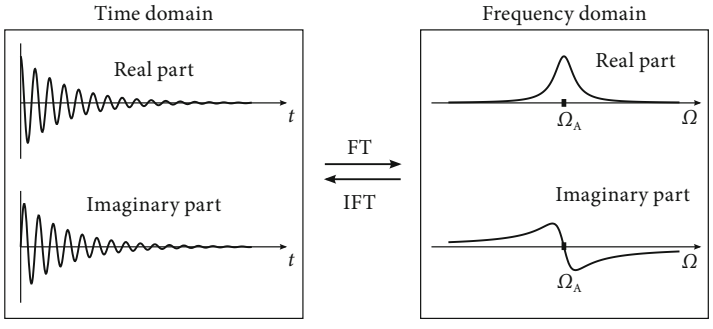

Figure 11.4 Fourier transform (FT) of an exponentially decaying sinoid. The FT of an exponentially damped sinoid yields absorptive and dispersive Lorentzian lines. IFT – inverse Fourier transform. Note that always both the real and the imaginary part of the signal contribute to the real and imaginary parts of the transformed domain.

11.2.2
Intensity, Integral, and Line Width

As described in Section 2.4, resonances may have different line widths related to varying transverse relaxation times T2. We have also seen that integrals, especially those of ^{1}H NMR spectra, can be used to derive stoichiometric ratios. With the help of the analytical expression for the shape of a resonance line (11.10), we can specify characteristic features of the signal such as the intensity, and the line width.

Clearly, the value of (11.10) is largest when the denominator is smallest, which applies for $\Omega = \Omega_A$. Thus, the Lorentzian line (Figure 11.5) has a maximum at Ω_A with intensity

$$I_{max} = \frac{s_0}{R_2} = s_0 T2 \tag{11.12}$$

in which we used $R_2 = T2^{-1}$.

The signal width at its half height, the so called full width at half height (FWHH), or $LW_{1/2}$, is usually specified to present the width of the line. From (11.10) we derive the line width as

$$\begin{aligned} LW_{1/2} = 2R_2 &= \frac{2}{T2} \quad (\text{rad s}^{-1}) \\ &= \frac{1}{\pi T2} \quad (\text{Hz}) \end{aligned} \tag{11.13}$$

We point out here that although we started with the analytical expression of a well-defined frequency (Ω_A), the output is rather a *distribution* of frequencies. This distribution has a certain width and is centered symmetrically about Ω_A. Thereby, the Fourier transform indicates that the time domain signal is composed of many tiny vectors (in the extreme corresponding to the individual magnetic moments of the nuclei) that rotate at slightly different frequencies. When we look at relaxation in a microscopic view later, we will see that this is indeed true (see Chapter 14).

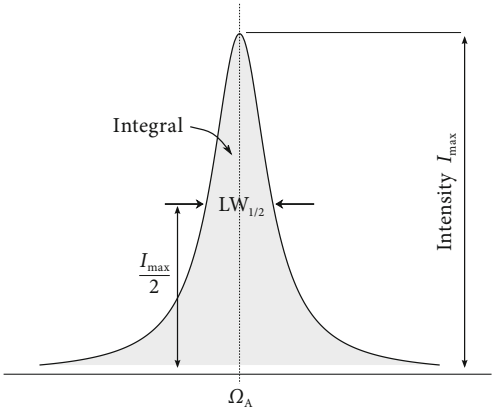

Figure 11.5 Characteristic quantities of the Lorentzian line. LW – line width.

Equations 11.12 and (11.13) reveal that intensity and line width are inversely related to each other. It remains to be shown that the integral (the area under the signal) has a constant value that is independent of T2. For this we integrate (11.10) using Ω as the variable in the limits $\pm\infty$, and obtain

$$\text{Integral} = s_0\pi \tag{11.14}$$

Remember, s_0 is proportional to the amount of initial xy magnetization and is therefore proportional to the absolute number of spins contributing to the signal. Thus, integral ratios can be used to derive quantitative information on the relative occurrence of spins.

11.2.3
Phases of Signals

Expression (11.9) was derived under the assumption that the phase ϕ of the time domain signal $s(t)$ is zero. Now we will consider the general case in which ϕ is different from zero. In view of (11.5) that means we need to take into account a factor of $\exp(i\phi)$. As this factor does not depend on time, we can write it just in front of the Fourier integral (11.9), resulting in

$$S(\Omega) = (\text{Abs}(\Omega) + \text{i}\,\text{Dsp}(\Omega))\exp(\text{i}\phi) \tag{11.15}$$

Using $\exp(\text{i}\phi) = \cos(\phi) + \text{i}\sin(\phi)$, we can express the real and imaginary parts of the spectrum as

$$\begin{aligned}\text{Re}(\Omega) &= \text{Abs}(\Omega)\cos(\phi) - \text{Dsp}(\Omega)\sin(\phi)\\ \text{Im}(\Omega) &= \text{Abs}(\Omega)\sin(\phi) + \text{Dsp}(\Omega)\cos(\phi)\end{aligned} \tag{11.16}$$

Unless ϕ is zero (or a multiple of 2π), both the real and the imaginary part present mixtures of absorptive and dispersive Lorentzians. This is shown in Figure 11.6, and we will see in Section 11.4.4 how we can correct for this.

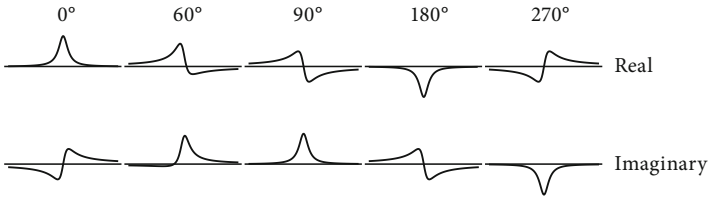

Figure 11.6 Signal phases. Line shapes of the real and imaginary parts of a resonance line as a function of the phase ϕ.

11.2.4
Truncation

The expressions for the absorptive and dispersive line shapes presented in (11.10) and (11.11) were obtained under the assumption that the time domain signal is known for an *infinite* time period. However, the FID is measured only for a *finite* time, and particularly in 2D or 3D NMR experiments but also sometimes in 1D NMR experiments signal acquisition is stopped even earlier when a considerable amount of signal still exists, so the FID is truncated. As shown in Figure 11.7 this results in a distortion of the line shape and some "wiggles" to the right and left of the signal are introduced, known as truncation artifacts. In general, truncation artifacts are severer the larger the residual signal intensity is at the last data point of the FID.

As we will see in Section 11.4.3, truncation artifacts can be strongly reduced by multiplying the time domain signals by appropriate smoothing functions.

11.2.5
Handling Multiple Frequencies

The real power of Fourier transformation is that it works equally well if the time domain signal consists of many different frequencies (possibly thousands). This

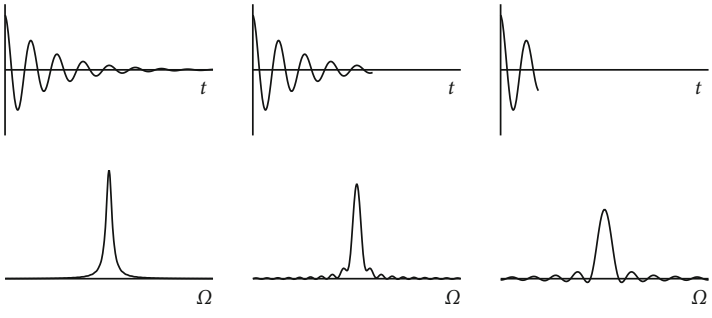

Figure 11.7 Truncation artifacts for different levels of truncation. Stopping signal acquisition before the signal has fully decayed results in broadening of resonance lines and introduces the typical truncation wiggles.

is because Fourier transformation is a linear operation. To show this property, we rewrite the time domain signal as the sum

$$s(t) = s_1(t) + s_2(t) + s_3(t) + \ldots \tag{11.17}$$

in which each term denotes a single resonance $s_i(t) = s_i e^{-\lambda_i t} e^{i(\Omega_i t + \phi_i)}$. Substituting it in into the Fourier integral (11.7) gives

$$\begin{aligned} S(\Omega) &= \int s(t) e^{-i\Omega t} dt \\ &= \int s_1(t) e^{-i\Omega t} dt + \int s_2(t) e^{-i\Omega t} dt + \int s_3(t) e^{-i\Omega t} dt + \ldots \\ &= S_1(\Omega) + S_2(\Omega) + S_3(\Omega) + \ldots \end{aligned} \tag{11.18}$$

in which each term in the last line represents a complex Lorentzian (11.16) centered at Ω_i.

11.2.6 Discrete Fourier Transform

So far we have been dealing with continuous functions. However, as we have seen already (see Figure 11.2) the FID is not recorded as a continuous (analog) signal but is sampled at regular time intervals as a discrete (digital) signal. The signal processing therefore comprises treatment of a digital signal, or more precisely a time series, from which we wish to extract the frequency components involved. Because of its discrete character we cannot use the Fourier integral as given by (11.7), and we need to use a somewhat modified variant of Fourier transformation known as the *discrete Fourier transform* (DFT). DFT is the equivalent of the continuous Fourier transform with the integral replaced by a summation running over all sampled time points t_k. Formally the DFT of a time series $s(t_k)$ into the spectrum $S(\Omega_n)$ can be expressed by

$$S(\Omega_n) = \sum_{k=0}^{N-1} s(t_k) e^{-i\Omega_n t_k} , \quad n = -\frac{N}{2}, \ldots, \frac{N}{2} - 1 . \tag{11.19}$$

with

$$\begin{aligned} t_k &= k\Delta t \\ \Omega_n &= n\Delta\Omega \\ \Delta\Omega &= 2\pi \mathrm{SW}/N \\ \mathrm{SW} &= 1/\Delta t \end{aligned}$$

Thus, the DFT transforms an N-point time series into an N-point spectrum. This is depicted in Figure 11.8.

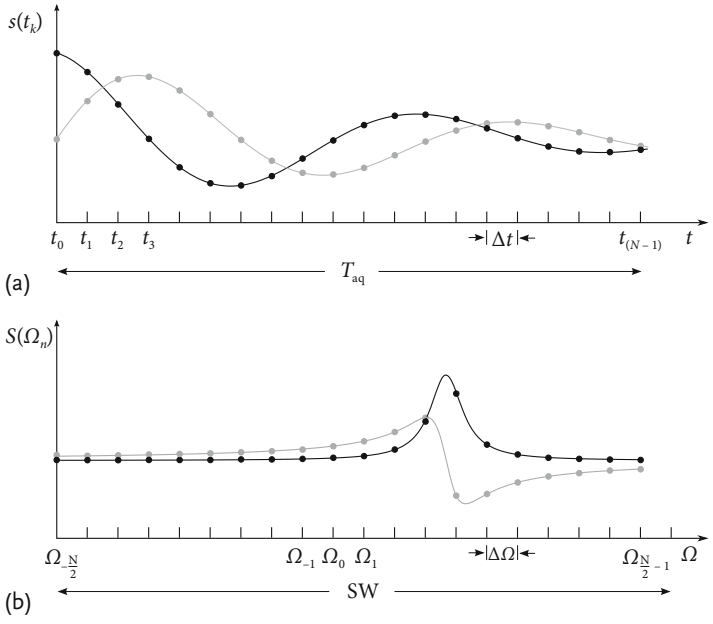

Figure 11.8 Fourier transform of discrete sampled data. The time domain signal (a) consisting of *N* real (black dots) and *N* imaginary (gray dots) intensity/time pairs (corresponding to *N* complex values) is transformed by the discrete Fourier transform into the spectrum (b) that consists of *N* complex intensity/frequency pairs. The spectral width (SW) is determined by the sampling interval Δt.

11.2.7 Sampling Rate and Aliasing

The fact that the NMR signal is sampled as discrete data points has an important consequence concerning the sampling rate. In order to encode all frequencies correctly, the sampling rate must be at least twice the frequency of the resonance with the highest offset. Or in other words, at least two data points per period must be sampled to encode a frequency component at its correct frequency. This is called the Nyquist theorem, and its source is illustrated in Figure 11.9.

When the sampling rate is too low, the signal (data points) can always be "explained" by a sinusoid of lower frequency and hence the signal will appear in the spectrum at a wrong position. Such signals are called *folded signals*. Furthermore, when both components of a rotating object (a complex signal) are being measured, the apparent frequency is not only too low, but also of opposite sign. Such signal are called *aliased signals*. Aliasing is a phenomenon that is widely observed for non-continuous time sequences. A prominent example from our daily life is wheels of cars as seen in movies: depending on how fast the wheel effectively rotates, the wheel seems to turn in one or the opposite direction. We will see that folding or aliasing of signals in indirect dimensions of 2D or 3D spectra is sometimes done

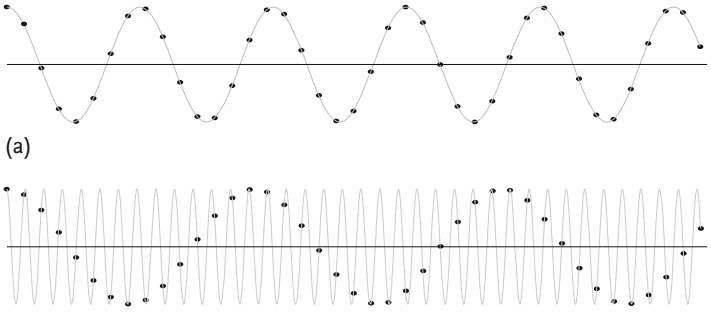

Figure 11.9 Two cosines of different frequency sampled with the same rate. For the signal in (a) the sampling rate is fine. The curve is properly captured by the data points and no lower frequency can equally well fit the points. In contrast, the sampling rate is too low for the signal in (b). From simple visual inspection we get the impression that the dots are caused by a signal of a much lower frequency.

on purpose. In the direct dimension these signals will usually be removed by audio or digital filters and hence are completely lost from the measurement.

But how do we control the spectral width (how do we determine whether a 15 ppm or a 20 ppm range is recorded)? The answer was partially given in the last paragraph. By setting the time spacing between consecutively sampled data points, we determine the highest frequency that is being sampled correctly. Any frequency higher than the so-called Nyquist frequency (and not removed by the audio filters) is, depending on the type of instrument, either folded into the spectrum (old instruments) or completely removed from the spectrum (new instruments with oversampling and digital filtering). The relationship between spectral width (in hertz) and the dwell time Δt is

$$\Delta t = \frac{1}{(2)\mathrm{SW}} \tag{11.20}$$

(whether a factor of 2 comes into play is determined by the type of quadrature detection that is used, see Section 11.3.2). We will see that this relation generally holds true. It is also valid for the indirect dimensions of 2D and 3D NMR experiments. In the indirect dimensions, folding and aliasing always occur with full intensity.

Whether signals are folded or aliased depends on the sampling scheme (Section 11.3.2). In particular, folding occurs with *real* quadrature detection and aliasing occurs with *complex* quadrature detection (Figure 11.10). However as both terms refer to the same phenomenon of the occurrence of "ghost" signals, they are often used interchangeably.

11.2.8
How Fourier Transformation Works

The problem of converting time domain data into frequency domain data has been solved for us by the French mathematician Jean-Baptiste Joseph Fourier (1768–

Figure 11.10 Folding and aliasing. Signals recorded by real quadrature detection are folded along the near edge, whereas aliased signals recorded by complex quadrature detection are "folded" along the distant edge.

1830). The Fourier theorem states that *any* periodic function $f(t)$ with period T can be expressed by a series of sines and cosines of different frequencies and amplitudes in terms of a so-called Fourier series:

$$f(t) = \sum_{k=0}^{\infty} (A_k \cos \Omega_k t + B_k \sin \Omega_k t) \quad \text{with}$$
$$\Omega_k = \frac{2\pi k}{T} \quad \text{and} \quad B_0 = 0 \tag{11.21}$$

The coefficients A_k and B_k characterize to what extent the frequency Ω_k is contained in the function. Importantly, our NMR signal represents a sum of sines and cosines, only damped by T2 relaxation. Computing the Fourier transform corresponds to finding the coefficients of the individual frequencies that are superimposed in the NMR signal.

11.2.8.1 Fourier Integrals

The basic principle of Fourier transformation is illustrated in Figure 11.11. Let us assume that our signal is a cosine of unknown frequency Ω_A, shown in the upper part of Figure 11.11 as a solid line. This signal is now multiplied by the cosine of a guess frequency Ω_{guess}, depicted by dotted lines. The result of the multiplication of the two functions is displayed in the center panel of Figure 11.11. Apparently, if Ω_{guess} and Ω_A match, they will remain in phase during the entire time interval and therefore their product will always be positive. In contrast, if Ω_{guess} and Ω_A are different, the two cosine functions run out of phase, resulting in products with both positive and negative parts. A measure of how well Ω_{guess} and Ω_A agree is the integral of the corresponding product. As shown at the bottom of Figure 11.11, it is maximum in the case $\Omega_{guess} = \Omega_A$ and close to zero if the frequencies strongly differ.

To summarize, to find out which frequency component(s) is contained in a signal, we need to multiply the signal function by a guess function and take the integral of that product, the so-called Fourier integral.

Unfortunately things become a bit more complicate if we are also interested in the sign of the frequency, or in other words, if we wish to know the sense of rotation of the magnetization vector in the rotating frame of reference, as is usually required in NMR experiments. Since $\cos(\Omega_{guess} t) = \cos(-\Omega_{guess} t)$, the spectrum obtained by calculating the cosine Fourier integral as described above will also show a max-

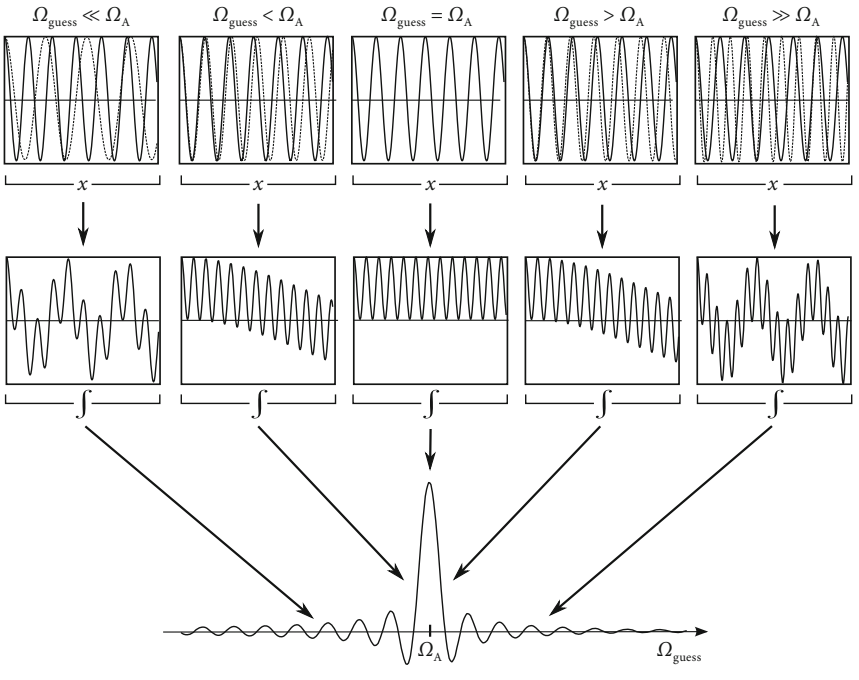

Figure 11.11 Principle of Fourier transformation. Integrals of the product of the measured signal times a cosine of guessed frequency. The integral is largest when Ω_{guess} matches Ω_A.

imum at $\Omega_{guess} = -\Omega_A$. As discussed in the next section, this unambiguity can be resolved by recording also the sine-modulated signal and calculating the sine Fourier integral.

11.2.8.2 Frequency Discrimination

To understand how the frequency discrimination works, we need to describe the Fourier transform in a more formal way. For that it is useful to remember the following trigonometric identities:

$$\cos(A)\cos(B) = \frac{1}{2}(\cos(A+B) + \cos(A-B)) \tag{11.22}$$

$$\cos(A)\sin(B) = \frac{1}{2}(\sin(A+B) - \sin(A-B)) \tag{11.23}$$

$$\sin(A)\cos(B) = \frac{1}{2}(\sin(A+B) + \sin(A-B)) \tag{11.24}$$

$$\sin(A)\sin(B) = \frac{1}{2}(-\cos(A+B) + \cos(A-B)) \tag{11.25}$$

The cosine Fourier integral considered above can be expressed as

$$S_{\cos}(\Omega) = \int s(t)\cos(\Omega t)\mathrm{d}t \tag{11.26}$$

in which $s(t)$ is the time domain signal and $S_{\cos}(\Omega)$ the cosine spectrum of $s(t)$. Assuming again our time domain signal is of the form $s(t) = \cos(\Omega_A t)$ and using the identity (11.22), we obtain

$$S_{\cos}(\Omega) = \frac{1}{2}\int \cos((\Omega_A + \Omega)t)\mathrm{d}t + \frac{1}{2}\int \cos((\Omega_A - \Omega)t)\mathrm{d}t \qquad (11.27)$$

Clearly, the integral of a cosine is largest when the argument is zero, in which case the cosine has a constant value of 1. For the first integral of (11.27) this is the case for $\Omega = -\Omega_A$, and for the second integral it is the case for $\Omega = \Omega_A$. Therefore, the cosine spectrum will show two peaks, one at the correct frequency Ω_A and one at the wrong frequency $-\Omega_A$ (see Figure 11.12a).

As mentioned before, we can distinguish between the correct and the wrong frequency by additionally recording the sine-modulated signal, and calculating its sine Fourier transform according to

$$S_{\sin}(\Omega) = \int s(t)\sin(\Omega t)\mathrm{d}t\ . \qquad (11.28)$$

With $s(t) = \sin(\Omega_A t)$ and the identity (11.25), we obtain

$$S_{\sin}(\Omega) = -\frac{1}{2}\int \cos((\Omega_A + \Omega)t)\mathrm{d}t + \frac{1}{2}\int \cos((\Omega_A - \Omega)t)\mathrm{d}t \qquad (11.29)$$

Again this results in two peaks in the spectrum, one at Ω_A and one at $-\Omega_A$. However, this time the peaks have opposite intensity. The peak at Ω_A is positive and that at $-\Omega_A$ is negative, as shown in Figure 11.12b. Combining the cosine and the sine spectrum results in a spectrum that contains onyl the peak at the correct frequency Ω_A (Figure 11.12c). Alternatively we may take directly the sum of (11.27) and (11.29), which results in the single term $\int \cos((\Omega_A - \Omega)t)\mathrm{d}t$, resulting in a single peak at $\Omega = \Omega_A$.

To summarize, the correct frequency is obtained by recording the cosine-modulated and the sine-modulated signal (which basically correspond to the x and y components of the magnetization), calculating the cosine Fourier transform of the cosine signal and the sine Fourier transform of the sine signal and combining the two spectra. Formally we can express this in a compact form by treating the

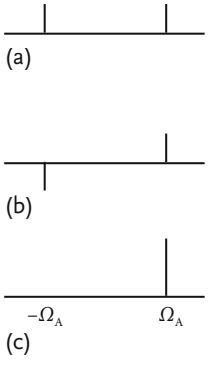

Figure 11.12 Frequency discrimination. Cosine spectrum of a pure cosine (a), sine spectrum of a pure sine (b), and the sum of both spectra (c).

signal as a complex quantity $s(t) = \cos(\Omega_A t) + i\sin(\Omega_A t)$ and using the complex "test function" $\cos(\Omega t) - i\sin(\Omega t)$. We can then write

$$S(\Omega) = \int [\cos(\Omega_A t) + i\sin(\Omega_A t)][\cos(\Omega t) - i\sin(\Omega t)]dt \tag{11.30}$$

Expanding this expression yields four terms, of which the two real terms correspond to the desired cosine and sine Fourier integrals as described above. The real part of the spectrum shows a single peak with absorptive line shape. Note, the other two terms, being products of sines and cosines, produce the imaginary part of the spectrum, again a single peak at the correct frequency $\Omega = \Omega_A$, however with dispersive line shape. Things become even more comprehensible if we use Euler's formula:

$$\begin{aligned} S(\Omega) &= \int e^{i\Omega_A t} e^{-i\Omega t} dt \\ &= \int e^{i(\Omega_A - \Omega)t} dt \\ &= \int \cos((\Omega_A - \Omega)t)dt + i\int \sin((\Omega_A - \Omega)t)dt \end{aligned} \tag{11.31}$$

The first integral in the last line represents the real part (absorptive line) and the second integral the imaginary part (dispersive line) of the spectrum.

11.3 Technical Details of Data Acquisition

11.3.1 Detection of the FID

As shown in Figure 11.13, rotating transverse magnetization M_{xy} will induce an oscillating voltage U in a coil placed orthogonal to the z axis. As mentioned in Section 2.1, this behavior is similar to the situation in an electricity generator, in which a loop is rotated by a mechanical force in a static magnetic field, with the difference being that in the NMR experiment it is the magnetic field (the magnetization) that rotates about the loop.

The frequency of the alternating voltage corresponds to the Larmor frequency of the observed nucleus and is therefore on the order of several hundred megahertz. In contrast, the frequency spread of individual signals due to chemical shift is usually on the order of some kilohertz at maximum, and frequency differences can be as small as a fraction of a hertz. This means that we need to record a very rapidly oscillating voltage with very high accuracy – a difficult task. To overcome this technical difficulty, the signal picked up by the receiver coil is mixed (multiplied) down to a much lower frequency by multiplying it by the transmitter (carrier) frequency. Multiplying a signal by another frequency results in two components, one with the sum and the other with the difference of the respective frequencies (compare

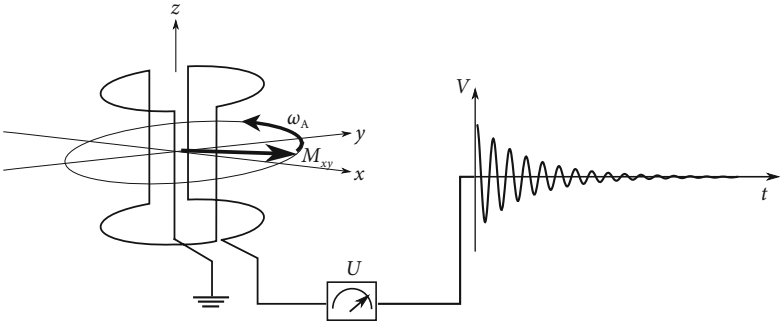

Figure 11.13 Transverse magnetization M_{xy} induces an alternating voltage in the receiver coil.

(11.22)–(11.25)). The high-frequency component is filtered out by low-pass audio filters such that only the low-frequency component which corresponds to the offset frequency is retained. It is this reduced frequency that is fed into the analog-to-digital converter (ADC).

As mentioned before, to distinguish positive and negative frequencies we need to know both the x component and the y component of the magnetization. The y component is artificially retrieved by multiplying the signal in addition by the 90° phase-shifted carrier signal (Figure 11.14). For a single component of frequency ω_A, the quadrature detection (omitting relaxation and signal amplitude s_0 for a moment) is mathematically expressed by

$$\begin{aligned} S_{RF}\, S_{ref}^{0^\circ} &= \cos(\omega_A t + \phi_A)\cos(\omega_{ref} t + \phi_{ref}) \\ &= \frac{1}{2}\cos((\omega_A - \omega_{ref})t + \Delta\phi) + \frac{1}{2}\cos((\omega_A + \omega_{ref})t - \Delta\phi) \end{aligned} \quad (11.32)$$

for the x (or real) component, and by

$$\begin{aligned} S_{RF}\, S_{ref}^{90^\circ} &= \cos(\omega_A t + \phi_A)\sin(\omega_{ref} t + \phi_{ref}) \\ &= \frac{1}{2}\sin((\omega_A - \omega_{ref})t + \Delta\phi) + \frac{1}{2}\sin((\omega_A + \omega_{ref})t - \Delta\phi) \end{aligned} \quad (11.33)$$

for the y (or imaginary) component. ω_{ref} is the reference frequency (the center frequency of the spectral range) with receiver phase ϕ_{ref} and $S_{ref}^{90^\circ}$ the 90° phase-shifted reference signal. If we discard the fast oscillating terms which are effectively filtered out and use $\omega_A - \omega_{ref} = \Omega_A$, the sum of both detector channels provides the required *complex* signal of the form

$$s(\Omega_A, t) = \cos(\Omega_A t + \Delta\phi) + i\sin(\Omega_A t + \Delta\phi) = e^{i(\Omega_A t + \Delta\phi)} \quad (11.34)$$

11.3.2 Simultaneous and Sequential Sampling

Quadrature detection corresponds to recording of the sine- and cosine-modulated signals in order to distinguish positive and negative frequencies. The two compo-

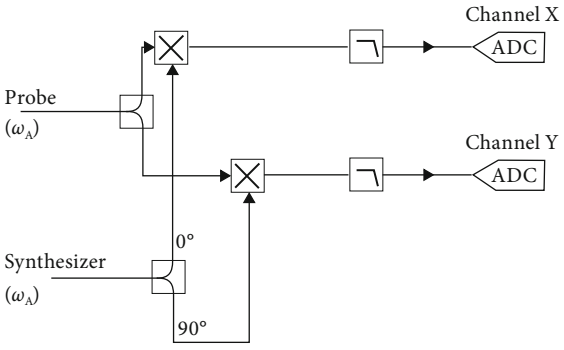

Figure 11.14 Simplified scheme of a quadrature detector. The signal picked up by the receiver coil (probe) is split into two components which are mixed either with the reference signal in phase (0°) or with the reference signal 90° out of phase. After removal of high-frequency components by antialiasing filters, the signal is digitized by the analog-to-digital converters (ADC).

nents can be sampled simultaneously or sequentially. In the case of simultaneous sampling at each time increment, both the x component and the y component of the magnetization are recorded (see Figure 11.15a). The (complex) time domain signal so obtained can be directly subjected to Fourier transformation to yield the desired spectrum. In contrast, during sequential sampling, x and y components are alternately sampled. Sequentially sampled time domain data, such as shown in Figure 11.15b, can not be directly subjected to Fourier transformation. As described below, some additional data manipulation is required.

Sequential sampling (also known as the *Redfield trick*) originates from the days when spectrometers were equipped with just a single-channel ADC and hence quadrature detection using simultaneous sampling was not available. Nowadays most spectrometers measure the FID using simultaneous sampling. Nevertheless, because frequency discrimination in the indirect dimension of multidimensional spectra is often achieved using a method very similar to sequential sampling (called

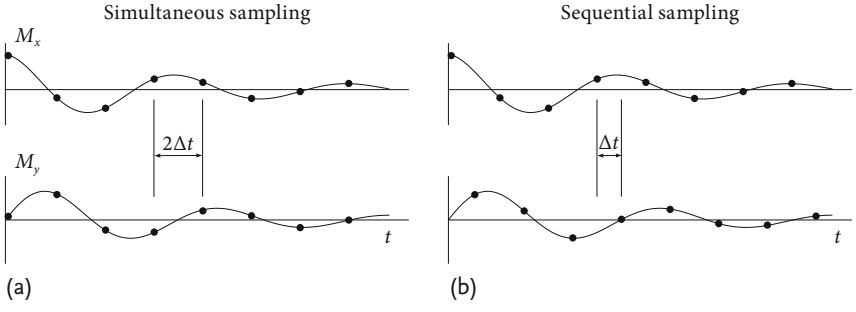

Figure 11.15 Detection of the FID using simultaneous (a) or sequential (b) sampling. For sequential sampling, in which at each time increment only one component is measured, the sampling rate must be twice as large as that in simultaneous sampling (see (11.20)).

time-proportional phase incrementation; Section 17.6.1), we will have a closer look at it in the following.

The concept of sequential sampling is depicted in Figure 11.16. The sequences of *X* and *Y* records are successively multiplied by 1 1 −1 −1 and stored in a single (real) array FID. This has the effect of artificially shifting the offset frequencies by SW/2. In addition, since the time domain signal now consists of a real part only, frequency discrimination in absolute terms is no longer possible and the Fourier transform results in a spectrum that exhibits a mirror image around the origin

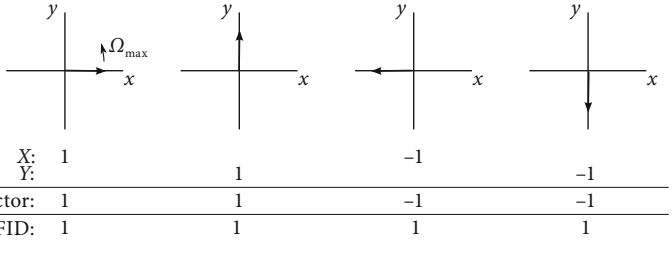

X:	1		−1	
Y:		1		−1
Factor:	1	1	−1	−1
FID:	1	1	1	1

(a)

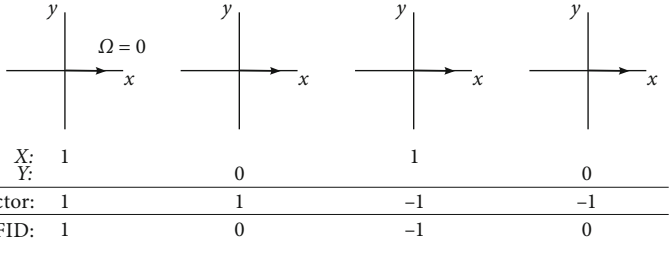

X:	1		1	
Y:		0		0
Factor:	1	1	−1	−1
FID:	1	0	−1	0

(b)

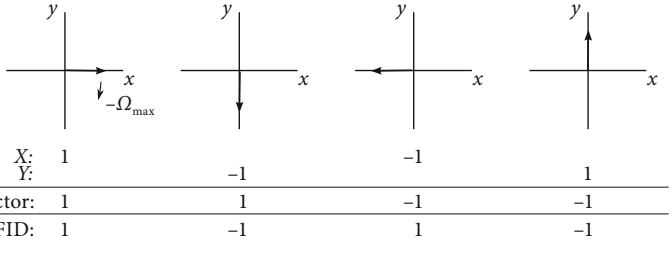

X:	1		−1	
Y:		−1		1
Factor:	1	1	−1	−1
FID:	1	−1	1	−1

(c)

Figure 11.16 Demonstration of the artificial frequency shift brought about by the sequential sampling scheme. As shown in (a), a vector at the high-frequency edge of the spectral window (Ω_{max} = SW/2) rotates between successive samples (separated by Δt = 1/2SW) by 90°, and the *X* and *Y* records read as 1 1 −1 −1. After multiplying by 1 1 −1 −1, we obtain FID = 1 1 1 1, the same result as if the vector has zero frequency. Similarly, for a resonance at the center of the spectral window (Ω = 0), shown in (b), the output sequence FID reads as 1 0 −1 0, equivalent to the *x* components of a vector that rotates with SW/2 or −SW/2. For a resonance at the low-frequency edge of the spectral window (Ω = −SW/2), shown in (c), the frequency translates to ±SW. As a result, the carrier frequency is apparently shifted by SW/2 to the edge of the spectral window.

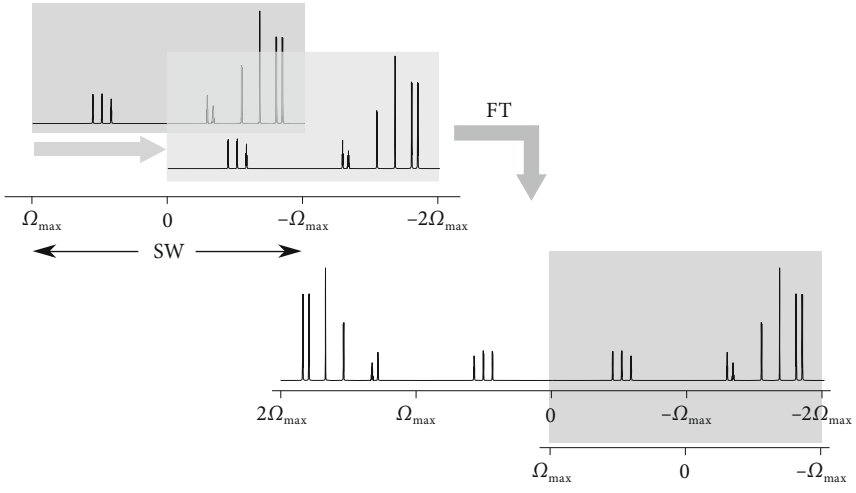

Figure 11.17 Pictorial representation of the sequential sampling method (see the text).

(Figure 11.17). This image is simply deleted, the frequency axis shifted by SW/2, and we obtain our final spectrum with correct frequencies.

This is essentially the same as if we acquired a spectrum with the carrier frequency set to one end of the spectral range, doubled the spectral width, and recorded the *x* component only. The advantage of the sequential sampling scheme is that the carrier can remain in the center of the spectrum to yield a more uniform excitation of the resonances (Section 6.6.4).

11.3.3 Digitizer Resolution

The input voltage of an analog signal is converted by the ADC into discrete binary values. For example, a 16 bit ADC digitizes an analog signal in the range of 2^1 to $2^{16} = 65\,536$ values. Thus, the analog signal is captured with finite precision and with intrinsic rounding errors (Figure 11.18). These quantization errors, also termed "digitization noise," result in a noise contribution in the spectrum. In addition, the number of bits and hence the number of quantization levels, the digitizer resolution, also determine the accuracy of measuring a weak signal in the presence of a much stronger signal, something referred to as the dynamic range of an ADC.

As both digitization noise and dynamic range improve with increased digitizer word lengths, it is advantageous to use ADCs with as many bits as possible. However, quantization with longer digital words also takes more time, which brings about some limitations regarding the maximum sampling rate and bandwidth. At present, typical values of digital resolution are 18, 20, and 22 bit.

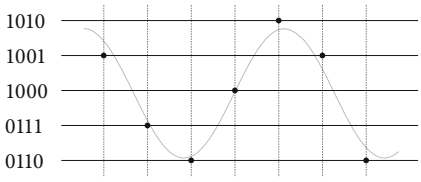

Figure 11.18 Quantization errors by digitization of an analog signal. Rounding errors will contribute to spectral noise.

11.3.4 Receiver Gain

In order to digitize the signal accurately and to make full use of the ADC's dynamic range, the maximum signal intensity should match the highest digitizer bits. Therefore, the signal is amplified *before* it is fed into the ADC. By adjusting the receiver gain, we determine to what extent the signal is amplified. As the signal intensity depends on the sample concentration, on the observed nuclei, and on the type of experiment, the receiver gain should be carefully adjusted for each experiment. If the receiver gain is set too low, the digitization noise will have a larger contribution to the spectrum and small signals could be lost. If the receiver gain is set too high, the FID becomes clipped, resulting in severe distortions in the spectrum, as is shown in Figure 11.19b.

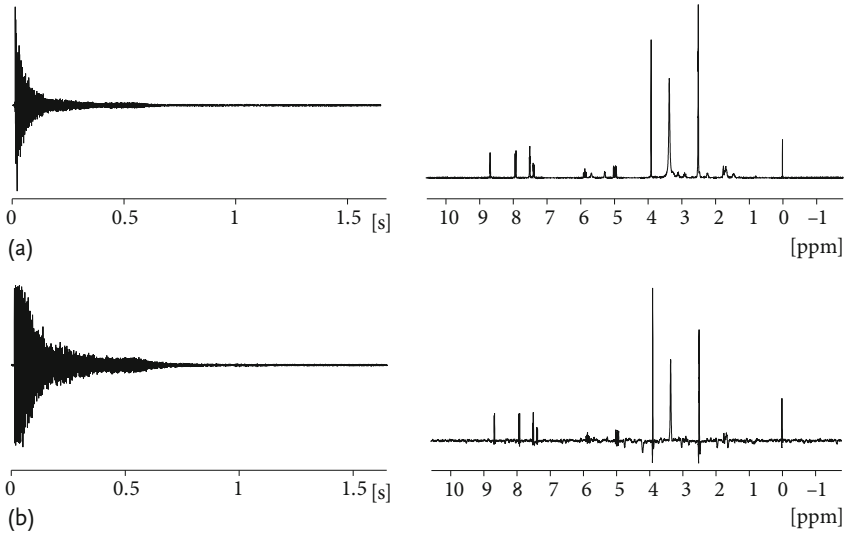

Figure 11.19 Effect of overloading the receiver. In (a) the receiver gain is just fine. In contrast, in (b) the FID is sampled using too high a receiver gain. The FID is clipped and the corresponding spectrum shows large distortions.

11.3.5
Analog and Digital Filters

The offset frequencies that are typically measured in NMR experiments are within a range of some kilohertz, which is the audio frequency range. Any frequency outside the spectral range of interest will be folded into the spectrum (see Section 11.2.7). Importantly, not only resonances outside the spectral width but also contributions from thermal noise will be folded. Thus, if such frequencies are not eliminated, the spectrum will become awfully crowded by noise and the signal-to-noise ratio will accordingly suffer. Therefore, the signal must be filtered before it can be fed into the ADC. This is achieved by analog *audio filters*. These filters are constructed so as to allow only frequencies lower than a specified value to pass and to reject any higher frequencies; accordingly they are called low-pass filters. Ideally the filter function should be described by a perfect "boxcar" function, that is, a function that is flat in the frequency range of interest and steeply falls to zero at the edge of this range. However, as shown in Figure 11.20, in practice the filter profile is not perfect and unfortunately introduces distortions of the peak intensities for signals close to the edge of the spectrum. When a larger filter width to chosen to avoid these distortions, a considerable amount of noise and other unwanted frequencies will be folded into the spectrum.

A solution to this problem is to record a larger spectral width by increasing the sampling rate and then select the small spectral range of interest as defined by the spectral window. The filter width of the analog antialiasing filter can then be chosen large enough to obtain a relatively flat filter function for the spectral range of interest. This is accomplished by using digital filters. In the digital filtering technique a much larger spectral range (e.g., 10-fold) is recorded than defined by the operator by sampling much faster and with many more points than necessary for a given spectral window (Figure 11.20). This is called *oversampling*. The spectral range outside of the region of interest is removed with a digital filter. Technically this corresponds to performing a Fourier transform on the oversampled FID, and then doing an inverse Fourier transform on the frequency range of interest only. This proce-

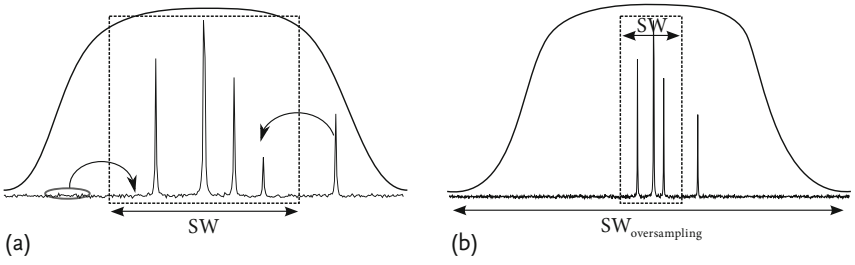

Figure 11.20 Concerted effect of an analog and a digital filter. The spectrum in (a) is acquired using an analog filter only. Noise and signals outside the spectral window within the transition band of the filter is folded into the spectral window. The spectrum in (b) is acquired using oversampling and a digital filter. No signals and no noise are folded into the spectral window anymore.

dure results in an FID that exclusively includes the frequencies of interest, which can be subsequently used for further processing. In practice a more efficient but slightly more complicated technique is used. In short, the oversampled FID is convoluted on the fly with an appropriate filter function, and the number of FID points is then reduced to the actual value the operator has set, a process called *decimation*. Decimation not only reduces the required memory but even more importantly also reduces digitization noise due to an averaging effect on the quantization errors.

11.3.6 Spectral Resolution

Spectral resolution determines whether two signals with a small frequency difference can be recognized as two signals or not, or whether a small coupling becomes visible in the spectrum. Whether such small frequency differences become observable depends on two properties: the line width of the signal and the inherent spectral resolution of the spectrum. When the line width (the signal width at half height) is 20 Hz, a value valid for large molecules such as proteins, it is impossible to observe a 3 Hz coupling. The inherent spectral resolution depends on for how long signal is contained in the FID.

Figure 11.21 depicts sampling of two different frequencies in which the frequency between the two signals differs by a factor of 10 between the two cases. The phase difference between the two magnetization vectors from the two signals

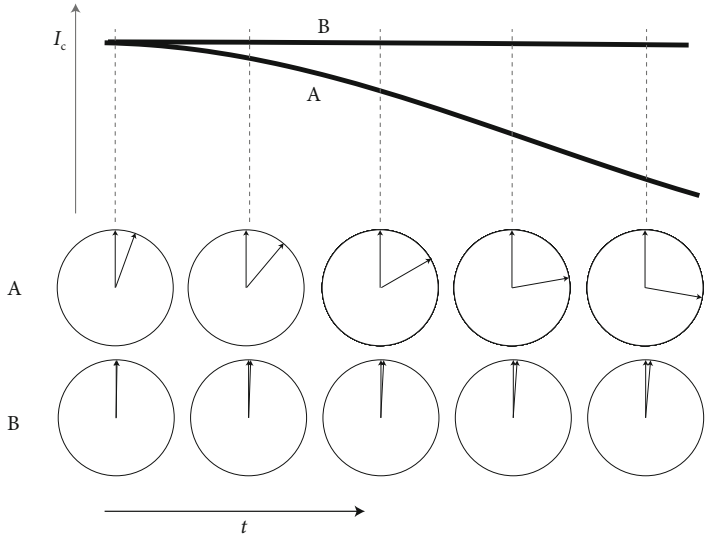

Figure 11.21 Resolution. The phase difference due to evolution of the chemical shift is depicted for two signals with a large (case A) or a small (case B) frequency difference. One of the two signals is always on-resonance, and hence its magnetization vector does not rotate but remains in the 12 o'clock position. The curves at the top are shown for the off-resonance signal.

is depicted at equally spaced time intervals. In case A in Figure 11.21, corresponding to a large frequency difference, an appreciable phase difference is visible soon, whereas for the small frequency difference (case B) even for the last sampled data point the phase difference is small. Ten times as many data points need to be sampled so that the two vectors assume the same phase difference as in case A. Signals will only be distinguished after the Fourier transform if an appreciable phase difference between the signals is present. Therefore, we need to sample for *much longer* if we want to distinguish small frequency differences. The resolution therefore depends on the number of data points sampled during acquisition. Unfortunately, extended sampling competes with T2 relaxation. There is no point in sampling a signal for 2 s if the magnetization has already decayed after 200 ms – only noise will be sampled for most of the time. The practically achievable resolution hence not only depends on the number of data points sampled but also on the transverse relaxation time, and both quantities need to be taken into consideration when setting up experiments. Therefore, its is usually much better to pay attention to the acquisition time(s) instead of the number of data points.

11.4 Data Processing

11.4.1 Digital Resolution and Zero Filling

The discrete Fourier transform as given in Section 11.2.6 transforms an N-point time series into an N-point spectrum. One should note, however, that the equality of points in the time and frequency domains is not a general feature of DFT. In principle, we could calculate the intensity at arbitrary frequencies. However, DFT is usually accomplished by using the fast Fourier transform, which relies on the Cooley–Tukey algorithm. This algorithm requires that the number of points in the time domain (FID) and the number of points in the frequency domain (spectrum) are the same, and that the number is a power of 2.

This means the number of points in the spectrum, and hence the frequency difference between succeeding points, the so-called digital resolution, is limited to the number of points in the FID. With a spectral window of SW Hz and an FID consisting of N points, the digital resolution is SW/N Hz. Considering that N is related to the acquisition time T_{aq} by $N = T_{aq}/\Delta t$ with $\Delta t = 1/\mathrm{SW}$, the digital resolution is related to the acquisition time by ${T_{aq}}^{-1}$. For example, if the FID is measured for 2 s, the point-to-point resolution of the spectrum is 0.5 Hz. In other words, if we have a resonance line of 1 Hz width (FWHH), the shape of the signal above half height is given by two points only and therefore it is relative poorly defined. Moreover, when the digital resolution is poor, line splitting due to a small coupling can be easily overseen or signals with small shift differences may accidentally be recognized as a single line.

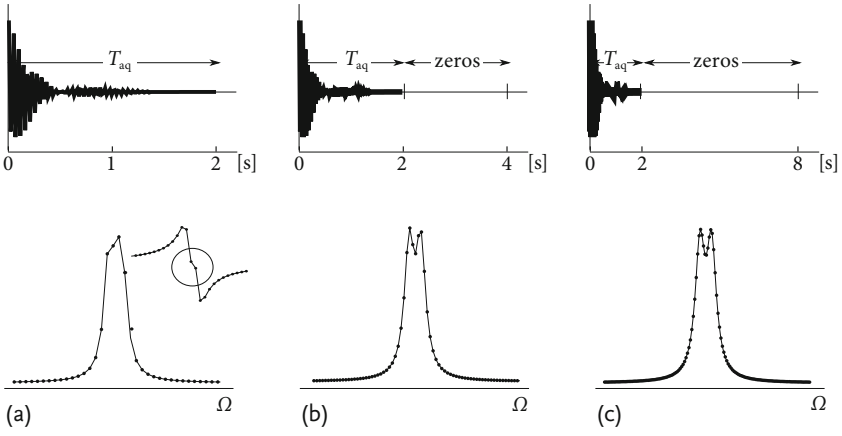

Figure 11.22 Effect of zero filling. FIDs and the corresponding spectra are depicted without zero filling (a), and when zero filling has been applied once (b) or twice (c). The insert on the spectrum in (a) shows the dispersive signal observed for the imaginary part of the spectrum.

To overcome this issue we have to increase the number of points in the spectrum. As mentioned above, this requires more points in the FID (a longer FID). However, lengthening the acquisition time is usually not a feasible solution as mainly noise will be sampled in the later part of the FID when the signal has decayed, and this will worsen the signal-to-noise ratio in the spectrum. Moreover, extending the interferograms in the indirect dimension of multidimensional spectra usually results in unacceptable long experiment times. One trick to extend the FID without lengthening the acquisition time is to artificially lengthen the FID by adding an appropriate number of zeros to the FID. This is called *zero filling* or zero padding. As the added zeros provide no additional information, this does not improve the inherent spectral resolution but rather results in a smoother curvature of the lines.

The effect of zero filling is shown in Figure 11.22. Therein the FID of two resonance lines with a shift difference of 1 Hz recorded for 2 s is Fourier transformed once without zero filling and once when the FID is extended by zero filling by a factor of 2 or 4. The example clearly demonstrates that the splitting is not recognized unless zero filling is applied at least once. Further zero filling has more or less cosmetic effects only.

It seems as if Fourier transformation without zero filling withholds some information, but this is not true. To understand this apparent contradiction, we need to consider not only the *real* part of the spectrum. This part includes only half of the points delivered by Fourier transformation, and thus essentially contains only half of the information. The other half is contained in the imaginary part, which is usually not displayed. In fact, if we look at the imaginary part of our example given in Figure 11.22, we recognize a disruption in the steep passage of the dispersive signal even when no zero filling was done. Such a feature does not occur for a single resonance, and if we were accustomed to interpreting spectra in dispersive mode we would probably immediately recognize it and interpret it in terms of two

adjacent resonance lines. But for many reasons dispersive-mode spectra are a nuisance to work with and it is much more convenient to apply zero filling. Usually we should at least double the size of the FID by applying zero filling once.

Another reason for zero filling is the requirement of the fast Fourier transform that the number of points is a power of 2. Due to restricted experiment time, this requirement is often not met for the indirect dimensions of multidimensional spectra, where, for example, we may measure 300 increments instead of 512 (2^9). In such a case zero filling is used to fill the time domain at least to the next power of 2.

11.4.2 Linear Prediction

A more sophisticated technique to extend the FID, other than zero filling, is called *linear prediction*. In this technique the FID is extended with predicted points using the information content of the measured data points. Thus, by use of linear prediction not only the *digital* resolution, but to some extent also the *spectral* resolution is increased.

Linear prediction models the future of the signal in terms of the measured data points by assuming that any further point x_n can be expressed as a linear combination of the immediately preceding points $[x_{n-1} \ldots x_{n-M}]$, such that

$$x_n = a_1 x_{n-1} + a_2 x_{n-2} + a_3 x_{n-3} + \ldots + a_M x_{n-M} \tag{11.35}$$

where the a's are the prediction coefficients and M is the prediction order. It can be shown that for a signal constituted of damped sinusoids, (11.35) holds true. In particular, for a signal of complex amplitude, the prediction order M must equal the number of damped sinusoids involved. Having measured at least $2M$ FID points, we can obtain the prediction coefficients by solving a system of M linear equations. However, in the presence of noise and when more than $2M$ data points are available, the coefficients must be computed in a least-squares sense, for example, by singular value decomposition. Usually the parameter M is not known and thus an estimate of M must be provided for linear prediction. If M is chosen too small, only the M largest signal components will be predicted; if M is chosen to large, also noise components will be predicted. In general, a reasonable estimate for M is two to three times the number of expected resonance lines.

From (11.35) it is clear that any error in the prediction coefficients will progressively propagate into the predicted signal. Therefore, we cannot extend the signal infinitely by linear prediction without introducing severe distortions in the spectrum. In practice, the FID can be reliably extended by up to the same number of points. For good results of linear prediction, the signal-to-noise ratio must be high.

Linear prediction is most advantageous in multidimensional spectra, generally the better the fewer data points have been measured. The FIDs in the indirect dimensions of multidimensional spectra are usually highly truncated. Accordingly, strong window functions must be used to suppress truncation artifacts, resulting in poor spectral resolution. When extending the FIDs by means of linear prediction,

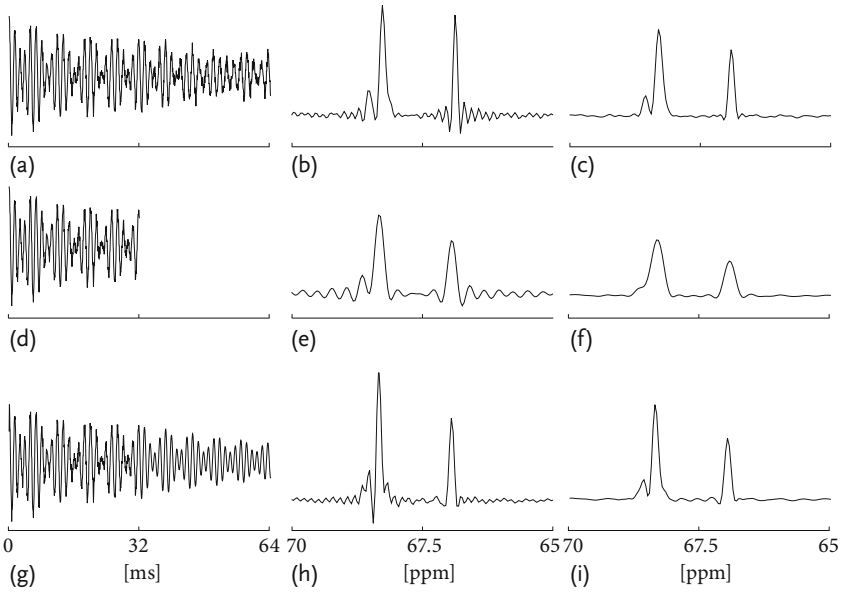

Figure 11.23 Example of the resolution enhancement obtained by using linear prediction. (a) A time domain signal (real part only) of the ^{13}C dimension of a heteronuclear single-quantum coherence spectrum is shown (1024 complex points). The corresponding spectra without and with apodization (squared cosine window function) are shown in (b) and (c), respectively. In (d) only the first 512 points of the spectrum in (a) are retained, resulting in a spectrum that lacks either from strong truncation artifacts when no window multiplication is used (e) or poor resolution when apodization is used (f). When the signal is extended to its original size of 1024 complex points by using linear prediction (g), the resolution of the corresponding spectra (h,i) is almost identical to that for the case in which the full signal has been acquired (b,c).

we can use smoother apodization functions (see Section 11.4.3), and accordingly better resolution is obtained. This is shown in Figure 11.23. It clearly demonstrates that, in combination with linear prediction, almost identical resolution is obtained when only half of the time domain data points are sampled. Another typical application of linear prediction is to reconstruct the initial part of an FID, called *backward linear prediction*. The very first FID points are sometimes distorted, for example, by residual RF pulse power in the receiver coil or by the presence of rapidly decaying signals (e.g., from background signals from the probe). Such distortions can result in severe baseline and phase problems. In that case the erroneous points can be replaced by the predicted ones using the undistorted part of the FID.

11.4.3
Pretreatment of the FID: Window Multiplication

By using window functions (also known as *apodization*), we can increase the signal-to-noise ratio, enhance the resolution and/or reduce truncation artifacts. For this,

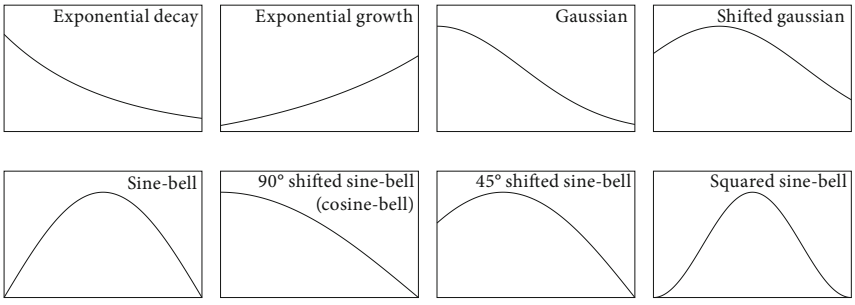

Figure 11.24 Commonly used window functions.

the FID is multiplied prior to the Fourier transform by so-called window or weighting functions. Some of the most widely used window functions are shown in Figure 11.24. The effect of multiplying the FID by a window function is to emphasize or attenuate different sections of the FID such that the desired properties become amplified in the spectra. As discussed before, sensitivity is mostly provided by the *initial* part of the FID, whereas resolution mostly depends on the signal content in the later parts of the FID. Thus, by emphasizing either the initial or the later part of the FID, we can enhance either the sensitivity or the resolution in the spectrum. In addition, truncated FIDs can be smoothly brought to zero at the end, thereby reducing truncation artifacts. Mathematically the effect of window multiplication can be understood as a convolution of the original spectrum with the spectrum of the window function (see Excursus 11.1). Do not worry. Things will become much clearer soon. In the following we will have a closer look at some of the most popular window functions used in NMR spectroscopy (Figure 11.24).

Excursus 11.1: Convolution Theorem

An important technique to predict the outcome of the Fourier transform is *convolution*. Mathematically speaking, convolution corresponds to the combination of two functions to give a third that is typically viewed as a modified version of one of the original functions. Technically, convolution is an integral that expresses the amount of overlap of one function G as it is shifted over another function F. It therefore "blends" one function with another. To better understand what that means, we will look at the Fourier transform of a damped cosine function. The cosine function itself will result in two delta functions, each representing a spike at the positive or negative frequency of the oscillation, but with no line width. The Fourier transform of an exponential is a Lorentzian. Multiplying the cosine by the exponential blends the properties of the cosine over the exponential and results in a damped cosine function. Blending the Lorentzian over the result of the Fourier transform of a cosine function results in two signals, but this time with Lorentzian line shape instead of the delta functions.

The convolution theorem states that the Fourier transform of the product of two functions $f(t)$ and $g(t)$ is the same as the convolution of their Fourier trans-

form:

$$\mathrm{FT}\{f(t)g(t)\} = F(\omega) \otimes G(\omega) \tag{11.36}$$

with $F(\omega)$ and $G(\omega)$ denoting the Fourier transforms of $f(t)$ and $g(t)$, respectively. Alternatively, when the convolution is done in the time domain, we can write

$$\mathrm{FT}\{f(t) \otimes g(t)\} = F(\omega)G(\omega) \tag{11.37}$$

In particular it is (11.36) that is helpful when discussing the effects of window functions. Convolution of two functions is obtained by stepwise integration of their product while continuously applying a shift to one of the functions. This is depicted in Figure 11.25 for the case of two discrete functions. For simplicity it is assumed that $G(\omega)$ has only three values different from zero.

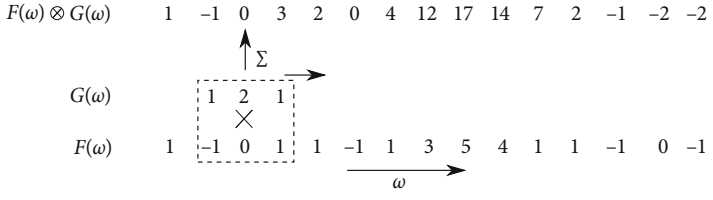

Figure 11.25 The principle of convolution of two functions F and G. The values of $F(\omega)$ are sequentially multiplied by the values of $G(\omega)$ and added up to give the values of $F(\omega) \otimes G(\omega)$ (e.g., $1 \cdot -1 + 2 \cdot 0 + 1 \cdot 1 = 0$). To obtain the next value in $F(\omega) \otimes G(\omega)$ (here 3), $G(\omega)$ is shifted to the right by one position.

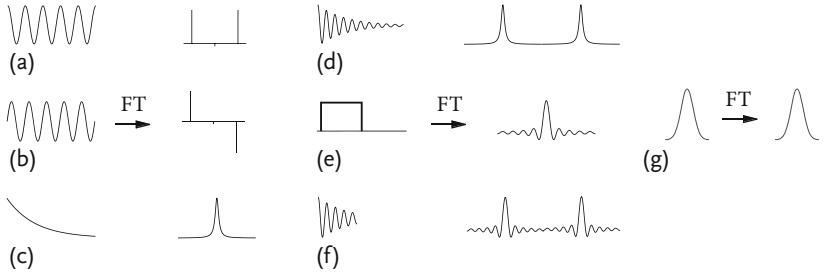

Figure 11.26 Fourier pairs. Time domain data and their corresponding Fourier transforms. The Fourier transform of a pure (not truncated) cosine function is a delta function (a) with signals at $\pm\Omega$. The Fourier transform of a sine function is again a delta function, but this time the signals at $+\Omega$ and $-\Omega$ have opposite sign (b). An exponential function results in a Lorentzian function, displaying the desired line shape of NMR signals (c). To predict the Fourier transform of an damped cosine (d), we just convolute the results from a cosine (a) and an exponential (c). The Fourier transform of a step function is the sinc function $(\sin(x)/x)$ with its characteristic side lobes (wiggles) (e). The Fourier transform of a nondecayed damped cosine (f) is simply the convolution of the functions represented by (a), (c), and (e). The Fourier transform of a Gaussian function yields the Gaussian function again (g).

Knowing the basic appearance of the Fourier transform of some simple functions as a cosine, an exponential decay, or a step function, we can then relatively easily deduce the Fourier transform of the product of such a function by using the convolution theorem as given by (11.36). Some examples are depicted in Figure 11.26. Similarly, we can deduce the effect of a window function on a spectrum by considering the convolution theorem.

11.4.3.1 Exponential Multiplication

Exponential multiplication is usually used to enhance sensitivity and to reduce truncation artifacts. For that purpose the FID is multiplied by a decaying exponential

$$e^{-\pi \mathrm{lb} t} \tag{11.38}$$

in which lb is the so-called *line-broadening* factor. If we consider a particular resonance that decays with $e^{-1/T2t}$ and use (11.13), exponential multiplication gives

$$e^{-\pi \mathrm{LW}_{\frac{1}{2}} t} e^{-\pi \mathrm{lb} t} = e^{-\pi\left(\mathrm{LW}_{\frac{1}{2}} + \mathrm{lb}\right)t} \tag{11.39}$$

where $\mathrm{LW}_{1/2}$ is the natural line width of the resonance. Fourier transformation of (11.39) results in a Lorentzian line shape of the line width (FWHH): $\mathrm{LW}_{\frac{1}{2}} + \mathrm{lb}$. Thus, by exponential multiplication, the resonance lines becomes broadened to an extent specified by the factor lb (in hertz). At first glance this may seem not to be very helpful as the resolution and the signal intensity are reduced. To perceive the strength of exponential multiplication we also have to consider the noise. The noise can usually be assumed to be randomly and hence uniformly distributed over the *entire* FID in contrast to the signal, whose intensity strongly falls off toward the end of the FID. When we multiply by a decaying exponential, the noise power at the end of the FID becomes substantially reduced and thereby so does the noise in the spectrum. Thus, exponential multiplication improves the signal-to-noise ratio at the expense of lower resolution. It can be shown that the improvement in the signal-to-noise ratio is largest when a value of lb that equals the natural line width is used (a so-called *matched filter*). Exponential multiplication is usually applied to spectra with inherent low sensitivity and for which resolution is usually not a problem, for example, for ^{13}C NMR spectra (see Figure 11.27). Moreover, the signal is forced to become zero at the end, thereby reducing truncation artifacts, and the Lorentzian line shape is maintained.

It is clear that we can also do the opposite by using exponential multiplication using negative values for lb. Then the decay rates becomes artificially reduced, resulting in narrower resonance lines and hence in an improvement of the spectral resolution. However, as shown in Figure 11.28, multiplication by an increasing exponential will also add a considerable amount of noise to the spectrum and result in strong truncation artifacts. As we will see below, there are better window functions for the purpose of resolution enhancement.

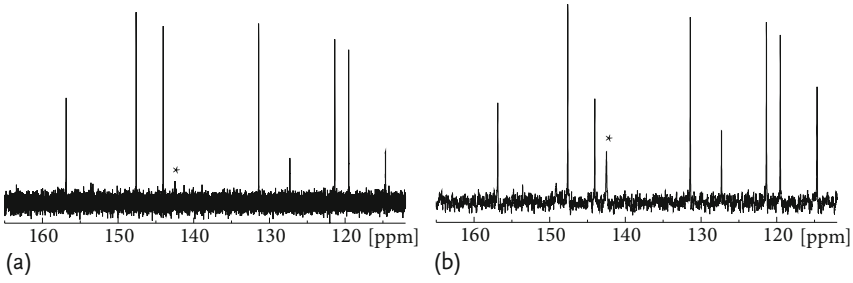

Figure 11.27 Effect of sensitivity enhancement by using exponential multiplication. Part of a ^{13}C spectrum without (a) and with (b) exponential multiplication using a line-broadening factor of 4 Hz. Note the remarkable sensitivity gain for the relatively broad signal labeled with an asterisk that can hardly be detected in the spectrum resulting from the untreated FID. Also note how exponential multiplication alters the relative signal intensities, which can be explained by considering the varying line widths (see (11.12)).

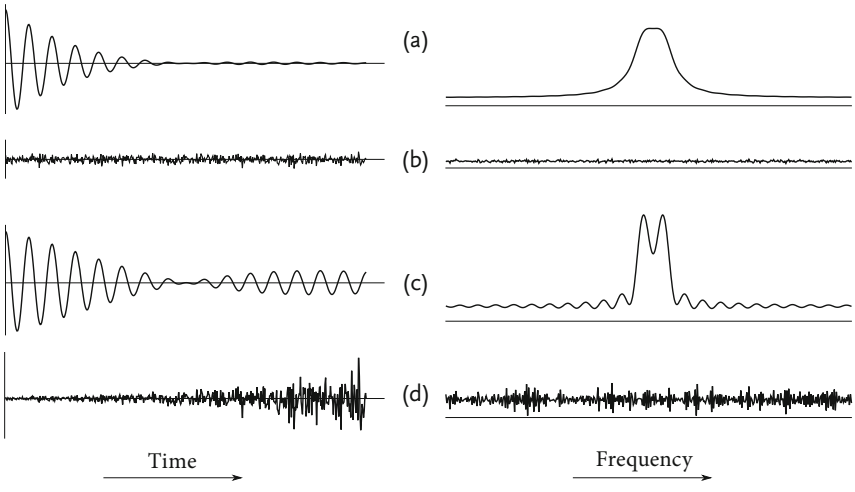

Figure 11.28 Resolution enhancement using exponential multiplication. The left panel shows the decay of two closely located resonances (a) and a simulated noise contribution (b). The corresponding spectra are shown on the right. In (c,d) the time domain data are multiplied by an increasing exponential prior to Fourier transformation, resulting in the spectra shown on the right.

11.4.3.2 **Gaussian Multiplication**

Use of a Gauss function $g(t) = \exp -(\frac{\mu - t}{\sigma})^2$ of width σ and centered at μ for window multiplication instead of a simple exponential allows a more sophisticated weighting of the FID. By adjusting σ and μ, we can specify the position of the maximum and the width of the Gaussian function. Thereby we can, for example, emphasize the central part of an FID while ensuring that the FID still decays smoothly to zero at its end to avoid truncation problems. *Gaussian multiplication* may ac-

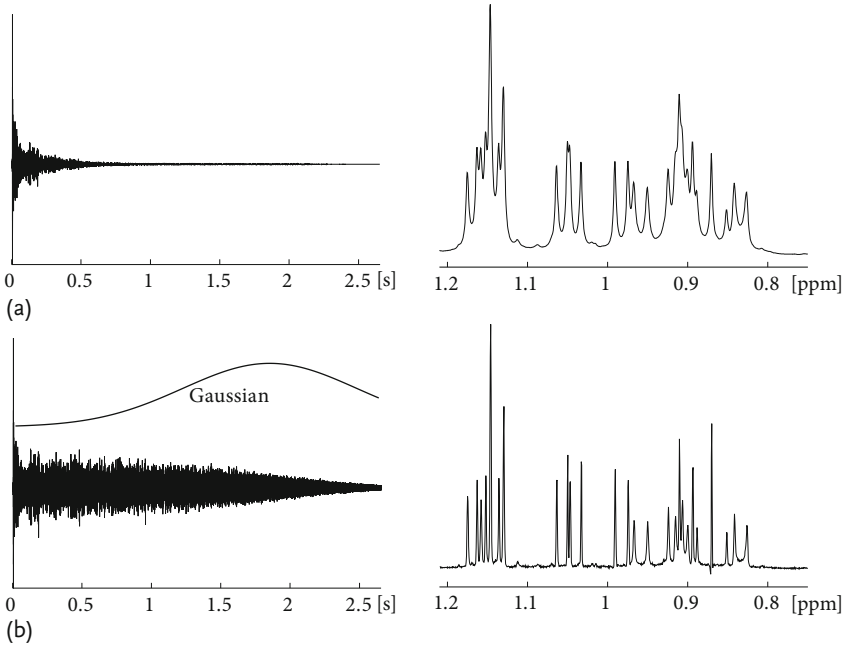

Figure 11.29 Resolution enhancement using Gaussian multiplication. (a) The FID and the spectrum in absence of Gaussian multiplication. (b) Gaussian multiplication is applied using a shifted Gaussian function, resulting in a dramatic increase in resolution of the spectrum.

complish different tasks. Firstly, we can multiply the FID by a nonshifted Gauss function. This allows sensitivity enhancement when the envelope of an FID is a Gaussian rather than an exponential decay – a rare case in high-resolution NMR experiments. Secondly, a shifted Gaussian can be used to enhance the sensitivity for FIDs that are characterized by an initial signal buildup, and where the maximum signal intensity is not at the beginning of the FID, for example, in COSY or spin-echo experiments. Thirdly, and this is the main purpose of Gaussian multiplication, using shifted Gaussians, we can enhance the resolution of spectra. The shifted Gaussian emphasizes the later part of an FID and therefore enhances the resolution, as shown in Figure 11.29. We can understand this if we consider that the initial slope of a shifted Gaussian acts to compensate for the natural decay of the FID, such that the weighted FID decays more slowly and hence narrower lines are obtained. By careful choice of the Gaussian, we can even cause the envelope of the FID to become entirely half-Gaussian. As the Fourier transform of a half-Gaussian yields another Gaussian (see Figure 11.26), this is referred to as Lorentz-to-Gauss transformation and is outlined in more detail in Excursus 11.2. Gaussian lines are narrower at their base than Lorentzian lines, resulting in less peak overlap.

Excursus 11.2: Lorentz-to-Gauss Transformation

In the Lorentz-to-Gauss transformation the FID is first multiplied by a growing exponential such that the T2 decay of the signal is compensated. Thereafter the FID is further multiplied by a half-Gaussian. As mentioned already, the resulting Gaussian lines obtained after Fourier transformation are narrower than Lorentzian lines. Grouped together, the window function has the form

$$\exp\left(-\frac{t^2}{\sigma^2}\right)\exp(\pi \mathrm{lb} t)\ , \tag{11.40}$$

in which lb specifies the natural line width of the signal in hertz. It can be shown that this expression corresponds to a shifted Gaussian centered at $\mu = \sigma^2 \pi \mathrm{lb}/2$. If we specify the position of the maximum relative to total acquisition time by the parameter gb, such that $\mu = \mathrm{gb}\, T_{\mathrm{aq}}$ with $(0 \geq \mathrm{gb} \leq 1)$, the width of the Gaussian is $\sigma^2 = 2\mathrm{gb}\, T_{\mathrm{aq}}/(\pi \mathrm{lb})$. Inserting this into (11.40), we obtain

$$g(t) = \exp\left(-\frac{\pi \mathrm{lb}}{2\mathrm{gb}\, T_{\mathrm{aq}}} t^2\right)\exp(\pi \mathrm{lb} t) \tag{11.41}$$

in which gb and lb are the adjustable parameters. In principle, all types of Gauss apodizations can be accomplished using the single window function specified in (11.41). Whether a pure Lorentz-to-Gauss transformation is obtained or not depends only on the choice of lb and gb. Note that lb is often also specified to be the negative natural line width, in which case lb in (11.41) must be replaced by −lb.

11.4.3.3 Sine-Bell Multiplication

Sine-bell multiplication is often used in multidimensional NMR experiments where signal truncation is a common issue. The sine–bell function is defined by

$$\mathrm{SB}(t) = \sin\left((\pi - a)\frac{t}{T_{\mathrm{aq}}} + a\right) \tag{11.42}$$

with $0 \leq a < \pi$. For $a = 0$, (11.42) describes a pure sine-bell function that presents the first half-lobe of a sine wave; for $a = \pi/2$ it describes the first quarter of a cosine wave and accordingly is called a cosine-bell or a 90°-shifted sine-bell window function. For other values of a it denotes the sine half-lobe starting at a and extending up to π. In any case the function forces the signal to zero at the end of the FID and thus reduces truncation artifacts. In addition, a pure sine-bell function emphasizes the center part of an FID, while a cosine-bell function emphasizes the initial portion. Accordingly, for FIDs showing the usual exponential decay of the signal, the sine-bell function will increase resolution at the expense of a lower signal-to-noise ratio, while the opposite is true for the cosine-bell function. For FIDs that have maximum signal intensity in a later portion of the FID (e.g., in the COSY experiment), a shifted cosine-bell function will be required for improved signal-

to-noise ratio. Using pure sine-bell functions for resolution enhancement usually introduces unacceptable line-shape distortions and a dramatic degradation of the signal-to-noise ratio. Thus, sine-bell and cosine-bell functions are primarily used to prevent truncation artifacts without compromising resolution to the same extent as in exponential multiplication. Accordingly, cosine-bell functions are used for experiments starting with full signal intensity (e.g., NOESY or HSQC experiments) and sine-bell functions are for experiments with initial signal buildup (e.g., in COSY experiments). Often also *squared* sine-bell functions are used for apodization that have smoother curvature and are more pronounced around the maximum.

To summarize, we have seen that the quality of spectra can be much improved by applying appropriate window functions. Such improvement can become extremely important in combination with automatic spectral analysis tools. While the human eye (at least that of an experienced spectroscopist) is capable of recognizing Fourier transform artifacts in the spectra (it can distinguish truncation wiggles from signals or broad signals from noise), this is much more demanding for software, and the quality of the spectra must be high when using computer tools.

11.4.4 Phase Correction

Directly after Fourier transformation, spectra usually look similar to the spectrum shown at the top of Figure 11.30. This is due to phase errors (for reasons given below), and we need to correct for them. We saw in Section 11.2.3 that unless the phase of the time domain signal is zero, the spectrum exhibits a mixture of absorptive and dispersive line shapes.

Basically there are two types of phase errors: an overall or *zeroth-order* phase error ϕ_0, which is the same for all resonances independent of their frequency, and a *first-order* phase error ϕ_1, which scales linearly with the offset frequencies; thus, $\phi_1 = c\Omega$. The total phase error for the ith resonance can be expressed as $\phi_i = \phi_0 + c\Omega_i$. Considering (11.15), we obtain

$$S(\Omega_i) = (\mathrm{Abs}(\Omega_i) + \mathrm{i}\,\mathrm{Dsp}(\Omega_i))\exp(\mathrm{i}(\phi_0 + c\Omega_i)) \tag{11.43}$$

From this expression it becomes clear that we can remove the phase errors simply by multiplying the spectrum by $\exp(-\mathrm{i}(\phi_0 + c\Omega_i))$ since $\exp(\mathrm{i}\alpha)\exp(-\mathrm{i}\alpha) = 1$. As ϕ_0 and c are not known to us a priori, phasing is a bit more complex. If we write the phase correction factor in the form $\exp(\mathrm{i}(c_0 + c_1\Delta\Omega))$, in which $\Delta\Omega$ is the frequency difference with respect to an arbitrary reference frequency, the so-called pivot point, the goal of phasing is to find the appropriate values of c_0 and c_1 to obtain a pure absorption spectrum for the real part. In practice this is usually done by setting the pivot point to a well-resolved resonance at one end of the spectrum, changing the value (here c_0) of the zeroth-order correction to phase it to the pure absorption line shape, and then correcting the phase of all other signals by adjusting the phase of a signal at the other end of the spectrum to pure absorption using the first-order correction only (here c_1).

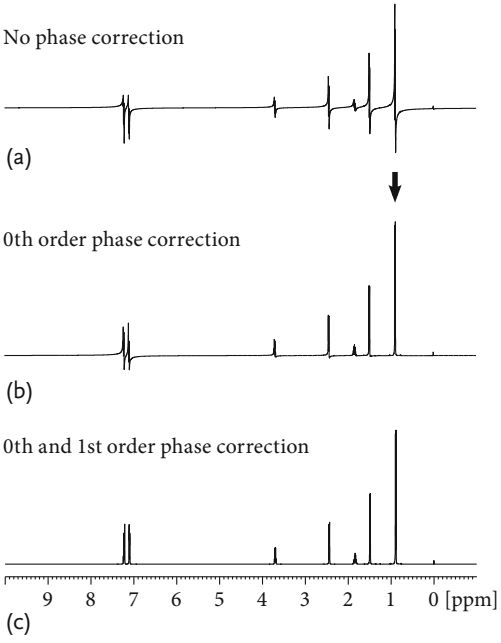

Figure 11.30 Phasing of spectra. Spectrum without any phase correction (a), spectrum after applying a zeroth-order correction with the reference set to the signal at the right end of the spectrum (marked by the arrow) (b), and the fully phase-corrected spectrum after additional first-order phase correction (c).

Now let us look at the origin of the phase errors. The zeroth-order overall phase error is due to an inherent phase offset of the RF signal received and the receiver reference signal. The RF signal is split, mixed, amplified, and filtered several times in the receiver path and each of these steps, as also the length of the RF cables itself, will alter the phase of the signal to some extent and there is no way to ensure that the reference signal has the same phase as the RF signal. One should note, however, that as long as all acquisition settings (e.g., receiver gain, spectral width) remain unchanged, the phase difference of the RF signal and the reference signal will not alter. For subsequent scans the phase offset is therefore identical, and the FID will add coherently. This characteristic feature is called *phase coherence* and will be treated in more detail in Section 12.3. The frequency-dependent first-order phase error is mainly caused by RF pulse offset effects and the *prescan delay*. The pulse offset effects were discussed in more in Chapter 6. The prescan or ring-down delay is a short delay (e.g., 10 μs) inserted after the RF pulse and before the start of signal acquisition. The delay protects the receiver and other electronics from the intense RF field of the pulse. However, as depicted in Figure 11.31, during this time period as well as during the pulse, shift evolution takes place and the magnetization vectors will fan out by an amount *proportional to their frequency offset*, resulting in the first-order phase errors.

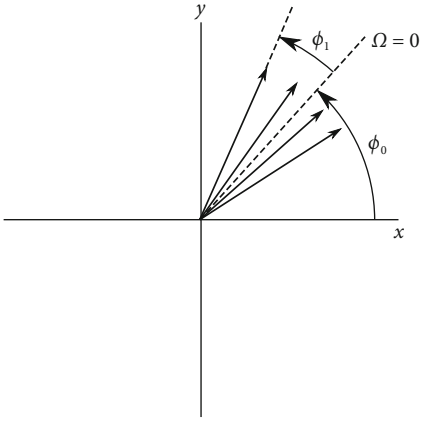

Figure 11.31 Magnetization vectors in the receiver reference frame. Zeroth-order phase error ϕ_0 due to a mismatch in the phases of the RF and the reference signals and first-order phase error ϕ_1 due to free precession during the prescan delay τ ($\phi_1 = \tau\Omega_i$).

11.4.5
Magnitude Mode and Power Spectra

As we will see later in this book, particularly in the multidimensional experiments discussed in Chapter 17, it is not always possible to record phase-sensitive spectra from which pure absorption line shapes can be obtained. Some types of experiments produce spectra that inherently exhibit mixtures of absorptive and dispersive line shapes, so we are not able to correct for them by a phase correction. Furthermore, the amount of absorptive and dispersive contributions may depend in a rather involved way on the actual offsets and coupling constants of the resonances, resulting in spectra that may look very strange due to the strong variation in the phases. In such cases it is useful to present spectra in *magnitude or absolute value mode*, which is computed as

$$\text{Spect}_{\text{magnitude}} = \sqrt{\text{Re}^2 + \text{Im}^2} \tag{11.44}$$

where Re and Im are the real and imaginary parts of the spectrum, respectively. For a single line and with use of (11.16), the magnitude line shape is independent of the actual signal phase and is given by $\sqrt{\text{Abs}(\Omega)^2 + \text{Dsp}(\Omega)^2}$. Using (11.10) and (11.11), we obtain

$$S(\Omega)_{\text{magnitude}} = \frac{s_0}{\sqrt{R_2^2 + (\Omega_A - \Omega)^2}} \tag{11.45}$$

Because of the square root dependence of the denominator, magnitude mode signals are much broader than the corresponding absorptive Lorentzian lines (see Figure 11.32a). Furthermore, (11.45) only applies for a isolated singlet line. When other signals are in close proximity, the large dispersive tails will interfere, resulting in asymmetric line shapes (Figure 11.32b).

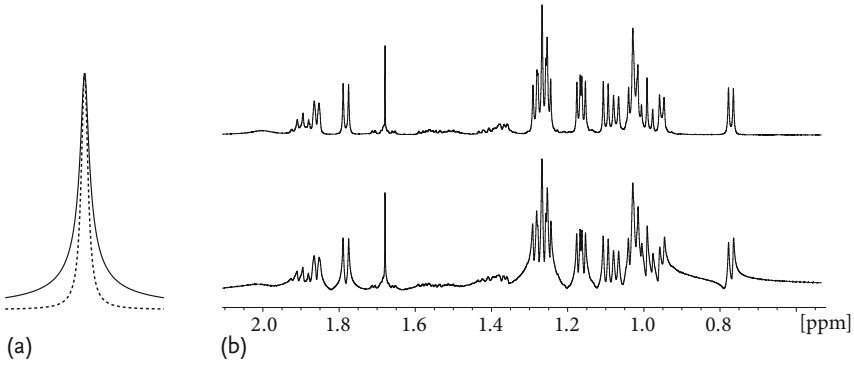

Figure 11.32 Magnitude mode versus pure absorption line shapes. (a) The line shape of an isolated resonance when using absorption mode (dashed line) or magnitude mode (solid line). (b) A section of an ^{1}H spectrum when using conventional absorption mode presentation (upper trace) or when using magnitude calculation (lower trace).

Alternatively, spectra can be presented as *power spectra*:

$$\text{Spect}_{\text{power}} = \text{Re}^2 + \text{Im}^2$$

Power spectra produce narrower line shapes than magnitude spectra. However, the signal intensities will scale by the square.

11.4.6 Baseline Correction

Curved baselines present a major problem in Fourier transform NMR experiments. Firstly, such baselines will distort integrals. Secondly, in spectra with baseline roll, small signals may not be recognized. Thirdly, those spectra are difficult to phase. Furthermore, peak-picking routines may not work properly. There are many reasons for poor baselines. In general, baseline distortions are caused by distortions of the first points of the FID or when very large first-order phase corrections are required. A frequent source is receiver overload that occurs when the receiver gain has been set too high (Section 11.3.4). In such a case the baseline cannot be corrected, and the measurement must be repeated with a lower receiver gain. Other baseline problems, such as baseline drifts (nonhorizontal but flat baseline) or systematic baseline curvature, can often be corrected either automatically or manually (Figure 11.33). Oversampling has been shown to reduce dramatically baseline problems in the directly sampled frequency dimensions originating from the audio filters. In principle we can recognize which data point is distorted from the shape of the baseline. A wrong first data point leads to a baseline offset, a wrong second one leads to distortions corresponding to a half-wave, a wrong third one leads to those of a full wave, and so on. In principle, spectra with (a few) wrong first data points can still be used if linear back-prediction of the first data points is used (Section 11.4.2).

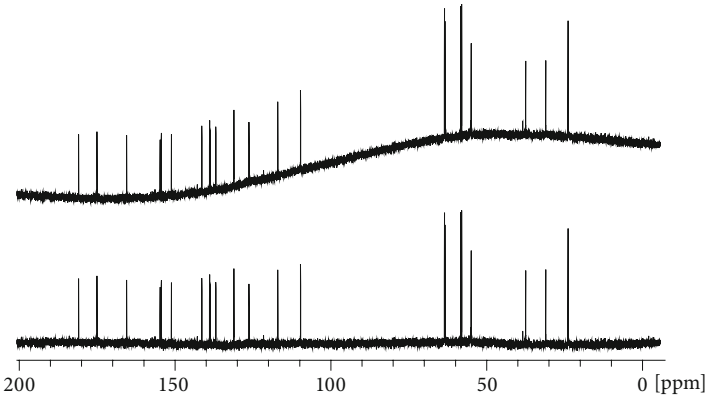

Figure 11.33 Baseline correction. ^{13}C NMR spectra with (lower trace) and without (upper trace) baseline correction.

11.5 Problems

11.1. Comment on the following statement: The Fourier transform approximates the time domain signal (FID) as a series of sines and cosines.

11.2. In NMR, the spectrum is usually kept by means of a *complex* Fourier transformation. What does the term complex mean? Which of the following answers is correct? (a) Fourier transformation of a discrete time domain signal, especially one that consists of multiple frequencies, by no means is a trivial task. Hence, a very complex form of Fourier transformation must be employed. (b) The complex Fourier transform prevents a folding of resonances outside the spectral range. (c) In order to distinguish between negative and positive frequencies relative to the carrier signal, the x and the y components of the magnetization must be detected. These two components are usually represented using complex numbers and the complex Fourier transform will then give the correct frequencies.

11.3. In order to measure the entire range of chemical shifts of a metal hydride the spectral width must be doubled. How do you then need to change the number of time domain data points in order to keep the maximal spectral resolution at a constant level?

11.4. Finally you have realized, that a measurement of the entire shift range of the metal hydride mentioned in 11.3 requires a spectral width that is even four times as large than that of the default ^{1}H parameter set. Accordingly, to maintain the spectral resolution, you also adjusted the number of time domain points. Unfortunately, after Fourier transformation you seem to have lost some previously observed signals while the intensities of other signals seem to be quite disturbed (especially that of the very sharp signals). What could be the reason for this?

11.5. The FID of a relatively intense resonance is sampled only up to about one times its T2 relaxation. What artifacts do you have to expect after FT of the FID? Give two possible pre-processing steps of the FID that help to reduces these artifacts.

11.6. Place the following items into the correct order in which they are performed: phase correction/window multiplication/Fourier transform/zero filling/baseline correction

11.7. What type of window function is most often applied to ^{13}C data and why?

Further Reading

Braun, S., Kalinovski, H.-O., and Berger S. (1998) *150 and More Basic NMR Experiments*, VCH-Wiley Verlag GmbH.

Hoch, J. and Stern, A. (1996) *NMR Data Processing*. John Wiley & Sons.

Keeler, J. (2010) *Understanding NMR Spectroscopy*, 2nd edn, John Wiley & Sons, Ltd.

12
Experimental Techniques

This chapter introduces the experimental techniques that form the core of modern NMR experiments. We will describe the art of crafting radio frequency (RF) pulses and pulsed field gradients (PFGs), introduce phase cycling, and explain the occurrence and effects of delays used in NMR experiments. In Chapter 13 we will look at the technical implementation of such experiments using modern NMR spectrometers – the art of pulse sequences.

For newcomers to the field of NMR spectroscopy, this chapter may contain a huge amount of new concepts and ideas in a quite condensed form. For a first reading it should be sufficient to take note of the content without trying to fully understand the underlying principles, and later when the reader really has a feeling for the subject should the specific sections be read with a bit more attention, which also should provide a starting point for reading other literature.

12.1
RF Pulses

RF pulses form the backbone of all NMR experiments. Through their use it is possible to manipulate magnetization in the course of an experiment in the desired way to form what we commonly call a "pulse sequence". In order to understand the flow of magnetization in the course of an experiment, it is essential to have an idea about the effect of different types of RF pulses, and how we can craft them in order to influence their impact profile. The different types of RF pulses can be roughly divided into two classes: *hard* and *soft* pulses. Hard pulses are applied for a very short duration at maximum RF power with the aim of exciting spins over a wide range of frequencies. In contrast, soft pulses are applied for much longer durations at much weaker RF power levels and are used to selectively excite resonances within a narrow frequency range. In order to improve the selectivity, soft pulses often have a specific shape. Other important classes are band-selective pulses, designed to influence spins in a certain frequency range, for example, the range of carbonyl resonances, and adiabatic pulses, which can cover a very broad frequency range.

Applied NMR Spectroscopy for Chemists and Life Scientists, First Edition. Oliver Zerbe and Simon Jurt.
©2014 WILEY-VCH Verlag GmbH & Co. KGaA. Published 2014 by WILEY-VCH Verlag GmbH & Co. KGaA.

We will start this chapter by considering the basics of RF pulses, and by describing some general aspects of RF pulses. Thereafter, some important classes of pulses are introduced and their purposes, benefits, and limitations are discussed. Finally, we will look at the sources and consequences of pulse imperfections.

12.1.1 General Considerations

We saw in Section 6.6 that the application of an RF field orthogonal to the static main or B_0 field results in a rotation of magnetization, and that this process is best described in a rotating frame of reference that rotates with the frequency of the RF field. Therein the on-resonant B_1 component is static and its direction is given by the pulse phase ϕ_{RF}. As depicted in Figure 12.1a, for a magnetization vector orthogonal to the B_1 field and which is exactly on-resonant, a pulse of duration t_p rotates the magnetization in a plane orthogonal to the B_1 vector by a certain angle, the so-called flip or tip angle β (in radians):

$$\beta = -\gamma B_1 t_p \tag{12.1}$$

The duration of the pulse is usually called the pulse width. Alternatively, when magnetization is not orthogonal to B_1, the vector evolves on the surface of a cone (Figure 12.1b). Most important are flip angles of 90° or 180° and commonly used pulse phases are 0°, 90°, 180°, and 270°.

We have also seen that for off-resonant spins, a residual B_0 field must be taken into account, and that in this case the axis of rotation is no longer in the xy plane. This results in a nonuniform excitation profile. Depending on the offset of a resonance, the actual flip angle differs from its nominal value, resulting in spectral defects, known as off-resonance effects.

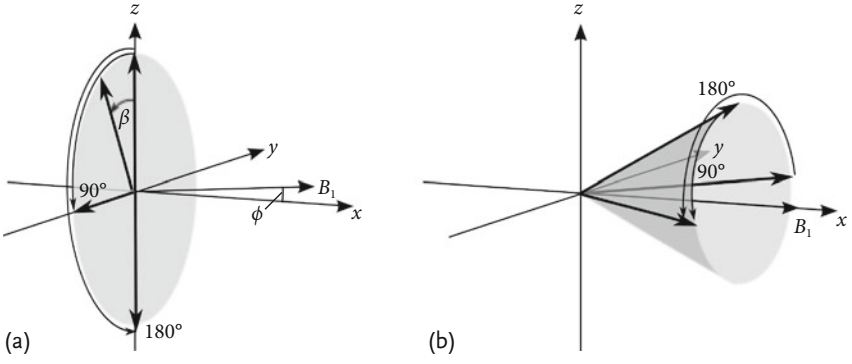

Figure 12.1 Effect of radio frequency (RF) pulses on the magnetization. In the case of z magnetization, the pulse rotates magnetization in a plane orthogonal to the direction of the B_1 field (a). When the starting magnetization is not orthogonal to the B_1 field, the evolution of magnetization is described by a cone, of which the central axis is formed by the B_1 field vector (b).

12.1.1.1 RF Field Strength

The B_1 field is a magnetic field and therefore in principle has the unit of tesla. However, similar to the case of the B_0 field, which is usually given in terms of the ^{1}H precession frequency (e.g., a 500 MHz magnet), it is common to specify the B_1 field strength in terms of the nutation frequency:

$$\nu_{\text{nut}} = \frac{|\gamma|B_1}{2\pi} \tag{12.2}$$

For example, if a 10 μs pulse is required to rotate magnetization by 90°, a pulse of 40 μs will be needed to rotate magnetization by 360°; hence, the nutation frequency corresponds to $1/(40 \times 10^{-6}\,\text{s}) = 25\,\text{kHz}$.

12.1.2 Hard Pulses

In order to excite resonances over a broad spectral range, short and powerful pulses are required, referred to as hard or high-power pulses. They are usually applied at maximum RF power for short durations in the range of a few microseconds. They are by far the most frequently used pulses and are an integral part of almost all NMR experiments. They are usually applied with the aim of rotating magnetization by either 90° or 180° over the entire spectral range of interest. A typical excitation profile of a hard 90° pulse is shown in Figure 12.2.

We already saw in Section 6.6 that the excitation bandwidth and the pulse duration are inversely related. Thus, the larger the spectral range of interest, the shorter and the more powerful the pulses are required to be in order to keep off-resonance

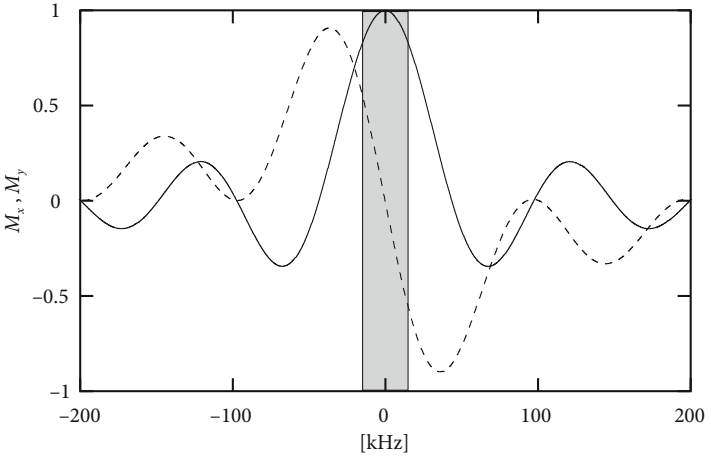

Figure 12.2 Excitation profile of a "hard" 90° pulse. The amount of *x* (solid line) and *y* (dashed line) magnetization after equilibrium *z* magnetization has been excited by a 10 μs RF pulse of phase *y* as a function of the pulse offset (simulated). A frequency range of 30 kHz is highlighted, which is the common shift range (200 ppm) for ^{13}C spectra at 600 MHz field strength.

effects at an acceptable level. However, because RF coils have power limitations, the pulse power cannot be increased at will and the pulse widths are restricted to a lower limit (bandwidth limitation). According to (12.2), the lower the γ of a nucleus, the lower the nutation frequency and hence the larger the 90° pulse width at a given B_1 field strength is. In the case of ^{1}H, for which chemical shifts are usually in a relatively narrow spectral range (e.g., about 6 kHz for a 600 MHz spectrometer) and pulse widths are typically short (around 10 μs), off-resonance effects are normally not that critical. However, they can become rather severe for nuclei that have much broader spectral ranges (e.g., about 30 kHz for ^{13}C for a 600 MHz spectrometer) and/or longer pulse widths. In particular, the 180° inversion or decoupling pulses often encountered in multidimensional experiments suffer from off-resonance effects. In such cases it can be necessary to replace them by using adiabatic or composite pulses (see Sections 12.1.5 and 12.1.6, respectively).

12.1.3 Soft Pulses

Sometimes we wish to irradiate exclusively a single line or a multiplet and hence the pulse should act within a relatively narrow frequency range, leaving other resonances essentially unaffected. In such a situation we can use soft or selective pulses. These pulses are of much longer duration (on the order of milliseconds) but also of much less RF power.

As an example, Figure 12.3b (solid line) shows the total amount of xy magnetization obtained from a 90° soft pulse of 20 ms duration. As expected, the excitation bandwidth is much reduced (to about 100 Hz) when compared with the 90° hard pulse. Unfortunately, there are also a number of sidebands for which a considerable amount of xy magnetization is created. These sidebands are strongly reminiscent of the "wiggles" observed for truncated free induction decays (see Section 11.2.4). This is not a coincidence and it can be shown that for small flip angles β, the excitation profile of a pulse is well described by its Fourier transform.

To introduce the desired selectivity of the soft pulses, they are often applied with a specific shape. That means that the pulse amplitude, and sometimes also the pulse phase, is modulated as a function of time. Accordingly we call them shaped pulses. As an example, a Gaussian-shaped pulse is depicted in Figure 12.3b (dashed line). As mentioned in Section 11.4.3.2, the Fourier transform of a Gaussian is yet another Gaussian and the excitation profile of a Gaussian pulse is therefore also of Gaussian shape. As can be seen from Figure 12.3b, this effectively eliminates the side lobes at the expense of a somewhat broader excitation band when compared with a simple square pulse.

Shapes other than Gaussian shapes are also used, for example, pulses shaped like the first positive lobe of a sinc function. We will not discuss them here, but we wish to mention that the most commonly used shapes are already included in the acquisition software of the spectrometer, and their use can simply be specified as an attribute of a generic soft pulse. It only remains then to adjust the power level of the pulse. In short, for a pulse of constant phase, the impact is given by the integral

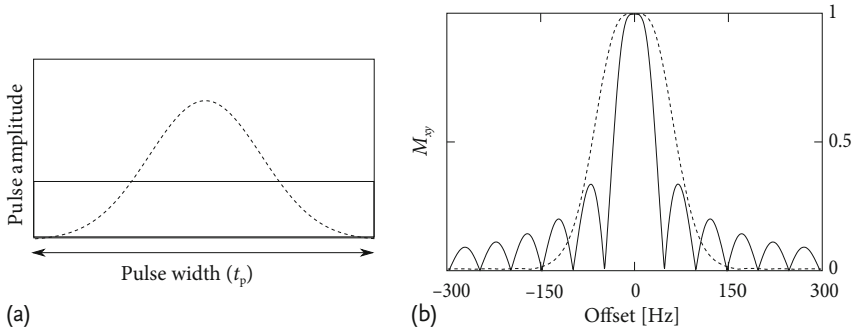

Figure 12.3 Comparison of the excitation profile of a Gaussian and a rectangular pulse. (a) The relative amount of transverse magnetization ($\sqrt{M_x^2 + M_y^2}$) as a function of resonance offset using selective pulses (20 ms) of square (solid line) or Gaussian (dashed line) shape as depicted in (b).

of the pulse shape (see (12.1)). The required pulse power for a shaped pulse is then calculated according to the integral ratio of the shaped and the square pulses. The hard 90° pulse is easily calibrated prior to the experiment (see Section 12.1.9). This calculation is usually accomplished by using appropriate spectrometer software.

12.1.4 Band-Selective RF Pulses

Band-selective pulses are a further class of shaped pulses. These pulses are designed to act on the spins within a certain frequency range exclusively without disturbing the spins outside that range. This is an essential prerequisite for many applications (e.g., in biomolecular NMR experiments). Ideally, the excitation profile of such pulses should look like a perfect "boxcar" function, with a uniform excitation within the selected frequency range and zero otherwise – a demand hardly met by the simple mathematical function usually used for line-selective pulses considered above. Thus, the shapes of band-selective pulses in general are a bit more complex and usually derived from computer optimization. One prominent example of such computer-optimized pulses is the family of *BURP* pulses (band-selective, uniform response, pure phase). Depending on their purpose, we distinguish between E (excitation), I (inversion), RE (refocusing), and U (universal rotation) BURP pulses. As an example, the pulse shape and the excitation profile of an E-BURP pulse are shown in Figure 12.4. Also belonging to this class are the *Gaussian cascade* (Q3 and Q5) pulses.

The band selectivity can be adjusted by the pulse duration. Again, short pulses result in broad excitation bandwidths and long pulses result in narrow excitation bandwidths. Furthermore, the pulse can be applied at any frequency offset by specifying the frequency of the shaped pulse as an additional acquisition parameter.

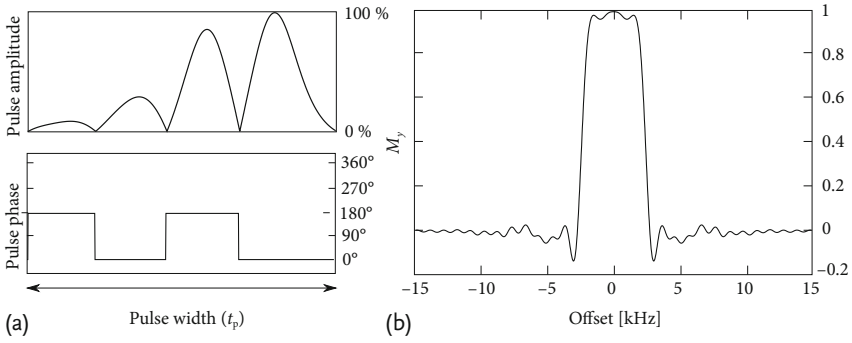

Figure 12.4 Pulse shape (a) and excitation profile (b) of an E-BURP pulse. With use, for example, of an E-BURP pulse of 1 ms duration, the spins are uniformly excited within a frequency band of about 4 kHz, while spins outside that range are virtually unaffected. In addition to the amplitude, the phase of the pulse is also altered, as depicted in (b).

12.1.5
Adiabatic RF Pulses

In order to selectively decouple or recouple spins from scalar spin–spin interactions, a number of hard 180° inversion pulses are often employed in heteronuclear experiments. If these pulses deviate from their nominal value of 180°, the inversion of the spin states is incomplete, and a considerable amount of signal may be lost and additional coherences may be created that may introduce artifacts.

As mentioned in Section 12.1.2, the relatively large spectral widths of some heteronuclei, especially when measured at higher magnetic fields, can easily result in large off-resonance errors of 180° hard pulses, making it necessary to replace them with more sophisticated RF pulses. Adiabatic pulses are very attractive because they achieve a very broad inversion bandwidth at comparably low power levels.

In adiabatic pulses the frequency of the RF field is swept over a large range, usually much larger than the spectral range of interest, as depicted in Figure 12.5. The term "adiabatic" indicates that the perturbation is slow so that the system can always follow the pulse. The *frequency sweep* has the effect that the effective field B_{eff} moves from the positive to the negative z axis or vice versa, describing an arc. As long as B_{eff} changes its direction (θ) much more slowly than the magnetization

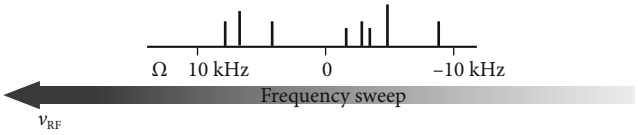

Figure 12.5 Frequency sweep in adiabatic pulses. The RF carrier is swept over the entire range of resonance frequencies.

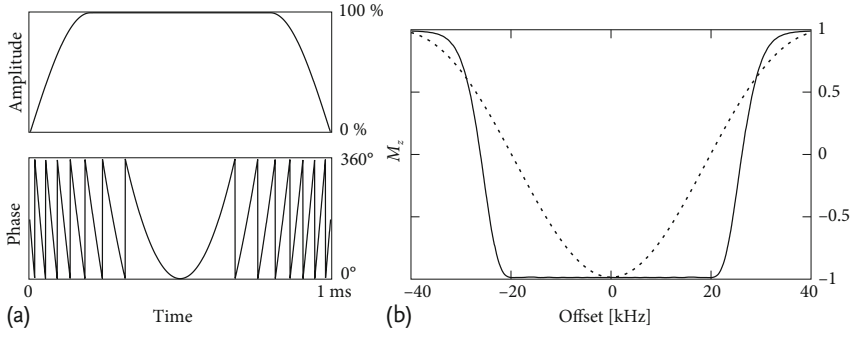

Figure 12.6 Shape (a) and inversion profile (b) of an adiabatic chirp pulse. A frequency sweep of 60 kHz and a pulse width of 1 ms (B_1 field 6.9 kHz) were used for the simulation. For comparison, the inversion profile of a 20 µs 180° hard pulse is indicated by the dashed line.

precesses around B_{eff}, so that the condition

$$\left|\frac{\mathrm{d}\theta}{\mathrm{d}t}\right| \ll |\gamma\, B_{\text{eff}}| \tag{12.3}$$

holds true, the magnetization will just follow the direction of the effective field and thereby is smoothly "dragged" from the positive to the negative z axis or vice versa. The slow perturbation is responsible for the term "adiabatic." Equation 12.3 is called the *adiabatic condition* and the process is known as an *adiabatic rapid passage*, in which the term "rapid" means that the inversion of magnetization is fast with respect to the relaxation times involved.

Thus, by applying the frequency sweep over a suitably large range, magnetization within a large range of offset frequencies can be inverted very accurately (Figure 12.6). In addition, because the adiabatic condition is maintained for a relatively large range of B_1 amplitudes, adiabatic pulses are quite insensitive to B_1 inhomogeneities (Section 12.1.8) and pulse miscalibration; in essence, the pulse power must be larger than a certain value. The frequency sweep is usually achieved by a phase modulation of the RF field throughout the pulse, as shown in Figure 12.6a.

The adiabatic full passage is best described in a rotating frame of reference that also undergoes the frequency sweep, such that the B_1 vector becomes static. To perceive how the magnetization evolves, we need to consider the effective field B_{eff}, which is the vector sum of the residual field B_0' and the RF field B_1. As an example, we follow a resonance that is 10 kHz off resonance starting from z magnetization and assume that the carrier frequency is linearly swept over a range from −25 to +25 kHz during the pulse. Accordingly, the rotating frame has an initial frequency of −25 kHz and a final frequency of +25 kHz. In this frame our particular resonance has an initial offset of 35 kHz, which decreases to a final value of −15 kHz and varies linearly in between, which results in a residual field B_0' along z. Together with the B_1 field, for which the amplitude is usually smoothed (see Figure 12.6a), the vector of the effective field B_{eff} describes an arc from the positive to the nega-

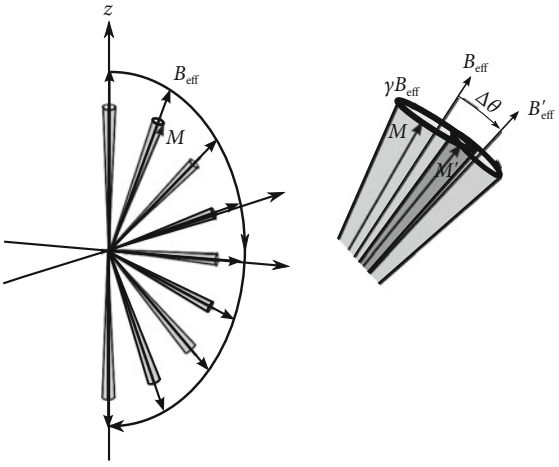

Figure 12.7 Principle of an adiabatic inversion pulse. The magnetization, initially along $+z$, is locked by the effective field. When the rotation about B_{eff} is fast with respect to the change in θ, the magnetization will remain nearly collinear to the effective field and is thus "dragged" to the negative axis.

tive z axis (Figure 12.7). The magnetization trajectory is then obtained by considering that the magnetization continuously precesses about B_{eff}. If the change in the direction of B_{eff} is much slower than the precession frequency of the magnetization, the adiabatic condition is fulfilled, and the magnetization is effectively spin locked along B_{eff} and is thus carried from the positive to the negative z axis, as depicted in Figure 12.7.

The "simple" adiabatic 180° inversion pulse considered above, where the carrier frequency is swept *once* through a certain frequency range, results in a point-to-point rotation (e.g., $M_z \rightarrow -M_z$) and therefore cannot be used as a 90° excitation pulse. Other point-to-point rotations (e.g., $M_x \rightarrow -M_x$) can be obtained by using composite adiabatic pulses where the frequency is swept back and forth several times. Although in fact there exist adiabatic pulses capable of rotating magnetization about any angle and any axis, so-called universal rotation pulses (e.g., the class of B1-insensitive rotation (BIR) pulses), they are not routinely used in NMR experiments.

12.1.6 Composite Pulses

Another possibility to overcome pulse imperfections is to use *composite pulses*. These are composed of a sequence of rectangular pulses of various widths and phases. The construction principle for these pulse cascades is that the errors of the individual pulses compensate each other, resulting in uniform overall rotations. One of the simplest composite pulses is the famous $90_x 180_y 90_x$ inversion pulse. The fate of magnetization starting from pure z magnetization for various

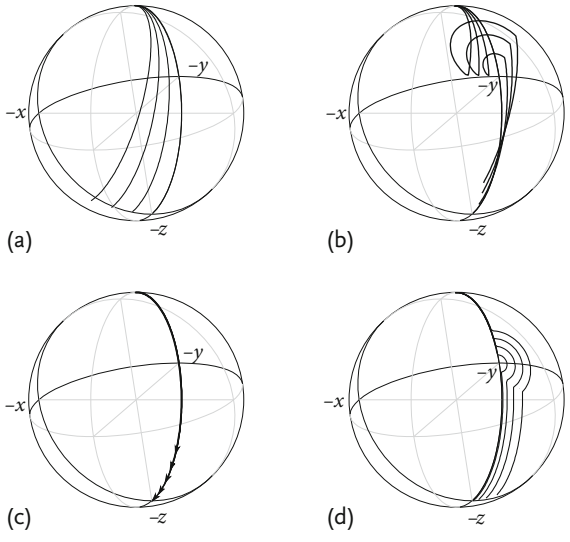

Figure 12.8 Improvement of the inversion performance using a $90_x\,180_y\,90_x$ composite pulse. The simulations shows Bloch-sphere trajectories starting from pure z magnetization for various pulse offsets (a,b) or B_1 mismatches (c,d) when using a single pulse (a,c) or a composite pulse (b,d). The pulse offsets are 2, 4, and 6 kHz at a B_1 field strength of 20 kHz. The B_1 mismatches result in effective 90° pulse angles of 70°, 75°, 80°, or 85°.

resonance offsets and when the pulse angle deviates from its nominal value is shown in Figure 12.8. It clearly demonstrates the benefits of the composite pulse. The central 180_y element largely compensates for the errors in the preceding and following 90_x elements. As a consequence the inversion bandwidth becomes much larger.

The $90_x\,180_y\,90_x$ composite pulse forms the central element of the *MLEV* decoupling sequences. Another often used element is the $90_x\,180_{-x}\,270_x$ pulse, which is used in the *WALTZ* decoupling schemes (Section 12.4.2).

12.1.7 Technical Considerations

12.1.7.1 Power Setting

While the pulse power in absolute terms is specified in watts (W), it is usually adjusted in relative terms using the decibel (dB) scale. The power P is related to the voltage U by $P = U^2/R$, with R denoting the resistance of the circuit. Since the B_1 field is proportional to U, the pulse power depends on the square of the RF field strength. For example, a 90° pulse of half the length requires a twice as large RF field (assuming a constant pulse angle) and hence four times as much RF power.

However, as mentioned above, the pulse power is usually adjusted using the decibel scale, which compares the actual power P relative to a reference value P_0 by

$$P_{\mathrm{dB}} = 10 \log_{10} \left(\frac{P}{P_0} \right)$$

As a rule of thumb, the power level must be changed by 6 dB in order to change the pulse width by a factor of two. Unfortunately, spectrometer manufacturers use the decibel scale in a different way, and sometimes the scale runs from −6 dB (full power) to +120 dB (zero output), while sometimes the scale is used in the opposite direction from 63 dB (full power) to 0 or −16 dB (zero output).

12.1.7.2 **Power Limitation**

As mentioned in Section 12.1.2, the pulse power can be increased only up to a maximum upper value. Usually the power limitation is dictated by the specifications of the RF coils, and the maximum allowed RF power for a specific coil is often found to be substantially lower than the maximum available RF power at the amplifier output, and also depends on the Larmor frequency of the nuclei of interest. It is important to note that these high power pulses should be applied only for very short durations and at relatively low pulse-repetition rates. For longer pulses the RF power needs to be substantially reduced. Pulsing with too high RF power can result in voltage breakdown (arcing) or even in destruction of the RF coil.

A further important point which must be considered when discussing power limitations is sample heating due to RF power dissipation. The electric field components of RF pulses can induce a considerable amount of sample heating. This must be clearly avoided because otherwise it can result in annoying effects such as frequency shifts of the resonances, instabilities in the lock system, wrong dynamic parameters such as relaxation time constants or diffusion coefficients, or in the worst case even sample degradation. In fact, sample heating is often the real limiting factor when considering RF power settings, especially during broadband decoupling and in spin-lock sequences (e.g., TOCSY), and is particularly troublesome for samples of high ionic strength (much salt). The occurrence of sample heating can often be recognized by a decrease in the amplitude of the lock level. The power dissipation is frequency dependent and tends to be larger for higher frequencies at similar power levels.

12.1.7.3 **Frequency-Shifted Pulses**

Many experiments require that pulses on one channel are applied at different frequencies. A typical application is to have selective pulses on both the C_α and carbonyl resonances during experiments. Instead of shifting the frequency of the channel back and forth, for technical reasons it is more convenient to shift the pulse by other means. This can be achieved by applying a certain phase increment $\Delta\phi$ to each slice of the selective pulse (see Figure 12.9). The phase increment required to achieve a frequency shift of $\Delta\nu$ is

$$\Delta\phi = 2\pi\Delta\nu\Delta\tau \tag{12.4}$$

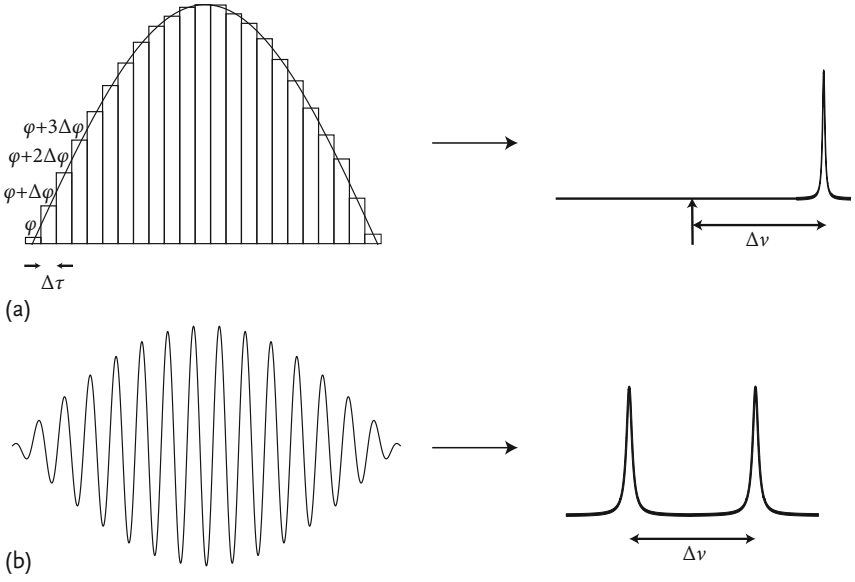

Figure 12.9 Phase- and amplitude-modulated pulses. Offset-shifted pulses are produced by shifting the phase of each slice of the pulse by a fixed phase increment (a). By multiplication of the amplitude of the pulse by a cosine function $\cos(2\pi\Delta\nu)$ the excitation band can be split in two (b). Note that the pulse power must be doubled in that case.

For completeness we also mention that a pulse can be split into two excitation bands by modulating the pulse amplitude with a cosine function.

12.1.8 Sources and Consequences of Pulse Imperfections

In this chapter we have learned about many different types of RF pulses. They are designed to transform the magnetization in a specific and accurate way. However, we have also seen that in practice it is not possible to achieve perfect pulse responses, neither for all resonances within a spectral range nor for all compartments within the active sample volume. As a brief summary, the sources of pulse imperfection are:

- off-resonance effects
- B_1 inhomogeneity
- misadjustment of pulse width and RF power.

Off-resonance effects and B_1 inhomogeneity are inherently given by the sample of interest (chemical shift range) and by the RF coil design, respectively, and there is not much we can do but to choose the most appropriate RF pulse. Imperfections due to misadjustment of pulse widths and RF power should be minimized by careful pulse calibration (Section 12.1.9).

To what degree pulse imperfections affect the quality of a spectrum depends on the type of experiment. The purposes of RF pulses are manifold: they are used to excite spins as in the case of the basic 1D experiment, but they are also applied for other tasks, for example, for refocusing of chemical shift and scalar coupling evolution, in order to transfer magnetization from one nucleus to another or to keep the magnetization along a specific axis (spin-lock pulses). Depending on the particular purpose, one or several of the following defects must be expected:

- reduced signal intensity
- additional signals (artifacts)
- phase distortions
- decoupling sidebands or residual spin–spin couplings.

12.1.9 RF Pulse Calibration

In order to minimize spectral artifacts in multipulse experiments due to pulse imperfections, the RF pulses have to be properly adjusted. You will usually find default pulse lengths and power level settings (as calibrated on a standard sample) stored in special setup files in your spectrometer. However, as the exact pulse widths may differ from sample to sample, depending on the particular sample conditions (solvent, temperature, ionic strength, and solute concentration), the RF pulses should be recalibrated for each new sample separately. For a given probehead, the largest influence is from different salt contents, followed by the solvent dependence. How much the pulse widths are influenced by the sample conditions depends on the nucleus (Larmor frequency) and whether the inner or the outer RF coil is used. The influence is largest for ^{1}H nuclei on the inner coil, in which case the pulse width may easily differ from sample to sample by 20% or more. Therefore, whenever the sample has been changed, the probe should be tuned and matched and at least the 90° ^{1}H high-power pulse should be recalibrated. While this can usually be accomplished on the sample of interest within a few minutes, it is mostly impractical for other nuclei such as ^{13}C and ^{15}N due to their much lower sensitivity, and therefore the pulse lengths as measured on a standard sample are usually used instead.

In most situations it is sufficient to calibrate the 90° high-power pulse and to calculate the power levels for the low-power pulses according to the values found for the hard pulse, assuming the amplifiers are highly linear. The method for determining pulses on the observe channel is different from that used for the other pulses because we can directly measure the signal, while we have to use indirect methods to calibrate pulses on the other channels. The observe channel is often also referred to as the transmitter channel, while the other channels are often called the decoupler channels. Many biomolecular NMR experiments use four different channels, with one of them dedicated to deuterium pulsing. Although the hardware of both channels is often virtually the same, the lengths of the pulses may slightly differ depending on whether they are applied on the observe or the decoupler channel.

12.1.10
Transmitter Pulse Calibration

The easiest way to determine the transmitter pulse is to perform a series of simple 1D experiments in which t_p, the duration of the pulse, is systematically increased. The pulse angle β is very small in the first experiment and becomes larger and larger as the pulse width is increased. The signal amplitude related to the amount of transverse magnetization will increase from an initially very small value to a maximum value when the entire magnetization is tipped to the xy plane, corresponding to a 90° pulse, and will decrease to zero for a 180° flip angle, become entirely negative for 270°, become zero again for 360°, and so on. In fact, as shown in Figure 12.10, if we plot the signal intensity versus pulse duration t_p, we obtain a sine according to $M_{xy} = M_{eq} \sin(\beta)$. During the experiment it is very important to chose the relaxation delay to be sufficiently long so that each scan starts from equilibrium z magnetization.

In principle, we could derive the required pulse width from a fit (Figure 12.10) but usually it is sufficient to search close around a characteristic point. Because the maximum of a sine curve is flat and hence cannot be determined accurately, we look for the zero crossing of the signal. It is better to determine the 360° pulse because then magnetization is already close to the equilibrium value at the end of the scan and the determination is less prone to errors due to incomplete T1 relaxation. In practice the procedure is as follows:

1. Look up the approximate value of the 90° pulse on the particular probehead.
2. Set up a standard 1D experiment, set the pulse length to a value shorter than t_{90}, run the experiment, and adjust the phase of the spectrum as usual.
3. Set t_p to a value that is about four times the expected value of the 90° pulse, run the experiment, but use the previously determined value for the phase correction during processing.
4. If the signals are positive, thus the flip angle is larger than 360°, decrease t_p a bit. On the other hand, if the signals are negative, increase the pulse length a bit and record another spectrum.
5. Repeat the previous step until you observe no or very small dispersion signals. The 90° pulse will then be one quarter of the actual t_{360} value.

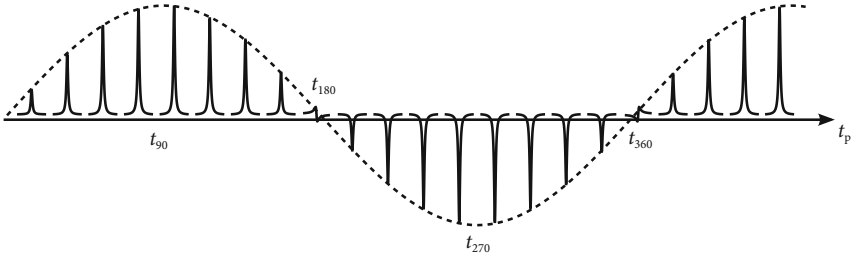

Figure 12.10 Dependence of signal intensity on pulse width t_p using the basic one-pulse experiment. The plot of a single resonance line versus pulse width describes a sine curve.

12.1.11
Decoupler Pulse Calibration (^{13}C and ^{15}N)

Since it is impossible to detect the signal via the decoupler channel, we need to calibrate the decoupler pulses in an indirect way. An elegant method to determine ^{13}C and ^{15}N decoupler pulses is to observe the influence of the decoupler pulse on an antiphase doublet. The pulse sequence is shown in Figure 12.11a. The initial ^{1}H pulse creates transverse ^{1}H magnetization that evolves during a time period of $1/(2J_{HX})$ into antiphase magnetization with respect to X (e.g., ^{13}C or ^{15}N):

$$I_z \overset{90^{H}_{x}}{\rightarrow} -I_y \overset{\tau}{\rightarrow} 2I_x S_z \tag{12.5}$$

The transmitter frequency is usually set to the middle of the multiplet, such that the shift offset is zero. The term with the two spin operators is called antiphase magnetization (see Section 8.1). Application of a 90° pulse on the decoupler (*X*) channel will convert this term quantitatively into multiple-quantum coherences (second term on the right in (12.6)), a form of magnetization that does not give rise to a detectable signal:

$$2I_x S_z \overset{\beta^{X}_{x}}{\rightarrow} 2I_x S_z \cos(\beta) - 2I_x S_y \sin(\beta) \tag{12.6}$$

When the decoupler pulse is exactly 180°, the doublet components are inverted. The dependency of the doublet intensities as a function of the decoupler pulse width is depicted in Figure 12.11b.

A sample often used to calibrate ^{13}C and ^{15}N decoupler pulses consists of a mixture of ^{13}C-labeled methanol and ^{15}N-labeled urea in dimethyl sulfoxide-d_6. When the appropriate pulse sequence is used, and after the spectrometer routing has been set and the probe has been properly tuned (transmitter and decoupler channels!), the procedure is as follows:

1. Set the pulse widths and power levels according to the standard values for high-power 90° pulses on the probe used. Set the transmitter and decoupler frequencies on-resonant with respect to the multiplet of interest.
2. Set the pulse width of the decoupler pulse close to zero so that the flip angle is very small. Record a spectrum and phase it to obtain an absorptive antiphase doublet for the signal of interest.

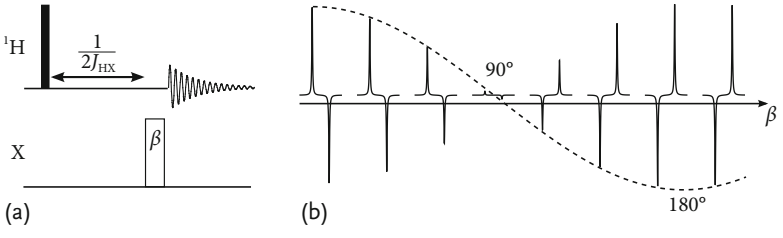

Figure 12.11 Decoupler pulse calibration. Variation of the pulse width of the RF pulse applied to the X channel (β) in the pulse sequence (a) alters the intensity of the ^{1}H antiphase doublet (b).

3. Set the decoupler pulse close to the nominal 90° pulse width.
4. Record a spectrum and inspect the doublet components. If they are still of same phase but with lower overall intensity, increase the duration of the decoupler pulse a bit. If the phase of the doublet component has changed, decrease the pulse duration a bit.
5. Continue with step 4 until the doublet components become virtually zero, and thus the 90° decoupler pulse width is found.

12.2 Pulsed Field Gradients

Usually we make a big effort to improve the field homogeneity by careful shimming so that the magnetic field within the active sample volume is as homogeneous as possible in order to obtain narrow line widths. However, sometimes it is useful to destroy the field homogeneity for a specific amount of time by applying a *pulsed field gradient* (PFG). Modern NMR spectroscopy makes excessive use of PFGs. Field gradients are an additional tool to manipulate magnetization in a specific way. By using PFGs, we can select or reject particular coherences. Because of this spectra can be recorded using shorter phase cycles, resulting in a much reduced experiment time and often also in spectra with fewer artifacts.

PFG technology was developed in the field of imaging. Here field gradients are used for spatial frequency and phase labeling to achieve spatial selection. As mentioned in Section 10.2.3, application of gradients allows us to map the B_0 field, a feature used in gradient shimming. Measurements of diffusion are other experiments that are based on spatial phase labeling using field gradients.

12.2.1 Field Gradients

Following application of a field gradient, the magnetic field varies in one or more directions within the sample. To a good approximation the gradient can be considered as constant over the sample volume and hence the field changes linearly. The gradients are produced by so-called gradient coils enclosing the sample and located in the probeheads (Figure 10.7). Depending on the type of probe, field gradients can be applied in all three spatial directions x, y, and z, or in the z direction only. For most applications it is sufficient to have a gradient in the z direction, the long axis of the sample tube. For simplicity, we will in the following consider that case only.

If we choose the center of the RF coil as the origin ($z = 0$), the effective magnetic field along z during the application of a field gradient is

$$B_{(z)} = B_0 + Gz \tag{12.7}$$

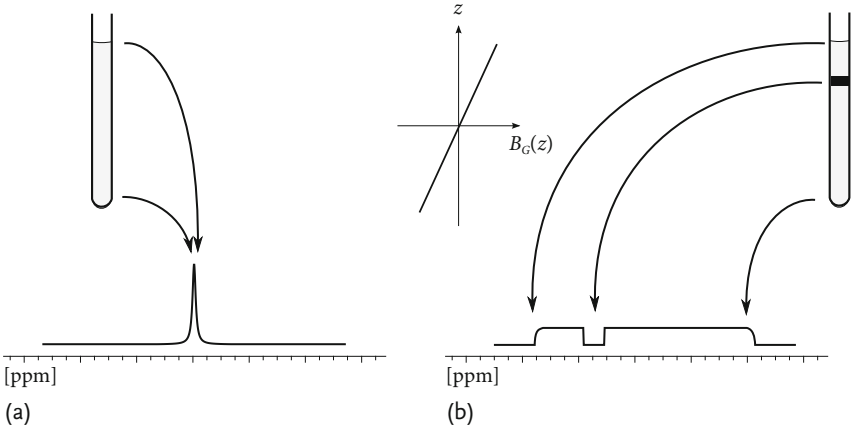

Figure 12.12 Spatial frequency encoding due to a gradient field. In the absence of a field gradient, all spins of a particular resonance experience the same magnetic field strength and accordingly have the same precession frequency, giving rise to a single narrow line (a). Application of a field gradient results in a frequency discrimination of spins according to their location along *z*. Placing a phantom into the sample will eliminate signals from those slices and accordingly also from the corresponding part of the spectrum (b).

where G is the gradient strength, which is normally given in gauss per centimeter (G/cm) (gauss is the "old" cgs unit for the magnetic field; $1\,\mathrm{G} = 10^{-4}\,\mathrm{T}$). The gradient can be applied with both polarities, which means G can be positive or negative. For example, for a positive G, the magnetic field strength is reduced at the bottom of the sample and enhanced at the top, while it varies linearly in between (see Figure 12.12). Accordingly, the precession frequencies become a function of the position of the spin along z. This can be easily observed by acquiring a spectrum while a gradient is applied. Especially suited are samples that give rise to a strong, single resonance, for example, a sample of pure water. According to the frequency distribution over the sample in the presence of a gradient, the spectrum will show a broad signal, as shown in Figure 12.12b. If we were to put a solid disk into the sample, we would observe a gap in the spectrum at the corresponding frequencies. While this example illustrates the basic principle of the imaging technique used in MRI, in NMR experiments the field gradients are usually applied not during signal acquisition, but for short time periods (on the order of milliseconds) throughout the pulse sequences, as PFGs.

12.2.2 Using Gradient Pulses

Field gradients cause the precession frequency to become a function of the location of the spins. If the sample is divided into thin slices along the z axis, the magnetization within each slice precesses at a different frequency, resulting in a dephasing of xy magnetization, as depicted in Figure 12.13. Note that z magnetization is not affected by PFGs. To what amount the magnetization is dephased depends on the

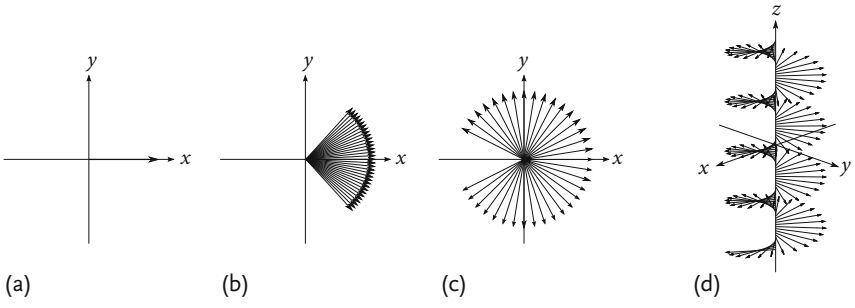

Figure 12.13 Dephasing of magnetization due to pulsed field gradients (PFGs). (a–c) The progressive dephasing of the *xy* magnetization vectors (when looking along the *z* direction) during a PFG. (d) If a gradient pulse of sufficient strength and duration is used, the magnetization becomes completely dephased and the vectors acquire a phase dependency along *z*.

strength (G) and the duration (τ_G) of the gradient pulse, as well as on its gyromagnetic ratio. The phase angle due to a gradient pulse depends on its vertical position along the z axis and is given by[1)]

$$\phi_{(z)} = \gamma G z \tau_G \tag{12.8}$$

By application of powerful gradient pulses, magnetization in the xy plane can be completely dephased such that the net magnetization becomes zero. A simple calculation is given in Excursus 12.1. PFGs act onyl on transverse magnetization. Using strong PFGs, we can, for example, destroy transverse magnetization while retaining the magnetization of interest that is stored along z.

Gradient pulses are often applied in pairs. Thereby, a first gradient pulse is used to dephase magnetization and a second gradient pulse, applied later, rephases the magnetization. In the simplest case, when no RF pulse is applied in between, we can refocus magnetization simply by applying the second gradient with inverted polarity, so the net effect of both gradients becomes zero for each spin. Another, more often encountered example of using gradients in pairs is the suppression of pulse imperfections in echo sequences as depicted in Figure 12.14 and described in more detail in Section 12.8.2.1. Flanking a 180° pulse with two gradients allows us to eliminate effects from imperfect 180° pulses. This is the case because the

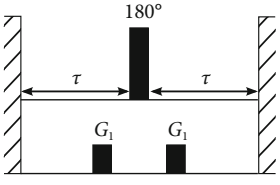

Figure 12.14 PFGs in spin-echo sequences. The pair of gradient pulses G_1 removes xy magnetization resulting from imperfections of the 180° RF pulse.

1) The dephasing from PFGs is also proportional to the order of coherences, for example, twice as large for proton double-quantum coherences. For simplicity we only look at the effects on observable magnetization (single-quantum coherences) here.

dephasing or rephasing effect is proportional to the coherence order. A 180° pulse inverts the coherence order, and only then the second gradient pulse refocuses the magnetization correctly.

As we will see in Section 12.3, we can eliminate the problems from pulse imperfections also by phase cycling. However, as the pulse sequence must be repeated with different phases in order to cancel the unwanted signals, this extends the total experiment time.

Excursus 12.1: A Simple Calculation of Signal Attenuation by PFGs

Assume, for example, we wish to know to what degree ^{1}H magnetization is attenuated by a gradient pulse of 50 G/cm and 1 ms duration. For that we need to calculate the phase twist over the active sample volume caused by the gradient. Let us assume the active sample volume along z is 2 cm. So the difference of the gradient field over that volume is 100 G. Using the fact that the magnetic field of a 600 MHz magnet is about 14 T (equivalent to 140 000 G), the field difference of 100 G corresponds to a frequency difference of $100 \times \frac{600\,000\,000}{140\,000} \approx 400\,000$ Hz. Multiplication by the duration of the gradient pulse (1 ms) gives a phase twist of about 400 turns. Magnetization within each turn will cancel, and only the last turn, which might not be complete, results in observable magnetization. Thus, the signal is attenuated by a factor of at least 400. A more detailed calculation reveals that the attenuation is even better by a factor π.

12.2.3 Technical Aspects

12.2.3.1 Gradient Recovery Delay

The fast rise and drop of the gradient field at the beginning and end of a rectangular gradient pulse triggers disturbances, so-called eddy currents, that are induced in conducting material close to the gradient coil. Such *eddy currents* produce disturbing magnetic fields, resulting in spectral artifacts. To prevent this, we have to wait until the eddy currents have decayed, and a delay, the so-called gradient recovery delay, must be inserted after each gradient pulse. These delays should be kept as short as possible. Alternatively, gradient pulses are often employed with a particular shape (e.g., a half sine lobe), to reduce the fast rise and drop at its edges and hence the eddy currents, permitting us to use shorter recovery times (typically some hundred microseconds or less).

12.2.3.2 Gradient Strength

For conventional high-resolution liquid-state probes, the maximum gradient strength is usually around 50 G/cm. For probes used for diffusion (Section 12.8.2.2) and imaging applications, the gradient strengths are usually substantially higher. The strength of a gradient pulse is set as a percentage of the maximum strength. The exact strength is, except for diffusion measurements, of minor importance.

However, it is important that the gradient pulses are applied at correct *relative* strengths. Often numerous gradient pulses are applied throughout a pulse sequence, and to prevent unwanted coherences being refocused by chance, they need to be applied at special ratios. Gradient pulses at high strength should never be applied for more than a few milliseconds.

12.2.3.3 Disturbances on the Lock

Field gradients will also affect the deuterium signal used by the field-frequency lock system (Section 10.5). This can be easily observed by the collapse of the lock signal when gradient pulses are applied. The lock circuit cannot work properly during application of PFGs and therefore the lock must be temporarily inactivated when PFGs are applied to prevent misregulation. The lock is then reactivated for periods that are free of field gradients, normally during acquisition and the interscan delay.

12.3 Phase Cycling

Phase cycling is a procedure in which an NMR experiment is repeated with identical pulse widths and delays, but for which the phases of the pulses are changed in a systematic manner. Phase cycling is employed to overcome pulse imperfections and imbalances in the quadrature detector (in older spectrometers) and for the purposes of coherence selection. The different types of coherences are affected by changes in the phases of RF pulses in different ways. By varying the pulse phases in concert with the receiver phase from scan to scan, we can determine which signals will coherently add up and which signals will cancel. The 2D DQF-COSY and NOESY experiments both use three 90° pulses but their information content is very different. The major difference between these two experiments is the phase cycle on the 90° pulses. Thus, a successful outcome of an experiment depends on proper phase cycling. Even if you do not plan to develop your own NMR experiment, it is still important that you can understand how many steps the phase cycle contains.

12.3.1 The Meaning of Phase Cycling

A pulse sequence may include one or several RF pulses. For each of them we can specify a phase (ϕ) defining the pulse axis in the rotating frame (Section 12.1.1). In addition we specify the phase of the receiver (ϕ_{rec}) (see Excursus 12.2). When we record more than one scan, the phases of all RF pulses as well as the receiver phase may be altered independently. This is called phase cycling. Thus, for each RF pulse and the receiver, an individual phase scheme can be employed. For example, if the phase scheme [$x\ y\ -x\ -y$] is associated with an RF pulse, the pulse will be applied along the x axis in the first scan, along the y axis in the second scan, along

the $-x$ axis in the third scan, and along the $-y$ axis in the fourth scan. For further scans the scheme will be repeated again. The length of a phase cycling scheme usually corresponds to a power of 2 and can be as long as 32 or more in rare cases. For many experiments it is essential that full phase cycles are always employed, which means that the number of scans must correspond to the longest phase cycle scheme used in an experiment or must be a multiple thereof. If a phase cycle is four steps long, you may perform a multiple of four scans per increment. Four scans is okay, so are eight scans. If you use six scans on the other hand, the spectra will contain more artifacts than with four scans.

Excursus 12.2: The Receiver Phase

Whereas the meaning of phases regarding RF pulses should already be quite clear, the phase of the receiver might need additional explanation at this point. Technically, the receiver phase denotes the phase setting of the reference signal used to down-mix the NMR signal in the quadrature detector (Section 11.3.1). Remember, as the source of RF pulses and the receiver reference signal a single RF signal produced by a master quartz is used. Pulse and receiver phases are then subsequently adjusted by applying appropriate phase shifts to the reference signal. This defines the pulse axis and the axis of signal acquisition in the rotating frame of reference. That is to say, the receiver phase defines the position of an "observer" in the rotating frame. Depending on its position, the observer will experience the rotating magnetization differently.

To better understand phase cycling let us look at Examples 12.1 and 12.2.

Example 12.1

In a first example we will look at the simplest pulse sequence, the one-pulse sequence consisting of a recycle delay, a single 90° RF pulse, and the acquisition period. In a first case let the phase scheme of the RF pulse be $[y\ -x\ -y\ x]$ and the receiver phase be constant. Thus, the observer will perform the observation in each scan from the same direction; arbitrarily we place the observer next to the x axis. The experiment is illustrated in Figure 12.15. According to the phase scheme, the magnetization will flip to the x axis in the first scan, to the y axis in the second, to the $-x$ axis in the third scan, and to the $-y$ axis in the fourth scan. The corresponding signals after Fourier transformation are shown in the lower traces. Clearly when adding up, the signal will cancel.

Now we will alter the receiver phase in concert with the pulse phase still being $[y\ -x\ -y\ x]$. As can be seen in Figure 12.16, the observer now follows the magnetization vector in each subsequent scan, and thus in each scan will perform the same observation, resulting in a coherent addition of the signal.

Scan	1	2	3	4
Pulse phase	Y	$-X$	$-Y$	X
Receiver phase	X	X	X	X

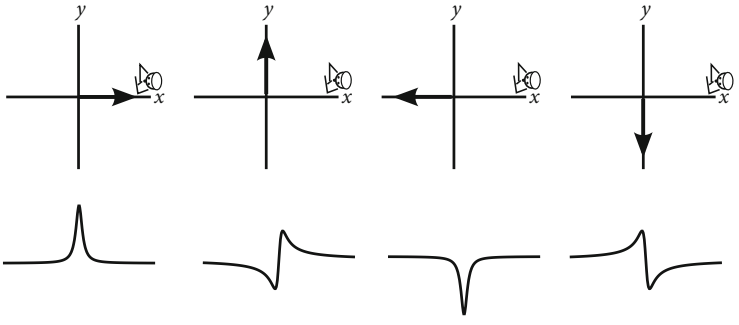

Figure 12.15 Illustration of the basic principle of phase cycling using a one-pulse experiment. When the pulse phase is incremented by 90° from scan to scan while the receiver phase is constant, the total signal will cancel every fourth scan.

You may now think, fine, we get four times the signal, obviously the same as if the pulse and receiver phase had been kept constant. So why the effort? In this case just think about what would happen if there would be, for whatever reason, an additional resonance in the *xy* plane not affected by the RF pulse, and which is of no interest to us and which should therefore be eliminated. This brings us to Example 12.2.

Scan	1	2	3	4
Pulse phase	Y	$-X$	$-Y$	X
Receiver phase	X	Y	$-X$	$-Y$

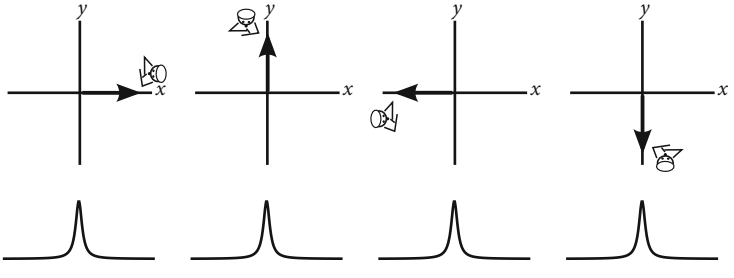

Figure 12.16 Phase cycling using the one-pulse experiment when the receiver phase is altered in concert with the pulse phase. In that case the signal will add up in a constructive way.

Example 12.2

Let us assume that we have net magnetization of two spins with resonances A and B. Resonance A is along z, and resonance B is found in the xy plane, as shown in Figure 12.17a. Such a state can be the result of a preceding pulse sequence. Now suppose our goal is to observe only resonance A in the final spectrum. Obviously we need to bring magnetization of resonance A by a 90° RF pulse into the xy plane, for example, by applying a 90° pulse along x to rotate it onto the $-y$ axis. At the same time the y component from resonance B is rotated to the z axis so that only the x component from resonance B resides in the xy plane (Figure 12.17b). Thus, prior to acquisition, the xy magnetizations of resonances A and B are orthogonal such that both signals are 90° out of phase in the spectrum. If we now repeat the experiment but use a 90° pulse along $-x$, resonance A is tipped to the y axis, while the x component of resonance B still remains along x (Figure 12.17c). Again the two magnetization vectors are 90° out of phase with respect to each other, but magnetization of resonance A is inverted with respect to the first scan, while magnetization of resonance B is not inverted. Inverting also the receiver phase gives a spectrum in which signal A has the same phase as in the first scan, while signal B is 180° out of phase between the two scans. Adding the two spectra will eliminate signal B.

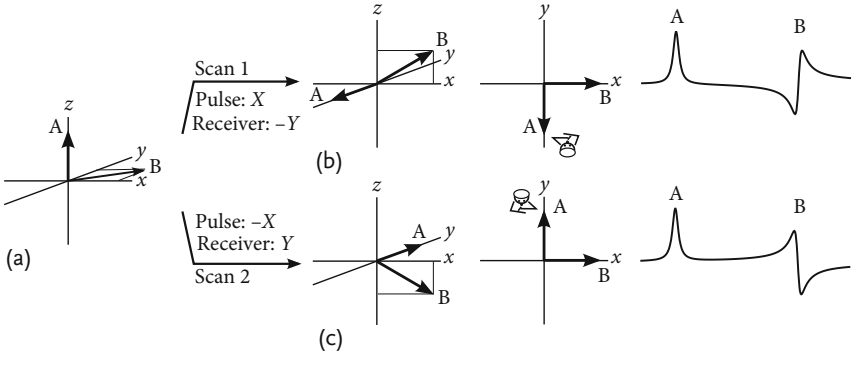

Figure 12.17 An advanced example of phase cycling. When magnetization (a) is affected by RF pulses with phases altered in a different way, by proper choice of the receiver phase we can influence which signals add up or cancel (b,c).

Writing phase cycles is an art on its own. Simple rules determine how to select changes in coherence order and so on. This is explained in more detail in Section 13.9.1.

12.4
Decoupling

By decoupling we remove the line splitting due to the scalar interaction so that for each resonance a single line at its chemical shift is observed. Although a certain amount of information is lost by this procedure, this is often more than compensated by an intensity gain and the much simplified spectra. Depending on the purpose of decoupling, we have to distinguish between heteronuclear, homonuclear, broadband, and selective decoupling. In this section we will focus on methods of heteronuclear broadband decoupling that are widely used, for example, as a standard in ^{13}C NMR spectroscopy.

12.4.1
How Decoupling Works

For the sake of simplicity we will discuss the principle of decoupling by considering an isolated heteronuclear pair of two spins I and S mutually coupled by the scalar coupling constant J. For example, I could be the ^{13}C spin and S the ^{1}H spin in a CH group. Imagine we wish to observe spin I while removing the line splitting due to coupling with the S spin. The splitting is related to the two possible spin states of S, α (spin up) and β (spin down), and therefore we simply need to ensure that the two states are interchanged much more frequently than the two components of the I spin diverge. This can be achieved by applying a series of 180° RF pulses to the S spins, as shown in Figure 12.18. The continually applied spin-flips of the S spins results in an averaging of the I spin precession frequencies such that a single line at its chemical shift is observed.

Unfortunately this is not the end of the story and there are some more important points we need to consider. Strictly speaking, the consideration above applies only when the carrier of the decoupler channel is exactly on-resonant on the S spins such that the spins are properly inverted by the decoupler pulses. When the spins are off-resonant, the spin inversion will be incomplete, resulting in residual line splittings or line broadening. Furthermore, to prevent sample heating and damage to the RF assembly, the decoupler pulses must usually be applied at relatively low power levels, which increases off-resonance effects of the pulses. Therefore, the

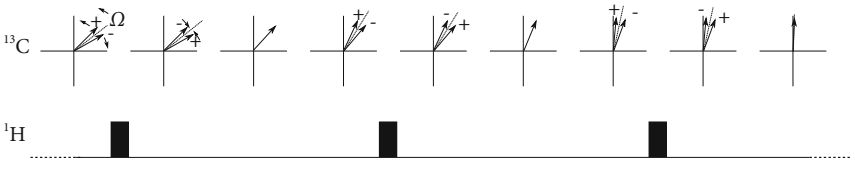

Figure 12.18 Principle of decoupling. In the upper panel the two components of a ^{13}C doublet are shown, one precessing with $\Omega + J/2$ (labeled with +) and the other with $\Omega - J/2$ (labeled with −). Applying 180° pulses to the ^{1}H spins will interchange the doublet components and therefore the − and + labels. This causes a cancellation of the J evolution, and the magnetization evolves solely by its chemical shift.

application of a series of simple 180° pulses is not a good choice and we need to use more powerful techniques as described below.

12.4.2 Composite Pulse Decoupling

A simple thing we can do in order to improve the efficiency of decoupling is to replace the 180° decoupler pulses by composite pulses. As described in Section 12.1.6, composite pulses invert the magnetization over a wider frequency range compared with a single 180° pulse. Importantly, for a cascade of such composite pulses, the inversion bandwidth can be further improved by a systematic variation of the pulse phases. Denoting the basic composite pulse element by R and the composite pulse with inverted pulse phases by $\overline{R}$, we can express the decoupler sequence by a series of R and $\overline{R}$ elements. For example, the sequence $R\,R\,\overline{R}\,\overline{R}$ with $R = 90_x180_y90_x$ corresponds to the MLEV-4 decoupler sequence, named after its contributor Malcolm Levitt. A cycling permutation of the elements in the MLEV-4 block will further improve the efficacy of decoupling and results in the supercycle of the MLEV-16 decoupling scheme $R\,R\,\overline{R}\,\overline{R}\ \overline{R}\,R\,R\,\overline{R}\ \overline{R}\,\overline{R}\,R\,R\ \ R\,\overline{R}\,\overline{R}\,R$. The WALTZ-16 decoupling scheme, which surpasses the decoupling bandwidth of MLEV-16 (see Table 12.1), makes use of a $90_x180_{-x}270_x$ composite pulse as the basic 180° rotation element R. A decoupling sequence that gives even larger decoupling bandwidth is GARP (globaly optimized alternating phase rectangular pulses), which was derived from a computer optimization, and its basic rotation element consists of 25 pulses. Because of its outstanding bandwidth, GARP is often used for X-nuclei decoupling in ^{1}H detected heteronuclear correlation experiments (e.g., HSQC) where the chemical shift range of X may encompass several tens of kilohertz (e.g., 30 kHz for ^{13}C with a 600 MHz magnet). As the magnetic field strengths becomes larger, the absolute spectral widths in hertz also become larger and more effective decoupling sequences are required to keep the decoupling power at reasonable levels. An attractive solution for that is to use adiabatic pulses for decoupling.

Table 12.1 Performance of some selected decoupling sequences. The bandwidth factor multiplied by γB_2 (where B_2 is the decoupling field strength) gives the bandwidth over which decoupling is effective (signal intensity is at least 80% of the fully decoupled signal).

Sequence	Bandwidth factor	Residual line broadening	Typical applications
MLEV-16	1.5	Large	Not used for decoupling any longer
WALTZ-16	2.0	Small	^{1}H decoupling
GARP	4.8	Moderate	X-nuclei decoupling
DIPSI-2	1.2	Very small	Decoupling in the presence of homonuclear interactions

When the nuclei from which we wish to decouple themselves show large *J* couplings among themselves, conventional decoupling sequences such as MLEV and WALTZ will work less effectively and sequences have been developed that take such homonuclear interactions into account. They are known as decoupling in the presence of scalar interaction (DIPSI) sequences.

12.5 Isotropic Mixing

Many decoupling sequences can also be used to transfer magnetization along a homonuclear spin system as is required in the TOCSY experiment discussed in Section 17.4.2. In this context the sequences are called *isotropic mixing* or *TOCSY spin-lock* sequences, and their ultimate goal is to suppress chemical shift evolution so that the spins become strongly *J* coupled. Under this condition, magnetization can flow from one spin to another.

TOCSY mixing sequences in widespread use are MLEV-17, WALTZ-16, DIPSI-2, and FLOPSY-16 (FLOPSY is the acronym for flip-flop spectroscopy). The seventeenth element of the MLEV-17 sequence is a 60° pulse that compensates for phase imperfections in the preceding 16 elements. The mixing sequences differ mainly in their transfer efficiency, the shift range over which magnetization transfer is effective (how large the shift difference of two spins can be), and to what extent T1 and T2 relaxation during the mixing sequence matters.

12.6 Solvent Suppression

Usually highly deuterated solvents (typically more than 99.9% ^{2}H) are used in liquid-state NMR experiments. This is for two reasons: firstly, the deuterium signal is used by the lock system; secondly, the use of deuterated solvents prevents the occurrence of very intense solvent signals, which otherwise would dominate the proton NMR spectra. However, sometimes solvents of much lower deuterium concentration must be used. For example, if a compound with labile protons is dissolved in pure D_2O, all labile protons will be exchanged for deuterium and hence will be absent in an ^{1}H NMR spectrum. Therefore, a mixture of D_2O/H_2O (e.g., 10% D_2O and 90% H_2O) is usually used for such compounds (e.g., carbohydrates, proteins or nucleic acids). Another example is liquid chromatography (LC)-NMR spectroscopy, where for economic reasons the LC solvent often comprises a mixture of protonated solvent and the much more expensive deuterated solvent. Moreover, sometimes the sample itself contains a huge ^{1}H resonance, for example, when biofluids are investigated by NMR spectroscopy (metabonomics). In all these situations we need efficient methods to suppress the solvent signal.

12.6.1
Presaturation

For presaturation the water resonance is selectively saturated by application of a weak (about 50 Hz), continuous RF field on the water signal. The carrier is placed exactly on-resonant at the water frequency and the saturation field is applied throughout the interscan delay for about 1–3 s (Figure 12.19a). The saturation occurs due to T1 and T2 relaxation during the time the water magnetization rotates about the RF field, and due to inhomogeneities in the B_1 field strength over the sample volume. The latter causes a variation in the spin's precession frequency about the B_1 field and thereby dephases the magnetization as shown in Figure 12.19b.

Presaturation is widely used in routine work; an example is depicted in Figure 12.20a. It is easy to implement and the only parameter which must usually be adjusted is the carrier frequency. However an excellent shim (B_0 field homogeneity) is required for this method to work properly. Further disadvantages are that exchanging protons may become partially saturated because of *saturation transfer* and that signals close to the solvent line may be suppressed. The resulting unde-

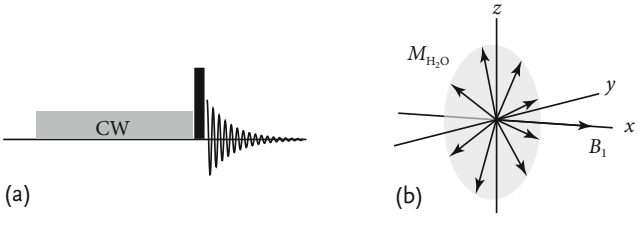

Figure 12.19 Solvent suppression by presaturation. (a) The solvent magnetization is saturated by applying a weak continuous RF field during the interscan delay. (b) The dephasing effect due to B_1 inhomogeneity. CW continuous wave.

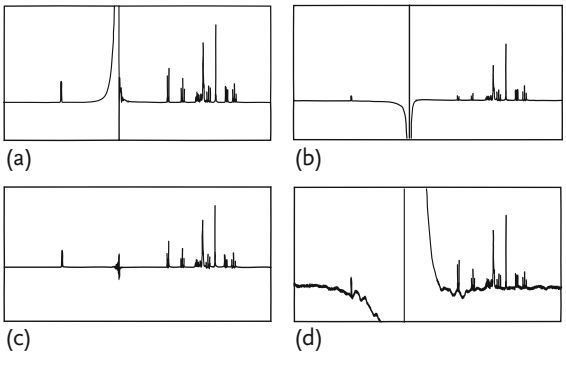

Figure 12.20 Water suppression using presaturation (a), water suppression through gradient-tailored excitation (WATERGATE) (b), and excitation sculpting (c) compared to the spectrum without water suppression (d).

sired signal attenuation can be so severe that presaturation is unsuitable in some applications (e.g., for proteins at elevated pH), and other methods, as discussed in the following sections, must be used.

12.6.2
Water Suppression through Gradient-Tailored Excitation

The water suppression through gradient-tailored excitation (WATERGATE) sequence exploits the fact that in a PFG spin-echo sequence only resonances become rephased for which the magnetization has been inverted in the center of the echo. Thus, if we invert the magnetization of all solute spins but not magnetization of the water spins, the solute magnetization is rephased by the second gradient pulse, while the water magnetization is dephased even further. In practice there are two approaches by which the selective inversion is achieved. One is to use a 180° hard pulse flanked by two 90° selective pulses as shown in Figure 12.21a. The two selective pulses applied to the water signal together with the hard pulse result in a 360° rotation (and thus in zero net rotation) for the water magnetization, while the magnetization of the solute signals, which is only affected by the hard pulse, is rotated by 180°.

The other approach uses a cascade of hard pulses, a so-called binomial pulse. For example, the 3-9-19 binomial pulse shown in Figure 12.21b will do the job. Binomial pulses produce zero excitation at zero offset frequency and at multiples of $1/\tau$ Hz, where τ is the interpulse spacing. Therefore, if τ is set in such a way that the first zeros occur outside the spectral range of interest, all "observed" solute spins are inverted, while the on-resonant water spins are not inverted. Binomial pulses produce a narrower notch in the excitation profile when compared with shaped pulses, and therefore resonances close to the water are less attenuated. Further benefits are that no soft pulses need to be calibrated, and that by small modifications the sequence can also be used for off-resonance water suppression. A disadvantage is that signals with large offsets may be attenuated due to the additional notches at multiples of $1/\tau$ Hz in the excitation profile. An example of a spectrum employing WATERGATE suppression is shown in Figure 12.20b.

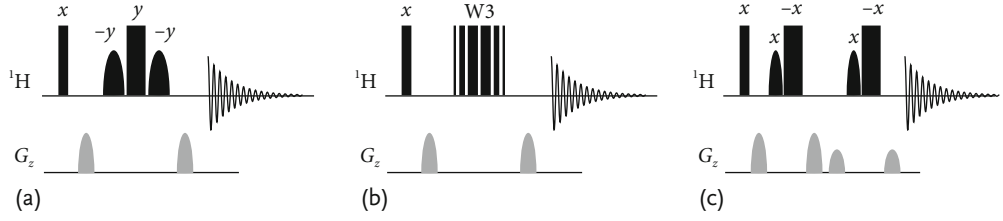

Figure 12.21 Sequences for water suppression: (a) WATERGATE using selective 90° pulses, (b) WATERGATE using 3-9-19 binomial pulses (W3), and (c) excitation sculpting. The binomial pulse train W3 consists of six hard RF pulses of $3\alpha_x - \tau - 9\alpha_x - \tau - 19\alpha_x - \tau - 19\alpha_{-x} - \tau - 9\alpha_{-x} - \tau - 3\alpha_{-x}$, with $\alpha = 90°/13$. Note that the soft pulses in the WATERGATE sequence are 90° pulses and in the excitation sculpting sequence are 180° pulses.

WATERGATE elements are usually placed at the end of the pulse sequence just before signal acquisition starts. Saturation transfer is therefore less critical when compared with the presaturation method.

12.6.3 Excitation Sculpting

The excitation sculpting sequence for solvent suppression is shown in Figure 12.21c. It is similar to the WATERGATE sequence discussed above. However, the use of a double spin echo results in spectra with less phase distortion and superior water suppression (Figure 12.20c). Furthermore, the sequence is very robust against miscalibration of the soft pulses. A disadvantage is that the sequence is twice as long and less selective when compared with the WATERGATE sequence.

12.6.4 WET

WET solvent suppression is often used in LC-NMR spectroscopy. The solvent signal is suppressed by means of four selective RF pulses, each followed by a PFG, as shown in Figure 12.22. The subsequent use of four selective pulses of different pulse angles largely cancels out the effects of B_1 inhomogeneity and T1 relaxation and results in superior spectra when compared with the use of a single 90° selective pulse. By modulation of the shaped pulses (Section 12.1.7.3), solvent signals at multiple sites can be suppressed simultaneously as is often required for the solvent mixtures in LC-NMR spectroscopy. The ^{13}C satellites that often remain as the strongest signals are best suppressed by ^{13}C decoupling during the selective pulses.

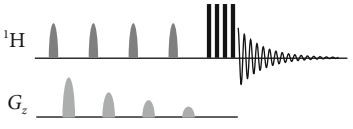

Figure 12.22 The WET scheme for solvent suppression. The solvent magnetization is destroyed by application of four selective RF pulses (81°_x, 101°_y, 69°_y, 161°_y) followed by four PFGs of ratio 8 : 4 : 2 : 1. The final excitation pulse is a 90° composite pulse (90°_y, 90°_{-x}, 90°_{-y}, 90°_x).

12.6.5 One-Dimensional NOESY with Presaturation

The 1D NOESY with solvent suppression (1D NOESY-presat) has become very popular in LC-NMR spectroscopy and metabonomics where low solute concentrations are detected. The 1D NOESY sequence with presaturation largely removes the "hump" of the residual solvent signal that is often observed using conventional presaturation. The hump stems from spins far outside the volume enclosed by the

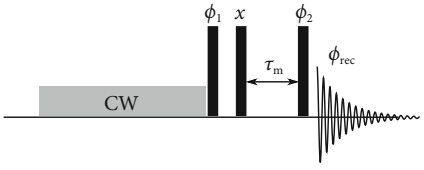

Figure 12.23 1D NOESY-presat sequence. The solvent is presaturated by application of a weak continuous wave (CW) RF field during the interscan delay. Residual solvent, off-resonant due to B_0 inhomogeneities, is suppressed by application of three 90° pulses. The phase cycling is ϕ_1 : $x, -x$; ϕ_2 : $x, x, -x, -x, y, y, -y, -y$; ϕ_{rec} : $x, -x, -x, x, y, -y, -y, y$. The mixing time τ_m is usually set to a very short value.

RF coil where B_0 homogeneity is poor and the spins therefore are not on-resonant with the saturating RF field. The 1D NOESY sequence (Figure 12.23) utilizes the fact that also the B_1 field, and hence pulse angles, will be substantially smaller in those regions. For the spins for which the pulse angles differ from the nominal values of 90°, the phase cycling scheme results in signal cancellation. This provides the basis of volume selection and can be easily verified by considering for example the first two increments of the phase cycling scheme.

12.6.6 Other Methods

Other methods for solvent suppression are based on selective excitation of the solute resonances while leaving the solvent signal effectively along z and thereby largely overcome the problem of saturation transfer. In the "*jump-and-return*" method, essentially a $90^\circ_x - \tau - 90^\circ_{-x}$ element, the *on-resonant* solvent magnetization is tipped back to the z axis by the second 90° pulse, while the x component of the solute magnetization, evolving during τ according to its offsets, remains in the transverse plane. The corresponding excitation profile describes a sine with maximum excitation at $\pm 1/2\tau$ Hz. By setting the interpulse time τ, we can adjust the width of the sine lobes to the right and the left of the center frequency. Usually τ is adjusted in such a way that the lobes span the entire spectral range of interest (typically τ is a few hundred microseconds). However, the signal intensities will be sine modulated and the signals to the left and to the right in the spectrum will have opposite phase. The *binomial sequence* $1\bar{3}3\bar{1}$, an $\alpha_x - \tau - 3\alpha_{-x} - \tau - 3\alpha_x - \tau - \alpha_{-x}$ pulse train ($\alpha = 90^\circ/8$), also yields an excitation profile with a notch at zero offset frequency and maximum excitation at $\pm 1/2\tau$ Hz but gives better solvent suppression than the $1\bar{1}$ pulse of the jump-and-return sequence. However a strong linear phase error must be expected, we can correct for by using first-order phase correction, but at the same time this introduces severe baseline distortions.

In some experiments the water magnetization is destroyed by using *spin-lock pulses*. For example, in an INEPT sequence the magnetization of the water spins and the magnetization of the solute spins are 90° out of phase at the end of the spin-echo sequence. Applying a strong spin-lock pulse at that time along the axis of the solute magnetization will lock the solute magnetization while purging the or-

thogonal water magnetization due to B_1 field inhomogeneities. Nowadays, in many experiments (especially those dedicated to biomolecular NMR) the water magnetization is effectively preserved along the z axis by using water-selective *flip-back pulses*, which thereby minimizes the effects from saturation transfer.

12.7 Basic 1D Experiments

In the remainder of this chapter we will introduce a few simple 1D experiments that are used to measure relaxation times, to measure diffusion rates, to increase the signal-to-noise ratio in (mainly in ^{13}C or ^{15}N NMR spectra), or to determine the number of attached protons.

12.8 Measuring Relaxation Times

12.8.1 Measuring T1 Relaxation – The Inversion-Recovery Experiment

Knowledge of longitudinal (spin–lattice) relaxation times T1 is important for several reasons. Rough estimates of T1 values are useful for the setting of recycle delays or mixing times in NOE experiments. Accurate T1 values even provide insight into the source of relaxation – the molecular dynamics (Chapter 14). For a rough estimate of T1 values, a very simple experiment, the so-called inversion-recovery experiment, can be used.

The pulse sequence of the inversion-recovery experiment is schematically shown in Figure 12.24. It consists of a 180° and a 90° pulse separated by a variable delay τ, the so-called recovery delay. As shown in Figure 12.25, the 180° pulse inverts equilibrium z magnetization. During the subsequent delay, the magnetization is gradually recovered due to T1 relaxation according to

$$M_{z(\tau)} = M_{eq}(1 - 2e^{-\frac{\tau}{T1}}) \tag{12.9}$$

For short recovery delays the magnetization will still point along the negative z axis, while for longer delays the magnetization will be along the $+z$ axis. The

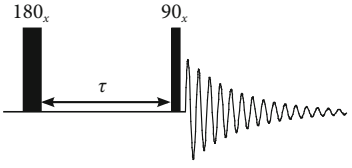

Figure 12.24 Pulse sequence of the basic inversion-recovery experiment. A 180° pulse is followed by a variable time delay and a 90° readout pulse.

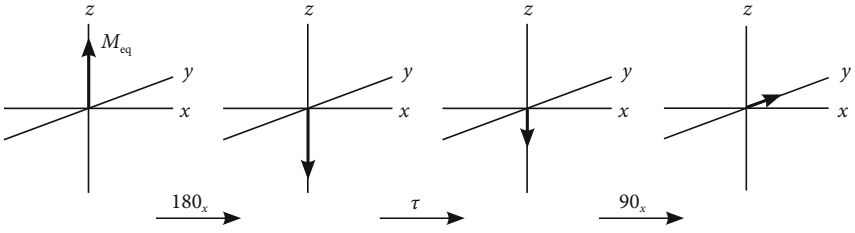

Figure 12.25 State of magnetization during the inversion-recovery experiment.

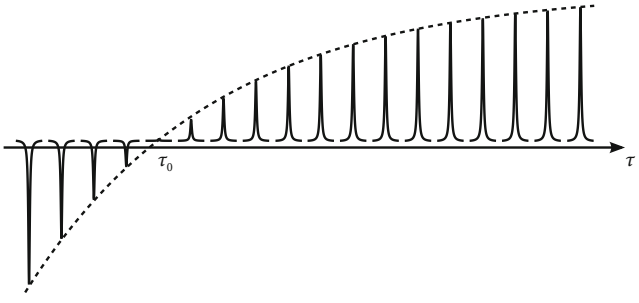

Figure 12.26 Recovery of z magnetization as measured by the inversion-recovery experiment. The plot shows a single line obtained from experiments with successively increased recovery delays. The envelope is described by an exponential buildup function starting from $-M_{eq}$ and asymptotically approaching $+M_{eq}$.

longer the recovery delay, the closer the magnetization will return to the value of thermal equilibrium M_{eq}.

The 90° readout pulse converts the z magnetization into detectable xy magnetization. Depending on whether the magnetization is along the $+z$ or $-z$ axis, the signal phase will change by 180°. The signal intensities measured for various recovery delays describe the magnetization recovery as given by (12.9) (see Figure 12.26).

In principle, T1 values can be derived from fitting the signal intensities to (12.9). However, for a rough estimate it is sufficient to look for the particular recovery delay τ_0 where the signal intensity becomes zero, from which we can calculate the relaxation time according to

$$\mathrm{T1} = \frac{\tau_0}{\ln 2} \approx 1.44\tau_0 \tag{12.10}$$

12.8.2 Measuring T2 Relaxation – The Spin Echo

In principle we could retrieve transverse relaxation time constants T2 directly from a line-shape analysis (see Section 11.2.2). Unfortunately, the line shape is usually at least slightly distorted by field inhomogeneities (poor shims). The total line width depends on the efficiency of spin–spin relaxation, the so-called homoge-

neous broadening, and the amount of line broadening due to B_0 field inhomogeneities, the so-called inhomogeneous broadening. A simple "trick" to eliminate the contributions from the inhomogeneous field is to apply spin echos. Because spin echos are used for many purposes in NMR experiments, we will look at them in more detail now.

12.8.2.1 The Principle of Spin Echos

The basic spin-echo sequence is shown in Figure 12.27. It consists of a 90° excitation pulse and a 180° pulse flanked by two equal delays. Briefly, the 180° pulse has the effect that magnetization dephased because of field inhomogeneities during the first time period τ is rephased during the second time period τ.

To understand the effect of this experiment it is convenient to divide the sample into many tiny subsamples. Each of them experiences a slightly different B_0 field due to field inhomogeneities across the sample. The evolution of a small collection of vectors from these different sample compartments during the spin echo is shown in Figure 12.28. After the initial 90° pulse all vectors coalign with the y axis. If we disregard effects from T2 relaxation for a moment, the vectors precess with their specific offset frequency according to the chemical shift, which, however, is additionally varied due to the different field strengths in the sample. Accordingly, the time course of magnetization during free precession throughout the first period τ is characterized by a vector bundle that rotates with an overall frequency Ω and it successively fans out according to the contributions of field inhomogeneities as shown in Figure 12.28. Applying a 180° pulse at the end of the first time period τ will flip the vectors by 180°. The vector bundle immediately after the pulse presents a mirror image with respect to the y axis. In the second time period τ the vectors will again evolve under free precession. The crucial point is that each vector will rotate through the same angle as during the first period τ. Therefore, all vectors will realign with the y axis again at the end of the second τ interval, and the only effect remaining is that of T2 relaxation. A spectrum acquired at this point will display reduced signal intensities according to the transverse relaxation by the factor $\exp(-2\tau/\mathrm{T2})$.

The amount of net xy magnetization during the spin-echo sequence is shown in the lower trace in Figure 12.28. During the first τ interval the magnetization successively decays and becomes smallest for $t = \tau$. Depending on the length of τ and the severity of the field inhomogeneity, the magnetization may even completely decay to zero. After the 180° pulse, the vectors starts to realign and accordingly the observed magnetization will increase, until for $t = 2\tau$ the vectors are fully rephased

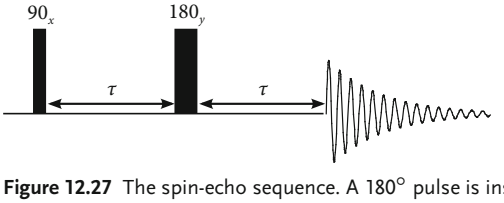

Figure 12.27 The spin-echo sequence. A 180° pulse is inserted into the center of a delay period.

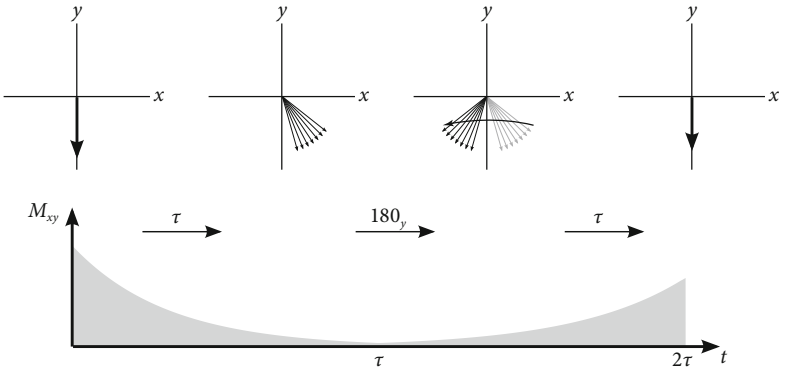

Figure 12.28 The spin echo. *y* magnetization created by the initial 90° pulse dephases due to field inhomogeneities during the first interval τ. The application of a 180° pulse along the *y* axis rotates the magnetization vectors by 180° about the *y* axis. After a second interval τ, the vectors will realign on the *y* axis. The lower trace displays the amount of net *xy* magnetization during the spin-echo sequence.

and a spin echo is observed with full signal intensity reduced only by T2 relaxation. Thereafter, magnetization starts to dephase again.

It is important to note that the 180° pulse not only refocuses contributions of field inhomogeneity, but also refocuses chemical shifts themselves. This must be seen as the real reason why spin echos have become so popular in multipulse experiments (see Chapter 13). We wish to add that spin echos do not refocus homonuclear couplings. Spin echos in which the delay–180°–delay element is repeated many times also serve to suppress the effects from chemical or conformational exchange as described in Chapter 16.

12.8.2.2 **The Effects from Diffusion and Convection**

Perfect echos are only obtained as long as spins do not move in the sample so that the field experienced by a spin is constant. Molecular diffusion may transport spins into other sample compartments where the field is different. Accordingly, the average precession frequency does not need to be the same within the first and the second echo time, resulting in an additional signal attenuation due to imperfect echo formations. How much the echos will be attenuated depends on the self-diffusion constant and the characteristics of the field inhomogeneity.

From these remarks it is clear that spin-echo experiments can be used to determine molecular self-diffusion constants. In the most popular sequence BPP-LED (bipolar pulse longitudinal eddy-current delay), magnetization is initially dephased, then stored in the *z* direction (to reduce losses due to transverse relaxation) during a diffusion delay Δ, reconverted into transverse magnetization, and rephased with a second gradient. The rephased signal is attenuated by the extent of diffusion. From a series of such spectra obtained at various gradient strengths, the diffusion constants can then be extracted by fitting signal intensities $I(G)$ to the following

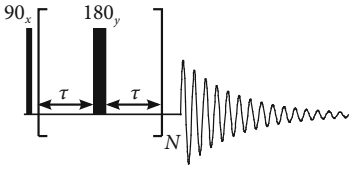

Figure 12.29 The Carr–Purcell–Meiboom–Gill sequence. A spin-echo sequence for measuring T2 relaxation.

equation:

$$I(G) = I_0 e^{-(\gamma \delta G)^2 (\Delta - \frac{\delta}{3}) D} \tag{12.11}$$

in which D is the diffusion constant, Δ is the length of the diffusion delay, and δ and G are the length and strength of the gradient. A similar source for imperfect echo formations is convection. An interesting feature of convection in combination with spin echos is that the effect of convection will cancel at every even echo.

12.8.2.3 Measuring T2 Relaxation

The effects of molecular diffusion, convection, and chemical exchange can be considerably reduced by applying many 180° refocusing pulses throughout the relaxation period. Thus, instead of applying a single 180° pulse in the middle of the relaxation period, one usually applies a cascade of equally spaced 180° pulses in sequences for measuring T2 relaxation, as shown in Figure 12.29, and this sequence has been dubbed the Carr–Purcell–Meiboom–Gill sequence. The interpulse or echo time τ should be chosen as short as possible, however without generating too much heat from the RF. From a series of spectra recorded for different relaxation periods, the T2 values can then be obtained by a two-parameter fit of the signal intensities: $I_{(t)} = I_0 \exp(-t/\mathrm{T2})$.

12.9 The INEPT Experiment

Insensitive nuclei enhancement by polarization transfer (INEPT) is a very useful technique and serves as an important building block in many heteronuclear shift correlation experiments (e.g., HSQC). As the name suggests, INEPT experiments benefit from transfer of polarization from the much more sensitive nucleus (usually ^{1}H) to the much less sensitive nucleus (e.g., ^{13}C or ^{15}N). For example, γ of ^{13}C is about four times smaller than that of ^{1}H. Accordingly, the population difference at thermal equilibrium is about four times larger for ^{1}H than for ^{13}C (see Section 6.2). With an INEPT experiment we can transfer the ^{1}H polarization onto the ^{13}C spins, resulting in a signal increase of ^{13}C spectra. The experiment is described in much more detail in Chapter 13.

In short, the INEPT experiment uses the scalar coupling between a sensitive nucleus (usually ^{1}H) and an insensitive nucleus to create a state which is called

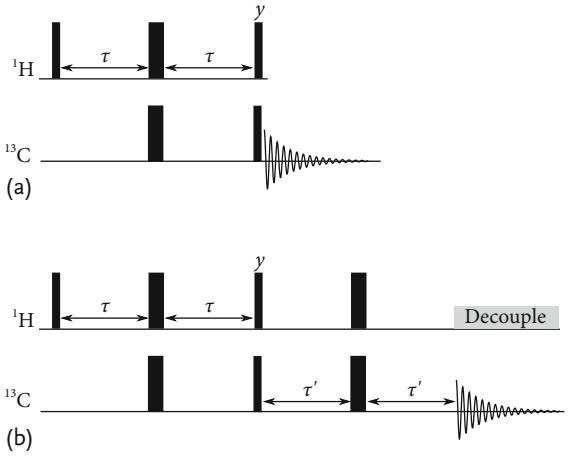

Figure 12.30 Pulse sequences of the INEPT experiment (a) and the refocused INEPT experiment (b). Narrow and wide rectangles represent 90° and 180° pulses, respectively. Unless indicated otherwise, all pulse phases are of phase *x*. The delay τ is $1/4J$, and τ' must be adjusted according to the multiplicity.

antiphase magnetization. Antiphase magnetization of the ^{1}H spins can be quantitatively transferred to antiphase magnetization of the insensitive nuclei (X) with two 90° pulses. The latter state then describes a particular form of transverse magnetization of the insensitive spin. What we have achieved is the creation of transverse magnetization of the insensitive spin, but the amount of this magnetization is related to the population difference of the more sensitive nucleus, and hence will be much more than if we had excited the insensitive nucleus directly. Any equilibrium z magnetization of the X nuclei is also brought into the transverse plane by the 90° pulse, giving rise to in-phase magnetization distorting the intensities of the antiphase doublet. This magnetization can be easily removed by using appropriate phase cycling (e.g., by altering the phase of the second 90° ^{1}H pulse and the receiver phase by $\pm y$).

It is important to note that if we simply recorded an ^{1}H decoupled spectrum after the INEPT we would not detect any signal since the antiphase magnetization components cancel each other. Therefore, the antiphase magnetization is often converted into in-phase magnetization prior to acquisition by adding another spin-echo element to refocus the heteronuclear coupling, called refocused INEPT (Figure 12.30b). Depending on the X nucleus multiplicity, the antiphase doublet is split into further components, as shown in Figure 12.31. In those cases where different multiplicities are present simultaneously (e.g., CH, CH_2, and CH_3) the delay τ' in the spin echos must be chosen as a compromise (e.g., $1/6J$ for CH, CH_2, and CH_3).

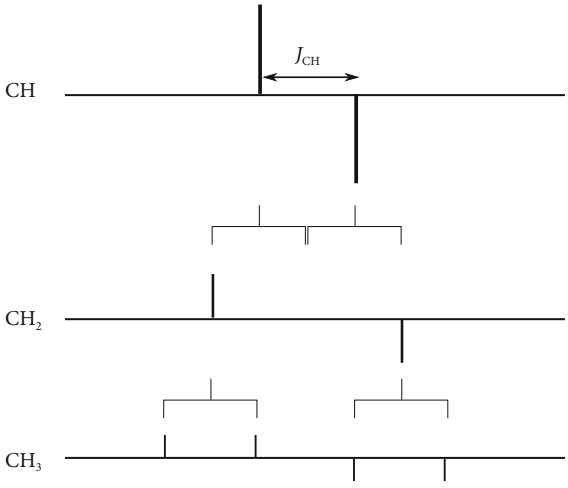

Figure 12.31 Splitting of the ^{13}C antiphase signal due to coupling to further protons. For a CH group the spectrum displays an antiphase doublet. For a CH_2 group each of the antiphase components is again split by the coupling to the second proton into two components separated by J_{CH}. Thereby the inner lines overlap and cancel. Further splitting due to the presence of a third proton in a CH_3 group results in a 1 : 1 : −1 : −1 quartet.

12.10 The DEPT Experiment

Distortionless enhancement by polarization transfer (DEPT) experiments are very useful since they allow us to discriminate between the ^{13}C atoms according to the number of directly attached protons. In DEPT-135 spectra the signals of methyl and methine carbons are phased to be positive, while those of methylene carbons are negative (Figure 12.32, spectrum a). In DEPT-90 spectra only methine carbons are present (Figure 12.32, spectrum b). In both spectra quaternary carbons are absent. Recording DEPT-135 and DEPT-90 spectra along with a conventional ^{13}C NMR spectrum allows one to differentiate between methyl, methylene, methine, and quaternary carbons. In addition, because the experiments rely on a polarization transfer from ^{1}H to ^{13}C, DEPT experiments in general are more sensitive than the conventional ^{13}C experiment. DEPT experiments basically can also be used to obtain multiplicities of X nuclei other than ^{13}C, for example, for ^{15}N. Another advantage of DEPT is that it starts with proton magnetization, and the experiment repetition delay can therefore be chosen to match the much shorter T1 values of protons (compared with carbon).

For completeness, there exists an additional variant, DEPT-45. In this experiment all but the quaternary carbons are detected, however, in contrast to DEPT-135, without editing of the signal phases (Figure 12.32, spectrum c). By appropriate combination of DEPT-45, DEPT-90, and DEPT-135 spectra, we can (assuming the sensitivity of the three subspectra matches) obtain spectra that include CH, CH_2, or CH_3 signals exclusively.

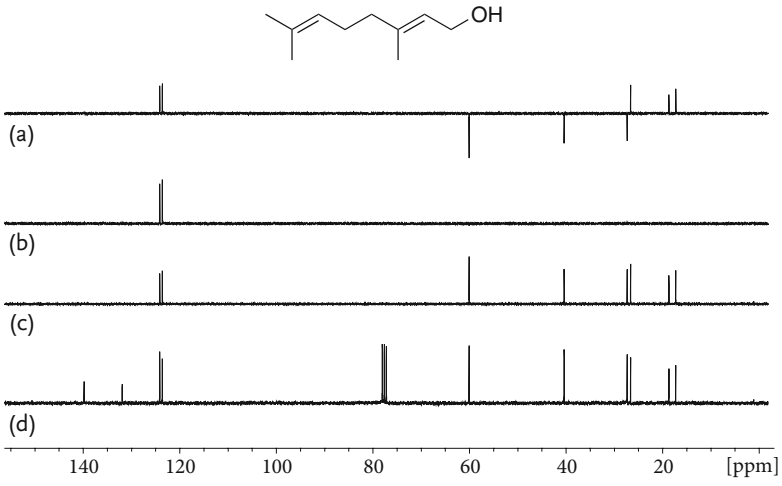

Figure 12.32 Distortionless enhancement by polarization transfer (DEPT) spectra of geraniol. The DEPT-135 spectrum (a) shows positive signals for CH and CH_3, whereas those for CH_2 are negative. Distinction between CH and CH_3 groups is observed in the DEPT-90 spectrum (b), which includes CH signals exclusively. The DEPT-45 spectrum (c) shows all but the quaternary carbons. Spectrum d is the routine ^{13}C NMR spectrum.

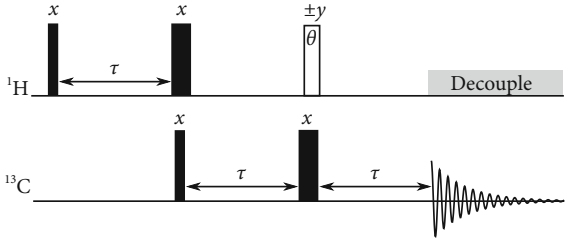

Figure 12.33 Pulse sequence of the DEPT experiment: The time periods τ have a value of $1/2J$. Depending on whether a DEPT-45, a DEPT-90, or a DEPT-135 spectrum is measured, the last ^1H pulse has a flip angle θ of 45°, 90°, or 135°, respectively.

The pulse sequence of the DEPT experiments is shown in Figure 12.33. Whether we obtain a DEPT-45, a DEPT-90 or a DEPT-135 spectrum depends solely on the flip angle of the last ^1H pulse, which not suprisingly is 45°, 90°, or 135°. A detailed description of the DEPT sequence is beyond the scope of this book. Suffice to say that multiple-quantum proton–carbon coherences are excited that, depending on the flip angle of the last proton pulse, are back-converted into observable magnetization. DEPT experiments are quite insensitive to variations in the J coupling constants. However, they are sensitive to variations in the final ^1H pulse. Relatively small deviations result in breakthrough of CH_2 and CH_3 signals in DEPT-90 experiments or result in distortion of the signal intensities in DEPT-135 experiments.

12.11 Problems

12.1. In a paper you read that for a certain type of experiment the ^{15}N 90° and 180° pulses were applied at an RF field strength of 5 kHz. Calculate the corresponding pulse widths.

12.2. A certain type of experiment requires that the magnetization is inverted very precisely over a large range of offset frequencies. Name two alternative classes of RF pulse shapes with an improved inversion profile when compared to a simple rectangular 180° pulse.

12.3. Transverse ^{13}C magnetization is dephased by applying a pulsed field gradient of 10 G/cm and 1 ms duration. The spatially encoded magnetization is then transferred by means of a sequence of RF pulses into transverse ^{1}H magnetization. Let us suppose that this magnetization has the same spatial phase relationship as the dephased ^{13}C magnetization, with the difference that the ^{13}C spins are now replaced by ^{1}H spins. What gradient strength do you need to refocus the ^{1}H magnetization (a) using a gradient pulse of the same duration of 1 ms or (b) using a gradient pulse of 0.5 ms duration?

12.4. Does the answer to Exercise 12.3 depend on the relative signs of the gyromagnetic ratios?

12.5. Does the phase cycling scheme of a one-pulse experiment [pulse phase: $X\ -X\ -Y\ Y$; receiver phase: $-Y\ X\ Y\ -X$] have (a) zero signal, (b) half signal, or (c) full signal intensity?

12.6. The basic INEPT sequence is shown below. To which parameter is the delay τ tuned to?

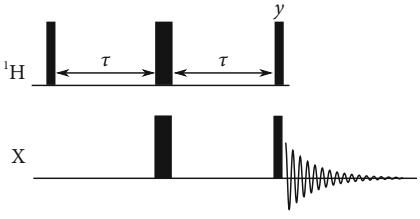

13
The Art of Pulse Experiments

13.1
Introduction

NMR of course obeys the rules of quantum mechanics. But the latter is also true for optical spectroscopy. So why has the NMR technique become so much more powerful than IR spectroscopy, despite it clearly needing much larger sample quantities? The answer is related to the fact that a number of NMR parameters, with the exception of sensitivity perhaps, are highly favorable, allowing one to manipulate spin systems in much detail, and observe the results with great precision. This can be done to the extent that researchers are trying to exploit the NMR phenomenon to build a quantum computer that would be capable of performing a vast number of calculations in a very short time.

Frequency and, hence, signal separation is reasonably good. A ^{13}C NMR spectrum of a comparably large molecule, for example, a peptide with 20 amino acids, will usually still display resolved carbonyl signals. In contrast IR spectra usually fail to resolve the individual CO frequencies, and often require tedious labeling procedures. Even if signals overlap, as is often the case in proton spectra or when considering larger molecules such as proteins or polysaccharides, higher-dimensional NMR spectroscopy will still allow one to assign the resonances. This is only possible because the relaxation times of excited spin states are long enough so that spins can be manipulated and coherences can be transferred from one nucleus to another, possibly a remote one.

Coherence transfer is achieved through RF pulses. The standard 1D proton NMR experiment consists of a single 90° RF pulse. Modern triple-resonance experiments, for example, experiments that transfer magnetization between proton, nitrogen, and carbon nuclei, as routinely used for assigning protein spectra, may easily contain more than 30 pulses, among them selective and nonselective 90° and 180° pulses. Still, the experimental result is highly predictable, and hence designing a new experiment usually starts with an idea of how magnetization should be shuffled around. The idea is then formulated in mathematical terms, using a formalism known as the product operator formalism (POF) (see Chapter 8). Once this

Applied NMR Spectroscopy for Chemists and Life Scientists, First Edition. Oliver Zerbe and Simon Jurt.
©2014 WILEY-VCH Verlag GmbH & Co. KGaA. Published 2014 by WILEY-VCH Verlag GmbH & Co. KGaA.

is done, the idea can be directly translated into the pulse experiment using standard building blocks. While for the novice pulse experiments are highly cryptic, in fact they can be assembled in a rational way. With a little training it is fairly easy to understand even more complicated triple-resonance experiments. This chapter is intended to provide the necessary tools to design or, more likely, understand NMR pulse experiments.

13.2
Our Toolbox: Pulses, Delays, and Pulsed Field Gradients

A well-defined sequence of RF pulses and time spacings between them, called delays, is used to manipulate the magnetization. Pulses can be classified according to the angle through which they rotate the magnetization (see also Section 6.6). Most often used are 90° and 180° pulses, although one sometimes also finds 45° or 60° pulses. We will follow the convention of many spectroscopists and use thin lines for 90° pulses and filled squares for 180° pulses (Figure 13.1). Pulses can also be of high power and short, so-called hard or nonselective pulses, or long and selective, the soft pulses. Soft pulses will usually not be rectangular in shape, and we will use a sinc or Gaussian shape to indicate that those pulses are selective.

Inserted delays are indicated by spacings between the pulses. Many delays involve fixed time settings, for example, to account for the evolution of a certain scalar coupling, and the length of the delay is the same in each experiment. They are denoted by the sign Δ, and are numbered consecutively in the sequence. Some delays that are used for frequency labeling in indirect frequency dimensions are modified, usually incremented or decremented, by a fixed amount of time for each new experiment. Since these delays give rise to the F1 or F2 frequency, they are denoted as t_1 or t_2 in the sequence. Figure 13.1 displays a short sequence composed of a soft pulse, a nonselective 90° pulse, and a delay with a hard 180° pulse in the center, followed by data acquisition.

Many experiments use pulses applied to more than one type of nucleus, for example, to manipulate proton as well as carbon nuclei. Each type of nucleus is pulsed via different hardware, and the routing is often for technical reasons referred to as being applied on a certain channel. In the graphical representation, pulses on different channels are drawn on different lines.

Sometimes the homogeneity of the magnetic field is destroyed by so-called pulsed field gradients (see Sections 12.2 and 13.9.2). The presence of them is shown on a separate line.

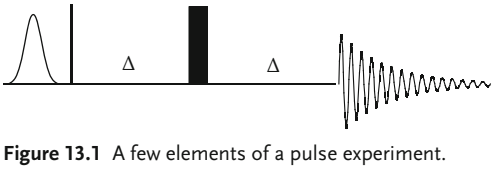

Figure 13.1 A few elements of a pulse experiment.

13.3
The Excitation Block

13.3.1
A Simple 90° Pulse Experiment

The simplest NMR experiment comprises a single 90° RF pulse. The NMR spectrometer, however, needs to do more than that. The entire pulse experiment consists of an initial delay, called the *relaxation delay*. The insertion of the delay ensures that the spin system has completely relaxed, when more than one NMR experiment is done (usually signal is added up from a number of separate experiments, called scans, to increase the signal-to-noise ratio). Then the 90° pulse with a certain phase follows. Thereafter, a very brief delay is inserted to prevent residual current from the pulse being detected in the receiver coil. This is necessary because the same RF coil is used for pulsing and for detection. Afterward the receiver is opened and the signal detected. This sequence of events is repeated with exactly the same timing ns times, with ns denoting the number of scans. A single 90° pulse converts equilibrium magnetization, I_z, into transverse magnetization, and therefore is usually the first element of almost every pulse sequence, however complicated it may be:

$$I_z \xrightarrow{90°(y)} I_x$$

13.3.2
The Effects of 180° Pulses

Pulses of 180° are usually inserted into the pulse sequence for three different purposes. Firstly, they help refocus chemical shifts during a delay. They are often inserted into a delay during which only a heteronuclear scalar coupling evolves. Secondly, a scalar coupling can be removed while chemical shifts evolve. Thirdly, 180° pulses may invert z magnetization, and thereby establish a nonequilibrium distribution of z magnetization (in fact, the vector of the z magnetization will be pointing in the $-z$ direction after application of the 180° pulse). The effects of 180° pulses are summarized in Figure 13.2.

If we assume that after the first dotted line transverse magnetization exists on the upper (I spin) channel, the sequence on the left will refocus chemical shifts for the I spin, and decouple the I spin from the S spin. The sequence in the center allows chemical shifts to evolve during 2Δ and will refocus the IS coupling. The

Figure 13.2 The effects of 180° pulses. Examples are depicted for a scalarly coupled *IS* system.

sequence on the right will refocus *I*-spin chemical shifts but leaves the *IS* coupling untouched so that it evolves during 2Δ.

An alternative way to achieve decoupling is to use a *composite-pulse decoupling* sequence (see Section 12.4.2). Such sequences consist of off-resonance-compensated 180° pulses, and flip spins constantly between the α and β states. Composite-pulse decoupling can be conveniently switched on during the beginning of a delay, and turned off when desired. Any antiphase terms present at the beginning of decoupling will be immediately destroyed by the decoupler sequence.

13.3.3 Handling of Solvent Signals

Many compounds need to be measured in the presence of strong signals from the solvent. The most prominent example is the measurement of biological macromolecules, for example, RNA and proteins, in water as the solvent. The concentration of the water protons is approximately five orders of magnitude higher than that of the solute protons, and hence very efficient methods for suppressing the water line are required.

The simplest method is low-power irradiation of the solvent line (Figure 13.3a). A very weak field (e.g., 50 Hz bandwidth) is used to saturate the water protons. Any other protons for which the chemical shift is very close to the water line will also be suppressed by this method. The method is highly sensitive to the line shape of the water line, and therefore an excellent shim is mandatory. High levels of suppression can be achieved. More modern methods such as excitation sculpting use a combination of soft pulses and gradients to selectively eliminate the water signal. They achieve higher levels of signal suppression and are less sensitive to poor magnetic field homogeneity (bad shims). Water suppression techniques are described in more detail in Section 12.6.

A undesired side effect of water suppression by low-power solvent irradiation is that any protons that exchange with the solvent signal are also suppressed to some extent, a phenomenon known as *saturation transfer*. A well-known example is the saturation transfer to amide protons in proteins. At unfavorable pH values, complete bleaching of solvent-exposed amide protons may occur. The above-mentioned experiments that use gradients and soft pulses also help one to record spectra that are less prone to such problems.

A number of other elements that can be used for solvent suppression are shown in Figure 13.3a.

In Figure 13.3b a delay alternating with nutation for tailored excitation (DANTE) pulse train is applied. The spacing of the 90° pulses determines the excitation profile. Figure 13.3c depicts a soft pulse, in this case shaped to a Gaussian function. In Figure 13.3e we see a series of four 90° pulses shifted in phase by 90° between consecutive pulses. In Figure 13.3f incorporation of a short spin-lock pulse into an insensitive nuclei enhancement by polarization transfer (INEPT) building block is shown.

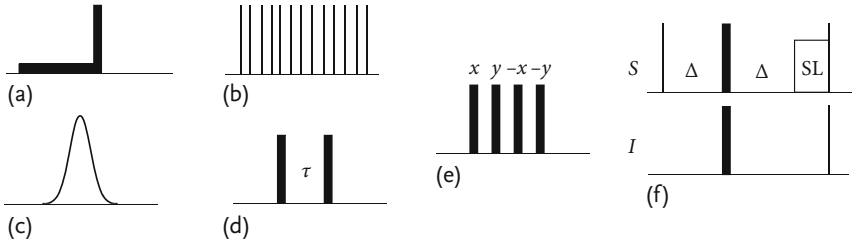

Figure 13.3 Elements for removing water signal. The simple presaturation (a), delay alternating with nutation for tailored excitation (DANTE)-type selective excitation (b), selective excitation using a soft pulse (c), the jump-return sequence (d), a four-pulse element (e) and a spin-lock purge pulse within an insensitive nuclei enhancement by polarization transfer (INEPT) element (f).

13.3.4
A Polarization Transfer Sequence

As described in Section 12.9, polarization transfer sequences are often used to transfer the z polarization from a sensitive nucleus (a nucleus with a large gyromagnetic ratio for which the population difference between α and β states is large) to a more insensitive nucleus. The most prominent example is the transfer of polarization from proton to carbon nuclei, and the standard building block used in NMR experiments to achieve such a transfer is called the *INEPT* experiment. Since the INEPT building block is found in most modern solution NMR experiments, we will describe it in more detail here. The INEPT sequence can only be understood when a more formal description of the experiment is used, the most convenient one being the POF introduced in Chapter 8.

The basic idea behind the experiment is to excite the sensitive nucleus first, and then use the scalar coupling to the insensitive nucleus to establish antiphase magnetization. The latter can be subsequently transferred to the insensitive nucleus with the help of 90° pulses simultaneously applied to the sensitive and the insensitive nucleus (Figure 13.4).

The sequence depicted on the left in Figure 13.4 suffers from the fact that during 2Δ the chemical shift will evolve and, depending on the offset of the I spin, only a fraction of I-spin polarization will be transferred to the S spin. In the original INEPT element depicted on the right in Figure 13.4, the insertion of a 180° pulse on the I channel refocuses the I-spin chemical shift. Unfortunately, this pulse also decouples the I spin from the S spin. Since evolution of the IS coupling is required

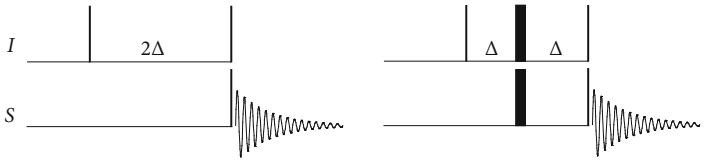

Figure 13.4 Polarization transfer with the INEPT sequence.

for the experiment, a 180° pulse must be applied to the S spin as well. Only when both spins are flipped simultaneously does the IS coupling evolve. In terms of the POF, the sequence is described as follows:

$$I_z \xrightarrow{90°(x)} -I_y \xrightarrow{\Delta-180(I,S)-\Delta} 2I_xS_z \xrightarrow{90°(I,y)} 2I_zS_z \xrightarrow{90°(S,x)} -2I_zS_y$$

As a result the S spin is excited, albeit with increased sensitivity. The sensitivity of an NMR experiment is proportional to $\gamma_{ex}\gamma_{det}^{3/2}$, in which the first term is the gyromagnetic ratio of the exited spin and the second term is the gyromagnetic ratio of the detected spin. The INEPT experiment is so much more sensitive because the gyromagnetic ratio of protons is four times larger than that of carbon spins or ten times larger than that of ^{15}N.

Other sequences that accomplish similar things are depicted in Figure 13.5.

The sequence in Figure 13.5c represents the refocused INEPT, which is used when in-phase S-spin magnetization is required, which is the case, for example, in relaxation experiments. The sequences in Figure 13.5b,d correspond to the creation of *heteronuclear multiple quantum coherences*. The sequences in Figure 13.5b are used in the heteronuclear multiple-quantum coherence (HMQC)-type experiment and the sequence in Figure 13.5d is used in the distortionless enhancement by po-

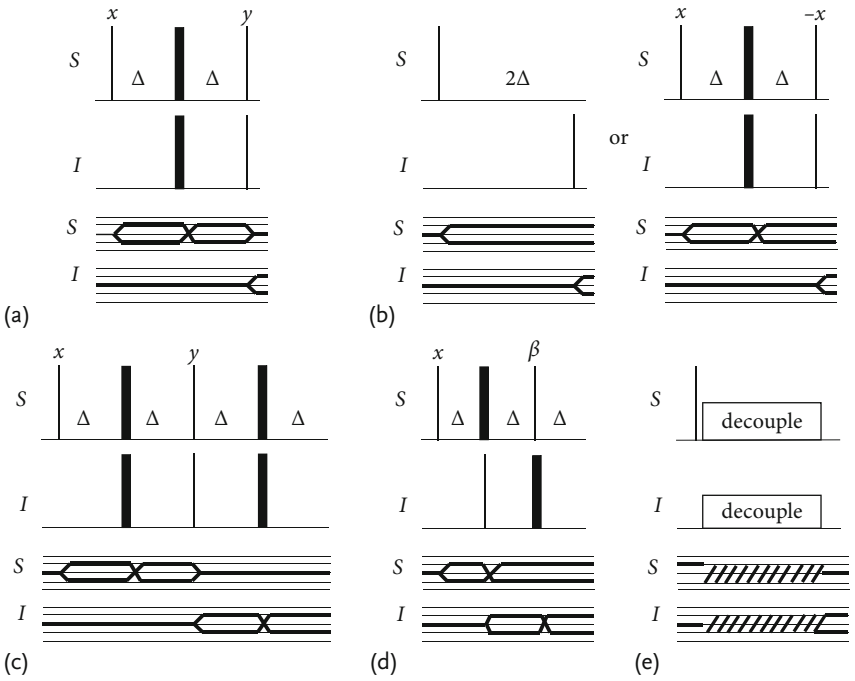

Figure 13.5 Polarization transfer elements. INEPT (a), heteronuclear multiple-quantum coherence (HMQC) type (b), refocused INEPT (c), distortionless enhancement by polarization transfer (DEPT) (d) and heteronuclear cross-polarization (e). Below the pulse-sequences the coherence level diagrams are shown.

larization transfer (DEPT)-type experiment. Figure 13.5e displays a building block more often used in solid experiments, known as *heteronuclear cross-polarization*. Two fields of exactly the same strength are applied to both the I and the S channel, fulfilling the Hartmann–Hahn condition ($\omega(I) \approx \omega(S)$) and resulting in coherence transfer.

The polarization transfer in these sequences can be described using the POF as

$$I_z \xrightarrow{90^\circ(x)} -I_y \xrightarrow{\Delta-180-\Delta} 2I_xS_z \xrightarrow{90^\circ(S,x)90^\circ(I,y)} -2I_zS_y \qquad \text{(Fig. 13.5a)}$$

$$I_z \xrightarrow{90^\circ(x)} -I_y \xrightarrow{2\Delta} 2I_xS_z \xrightarrow{90^\circ(S,x)} -2I_xS_y \qquad \text{(Fig. 13.5b)}$$

$$I_z \xrightarrow{90^\circ(x)} -I_y \xrightarrow{\Delta-180-\Delta} 2I_xS_z \xrightarrow{90^\circ(S,x)90^\circ(I,y)} 2I_zS_y \xrightarrow{\Delta-180-\Delta} -S_x \qquad \text{(Fig. 13.5c)}$$

$$I_z \xrightarrow{90^\circ(x)} -I_y \xrightarrow{2\Delta} 2I_xS_z \xrightarrow{90^\circ(S,x)180(I,x)} 2I_xS_y \qquad \text{(Fig. 13.5d)}$$

$$I_z \xrightarrow{90^\circ(x)} -I_y \xrightarrow{\mathrm{CP}_x} -S_y \qquad \text{(Fig. 13.5e)}$$

13.4 The Mixing Period

In the mixing period magnetization is transferred from one spin onto another one, thereby providing the crucial step for detecting correlations. This can be accomplished either via a coherent process (correlation spectroscopy (COSY)-type transfer, Figure 13.6a,b) or via an incoherent transfer (nuclear Overhauser effect spectroscopy (NOESY)-type transfer, Figure 13.6c,d):

$$I_x \xrightarrow{\Delta-\pi-\Delta} 2I_yS_z \xrightarrow{(\pi/2)_x} -2I_zS_y \qquad \text{(Fig. 13.6a)}$$

$$I_x \xrightarrow{\mathrm{MLEV16}} \frac{1}{2}I_x + \frac{1}{2}S_x + (I_yS_z - I_zS_y) \qquad \text{(Fig. 13.6b)}$$

$$I_x \xrightarrow{90^\circ(-y)} -I_z \xrightarrow{\tau_m} -S_z \xrightarrow{90^\circ(x)} S_x \qquad \text{(Fig. 13.6c)}$$

$$I_x \xrightarrow{\mathrm{CW}_x} S_x \qquad \text{(Fig. 13.6d)}$$

The working principle of COSY-type experiments is to establish antiphase magnetization, and use that for coherence transfer. In isotropic mixing experiments such as total correlation spectroscopy (TOCSY), in-phase terms are transferred (Figure 13.6b). The resulting mixture of phases usually needs to be purged. In

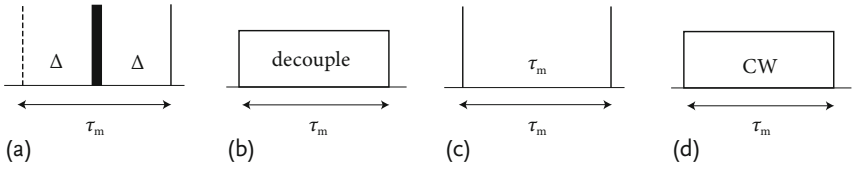

Figure 13.6 Mixing elements for correlation spectroscopy (COSY)-type (a), total correlation spectroscopy (TOCSY) (b), nuclear Overhauser effect spectroscopy (NOESY) (c), and rotating-frame NOESY (ROESY) (d) sequences.

the NOESY experiment, longitudinal magnetization is established with inversion of the normal population, and the nuclear Overhauser effect (NOE) then transfers this to another nucleus (Figure 13.6c). The rotating frame NOESY (ROESY) sequences are very similar, but spin-locked transverse magnetization instead of longitudinal magnetization is transferred by the rotating-frame NOE.

Sequences in which heteronuclear coherence transfer occurs during the mixing period uses the above-described INEPT or heteronuclear cross-polarization building blocks.

13.5
Simple Homonuclear 2D Sequences

Two-dimensional NMR experiments will produce a spectrum that contains two frequency dimensions. In the NMR experiment this is achieved by simply inserting a variable delay. Two-dimensional spectra are acquired as an array of 1D spectra, and the only difference in the individual experiments is that a time variable is systematically incremented (see Chapter 17). Figure 13.7 displays one of the simplest 2D homonuclear shift-correlation experiments, well known as the COSY experiment.

All the 2D NMR experiments are composed of four building blocks: *excitation–evolution–mixing–detection*. In the COSY sequence the excitation element is just the first 90° pulse. The evolution period serves to label the chemical shift in the indirect dimension and is given by the t_1 delay. The mixing period transfers coherences from one spin to another, such that correlations between different spins become visible. In the COSY experiment this is simply another 90° pulse. Finally the signal is detected during acquisition.

The COSY experiment belongs to the class of homonuclear shift-correlation experiments. Suppose we insert a 180° pulse into the center of the t_1 delay and remove the second 90° pulse. The result is the *J*-resolved experiment, which was one

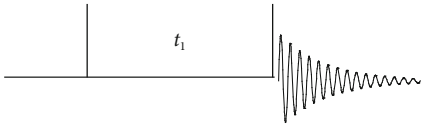

Figure 13.7 Pulse sequence for a simple COSY experiment.

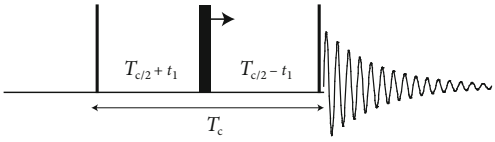

Figure 13.8 Constant-time COSY variant.

of the first 2D NMR sequences. The 180° pulse in the center of t_1 refocuses the chemical shifts and only homonuclear couplings evolve, which will be displayed along the indirect dimension in the corresponding spectra.

In the COSY example described above the delay t_1, corresponding to the time evolution in the F1 dimension, is incremented from experiment to experiment by a fixed amount of time. Another possibility for shift labeling is used in the so-called constant-time experiments (Figure 13.8). In these experiments, a 180° pulse is systematically shifted through a period of constant length. In the first experiment the 180° pulse is perfectly centered in the middle of the delay, so that chemical shifts are completely refocused. When the pulse is moved toward one end of the delay, keeping the overall length of the delay the same, chemical shift evolves during a time period which corresponds to the difference in length between the time spacings before and after the 180° pulse.

Constant-time methods have important advantages and disadvantages. The advantage is that *homonuclear* couplings are not removed by the 180° pulse, and hence they will always evolve over the full length of T_c. Because the homonuclear couplings are not modulated during t_1, they will not give rise to a splitting of the signal in the indirect dimension. Such experiments are used when homonuclear couplings are relatively large, as is the case for ^{13}C signals in ^{13}C-labeled proteins. The disadvantage is that the magnetization is always transverse over a long period during which T2 relaxation is active, and hence these experiments are inherently much more insensitive compared with their non-constant-time counterparts.

13.6
Heteronuclear 2D Correlation Experiments

A large class of experiments correlate the chemical shifts of nuclei of different types, for example, protons, with their directly bonded carbon nuclei. Usually, these sequences incorporate a polarization transfer step as the mixing element, mostly an INEPT block. Figure 13.9 depicts a number of different sequences, all of which can be used to record ^1H–^{13}C correlation spectra. In Figure 13.9a the original HETCOR sequence is shown, which starts from proton magnetization, and transfers coherences to carbon nuclei via the one-bond coupling. The sequence will produce antiphase magnetization, and therefore does not allow decoupling. Insertion of a refocusing delay, as shown in Figure 13.9b, refocuses this coupling and allows decoupling. The sequences in Figure 13.9c,d contain two polarization transfer steps.

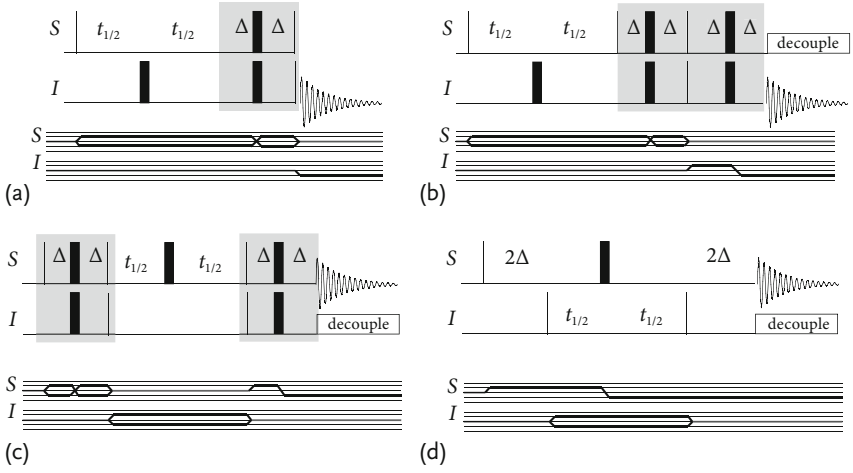

Figure 13.9 Different pulse sequences for heteronuclear correlation experiments: heteronuclear shift correlation (HETCOR) without (a) and with (b) decoupling, heteronuclear single-quantum coherence (HSQC) (c), and HMQC (d) experiments.

They start with proton magnetization and detect proton magnetization, and therefore are much more sensitive than the HETCOR sequence.

The sequences in Figure 13.9c,d differ from each other in an important way. The experiment shown in Figure 13.9c is called the *heteronuclear single-quantum coherence* (*HSQC*) experiment, and the one in Figure 13.9d is called the *heteronuclear multiple-quantum coherence* (*HMQC*) experiment. During the t_1 period only *I*-spin magnetization is transverse in the HSQC experiment, while both proton and carbon magnetization are present in the HMQC experiment. The literature extensively discusses the relative merits of the two sequences. The HMQC sequence has much fewer pulses, in particular 180° pulses, and hence will work better when the X-nucleus chemical shift range is very wide. Moreover, the multiple-quantum coherences relax more slowly for large molecules. As a disadvantage, the homonuclear ^{1}H,^{1}H couplings are present in the indirect dimension, and the spectra are therefore less well resolved.

Homonuclear couplings cannot be removed by nonselective 180° pulses. In [^{13}C,^{1}H] HSQC spectra recorded on ^{13}C-labeled proteins, the ^{13}C,^{13}C couplings will broaden the peaks in the indirect dimension enormously, resulting in poor resolution. Figure 13.10 depicts the implementation of a constant-time HSQC experiment that avoids splittings due to homonuclear couplings. The sequence in Figure 13.10b additionally decouples the aliphatic carbons from carbonyls. This is possible because of the large chemical shift difference of the CO (170 ppm) and aliphatic (10–70 ppm) carbon range, allowing one to use CO-selective pulses.

Another variant of heteronuclear correlation NMR experiments uses the *transverse-relaxation-optimized spectroscopy* (*TROSY*) principle. This experiment recently became very popular because it results in much narrower lines for large molecules at high fields. The principle is based on the compensation of dipolar relaxation

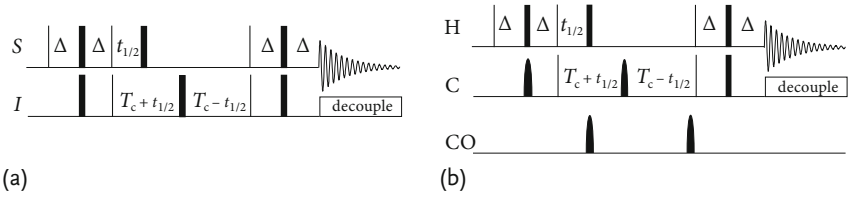

Figure 13.10 Constant-time HSQC experiments without (a) and with carbonyl (b) decoupling.

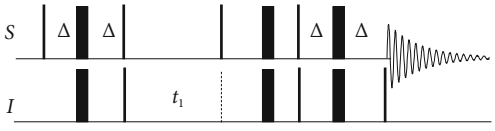

Figure 13.11 Transverse-relaxation-optimized spectroscopy (TROSY) experiment. Note that the dotted line does not indicate the presence of a pulse.

and chemical shift anisotropy (see Chapter 14), and hence the application is only recommended for nuclei with significant chemical shift anisotropy contributions (e.g., ^{15}N,^{31}P, sp^2-^{13}C). The original sequence is shown in Figure 13.11.

A detailed description is beyond the scope of this book, but a few features should be mentioned here. The most important point is that the signal is not decoupled, neither in the direct nor in the indirect dimension, to not mix the transitions. An NH cross peak displays four components, two for each dimension due to the coupling. The phase cycle is designed to select for the narrowest component, leaving just one of the four (see also Chapter 14).

13.7 Experiments for Measuring Relaxation Times

Knowledge of T1 and T2 values is important for a number of reasons. T1 values determine the scan-repetition rate and hence the setting of the relaxation delay for an experiment. In a small molecule at moderate B_0, a carbonyl ^{13}C spin, for example, can easily have a T1 of 20 s or longer. If the ^{13}C 1D NMR experiment is repeated with a relaxation delay of 2 s, the carbonyl carbons will be kept in a semisaturated state and will never return to thermal equilibrium. As a consequence, the signal will be very small. T2 relaxation times reflect the line width of signals. As a rule of thumb, magnetization can only be transferred along a certain coupling if the line width of the signal involved is smaller than this coupling. In the case of a 2D COSY experiment, that means that line widths should not exceed 7 Hz if couplings of vicinal protons are to be observed. Knowledge of relaxation times is not only mandatory for the proper setup of NMR experiments, but also provides a wealth of information on dynamics of molecules. For example, ^{15}N relaxation has been extensively used in protein NMR experiments to characterize internal motions.

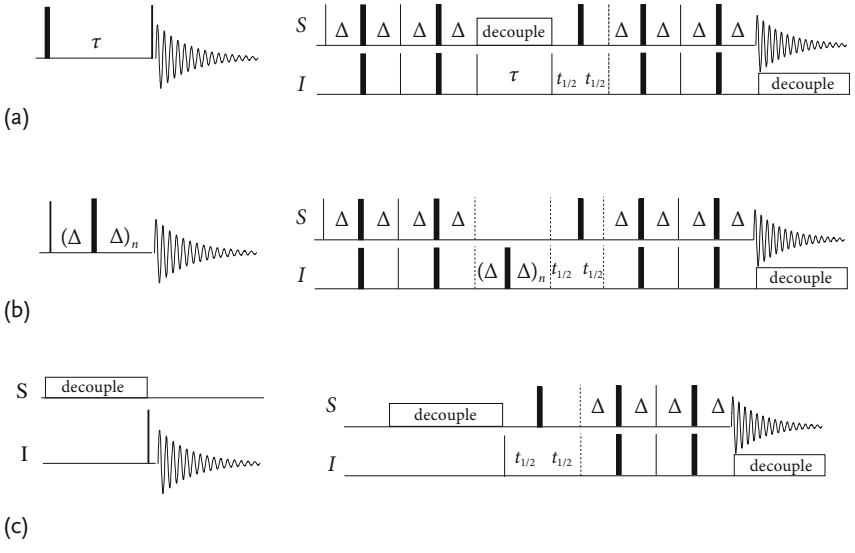

Figure 13.12 Experiments for measuring T1 (a), T2 (b), and the X{^{1}H} nuclear Overhauser effect (c) via HSQC-type experiments. The corresponding simple 1D sequences are depicted on the left.

The T1 relaxation time is mostly measured with the *inversion-recovery* sequence (Figure 13.12a). Therein, equilibrium magnetization is inverted $I_z \rightarrow -I_z$. A variable delay then follows to allow T1 relaxation to occur. Since the decay will not produce transverse magnetization, a 90° readout pulse is required.

To measure T2 values the *Carr–Purcell–Meiboom–Gill* (see also Section 12.8.2.3) sequence is used (Figure 13.12b). This, in principle, simply measures the decay of transverse magnetization. However, if one were to extend the delay during which transverse magnetization is present, any field inhomogeneity would also contribute to the decay. To avoid the latter, a series of 180° pulses are inserted, and it can be shown that these must be repeated by an even number for complete cancellation of artifacts.

The heteronuclear NOESY experiment is simply a one-pulse experiment in which a saturating decoupler field is applied to the other spin (usually to the protons) (Figure 13.12c). The NOE itself then corresponds to the difference of two experiments, one with decoupling of the protons, the other one without.

Figure 13.12 summarizes all the sequences on the left as well as their HSQC counterparts of the more sensitive 2D detection via protons.

13.8
Triple-Resonance NMR Experiments

Many experiments that are routinely used in NMR laboratories working on proteins or nucleic acids involve the use of three different types of nuclei. Typical examples are proton, carbon, and nitrogen nuclei. We will briefly describe the HNCA experiment to show how clever concatenation of INEPT building blocks allows the transfer of magnetization through a molecule in a highly efficient manner.

The HNCA experiment connects the amide moiety of a protein with the α carbon, and forms part of the experiments used to assign the backbone of a $^{13}C,^{15}N$-labeled protein (Figure 13.13).

The triple-resonance experiments use the comparably large one-bond couplings to efficiently transfer magnetization. In addition, these sequences allow nuclei to be connected in a highly specific manner and thereby tailor the sequences to deliver unambiguous answers. An HN(CO)CACB experiment, for example, will connect the amide proton and nitrogen of residue i via the carbonyl nucleus with the C_α and C_β of residue $i-1$, and no other correlations will be observed. The addition of many NMR-active nuclei along the transfer pathway provides additional frequencies along which the peaks can be dispersed, resulting in less peak overlap. Last but not least, knowledge of C_α and C_β chemical shifts is very helpful in establishing the type of amino acid.

In order to design such an experiment, we need to accomplish the following series of events:

- excitation of the amide proton and transfer of magnetization to the directly attached ^{15}N nucleus (INEPT 1)
- chemical shift labeling of ^{15}N (insertion of a t_1 period)
- transfer from the amide nitrogen to the C_α (INEPT 2)
- chemical shift evolution of the C_α magnetization to derive the C_α chemical shift (insertion of a t_2 period)
- back transfer from C_α to ^{15}N (INEPT 3)
- back transfer to the amide proton for detection (INEPT 4).

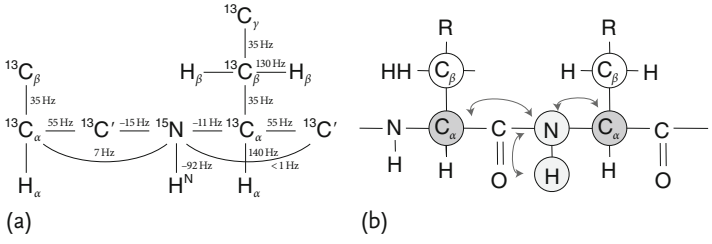

Figure 13.13 Magnitude of scalar couplings in an isotope-enriched protein (a) and magnetization transfer flow in an HNCACB experiment (b).

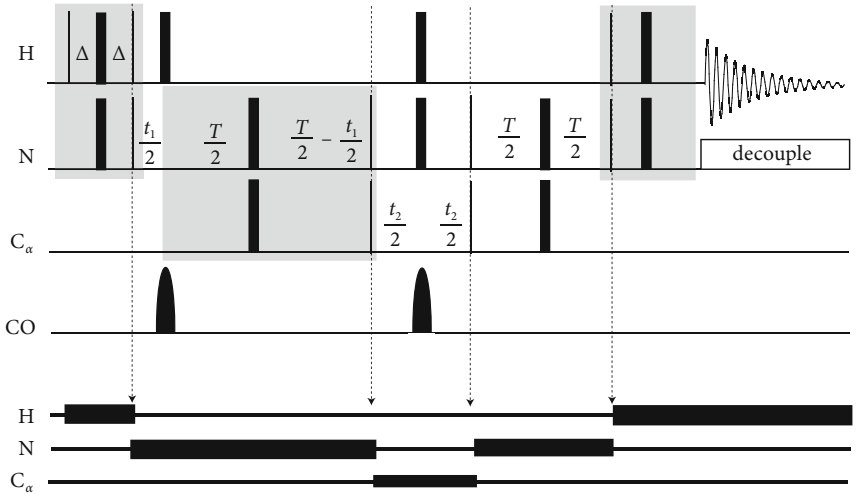

Figure 13.14 The pulse sequence of an HNCA experiment.

The complete sequence is depicted in Figure 13.14, and the individual INEPT transfer blocks are shaded in gray. For improved understanding, the presence of transverse magnetization on a particular nucleus is indicated by thick bars below the sequence. A few comments need to be made. Firstly, in all evolution periods (t_1 and t_2), 180° pulses must be inserted in the center to refocus all resolved heteronuclear couplings in order to improve resolution and to reduce the number of peaks. Secondly, the second INEPT block has been used additionally for nitrogen chemical shift labeling. This is possible because the delay required for building up the N,C_α coupling is long enough to be used as a constant time period for ^{15}N shift labeling. Another striking feature of this experiment is the symmetry in the sequence. The experiment belongs to the so-called class of *out-and-back* triple-resonance experiments, in which magnetization is transferred along one path and then all the way back.

Modern sequences are even more complicated. They incorporate pulsed field gradients for improved selection of the proper coherence pathway and better solvent suppression. Nevertheless, their overall appearance is very similar.

13.9 Experimental Details

13.9.1 Selecting the Proper Coherence Pathway: Phase Cycles

The correct order of pulses on the various channels does not automatically guarantee the correct flow of magnetization in the experiment. In fact, the NOESY experiment and the double-quantum-filtered COSY experiment all contain three 90°

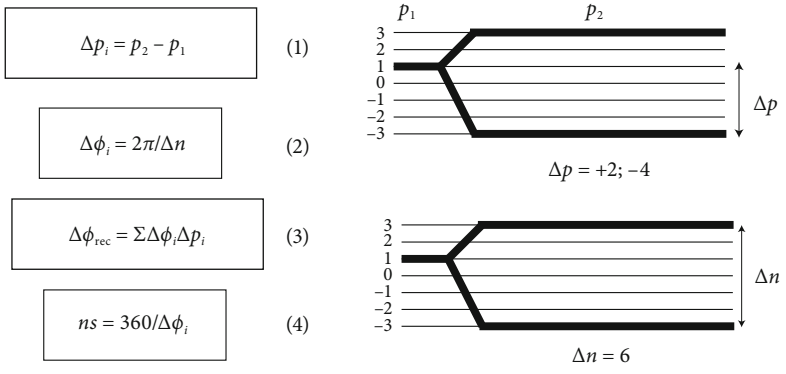

Figure 13.15 Rules for constructing phase cycles.

pulses. To select the correct flow of magnetization, the phases of the pulses are changed between different scans, a procedure known as phase cycling. Phase cycling, however, also serves to remove the effects from miscalibrated pulses or from off-resonance effects. A phase cycle contains a certain number of steps. A four-step phase cycle that removes an important source of artifacts requires also a multiple of 4 as the number of scans. Pulse programs usually contain the phase cycle at the end, and the interested reader is recommended to check this for the sequence of interest.

The underlying principle is that a coherence is shifted in phase by $\Delta\varphi \times \Delta p$ when a pulse that changes the coherence order by Δp is phase shifted by $\Delta\varphi$, and usually this coherence change is followed by shifting the receiver phase appropriately.

There are a small number of rules for designing phase cycles (Figure 13.15). For example, the selection rule for the coherence order (rule 2) requires for selection of triple-quantum coherence ($\Delta n = 6$) that the phase is changed by $360/6 = 60°$ in successive scans, requiring a six-step phase cycle (rule 4) for the corresponding pulse. If the initial state was $+1$, the change in coherence order, Δp, is $+2$ for selecting the $+1 \rightarrow +3$ pathway. To select for the triple-quantum coherences, the receiver phase must be shifted by $2 \times 60° = 120°$. The phase program for this particular selection would then be as follows: φ(pulse) = 0, 60, 120, 180, 240, 300 and φ(rec) = 0, 120, 240, 0, 120, 240.

As an example, triple-quantum-filtered COSY together with the phase cycle as implemented in a Bruker standard pulse program is depicted in Figure 13.16. In Bruker's nomenclature, 0, 1, 2, and 3 correspond to x, y, $-x$, and $-y$. The (12) indicates that the numbers correspond to multiples of $360/12 = 30°$ instead of the standard 90°.

In this sequence the first two pulses are cycled together. The total change in coherence order for these two pulses is ± 3. Again, $\Delta n = 6$ and therefore six $360/6 = 60°$ phase shifts are required (rule 2). These are applied to phases 1 and 2 together (shown in gray; note that the phase of the receiver phase is given in multiples of 90°). From step 1 to step 2 in the phase program, $\varphi(1)$ and $\varphi(2)$ are changed from 0 to $6 \times 30 = 180°$. To follow this coherence pathway the receiver

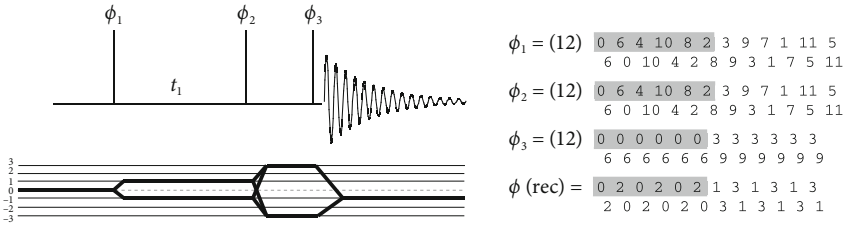

Figure 13.16 The triple-quantum-filtered COSY experiment (a), and a phase cycle for this experiment (b).

phase must be ($\Delta p = 3$; $\Delta\varphi = 180$) changed by $3 \times 180° = 540° \equiv 180°$. In step 6, the phases of $\varphi(1)$ and $\varphi(2)$ are changed from 0 to $2 \times 30 = 60°$ with respect to the first phase. To follow this coherence pathway, the receiver phase must be changed by $3 \times 60° = 180°$. In addition to that six-step phase cycle, all phases are shifted in four steps by 90° simultaneously by changing each of the six phases from the first step by 90°, giving the next six phases and so on. The last phase cycle is called a cyclically ordered phase sequence (CYCLOPS) and is intended to remove artifacts from improper quadrature detection. Since this is not really a problem with modern spectrometers any longer, six scans are sufficient. It is important to use a multiple of 6 as the number of scans so that the phase cycle can always be completed.

13.9.2 Pulsed Field Gradients

The development of pulsed field gradients was stirred by the fact that dephasing of coherences by field gradients is proportional to the order of the coherence and the gyromagnetic ratio of the nuclei involved. If a gradient of strength G (usually in units of gauss per centimeter) is applied, coordinate z and length τ will shift the phase is a spatially dependent manner by

$$\varphi(z) = -p \times \gamma\, G z \tau$$

It is important to recognize that the z gradient will only affect transverse magnetization since the phase shift is proportional to the coherence order. The application of pulse field gradients will enable one to select for a certain coherence, or to follow a coherence pathway. An important difference from accomplishing a similar task by phase cycling is that the selection is done *within a single scan*, in contrast to the addition/subtraction procedure used in phase cycling. Therefore, instrumental instabilities are much less relevant, and experiments using pulsed field gradients often display significantly fewer noise artifacts. Moreover, the dynamic range can be exploited much more favorably because only coherences of interest contribute to the signal. In addition, the necessary number of scans can be reduced, thereby having an enormous time saving for 3D experiments if sufficient sample concentration permits a few scans.

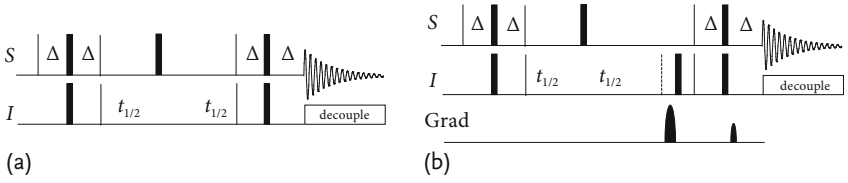

Figure 13.17 HSQC experiments without (a) and with *coherence selection* via pulsed field gradients (b).

In principle, pulsed field gradients are used in two different ways, namely, *coherence selection* schemes and *coherence rejection* schemes. The former method labels a particular coherence for selection, while the latter rejects all the unwanted coherences. While the coherence selection schemes usually result in much cleaner spectra and better artifact suppression, they are mostly (not always) accompanied by a loss of sensitivity. If a gradient is applied during an evolution period, where coherence orders $+1$ and -1 are present, the gradient will select only for one of the two coherence orders, and usually alternative experiments will be used to sample both pathways, which is required for phase-sensitive detection. Figure 13.17 compares coherence selection and rejection schemes in a standard HSQC experiment.

In this sequence the sign of the last gradient is inverted every second experiment (every increment is measured twice) to record both n-type and p-type signals for quadrature detection. If this sequence is used for an $^{15}N,^{1}H$ correlation, the strength of the second gradient must be 10% of that of the first one because $\gamma(^{1}H)/\gamma(^{15}N) \approx 10$. This sequence does perfectly dephase the solvent signal, so no other solvent suppression method is necessary, thereby also largely avoiding the effects from saturation transfer.

The sequence in Figure 13.18 demonstrates the use of *coherence rejection* schemes. The two pairs of bold gradients flanking the 180° pulses in the INEPT steps help eliminate pulse imperfections from the 180° pulses. Since the coherences are inverted through the 180° pulse (e.g., $-1 \rightarrow +1$), the second gradient will refocus the effect of the first one. The second gray gradient is a so-called crusher gradient that eliminates any transverse coherences during a period where only z magnetization should be present. The first gray gradient eliminates any steady-state I-spin magnetization.

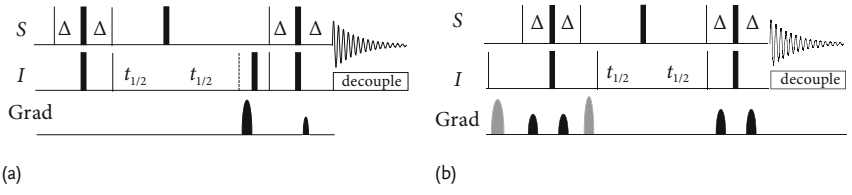

Figure 13.18 HSQC experiments with coherence selection (a) and coherence rejection (b) schemes.

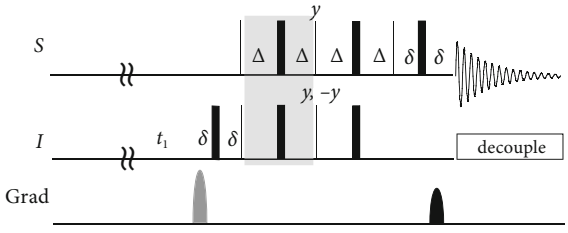

Figure 13.19 Building block for sensitivity enhancement.

13.9.3
N-Dimensional NMR and Sensitivity Enhancement Schemes

The mixing step in a multidimensional NMR experiment serves to transfer coherences from one type of spin to another. This usually requires a fixed phase relationship, for example, a y pulse to transfer $I_x S_z$ antiphase magnetization. Chemical shift evolution during a t_1 period will, however, produce a mixture of $I_x S_z$ and $I_y S_z$, and only one of the two terms will be transferred. Addition of an extra frequency dimension therefore reduces the signal by a factor of $1/\sqrt{2}$. In the case of an ^{15}N,^{1}H HSQC correlation, an ingenious invention, called *sensitivity enhancement*, serves to circumvent this loss by transferring both the $I_x S_z$ and $I_y S_z$ components (Figure 13.19).

Two types of magnetization that contribute to the signal exist at the end of t_1: $I_z S_x$ and $I_z S_y$. In this scheme (we show here only the pulses after the t_1 period) $I_z S_x$ is converted to $I_y S_x$ by the two 90° pulses after t_1 and stored as such during the first spin echo (highlighted in gray), while the other component $I_z S_y$ is converted to $I_y S_z$ and refocused to I_x. The two 90° pulses with y phases then transfer the latter to I_z, which is not altered during the second spin echo, and is transferred to I_y by the last 90° pulse. The $I_y S_x$ component is transformed to $I_y S_z$ by the S_y pulses and refocuses to I_x during the second spin echo. The latter is not affected by the last 90° proton pulse, so in the end both components have been transferred as $I_x + I_y$. This is an undesired mixture of phases. However, when the 90° y pulse on the I channel is changed to a $-y$ pulse, it will result in $I_x - I_y$. Adding this to the result from the first experiment will produce I_x and subtracting it will produce I_y, which can be stored separately and processed in the usual way. Another advantage of this sequence is that the gradient selection during t_1 does not select only p-type or n-type signals, so no loss of intensity occurs for this coherence selection scheme.

13.10 Problems

13.1. Describe the basic building blocks of an HSQC experiment.

13.2. The following element is to be inserted as an INEPT transfer block into a heteronuclear experiment. It contains two errors. Which ones?

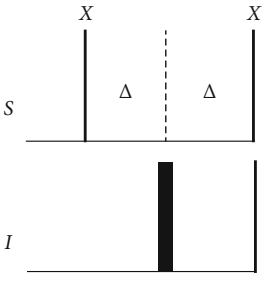

13.3. Describe the difference between the HETCOR and the HSQC experiment.

13.4. In the double-quantum filtered COSY experiment, you want to allow +2 and −2 coherences past the filter, and block all others. How many steps must the phase cycle contain on the first 90° pulse of the filter element?

13.5. For gradient coherence selection you cannot simply place a gradient into the evolution period. Why?

13.6. Compare the relative sensitivity of an HSQC experiment using phase cycles for coherence selection, the corresponding experiment with gradient selection during t_1, the sensitivity-enhanced HSQC, and the sensitivity-enhanced HSQC with gradients in t_1.

13.7. Describe the spin-lock element in TOCSY experiments.

13.8. The gradient version of the HMBC gives much superior spectra when compared to the version using just phase-cycling. Explain why!

Further Reading

Cavanagh, J., Fairbrother, W.J., Palmer III, A.G., Rance, M., and Skelton, N.J. (2007) *Protein NMR Spectroscopy*, 2nd edn, Academic Press.

Rule, G.S. and Hitchens, T.K. (2006) *Fundamentals of Protein NMR Spectroscopy*, Springer.

Sattler, M. and Schleucher, J. (1999) Heteronuclear multidimensional NMR experiments for the structure determination of proteins in solution employing pulsed field gradients. *Prog. Nucl. Magn. Reson. Spectrosc.*, **34**, 93–158.

Kessler, H., Gehrke, M., and Griesinger, C. (1988) Two-dimensional NMR-spectroscopy: Background and overview of the experiments. *Angew. Chem. Int. Ed. Engl.*, **27**, 490–536.

Part Four
Important Phenomena and Methods in Modern NMR

By now you should have a solid knowledge of the basic principles of NMR spectroscopy. In this part we would like to introduce special topics that are of central importance for modern NMR experiments. For example, we explain the working principle of two-dimensional NMR and introduce the most important 2D NMR experiments. The NMR literature is full of acronyms, and abbreviations such as COSY (correlation spectroscopy) or HSQC (heteronuclear single-quantum coherence) can be found in almost every paper describing the use of NMR. Furthermore, we give you a glimpse on solid-state NMR, introduce exchange spectroscopy, and present a more in-depth account on relaxation as well as on the nuclear Overhauser effect. Clearly, the latter two topics are advanced and you will profit from prior reading of Part Two of this book. We finally describe methods for looking at intermolecular interactions by NMR – experiments that are widely used in biochemistry and pharmaceutical sciences. After reading these chapters you will be more familiar with the experiments, and you have obtained an overview of which of the various NMR methods may be best suitable to solve your particular problem.

14
Relaxation

14.1
Introduction

Relaxation describes the return of any perturbed system to its equilibrium state. In NMR experiments, perturbations can be caused through the effect of radio frequency (RF) pulses but also by relaxation pathways themselves, and the latter give rise to the *nuclear Overhauser effect* (NOE). The efficiency of relaxation determines the line widths and the signal intensities in our spectra, and has a large influence on what types of NMR experiments are possible. As we will see in a moment, relaxation is largely governed by motion, either overall tumbling of the molecule in solution, or in case of larger molecules, motions of parts of the molecule. We introduced the basic features of longitudinal and transverse relaxation in Section 6.4.2. In this chapter we provide a better description of the mechanism that gives rise to the phenomenon of relaxation. But first we briefly summarize the basic aspects of relaxation.

14.2
Relaxation: The Macroscopic Picture

In the following we describe how a perturbed system returns to the equilibrium state. Let us start by reminding you of the properties of the thermal equilibrium state. As described in detail in Chapter 2, the state of a spin ensemble in such a state is governed by the Boltzmann distribution: a small excess of spins are in the energetically lower states, for which the magnetic dipole moment is aligned with the positive z axis, giving rise to thermal equilibrium z magnetization M_{eq}. Whenever this state is disturbed, relaxation drives the system back to thermal equilibrium. For example, if we invert the z magnetization by applying a 180° RF pulse such that the population of α or β states is inverted, we create a state that is higher in energy. This state will eventually relax back to equilibrium by *longitudinal, T1, or*

Applied NMR Spectroscopy for Chemists and Life Scientists, First Edition. Oliver Zerbe and Simon Jurt.
©2014 WILEY-VCH Verlag GmbH & Co. KGaA. Published 2014 by WILEY-VCH Verlag GmbH & Co. KGaA.

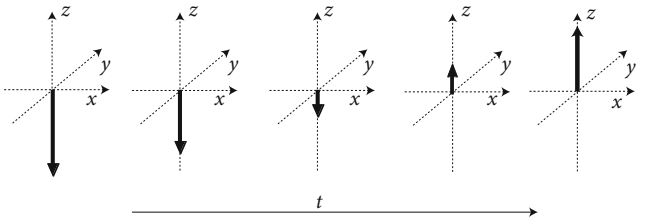

Figure 14.1 Recovery of equilibrium z magnetization by T1 relaxation. The return of the z magnetization is shown at certain time snapshots following an increasing delay time after the initial 180° pulse from the left to the right.

spin–lattice relaxation (Figure 14.1). Since α and β states are associated with different energies, this process is *enthalpic* in nature.

On the other hand, any transverse magnetization (or coherences) formed by spin alignment in the xy plane (e.g., after application of a 90° pulse) will vanish due to transverse (T2) relaxation. *T2, spin–spin*, or *transverse relaxation* destroys phase coherence over time. It is this process that ultimately leads to the decay of the signal detected by the receiver coil, and is responsible for the line width of the signal. Short T2 times result in broad lines and poor resolution. Since a reorientation of the spin component in the xy plane is not associated with a change in energy but the loss of phase coherence decreases the order in the spin ensemble, T2 relaxation is an *entropic* process.

As shown in Figure 14.2, dephasing of the spins decreases the magnitude of the transverse magnetization vector, and as a result will lead to a decrease of the signal detected by the coil. Both T1 and T2 relaxation are first-order processes characterized by exponential decays:

$$M_z(t) = [M_z(0) - M_{\mathrm{eq}}]\mathrm{e}^{-t/\mathrm{T1}} + M_{\mathrm{eq}} \tag{14.1}$$

$$M_{xy} = M_{xy}(0)\mathrm{e}^{-t/\mathrm{T2}} \tag{14.2}$$

where T1 and T2 the characteristic longitudinal and transverse relaxation time constants, respectively, which alternatively may be expressed by the corresponding rate constants ($R_1 = \mathrm{T1}^{-1}$; $R_2 = \mathrm{T2}^{-1}$). $[M_z(0) - M_{\mathrm{eq}}]$ denotes the initial deviation of the z magnetization $M_z(0)$ from its thermal equilibrium value M_{eq}.

14.3 The Microscopic Picture: Relaxation Mechanisms

If relaxation processes occur spontaneously, relaxation times can be very short and line widths very large. The transition probability per unit time for a transition from higher to lower energy by spontaneous emission of a photon of energy $\Delta E = \hbar\omega_0$ is given by

$$W = \frac{\mu_0 \gamma^2 \hbar \omega_0^3}{6\pi c^3} \tag{14.3}$$

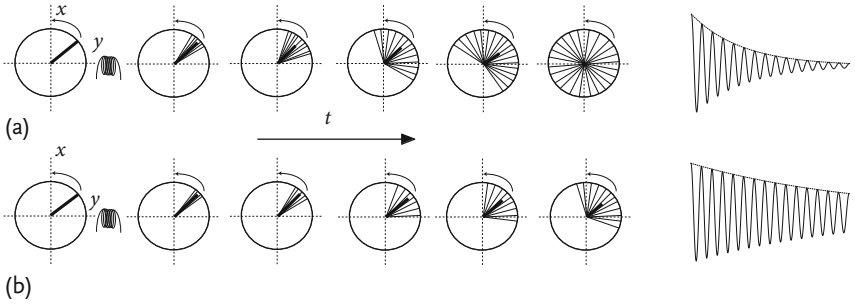

Figure 14.2 Mechanism of T2 relaxation. The decay of transverse coherence due to the loss of phase coherence in a frame rotating at the resonance frequency is shown for a quickly (a) and a slowly (b) relaxing resonance. The length of the vector representing transverse magnetization is depicted in bold. The influence on the free induction decay is depicted on the right.

(in which c is the speed of light and μ_0 and $\hbar$ have their normal meanings). Due to the low frequency of NMR transitions when compared with the frequencies of other forms of spectroscopy (e.g., UV spectroscopy) (note that the NMR frequency enters the equation as the *cube*) the probability is virtually zero, and spontaneous emission is completely ineffective. Relaxation is rather due to interactions with the surroundings (mostly with nearby spins acting as dipoles), often referred to as the *lattice*. In the following we will describe the most important mechanisms of interactions that result in relaxation. We only intend to remind the reader of the most important features of these interactions, which are described in much more detail in Chapter 7.

14.3.1 Dipole–Dipole Relaxation

The dipole–dipole interaction is the most important source of relaxation for many nuclei, in particular for ^{1}H nuclei. We have described the dipolar field due to the magnetic moment of a single spin already. During dipolar relaxation nuclear spins in close proximity to the observed spin produce fluctuating magnetic fields. These magnetic dipole fields slightly alter the effective field at the site of the observed spin. The strength of the dipolar field depends on the distance r^{-3} and on the orientation of two interacting nuclei relative to the external field, as expressed by the angle θ (for a more exact definition of the dipolar field, see Section 7.2.3).

As the molecule tumbles, the relative orientation changes, and hence the effective field is modulated. This behavior is sketched in Figure 14.3 for the dipolar coupling between two ^{15}N and ^{1}H spins. Similar to a very weak RF pulse, such a field modulation can induce transitions between spin states. However, in contrast to an RF pulse, which acts in the same way for spins in all molecules, the modulation by the dipolar field is different for each molecule because the motions of different molecules are uncorrelated. Dipolar interaction therefore results in incoherent or

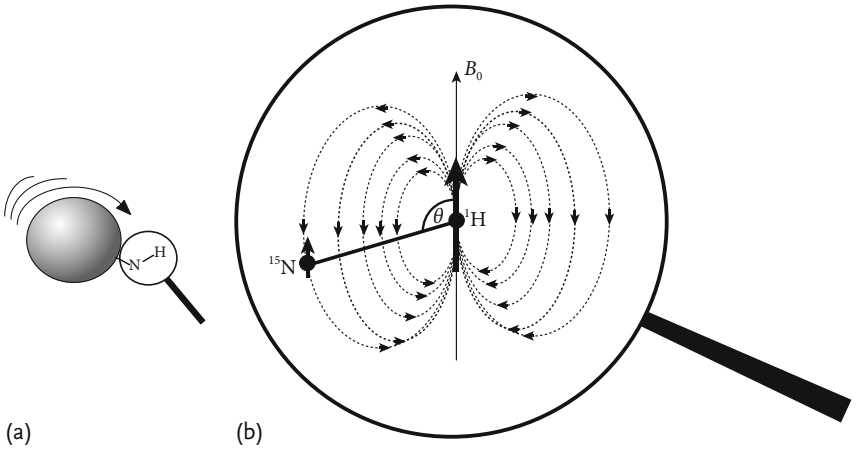

Figure 14.3 Dipolar coupling for a pair of directly bonded ^{15}N and ^{1}H nuclei. (a) Overall tumbling changes the orientation of the connecting vector with respect to the static field. (b) A zoom that illustrates the dipolar field.

nonsynchronized transitions, which will destroy any existing phase coherence over time (T2 relaxation) or will flip spins from the α state into the β state or vice versa (T1 relaxation).

T1 and T2 processes depend on the *mutual* dipolar coupling, and therefore on the square of the additional field (R1 (or R2) $\propto B_{\text{loc}}^2$). Accordingly, relaxation processes depend on the inverse distance to the power of 6($\propto \frac{1}{r^6}$), making it highly sensitive to how close the next NMR-active spin is. The efficiency of relaxation due to dipolar coupling of two spins I and S also depends on $\gamma_I^2 \gamma_S^2$. For an exact definition of the dipolar coupling, see (7.23).

Now we wish to investigate what the effect of these dipolar fields is. As stated above, the dipolar field from another spin close in space acts like a very weak RF pulse. For these fields to be effective they must occur in a certain direction in space. As shown in Figure 14.4, dipolar fields along a direction orthogonal to the direction of the static field can flip spins from the β state into the α state, a process that will result in T1 relaxation.[1)] Alternatively, they can rotate the spins such that their phases, as defined as the orientation in the xy plane, change. This process reduces the phase coherence in the spin ensemble, and will lead to T2 relaxation. The result of a dipolar field along the z direction is the direct increase or decrease in precession frequency, which also results in phase decoherence. In contrast, dipolar fields along the z direction do not change the relative population of α and β states, and hence do not trigger T1 relaxation.

So far, we have investigated the action of these fields in a rotating frame. Of course, the spins are precessing, and therefore the local dipolar fields along the x or y axis must also rotate to have an influence, for the same reason as the B_1 field

1) In general, spins can be in superposition states. In those cases the coefficients of α and β states will be swapped upon a 180° rotation.

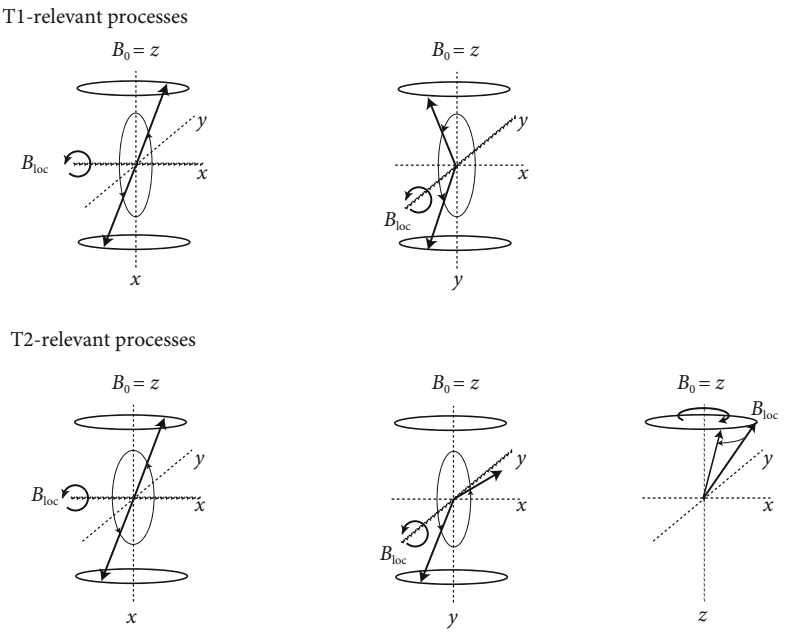

Figure 14.4 The effects from dipolar fields along the *x*, *y*, or *z* axis. The pictures correspond to a frame rotating at the Larmor frequency of the spin, and the initial state of the spin is such that it is in the *yz* plane. Although rotation about arbitrary angles is possible, we show only rotations by 180°, with the exception of the T2-relevant rotation about the *y* axis. In that specific case a 180° flip does not alter the phase of the spins (but any other rotation angle will).

during a pulse must rotate about the *z* axis to be effective. The required rotations come from molecular motions, and we will discuss this topic in more detail in Section 14.4. We will then also see that there is a very different dependence on motion for the component along the *z* axis. But before we look at motion in more detail, we will introduce other mechanisms that also contribute to relaxation.

14.3.2 Chemical Shift Anisotropy

For those nuclei that do not have a spherical electron distribution, the shielding of the chemical shift depends on the orientation of the nucleus relative to the magnetic field (see also Section 7.1.1.3). This phenomenon is called chemical shift anisotropy (CSA). CSA is defined as the difference between the largest and the smallest chemical shift for different orientations. CSA is very small for protons, but can become significant for ^{15}N due to the lone pair at the nitrogen. CSA for ^{15}N can be as large as 180 ppm. In the case of the ^{13}C nucleus, sp^3-hybridized carbons posses little CSA, whereas sp^2-hybridized carbons such as aromatic or carbonyl carbons display large values of CSA. Another common nucleus with a large CSA

is ^{31}P. When molecules tumble in solution, the chemical shift of these atoms will fluctuate because the electron shielding is anisotropic. If this fluctuation occurs at the frequency of an NMR transition, the nucleus can relax.

The electron distribution in sp^2 carbons is not longer isotropic about the carbon atom. However, the asymmetry in electron distribution is low and difficult to visualize. Since the NMR shielding is very sensitive towards the electron density the rotation of a CO moiety in space results in a considerable fluctuation of the chemical shift, for example from maximum values of −20 to +240 ppm.

The efficiency of CSA-mediated relaxation depends on the square of the external magnetic field. For an amide ^{15}N relaxing via both dipolar interaction with its directly bound proton and CSA, the CSA contribution to relaxation at 400 MHz is 5%, whereas it is 35% at 1 GHz.

14.3.3 Scalar Relaxation

Scalar relaxation occurs in the situation where the scalar coupling is not constant but fluctuates in time. This stochastic modulation of the scalar coupling interaction acts as a relaxation mechanism. The modulation of the scalar coupling can be due to exchange (*scalar relaxation of the first kind*) or due to rapid self-relaxation because of a short T1 of the coupled partner (*scalar relaxation of the second kind*). An example of scalar relaxation of the first kind is when ^3J couplings are time modulated because the dihedral angle varies with time. Another example is given by the exchange of hydroxyl protons. Because of exchange, the hydroxyl proton will be replaced by a proton from water, and this proton will be in either the α or the β state, both with similar probability. This effect is reminiscent of decoupling, a process where the spin state of the coupled nucleus is constantly switched between α and β states through application of 180° pulse rotations. Therefore, this effect is also sometimes referred to as self-decoupling.

Scalar relaxation of the second kind is mostly observed for spin-1/2 nuclei coupled to quadrupolar nuclei. A commonly encountered example is a CN group, in which the ^{14}N–^{13}C coupling is not visible due to the rapid T1 decay of the ^{14}N nucleus.

Scalar relaxation may have an influence on the transverse relaxation time but not on the longitudinal relaxation time.

14.3.4 Quadrupolar Relaxation

Spin-1/2 nuclei posses a more or less perfectly spherical charge distribution. As a result their interaction with electric fields is not orientation dependent. In contrast, for nuclei with $I > 1/2$ the charge distribution is no longer spherical, and therefore the electric energy of the nucleus depends on its orientation in the ligand field (see Section 7.2.2). Nuclei with spin $I > 1/2$ relax rapidly under the influence of an electric field gradient. T1 relaxation and T2 relaxation are very fast for these

nuclei provided that the ligand environment of the nucleus is nonsymmetric. Line widths for nuclei with large values of the quadrupole moment can be very large (tens of kilohertz). Importantly, this effect almost completely vanishes when the ligand field is highly symmetric. This is seen in ^{14}N NMR experiments, in which a narrow resonance is observed in the tetrahedral NH_4^+ ion but much broader lines are observed when the ^{14}N nucleus is in an asymmetric environment such as in pyrrole.

14.3.5
Spin–Spin Rotation Relaxation

Rapid rotation of molecules in solution leads to a circulating charge, which in turn induces a magnetic field. These currents are purely the result of the fact that the electron cloud rotates about a fixed point through molecular tumbling. These local magnetic fields may interact with the nuclear spins, resulting in a contribution to relaxation. Since this mechanism is of marginal importance in solution NMR experiments, it will not be discussed further here.

14.3.6
Paramagnetic Relaxation

Paramagnetic relaxation describes the dipolar interaction of an NMR-active nucleus with an electron. In principle the effect is governed by the same physics as the dipolar interaction of two nuclear spins, and is described in more detail in Section 14.3.6. However, the effect is much stronger due to the approximately 2000 times larger gyromagnetic ratio of the electrons. Paramagnetic impurities are usually an unwanted contamination in samples. Often they stem from metals in an unfavorable oxidation state. Some chromatography column materials can be paramagnetic. Introduction of paramagnetic moieties into molecules at distinct places can be used to obtain structural information. Due to the magnitude of the effect, paramagnetic relaxation effects can be observed over much larger distances (up to 30 Å) than NOEs.

14.4
Relaxation and Motion

The efficiency of relaxation processes is coupled to motional properties of the molecules, and because of this relation NMR is a very powerful probe of dynamics. In this section we will explain the relationship between motional properties and the efficiency of T1 and T2 relaxation.

We stated above that the dipolar field from another spin close in space acts like a very weak RF pulse. The dipolar field is, of course, much weaker than the B_0 field and is even weaker than the B_1 field. In Section 6.6, we discussed that a static field has no influence in the presence of a much stronger orthogonal field. In the

context of RF pulses, we have learned that the trick is to apply the additional field such that it oscillates in the transverse plane with a frequency close to the Larmor frequency. In the context of relaxation, the rotation of the dipolar field about the z axis must stem from rotation of the molecule (or motion of parts of the molecule). The fraction of molecules tumbling at a frequency very close to one of the NMR transitions will then determine the efficiency of the process. We have also discussed that an additional dipolar field along the z axis directly alters the Larmor frequency. We will see later why the efficiency of this process is greatest when the molecule is at rest.

In order to describe this motional component more precisely, we need to understand how we can mathematically express the fraction of molecules that happen to tumble at the correct frequency. We also need to understand what we mean by "correct frequency," and we will see that this may be more than just the Larmor frequency of the nucleus. But let us first have a closer look at the motional properties of molecules in solution.

Molecules tumble around all possible axes in solution. Small molecules may tumble very rapidly; large molecules will on average tumble more slowly. The average time required for the molecule to rotate by 180° about an axis is called the *correlation time* (or reorientation time), abbreviated as τ_c. Molecules do not tumble at the same rate all the time, and their motional states in solution are largely determined by collisions with solvent molecules, which will change the direction and rate of their rotation. Their size and shape, however, determine the upper limit of the rotation frequency. Accordingly, the rotational rates of ensembles of molecules can be described as a smooth distribution of frequencies, with an upper limit depending on their size. This function is called the *spectral density* and describes the fraction of molecules at particular rotational frequencies.

In the description above, motion was assumed to be entirely due to overall tumbling. While this is true for rigid molecules, large molecules with structured and unstructured parts may possess additional *internal motion* in the regions that are flexible.

14.4.1
A Mathematical Description of Motion: The Spectral Density Function

How do we mathematically distinguish between a state that rapidly changes its orientation from one that does not? For this task we will need to introduce the *autocorrelation function* $g(\tau)$, which is defined as

$$g(\tau) = \overline{f(t) \cdot f(t+\tau)} \tag{14.4}$$

The autocorrelation function g is defined as the scalar product of two vectors, one describing the initial state and the other describing the state after some time increment τ, averaged over the whole ensemble. The autocorrelation function goes rapidly to zero for quickly changing states. This is illustrated in Figure 14.5.

A vector at $t = 0$ is shown together with (four) snapshots after some time increment $t = \tau$. Note that the four snapshots correspond to four different entities

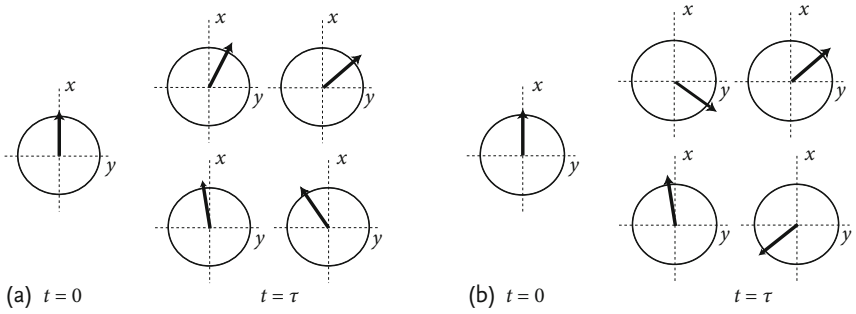

Figure 14.5 Definition of correlation functions. Ensemble of vectors of slowly (a) or rapidly (b) reorienting objects.

from the ensemble, all taken at the same time. Although the orientation in all four states is different, in the slowly reorienting system (Figure 14.5a) they are closer to the original state than in the rapidly reorienting system (Figure 14.5b). Since these are vector quantities, they have a sign, and states in which the orientation relative to the original state have changed by more than 90° (disregarding the sense of the rotation) will have a negative sign. The product $f(t) \cdot f(t+\tau)$ will therefore be positive *and* negative in Figure 14.5b, while it is only positive in Figure 14.5a. Averaging over the ensemble in Figure 14.5b (which means averaging over a spread of positive and negative numbers) will lead to a small number (or zero). Accordingly, the autocorrelation function g will decay quickly to zero for rapidly rotating systems, while it will only very slowly approach zero for slowly reorienting systems. The autocorrelation function therefore expresses how rapidly molecules rotate about arbitrary axes. Since observed NMR signals decay exponentially (this can be concluded from the line shape, which is Lorentzian as expected for exponential decays), $g(\tau)$ is believed to decay exponentially:

$$g(\tau) = \mathrm{e}^{-\tau/\tau_\mathrm{c}} \tag{14.5}$$

We are less interested in the time it takes for a molecule to change its spatial arrangement than in the frequency with which these changes take place. We already know how to transform a property from the time domain into the frequency domain, because we use this procedure for processing NMR data: the Fourier transform. The *spectral density* $J(\omega)$ is the Fourier transform of the autocorrelation function. $J(\omega)$ tells us how much power is available from the motion of the molecule to cause fluctuations at frequency ω. The normalized spectral density is given as

$$J(\omega) = 2\int g(\tau)\mathrm{e}^{\mathrm{i}\omega t} = \frac{\tau_\mathrm{c}}{1+\omega^2\tau_\mathrm{c}^2} \tag{14.6}$$

The dependence of the spectral density on the frequency is shown in Figure 14.6 for small, medium-sized, and large molecules. It is clear that the spectral densities at low frequencies, in particular close to $J(0)$, strongly increase with increasing correlation times (e.g., larger molecules). This can be rationalized in the following

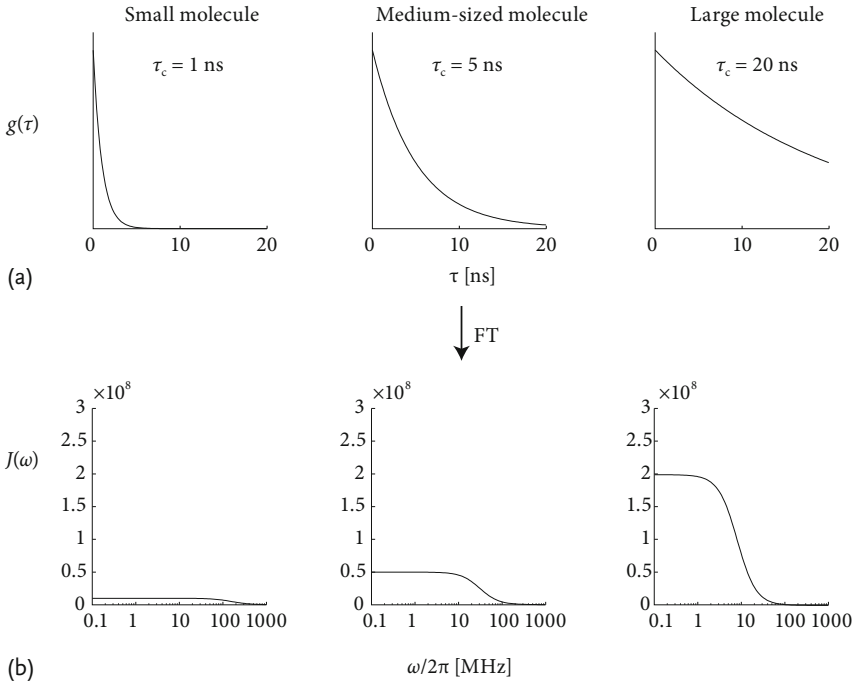

Figure 14.6 Correlation functions (a) and corresponding spectral densities (b). Correlation functions for small, medium, and large molecules (from left to right) and the corresponding spectral densities. Note that the integral under the spectral density functions is the same for the three cases. That this does not seem to be the case is due to the logarithmic representation of the *x* axis. FT – Fourier transform.

way. The overall power from all frequencies (the integral under the spectral density function) must remain the same because it corresponds to the total number of molecules. However, smaller molecules may rotate faster than larger molecules, so the highest possible frequency is lower for larger molecules and hence the spectral density at $J(0)$ increases with molecular weight. As we will see, this is important because it results in more efficient T2 relaxation, and unfortunately places a physical limit on the size of large molecules that can be studied by solution NMR techniques.

14.4.2 NMR Transitions That Can Be Used for Relaxation

In Sections 14.3.1 and 14.4 we saw that spins can change their state due to dipolar interactions with other nearby nuclear spins. We have also explained that the molecule needs to tumble at a frequency that corresponds to one of its NMR transitions in order for T1 relaxation to occur, because only then will the dipolar field be effective in causing transitions. While in isolated spins this frequency corresponds to the Larmor frequency of the spin, for scalarly coupled spins additional frequen-

cies may be used. For two coupled spins I and S the possible frequencies that can be used for relaxation are the single-quantum, double-quantum, and zero-quantum frequencies.

The frequencies for single-quantum transitions correspond to the Larmor frequencies of the I or S spin (ω_I or ω_S). The zero-quantum transitions occur at the difference between the Larmor frequencies ($\omega_I - \omega_S$), and the double-quantum frequencies occur at the sum frequency ($\omega_I + \omega_S$). These frequencies are very different, depending on whether a homonuclear spin pair is involved or not. In the case where I and S are both protons, with a 600 MHz instrument the double-quantum transitions occur at 1.2 GHz, whereas the zero-quantum transitions are in the audio range (below 6000 Hz). If the I spin is a proton and the S spin is an ^{15}N nucleus, the double-quantum frequency is about 660 MHz, and the zero-quantum frequency is about 540 MHz, both fairly close to the proton Larmor frequency.

14.4.3 The Mechanisms of T1 and T2 Relaxation

For T1 relaxation to occur spins need to be flipped from the β state to the α state or vice versa. We have seen previously that this requires the presence of dipolar fields in a direction orthogonal to the static field. Moreover, the molecule must contain sufficient motion at the frequency of an NMR transition, because only then is the very weak dipolar field effective. To formulate this more mathematically, we postulate for the longitudinal relaxation time of spin I

$$\frac{1}{\mathrm{T1}} \propto \gamma_I^2 \left(\overline{B}_x^2 + \overline{B}_y^2 \right) J(\omega) \tag{14.7}$$

where $\overline{B}_i$ is the average dipolar field strength along axis i produced by spin S, and $J(\omega)$ is the spectral density at the single-quantum transition frequency. This equation is valid only for isolated spins; scalarly coupled spins can use additional frequencies (see Sections 14.4.2 and 14.5).

In the case of T2 relaxation the situation is more complicated. Dipolar fields along a direction orthogonal to the axis of the static field in conjunction with motion at the Larmor frequency will flip a spin, and thereby reduce the phase coherence among all the spins. In addition, a dipolar field along z or $-z$ will add to the static field, thereby locally altering the precession frequency of a spin directly, and as a result will also reduce phase coherence. Interestingly, the dephasing effect of the dipolar field along the z axis of the static field has a different dependence on motion. In fact, its capability to dephase coherences becomes increasingly effective as the molecular rotation slows. When the molecule rotates by, for example, 90° the dipolar field will subtract from instead of add to the static field (see Figure 14.7) Any motion will change the position of that field and average out this effect.

For this process to contribute significantly to transverse relaxation, zero or very little motion is needed, and accordingly the spectral density at frequency zero, $J(0)$, is important. To summarize, two processes are important; one similar to the one

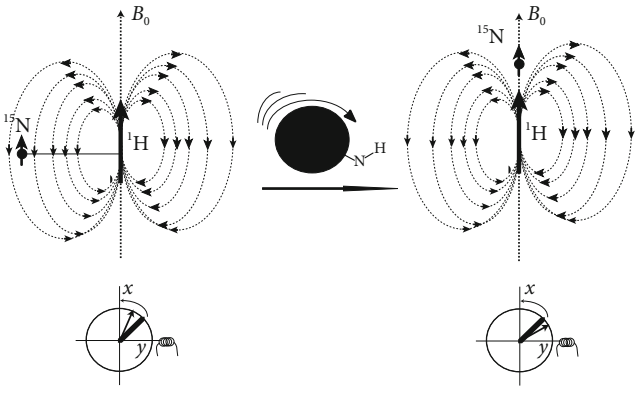

Figure 14.7 Dipolar fields. Orientation of a dipolar field at the site of an ^{15}N nucleus due to a neighboring ^{1}H nucleus and the effect on the Larmor frequency of the ^{1}H nucleus. The relative orientation determines whether the dipolar field will increase or decease the effective field.

active for T1 relaxation, the other one depending on zero (or no) motion:

$$\frac{1}{\mathrm{T2}} \propto \gamma_I^2 \left[\left(\overline{B}_{x,y}^2 \right) J(\omega) + \left(\overline{B}_z^2 \right) J(0) \right] \tag{14.8}$$

We have already seen (Figure 14.7) that the spectral density at zero frequency, $J(0)$, increases with molecular weight (or with τ_c). This means that transverse relaxation becomes more and more effective as the molecular weight increases. This imposes a physical limit on what type of molecules we can measure using solution NMR techniques, because resonance lines inevitably become too broad when the molecular weight is too large.

14.4.4 Transition Probabilities

For isolated spins only motions at the Larmor frequency contribute to T1. For coupled spins, however, also zero-quantum and double-quantum frequencies are important. But even if similar spectral densities exist at the single-quantum and double-quantum frequencies, the transition probabilities for these two transitions are not the same. A calculation (which is beyond the scope of this book) results in the following transition probabilities for the single-quantum, double-quantum, and zero-quantum transitions:

$$W_1 = \frac{3}{20} d^2 J(\omega_I) \tag{14.9}$$

$$W_2 = \frac{3}{5} d^2 J(\omega_I + \omega_S) \tag{14.10}$$

$$W_0 = \frac{1}{10} d^2 J(\omega_I - \omega_S) \tag{14.11}$$

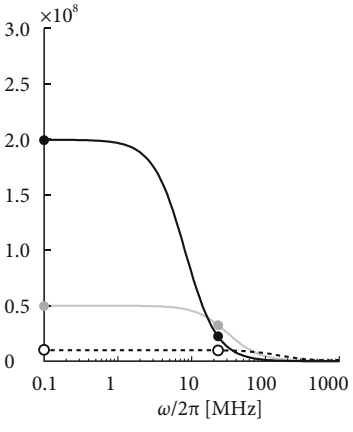

Figure 14.8 Spectral densities. Spectral densities at two different frequencies for molecules with differing molecular weights.

where d is the dipolar coupling constant

$$d = \frac{\mu_0 \hbar}{4\pi} \frac{\gamma_I \gamma_S}{r_{IS}^3} \tag{14.12}$$

If we examine the spectral density functions of small and large molecules (Figure 14.8), it becomes clear that for small molecules with short τ_c, $W_2 > W_1 > W_0$, whereas for large molecules with long τ_c, $W_0 > W_1 > W_2$.

It should again be emphasized that zero-quantum transitions for an ^{15}N–^{1}H spin pair still occur at very high frequency, whereas for a proton–proton pair the frequency is close to zero, thereby probing spectral densities at very different frequencies!

The different dependencies of T1 and T2 relaxation on spectral densities at $J(0)$ result in a different behavior of these relaxation times with respect to size. This is illustrated in Figure 14.9.

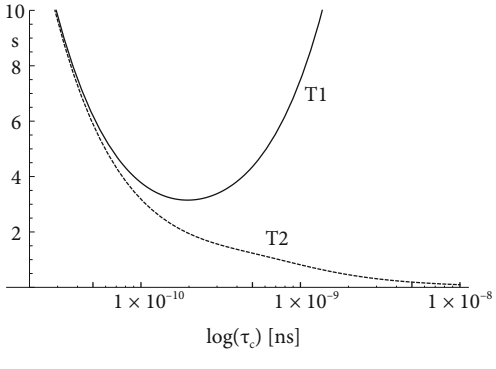

Figure 14.9 Dependence of T1 and T2 on the overall tumbling time τ_c.

For small molecules (rapid reorientation), T1 $\approx$ T2, while for large molecules T2 $\lll$ T1. We can now understand this behavior. For large molecules $J(0)$ increases all the time, and hence T2 becomes smaller and smaller, while for small molecules the contribution at $J(0)$ is insignificant and therefore T1 $\approx$ T2. The size regime in which T1 $\approx$ T2 is sometimes called the *extreme narrowing* regime, whereas the range with T2 $\lll$ T1 is called the *spin-diffusion regime* (see Section 15.2.1).

14.4.5
Measuring Relaxation Rates

As described in much more detail in Section 12.8.1, T1 measurements use an *inversion-recovery* sequence. The T2 relaxation rate is determined using the *Carr–Purcell–Meiboom–Gill* (CPMG) experiment (Section 12.8.2.3). The heteronuclear NOE experiment records X-nucleus spectra with and without proton presaturation. Two-dimensional implementations of these experiments based on heteronuclear single-quantum coherence (HSQC) are described in Chapter 13.

14.5
Measuring ^{15}N Relaxation to Determine Protein Dynamics

Measuring ^{15}N relaxation has become a very popular tool to probe protein backbone dynamics. The ^{15}N nucleus of the amide backbone moieties almost entirely relaxes via dipolar interaction with the directly bonded amide proton, other protons are too far away (remember that the dipolar coupling strength according to (14.17) depends on r^{-6}), and the relaxation with the attached carbons is also less important because of the lower gyromagnetic ratio of ^{13}C. Depending on the field strength, CSA may contribute significantly to relaxation. However, the CSA for ^{15}N has been accurately determined. Therefore, ^{15}N relaxation is comparably easy to interpret. Moreover, relaxation rates can be determined from 2D [^{15}N,^{1}H]-HSQC-type experiments, which display superior signal dispersion and good sensitivity.

The experiments based upon the HSQC used to measure T1, T2, and the ^{15}N{^{1}H} NOE of proteins are described in Chapter 13. In the T1 and T2 experiments the relaxation delay is varied and [^{15}N,^{1}H] correlation spectra are recorded. The peak intensity will decrease with increasing length of the relaxation delay. A series of spectra obtained with T1 and T2 experiments performed with different settings of the relaxation delay are recorded, peaks are integrated, and the peak intensity is then plotted against the relaxation delay. These curves usually display monoexponential decays, and a fit to a function of the type

$$I = I_0 e^{\frac{t}{Ti}} \tag{14.13}$$

allows the relaxation time constants T1 and T2 to be extracted. In the case of the ^{15}N{^{1}H} NOE, two experiments, one without (the reference) and one with (the

NOE spectrum) proton saturation, are performed. The ratio of the peaks of the two spectra directly yields the $^{15}N\{^1H\}$ NOE.

The analytical dependence of the ^{15}N R1, R2, and cross-relaxation rates (σ_{IS}) on the dipolar coupling and the CSA is given by

$$R1 = \frac{d^2}{4}\{J(\omega_H - \omega_N) + 3J(\omega_N) + 6J(\omega_H + \omega_N)\} + \frac{\Delta^2\omega_N^2}{3}J(\omega_N) \quad (14.14)$$

$$R2 = \frac{d^2}{8}\{4J(0) + J(\omega_H - \omega_N) + 3J(\omega_N) + 6J(\omega_H) + 6J(\omega_H + \omega_N)\} + \frac{\Delta^2\omega_N^2}{3}\left\{\frac{2}{3}J(0) + \frac{1}{2}J(\omega_N)\right\} \quad (14.15)$$

$$\sigma_{IS} = \frac{d^2}{4}\{-J(\omega_H - \omega_N) + 6J(\omega_H + \omega_N)\} \quad (14.16)$$

where d denotes the dipolar coupling constant, defined as

$$d = \frac{\mu_0\hbar\gamma_H\gamma_N}{4\pi^2} \cdot \frac{1}{\langle r_{N,H}^3\rangle} \quad (14.17)$$

In the formulas for R1 and R2, the first term always describes the dipolar coupling and the second term describes the CSA contribution. μ_0 denotes the permeability of free space, Δ denotes the CSA, and all other constants have their usual meaning.

The spectral density functions can be calculated as

$$J(\omega) = \frac{\tau_c}{1 + \omega^2\tau_c^2} \quad (14.18)$$

According to these expressions, R1 and R2 as well as the NOE should be the same for all residues because the correlation time of the molecule is the only variable. In reality R1 and R2 values span a large range in proteins, with the values of flexible residues having small values of R1, R2, and the NOE, while residues in rigidly folded regions are characterized by large R1, R2, and $^{15}N\{^1H\}$ NOE values close to 0.8. The reason for the spread of relaxation rates is the presence of additional local motion at certain residues, making the assumption of a single overall correlation time invalid.

14.5.1 The Lipari–Szabo Formalism

The Lipari–Szabo (LS) formalism introduces an internal correlation time to account for the additional flexibility. Let us try to understand this using an analogy from daily life. Suppose we are interested in the traveling behavior of an NMR spectroscopist. Being placed on planet Earth, he will continuously change his position

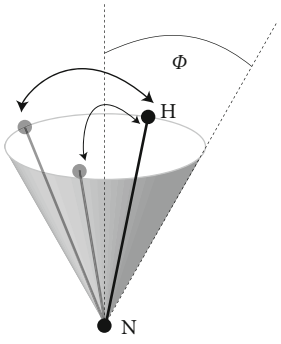

Figure 14.10 Wobbling-in-a-cone motional model. Spatial restriction of jumps is presented by the half-angle ϕ.

because our planet rotates about its own axis, rotates about the sun, and in principle the universe is also expanding. All these motions are of no interest to us, and therefore we will try to factor them out. This again corresponds to transformation into a rotating coordinate system. In such a coordinate system our spectroscopist should be at rest when he sits in his chair in his office. Now, if he gets on a plane and goes to a conference, he should move also in this coordinate system. In a similar way we try to separate motions due to overall tumbling from internal motions in the LS formalism.

Formally this is achieved by expressing the autocorrelation function as a product of two autocorrelation functions, one that specifies overall motions (g_o) and one that specifies internal motions (g_i):

$$g(t) = g_o(t) \cdot g_i(t) \tag{14.19}$$

As described in Section 14.4.1, the overall autocorrelation function is assumed to decay exponentially:

$$g_o(t) = e^{\frac{t}{\tau_c}} \tag{14.20}$$

The autocorrelation function for internal motions $g_i(t)$ is expressed as

$$g_i(t) = S^2 + (1 - S^2)e^{\frac{t}{\tau_e}} \tag{14.21}$$

The parameter S^2 is called the *generalized order parameter*. Its formal definition is complicated, but its meaning is fairly simple. A value of 1.0 indicates that the motion of that moiety is totally correlated to overall tumbling; there is *no* internal motion. S^2 of 0 means that the moiety is completely decoupled from overall motion (totally flexible). The strength of the LS formalism is that it does not require a specific motional model for interpretation, and therefore the formalism is also often referred to as the *model-free formalism*. However, S^2 values are often interpreted in a certain motional model, for example, the *wobbling-in-a-cone* model (Figure 14.10). In this model the bond vector makes arbitrary jumps; these are, however, spatially restricted within a cone.

The half-angle of the cone (ϕ) describes to what extent the internal motion is restricted (180° corresponds to complete flexibility and 0° corresponds to a perfectly

rigid system). It can be shown that

$$S^2 = \left(\cos\phi \frac{1+\cos\phi}{2}\right)^2 \tag{14.22}$$

The LS formalism can only be applied to systems where the timescales of internal and overall motions are separated by at least a factor of 10, and when internal and overall motions are decoupled. While the theoretical framework of the LS formalism is complicated, the S^2 values are very descriptive and yield a good picture of which parts of the molecule are flexible and which parts are rigid. In that respect they are similar to the B factors from crystallographic studies, but their information content is higher. The LS formalism will under certain circumstances also allow one to extract internal correlation times, and often the autocorrelation function of the internal motions needs to be further modified when internal motions on different timescales are present.

Excursus 14.1: Cross-Correlated Relaxation and Relaxation Interference

When two motional process are coupled, they are said to be cross-correlated. For example, the dipolar interactions of two spin pairs that are part of the same covalently rigid skeleton, so that they cannot move relative to each other, are cross-correlated. An example is two different CH dipolar couplings in an aromatic ring, or two CH dipolar couplings in a monosaccharide unit. Whenever one unit moves, the other will follow. This can in principle also be true for moieties that are separated by rotatable bonds but adopt a well-defined structure (e.g., in folded proteins). Mathematically, cross-correlation can be expressed as

$$k(\tau) = \overline{f(t)\cdot g(t+\tau)} \tag{14.23}$$

The cross-correlation function characterizes to what extent a vector g after some time increment τ is correlated to another vector f.

Two important examples are cross-correlation between two dipole interactions and cross-correlation between dipole interactions and CSA. An important application is the dipole–dipole/CSA cross-correlation that results in the transverse-relaxation-optimized spectroscopy (*TROSY*) effect. Let us look at the cross peak from an amide moiety in an $^{15}N,^{1}H$ correlation experiment. If we do not decouple in both dimensions, we will detect a doublet separated by about 90 Hz due to the coupling of the ^{15}N nuclei with the attached protons. For large molecules the two doublet lines have very different line widths, and this effect is due to dipole–dipole/CSA cross-correlation (or *relaxation interference*). In Section 14.5 we saw that the R2 rate constant is proportional to contributions from dipolar interactions and CSA. In the amide moiety, the motion of the amide nitrogen is 100% correlated to the motion of the N–H dipolar vector, because the nitrogen and the amide proton are connected by a covalent bond. As a consequence, contributions from dipole–dipole/CSA cross-correlation arise. For large molecules,

all spectral densities other than $J(0)$ become vanishingly small, and the transverse rate constants for the two double lines are

$$\mathrm{R2(line1)} = \frac{1}{10}d^2\frac{1}{2}J(0) + \frac{2}{45}c_\mathrm{N}^2 J(0) + \frac{2}{15}c_\mathrm{N} d\frac{1}{2}(3\cos\phi - 1)J(0) \quad (14.24)$$

$$\mathrm{R2(line2)} = \frac{1}{10}d^2\frac{1}{2}J(0) + \frac{2}{45}c_\mathrm{N}^2 J(0) - \frac{2}{15}c_\mathrm{N} d\frac{1}{2}(3\cos\phi - 1)J(0) \quad (14.25)$$

with d as defined in (14.17) and $c = \gamma_\mathrm{N} B_0(\sigma_{\mathrm{N},\parallel} - \sigma_{\mathrm{N},\perp})$.

In (14.24) and (14.25) the first term corresponds to the dipolar coupling, the second to the CSA, and the third to dipole–dipole/CSA cross-correlation. The important feature here is that the third term, the cross-correlation term, has a different sign for the two lines. As a result, in one case it adds to the other relaxation mechanisms and in the other case it partially compensates them, resulting in a decrease of the relaxation rate constant and hence a narrower line.

Dipole–dipole/CSA relaxation interference is exploited in *TROSY*. An experimental example is shown in Figure 14.11. Normally, proton couplings are removed in ^{15}N,^{1}H correlation experiments by decoupling. In TROSY this is not done, so the four components of a single correlation (two components in each dimension due to the ^{15}N,^{1}H coupling) are detected. It is clearly visible that the cross peak at the lower right of the spectrum (Figure 14.11b) is much narrower and more intense than the other cross peaks, in particular when compared with the one at the upper left of the spectrum (the so-called anti-TROSY component). The most intense and narrowest cross peak corresponds to the transition in which in both dimensions cross-correlation partially compensates the two relaxation mechanisms. The TROSY effect is field dependent because c in (14.24) and (14.25) depends on B_0, and is optimal close to 1.2 GHz for ^{15}N,^{1}H couplings. In the TROSY experiment the broader component is usually removed by phase-cycling.

The direction of the dipolar field reverses depending on whether the other spin (in this case the proton) is in the α state or the β state as depicted in Figure 14.12. In one case the dipolar field B^DD adds to the field from the CSA tensor B^CSA; in the other case it partially cancels it.

14.6 Measurement of Relaxation Dispersion

We will discuss effects of chemical or conformational exchange in much more detail in Chapter 16. Here were merely point out that they result in additional line broadening. As described in Section 14.4.5, transverse relaxation rates are measured using the so-called CPMG pulse train. The CPMG sequence comprises a

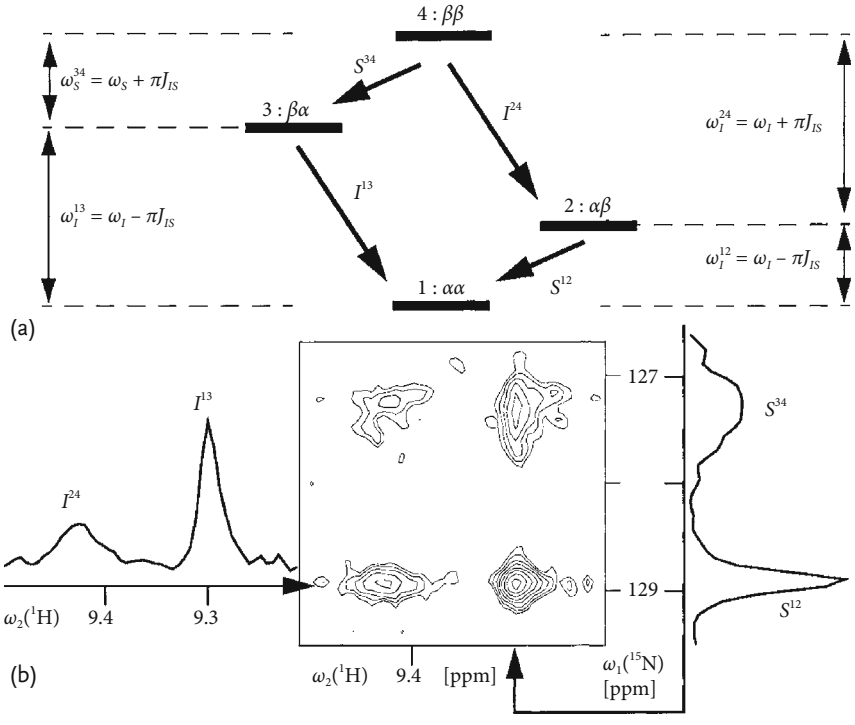

Figure 14.11 Transverse-relaxation-optimized spectroscopy (TROSY) spectrum. Multiplet pattern in a nondecoupled $^{15}N,^1H$ spectrum (b). Horizontal and vertical traces through the cross peaks are depicted at the side of the spectrum. The TROSY component in that case is represented by the lower-right component. The location of the corresponding transitions in the energy level diagram is depicted in (a). Reproduced with permission from Zerbe (Ed.) BioNMR in Drug Design, Chapter 10).

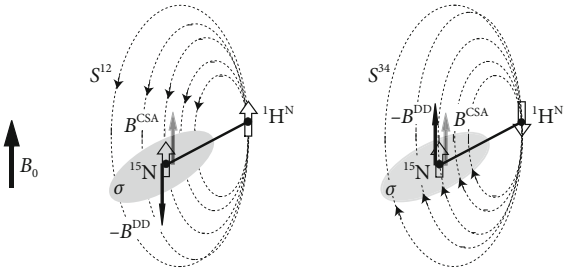

Figure 14.12 Orientation of tensors: Direction of dipolar field (black arrow) and chemical shift anisotropy tensor (gray arrow) at an ^{15}N site.

train of equally spaced 180° pulses. When exchange is present, the apparent R2 rate depends on the time spacing of the 180° pulses, a phenomenon named *relaxation dispersion*. Relaxation dispersion experiments help to identify exchanging sys-

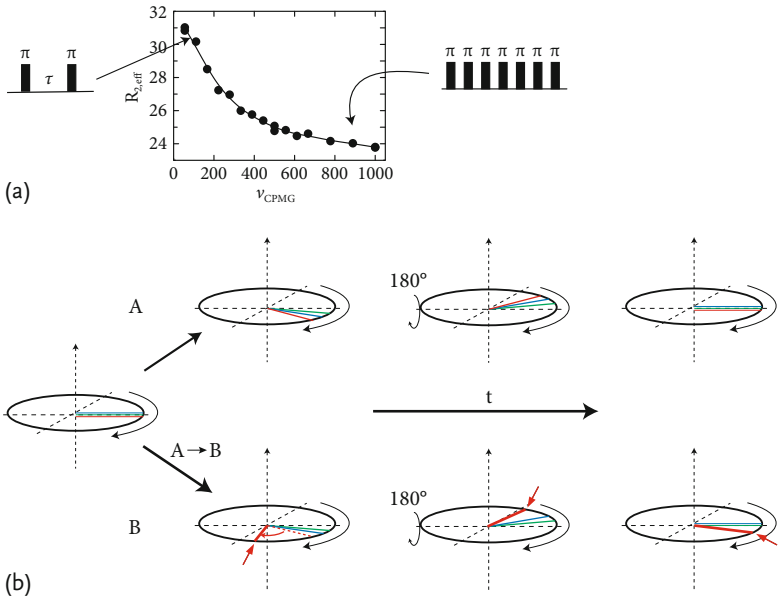

Figure 14.13 Relaxation dispersion. Two spins A and B interconvert with rates k_{AB} and k_{BA} through exchange, resulting in two signals ω_A and ω_B in a 1D spectrum or two cross peaks in a 2D spectrum. The extracted R2 rate depends on the delay τ that separates the 180° pulses in the Carr–Purcell–Meiboom–Gill (CPMG) pulse train (a). The higher the pulse repetition rate is, the closer the apparent R2 is to the true value. (b) The transverse magnetization from a few spins during the spin echo in the absence (case A) or presence (case B) of exchange. The magnetization from the spin in red undergoes a two-site exchange and precesses with a higher frequency afterward and hence will not be perfectly aligned with the others at the end of the spin echo.

tems. Moreover, using sophisticated analysis, we can extract rates for the exchange process as well as the frequencies involved.

Transverse relaxation characterizes the loss of transverse phase coherence. An exchange process by which a frequency ω_A interconverts into a different frequency ω_B will change the phase of the corresponding spin, and therefore contribute to line broadening. A scenario is depicted in Figure 14.13b. The magnetizations from three different resonances indicated by red, blue, and green lines have slightly dephased due to T2 processes. Application of a 180° pulse in the spin echo flips them such that after an additional period τ they are coaligned (case A). However, if a frequency shift due to exchange occurs, the corresponding spin may continue precessing at a very different frequency for the remaining time. If the precession frequency difference $\Delta\omega = \omega_A - \omega_B$ is large relative to $\Delta\nu_{CPMG}$, the corresponding spin is not properly refocussed and therefore not aligned with the others at the end of the spin echo (case B). If we vary the time spacing between the pulses systematically, we modify the sensitivity of the measured R2 rates to exchange to obtain a typical relaxation dispersion curve as depicted in Figure 14.13a.

The relaxation dispersion profile for an exchanging system clearly demonstrates that R2 depends on ν_{CPMG}, while it is independent in the absence of exchange. By fitting the curves to an analytical function, we can extract the rate constants as well as the frequency separation $\Delta\omega$. Knowledge of $\Delta\omega$ is important because it allows us to obtain information about *invisible states*, states that are populated to such a small extent that their corresponding signals cannot be observed in the spectra directly.

14.7 Problems

14.1. Describe the most important relaxation mechanisms for the following spins (we look at the spins printed in bold): (a) –C**H**$_2$CH$_3$, (b) –^{13}**C**–^{14}N, (c) –^{13}**C**=O

14.2. Which relaxation mechanisms lead to enthalpic and which to entropic changes?

14.3. What is the observable effect of short T2 and long T1 times in spectra?

14.4. How do you measure T1 and T2 relaxation times (name of the experiments)?

14.5. Suppose you have a pair of ^{1}**H**–^{1}H and ^{1}**H**–^{15}N spins in the same distance. Are the proton T1 and T2 times the same?

14.6. Describe qualitatively the difference between amide moieties with an S^2 of 0.8 and 0.3.

14.7. Describe the principle behavior of the T1 and T2 curve against molecular weight.

14.8. Under which conditions are TROSY spectra most useful (with respect to molecular weight, magnetic field, and deuteration level)?

15
The Nuclear Overhauser Effect

15.1
Introduction

The nuclear Overhauser effect (NOE) is used extensively to establish the stereochemistry of molecules by measuring spatial proximities of (mainly proton) nuclei. It is still the principal technique used in determining structures of proteins or nucleic acids in solution. The NOE is a relaxation phenomenon. If you are interested in understanding how it works, we recommended you read Chapter 14 before you start reading this chapter. The original article on this effect was by Overhauser, an American physicist, in 1953. He stated that nuclear spin polarization can be enhanced through microwave irradiation of electrons, and this was soon verified by Slichter. Kaiser then applied the phenomenon to measure the proton–proton NOE, for which this effect became really famous and useful.

In the classic 1D NOE experiment a single resonance is perturbed such that the population of α and β states is different from the Boltzmann distribution. Such a perturbation can be achieved by applying low-power (and therefore selective) irradiation on a single resonance. As a result, the resonance is *saturated*, and α and β states are then populated to the same extent. Alternatively, one can apply a selective 180° pulse, and thereby *invert* populations. Both ways of manipulating resonances are depicted in Figure 15.1. One set of lines, labeled as *S*, correspond to the lines of the *S* resonance; the others correspond to the *I* resonance. After the inversion pulse has been applied, the populations corresponding to the *S*-spin resonances are inverted, while they are equalized when using saturation. Note that saturation leads to the (usually only almost) complete disappearance of the signal from the spectrum, while inversion results in a signal with full amplitude but opposite sign.

What happens once we have saturated or inverted the resonance? Since this process has changed population levels, the system will relax back to equilibrium population levels via T1 relaxation. It can do so via a process called *autorelaxation* or via a process called *cross-relaxation*. As we learned in Chapter 14, both processes occur mostly via dipolar coupling (and for some nuclei additionally via chemical shift

Applied NMR Spectroscopy for Chemists and Life Scientists, First Edition. Oliver Zerbe and Simon Jurt.
©2014 WILEY-VCH Verlag GmbH & Co. KGaA. Published 2014 by WILEY-VCH Verlag GmbH & Co. KGaA.

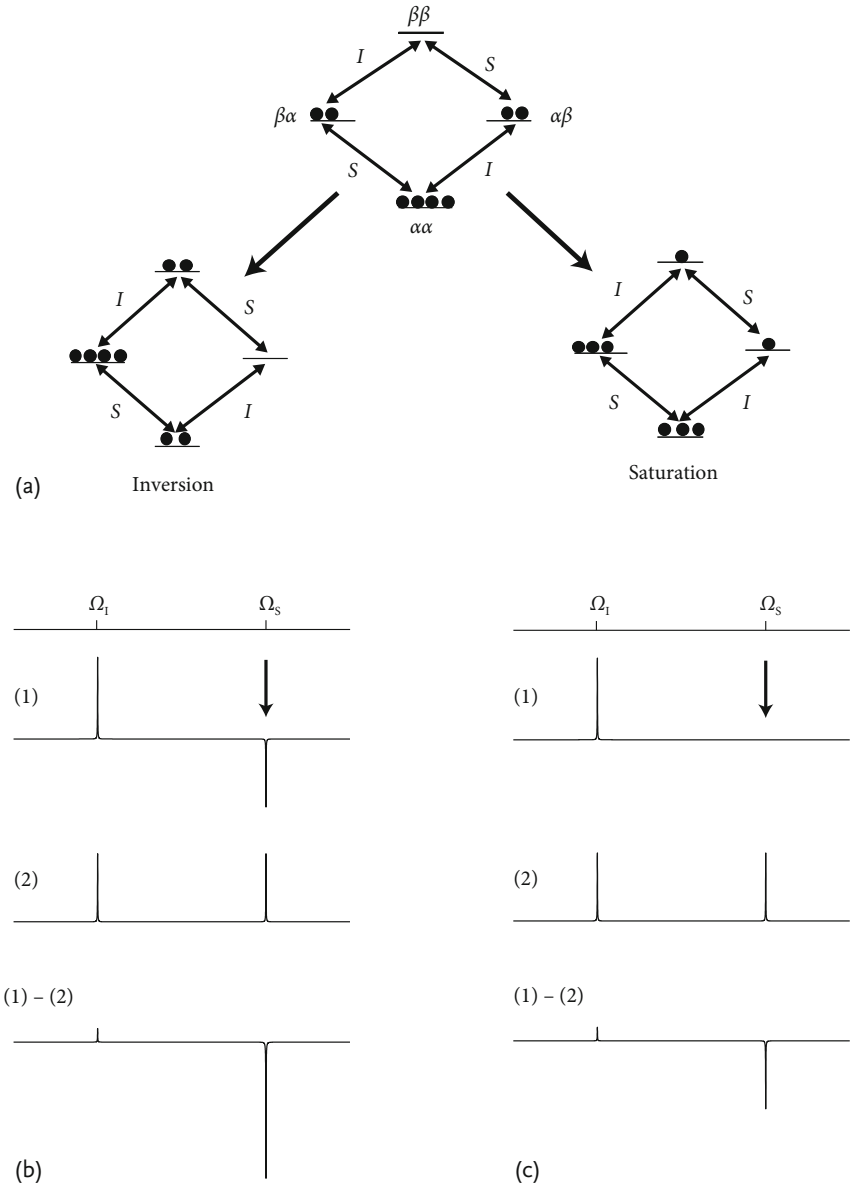

Figure 15.1 Definition of a two-spin system (a); population levels and spectra following inversion (b) and saturation (c).

anisotropy). When the system relaxes back to equilibrium through cross-relaxation, this will, however, alter the population levels of *other* spins. Accordingly, they will appear in the spectrum afterward with slightly altered intensities. The change in intensity of a resonance as the result of cross-relaxation with another nucleus is

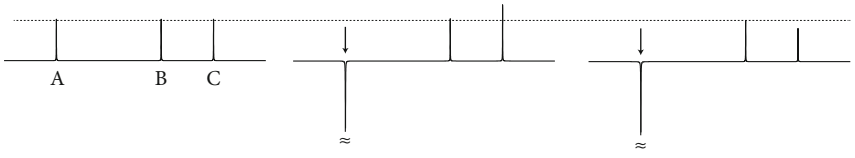

Figure 15.2 Definition of the nuclear Overhauser effect (NOE). After inversion of resonance *A*, the intensity of resonance *C* is increased (positive NOE; center) or decreased (negative NOE; right). Resonance *B* is not affected.

called the NOE. The result of cross-relaxation can be such that the intensity of the noninverted (nonsaturated) line becomes larger or smaller, and the corresponding NOE is then called positive (increase in intensity) or negative (decrease in intensity). This is shown in Figure 15.2.

To explain this effect we use the analogy in Figure 15.3. Let us assume we place three iron bowls in space. The temperature of the environment is 10 °C. Now we start to heat up one of the bowls to 500 °C. Once we stop heating, the bowl will cool down again. If the other two bowls are a large distance apart the hot bowl will cool down only very slowly (case *A*). If another bowl is sufficiently close, it will take up some heat from the hot bowl, and it will do that more quickly (case *B*) or slowly (case *C*) depending on its distance from the hot bowl. Accordingly, the hot bowl will cool down more quickly, but the second bowl will also warm up. If we place two cold bowls close to the hot one (case *D*), the closer one will take up most of the heat.

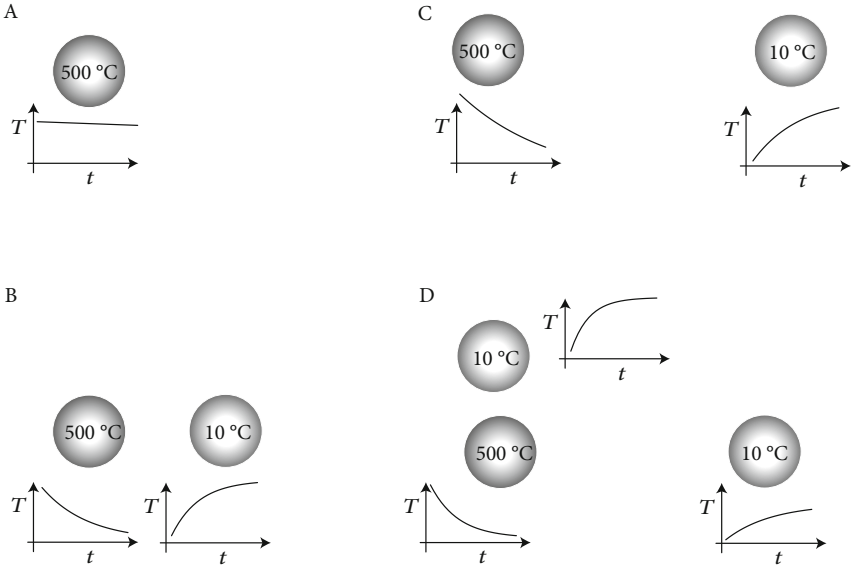

Figure 15.3 Analogy for the NOE using bowls of different temperature. The initial temperatures are printed on the bowls, and the time-dependent temperature profiles of the bowls are depicted below them. The temperature profiles of the cold and hot bowls are drawn to different scale.

Two points are important to remember: (i) the proximity of a second bowl results in much faster cooling of the hot bowl and (ii) the amount of heat taken up by the cold bowl at the larger distance is less in case *D* compared with case *C*, although the distance to the hot one is the same. The reason is that in case *D* the closer bowl takes up most of the heat (it acts as a heat sink). In our NMR experiment the hot bowl is the perturbed spin, and the two cold ones are the nonperturbed spins. Relaxation depends on the distance between the spins. We learned about dipolar interaction in Section 2.4 and Chapter 14, and we have seen that the dipolar interaction scales with r^{-6}. This analogy tells us that not only the distance between the two spins influences cross-relaxation, but so does the presence of other spins.

15.1.1
Steady-State and Transient NOEs

In the previous section we learned that in principle two different ways exist to alter the populations of spin systems, and accordingly two different sets of experiments are available to measure NOEs. One of these experiments is the so-called *steady-state NOE* experiment, in which a resonance is selectively irradiated with low power for a time τ_m sufficiently long to completely saturate the transition and propagate the NOE (approximately more than 0.5 s). A second spectrum, the reference spectrum, is recorded either without irradiation or with irradiation far away from any resonance and is subtracted from the first spectrum. The difference spectrum shows only signals with altered intensities, and these are due to spins that have received an NOE that means, that have changed their intensity (apart from the signal from the irradiated resonance). The second type of experiment is called the *transient NOE* experiment. In this experiment a resonance is selectively perturbed, usually either by selective 90° or 180° pulses but sometimes also by a *short* period of selective irradiation. After a delay τ_m for NOE buildup, a 90° readout pulse is applied and a 1D spectrum is acquired. Again, one experiment with and one without the selective 180° pulse is performed, and the corresponding spectra are subtracted from each other. The famous NOESY experiment is the 2D variant of the transient NOE experiment.

The two types of experiments differ according to whether the perturbation is driven (continuous saturation; steady-state NOE) or effectively instantaneous (selective pulse, transient NOE).

15.2
The Formal Description of the NOE: The Solomon Equations

Perturbation of a resonance possibly alters the populations of other resonances. The steady-state NOE η is formally described as

$$\eta = f_I\{S\} = \frac{(I - I^0)}{I^0} \tag{15.1}$$

in which $f_I\{S\}$ denotes the fractional change in intensity of the resonance of spin I upon manipulation of spin S (I is the intensity after irradiation, I^0 is the intensity without irradiation).

In the following we will describe this process more formally and look at the change of I-spin magnetization over time ($\mathrm{d}I/\mathrm{d}t$). To again use the analogy in Figure 15.3, we wish to understand how fast the hot bowl cools down. This process depends on a number of parameter: (i) the temperature of the hot bowl, (ii) how many other bowls are around, (iii) what their distances to the hot bowl are, and (iv) what their temperature difference with respect to the hot bowl is. In the NMR experiment the temperature corresponds to the extent by which populations have been changed with respect to the equilibrium values. We wish to express these rates individually first, and then sum them. Before we do that, we need to look in a bit more detail at which processes can lead to the exchange of spin states through dipolar coupling in a two-spin system. As explained in much more detail in Section 14.4.2, in a two-spin system these are the single-, zero-, and double-quantum transitions. These are associated with the frequencies ω_I, $\omega_I - \omega_S$, and $\omega_I + \omega_S$, respectively. In fact, what is really relevant are not the frequencies themselves, but rather the probabilities with which these transitions occur, usually denoted as W_I, W_{0IS}, and W_{2IS}. The relaxation of the I spin depends on

$$\frac{\mathrm{d}I_z}{\mathrm{d}t} = \left(I_z - I_z^0\right)\left(2W_I + W_{0IS} + W_{2IS}\right) - \left(S_z - S_z^0\right)\left(W_{2IS} - W_{0IS}\right) \quad (15.2)$$

In this difference, the first term denotes all pathways by which nonequilibrium I-spin magnetization relaxes, whereas the second term denotes all processes in which nonequilibrium S-spin populations will alter I-spin populations. It is clear that for the second term only pathways can contribute that will affect *both* spins, and those are only the zero- and double-quantum transitions.

At equilibrium, $\mathrm{d}I_z/\mathrm{d}t = 0$ and $S_z = 0$, resulting in

$$0 = \left(I_z - I_z^0\right)\left(2W_I + W_{0IS} + W_{2IS}\right) + S_z^0\left(W_{2IS} - W_{0IS}\right) \quad (15.3)$$

which we can rearrange to

$$\frac{\left(I_z - I_z^0\right)}{S_z^0} = \frac{\left(W_{2IS} - W_{0IS}\right)}{\left(2W_I + W_{0IS} + W_{2IS}\right)} \quad (15.4)$$

Using $S_z^0 = \frac{\gamma_S}{\gamma_I} I_z^0$ and substituting it into (15.4), we obtain

$$f_I\{S\} = \frac{\left(I_z - I_z^0\right)}{I_z^0} = \frac{\gamma_S}{\gamma_I}\frac{\left(W_{2IS} - W_{0IS}\right)}{\left(2W_I + W_{0IS} + W_{2IS}\right)} \quad (15.5)$$

or in shorthand

$$f_I\{S\} = \frac{\gamma_S}{\gamma_I}\frac{\sigma_{IS}}{\rho_{IS}} \quad (15.6)$$

Equation 15.6 has become famous as the *Solomon equation*. σ_{IS} is the so-called *cross-relaxation rate*. It determines how fast the NOE is transferred from the S spin

to the I spin during longitudinal relaxation of the S spin. ρ_{IS} denotes the *direct dipolar relaxation rate*. This term characterizes how quickly a selectively inverted S spin relaxes through exclusive interaction with the I spin. In our analogy, the cross-relaxation rate determines how fast a cold bowl is heated up by the presence of a hot bowl, whereas the direct dipolar relaxation rate characterizes how quickly the hot bowl cools down if it can only interact with a particular cold one (the one to which the NOE is transferred). Since only cross-relaxation will change populations of spins that have not been directly perturbed, this is the process that is important for the NOE transfer.

15.2.1 Different Regimes and the Sign of the NOE: Extreme Narrowing and Spin Diffusion

The magnitude and sign of the NOE is determined by the ratio of the cross-relaxation rate to the autorelaxation rate. The cross-relaxation rate is given by the difference between the double-quantum transition rate and the zero-quantum transition rate (see (15.6)). The probability of using double- or zero-quantum transitions is related to motional properties of the molecule. This is described in much more detail in Section 14.4. For the moment we wish to briefly remind you that double- and zero-quantum transitions take place at very different frequencies. In the case of a proton–proton NOE, the double-quantum transitions will be close to 1 GHz for a 500 MHz spectrometer, while the zero-quantum transitions are in the audio range (below 10 kHz) since they correspond to the chemical shift difference. Which of the transitions are used depends on the motional properties of the molecules (for small rigid molecules this is the time required for overall tumbling, τ_c). To use double-quantum transitions a significant fraction of molecules must tumble at those high frequencies (τ_c must be on the order of the inverse of the double-quantum-transition frequencies, approximately 10^{-9} s), and similarly to use zero-quantum transitions a large fraction of the molecules must tumble very slowly. The statistical distribution of rotational states for the ensemble of molecules is described by the spectral density function. Here we summarize a couple of important features of this function: (i) small molecules may tumble very quickly, and have a broad distribution of rotational states with high and low frequencies similarly distributed; (ii) large molecules tumble at low rates, and the very low frequencies are increasingly populated with size. As a result, large molecules will largely use zero-quantum transitions for cross-relaxation, while small molecules will primarily use double-quantum transitions.

The cross-relaxation rate σ_{IS} is the difference $W_{2IS} - W_{0IS}$, and, depending on which of the two transitions dominates, the sign of the NOE is positive or negative. This is demonstrated in Figure 15.4. For small molecules the double-quantum transitions are used more effectively, and hence the NOE is positive, while for large molecules zero-quantum transitions are more favorable and hence the NOE is negative. There is a little confusion about the sign of cross peaks in NOESY spectra (the 2D NOE experiment): for small molecules the NOE is positive but the cross peaks

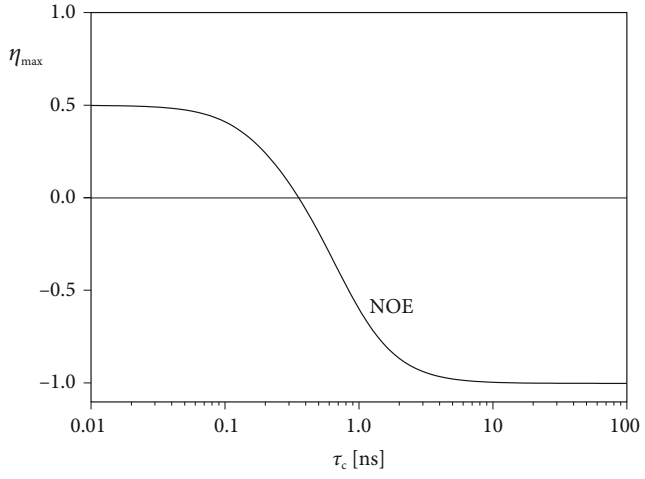

Figure 15.4 Dependence of the NOE on the correlation time.

are negative (when phasing the diagonal peaks to be positive); for large molecules the NOE is negative, but the cross peaks are positive.

At some particular motional state, the NOE is zero irrespective of the distance between the protons involved, and this is the case when $W_{2IS} - W_{0IS}$ becomes zero. Traditionally, the regime characterizing small molecules (those that result in positive NOEs) is called the *extreme-narrowing* regime, because the resonance lines are comparably sharp. For molecules in that regime, the transverse and longitudinal relaxation times are similar (T1 $\approx$ T2). The regime characterizing large molecules is called the *spin-diffusion* regime. Lines are broad, and spin diffusion (the transmission of NOEs down a chain of close contacts) is very effective. Transverse relaxation times are short, and with increasing size the difference between T1 and T2 becomes larger because longitudinal relaxation is less efficient for large molecules again, while transverse relaxation becomes increasingly more efficient.

15.2.2 The Steady-State NOE

In the steady-state NOE experiment a single resonance is irradiated long enough to completely saturate the transitions. Without deriving the equation describing the NOE in that case in detail, we will present it and rather spend some time trying to understand what it means:

$$f_I\{S\} = \eta_{\max}\frac{r_{IS}^{-6}}{r_{IS}^{-6} + \sum_x r_{IX}^{-6}} - \eta_{\max}\sum_x \frac{f_x\{S\} r_{IX}^{-6}}{r_{IS}^{-6} + \sum_x r_{IX}^{-6}} \tag{15.7}$$

In this equation $\eta_{\max}$ is introduced to factor out all contributions to the NOE other than distances; as shown in Figure 15.4, it is the maximum two-spin NOE. For a multispin system, all spins other than I and S are denoted here as X (note that

in (15.7), for a two-spin system where there are no spins X the equation reduces to $f_I\{S\} = \eta_{\max}$). The first term in the difference describes the direct contribution to the NOE, while the second term denotes indirect contributions. Indirect contributions are also known as the *three-spin* or *spin-diffusion* effect. This effect is a very serious source of errors in the interpretation of NOE data, and its impact is particularly bad for large molecules. But let us first look at the direct contribution (the first term). The maximum NOE is attenuated by a factor that depends on $\sum r_{IX}^{-6}$. This term sums up all close distances to other spins. These spins act as relaxation sinks, and help the perturbed spin relax via other pathways. In our analogy they represent other cold bowls to which the hot one is transferring its heat. Particularly for remote protons, NOE transfer is low not only because of the large distance (one might expect that the NOE buildup will simply take longer), but more importantly because other spins help the spins to relax more efficiently and long before the NOE has built up on remote spins. To rephrase that, the NOE depends not only on the distance between two spins but also on the presence of other spins. This fact should always be kept in mind when the absence of an NOE is used as a stereochemical argument!

The spin diffusion term reports on the NOE transfer via third spins that serve as relay spins for the NOE transfer. Upon saturation of spin 1, the population levels on spin 3 change. This itself is an effect similar to that which would have occurred as if we had irradiated spin 3 in the first place. Accordingly, spin 3 will cross-relax also via spin 2. We have irradiated spin 1 and observe an NOE on spin 2 although spins 1 and 2 are too far apart. This is depicted in Figure 15.5, in which the distance between spins A and B is varied through changes in α. For small values of α, that means when the distance is short between spins A and B; the NOE is strong and corresponds entirely to the direct effect (in our case up to approximately 40°). In

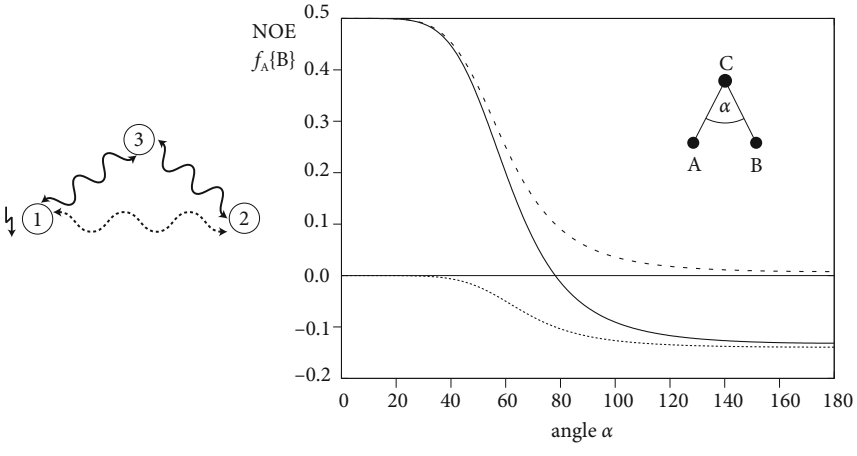

Figure 15.5 The three-spin effect in the extreme-narrowing regime. The plot shows the dependence of the NOE between spins A and B on the angle α. The dashed line corresponds to the direct NOE, the dotted to the indirect effect, and the solid line to (observed) overall NOE.

contrast, when α is close to 180° and hence the distance between *A* and *B* is large, the NOE between spins *A* and *B* is entirely due to the indirect effect (the second term in (15.7)). For molecules in the extreme-narrowing regime (small molecules) the sign of the NOE reverses with every relay step, and hence the direct and the three-spin effect cancel at about 80°.

In the case of large molecules (those in the spin-diffusion regime), long irradiation periods will very effectively propagate the NOE through the entire molecule, and the steady-state experiment essentially becomes useless for measuring distances. This is depicted in Figure 15.6. Note that the x axis denotes $\omega\tau_c$, which is related to the molecular weight. For small molecules (between 0.01 and 0.1), the NOE in principle correctly reports on the relative distances. For $\omega\tau_c = 100$ the NOE is essentially the same for all protons irrespective of their mutual distances. This fact is exploited in a set of experiments called *saturation transfer difference* experiments (see Section 19.4).

A feature of the steady-sate NOE that is worth mentioning is that *enhancements are asymmetric*. This means if we irradiate a methyl group and we observe the NOE of a remote methine proton, the NOE can be substantially different from that if we had performed the reverse experiment in which we irradiate the methine proton. This is due to the fact that the protons have a different environment and hence different relaxation sinks!

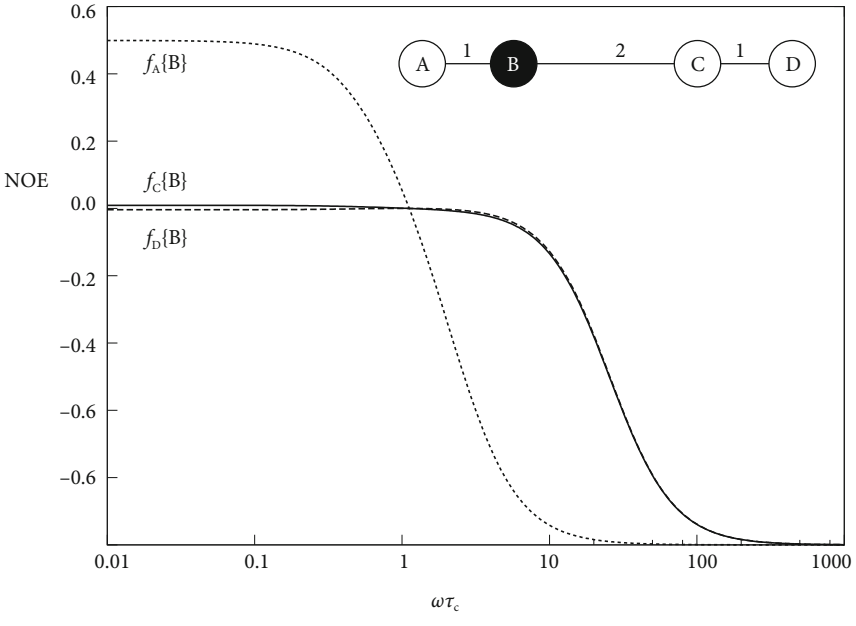

Figure 15.6 Spin diffusion in a four-spin system. The calculations assumed a linear arrangement of a four spins, with spin *B* being irradiated and the relative distances to spin *B* as indicated at the top.

15.2.3
The Transient NOE

The transient NOE is remarkably different from the steady-state NOE. In particular, enhancements are symmetric, and when used in the correct way, the transient NOE will still provide useful stereochemical information for large molecules. The 2D variant, the NOESY experiment, in fact delivers beautiful spectra for medium-sized proteins. The transient experiment starts with an instantaneous inversion of the population of one spin, which then relaxes back to equilibrium by autorelaxation and cross-relaxation. The crucial difference from the steady-state experiment is that there is an instantaneous perturbation, whereas in the steady-state experiment the spins are saturated until an equilibrium is reached.

For a formal description we again need to take both autorelaxation and cross-relaxation into account. For an I and an S spin, the time course can be described as

$$\frac{\mathrm{d}I_z}{\mathrm{d}t} = -R_1^I\left(I_z - I_z^0\right) - \sigma_{IS}\left(S_z - S_z^0\right) \tag{15.8}$$

$$\frac{\mathrm{d}S_z}{\mathrm{d}t} = -R_1^S\left(S_z - S_z^0\right) - \sigma_{IS}\left(I_z - I_z^0\right) \tag{15.9}$$

For a formal solution we refer the interested reader to the original Solomon article (see Further Reading), and we just present the result as

$$f_I\{S\}(\tau) = 2\mathrm{e}^{-R_1\tau}\sinh(\sigma_{IS}\tau) \tag{15.10}$$

where τ denotes the delay after the initial inversion pulse. Furthermore, we have assumed that R_1^I is equal to R_1^S. This function is depicted in Figure 15.7. The initial buildup is almost linear, after which the curve becomes flat. Finally, due to T1 relaxation, the NOE decreases again for large values of τ. In the 2D version of the transient NOE experiment, the NOESY experiment, the delay τ is called the *mixing time*. Proper choice of it depends on how fast the NOE builds up and therefore depends on the molecular weight.

15.2.4
The Kinetics of the NOE

The kinetics of the NOE buildup are different for the steady-state and the transient NOE because the effects of T1 relaxation result in a decrease of the NOE for long mixing times in the transient NOE experiment, whereas the continuing irradiation in the steady-state NOE experiment prevents the decrease of the NOE for long mixing times (see Figure 15.7). The rise of the NOE is faster in the transient experiment, but the maximum NOE that can be reached is larger in the steady-state experiment.

Depending on the molecular weight the NOE will be positive or negative (or possibly zero when $\omega\tau_c$ is close to 1) (see Section 15.2.1). In a two-spin system the transient NOE builds up exponentially over time until it reaches a plateau value. At the

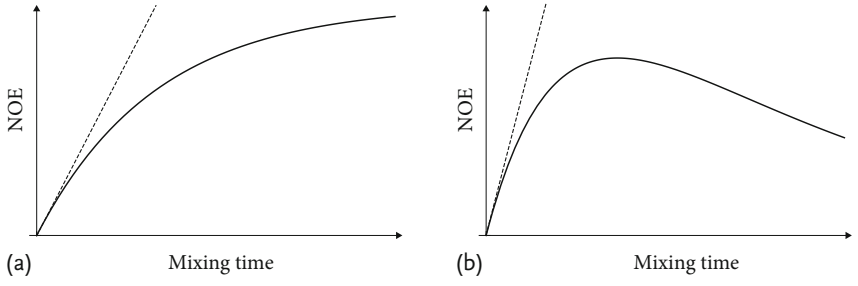

Figure 15.7 Buildup of the NOE. Curves are depicted for the steady-state (a) and transient (b) experiments for an isolated two-spin system in the extreme-narrowing regime. The dotted lines indicate the linear functions corresponding to the initial-rate approximation. The graphs are drawn with an arbitrary *y* scale but identical *x* scale. Identical cross-relaxation and autorelaxation rates were used in the simulations. Note the slope of the initial rate is twice as large in the transient experiment.

beginning the buildup is close to linear, and for short mixing times or irradiation periods the so-called *linear approximation* can be used. In the linear approximation the NOE intensity is proportional to r^{-6}, with r denoting the distance between the two spins, while at longer mixing times effects from spin diffusion start to occur. When determining the structure of molecules from NOEs, one therefore records spectra with short mixing times to ensure that the two-spin approximation is valid. In multispin systems the NOE buildup rates may be difficult to analyze quantitatively. An important feature of the buildup of so-called spin-diffusion peaks is that they have an induction period. During that period no NOE buildup for those peaks is observed, and hence the resulting buildup curve is sigmoidal. Therefore, to recognize spin diffusion, a series of spectra with increasing mixing times or irradiation periods are recorded, starting with fairly short values. In the case of small molecules, spin-diffusion peaks arising from the three-spin effect have opposite sign. Spin diffusion, however, is a much more serious problem for large molecules, for which NOE buildup is very fast. In those cases very short mixing times must be used. On the other hand, buildup is fast and the maximum NOE is twice as large as for small molecules, so NOESY spectra of macromolecules are usually nice spectra even when short mixing times are used!

15.2.5
The 2D NOESY Experiment

The archetypical experiment for measuring distance relationships is the 2D NOESY experiment. It provides all distance relationships in a single experiment, and does not require tedious optimization of selective pulses. NOESY spectra of large molecules are nice spectra. For a small to medium-sized molecule, the rotating-frame NOESY (ROESY) experiment is preferable (see Section 15.2.6). The NOESY experiment uses a single parameter, the mixing time (Figure 15.8), which can be varied between 20 ms and approximately 1 s and needs to be adjusted to

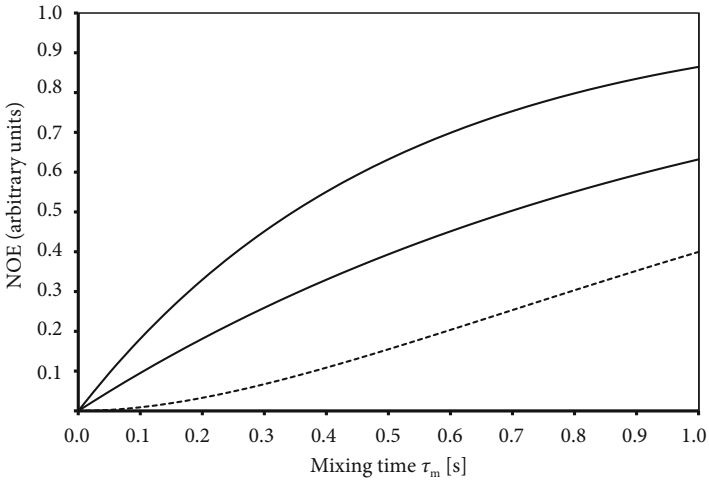

Figure 15.8 Buildup curves for NOEs in NOE spectroscopy (NOESY) experiments. Solid curves depicted NOEs corresponding to two proton pairs for which the cross-relaxation rates differ by a factor of 2. The dotted curve corresponds to an NOE due to spin diffusion.

the molecular weight of the compound of interest. For small molecules (those in the extreme-narrowing regime) the mixing time is chosen to be approximately T1 (we usually use values of 0.5–1.2 s). For proteins, mixing times have to be short in order to avoid artifacts from spin diffusion (typically below 150 ms). In the extreme-narrowing regime (positive NOEs), cross peaks are negative when diagonal peaks are phased to be positive, while cross peaks for large molecules have the same phase as diagonal peaks.

NOEs are weak signals. Accordingly, NOE cross peaks are a small percentage of the intensity of the diagonal peaks and artifacts can be very strong, often obscuring genuine NOEs. Artifacts in NOESY spectra, for example, may be due to exchange. Since exchange processes are usually fast, they can be detected by the presence of strong cross peaks even if the mixing times are very short. Exchange peaks are always positive. For small molecules a serious problem is zero-quantum artifacts or so-called COSY with a *zz* filter cross peaks. When not obscured by overlap with genuine NOEs, they can be recognized as COSY-type peaks with antiphase multiplet structure. If they overlap with genuine cross peaks, the result is tilted line shapes as presented in Figure 17.10. For large molecules zero-quantum coherences usually relax during the mixing times and do not present a problem. Moreover, these artifacts are only present when the two correlated protons are directly scalarly coupled, which usually means they are vicinal or geminal protons. The presence of spin-diffusion peaks can be detected when recording buildup curves of NOEs with a series of NOESY spectra using different mixing times. Spin-diffusion peaks will be absent in spectra recorded with short mixing times.

15.2.6 The Rotating-Frame NOE

The cross-relaxation term is the difference between double-quantum and zero-quantum transition probabilities. Depending on the size of the molecules, the two terms may become similar such that the NOE vanishes, even for short distances. Our experience working in this field is that it is likely your molecule of interest displays no NOE due to an unfavorable tumbling time (this is also sometimes stated as Murphy's law). Fortunately, the set of rotating-frame NOE (ROE) experiments have been designed to work also for these molecules. The prototypical example is the ROESY experiment, the rotating frame equivalent of the 2D NOESY experiment.

Let us quickly recapitulate how the NOE works. A spin is perturbed such that nonequilibrium populations of α and β states exist. In the NOESY experiment this is achieved with a nonselective pulse, and in the transient 1D NOE experiment is achieved with a selective 180° pulse. During the mixing time magnetization is along $-z$, and cross-relaxes during this period. The ROESY experiment is rather similar. Following an initial 90° pulse that brings magnetization into the transverse plane, a fairly weak field is applied along the x or y axis. Which axis is chosen actually matters a lot. If the original 90° pulse is applied along the y axis, magnetization is turned from the $+z$ to the x axis (see Section 8.1). Immediately thereafter a weak field is placed along the x axis. The purpose of the field is to prevent the transverse magnetization from precessing about the z axis; instead it will precess about the axis of the weak B_1 field. The magnetization is so to say locked along the x axis in the rotating frame due to the B_1 field, and therefore this field is referred to as the *spin lock*. If we compare the spin states during the mixing time in the NOESY and ROESY experiments as shown in Figure 15.9, we recognize that the two states are very similar. In the NOESY experiment, spins precess about the $-z$ axis, while they precess about a transverse axis in the ROESY experiment. Both states are nonequilibrium states, and relaxation will bring magnetization back to the equilibrium states. In the case of the NOESY experiment, the relevant time for achieving this is the longitudinal relaxation time T1, while in the ROESY experiment it is the rotating-frame relaxation time, T1ρ. We do not wish to provide a formal treatment of the relaxation process; for us it is sufficient to recognize that both processes are very similar. Again, there is cross-relaxation in the rotating frame that gives rise to the ROE, and it depends on zero- and double-quantum transitions in the rotating frame. The crucial difference is the frequencies of the processes in the static frame and the rotating frame. In the NOESY experiment, proton double-quantum frequencies are in the gigahertz range. In the ROESY experiment, the B_1 field is very much weaker: usually the field strength is set to approximately half of the spectral width (for a 10 ppm spectral width on a 500 MHz instrument that is 2500 Hz, corresponding to a 90° pulse of 100 µs – a very weak field). As a consequence, also the double-quantum frequencies are in the audio range (below 10 kHz), and therefore there is no zero crossing of the ROE for relevant molecular weights (see Figure 15.9)!

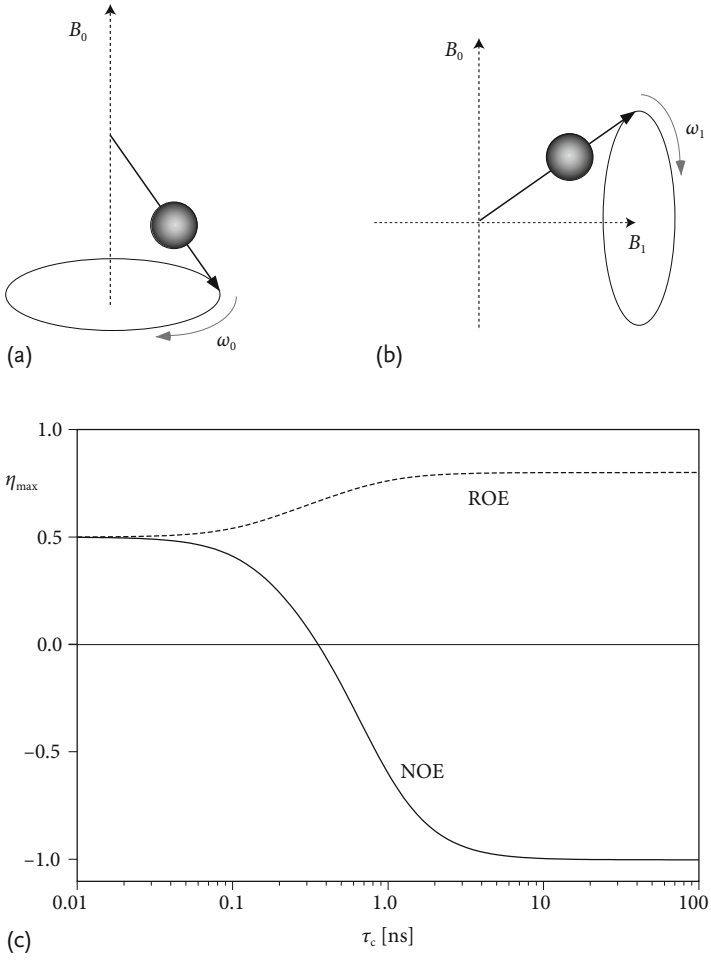

Figure 15.9 States for individual spins during the NOE (a) and the rotating frame NOE (ROE) (b) experiments relevant for the transfer; (c) dependence of the maximum NOE and ROE enhancements on the correlation time.

The ROESY spectrum will always result in ROEs for protons in close proximity (depending on the molecular weight between 4–5 Å). Is there any disadvantage of using the ROESY experiment? Of course, there is. Relaxation during the mixing times occurs with T1ρ, which is similar (although not identical) to T2. Transverse relaxation times are short for large molecules, and hence the ROESY experiment is much less sensitive for macromolecules such as proteins or nucleic acids. However, the ROESY experiment is really the experiment of choice for small synthetic molecules or natural products (except for biomacromolecules).

Another advantage of using the ROESY experiment is that artifacts can be recognized very easily. As a rule of thumb, all genuine ROEs display the opposite

sign compared with the artifacts. Artifacts are spin-diffusion peaks, TOCSY transfer peaks, and peaks due to chemical or conformational exchange. TOCSY transfer peaks are due to transfer across scalar instead of dipolar couplings, and usually occur between resonances that are similar in frequency (e.g., between diastereotopic methylene protons, or between sugar ring protons that all have similar chemical shifts) and hence are close to the diagonal. Exchange peaks can be very strong, but are recognized easily because of the sign of the signal (this is much more difficult in the NOESY experiment).

15.2.7
The Heteronuclear NOE and the HOESY Experiment

Instead of using the homonuclear ^1H–^1H NOE, in principle we could also measure the heteronuclear NOE, for example, the ^1H–^{13}C NOE. Since the strength of the dipolar coupling depends on the gyromagnetic ratios, the heteronuclear NOE is intrinsically much weaker, and hence has been used rarely for structural purposes. For heteronuclei with a comparably high gyromagnetic ratio, for example, ^{19}F, the heteronuclear NOE experiment however is a fairly sensitive experiment. The 2D experiment that exploits the heteronuclear NOE is called heteronuclear Overhauser effect spectroscopy (HOESY).

In contrast to structural work, the heteronuclear NOE, in particular the $^{15}N\{^1H\}$ NOE, is frequently determined in dynamics studies (see Section 14.5). The magnitude of the heteronuclear NOE depends on the correlation time. Figure 15.10 depicts the curves for ^{15}N, ^{13}C, ^{19}F, and ^{31}P. The maximum NOE enhancements change their sign for ^{19}F and ^{15}N nuclei.

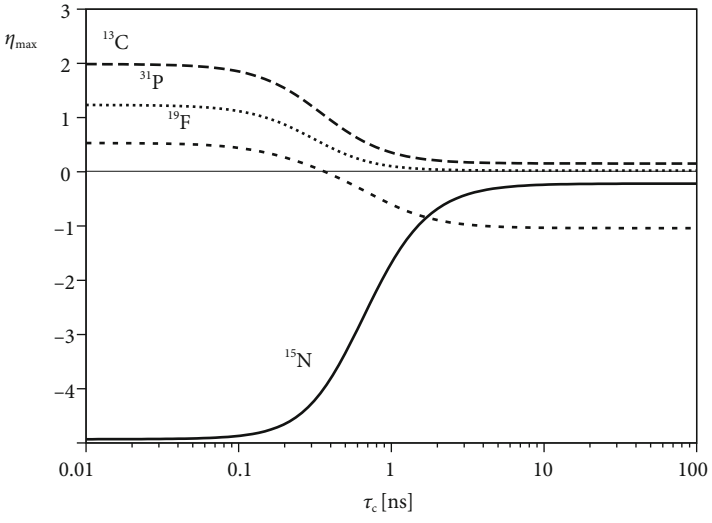

Figure 15.10 $X\{^1H\}$ NOEs for a number of important heteronuclei.

The large difference in magnitude and the different sign of the $^{15}N\{^{1}H\}$ NOE explain why measurements of that NOE have often been conducted in protein dynamics studies.

An important consequence of the heteronuclear NOE is signal amplification or decrease of signal intensity during decoupling. For example, when proton-decoupled carbon spectra are recorded, the heteronuclear NOE may result in a signal increase of up to 200%. For some nuclei this may result in total signal loss, for example, in ^{15}N and ^{19}F spectra (a −100% NOE enhancement essentially means that no signal remains!). In those cases it is better to record inverse-gated spectra (see Section 4.3.4).

15.3 Applications of the NOE in Stereochemical Analysis

NOEs are extensively used to establish stereochemistry in molecules. It is very important to emphasize that NOEs are useful to establish relative stereochemistry rather than absolute stereochemistry. Often heard arguments use statements along the line "assuming the stereochemistry of this proton is *X*, then the fact that we are able to observe an NOE to proton *Y* indicates that their relative stereochemistry is cis." In principle there is nothing wrong with an such argument. However, we need to be very careful when using such arguments, and be sure that positioning of groups in space is really as we imagine, and that there are no other possibilities that might explain the presence of such an NOE. A second possible complication may arise due to rotatable bonds.

To eliminate complications due to rotatable bonds, let us first look at six-membered rings. Often, a 1,2 cis relationship is claimed to be cis because of the presence of an NOE. Figure 15.11 summarizes the distances of axial proton 1 to a number of other protons in the ring. The distance to the proton in cis relationship (H_{2e}) is short, approximately 2.5 Å. The distance to the trans proton (H_{2a}) is longer (3 Å) but sufficiently short to result in an NOE. *Much* more conclusive are the distances to the protons on C-3, with the diaxial relationship being 2.5 Å and the axial–equatorial distance being 3.7 Å. Up to what distance NOEs can still be observed depends on a number of variables, obviously the distance but also the presence of other protons close to H1 and the molecular weight. For a small molecule, a distance of 3.7 Å will result in no or a very weak NOE since the distance is quite large and the proton will efficiently relax by its neighbor.

The second important point is to be sure that the molecule in three dimensions really looks like we believe! Particularly when many rings are fused our imagination may provide a very poor picture of reality. An example from our own research is presented in Figure 15.12. When we had to establish the stereochemistry of this polycyclic compound, we built up the two stereoisomers in three dimensions using a graphics program. These are inexpensive nowadays. Although this will not be a perfect model, in polycyclic molecules with a low number of degrees of freedom it is sufficiently accurate. Inspection of the two different models then allows us to

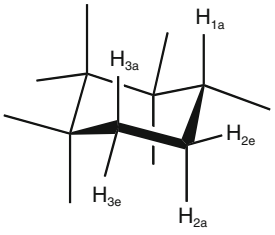

Distances:

$H_1 \rightarrow H_{2e} = 2.47$ Å

$H_1 \rightarrow H_{2a} = 3.02$ Å

$H_1 \rightarrow H_{3e} = 2.52$ Å

$H_1 \rightarrow H_{3a} = 3.71$ Å

Figure 15.11 Typical distances of protons in a six-membered ring (chair conformation).

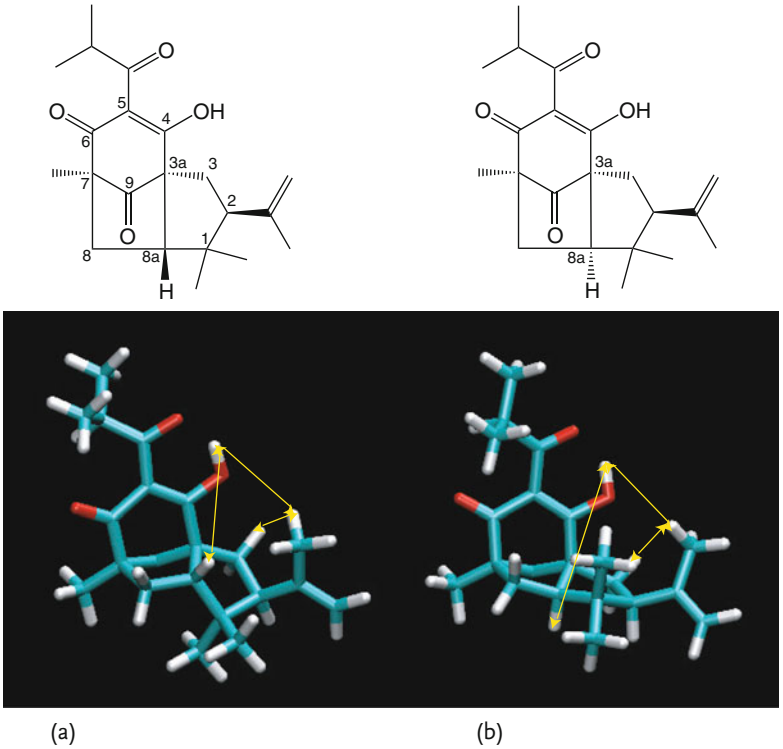

Figure 15.12 Structures of two phloroglucinol-derived isomers with (a) cis- or (b) trans-fused five-membered rings. Important NOEs used to discriminate the two isomers are marked with arrows.

pick a proton pair for which the distance varies very substantially between the two stereoisomers, and which therefore may serve to distinguish between the two by means of the NOE.

Extensive use of NOEs is made in the chapters devoted to the identification of natural products and therefore we will keep this section short and rather encourage readers to go through those examples. Nevertheless, we wish to close with two additional remarks. Firstly, often scalar couplings are even more helpful to estab-

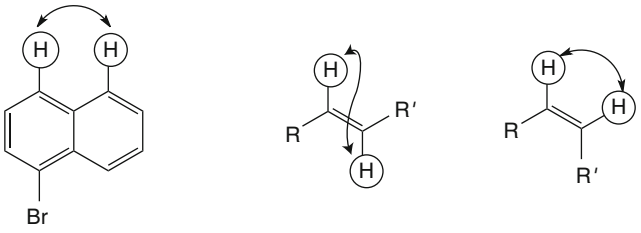

1 2a 2b

Figure 15.13 Important NOEs to assign compounds *1* and *2*.

lish stereochemistry. This will be extensively discussed in Chapter 20, which is devoted to carbohydrates. Finally, sometimes NOEs are really helpful for assignment purposes, even if they do not involve any variable distances. Two examples are presented in Figure 15.13.

An example in which an NOE helps assign the proton spin systems is shown in Figure 15.13 for molecule *1*. Herein, the two encircled protons are close and this will help to easily establish their location in the molecule. Scalar couplings or chemical shift arguments will be much less unambiguous!

Another example is the question of whether a disubstituted double bond is cis or trans (molecules *2a* and *2b*). The obvious answer is usually to measure the scalar coupling between the two protons – the trans coupling is larger. This, however, requires knowledge of both the cis and the trans coupling since electron-withdrawing or electron-donating groups have a large influence on the scalar coupling constant. When reference values of the cis and trans couplings are not known, the NOE between the two protons might help. For the cis form we expect to see a strong NOE (r is approximately 2.3 Å), while for the trans form we will see a weaker NOE. A combination of both methods is certainly the best!

15.4 Practical Tips for Measuring NOEs

NOEs are small. Any experimental instability will result in baseline problems or increased T1 noise and will obscure weak peaks. Stability of the instrument and temperature are therefore of prime importance as is always true for methods that rely on differences. For the same reason, never use sample spinning in NOE measurements! Measuring overnight or on weekends in many places will give better spectra because on those days there is less traffic in the building. Many of the artifacts from instrument instabilities are pronounced in experiments that use differences of spectra (such as the 1D NOE experiments). As described in Section 13.9.2, pulsed field gradients select for certain coherences *within a single scan*, and hence are much less susceptible to such artifacts. Therefore, we highly recommend using sequences that employ pulsed field gradients because they contain *many* fewer

artifacts, and small NOEs are more easily recognized in spectra from those experiments. The following are recommendations based on our experience:

- Calibrate the temperature control. To ensure constant temperature, nowadays cold air is blown into the probeheads, and a heater warms up the cold air. The control parameter for this circuit must be optimized. The settings depend on the temperature and the airflow. Usually spectrometers have automatic procedures for optimizing the settings. This really makes a difference! The setting must be adjusted when changing the temperature by more than just a few degrees.
- Lock instabilities are responsible for most of the problems seen in NOESY spectra. Optimize the lock power; set the lock power just below saturation to give a strong lock signal. A strong signal allows better lock regulation. Often forgotten but also important is to adjust the lock phase!
- Avoid paramagnetic impurities because they lower T1 values!
- The sample should be sufficiently concentrated but not too concentrated to avoid problems arising from viscous solutions.
- Pay attention to the choice of the solvent. Use a solvent, that gives an intense lock signal (dimethyl sulfoxide or acetone, and rather not $CDCl_3$ or D_2O if possible), because then the lock is more stable. D_2O also has a large temperature shift of the solvent line, so the lines easily change frequency when the temperature is not stable.
- The mixing time has to be optimized for the size of the molecule. Do not use too long mixing times in large molecules in order to avoid spin diffusion.
- In 1D steady-state NOE experiments, for observation of NOEs between methyl groups and other protons, irradiate the methyl group, because relaxation of methyl protons is mainly governed by the other methyl protons.
- If the NOE is very small, the tumbling time may be such that the NOE is near the zero crossing, and changing from a nonviscous solvent (e.g., acetone) to a viscous solvent (e.g., dimethyl sulfoxide) or measuring at lower temperatures may increase the magnitude of the NOE dramatically (note that at very low temperatures the danger is high that the temperature is not stable).
- Use sufficiently long irradiation times (three to five times T1) when measuring steady-state NOEs on small molecules.

15.5 Problems

15.1. Describe the difference between saturation and inversion of spins.

15.2. Draw NOE buildup curves for steady-state and transient effects.

15.3. How do you choose the values for the mixing times for NOESYs of (a) small and (b) large molecules?

15.4. Draw the dependence of the NOE on the molecular weight. At one particular temperature you cannot observe any NOEs in your molecule. What can you do to improve the situation?

15.5. Draw the buildup curve for a spin-diffusion NOE peak.

15.6. Why is it advantageous to use inverse-gated experiments when measuring ^{15}N or ^{29}Si spectra?

15.7. NOESY spectra of small peptides allow measurement of distances up to 4.0 Å, whereas distances of 5 Å can be measured on large proteins. Why?

15.8. Which parameter in general determines whether you can observe an NOE between two remote protons?

15.9. Why can you use long mixing times when measuring spectra on perdeuterated proteins?

Further Reading

Neuhaus, D. and Williamson, M. (2004) *The Nuclear Overhauser Effect in Structural and Conformational Analysis*, 2nd edn, Wiley-VCH Verlag GmbH.

Keeler, J. (2010) *Understanding NMR Spectroscopy*, Chapter 9, 2nd edn, John Wiley & Sons, Ltd.

Solomon, I. (1955) Relaxation processes in a system of two spins. *Phys. Rev.*, **99**, 559–565.

16
Chemical and Conformational Exchange

Dynamic processes are at the heart of chemistry and biology. Modern catalysts exert their action in an orchestrated fashion of ligand exchange reactions. Similarly, the function of enzymes comprise substrate binding, the catalytic reaction, and product release. All these events require conformational changes. It is one of the particular strengths of NMR spectroscopy to be able to follow these events, at least in principle, under certain circumstances. By doing so, as we will see later, we can obtain structural information on the interconverting species, on their rates of interconversion or the lifetimes of the various states, and on the activation energy that separates the two species. A lot of this information can be derived from simple 1D spectra recorded at different temperatures, a technique known as variable-temperature NMR spectroscopy or dynamic NMR spectroscopy. More sophisticated methods involve measurements of relaxation rates, and these methods are described in Chapter 14.

16.1
Two-Site Exchange

The exchange process may be due to a chemical transformation resulting from the breakage or formation of a bond. A famous example of *chemical exchange* depicted in Figure 16.1 and much investigated by NMR experiments is the bond isomerism of bullvalene due to a Cope rearrangement. In fact, only one of many transformations of bullvalene is shown in Figure 16.1.

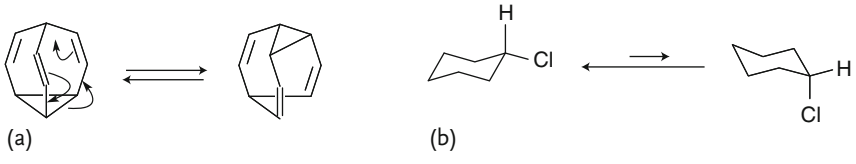

Figure 16.1 Examples of chemical (bullvalene; a) and conformational (chlorocyclohexane; b) exchange.

Applied NMR Spectroscopy for Chemists and Life Scientists, First Edition. Oliver Zerbe and Simon Jurt.
©2014 WILEY-VCH Verlag GmbH & Co. KGaA. Published 2014 by WILEY-VCH Verlag GmbH & Co. KGaA.

During this process carbon atoms change their hybridization from sp^2 to sp^3, so the corresponding ^{13}C chemical shifts change dramatically. An example of *conformational exchange* is the ring inversion in chlorocyclohexane. The conformer with chlorine occupying the equatorial position is energetically more favorable, and the two forms are separated by a comparably large energy barrier. Variable-temperature proton NMR spectra recorded on chlorocyclohexane at different temperatures are depicted in Figure 16.6.

But how do we notice the presence of a chemical or conformational exchange process? The most obvious indication of such a process is a remarkable increase in line width, to an extent that scalar couplings are not visible anymore. Alternatively, we may notice far too many peaks. However, there are many reasons why spectral lines can be broad: poor field homogeneity (poor shims) and the presence of paramagnetic impurities to name just two. So how do we know that the cause is exchange broadening? The best answer is to look at the line shape of the solvent signal. Exchange processes are not expected to influence the solvent line, but poor shim or paramagnetic contaminations will. Exchange process can affect a few, many, or all lines of a molecule.

Let us now look at exchange in a bit more formal manner. For that we assume that a systems interconverts between two different states A and B, the so-called *two-state exchange*, both of which are characterized by defined (and different) resonance frequencies δ_A and δ_B,

$$\delta_A \overset{k_+}{\rightarrow} \delta_B \tag{16.1}$$

and

$$\delta_B \overset{k_-}{\rightarrow} \delta_A \tag{16.2}$$

with the lifetimes of the individual states *A* and *B* defined as $\tau_A = 1/k_+$ and $\tau_B = 1/k_-$ and k_+ and k_- being the rate constants of the forward and backward reactions. The rate at which the two states interconvert determines whether the spectra will display a single peak at the population-weighted average frequency, the so-called *fast exchange* regime, or two different signals at δ_A and δ_B, referred to as *slow exchange*. The two regimes are separated by *intermediate exchange*, and it is this state which shows a very significant modification of the line shapes. Whether a system is in slow, intermediate, or fast exchange depends on the relation between the exchange rate and the frequency separation of the two signals δ_A and δ_B. This spectroscopic ruler is called the *NMR timescale*. However, not only chemical shifts may be averaged by exchange processes, but also scalar couplings and transverse relaxation rates. The definitions of slow, intermediate, and fast exchange are summarized in Table 16.1.

Obviously, the lifetime of the state must be longer than the inverse of the frequency separation in order to resolve the two lines as separate lines.

Figure 16.2 displays a simulation for a two-spin system that is in exchange spanning the full range from slow to fast exchange. In the simulation the frequency

Table 16.1 Definition of exchange regimes for various forms of exchange.

	Timescale		
	Slow	**Intermediate**	**Fast**
Chemical shift	$k \ll \delta_A - \delta_B$	$k \approx \delta_A - \delta_B$	$k \gg \delta_A - \delta_B$
Scalar coupling	$k \ll J_A - J_B$	$k \approx J_A - J_B$	$k \gg J_A - J_B$
Transverse relaxation	$k \ll R_{2,A} - R_{2,B}$	$k \approx R_{2,A} - R_{2,B}$	$k \gg R_{2,A} - R_{2,B}$

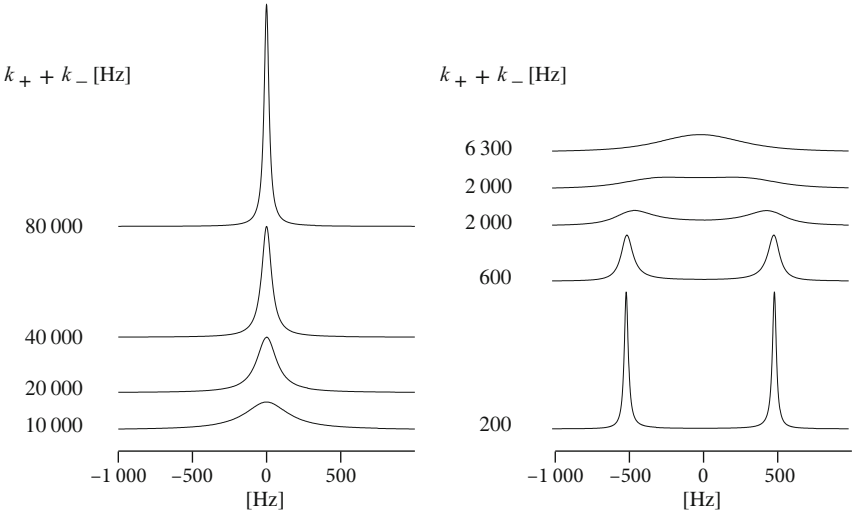

Figure 16.2 Line-shape simulation for a two-state exchange with equal populations of both states.

difference was set to 1000 Hz, and the exchange rate was varied between 100 Hz and 40 kHz. The simulation was performed for the case where the two states are equally populated.

The simulation clearly demonstrates the transition from a spectrum with two narrow lines (slow exchange) to a spectrum with a single, again narrow line (fast exchange). When the rate of the exchange process is about 2000 Hz, the two individual resonances are no longer visible, and this state is called *coalescence*. The situation changes slightly when the two states in exchange are not equally populated (see Figure 16.3).

Figure 16.3 displays the situation for two sites, both in exchange in two states. In one case the second state has a large chemical shift difference (site A), and in the other case the shift difference is comparably small (site B). We wish to draw your attention to two points. Firstly, the simulation at an exchange rate of 1000 Hz displays two signals, the minor forms are so broadened that they escape detection. Moreover, the transition from slow to fast exchange is different for the two sites because the chemical shift difference is not the same. Upon crossing from slow

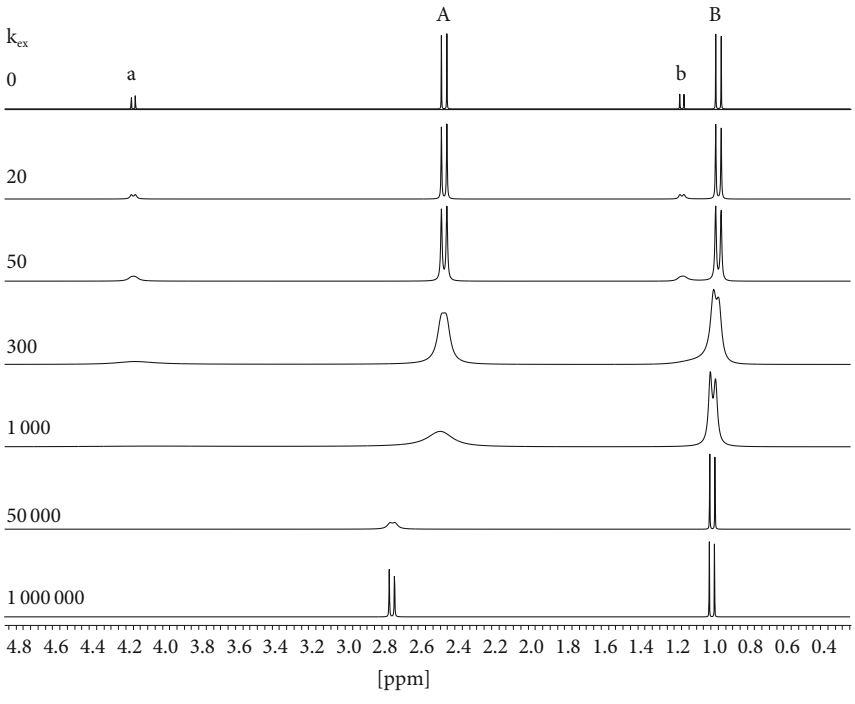

Figure 16.3 Line-shape simulation for two sets of resonances due to spins A and B, which are in exchange with minor populated states a and b.

to fast exchange the position of resonance A changes significantly but not for resonance B. In a molecule in which many sites are affected by the exchange process we are likely to encounter different chemical shift differences, and so this is a realistic scenario.

In the following we will describe the three regimes of chemical exchange timescales in more detail.

16.1.1 Fast Exchange

In fast exchange a single resonance line is observed at frequency

$$\delta_{ave} = p_A \delta_A + p_B \delta_B \tag{16.3}$$

Therein the resonance position of the averaged signal is not simply the arithmetic mean of the resonance positions of the two exchanging lines because the population of the two states has to be taken into account (usually an unknown). Only for equally populated states the average frequency is exactly the arithmetic mean. Often, populations are largely skewed. An example is the exchange of hydroxyl protons of a sugar when using water as the solvent. The concentration of water protons is so much higher than that of the hydroxyl protons, that even if exchange

were slow enough (which is usually not the case) the average frequency would almost perfectly coincide with the frequency of the water signal. Another important point about fast exchange is that peak positions will change during a titration. Assume we mix two components that form a complex that is in fast exchange. Adding more and more equivalents from one partner will shift the peak positions. This is particularly important because sometimes it is not clear whether both resonances can be observed for systems in slow exchange, in particular when the concentration of one state is low or when it displays broad lines for some reason. Signals that shift their positions during titrations will always identify the system as being in fast exchange!

The exchange reaction causes an additional contribution to the line width of

$$\Delta\nu = \frac{1}{2}\frac{\pi(\nu_A - \nu_B)}{k_{+1}} \tag{16.4}$$

Accordingly, the faster the exchange process or the smaller the frequency difference (provided that a single line is observed), the narrower the line will be. Once the system has been identified to be in fast exchange it is best to heat the system or to acquire the spectra using a lower-field spectrometer. In fact in a lower-field spectrometer the chemical shift difference (expressed in hertz) is smaller, and the same rate constant will result in a narrower line. For non-heat-sensitive compounds (larger), changes of temperature can accomplish much more than changes of the field.

A similar situation exists with averaging of couplings:

$$J_{ave} = p_A J_A + p_B J_B \tag{16.5}$$

Such averaging of scalar couplings is common for aliphatic protons on acyclic chains for which bonds are freely rotating. The often observed 7 Hz proton–proton coupling for vicinal protons is due to a weighted average of two gauche states (^3J approximately 3.5 Hz) and one trans state (^3J 14.0 Hz). Another important example of averaging of couplings is the exchange of hydroxyl protons of alcohols with solvent water protons. Hydroxyl protons will almost never display line splittings due to scalar couplings (unless they are strongly hydrogen bonded) but are usually characterized by broad singlets, often broadened to the extent that they escape detection. In Figure 16.4, the encircled methylene proton "feels" the vicinal hydroxyl proton to be in the α state (left side). Through chemical exchange that proton is substituted by a proton that comes from water and is with equal probability in the α or β state. When exchange is very slow, both lines of the doublet are visible, but for the fast exchange case, only the average singlet will be observed. This mechanism has been termed *self-decoupling* and is the reason why scalar couplings to hydroxyl protons in alcohols usually are not visible.

While the hydroxyl proton rapidly changes its spin state from α to β or vice versa through the exchange process, in decoupling this is achieved through application of 180° pulses that flip spins back and forth between the two states (see also Section 12.4).

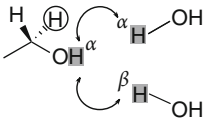

Figure 16.4 Exchange of the hydroxyl proton with a proton from water results in a change of the spin state of the hydroxyl proton.

16.1.2 Slow Exchange

When two separate signals are observed, the additional contribution to the line width due to exchange is

$$\Delta\nu = \frac{k_{+1}}{\pi} \tag{16.6}$$

Hence, a temperature decrease that reduces the rate of the interconversion process will lead to a sharpening of the lines. A typical example where both situations (slow and fast exchange) are simultaneously encountered is exchange of amide and hydroxyl protons of peptides with the solvent in aqueous solution. At slightly acidic pH the amide protons give separate, sharp lines and the exchange rate is on the order of 1–10 s^{-1}. In contrast, exchange between hydroxyl and water protons is so fast that resonance frequency of the hydroxyl protons coincides with the water chemical shift and cannot be observed separately.

16.1.3 Intermediate Exchange

The line shape of the signals changes characteristically upon passing from the slow exchange to the fast exchange regime. In general the line shape of signals that are in exchange is described as

$$g(\nu) = \frac{2\tau_A(\nu_A - \nu_B)^2}{\left[\nu - \frac{1}{2}(\nu_A - \nu_B)\right]^2 + \pi^2\tau_A^2(\nu - \nu_A)^2(\nu - \nu_B)^2} \tag{16.7}$$

Figure 16.5 shows calculated line shapes for two signals 100 Hz apart depending on their lifetime (Figure 16.5a) and for two signals with 0.1 s lifetime depending on the frequency separation (given in hertz; Figure 16.5b). Figure 16.5a corresponds to the situation where we change the temperature of the measurement, whereas Figure 16.5b corresponds to changes in the magnet field strength.

The point at which the two separate lines are broadened to an extent that they cannot be distinguished any longer is called *coalescence*, and the corresponding temperature is the *coalescence temperature*. At coalescence the line shape is characterized by a flat top. The corresponding lifetime for resonance A at coalescence τ^c is given by

$$\tau_A^c = \frac{\sqrt{2}}{\pi(\nu_A - \nu_B)} \tag{16.8}$$

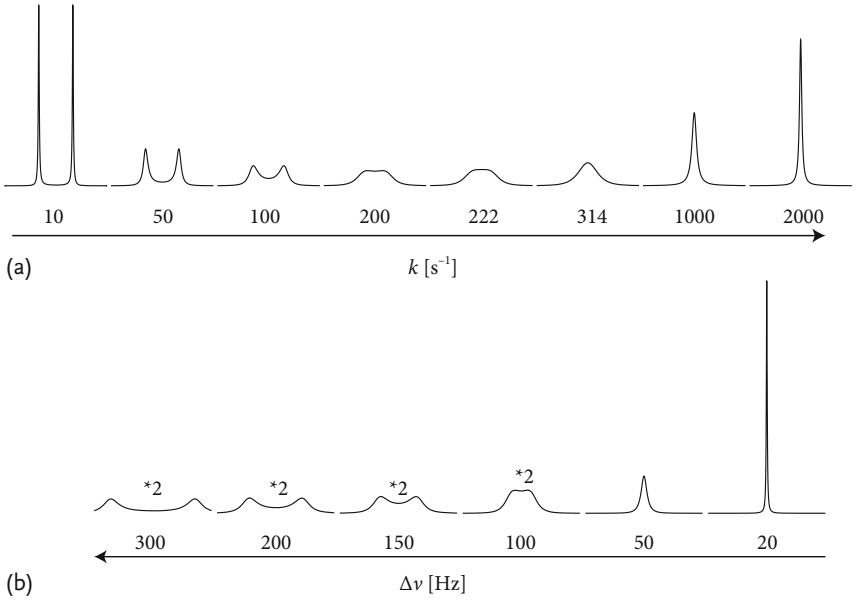

Figure 16.5 (a) Simulation of spectra from two resonances separated by 100 Hz with exchange rates between 10 and 2000 Hz. (b) Simulation of spectra from two resonances in exchange at the same temperature with a rate of 200 Hz with varying frequency separations (20–300 Hz).

The exact measurement of the coalescence temperature allows us to compute the activation energy of the exchange process (see below).

Usually, we are not interested in recording spectra with exchange-broadened lines. In fact it is often cumbersome to work out the conditions needed to record spectra of reasonable quality for these exchanging systems. In general you can find the proper measuring conditions as follows:

- *Record spectra at higher temperature*. When the lines become sharper, increase the temperature further until the lines are sufficiently narrow. If that temperature cannot be reached (the sample is not heat stable or the solvent is volatile), *record spectra at lower field*.
- When the lines become broader when the temperature is raised, cool the sample or proceed at higher field.

If you are unable to record spectra with reasonably sharp lines by following this procedure, it is worth trying to *change the solvent*, which may have a dramatic effect. Often cyclic compounds display such dynamic behavior due to slow conformational interconversions.

16.1.4
Examples

Let us look now at a few examples. The first one (an easy one) is 1-chlorocyclohexane.

Chlorine as a bulky substituent prefers to be placed equatorially. At low temperature (–75 °C) we observe two signals for the proton attached to the same carbon as the chlorine atom (Figure 16.6). The ratio of the two signals is about 4 : 1, and the signal due to the equatorial form clearly displays scalar couplings. In this conformation the trans–diaxial coupling constants are easily recognized, whereas in the minor conformation the broad peak results from the superposition of small equatorial–equatorial coupling constants. At –55 °C the signal from the minor form is broadened so much that it is almost invisible, and the major signal is also significantly broadened such that the scalar couplings are not resolved any longer. Notice there is a jump in frequency on going from –55 to –25 °C because the system crosses from slow to fast exchange, and the average frequency is not in the arithmetic center of the two signals but is closer to the signal of the major component. When the temperature is increased to 22 °C, the signal sharpens so much that scalar couplings are resolved again.

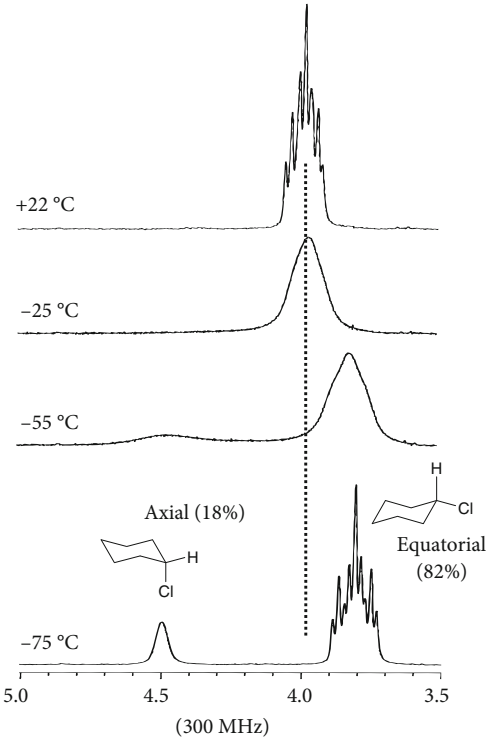

Figure 16.6 Variable-temperature proton NMR spectra of 1-chlorocyclohexane.

The next example is slightly more complicated. In this molecule two naphthalene units are para substituents to benzene.

The rotation about the aryl–aryl C–C bonds is hindered at low temperature and the naphthalene rings are perpendicular to the phenyl ring. As a consequence, two separate signals are observed for the two methyl groups, one corresponding to the syn rotamer and one to the anti rotamer (Figure 16.7). Coalescence is observed at about 114 °C. Also note the perfect reproduction of the spectra in the simulations, so the rate constants can be extracted with great accuracy!

The last example is taken from the field of atropisomerism. Atropisomerism is also known as axial chirality. As shown in Figure 16.8, two rotamers exist that are mirror images of each other about the C-aryl bond . Of course if the rotation about the C-aryl bond were fast, these two rotamers would rapidly interconvert. At –40 °C rotation about the C-aryl bond is very slow. Due to the axial chirality, the methylene protons of the carboxyethyl group are diasterotopic and hence show up as two different signals. At 60 °C interconversion of the two rotamers is fast, axial chirality vanishes, and hence only one signal is observed for the two methylene protons. In that respect the methylene group becomes a chirality sensor!

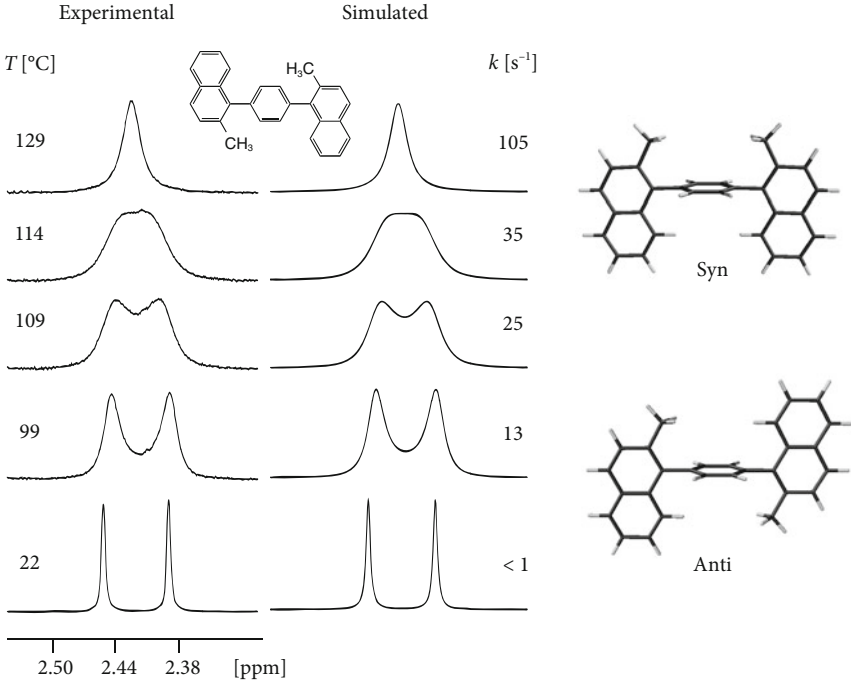

Figure 16.7 Variable-temperature proton spectra for a *binaphthyl* compound (reproduced with permission from Grilli *et al.* (2004) *Tetrahedron*, **60**, 4451.).

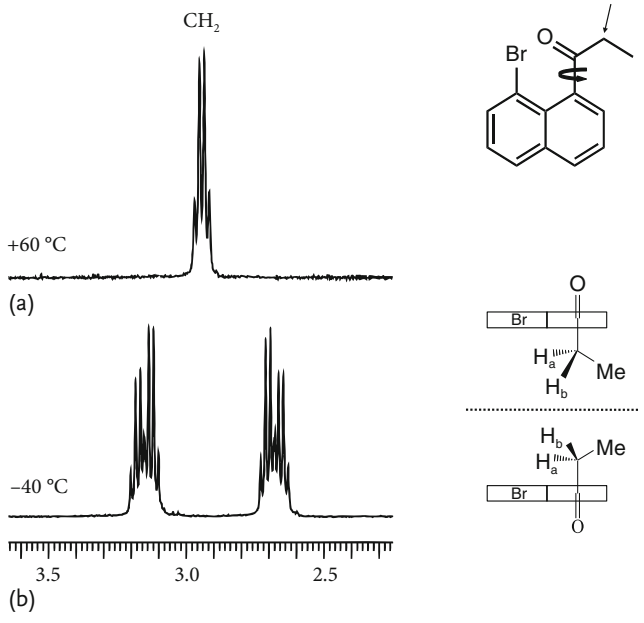

Figure 16.8 Proton signal of the methylene protons (arrow) in slow (b) and fast (a) exchange (reproduced with permission from Lunazzi *et al.* (2000) *J. Org. Chem.*, **65**, 3200).

16.2
Experimental Determination of the Rate Constants

In this section we will learn about two methods to determine exchange rates. The first method has become known as *saturation transfer*. One of the related techniques, *saturation transfer difference*, is very popular nowadays to investigate binding of small molecules to macromolecules, for example, association of drugs with receptors. In the saturation transfer experiment one resonance is selectively saturated (or its intensity is inverted by application of a selective 180° pulse). That resonance will disappear from the spectrum or show up as an inverted peak. However, any other resonance that is in exchange with that resonance will experience a reduction in signal intensity. A well-known example is the saturation transfer due to water presaturation. If carbohydrates are measured in water, the water resonance is saturated by selectively irradiating the water line. Through exchange of the water protons with hydroxyl protons, the intensity of the hydroxyl protons is reduced, possibly to an extent that the signals cannot be observed any longer.

The outcome of such an experiment is depicted in the simulation in Figure 16.9. In this experiment resonance *B* is inverted through action of a selective 180° pulse. Accordingly, a spectrum taken immediately after this pulse will display (full) inverted intensity resonance *B*. If no exchange with resonance *A* is present, the signal of resonance *B* will recover over time following an exponential curve (see also Chapter 14 for more details on T1 relaxation). If, however, resonance *B* is in exchange

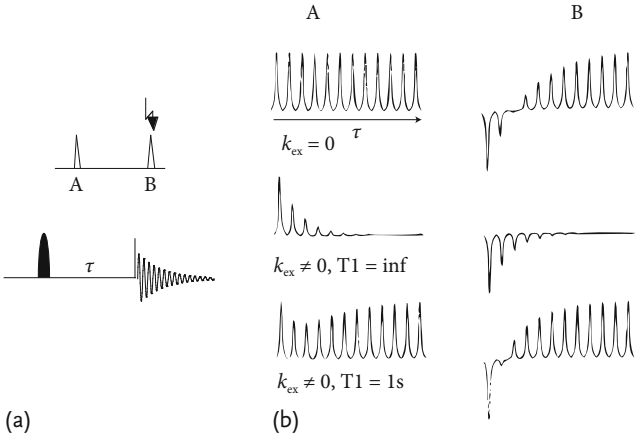

Figure 16.9 Saturation transfer. Data are recorded in an inversion-recovery experiment in which a resonance *B* is selectively inverted with a soft 180° pulse, followed by a delay τ and a readout pulse (a). The dependences of the signals of resonances *A* and *B* on the delay τ are shown in (b). Reproduced with permission from Neuhaus and Williamson (2000) *The Nuclear Overhauser Effect*, Wiley-VCH Verlag GmbH.

with resonance *A*, the intensity of resonance *A* will decrease as the intensity of resonance *B* recovers. If no T1 relaxation is present, after some time both signals will decay to zero (middle spectra in Figure 16.9b). The realistic situation with a finite T1 relaxation time is shown in the spectra at the bottom of Figure 16.9b, where both signal recover additionally due to T1 relaxation.

But how do we know which signals are related to each other in slow exchange? If an exchange process is present, we may notice too many signal in the spectrum. A simple 2D experiment to reveal the related signals is the so-called *exchange spectroscopy* (*EXSY*) experiment. In fact, an EXSY experiment is a NOESY experiment. Cross peaks will connect nuclei that interconvert. Figure 16.10b depicts an expansion from an EXSY spectrum recorded on an aromatic compound, displaying the region of aromatic resonances.

Quite surprisingly, rotation about the amide bond affects many aromatic resonances in this case. Since we are using a NOESY experiment, the cross peaks can of course also be due to genuine NOEs. For small molecules the two different types of signals can be easily distinguished on the basis of the sign of the signal: a true NOE will have a negative intensity, while exchange peaks are positive. For larger molecules, the NOEs also result in positive cross peaks. Here we can use another trick: the exchange process is usually faster than the NOE buildup. If we use short mixing times (less than 20–30 ms), we will mostly see exchange peaks, while NOEs are very weak. Varying the duration of the mixing time τ_m in the EXSY experiment alters the intensity of the exchange peaks. From a series of EXSY spectra recorded with different mixing times, the exchange rates can be extracted.

The cross-peak amplitudes in these experiments unfortunately additionally depend on the longitudinal relaxation times. However, the ratio of the diagonal-peak

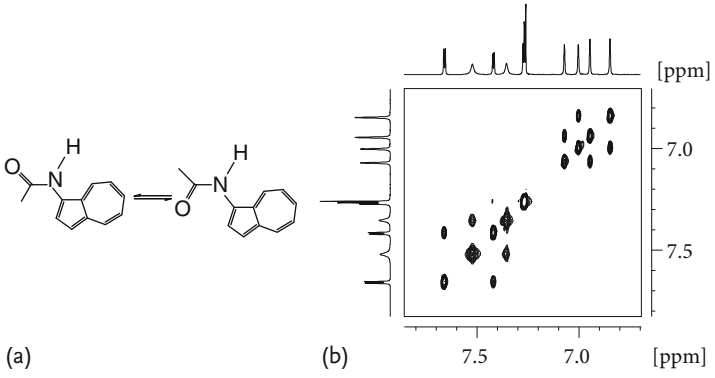

Figure 16.10 EXSY spectrum (b) recorded on the compound depicted in (a).

to the cross-peak intensity is independent of T1 and is given by

$$\frac{I_{\text{cross}}}{I_{\text{diag}}} = \frac{\sinh(k\tau_{\text{m}})}{\cosh(k\tau_{\text{m}})} \tag{16.9}$$

At short mixing times the ratio approximates to (called the *initial-rate approximation*)

$$\frac{I_{\text{cross}}}{I_{\text{diag}}} \approx k\tau_{\text{m}} \tag{16.10}$$

Determination of k using EXSY data therefore comprises measuring a set of spectra with different mixing times, and then fitting the ratio of the cross-peak intensity to the diagonal-peak intensity to (16.9).

16.3 Determination of the Activation Energy by Variable-Temperature NMR Experiments

The rate of a chemical reaction is determined by the height of the barrier to the transition state, referred to as the activation energy. The observation of dynamic processes by NMR experiments allows us to calculate the activation parameters of the exchange process. Empirically, the relation between the reaction rate and the temperature was postulated by Arrhenius in 1889 as

$$k = A\exp\left(-\frac{\Delta G^{\#}}{RT}\right) \tag{16.11}$$

in which A is the pre-exponential factor, R the gas constant and $\Delta G^{\#}$ the activation energy. In Eyring's transition-state theory of the activated complex, the pre-exponential factor is expressed as $k_{\text{B}}T/h$. k is the equilibrium constant for the formation of the activated complex. Thermodynamics states that the activation energy

can be decomposed into the activation enthalpy and entropy, $\Delta G^{\#} = \Delta H^{\#} - T\Delta S^{\#}$, so

$$k = \kappa \frac{k_B T}{h} e^{-\Delta H^{\#}/(RT)} e^{\Delta S^{\#}/R} \tag{16.12}$$

in which κ is the transmission coefficient (usually 1), k_B the Boltzmann constant, T the temperature, and h the Planck constant. A plot of $\ln(k/T)$ versus $1/T$, the so-called Arrhenius plot, yields a line with slope $(-\frac{\Delta H^{\#}}{R})$ and intercept $(\ln(\frac{k_B}{h}) + -\frac{\Delta S^{\#}}{R})$. $\ln(\frac{k_B}{h})$ is approximately 23.76 s^{-1} K^{-1}. The rate constants may be extracted from the line-shape (often also called band-shape) fitting procedures. Many programs (e.g., DNMR, G-NMR, and WIN-NMR) allow one to fit line shapes and require the chemical shifts, transverse relaxation times, and rate constants as an input. Through systematic variation of k the experimental spectrum can be reproduced. With use of band-shape analysis, barriers in the range from 4.5 to about 20–21 kcal/mol (at 300 MHz field) can be determined. However, the temperature range in which the values of k can be determined reliably is small.

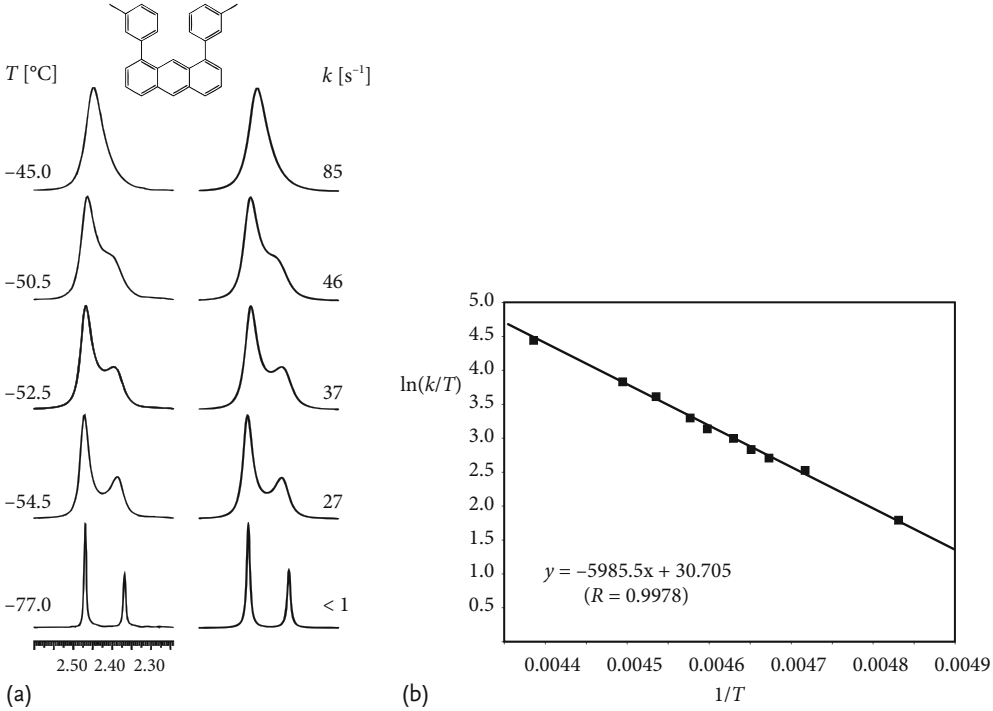

Figure 16.11 Variable-temperature NMR spectra of 1,8-ditolylanthracene. (a) The 600 MHz proton spectra in CD_2Cl_2 (right), and the spectra from the results from the simulation (left). (b) The corresponding Arrhenius plot. The thermodynamic parameters derived are $\Delta G^{\#} = 11.22$ kcal/mol, $\Delta H^{\#} = 11.45$ kcal/mol, $\Delta S^{\#} = 1.1$ cal/(mol K), and $E_a = 11.9$ kcal/mol (*J. Org. Chem.* 2007, *72*, 5391–5394).

An example of how line-shape analysis can be used to determine the activation energy for an anthracene derivative is depicted in Figure 16.11. Rotation about the aryl–aryl bond is hindered, resulting in two signals for the methyl protons at low temperature.

Alternatively, we may use the relation

$$\Delta G^{\#} \approx R T_C \left[22.96 + \ln \left(\frac{T_C}{\nu_A - \nu_B} \right) \right] \tag{16.13}$$

and experimentally determine the coalescence temperature. To improve the precision of the extracted value of the activation energy, we best determine the coalescence temperature at more than one field B_0. One inherent problem with the method is that the frequencies of the two states must be determined at sufficiently low temperature where signals are narrow, but the coalescence temperature is much higher. Many systems display strongly temperature dependent chemical shifts, so the frequency separation at the coalescence temperature may not be really known. Another complication arises from the fact that activation energies are temperature dependent (due to the $T\Delta S$ term). Only when the activation entropy is zero, which is fortunately frequently the case, can this complication be ignored. Finally, obtaining exact knowledge of the temperature inside the sample is far from trivial. The best way to measure it is to insert a thermocouple inside a dummy sample and produce a calibration curve. Due to these technical problems, the line-shape simulation of spectra recorded at different temperatures seems to us to be the most reliable and precise method for the evaluation of the activation parameters.

16.4 Problems

16.1. Describe the difference between slow and fast exchange.

16.2. Hydroxyl protons cannot be observed in proton spectra of peptides and proteins measured in water. Why?

16.3. Your proton spectrum is characterized by broad lines. How can you distinguish whether this is due to exchange processes or bad shims (poor field inhomogeneity)?

16.4. Is it possible that you have broad and sharp lines in the spectrum at the same time?

16.5. Describe methods to derive the activation energy of an exchange process from variable-temperature NMR spectra.

16.6. In 1D proton spectra recorded with water presaturation, signals of exchangeable protons are sometimes lost or severely attenuated. Describe why!

16.7. How do you determine exchange rates from EXSY spectra?

Further Reading

Harris, R.K. (1986) *Nuclear Magnetic Resonance Spectroscopy*, Chapter 5, Longman.

Roberts, G.C.K. (ed.) (1993) *NMR of Macromolecules*, Chapter 6, IRL Press.

Perrin, C.L. and Dwyer, T.J. (1990) Application of two-dimensional NMR to kinetics of chemical exchange. *Chem. Rev.*, **90**, 935–967.

Bain, A.D. (2003) Chemical exchange in NMR. *Progr. NMR Spectrosc.*, **43**, 63–103.

Casarini, D., Lunazzo, L., and Mazzanti, A. (2010) Recent advances in stereodynamics and conformational analysis by dynamic NMR and theoretical calculations, *Eur. J. Org. Chem.*, **2010**, 2035–2056.

17
Two-Dimensional NMR Spectroscopy

17.1
Introduction

Identification of the chemical nature of synthesized compounds by NMR experiments used to be very challenging, in particular in the (early) days when a 60 MHz spectrometer was considered as high field. But the severest problems during assignment were the amount of signal overlap and the fact that neighboring protons could not be simply identified from scalar couplings as demonstrated for the case of ibuprofen (see Chapter 1). Nowadays, with the availability of a large set of 2D NMR experiments, assignments for small to medium-sized molecules are usually achieved fairly rapidly and the procedures are straightforward.

Two-dimensional NMR spectroscopy was originally suggested by Jean Jeener at the Ampere Summer School in Basko Polje in 1971 as a gedankenexperiment (we believe it was a blackboard presentation). Richard Ernst, a Nobel laureate in chemistry 1991, was attending the lecture, became attracted by this idea, and decided to put it into practice (which he and his coworkers did!). The start of 2D NMR specroscopy was largely driven by technical issues: computing power was limited, the limited disk space on hard drives in those days in combination with the large data sets from 2D measurements as well as the requirements for improved long-term spectrometer stability and so on made experiments challenging. One of the first 2D experiments was a *J*-resolved proton experiment, and it was particularly chosen for the reason that it did not require large data sizes.

Why is 2D NMR spectroscopy so important? Undoubtedly, biomolecular structure determination would not have been possible without 2D or even 3D NMR techniques. An important feature of 2D NMR spectra is that such spectra display *correlations*. Instead of indirectly deducing neighboring relationships from scalar couplings, one can use cross peaks between signals to indicate such correlations directly. Another advantage of 2D NMR experiments is that signals are dispersed in a plane, so peak overlap occurs much less frequently.

We will now introduce some nomenclature. Two-dimensional NMR experiments are classified as *homonuclear* or *heteronuclear* experiments depending on whether

Applied NMR Spectroscopy for Chemists and Life Scientists, First Edition. Oliver Zerbe and Simon Jurt.
©2014 WILEY-VCH Verlag GmbH & Co. KGaA. Published 2014 by WILEY-VCH Verlag GmbH & Co. KGaA.

the two correlated spins are of the same type (e.g., both proton spins) or different type (e.g., correlations between proton and carbon spins). The vast majority of experiments correlate chemical shifts of two spins with each other, and these are referred to as *shift-correlation* experiments. Alternatively, sometimes a scalar coupling is correlated with a chemical shift, and such experiments are named *J-resolved* experiments. Even in the case of shift-correlation experiments, hundreds of experiments have been published that differ in the exact mechanism by which the two spins are correlated. In principle, this can be through scalar couplings, dipolar couplings, or exchange, but there are many more ways for how to manipulate magnetization transfers. In this chapter we will only describe the most often used experiments. Those readers who are actually interested in how these experiments work are encouraged to read Chapter 13.

17.2 The Appearance of 2D Spectra

After 2D Fourier transform of the array of free induction decays (FIDs), a spectrum as depicted in Figure 17.1 is obtained. The spectrum in Figure 17.1a corresponds to a *homonuclear* shift-correlated spectrum. The dimension corresponding to the directly detected frequency is usually called F2, and the indirectly obtained dimension is usually called F1. Signal frequencies in F1 or F2 are obtained by the projections onto the F2 or F1 axis. Homonuclear spectra mostly (although not always) contain a diagonal, characterized by peaks that possess the same frequency in F1 and F2, and these *autocorrelation peaks* are of little interest. In contrast, off-diagonal peaks, called *cross peaks,* are characterized by different frequencies in F1 and F2, and hence correlate different spins.

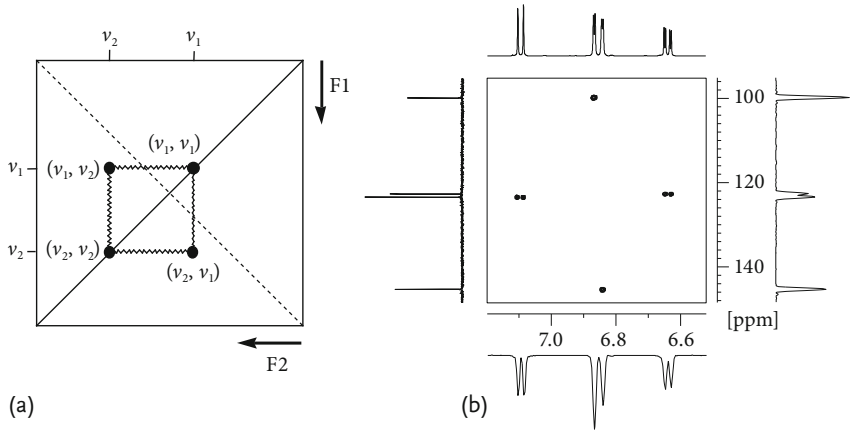

Figure 17.1 (a) Schematic representation of a homonuclear 2D spectrum. (b) Depiction of an expansion of the proton–carbon correlation of an aromatic compound; external (top, left) and internal (right, bottom) projections are plotted at the sides.

Peaks that are located on the antidiagonal are often artifacts. In heteronuclear shift-correlated spectra (Figure 17.1b) and of course in *J*-resolved spectra no diagonal peaks are found because the frequencies in F1 and F2 are different.

Two-dimensional spectra are 3D objects (two frequencies plus the amplitude of the cross peak). To visualize these, contour plots are used, which are very much like topological maps (see Figure 17.2). In the latter, mountains are indicated by contour lines that connect points of similar height. Figure 17.3c depicts a so-called *stacked plot*, which looks nice but is more or less useless for data interpretation. Next to the spectrum, *projections* are often plotted so that peak positions can be more easily traced back to the signals in the 1D spectra. If available, *external projections* from separately recorded 1D spectra may be plotted. Alternatively, *internal projections* computed from the 2D spectrum by summing up the signal along horizontal or vertical lines may be depicted. Considering that ^{13}C signals are much more sensitively recorded from certain 2D spectra (see Sections 4.2 and 13.6), this is sometimes the only way to obtain ^{13}C chemical shifts for compounds for which only very little substance is available!

When we zoom into a single cross peak, a multiplet structure may become visible. Figure 17.2 displays cross peaks from COSY spectra. In this figure contours corresponding to positive peaks are filled, and negative contours are indicated by a single line. *Active couplings* are those that gave rise to the cross peak. It is best if we look at an example, so let us assume a three-spin system ABC. In the cross peak at the Ω_A(F1), Ω_B(F2) frequency, the J_{AB} coupling is the active coupling. However, if spin A is also coupled to spin C, then the J_{AC} coupling is also present, and is called the *passive coupling*. If we look at the cross peak depicted in Figure 17.2b, we see four components of the peak along the F2 dimension: the active coupling is in antiphase (opposite phase for the components), and the passive coupling is in phase. Similarly, the signal corresponding to spin A in the 1D spectrum is a doublet of

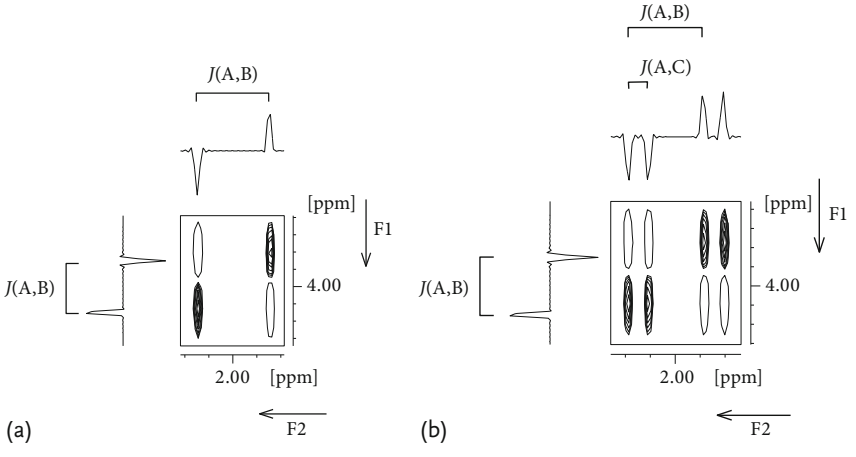

Figure 17.2 Schematic representation of cross peaks (a,b) in a 2D correlation spectroscopy (COSY) experiment. As projections, traces through the peaks along F1 or F2 are depicted.

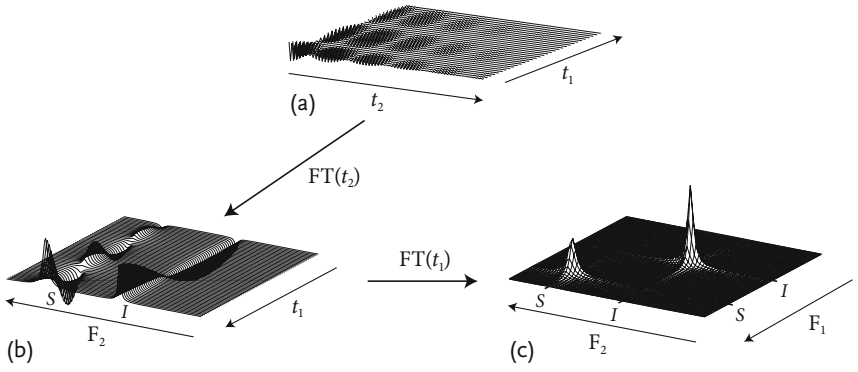

Figure 17.3 Principle of 2D NMR spectroscopy. An array of FIDs (a) is Fourier transformed, resulting in an array of 1D spectra (b), in which the signal intensities are modulated by the frequency in the indirect dimension. A second Fourier transform, this time taking corresponding data points from the different 1D spectra, results in the 2D spectrum (c). FT – Fourier transform.

doublets. When signals overlap, scalar couplings can (with some caution) still be extracted from 2D spectra; we will make use of this when we discuss carbohydrates (Chapter 20).

17.3 Two-Dimensional NMR Spectroscopy: How Does It Work?

In the simple 1D NMR experiment, an oscillating current is induced in the receiving coil that directly reflects the precession frequency of the spins. The frequency in the second dimension, referred to as the *indirect dimension*, is derived indirectly. To understand how that works we briefly recall that signals are sampled in 1D NMR experiments *stroboscopically*, with a time separation between two consecutive data points that is inversely related to the spectral width. The receiver is gated on and off during recording of the FID. In principle, the frequencies in the indirect dimension are sampled similarly, but this time two consecutive data points are sampled in two different FIDs! In fact, 2D NMR spectra are recorded as a set of a number of (usually a few hundred) 1D NMR spectra.

After these FIDs have been processed, a series of spectra are obtained that contain signals always at the same frequencies, but in which the signal intensities vary from 1D spectrum to the next one. It is this modulation of the signal intensity (amplitude) that defines the frequency in the indirect dimension. To translate the amplitude modulation into the corresponding frequency we apply a second Fourier transform, this time in the t_1 direction (Figure 17.3)!

Each 2D NMR experiment is composed of at least *four building blocks*: *excitation*, *evolution*, *mixing*, and *detection*. In the excitation block magnetization is flipped into the transverse plane. During evolution, chemical shift labeling for the indirect dimension occurs, which means the amplitude modulation encoding the frequency

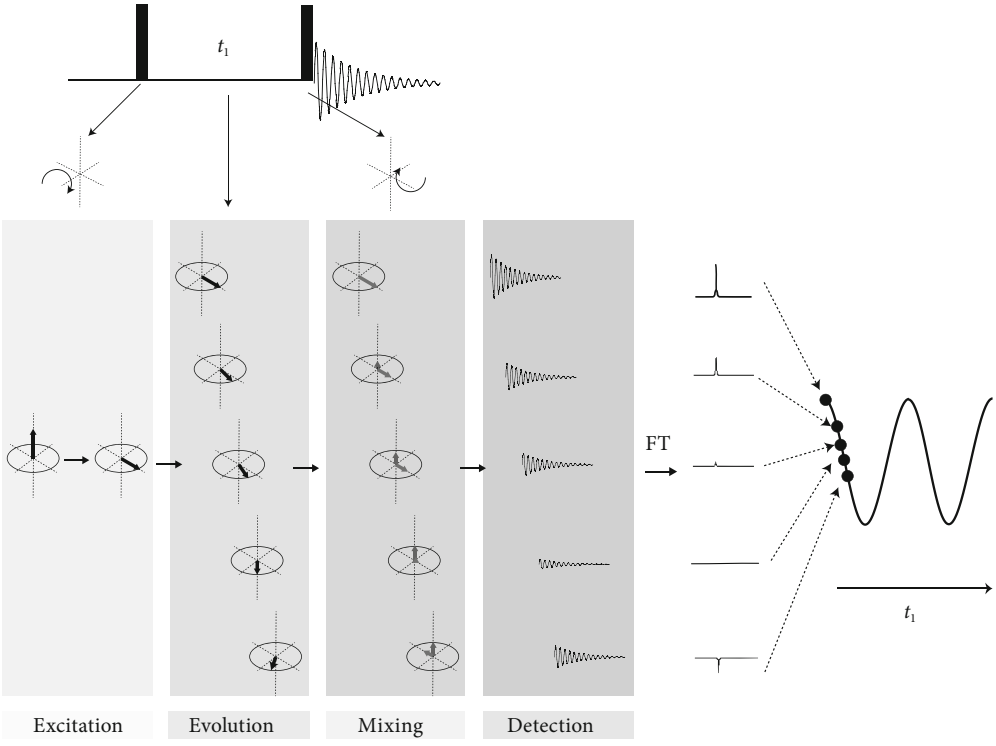

Figure 17.4 Origin of amplitude modulation in a COSY-type experiment.

in the indirect dimension is introduced. During mixing, coherences are transferred from one spin to another. The exact mechanism by which this occurs can be scalar or dipolar coupling, or via exchange processes. During the detection period the signal is acquired. This is schematically depicted in Figure 17.4.

The first 90° pulse of the COSY sequence rotates the magnetization into the transverse plane (excitation). Subsequently, this magnetization rotates in the transverse plane at a frequency that corresponds to its chemical shift (evolution). The mixing pulse is meant to transfer the magnetization from one spin to another (mixing). The nontransferred component, which will later lead to the diagonal peak, is partially rotated to the z axis and the x axis depending on the position of the magnetization vector (Figure 17.5)

In another increment, the magnetization vector has rotated to another position, and accordingly the length of the magnetization component that remains in the transverse plane after the 90° pulse changes from increment to increment. To be precise, the amount of transverse magnetization is modulated by the frequency with which the spin precesses in the transverse plane due to its chemical shift. We wish to emphasize the analogy with the simple 1D experiment, in which data points are consecutively sampled within one experiment, and the individual data points are always separated by the same amount of time. In the 2D experiment

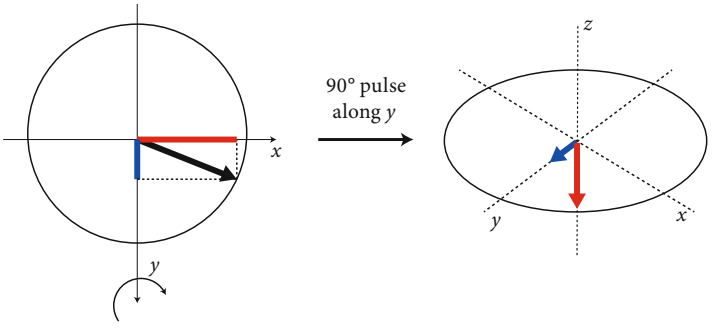

Figure 17.5 Effect of a 90° pulse along the *y* axis on a magnetization vector in the *xy* plane. To compute the effects from the pulse, the magnetization vector (depicted in black) is projected onto the *x* axis and the *y* axis, and the component along the *x* axis (shown in red) is rotated onto the *z* axis, while the component along the *y* axis (shown in blue) is not affected by the pulse and remains in the transverse plane. Note that the perspective of the observer has changed on the right to also show the *z* component.

the individual data points are derived from a series of 1D experiments. The increment of the evolution time again separates consecutive data points by the same amount of time. The only difference between 1D and 2D experiments is that in the 1D experiment data points are sampled in one experiment, whereas in the 2D experiment data points are sampled in different (1D) experiments.

Excursus 17.1: Description of the 2D COSY Experiment using the Product Operator Formalism

So far we have tried to describe the working principle of 2D NMR experiments using the vector picture. However, we cannot really understand the coherence transfer step using the vector picture. To really comprehend how 2D NMR spectroscopy works in all its facets we need the product operator formalism. The reader is encouraged to read Chapter 8. Believe it or not, the formalism is very simple to use, try it!

As always we start with equilibrium z magnetization, to which we apply a 90° pulse along y:

$$I_z \xrightarrow{90°(x)} -I_y \tag{17.1}$$

This magnetization will precess in the transverse plane according to its chemical shift:

$$\xrightarrow{\Omega_I t_1 I_z} -I_y \cos(\Omega_I t_1) + I_x \sin(\Omega_I t_1) \tag{17.2}$$

It will also evolve scalar couplings, possibly to another spin S, which we simply compute on top of the shift evolution:

$$\begin{aligned} \xrightarrow{2\pi J_{IS} t_1} \quad & -I_y \cos(\Omega_I t_1)\cos(\pi J_{IS} t_1) + 2 I_x S_z \cos(\Omega_I t_1)\sin(\pi J_{IS} t_1) \\ & + I_x sin(\Omega_I t_1)\cos(\pi J_{IS} t_1) + 2 I_y S_z \sin(\Omega_I t_1)\sin(\pi J_{IS} t_1) \end{aligned} \tag{17.3}$$

Phew, a lot of terms... Now, we calculate the effect of the final mixing pulse:

$$\begin{aligned} \xrightarrow{90^\circ(I,S)y} \quad & -I_y \cos(\Omega_I t_1)\cos(\pi J_{IS} t_1) - 2 I_z S_x \cos(\Omega_I t_1)\sin(\pi J_{IS} t_1) \\ & - I_z \sin(\Omega_I t_1)\cos(\pi J_{IS} t_1) + 2 I_y S_x \sin(\Omega_I t_1)\sin(\pi J_{IS} t_1) \end{aligned} \tag{17.4}$$

and now chemical shift evolution during the detection period t_2 (neglecting coupling and all sine-terms from shift evolution)

$$\begin{aligned} \xrightarrow{\Omega_{I,S} t_2} \quad & -I_y \cos(\Omega_I t_1)\cos(\pi J_{IS} t_1)\cos(\Omega_I t_2) \\ & - 2 I_z S_x \cos(\Omega_I t_1)\sin(\pi J_{IS} t_1)\cos(\Omega_S t_2) \\ & - I_z \sin(\Omega_I t_1)\cos(\pi J_{IS} t_1) \\ & + I_y S_x \sin(\Omega_I t_1)\sin(\pi J_{IS} t_1)\cos((\Omega_I \pm \Omega_S) t_2) \end{aligned} \tag{17.5}$$

The first term corresponds to I-spin magnetization evolving at the I-spin frequency in t_1 and t_2, and hence will lead to the diagonal peak at the I-spin frequency. The second term evolves at the I-spin frequency in t_1 and at the S-spin frequency in t_2, and hence will lead to the I–S cross peak. The third term is z magnetization, and will not result in a detectable signal. Finally, the fourth term is the so-called multiple-quantum coherence (more than one transverse term) and will not result in observable magnetization. If we started from S_z instead of I_z, we would only need to replace I with S in the description. The second term then would represent the symmetry-related second cross peaks, and the first term the diagonal peak at the S-spin frequency.

17.4 Types of 2D NMR Experiments

In this section we describe the commonest 2D NMR experiments. The choice is based on what we use most in the structure elucidation at our institute. Probably many hundreds of experiments have been designed, most of them required for special applications. Many sequences have been created in the BioNMR field, and the interested reader is encouraged to consult monographs in that field.

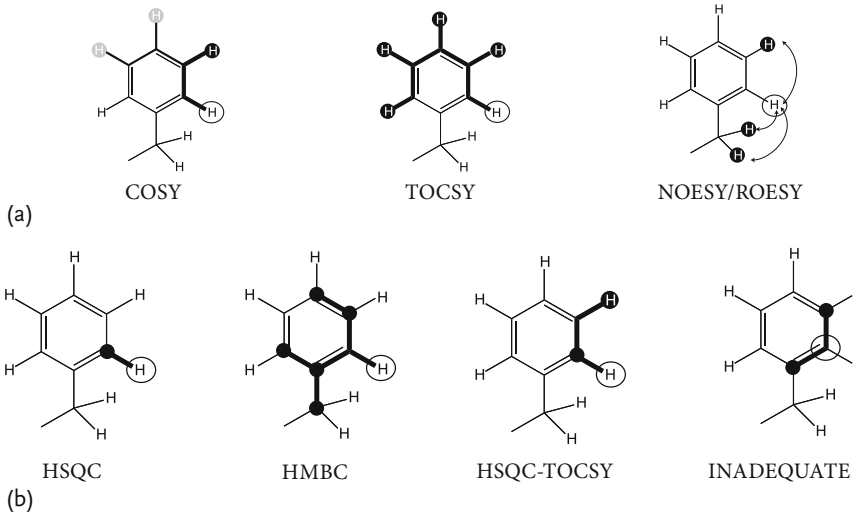

Figure 17.6 Magnetization flow in standard 2D NMR homonuclear (a) or heteronuclear (b) experiments using an aromatic spin system linked to an aliphatic anchor as an example. The starting nucleus (at the ortho position) is highlighted by an open circle. Bonds along which magnetization is transferred are depicted in bold. Locations of correlated nuclei are shown as filled black circles. The faint circles in the COSY example indicate positions for which correlation can only be observed under favorable circumstances (sharp lines). TOCSY – total correlation spectroscopy, NOESY – nuclear Overhauser effect spectroscopy, ROESY – rotating-frame nuclear Overhauser effect spectroscopy, HSQC – heteronuclear single-quantum coherence, HMBC – heteronuclear multiple-bond correlation, INADEQUATE – incredible natural abundance double quantum transfer experiment.

Two-dimensional NMR experiments have acronyms, and creating a fancy acronym is almost as developing the experiment itself. The names of many sequences end with "SY," which stands for "spectroscopy." We summarize the shift-correlation experiments that are most useful for synthetic organic molecules or natural products in Figure 17.6.

17.4.1 The COSY Experiment

The COSY experiment is one of the most commonly performed 2D experiments. It is a homonuclear 2D experiment usually used to correlate protons via scalar couplings. Correlations will be seen if the coupling is not smaller than the line width of the signal. The experiment also involves one of the simplest pulse sequences.

The COSY experiment comes in many flavors, for example, *double-quantum-filtered and triple-quantum-filtered* experiments. A disadvantage of using a simple COSY experiment is that the diagonal peaks are dispersive when cross peaks are phased absorptive. Since dispersive peaks are broader, cross peaks near the diagonal cannot be recognized anymore. In the alternative double-quantum-filtered COSY experiment (Figure 17.7), both diagonal peaks and cross peaks are absorp-

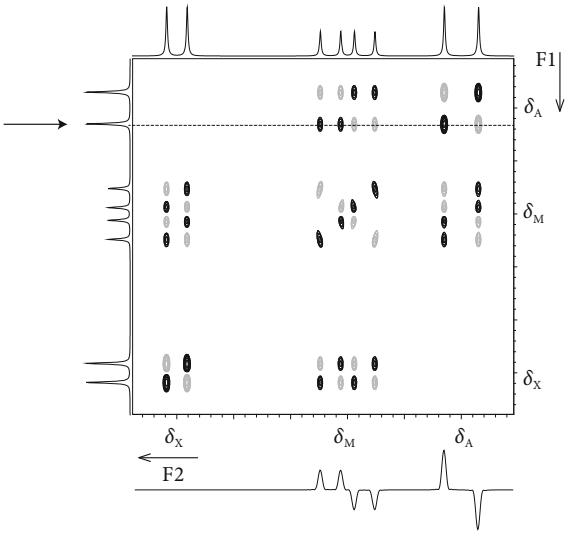

Figure 17.7 Appearance of an AMX spin system in a double-quantum-filtered COSY experiment with a linear A–M–X topology.

tive, and this is the type of COSY we use the most. In the triple-quantum-filtered COSY experiment, certain peaks will be eliminated. To create triple-quantum coherence, three protons must couple to each other. If a single proton just couples with another one, this coupling will not be visible. What remains are, for example, methine protons coupled to CH_2 groups. In the double- or triple-quantum experiments, 50 or 75% of the signal is inherently lost, and so they are less sensitive.

We have seen before that cross peaks in COSY experiments display a multiplet fine structure with antiphase contributions. When lines become broader (or when the resolution in F1 is low), these components will cancel each other. Therefore the COSY experiment is not an experiment for large molecules with broad lines. In this case use of a short-mixing-time TOCSY experiment is much better.

COSY experiments are prone to many artifacts. Some of them arise if the relaxation delay is set too short, and these artifacts are usually found on a line with twice the slope of the diagonal.

17.4.2 The TOCSY Experiment

The TOCSY experiment is a very useful experiment as well, in particular for slightly larger molecules, in which signal overlap commonly occurs. It is particularly well suited for molecules that comprise many spin systems. Classic examples are peptides and proteins, in which the amino acids exhibit individual spin systems, and oligosaccharides, in which the monosaccharide building blocks also exhibit individual spin systems.

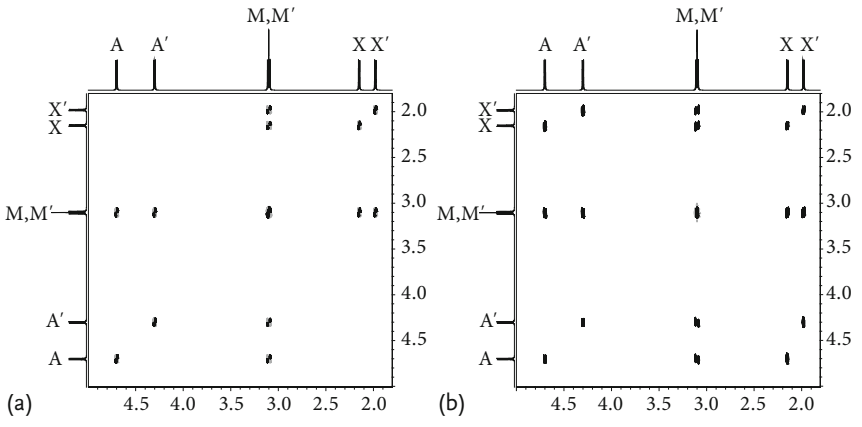

Figure 17.8 Comparison of COSY (a) and TOCSY (b) spectra of two mixtures of two AMX spin systems, in which the M and M′ resonances overlap.

During assignment in COSY-type experiments, traditionally we start by correlating spin *a* with spin *b*, spin *b* with spin *c*, and so on. If at some point a resonance overlaps with another one, we do not know how to proceed because further correlations may be due to either of the two overlapping resonances. In the TOCSY experiment, in principle correlations are achieved throughout the entire spin system. Accordingly, only a single well-resolved resonance is required, from which correlations to most other if not all members of the same spin system are seen. This is highlighted in Figure 17.8.

In the COSY experiment, A is correlated with M. But since M and M′ overlap, we do no know whether we need to move on to X or to X′. If we look at the TOCSY spectrum, we see that A is correlated with M (or M′) and X but not with X′. Again, a single resolved resonance is required. For peptides this is usually the amide proton, while it is the anomeric proton in the case of oligosaccharides.

The TOCSY experiment achieves coherence transfer through the entire spin system by temporarily creating a state of strong coupling. We discussed strong coupling in Section 3.4.2: it is characteristic of situations when the chemical shift difference is not large compared with the scalar coupling. The ultimate limiting case is when the chemical shift difference is zero. Magnetization then freely flows between strongly coupled spins, and they do not behave like separate entities any longer. The trick in the TOCSY experiment is to temporarily create a state in which the precession frequencies of all spins are the same (the so-called *Hartmann–Hahn condition*). This can be achieved by using a spin-echo pulse train, during which chemical shift is constantly refocused (see Figure 17.9).

As long as the pulse train of the spin-echo sequence is applied, the artificial strong coupling case applies and magnetization can flow between coupled spins.

The mixing process is sometimes compared to a set of coupled pendulums. At the beginning only the first pendulum moves. After some time the second one moves and it slowly propagates to all other coupled pendulums. How far we dis-

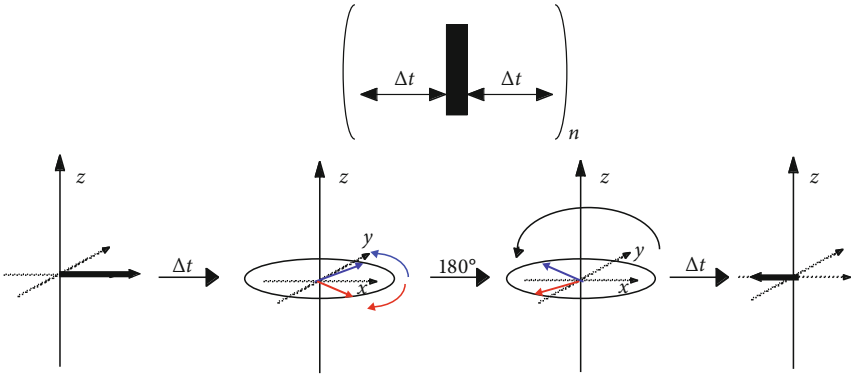

Figure 17.9 The spin-echo sequence. During a short delay Δt spins evolve at different frequencies. A central 180° pulse flips the spins, which are coaligned after a second delay Δt again. Thereby the dephasing effects due to precession according to different frequencies are eliminated at the end of the spin-echo sequences. In the TOCSY experiment, so-called offset-compensated sequences are used that achieve a nearly perfect 180° pulse over a large bandwidth. The spin-echo element is repeated over and over again for a total amount of time that is called the mixing time. This train of 180° pulses is sometimes also referred to as the *spin lock*.

tribute magnetization within a spin system depends on the mixing time (the period during which the spin lock is applied). A 12 ms ^{1}H,^{1}H TOCSY experiment will achieve only transfer to the direct neighbors, and hence corresponds to the COSY experiment. A 60–80 ms TOCSY experiment will usually result in transfer among the entire spin system. During the spin lock, T2 (to be more precise T1ρ) relaxation is active. Keeping proton magnetization transverse for 60 ms may lead to the complete decay of magnetization from macromolecules, and the TOCSY experiment therefore is not suitable for larger proteins any longer (but works well for peptides).

Short-mixing-time TOCSY experiments are a good alternative to COSY experiments for molecules with broader lines, because the multiplet components of the peaks are all in phase and hence do not cancel each other.

The pulse train during the spin lock is applied at comparably high power, although the power is less than for the other 90° pulses in the sequence. Nevertheless, the continuous pulsing results in sample heating, which may easily be 1–2 °C or more for long mixing times. Experimentally, you can try to compensate for that a bit by increasing the airflow in the probe so that the heat produced is more efficiently transported away. We often observe that the frequencies in F1 are slightly different from those in F2 because the measuring temperature after the relaxation delay (at the beginning of the sequence which is important for the frequency in F1) is less than after the spin lock when the signal in F2 is recorded, so both dimensions need to be slightly differently calibrated.

One final remark: TOCSY spectra sometimes display phase problems (and in particular a mixture of positive and negative signals).

17.4.3
The NOESY Experiment

The nuclear Overhauser effect spectroscopy (NOESY) experiment is the most important experiment for determining stereochemistry or conformational preferences of molecules. By the way, exactly the same experiment is called exchange spectroscopy (EXSY) when it is used to determined exchange effects (see Section 16.2). The mixing time in the NOESY experiment must be adjusted to the transverse relaxation time of the molecule under study: for small molecules the mixing time can be chosen to be slightly less than T1 (e.g., 0.8–1.0 s). For large molecules (those in the so-called spin-diffusion limit) the mixing time should be considerably less (50–100 ms); the correct choice is difficult and needs some experience. Note that this parameter depends on the measuring temperature because overall tumbling changes with temperature. As a rule of thumb, decreasing the temperature by 20 °C corresponds to doubling the molecular weight! For large molecules it is sometimes advisable to monitor the nuclear Overhauser effect (NOE) buildup by recording a series of NOESY spectra at different mixing times to detect spin-diffusion effects (see Section 15.2.2 for a discussion on this issue).

The most often encountered artifacts in NOESY spectra are zero-quantum interference peaks, exchange peaks, and t_1 noise. Zero-quantum interference peaks are observed between protons that are scalarly coupled, and will lead to COSY-type peaks with multiplet patterns. An overlap of this signal with a true NOE results in a typical tilted peak shape (similar to exclusive correlation spectroscopy (E.COSY) peak shapes) (Figure 17.10).

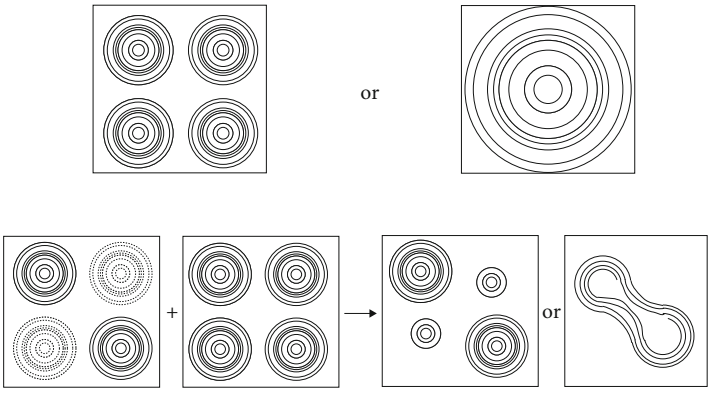

Figure 17.10 Peak shapes in NOESY spectra for a cross peak from a doublet signal (top left). For molecules with broader lines the individual, in-phase components will merge into a single peak (top right). Zero-quantum artifacts have positive and negative components (bottom left). Overlap of these peaks with true nuclear Overhauser effects results in mutual partial cancellation of positive and negative components (bottom, third from the left). Again for larger molecules these components merge (bottom right).

Zero-quantum interference is more a problem for molecules with sharp lines (for large molecules the zero quantum coherences decay during the mixing time). In principle there are experiments for suppressing artifacts of this type.

As described before, exchange peaks are strong, and are present even when short mixing times are used (unless the exchange is very slow). One source of artifacts that is always present, except for in the spectra used by manufacturers in advertising, is t_1 noise. This is characterized by strong vertical noise bands and is proportional to the signal intensity, and will therefore be strongest for an intense peak, usually the methyl singlets, and in particular for methyl signals from tertiary butyl groups. Interestingly, t_1 noise is much less a problem for molecules with broad lines because a field drift by a fraction of a hertz due to lock instabilities does not change the intensity at a certain position so much in a broad line. When setting up a series of 2D spectra, it is good to perform the NOESY experiment during the night when there is much less environmental disturbance!

17.4.3.1 The Alternative for Small Molecules: The ROESY Experiment

As discussed in Section 15.2.1, the NOE depends not only on the distance between the dipolarly interacting nuclei, but also on the tumbling properties of the molecule, and for some specific correlation time the NOE becomes zero. At 25 °C this is the case for molecules with a molecular weight of about 1000 when measurement are performed in water. Often, for small molecules it is unclear whether the molecule of interest is close to the zero crossing of the NOE. Fortunately, an alternative experiment, the rotating frame NOESY (ROESY) experiment can be used, and we prefer this experiment over the NOESY experiment for small molecules in general.

In ROESY spectra, cross peaks arising from true rotating-frame NOEs (ROEs) display negative sign when diagonal peaks are phased to positive absorption. As artifacts we encounter exchange peaks, TOCSY transfer peaks, spin-diffusion transfer peaks (ROE-ROE relay peaks), (rarely) TOCSY-ROESY transfer peaks, and of course t_1 noise. With the exception of the TOCSY-ROESY transfer peaks all peaks have positive sign and hence can be easily recognized as artifacts. In our opinion, the ease with which artifacts are recognized is an important advantage of ROESY experiments.

The ROE buildup is almost twice as fast as the NOE buildup, and hence shorter mixing times can be used (shorter than 500 ms usually). During the ROE transfer period (the spin-lock) magnetization relaxes with T1ρ, which is close to T2 and hence short for large molecules. Therefore, the ROESY experiment is really an experiment for small molecules, while the NOESY experiment gives good spectra particularly for larger molecules.

17.4.4 HSQC and HMQC Experiments

The heteronuclear single-quantum coherence (HSQC) experiment is *the* experiment for recording heteronuclear shift correlations along the one-bond coupling. Its is mostly used for correlating protons with their directly attached carbon nuclei (or in BioNMR experiments with their attached ^{15}N nuclei). One-bond carbon–proton couplings are rather uniform (see Section 4.3.2.1) and span the range of 120–160 Hz (for triple bonds the C–H coupling is about 250 Hz). Because the coupling is fairly large, the transfer from the proton to the carbon (and back) is highly efficient, and the experiment works very well even for large molecules or when lines are broad for some reason. Of course, sensitivity is reduced by the fact that the natural abundance of ^{13}C is only 1%, but in particular when cryoprobes are used good signal-to-noise spectra can still be recorded with a few milligrams of a natural product in a few hours (or with 1 mg overnight). When only 1 mg of a natural product is available recording a ^{13}C NMR spectrum directly is not feasible within a reasonable time frame, and hence measuring HSQC spectra is the only way to get to the carbon shifts.

The HSQC experiment uses a so-called double polarization transfer (see Section 13.6), which contains a number of 180° pulses that are prone to offset effects, and therefore the performance of the experiment is lowered when the chemical shift range is very large, or when the chemical shifts are unknown. Heteronuclear spectra may be used to record proton–metal correlations (e.g., we have measured many proton–cadmium correlations). At the beginning, the carrier of the heteronuclear channel can easily be off by 1000 ppm. Then it is better to use the heteronuclear multiple-quantum correlation (*HMQC*) experiment, which has only one 180° pulse on ^{1}H and none on X, and is therefore less prone to offset effects. The HMQC experiment is also better suited for large molecules with short T2 times. The disadvantage of the HMQC experiment is that it additionally displays proton–proton couplings in F1, and hence the maximum resolution is lower than in the HSQC experiment. Therefore, for small molecules we generally prefer the HSQC experiment over the HMQC experiment.

The HSQC experiment belongs to the so-called class of "inverse" experiments. Initially, experiments were used that were based on a single instead of a double polarization transfer. They started with proton magnetization and transferred the signal via the proton–carbon coupling to carbon for detection. The corresponding experiment is called the heteronuclear shift correlation (*HETCOR*) experiment. It is quite a bit less sensitive compared with the HSQC experiment because carbon magnetization instead of proton magnetization is detected. However, when the sample is sufficiently concentrated, it may be still be preferred over the HSQC experiment because the resolution in the carbon dimension can easily be increased by adding more data points during acquisition without increasing the measuring time significantly. Sometimes high resolution in the carbon dimension is required and then the HETCOR experiment may be more suitable.

17.4.5
The HMBC Experiment

Since the HSQC experiment correlates protons with their directly attached carbons, quaternary carbons or carbonyls will be missing in these spectra, and to measure their chemical shifts experiments that use long-range couplings must be used. The classic experiment for that purpose is the *heteronuclear multiple-bond correlation* (HMBC) experiment. The proton–carbon ^{2}J and ^{3}J couplings are between 0 and 20 Hz. The three-bond couplings follows a Karplus relationship, and their magnitude therefore depends on the dihedral angle involved. We usually use a coupling of 5–10 Hz as a general compromise, but it may sometimes be good to perform a second experiment with a different setting for the long-range coupling. The HMBC experiment uses a so-called *low-pass filter* to eliminate correlations due to the one-bond coupling. This filter is optimized for a certain coupling (e.g., 140 Hz), and, due to the spread in one-bond couplings, often residual signals due to the one-bond coupling are present in the spectra. These artifacts can be easily spotted, because they show up as two peaks separated by the coupling in F2 (see Figure 17.11). Even more important, there is not necessarily a corresponding signal at these positions in the proton dimension. This is because these experiments are performed without carbon decoupling. For the much smaller two- or three-bond couplings, the corresponding couplings may not be resolved in the spectra.

Signal intensities vary a lot in these spectra. HMBC spectra are much less sensitive than HSQC spectra, but nevertheless are very useful for structure elucidation. Because the couplings are much smaller, they will only give satisfactory results

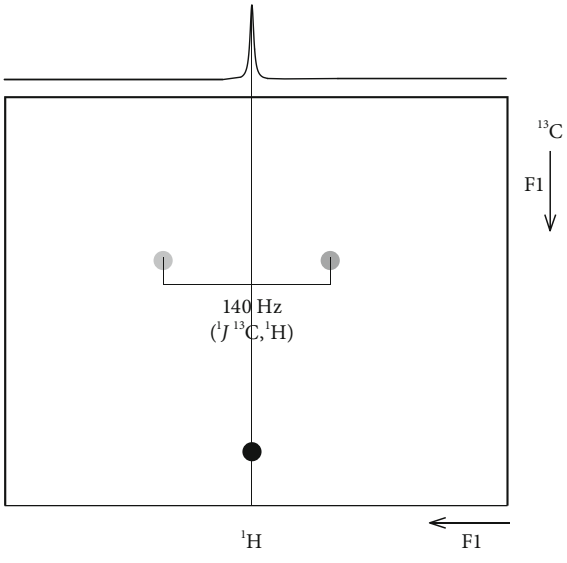

Figure 17.11 Signals in HMBC spectra. Artifacts due to nonsuppressed one-bond couplings (depicted in gray) and true HMBC peaks (black circle) are shown.

for molecules with sharp lines (in contrast to HSQC experiments). We will make extensive use of them in Part Five.

As the HETCOR experiment was the carbon-detected version of the HSQC experiment, the COSY via long-range coupling (*COLOC*) experiment is the carbon-detected variant of the HMBC experiment. For similar reasons it may be useful in cases where high resolution in the carbon dimension is required.

17.4.6 The HSQC-TOCSY Experiment

The HSQC-TOCSY experiment is an experiment in which two different 2D experiments have been concatenated to form a single 2D experiment. These experiments are derived from 3D experiments. In the HSQC-TOCSY spectrum, not only the correlations of the carbon with its directly bonded proton(s) but also the correlation of the carbon with the protons within the same spin system are shown. Usually the TOCSY transfer is limited to yield correlations to protons on neighboring carbons. This is schematically depicted in Figure 17.12. The direct correlation corresponding to the HSQC signal will usually be much stronger, but in principle comparison with an HSQC spectrum is required to distinguish direct correlations from relay peaks.

HSQC-TOCSY spectra contain in addition to HSQC-type information also COSY-type information. Since everything is filtered via ^{13}C, for molecules with natural-abundance ^{13}C, the experiment is much less sensitive compared with a COSY experiment. So what is the advantage of using a HSQC-TOCSY experiment? The dramatic advantage of this experiment is that is uses the resolution in the ^{13}C dimension to disperse these peaks. This becomes very useful when the resolution is low in the proton dimension, for example, for molecules with few functional groups. For two protons that are close in chemical shift, their mutual correlation in a COSY spectrum will be very close to the diagonal, often too close to be iden-

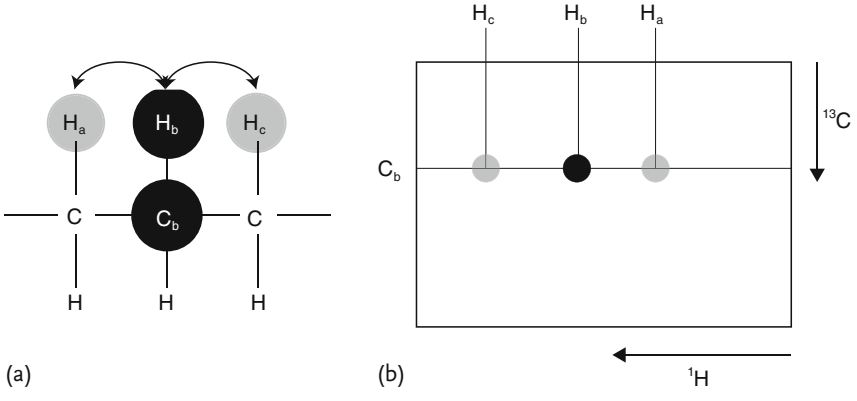

Figure 17.12 Schematic drawing of a HSQC-TOCSY experiment. A linear carbon chain is depicted in (a), and the correlations at the carbon frequency of C_b are depicted in (b).

tified. Moreover, these correlations may (hopelessly) overlap with others. Carbon spectra are almost always well dispersed, and because of this, correlations to the neighboring protons can be easily identified. These spectra are really very useful, and the sensitivity is reasonable though not as good as for the HSQC experiment. But for steroids or oligosaccharides, this is the only way to work your way through the proton spin systems!

17.4.7 The INADEQUATE Experiment

The incredible natural abundance double quantum transfer experiment (INADEQUATE) is an experiment to directly correlate carbon spins with each other. For a correlation to show up, two ^{13}C nuclei must be next to each other, for which the probability is $0.01 \times 0.01 = 0.0001$, or 0.1‰! Accordingly, a lot of sample is required, and we really mean *a lot*. The more the better in principle. Depending on the sensitivity of the probe, this can easily be 50–100 mg for a small molecule. We have recorded INADEQUATE spectra on samples where half of the sample was solvent and the other half the compound of interest! Obviously, the compounds must be highly soluble. As a rule of thumb, to be able to successfully record an INADEQUATE spectrum, we must get a good signal-to-noise ^{13}C spectrum with *a single scan*!

The incredible insensitivity of the INADEQUATE obviously severely limits its applicability. However, for some compounds, in particular for highly substituted compounds that contain only a few protons, this experiment may be the only tool to build up the covalent structure. Should good spectra be obtained, building up the structure is very fast! The problem is that it is difficult to measure good spectra, and this is mainly due to the insensitivity of the experiment. Again, if you do not have at least tens of milligrams of the substance or if the solubility is low, *don't even think* of recording INADEQUATE spectra.

A few tips: First of all, if you can, use small-volume tubes such as Shigemi tubes to achieve the highest possible concentration. Since the INADEQUATE is basically a carbon experiment, the relaxation delay should be tuned to the T1 times of the carbons, and these can be long (too long for practical purposes). Therefore, we usually add *a tiny bit* of a relaxation reagent such as chromium acetylacetonate to bring the T1 times down to approximately 1 s so that we can record the spectra using a relaxation delay of 1 s. Do not add too much of the reagent because otherwise the carbon lines will become too broad! It is also a good idea to quickly check the T1 times with an inversion-recovery sequence (see Section 14.4.5).

The appearance of INADEQUATE spectra is unusual in that double-quantum frequencies are displayed in F1. These are the sum of the chemical shifts of the two correlated carbon nuclei. However, this is not really a problem, since correlations to the two carbons involved are displayed at that frequency along F2 (see Figure 17.13)! Each cross peak usually comprises two components separated by the one-bond C–C coupling, and the two components are in antiphase (they have opposite sign). Due to the often poor signal-to-noise ratio, sometimes one of the

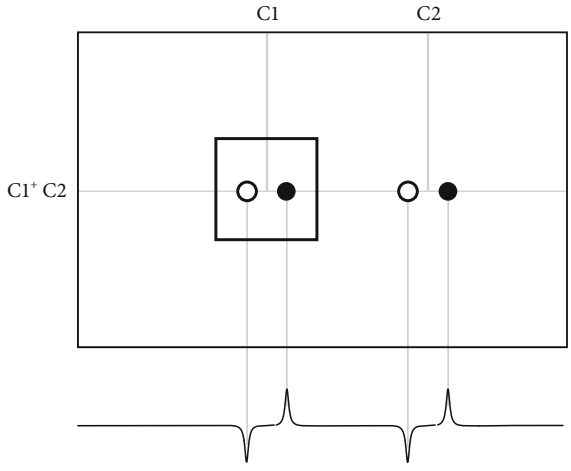

Figure 17.13 Schematic drawing of a spectrum from an INADEQUATE experiment. Two cross peaks occur on a vertical line at the sum of the frequencies of the two carbon resonances in F1. In F2 the positions correspond to the chemical shifts of the two carbons involved.

two cross peaks is not clearly visible (or is not visible at all). Here it helps that the frequency in F1 is the sum of the two chemical shifts. If we only observe one of the two cross peaks, we can calculate from the double-quantum frequency what the frequency of the missing peak must be!

How INADEQUATE spectra can be used to assign molecules is demonstrated in Figure 17.14 for the case of melatonin. Two cross peaks are always observed on a horizontal line, whose locations reveal the two carbon nuclei that are coupled. Walking along a vertical line to the next cross peak reveals the double-quantum frequency at which the second neighbor of that carbon nucleus is located.

Despite all the disadvantages of the INADEQUATE, for some applications it is perfectly adequate to use it.

If we want to detect carbon–carbon correlations, why do we not just use the normal COSY sequence? Well, the reason is that it does not suppress the ^{12}C–^{13}C isotopomers to a sufficient extent, and therefore we will only be able to observe the diagonal peak from the ^{12}C–^{13}C species and not the cross peaks from the ^{13}C–^{13}C isotopomers.

17.4.8 *J*-Resolved NMR Experiments

One of the first 2D NMR experiments that was developed was the *J*-resolved NMR experiment. In the *J*-resolved experiment scalar couplings are displayed along F1 and the chemical shifts along F2. This in principle is a good experiment to extract scalar couplings in cases where the 1D spectra are crowded and multiplets overlap such that the couplings cannot be extracted easily from the 1D spectrum directly. The *J*-resolved spectrum displays the multiplets in a tilted way, and therefore a so-

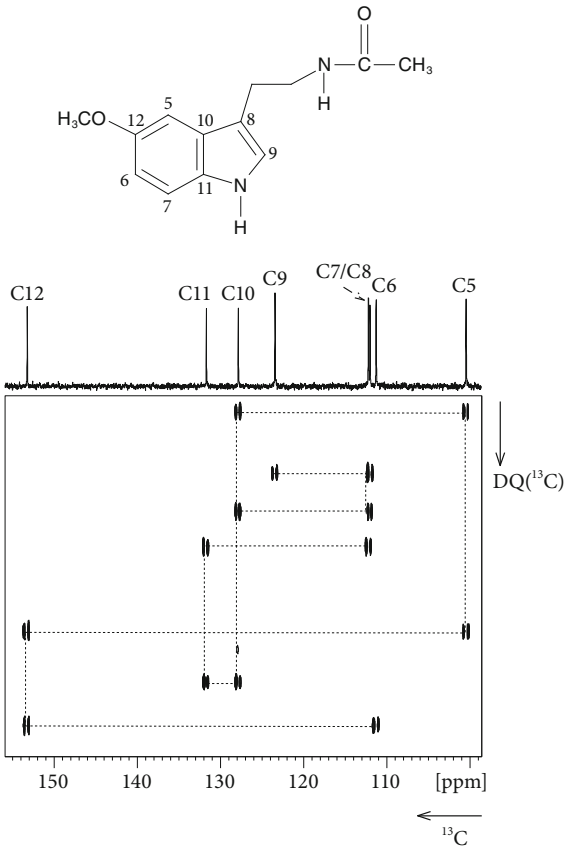

Figure 17.14 INADEQUATE spectrum of melatonin, and the chemical structure and the assignment.

called tilt procedure is required to rotate them so that the multiplets are really orthogonal to F2 (see Figure 17.15). Maybe you realize that projecting all peaks onto the F2 axis will result in a proton-decoupled proton spectrum, something that is

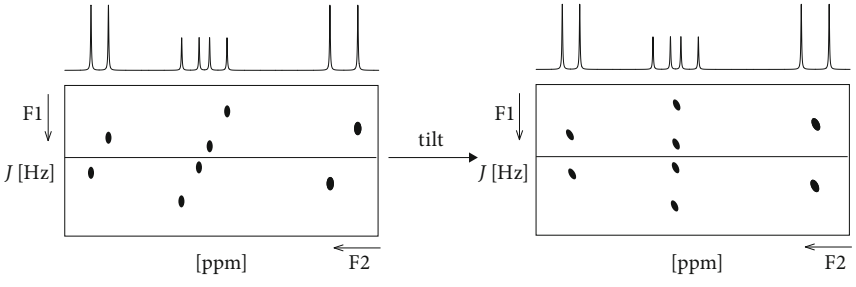

Figure 17.15 Schematic representation of a *J*-resolved spectrum, and the tilt procedure applied to it.

very difficult to obtain otherwise. Because of the much improved resolution of decoupled proton spectra, this seems highly desirable, and much work has been done on this. Unfortunately, *J*-resolved spectra contain many artifacts, strong coupling being a particular severe problem. In fact, the projections contain many spurious additional peaks, and poor baselines and line shapes. Nevertheless, for certain compounds, such as steroids, *J*-resolved spectra allow one to extract coupling constants from highly overlapped spectra, and the extracted couplings are very useful for establishing stereochemistry.

17.5 Three-Dimensional NMR Spectroscopy

Three-dimensional NMR spectroscopy is a logical extension of 2D NMR spectroscopy, and requires the introduction of a second evolution time into the experiments. Technically, two 2D experiments are concatenated. The excitation element of the second experiment is removed, and the two evolution times are incremented independently. Because two evolution periods are incremented independently, a lot of FIDs are recorded, a few thousand in general. The resolution in each domain is even less than in 2D NMR spectroscopy to keep the data matrices at a size that can still be handled by computers quickly and to save experiment time. Many experiments record only approximately 40 increments in one of the indirect dimensions. Still, 3D experiments usually run for at least one day at realistic sample concentrations.

Homonuclear 3D NMR sperectroscopy is hampered by many signals that do not contain interesting information, and is not used a lot. Heteronuclear 3D spectra, such as ^{13}C-resolved NOESY spectra or triple-resonance spectra for protein resonance assignments, are very helpful. However, these experiments require isotopically enriched compounds, for example, ^{13}C-labeled proteins for a ^{13}C-resolved NOESY experiment. Although we perform many 3D NMR experiments for proteins in our laboratory, we feel that these experiments are not really useful for small molecules and also not required generally. Hence, we will not describe these experiments in more detail, and instead we direct the interested reader to monographs on protein NMR spectroscopy or reviews on that topic.

17.6 Practical Aspects of Measuring 2D Spectra

17.6.1 Frequency Discrimination in the Indirect Dimension: Quadrature Detection

As we have seen, a 2D experiment is performed as a series of 1D experiments in which a specific delay (t_1) is systematically incremented from experiment to experiment. The modulation of the signal intensity provides us with the frequency in the

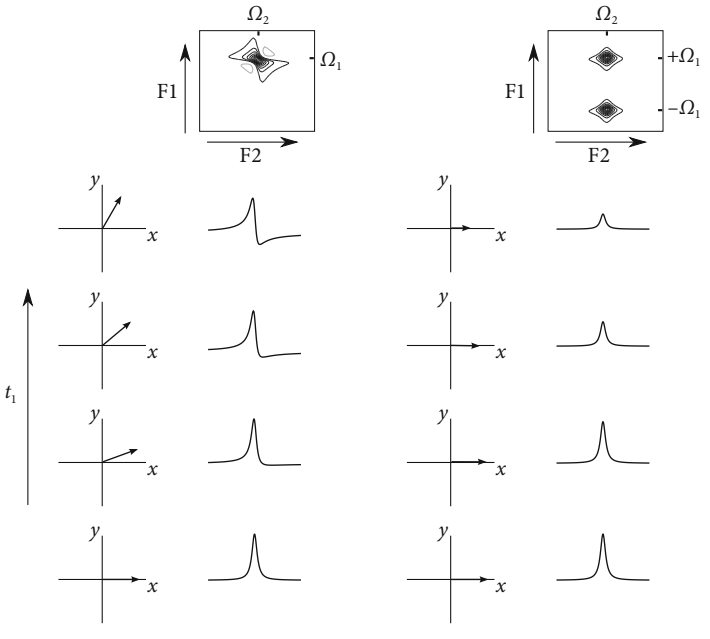

Figure 17.16 Phase (a) versus amplitude (b) modulation. The vector diagrams depict the magnetization in the *xy* plane at the beginning of acquisition of the individual 1D spectra as a function of t_1 evolution. The corresponding signals obtained after the Fourier transform in F2 are shown to the right. The corresponding 2D spectra after the Fourier transform in F1 are depicted at the top.

indirect dimension. The signal can be modulated in two different ways, by either phase modulation or amplitude modulation. We call a signal *phase modulated* when it is the phase of the magnetization that varies in successive t_1 increments. This is depicted in Figure 17.16a. In contrast, a signal is said to be *amplitude modulated* when it is the amount of *xy* magnetization that varies in successive t_1 increments while the phase remains constant, as depicted in Figure 17.16b. Accordingly, it is the amplitude of the signal that is modulated in the individual 1D spectra. Whether phase-modulated or amplitude-modulated data are obtained depends on the type of experiment.

The 2D spectra obtained after the Fourier transform in both dimensions are shown at the top in Figure 17.16, both having shortcomings. The phase-modulated data result in a signal that exhibits a mixture of double absorptive and double dispersive line shapes, the so-called *phase-twist line shape*. Such a line shape is highly undesirable since the dispersive contribution introduces broad wings. The amplitude-modulated data result in the desired double absorptive line shape, however we obtain two signals and therefore it lacks frequency discrimination. To achieve frequency discrimination with the desired absorptive line shape, we have to distinguish between phase-modulated and amplitude-modulated experiments. For

amplitude-modulated data we usually use the States, TPPI, or States-TPPI methods, and for phase-modulated data we usually use the echo/antiecho method.

Excursus 17.2: Amplitude Modulation

The 90° pulses preceding the evolution time t_1 in 2D NMR experiments will simultaneously create both positive and negative single-quantum coherences. These evolve at the positive or negative frequency $\pm\Omega_A$ and (in the rotating frame) correspond to two vectors that rotate at the same frequency but in the opposite sense. The chemical shift evolution for these two coherences can be described as

$$S(t) = \exp(i\Omega_A t_1) + \exp(-i\Omega_A t_1) \tag{17.6}$$

which according to the Euler formula $e^{i\Omega_A t} = \cos(\Omega_A t) + i\sin(\Omega_A t)$ yields

$$S(t) = 2\cos(\Omega_A t_1) \tag{17.7}$$

Note that each of the two terms on the right of (17.6) represent phase-modulated signals, but the *sum* of both is purely amplitude modulated! Equation 17.6 describes two vectors rotating in opposite sense. A well-known analogy is circularly polarized light. If you just use left *or* right circularly polarized light, the electromagnetic field vector rotates in one sense. If you superimpose left-handed and right-handed circularly polarized light, you obtain linearly polarized light that only oscillates in one plane, and hence is only amplitude modulated.

The trick to obtain pure phases for most spectra therefore is to retain both the positive and the negative coherences to obtain the amplitude-modulated signal. As demonstrated in Figure 17.16b, this procedure unfortunately results in peaks at $\pm\Omega_A$. In the following section we will therefore introduce different methods to achieve frequency discrimination *and* pure phases. As we will see, the echo/antiecho method samples the two coherences separately, but recombines them later appropriately. If only one of the two pathways is recorded, signals cannot be phased to absorption any longer and an alternative way of processing, called absolute value, must be used.

17.6.1.1 States, TPPI, and States-TPPI Methods

As we saw in Section 11.3.2, frequency discrimination in the *direct* dimension can be achieved by simultaneously recording the x component and the y component of the magnetization to obtain a complex time domain signal of which one part is cosine modulated and the other sine modulated. This scheme can also be extended to the *indirect* dimension of 2D experiments. With regard to Figure 17.16b, the signal is purely cosine modulated in F1, resulting in two signals centered at $\pm\Omega_A$. However, we can modify the pulse sequence to obtain a sine-modulated signal. Usually this is achieved by changing the phase of one specific RF pulse, the so-called quadrature pulse, by 90° (see Figure 17.17). The Fourier transform of a sine-

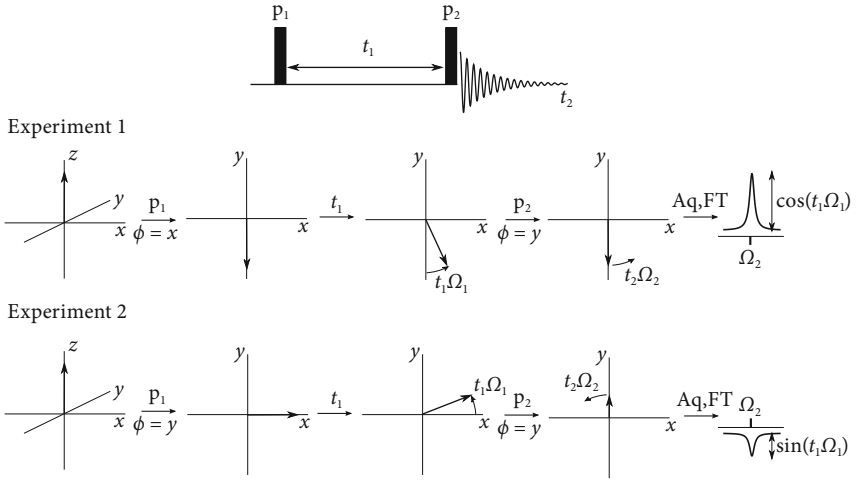

Figure 17.17 The States principle for quadrature detection. Depending on whether the first pulse of the COSY pulse sequence (shown at the top) is of phase *x* or *y*, the amplitude of the signal after the Fourier transform in F2 is cosine modulated or sine modulated.

modulated signal also results in two signals centered at $\pm\Omega_A$ but having opposite intensity. Combining the cosine- and sine-modulated data will cancel the wrong frequency such that the final spectrum shows only the signal of correct frequency. In practice, the pulse sequence is repeated for each t_1 increment twice, once with the unmodified sequence and once with the 90°-shifted RF pulse, and the FIDs are stored separately, whereby one FID is considered to be the imaginary component, resulting in a hypercomplex data matrix (complex in F2 and F1). This sampling scheme is referred to as the *States* or *hypercomplex* method originally proposed by States, Haberkorn, and Ruben.

Another method is *TPPI*. This method is closely related to the sequential sampling scheme discussed in Section 11.3.2. In that scheme frequency discrimination is achieved by causing an apparent frequency shift of SW/2 such that all resonances have the same sign. For the indirect dimension this is achieved by incrementing the phase of the quadrature pulse by 90° for each successive t_1 increment. Note, in contrast to the States method discussed above, only one FID is recorded for each increment. However, since the sampling rate in the TPPI method must be twice as fast as when using the States method, and therefore twice as many t_1 increments must be measured to obtain a specific resolution, the total experiment time for both methods is the same.

The advantage of the TPPI method over the States method is that *axial peaks* are shifted to the *edge* of the spectrum. Axial peaks are spectral artifacts originating from longitudinal relaxation during the shift evolution time t_1. Magnetization that has relaxed during t_1 is re-excited by the final 90° pulse. This magnetization is not amplitude modulated and hence behaves like on-resonant magnetization and therefore the axial peaks will appear in the *center* of the spectrum when using States

Table 17.1 Quadrature detection schemes: phase cycle and increments in the States, time-proportional phase incrementation (TPPI), and States-TPPI methods. Note that the increment Δt_1 is $\frac{1}{SW}$ for the States and States-TPPI methods, and is $\frac{1}{2SW}$ for the TPPI method.

States			TPPI			States-TPPI		
t_1 increment	ϕ_1	ϕ_{rec}	t_1 increment	ϕ_1	ϕ_{rec}	t_1 increment	ϕ_1	ϕ_{rec}
$1\Delta t_1$	x	y	$1\Delta t_1$	x	y	$1\Delta t_1$	x	y
$1\Delta t_1$	y	y	$2\Delta t_1$	y	y	$1\Delta t_1$	y	y
$2\Delta t_1$	x	y	$3\Delta t_1$	$-x$	y	$2\Delta t_1$	$-x$	$-y$
$2\Delta t_1$	y	y	$4\Delta t_1$	$-y$	y	$2\Delta t_1$	$-y$	$-y$
$3\Delta t_1$	x	y	$5\Delta t_1$	x	y	$3\Delta t_1$	x	y
$3\Delta t_1$	y	y	$6\Delta t_1$	y	y	$3\Delta t_1$	y	y

quadrature detection. This is undesirable since they may overlap with signals of interest. We can shift the axial peaks to the edge by using a modified variant of the States scheme, the so-called States-TPPI method. Therein, we exploit the fact that TPPI shifts the whole spectrum by SW/2. Accordingly, frequencies from the center such as the axial peaks are moved to one edge, where they do not interfere with genuine peaks any longer. In the *States-TPPI* method, the phases of the quadrature pulse and the receiver phase are inverted in every second t_1 increment (see Table 17.1). As both phases are inverted in concert, the amplitudes of the desired signals are unchanged. However, magnetization that relaxes during t_1 (giving rise to axial peaks) will alternate because it does not experience the 180° phase shift of the quadrature pulse. Therefore, its signal amplitude is inverted with each new t_1 increment, resulting in an apparent frequency of SW/2. Consequently the axial peaks are shifted to the edge of the spectrum. The phase cycling schemes employed in the States, TPPI, and States-TPPI methods are summarized in Table 17.1.

The working principles of the three methods are summarized in Figure 17.18.

17.6.1.2 Echo/Antiecho Method

As we have seen before, we can obtain correct frequencies from phase-modulated 2D data (Figure 17.16) which, however, unfortunately display the highly undesirable phase-twist line shape. However, even then we can obtain pure absorption line shapes when combining two sets of phase-modulated data. In Figure 17.16a, the phase of the magnetization prior to acquisition in F2 is modulated by $+\Omega_1$. However, most often we can also record a spectrum in which the phase is modulated by $-\Omega_1$. As shown in Figure 17.19, taking the sum of these two data sets yields pure cosine-modulated data, whereas taking the difference yields pure sine-modulated data. Similar to the States method, these two new data sets can be combined to give a spectrum with pure absorption line shapes after the Fourier transform in F1.

The signal of which phase is modulated by $+\Omega_A$ is usually called the *P-type* ("P" for "positive") or *antiecho* signal, the other, modulated by $-\Omega_A$, is called the *N-type* ("N" for negative) or *echo* signal. Whether the echo or the antiecho is ob-

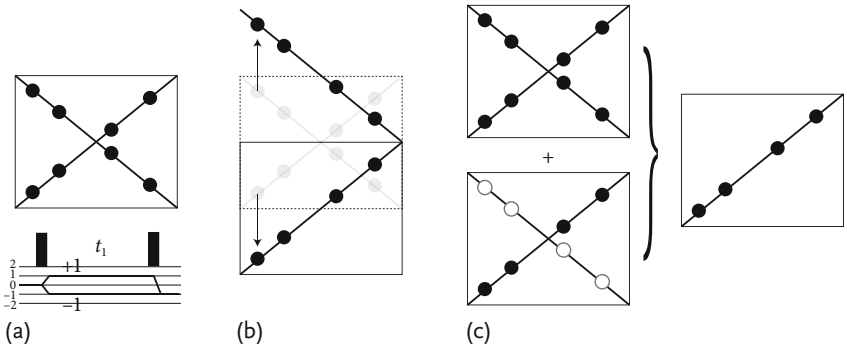

Figure 17.18 Methods for obtaining quadrature detection. Retaining both positive and negative coherences results in absorptive line shapes but with peaks at both positive and negative frequencies (a). In the time-proportional phase incrementation (TPPI) method, positive and negative frequencies are shifted by SW/2 in opposite directions (b). In the States method, sine- and cosine-modulated signals are combined (c).

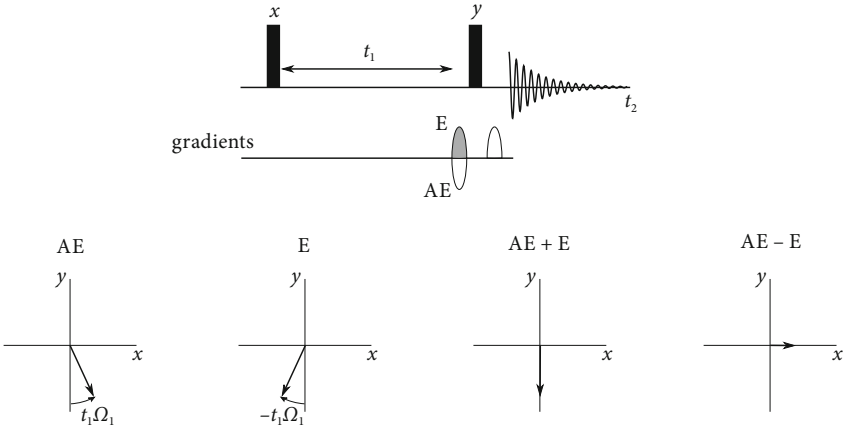

Figure 17.19 Recording phase-sensitive spectra by the echo (E)/antiecho (AE) method. Depending on whether the gradients are of the same or opposite polarity, the magnetization rephases on a different axis and thereby seems to rotate with Ω_A (AE) or $-\Omega_A$ (E) during t_1. Combining these two experiments results in cosine-modulated data (AE + E) or sine-modulated data (AE − E), from which we can obtain the desired absorptive line shape spectra.

tained is usually selected by setting the polarity of a gradient pulse. Note, in the echo/antiecho detection scheme the axial peaks are completely removed since any recovered z magnetization is completely dephased by the second gradient pulse and only magnetization that was dephased by the first gradient pulse becomes rephased by the second gradient pulse.

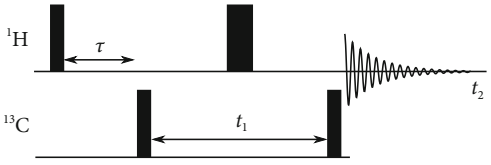

Figure 17.20 Pulse sequence of the phase-insensitive HMBC experiment.

17.6.1.3 Absolute Value (Magnitude) Spectra

In some experiments it is not possible to obtain pure absorption line shapes for all signals. A prominent example is the HMBC experiment. Its pulse sequence is depicted in Figure 17.20.

The HMBC experiment presents a long-range proton carbon correlation. How this experiment works exactly is explained in detail in Section 13.6. We would like to focus here on one particular feature of this experiment: The central 180° pulse on the proton channel refocuses chemical shift evolution only during t_1. The signal phases at the beginning of data acquisition (at the start of the FID) are not coaligned due to the chemical shift evolution during τ and due to the development of homonuclear proton–proton couplings during the experiment. Processing the HMBC data in a conventional way will result in a spectrum displaying broad dispersive wings and complicated signal patterns consisting of positive and negative contributions. A simple way to improve the appearance is to present such spectra in magnitude mode. As discussed in Section 11.4.5 for magnitude calculation, the absolute values of the real and the imaginary part are combined to result in pure positive signals.

An advantage of presenting spectra in magnitude mode is that no phase correction must be applied. A disadvantage of magnitude spectra is the increased line width and that any information presented by the sign of the signal will be lost (e.g., multiplet patterns in double-quantum-filtred COSY or NOESY cross peaks). Because of that, for high-resolution work phase-sensitive spectra are usually preferred. For processing magnitude-mode spectra, usually window functions are used that remove the dispersive wings at the expense of reduced sensitivity. Sine-bell window functions are functions that are often employed for that purpose.

17.6.2 Folding in 2D Spectra

Nowadays the States-TPPI method is generally the preferred quadrature detection method for indirect dimensions in multidimensional NMR experiments. We have seen that the location of axial peaks is more convenient compared with States spectra. But why do we not use the TPPI method in general? The answer is that folded signals do not cause so much trouble in States spectra, in fact they are often folded on purpose to keep the spectral width small, this time without loss of intensity since there is nothing like an audio filter that would attenuate them. To remind you, folded signals in complex acquisition schemes are folded about the *distant*

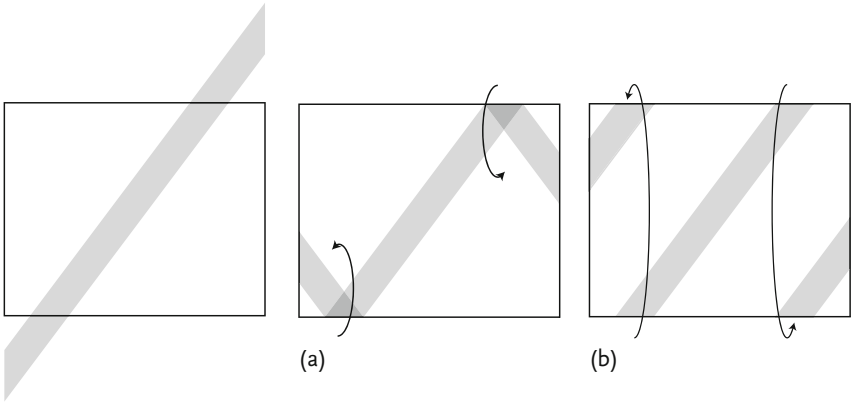

Figure 17.21 Folding in 2D spectra. (a) depicts folding in real (TPPI), (b) in complex (States, States-TPPI) spectra.

edge, while in sequential (real) schemes they are folded about the *near* edge (see Figure 17.21).

Many heteronuclear spectra such as proton–carbon correlations display a pseudo-diagonal-like shape: shielded protons are correlated to shielded carbons and deshielded protons to deshielded carbons. If we fold signals about the distant edge, as done in the States-TPPI method, the folded signals are placed into empty regions of the spectrum where they are much less likely to overlap with other (non-folded) peaks. In protein NMR experiments, the carbon range is about 70 ppm, which can be reduced to 25 ppm by folding the low-field and high-field peaks. This is of particular interest in 3D NMR experiments, where we record only a few increments, so that resolution is inherently low.

17.6.3
Resolution in the Two Frequency Domains

Resolution in 2D data sets is inherently lower than in 1D spectra. The reasons for this are that (i) the size of the data matrices would be too large to handle them (remember a 2D data set consist of hundreds of FIDs!) and that (ii) because for each additional data point in the F1 dimension another FID must be measured, the experiment time linearly increases with the resolution in F1. Fortunately, the requirements for resolution in 2D spectra are much less because peaks are dispersed in a plane. In 1D spectra we are interested in extracting coupling constants, and therefore the resolution should be a fraction of a hertz. In 2D spectra we are mostly interested in recognizing where the center of the peak is. Let us be a bit more specific. Suppose we have two signals that are multiplets, and their chemical shift differs by 10 Hz. In proton NMR spectra that means that the corresponding multiplets are overlapped to a large extent. To be able to resolve these two signals, our resolution must be better than 10 Hz. The resolution is approximately defined as the spectral width (in hertz) divided by the number of data points (for a more

thorough discussion on this, see Section 11.4.1). If our spectral width is 10 ppm on a 600 MHz instrument, the spectral width is 6000 Hz. To resolve 10 Hz we must record approximately 600 data points. In the direct dimension this is not a problem, usually more than 1024 data points are taken. In the indirect dimension we would need to record 600 increments, and this is already a lot. As we saw in Section 11.4.2, computationally the number of data points can be extended by using *linear prediction*. In general, the resolution in F2 is much higher than that in F1.

Recording more data points increases the resolution, however only to a certain extent. When we double the number of data points, we automatically double the acquisition time. At some point the acquisition time will exceed the transverse relaxation time and hence we will only record noise in the last data points. The acquisition time has to be adjusted to T2. For small molecules with sharp lines more data points can be recorded than for macromolecules (such as proteins) with their broad lines.

17.6.4 Sensitivity of 2D NMR Experiments

The sensitivity of 2D NMR experiments is inherently reduced by a factor of $\sqrt{2}$ when compared with a 1D NMR experiment. The reason for this is that the mixing pulse depending on the phase of the pulse can transfer only the x or y component, and hence part of the signal is lost. A mixture of phases will always occur due to the chemical shift modulation of the signals during the evolution time.

For the beginner it is sometimes difficult to estimate how many scans are required to have a sufficient signal-to-noise ratio for the cross peaks. We wish to remind the reader that the number of scans is related to the phase cycle, and hence must often be a multiple of 4, 8, or 16, depending on the experiment. Inspection of the first FID allows us to get a feeling of how much signal we can expect. However, it is important to realize that all FIDs sum up for the cross peaks, and good spectra are often obtained even when the signal-to-noise ratio in the first trace is poor. In almost all experiments the signal is reduced in later FIDs due to transverse relaxation during t_1, with the exception of the so-called constant-time experiments. How strong the reduction of signal due to transverse relaxation really is depends on T2 and hence will increase with size. Another important point to keep in mind is that for most homonuclear experiments a lot of the signal actually goes into the noninformative diagonal peaks. In contrast, in heteronuclear experiments, for example, in a [^{13}C,^{1} H] HSQC experiment, all signal will add up for the cross peaks. In our experience for small to medium-sized molecules good spectra are obtained as long as the signal is visible in the first FID (even if the signal-to-noise ratio is only 2). We wish to add that some experiments, for example, the often used double-quantum-filtered COSY experiment, do not display any signal in the first FID. Depending on the phases, it can also be that the first FID has no signal but the second does. So better look at FIDs up to number 10 or later.

17.6.5 Setting Up 2D Experiments

For most 2D experiments the most important parameters are the spectral widths and the number of scans. As discussed in Section 17.6.3, the resolution in 2D experiments is inherently lower than in the corresponding 1D experiments. Increasing the resolution in the indirect dimension comes at the expense of recording more increments. Doubling the resolution in the indirect dimension will double the measuring time!

The spectral width in the direct dimension (in F2) is usually chosen to be 10–20% larger than actually required to exclude the edges of the spectrum, which often display slight baseline problems. The number of data points in that direction is usually between 1024 and 4096 depending on the desired resolution and the transverse relaxation times. Typical acquisition times will range between approximately 50 and 500 ms. The number of increments in F1 very much depends on the desired resolution and the transverse relaxation time T2. Note that in a [^{13}C,^{1}H] HSQC experiment (a proton–carbon correlation) it is the ^{13}C nucleus that is shift labeled during t_1, and hence it will be the T2 times of the ^{13}C nuclei that influence the choice of the number of t_1 increments! It is not always required to record spectra with high resolution if signals are well separated. Some experiments such as the homonuclear COSY experiment display cross peaks with an antiphase multiplet pattern (see Figure 17.2). When the resolution is low in F1, the positive and negative components tend to cancel each other and cross peaks will completely disappear! Such spectra should always be recorded with high resolution.

The number of scans of course has a direct influence on the measuring time. Its choice depends on the phase cycle (see Section 13.9.1). For the NMR novice, it is a bit difficult to read phase cycles, and a 16-step phase cycle does not necessarily require the use of 16 scans. Often pulse programs contain descriptions in which the minimum number of scans is indicated to help set up the experiment. It is important to use multiples of the minimum number of steps in the phase cycle. If this is, for example, 8, experiments may be recorded with 8, 16, 24, or 32 scans but not with 12 scans. If you used 12 scans, a number of artifacts might appear in spectra that will not be there with 8 scans.

Given a certain amount of available measuring time, is it better to record spectra with more scans or more increments? The answer is not so easy: it depends on the relaxation properties. There is no point in recording 512 increments if the T2 times are so short that after half of the increments the FIDs do not contain any more signal! In addition, linear-prediction methods can often help a lot to increase resolution, but the FIDs must contain a sufficient amount of signals so that these methods work stably. When highly concentrated samples are used (as is often the case when synthetic compounds are measured), the number of scans needs only correspond to the minimum phase cycle.

A good setup of the spectrometer is important for acquiring high-quality 2D spectra: good shims, a stable lock, and temperature. For 2D experiments proper tuning and matching of the probe is essential! If the probe is not tuned and matched

properly, a 90° pulse may in fact not be a 90° pulse but rather a 60° pulse, and the spectra will be full of artifacts or the signal-to-noise ratio will be much lower. Mismatched probes are the most often encountered source of errors when experiments fail to deliver the expected results! At least the length of the proton 90° pulse should be determined on the sample (it takes not much more than 1 min!). Remember that a series of 2D experiments can easily run for 12 h or more, and therefore it is reasonable to invest a few minutes in a perfect spectrometer setup!

Finally, some experiments require a special parameter such as the length of the mixing time in NOESY experiments, or the magnitude of couplings in heteronuclear correlation experiments. We will discuss these parameters when we describe the experiments in more detail. In general, it is best practice to start from parameter sets that have been taken from the manufacturer's library or created by trained personnel. These parameter sets contain reasonable settings for the acquisition but also for processing and plotting of the spectra and will help in minimizing errors at the beginning!

17.6.6 Processing 2D Spectra

Proper processing of 2D spectra can dramatically improve the appearance of spectra. The complete procedure comprises (i) choosing the correct window functions for manipulating the FID prior to the Fourier transform, (ii) setting parameters for linear prediction and the Fourier transform, (iii) 2D Fourier transform, (iv) phase correction in F1 and F2, and (v) baseline correction in F1 and F2.

FIDs from 2D experiments have usually not decayed completely because the number of data points is limited. As discussed in Section 11.4.3, we will need to multiply the FID by a function that decays to zero to force the last data points to become zero. The most frequently used window function for that purpose is the sine-bell function. The nonshifted sine-bell function is zero at the beginning, and will lead to undesired line shapes. For most cases, a 90°-shifted sine-bell function (or a cosine window function) will do the job best. If resolution enhancement is desired, a 70°-shifted instead of a 90°-shifted sine-bell function can be used. For a few experiments in which the signal at the beginning of the FID is zero (e.g., the DQF-COSY experiments) a function that is close to zero at the beginning will actually help increase the signal-to-noise ratio. We store these settings in the experiment-specific parameter sets, and usually do not vary them much.

Selecting parameters for the linear prediction basically amounts to setting the number of coefficients in the linear-prediction routine (see Section 11.4.2).

Phasing of 2D spectra can be tricky for the beginner. It may be particularly difficult because the phase is usually incorrect in both dimensions. To phase spectra, we recommend the following procedure. Extract a row with a (strong) signal at the right edge of the spectrum. To this add a row with a (strong) signal at the left, and phase the corresponding 1D trace. This will give you the zero- and first-order phase correction in F2. Now, apply this to the 2D spectrum. After that only phase errors in F1 should remain. Apply the same procedure but extract columns instead of rows now. After the phasing in F1, the 2D spectrum should be correctly phased. Begin-

ners often have problems because of the phase errors in both dimensions. If you have problems with finding the correct values for the phase correction, set the values manually to zero, and start again. The first-order phase correction should never be much greater than 180°, otherwise you will introduce severe baseline problems!

Baseline correction is crucial in experiments in which the cross peaks of interest are weak (e.g., NOESY experiments), or when using solvent suppression schemes. Weak cross peaks may easily escape detection when the baseline is poor. In spectra from experiments performed with water suppression, it is best to perform the baseline correction twice: once from the left edge of the spectrum to the solvent line, and then from the solvent line to the right edge of the spectrum. Baseline correction in 2D spectra usually uses automatic (noninteractive) routines.

17.7 Problems

17.1. 2D NMR pulse experiments consist of four different building blocks. Specify the names of the four blocks in the correct order.

17.2. How do you determine the spectral width in the indirect dimension?

17.3. How do you determine the resolution in the indirect dimension?

17.4. Suppose you want to double the resolution in the indirect dimension. How will the total measuring time change?

17.5. The following COSY spectrum displays a mixture of butylbromide and butanal. Determine which signals belong to the bromide and which to the aldehyde.

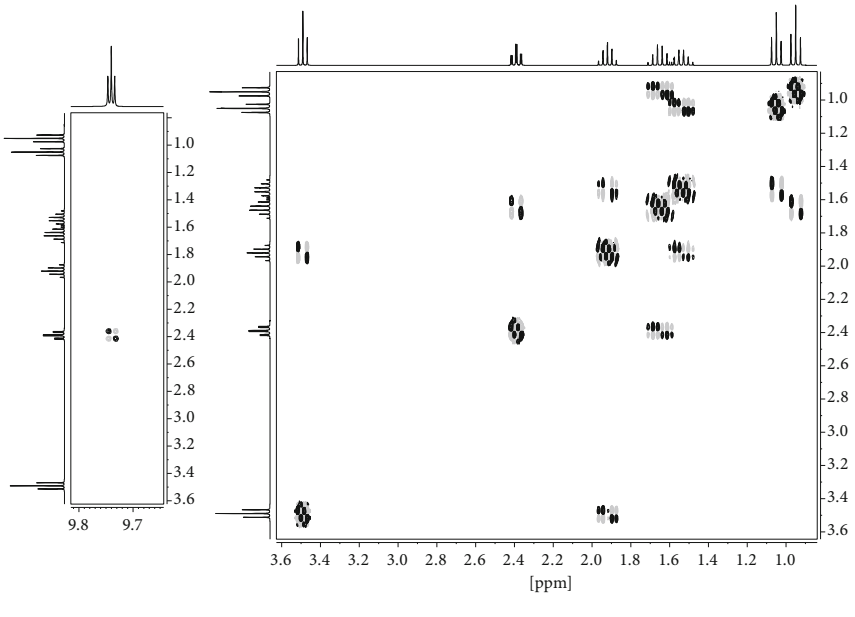

17.6. Which 2D NMR experiments do you generally need to get all ^{13}C chemical shifts of a compound?

17.7. Arrange the following 2D NMR experiments in order of decreasing sensitivity: [^{1}H,^{1}H]-COSY, [^{13}C,^{13}C]-INADEQUATE, [^{13}C,^{1}H]-HSQC, [^{13}C,^{1}H]-HMBC

17.8. Describe the difference between active and passive couplings. How do you extract them from 2D COSY spectra?

17.9. Explain the terms t_1 noise and axial peaks.

17.10. In 2D NMR experiments we are often forced to use a multiple of a certain number of scans per t_1 increments (e.g., 8 or 16 but not 9 scans). What is the reason for that?

17.11. For experts only: Why do the first increments of double-quantum filtered COSY spectra contain little or no signal?

18
Solid-State NMR Experiments

18.1
Introduction

In solid-state NMR experiments samples are usually powders of compounds, and small cylindrical containers called *rotors* are filled with these powders. In special applications samples can also be oriented between glass plates, but most of the time samples are measured as *powders* that often contain *microcrystals*. As we will see in a moment, a number of additional interactions are present in the solid state, and therefore line widths are much larger and the resolution is accordingly much reduced. So why should we use solid-state NMR experiments? The answer is that such experiments are very useful in cases where solubility is poor, an often encountered situation for polymers or inorganic materials. Another reason for doing such experiments is to learn about particular properties of a compound in the solid state, a question often relevant in materials science.

Spectra recorded in solution display dispersion due to the chemical shift, and line splittings due to scalar couplings. The effects of dipolar coupling (see Section 7.2.3) and chemical shift anisotropy (CSA; see Section 7.1.1.3) may contribute to the line width of the signal, but cannot be extracted from the spectra directly because rapid tumbling of the molecules in solution completely averages those interactions, at least for small molecules. In the solid, no tumbling occurs, and hence the effects from dipolar couplings or CSA will be present in the spectra. A powder contains molecules in a statistical distribution of orientations, and therefore all orientations relative to the magnetic field are present to an equal extent. Dipolar couplings are on the order of many tens of kilohertz, and the CSA can also cover hundreds of parts per million. A summary of the relevant values for the proton, carbon, and nitrogen is presented in Table 18.1.

A 20 kHz dipolar coupling corresponds roughly to 400 ppm on the ^{15}N shift scale for a 500 MHz spectrometer. Therefore, these interactions may cover a range comparable to the total chemical shift range, and this is even true for a single site in a molecule that in solution is defined by a sharp line (a few hertz)! Powder spectra, therefore, are extremely broad and, in principle, rich in information. However, the

Applied NMR Spectroscopy for Chemists and Life Scientists, First Edition. Oliver Zerbe and Simon Jurt.
©2014 WILEY-VCH Verlag GmbH & Co. KGaA. Published 2014 by WILEY-VCH Verlag GmbH & Co. KGaA.

Table 18.1 Typical magnitude of interactions in the solid state in biological applications.

Interaction	Nuclei	Typical magnitude
Chemical shift range	^{1}H	$\sim$ 15 ppm
	^{13}C	$\sim$ 220 ppm
	^{15}N	$\sim$ 200 ppm
Chemical shift anisotropy	^{1}H	$<$ 10 ppm
	^{13}C	$<$ 140 ppm
	^{15}N	$<$ 200 ppm
Anisotropy of one-bond dipolar coupling	^{1}H–^{13}C	$\sim$ 22 kHz
	^{1}H–^{15}N	$\sim$ 20 kHz
	^{13}C–^{13}C	$\sim$ 4.5 kHz
	^{13}C–^{15}N	$\sim$ 2 kHz
	^{15}N–^{15}N	$<$ 1 kHz
^{1}J scalar coupling	^{1}H–^{13}C	120–160 Hz
	^{1}H–^{15}N	$\sim$ 90 Hz
	^{13}C–^{13}C	30–60 Hz
	^{13}C–^{15}N	$\sim$ 15 Hz

resolution is not sufficient to extract the information in the absence of selective labeling.

Fortunately these interactions can be removed experimentally to some extent. Solid-state NMR spectroscopy has undergone very rapid development in the last 20 years, and some of the 2D spectra recorded on favorable samples look not so different from the corresponding solution spectra.

18.2 The Chemical Shift in the Solid State

If we recall what we learned in Section 7.1.3, the chemical shift tensor is a mathematical instrument that rotates a vector describing the direction and magnitude of the external field into another vector that denotes the direction and magnitude of the *effective* field:

$$\boldsymbol{B}_{\text{eff}} = (1-\sigma)\cdot\boldsymbol{B_0} = \begin{bmatrix} 0 \\ 0 \\ B_0 \end{bmatrix} - \begin{bmatrix} \sigma_{xx} & \sigma_{xy} & \sigma_{xz} \\ \sigma_{yx} & \sigma_{yy} & \sigma_{yz} \\ \sigma_{zx} & \sigma_{zy} & \sigma_{zz} \end{bmatrix} \begin{bmatrix} 0 \\ 0 \\ B_0 \end{bmatrix} \tag{18.1}$$

The chemical shift tensor σ is a second-rank tensor that can be described by a 3×3 matrix. In the principal axis system (PAS) it consists of three diagonal elements, the principal components σ_{xx}, σ_{yy} and σ_{zz}. The trace of this tensor (the average of the diagonal elements) is called the isotropic chemical shielding σ_{iso}, and the *anisotropy* $\Delta\sigma$ and the *asymmetry* η report on distortions from perfect octahedral

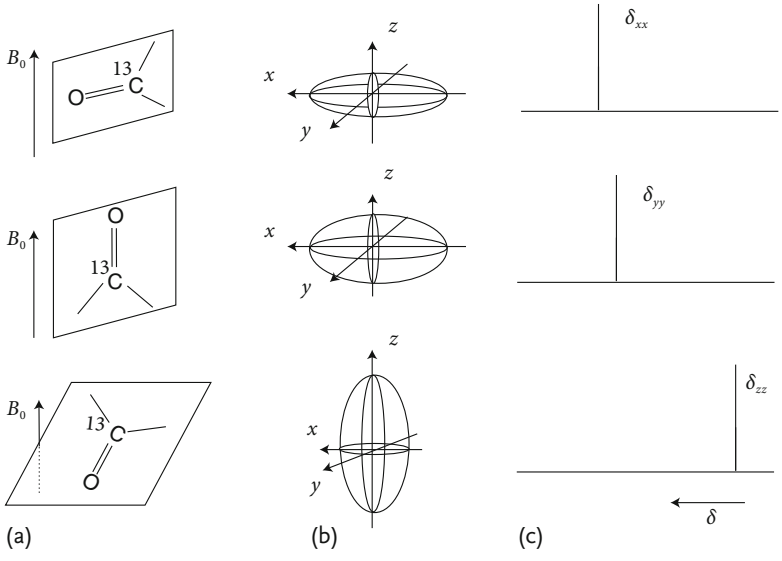

Figure 18.1 Chemical shift tensor for a carbonyl ^{13}C nucleus. The CO moiety is shown in (a) in three different orientations, and for each orientation the chemical shift anisotropy tensor is depicted in (b). The corresponding signal in the spectrum is depicted in (c).

symmetry of the tensor (for a more detailed definition of these, see Section 7.1.3). The coordinate system is usually chosen such that $\sigma_{zz} > \sigma_{yy} > \sigma_{xx}$; the term $\sigma_{xx} - \sigma_{yy}$ is also called the *rhombicity* of the tensor, and defines the difference in shielding in the x and y directions. The *axiality* denotes the difference of the shielding in the z direction from the average shielding in the transverse plane. The direction of the largest shielding by definition is along z.

The chemical shift tensor can be visualized as a rotation ellipsoid with the three principals denoting the values of σ_{xx}, σ_{yy}, and σ_{zz}. Let us try to put this into a well-known context and look at the chemical shift tensor of a carbonyl ^{13}C nucleus. The shielding is largest in the direction of the π orbital, which has been formed from the p_z orbital of the carbon and oxygen atoms. By definition, we call the chemical shift along the direction of the largest shielding δ_{zz} (see Figure 18.1) and the chemical shift in the two orthogonal directions δ_{xx} and δ_{yy}. In the orientation depicted at the bottom of Figure 18.1c, the p_z orbital points in the direction of the static field, and shielding is therefore largest. Accordingly, the frequency (or the chemical shift) in the spectrum is lowest.

In a powder all orientations are possible and, due to the very large number of molecules, all orientations will occur with the same probability.

Figure 18.2 shows typical powder patters for signals depending on specific values of the anisotropy and asymmetry. For asymmetric environments the signal is largest in the center. The higher the symmetry is, the more the location of the largest intensity moves to one edge of the line.

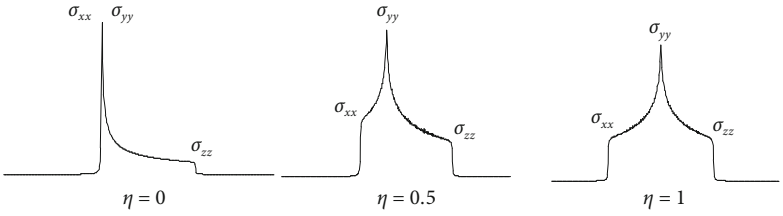

Figure 18.2 Powder patterns of signals of spin-1/2 nuclei in solid-state NMR spectra for nuclei with values of the anisotropy larger than 0. For negative values of the anisotropy the patterns would be similar but mirrored about a vertical axis through the center of the signal (e.g., for the example on the left, the strongest intensity would occur on the right-hand side of the signal).

18.3 Dipolar Couplings in the Solid State

As described in Section 7.2.3, the magnitude of the dipolar coupling depends on the distance between the two interacting nuclei, the angle θ the connecting vector makes to the external field, and the gyromagnetic ratios of the two nuclei involved (Figure 18.3).

In contrast to the situation in solution, in the solid state the angle θ does not change with time because the molecules do not tumble, and the dipolar coupling interaction is not averaged to zero but takes rather large values on the order of tens of kilohertz. Typical values are depicted in Table 18.1. The magnitude of the

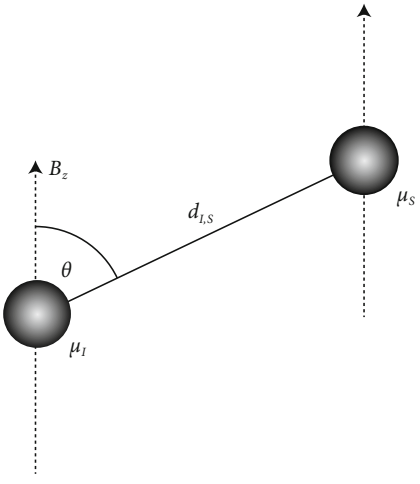

Figure 18.3 Definition of the dipolar coupling between two spins *I* and *S*.

dipolar coupling scales with γ of the two nuclei and therefore is largest for dipolar couplings involving protons.[1)]

Formally, the dipolar interaction between two spins I and S is described by the following Hamiltonian:

$$H_d \sim d^{-3} \cdot (3\cos^2\theta - 1) \cdot I_z S_z \tag{18.2}$$

Therein, the term in parentheses following the distance dependence denotes the spatial component, while the other term characterizes the so-called spin part. In principle, we could try to average both of these to zero to remove the dipolar interaction. We will see in the following two sections that both methods are used!

18.4 Removing CSA and Dipolar Couplings: Magic-Angle Spinning

In solution rapid overall tumbling of the molecule averages the $(3\cos^2\theta - 1)$ term to zero. In the solid state rapid rotation of the sample at an angle of approximately 54.7° causes the first term in (18.2) to approach zero. This particular value of θ is called the magic angle, and hence the technique is referred to as *magic-angle spinning* (*MAS*). A rotor, a cylindrical container with an outer diameter between approximately 0.8 and 7 mm, with sample volumes between 2 µl (1.3 mm rotor) and approximately 400 µl (7 mm rotor), is filled with the powder sample. Inside the magnet the rotor is tilted to the magic angle, and then spun at a few tens of kilohertz pneumatically. The maximum rotor frequency depends on its diameter, and is usually between 10 and 70 kHz. The spectra recorded under MAS conditions display dramatic line narrowing:

Unfortunately, so-called spinning sidebands at multiples of the spinning frequency remain in the spectra. These are most prominent at low spinning frequencies. To avoid problems in data interpretation due to spinning sidebands, MAS spectra are recorded at the highest possible spinning frequencies, at which signals due to the first spinning sidebands are outside the region of interest, and occur with relatively low intensities. Alternatively, spectra may be recorded at different spinning rates. The signal at the true chemical shift will remain at the same frequency, whereas the spinning sidebands change their location (see Figure 18.4).

Rapid rotation significantly heats the sample and must be compensated by lowering the temperature of the air around the sample.

MAS removes effects from dipolar coupling and, very importantly, also from CSA. However, it leaves scalar couplings, and the effects from heteronuclear (but not homonuclear) couplings can be eliminated by decoupling. Nevertheless ^{13}C MAS NMR spectra for favorable samples (natural abundance ^{13}C) at first glance

1) Similarly to the CSA tensor, the tensor describing dipole–dipole interactions is a *traceless* second-order tensor. Rapid rotation will therefore average both CSA and dipole–dipole interactions to zero.

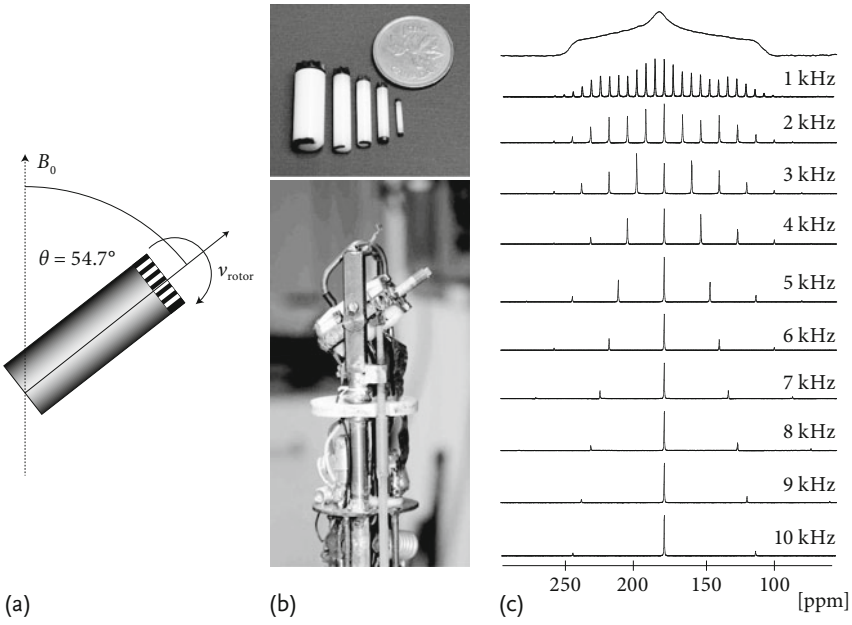

Figure 18.4 Magic-angle spinning (MAS) spectroscopy. (a) Orientation of the rotor relative to the magnetic field, (b) pictures of various rotors in the range between 1.3 and 7 mm (the coin size is 19 mm; top) and a MAS probehead (bottom), and (c) spectra that were recorded with MAS using various rotor spinning speeds.

look like high-resolution spectra and clearly allow one to extract chemical shifts of unique sites. A comparison of solid-state ^{1}H and ^{13}C NMR spectra is depicted in Figure 18.5.

Obviously, powder spectra for large molecules are featureless spectra with very broad lines. The resolution is much improved under MAS conditions. Additional narrowing of carbon lines occurs when the protons are decoupled. Interestingly, while individual lines start to become resolved in the carbon NMR spectra, proton NMR spectra even under MAS conditions display very broad lines. In fact, most experiments use ^{13}C instead of ^{1}H detection for that reason.

18.5
Reintroducing Dipolar Couplings under MAS Conditions

Distance measurements are performed by exploiting effects from the dipolar coupling, both in solution and in the solid-state. However, when we use MAS techniques, we remove the effects from dipolar coupling, and accordingly will not be able to use them for distance measurements. An apparent solution to this problem is to turn spinning on only during data acquisition, but this is technically impos-

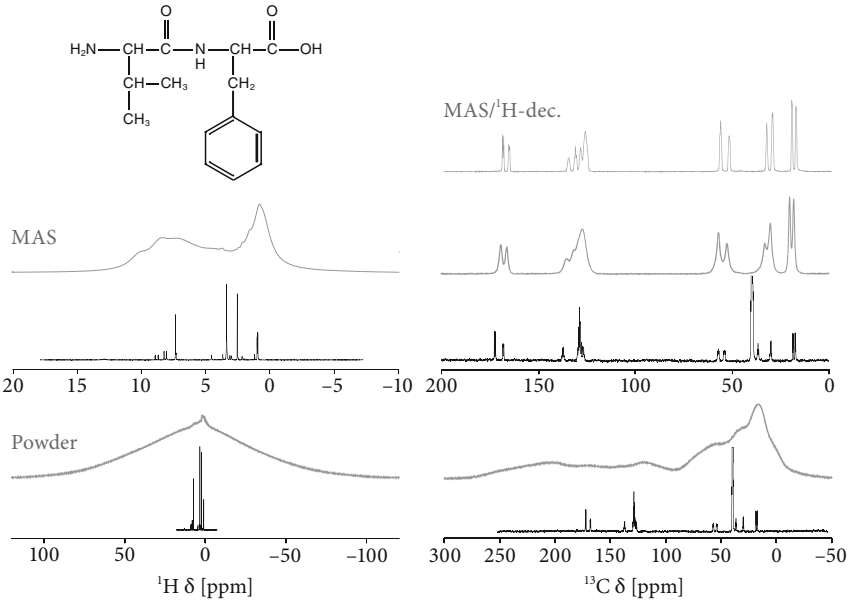

Figure 18.5 Comparison of solid-state spectra. Solid-state ^{1}H and ^{13}C NMR spectra of the Val-Phe dipeptide (top left) are depicted. Solid-state spectra are shown in gray lines and solution-state spectra are shown in black lines. Powder spectra (bottom) as well as spectra recorded under MAS (center) or MAS with proton decoupling (top right) are presented. Note that the region depicted for the powder spectra is wider to cover the extremely broad lines.

sible, since we would need to stop or start rotation in a fraction of a millisecond.[2)] A solution to this problem was the ingenious idea of applying *rotor-synchronized RF pulses*. The technique has been dubbed *rotational-echo double-resonance NMR (REDOR)*.

Since RF pulses can be turned on and off within a fraction of a microsecond, this is a convenient way to reintroduce such interactions during the experiment. Instead of turning on and off the rotor, MAS conditions are maintained throughout the experiment, and rotor-synchronized pulses are applied whenever dipolar interactions are required during the pulse sequence. The important idea behind the REDOR experiment is that if the spin and the spatial component of the dipolar interaction Hamiltonian are flipped simultaneously (the spatial part through the MAS rotation, the spin component by applying a 180° pulse whenever the sample has rotated by 180°), part of the dipolar interaction is reintroduced (see Figure 18.6).

2) In principle the rotation angle θ can be altered rapidly so that averaging is less complete. This can be done within a few milliseconds.

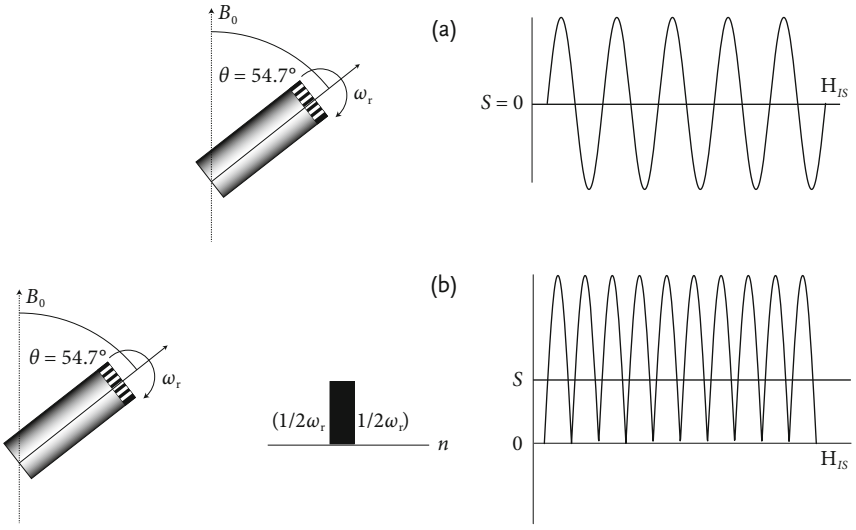

Figure 18.6 Reintroducing orientation-dependent interactions through rotor-synchronized pulses. The averaged effect of MAS on an orientation-dependent signal is demonstrated in (a), the same signal under MAS but when a 180° pulse is additionally applied after each half-rotation of the rotor is depicted in (b). The line at position *S* corresponds to the value of the averaged signal. Reproduced with permission from Zerbe, O. (Ed.) BioNMR in Drug Research, Chapter 11.

18.5.1
An Alternative to Rotor-Synchronized RF Pulses: Rotational Resonance

Solid-state NMR spectroscopists observed that when the sample spinning rate is adjusted to a frequency corresponding to the resonance frequency difference between two spins a and b (their zero-quantum frequency) the peaks broadened, indicating that the dipolar interaction was reintroduced. This phenomenon is called *rotational resonance*:

$$n\omega_{\mathrm{rot}} = \omega_{\mathrm{a}} - \omega_{\mathrm{b}} \tag{18.3}$$

Additionally, a rapid oscillatory exchange of Zeeman magnetization occurs. To monitor the exchange of magnetization, one of the two spins is selectively inverted and the oscillatory exchange of magnetization at the other spin is monitored over time.

We now have most of the tools to create solid-state NMR experiments. Before we can start building our own experiment we, however, need to take care of the inherent insensitivity of ^{13}C NMR.

18.6
Polarization Transfer in the Solid State: Cross-Polarization

Solid-state proton NMR spectra even under conditions of MAS are characterized by broad lines. Moreover, the chemical shift range is comparably small, the resolution is low, and hence these experiments are rarely performed. In fact, ^{13}C or ^{15}N NMR spectra are much better resolved, but these nuclei are less sensitive due to the lower γ of the heteronuclei and their low natural abundance. As in solution NMR experiments, polarization transfer methods are used in solid-state NMR experiments to increase the signal intensity. The standard technique for achieving signal enhancements for heteronuclei in solution is insensitive nuclei enhancement by polarization transfer (INEPT) (see Section 12.9), in which proton polarization is transferred to the heteronuclei via the one-bond scalar coupling. In solid-state NMR experiments, *heteronuclear cross-polarization* (*CP*) is used instead. The transfer mechanism uses *heteronuclear Hartmann–Hahn matching* and the large dipolar coupling.

In heteronuclear CP elements, pulse trains are simultaneously applied on both the proton and the carbon (or nitrogen) channel. Hartmann–Hahn matching of static samples requires that the precession frequencies of all nuclei are approximately the same ($|\omega_I| \approx |\omega_S|$) (Figure 18.7). In the case of sample spinning under MAS conditions, additional conditions with

$$|\omega_I| = |\omega_S| + n \cdot \omega_r \tag{18.4}$$

in which ω_r denotes the rotor frequency and $n = \pm 1, 2$, allow recoupling (but the bandwidth at the spinning sidebands is reduced).

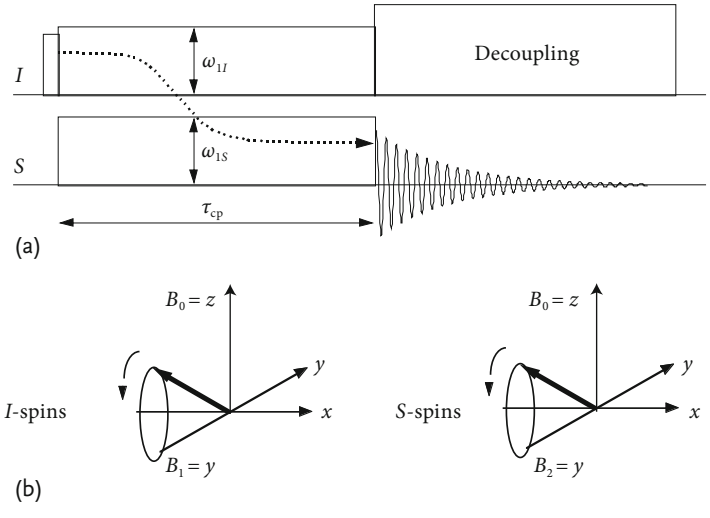

Figure 18.7 Heteronuclear cross-polarization NMR (a). Immediately following the 90° *x* pulse on the *I* channel, spin-locking fields of the same strength are applied to both the *I* and the *S* spins (b).

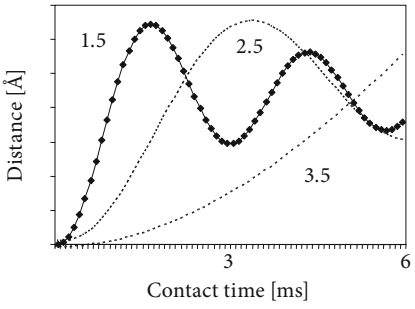

Figure 18.8 Buildup curve as determined by heteronuclear cross-polarization MAS. Theoretical curves are depicted for three different distances.

This is achieved by locking proton and X nuclei with RF fields of similar strength (see Figure 18.7). Technically speaking, that means you need to adjust the power levels on both channels such that the X signal is of maximum strength. This is a bit unusual since we are usually used to determining the length of pulses at a certain power level instead of adjusting power levels to achieve a certain pulse duration. When Hartman–Hahn matching conditions are achieved, the *strong coupling case* applies for all spins and magnetization can (more or less) flow freely. The length of the mixing time τ_{cp}, the so-called *contact time*, is often adjusted to the large dipolar couplings in the system and is 1–5 ms (Figure 18.8).

In solution-state NMR experiments the amount of polarization transfer depends on how well the length of the spin-echo period matches the scalar coupling. In an analogous fashion, the *S*-spin magnetization can be measured for a larger number of contact times, and the fit of measured signal intensity to the analytical function allows one to extract the magnitude of the dipolar coupling, which is related to the distance between the two nuclei (see (18.2)). An example for such an experiment is presented in Excursus 18.1.

Excursus 18.1: A Solid-State NMR Experiment to Measure Distances

We have now introduced all elements that we need to build a solid-state NMR experiment for measuring distances. Clearly, we will need MAS to narrow lines so that we can distinguish resonances. And we also need to introduce CP elements to shuffle magnetization between nuclei of different types. Another important difference from solution-state NMR techniques is that rarely proton spectra are recorded because proton lines despite MAS as still too broad, and therefore in most cases either ^{13}C or ^{15}N magnetization is detected.

The following sequence (Figure 18.9) is designed to measure carbon–nitrogen distances using the REDOR method. Following an initial polarization transfer from a proton to carbon, a dephasing element is introduced during which rotor-synchronized nitrogen 180° pulses are applied. In this period the dipolar nitrogen–carbon coupling is reintroduced and the ^{13}C signal is therefore dephased.

A series of measurements with different lengths of the dephasing period are performed and the measured change in signal intensity is fitted to theoretical curves.

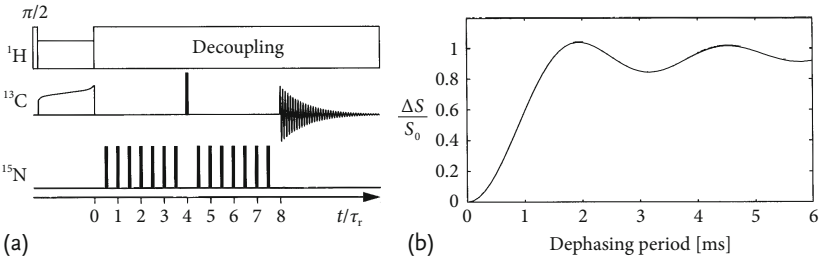

Figure 18.9 Experimental scheme for measuring carbon–nitrogen distances (a), the dephasing of the signal (change in signal intensity versus length of dephasing period) (b). The experiment was originally proposed by Guillion and Schaeffer (1989), J. Magn. Reson., 81, 196. Reproduced with permission from Zerbe, O. (Ed.) BioNMR in Drug Research, Chapter 11.

18.7 Technical Aspects of Solid-State NMR Experiments

The theory of solid-state NMR techniques is more complicated than that for solution techniques, and we have only described it very briefly. The experiment itself of course is an NMR experiment, and can be run on a standard high-resolution magnet. However, the hardware, both the electronics and the probes, need to be adapted to run solid experiments. In principle, the pulses required for solid-state NMR experiments are shorter and hence amplifiers capable of delivering more power are required due to the large values of the dipolar couplings compared with the isotropic *J* couplings. Moreover, a pneumatic unit for MAS is needed. The probes are very different since measurements are done in rotors (except for measurements on oriented sample, which we have not described here), and the probes must also be able to handle much more power. For all these reasons, special hardware is required, and a significant amount of money must be spent to upgrade a console from solution to solid-state applications.

Sample quality is *very* important. The isotropic chemical shift is highly sensitive to the environment, and therefore highly homogeneous samples are required. Otherwise, signals will be additionally broadened by different values of the isotropic shift. Semicrystalline material usually results in much improved spectra. The preparation of protein samples for solid-state NMR experiments is an art on its own. Recently, experiments performed at low spinning speeds (high-resolution MAS) have gained some attention. An example of an application is small peptides from solid-phase peptide synthesis that under favorable conditions can be mea-

sured while still coupled to the resin when using moderate (below 5 kHz) spinning rates. These techniques can also be used for samples that contain material that is not dissolved properly.

18.8 Problems

18.1. Which *additional* interactions become visible in solid-state NMR spectra compared to solution data?

18.2. How do you get rid of those interactions?

18.3. Describe the basic features of powder patterns.

18.4. Describe recoupling techniques in simple words.

18.5. Which SS-NMR techniques can be used to determine distances?

18.6. Describe the difference between polarization transfer techniques in solution and in solid-state NMR.

Further Reading

Duer, M. (2004) *Introduction to Solid-State NMR*, Blackwell Publishing.

Apperley, D.C., Harris, R.K., and Hodgkinson, A.H. (2012) *Solid-State NMR Basic Principles and Practice*, Momentum Press.

Laws, D.D., Bitter, H.-M.L., and Jerschow, A. (2002) Solid-state NMR spectroscopic methods in chemistry. *Angew. Chem. Int. Ed.*, **41**, 3096.

19
Detection of Intermolecular Interactions

19.1
Introduction

So far, we have mostly discussed how NMR experiments can be used to elucidate the chemical structure of a certain compound. But we are often interested in knowing whether two molecules interact with each other. The archetypical example is the interaction of small molecules such as drugs with protein targets. Pharmaceutical companies have made great efforts to detect such interactions using NMR experiments. While there are a number of techniques available to probe for such interactions, NMR experiments have the advantage of being capable of detecting interactions even when they are very weak. Since we need only two components, the drug and the receptor, false-positive results are limited, in contrast to assays that work in a complicated biological matrix. Drawbacks are the comparably low sensitivity of the NMR experiment and that it is inherently a low-throughput method, which requires high amounts of target and test compounds of good solubility.

When investigating interactions between a small molecule, the ligand, and a large molecule, the receptor, we can in principle monitor changes in NMR properties of the ligand or the receptor. The former methods are referred to as *ligand-observe* methods, while the latter are called *target-observe* methods. Ligand-observe methods have the advantage that we do not need to label the receptor. Since the receptor is often a protein or another molecule that is more difficult to make, it is also an advantage that we need small quantities of the receptor in these experiments. Usually, although not always, data analysis is easier because the spectra of the ligand are much simpler. However, only target-observe methods will reveal the site of ligand binding, and they are also less prone to artifacts.

The are a number of parameters that change when two molecules interact. The chemical shift may be different, because the environment changes or a hydrogen bond is formed. This method is called *chemical shift perturbation* or *chemical shift mapping*. Secondly, the transverse relaxation time, directly related to the line width, may change (dramatically). Thirdly, the diffusion rate may be altered. Both transverse relaxation times and diffusion rates change significantly only when the

Applied NMR Spectroscopy for Chemists and Life Scientists, First Edition. Oliver Zerbe and Simon Jurt.
©2014 WILEY-VCH Verlag GmbH & Co. KGaA. Published 2014 by WILEY-VCH Verlag GmbH & Co. KGaA.

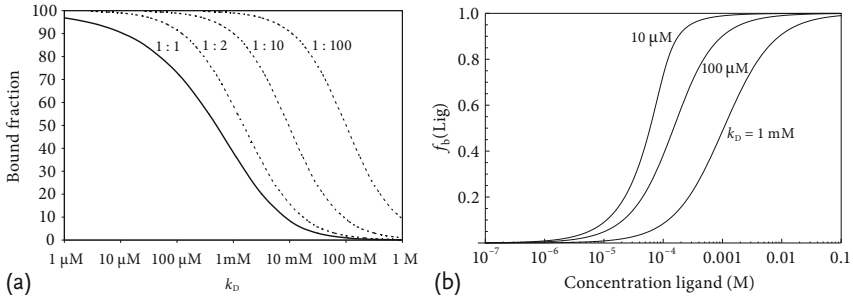

Figure 19.1 Bound fraction. (a) Fraction of complex formed, assuming that the concentration of one partner is 1 mM. Different curves are shown for various relative stoichiometries. (b) Fraction of bound target for various values of the k_D. The concentration of the target is 100 µM. Note the logarithmic scale on the *x* axis in both graphs.

molecular weight difference between the two molecules is large.[1)] Finally, provided that the lifetime of the complex is sufficiently long (the dissociation constant is sufficiently small), we can directly detect intermolecular nuclear Overhauser effects (NOEs). We will briefly discuss these methods in this short chapter.

We wish to mention here that the extent by which the complex between a ligand L and a receptor R is formed depends on the dissociation constant of the complex (19.1):

$$k_D = \frac{[L][R]}{[LR]} = \frac{([L_{tot}] - [LR])([R_{tot}] - [LR])}{[LR]} \tag{19.1}$$

where $[L_{tot}]$ and $[R_{tot}]$ denote the total concentrations of the ligand and receptor, and $[L]$, $[R]$, and $[LR]$ denote the concentrations of free ligand, free receptor, and the complex, respectively. This is illustrated in Figure 19.1. For a very strong binder (k_D in the nanomolar range or even better), the binding site is essentially saturated with 1 equiv of ligand. In contrast, for weaker binders more equivalents are required. For a very weak binder with k_D of 1 mM, only approximately 38% of the complex is formed with 1 equiv of ligand, whereas 90% is formed for k_D of 10 µM.

Often, although not always, one of the two interacting molecules is much larger. A classic example is drugs binding to protein targets. Some of the methods that are described below look at the small molecule, and are referred to as *ligand-observe* methods. Other methods detect changes on the receptor, and these methods are called *target-observe* methods. We will see that both ligand-observe and target-observe techniques are capable of detecting interactions, but they differ widely in what type of information they provide. For example, target-observe techniques often allow one to additionally establish the binding site. We will in the following therefore always indicate to which of the two categories the particular method belongs.

1) Due to chemical exchange broadening, the line width may also increase in cases where the difference in the molecular weight is not large.

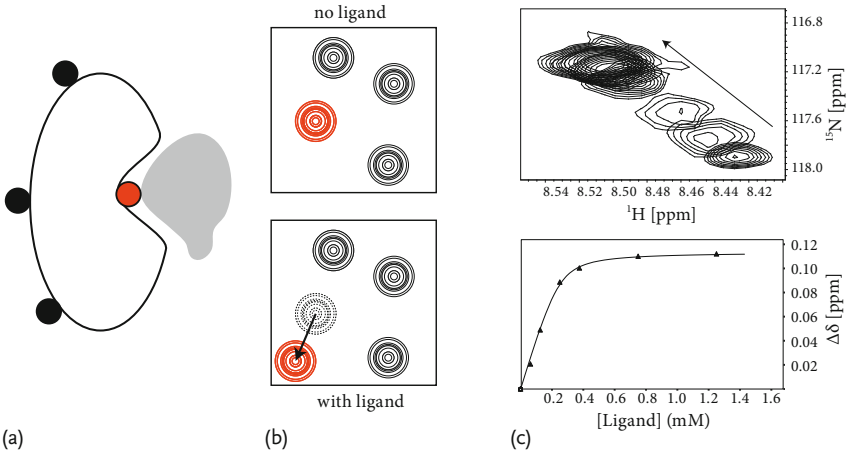

Figure 19.2 Chemical shift mapping. Upon interaction of the two molecules, an amide proton highlighted by the red circle shifts because its environment changes (a). Accordingly, the peak corresponding to the atom involved will shift in the 2D spectrum (b). Peaks due to other moieties (black spheres) that are not involved in binding will not move. A cross-peak from an [^{15}N,^{1}H] heteronuclear single-quantum coherence spectrum upon titration of a binder is depicted at the top in (c), and the bottom in (c) shows the fit of the proton chemical shift to the concentration of the binder.

19.2 Chemical Shift Perturbation

The method is particularly simple, and for that reason it is used a lot. You mix two compounds and monitor whether the chemical shifts of one of the two compounds (or both) change. You can try to either observe ligand resonances (ligand-observe methods) or receptor resonances (target-observe methods). Since the receptor is often a large macromolecule, the problem with target-observe methods is to recognize a few chemical shift changes in the presence of a lot of other signals in the spectrum. It is easiest if the receptor is isotope labeled, for example, ^{13}C or ^{15}N labeled. Then you can just record a proton–carbon or proton–nitrogen correlation map, which will only display signals from the receptor, and the good signal dispersion in the 2D spectrum allows you to spot shifting signals quickly (see Figure 19.2). In ligand-observe techniques you apply a short T2 filter (a spin lock) to suppress the broad receptor signals. However, as we will see later, instead of monitoring chemical shift changes of ligands, it is more convenient to monitor changes in line widths of the signals.

A particular form of chemical shift perturbation occur when a molecule displays concentration-dependent oligomerization. Chemical shifts at low concentration will then be different from those at high concentrations. If you suspect that your molecule is aggregated, you can dilute it and see whether the resonance position(s) changes!

Almost all interactions in complexes have a limited lifetime. When the lifetime is short, the system is in rapid exchange, and the chemical shifts will represent the population-weighted average. When the lifetime is much longer, the system is in slow exchange, and possibly two sets of signals can occur, one belonging to a particular moiety in the complex, the other one to its free form. This phenomenon is explained in much more detail in Chapter 16. For the moment let us assume our system is in rapid exchange. When we titrate one component into the other, affected resonances will shift until saturation occurs. Analytically, the observed chemical shift δ_{ave} when titrating a ligand L into a solution of a receptor R can be expressed as

$$\delta_{ave} = \delta_f + (\delta_b - \delta_f) \times \left(\frac{[L_0] + [R_0] + k_D - \sqrt{([L_0] + [R_0] + k_D)^2 - 4[L_0] \cdot [R_0]}}{2[R_0]} \right) \quad (19.2)$$

in which δ_f and δ_b refer to the chemical shifts of free and bound species, $[L_0]$ and $[R_0]$ refer to the total concentrations of ligand and protein, and k_D refers to the dissociation constant of the complex. The curves correspond to typical binding isotherms, and the fit of measured chemical shifts to the theoretical curve allows one to extract the dissociation constant.

The most important point is to make sure that nothing changes in the sample when you titrate in the second molecule. In particular, acidic groups often change the pH (even in buffered systems!) and that will almost always alter resonance positions. Of course, the measuring temperature, solvent composition, buffer, and so on must be *exactly* the same. An advantage of chemical shift mapping is that when resonances have been assigned, the location of binding can also be deduced.

One important point to note is that the concentration at which these experiments are performed matters! In order to determine k_D for a complex, it is important to chose a good concentration. To measure a proper binding curve we need to have as many data around the inflection point of the curve (this is the concentration at which 50% of the complex is formed). If we have a binder with k_D of 1 μM, we need to obtain data around that concentration! This is a very low concentration, and likely we will not be able to get decent spectra. If k_D is 1 mM, we need to measure in that range. We can certainly acquire decent spectra in the 100 μM to 5 mM range (a problem may be solubility at higher concentrations). You may realize that determining k_D by NMR experiments is more of a method for weak than really good binders! In any case, we need large quantities when compared with fluorescence-based readouts or other biophysical methods such as surface plasmon resonance.

19.3 Methods Based on Changes in Transverse Relaxation (Ligand-Observe Methods)

When two small molecules of molecular weight of 500 interact tightly with each other, they will form a complex with a molecular weight of 1000. This will not

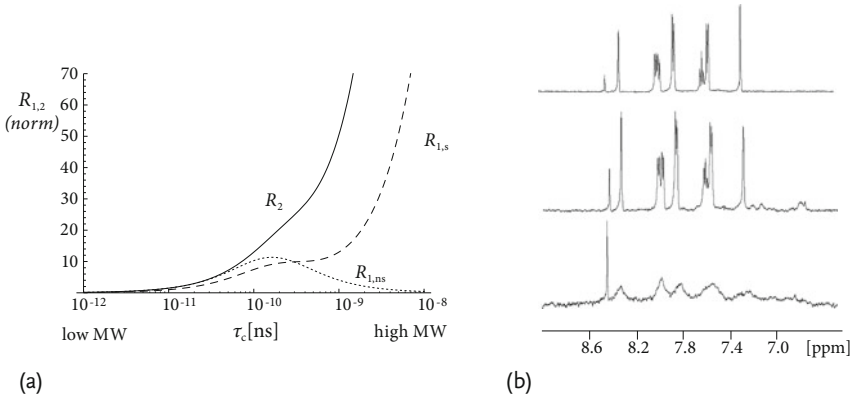

Figure 19.3 Dependence of R_1, R_2, or selective R_1 time (a). The relaxation rates are normalized for the distance *r*. (b) Proton spectrum of a small organic compound in the absence (top) or presence of a non-binding (center) or binding protein (bottom). The asterisk (*) corresponds to a non-binding impurity.

really result in a noticeable change in the transverse relaxation time, and hence the line width may remain the same. In contrast, when a small molecule interacts with a protein, its tumbling properties will change dramatically(see also Section 14.4). In drug screening, proton spectra of mixtures of small molecules are recorded, resulting in spectra with many but narrow lines. Then the protein target is added, and the spectrum is recorded again. If one of the small molecules in the mix binds to the protein, its line(s) will become much broader or completely disappear (Figure 19.3). The advantage of this method is that no labeling is required, and that protein consumption is reduced by a factor of more than 10.

In principle, changes will occur for both the longitudinal and the transverse relaxation time. However, the changes in T2 (respectively R_2) are much larger and more predictable than the changes in T1. As a rule of thumb (see Chapter 14), T2 times will decrease with increasing molecular weight, and if the binding partner is a macromolecule, the additional line broadening is very strong, to the extent that signals may completely disappear from the spectrum!

For molecules in rapid exchange with the target, there is a substantial contribution from exchange broadening to the line width (Figure 19.4).

It can be easily seen from Figure 19.4 that additional exchange contribution can easily outweigh the increase in line width due to the increase in molecular weight of the complex. The additional contribution to line broadening is

$$R_2^{\text{ex}} = (\delta_b - \delta_f)^2 \frac{f_f^2 f_b}{k_{\text{off}}} \tag{19.3}$$

where k_{off} is the off rate of the complex, and f_f and f_b are the fractions of the bound form and the free form.

To detect line broadening you can use the rotating-frame NOE spectroscopy (ROESY) experiment with a short spin-lock period. During the spin lock, $T_{1\rho}$ (very similar to T2) decay occurs, and signals with increased transverse relaxation times

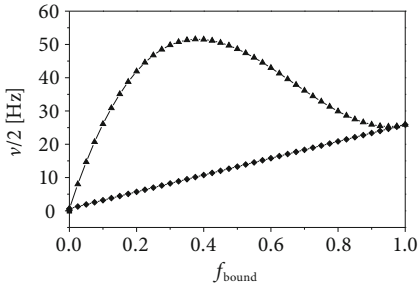

Figure 19.4 Exchange broadening. Dependence of the line width of a signal on the fraction bound, both in absence (diamonds) and in the presence (triangles) of exchange.

are strongly attenuated. Comparing data recorded in the presence and absence of a large molecular weight receptor reveals dramatic differences in the residual signals in the spin-lock experiment.

19.4 Methods Based on Changes in Cross-Relaxation (NOEs) (Ligand-Observe or Target-Observe Methods)

The most obvious and reliable approach to detect binding of one molecule to another is to measure *intermolecular* NOEs. The direct measurement of intermolecular NOEs may be hampered by two complications. Firstly, if the binding affinity is too low, the lifetime of the bound species may be too short for significant NOE buildup, even if the distances involved are short. In our experience, it is difficult to measure intermolecular NOEs if the complex is in fast exchange on the NMR timescale; in other words, if the binding constant is in the micromolar range or higher. Even if binding is tight and in the slow exchange regime, it may be that the experiment does not work for two reasons. There may be simply too many signals in the NOE spectroscopy (NOESY) spectrum (too many *intramolecular* NOEs), which may obscure the few *intermolecular* NOEs. In these cases often one of the two molecules is isotope labeled (^{13}C or ^{15}N) and so-called isotope-edited/isotope-filtered NOESY spectra are recorded (see Figure 19.5).

In these experiments only those NOEs are retained in which one proton is bound to ^{13}C and the other is *not* bound to ^{13}C. When only one of the two molecules is ^{13}C labeled, the experiment will automatically select for *intermolecular* NOEs. Another complication may be that one of the two molecules is so large that the line widths in the complex become too broad to be observed. When the two molecules are sufficiently small and so the lines do not display too much overlap, a standard NOESY experiment may be sufficient. Because measuring intermolecular NOEs requires assignments, it is not a high-throughput method, and serves to establish the nature of the complex rather than to detect binding!

When binding is weak (fast exchange regime) another set of methods can be used, in which the buildup of the intermolecular NOE is monitored on one of

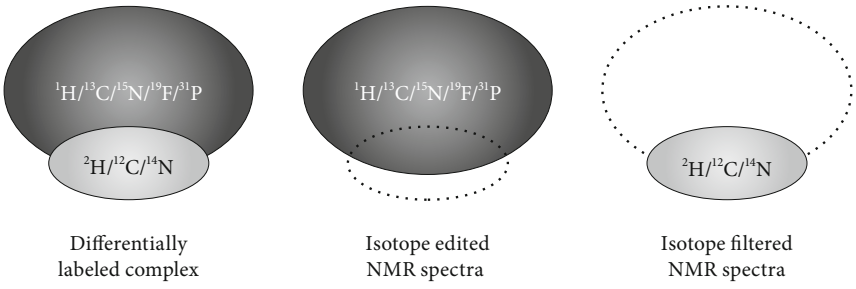

Figure 19.5 Isotope-filtered/isotope-edited spectra. Samples for isotope-filtered/edited experiments. In the isotope-edited spectra, only resonances from the labeled moiety remain, whereas in the isotope-filtered spectra, only the nonlabeled part is visible.

the two binding partners. In the *transferred NOE* experiment, a NOESY spectrum is recorded twice, once in the absence and once in the presence of the potential binding partner. A significant change in the NOESY spectrum indicates binding. If possible, the conditions should be chosen such that *no* intramolecular NOEs are observed for the low molecular weight binding partner. This can often be accomplished by careful choice of the temperature to select for a range close to the zero crossing of the NOE (see Section 15.2.1). When the binding partner is added, the molecular weight of the complex (even if it is only transiently formed) is large enough for effective NOE buildup. In the transferred NOE experiments, high affinity is undesired, because the off rate is then too small. It works best when the dissociation constant is in the micromolar range. This is the case when we are in the fast exchange regime. As we will see below, the experiment requires detection in the *free* state, but reveals NOEs that have built up in the bound state.

In these experiments, typically one molecule is large (e.g., a protein or an oligosaccharide). The small molecule is added in 10–100-fold excess. Its proton signals will dominate the spectrum for the reason that the small molecule is present in much higher concentration, and because its lines are much sharper. Because of fast exchange, bound small molecules will rapidly exchange with nonbound ones, so the NOE will spread over the whole population of small molecules. But because the NOE buildup in the free ligand is close to zero or slow, it will mostly occur when the ligand is bound. The NOESY spectrum will therefore display NOEs of the bound species mostly. The high molecular weight receptor does display intermolecular NOEs, but because its concentration is so low (possibly 1/100 of the ligand concentration) and because its lines are so broad, these signals do not contribute to the NOESY spectrum significantly. This is one of the few NMR experiments that work better the larger the receptor is! The NOESY experiment hence reports on the conformation of the bound ligand, and because the molecule is not too large, the spectra can usually be interpreted rapidly. We need to emphasize that transferred NOE spectra do not report on the intermolecular contacts, the experiment simply confirms if the ligand binds, and what its conformation in the receptor-bound state is.

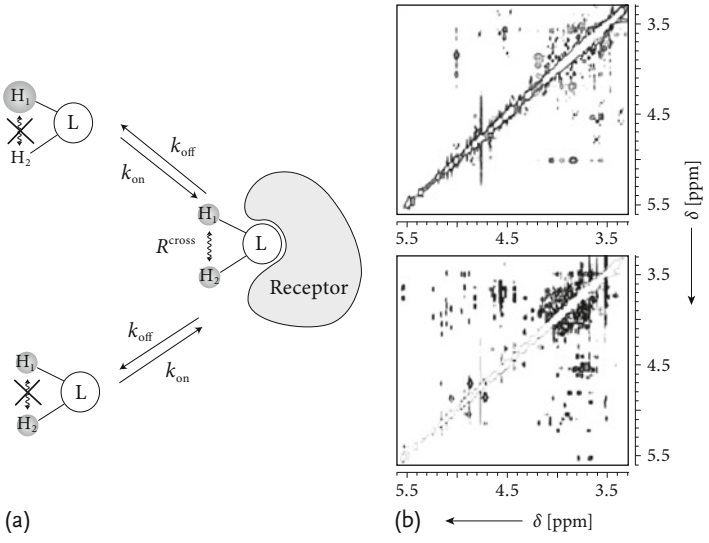

Figure 19.6 The transferred nuclear Overhauser effect (NOE). A ligand binds to a receptor (a). In the free state no NOE occurs between H_1 and H_2. Upon formation of the complex, cross-relaxation between H_1 and H_2 is effective, resulting in strong NOE buildup. After dissociation of the complex, no more cross-relaxation takes place. (b) A NOESY spectrum of a mixture of sugars is depicted in absence (top) or presence (bottom) of a receptor. Note that many cross peaks are only observed in the presence of a receptor, and are absent otherwise.

A 1D variant of the transferred NOE experiment is the *saturation transfer difference* experiment (Figure 19.7), although technically it is somewhat different. Again, the experiment is performed on a mixture of a small molecules and a macromolecule that are in fast exchange. In the experiment a resonance of the macromolecule is selectively irradiated and saturated with low power. Spin diffusion then rapidly transfers the saturation across the entire macromolecule (see Figure 15.6).

During the times when the small molecule is bound, the saturation will also be transferred to it, and will alter the intensity of ligand-related resonances. The experiment is performed twice: once with selective irradiation, once without, and the

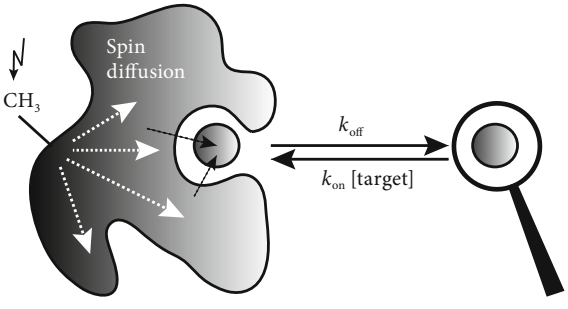

Figure 19.7 Saturation transfer difference.

difference of the two spectra is taken. In the difference spectra all resonances of the small molecule that have changed intensity due to the intermolecular saturation transfer will show up. The experiment is very simple, and very effective, and therefore has gained much popularity. It will show whether a ligand binds to the receptor, and possibly also which parts are involved in the binding. The most critical part of the experiment is to make sure that the saturation does not accidentally affect ligand resonances directly.

Let us look at two different cases. In the first one we will look at a mixture of sugars in the presence of a protein. In this case selective irradiation is comparably simple to achieve because all sugar resonances are in the region between 3 and 5 ppm. When we irradiate the mixture at 1 ppm, where the protein methyl resonances occur, we will not affect sugar resonances. The second case is binding of a peptide to a protein. This is much more difficult, because the signals of the two binding partners largely overlap. The difference, however, is that the lines of the protein are much broader. If we have Lorentzian line shapes, the outer parts of the signals will extend very far, and hence irradiation at, for example, −5 ppm may still affect protein resonances but not the ones of the peptide, which are fairly sharp.

19.5
Methods Based on Changes in Diffusion Rates (Ligand-Observe Methods)

The diffusion of molecules in solution depends on their hydrodynamic radius, which is related to the molecular weight. In protein NMR, the relationship

$$r_{\mathrm{H}} = \frac{\mathrm{MW\ (kDa)}^{0.41}}{1.55} \tag{19.4}$$

can be used approximately. The Stokes–Einstein relation then allows us to estimate the *diffusion coefficient* according to

$$D = \frac{k_{\mathrm{B}} T}{6\pi\eta r_{\mathrm{H}}} \tag{19.5}$$

in which η denotes the viscosity of the solvent. Upon binding, the change in the diffusion constant is more pronounced the larger the difference in the molecular weight between the two binding partners is. This is illustrated in Figure 19.8, which nicely demonstrates that the diffusion coefficient is a convenient tool to monitor binding, however only when the change in molecular weight upon binding is very large (at least by a factor of 1000–10 000!).

Diffusion rates are measured with a so-called stimulated gradient spin echo (see Section 13.9.2). Therein, magnetization is dephased by a gradient. A later gradient is applied which refocuses the magnetization again. However, any magnetization from protons of molecules that have diffused in the z direction in the NMR tube is lost. A series of spectra are recorded with different settings of the gradient strength. The gradient strength is plotted versus signal intensity, and the signal decay is fitted

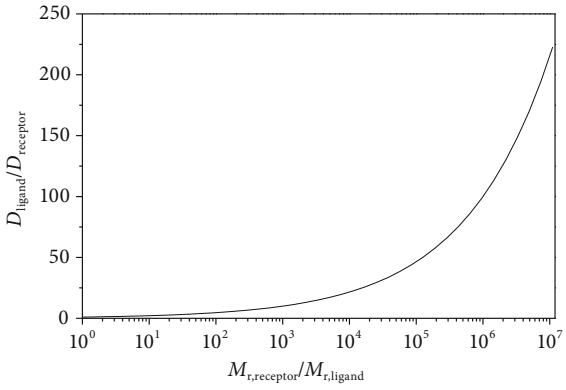

Figure 19.8 Diffusion-weighted NMR. Dependence of the relative change in the diffusion coefficient on the relative change in the molecular weight.

to an analytical function of the form

$$I(G) = I(G = 0)e^{-(\gamma \delta G)^2(\Delta - \delta/3)D} \tag{19.6}$$

where γ is the gyromagnetic ratio of the observed spin, δ and G are the duration and strength of the gradient, Δ is the delay time between the defocusing and refocusing gradients, and D is the diffusion constant (this equation holds true for the so-called longitudinal encode/decode experiment).

19.6 Comparison of Methods

Some of the methods that we have described require the addition of a compound to a sample, and hence compare spectra of two different samples. Any change in the sample, for example, changes in pH, salt, or buffer composition, may give rise to erroneous results. If these factors are carefully controlled, for example, by dissolving both components in the same buffer, chemical shift mapping can yield very reliable information.

Table 19.1 compares the sample quantities for the various methods:

Table 19.1 Comparison of sample quantities for screening.

	Ligand-observe methods	Target-observe methods
Ligand concentration/amount	> 100 µM or 10 µg	Typically 1 mM or 100 µg
Target amount	> 10 µg per sample	> 100 µg per sample
Labeling of target	No	Yes
Experiment time	> 10 min	> 20 min

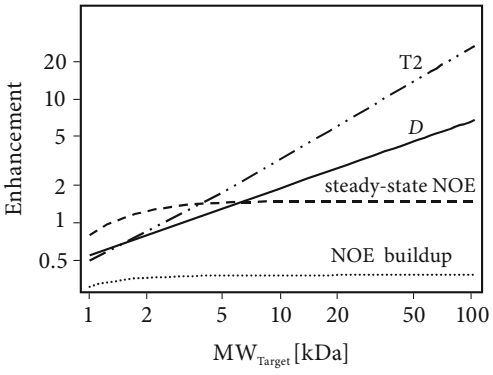

Figure 19.9 Comparison of NMR methods to detect binding. The effects of changes in the molecular weight on T2 (dashed-dotted line), on the translational diffusion rate *D* (solid line), on the steady-state NOE (dashed line), and on the buildup of the NOE (dotted line) are compared. All values are normalized to a 300 Da molecular mass molecule.

Figure 19.9 compares the changes in T2, *D*, steady-state NOE, and NOE buildup when a receptor in the 1–100 kDa range is added to a compound with a molecular mass of 300 kDa.

As we can see, methods based on relaxation tend to be more sensitive than those based on diffusion. We wish to finally mention that often a competition experiment is used. Therein a spy molecule with moderate binding affinity is replaced by the ligand of interest as long as the latter binds the target. As soon as the spy molecule has been released from the target, its resonance lines will become much sharper and they can be seen in the spectrum. Conveniently, such a molecule has a resonance outside the crowded regions of the spectrum.

In this chapter we have only introduced the most common experiments. However, a large selection of experiments have been described in the literature, and some of them represent very valuable additions to the methods described. The interested reader is strongly encouraged to consult reviews from the literature.

19.7 Problems

19.1. Describe the difference between ligand-observe and target-observe techniques.

19.2. Describe "Chemical Shift Mapping" in simple terms. What type of artifacts are possible? What complications can arise?

19.3. A small molecule (e.g., a drug) binds to a large receptor (e.g., a protein). Which parameters change that can be picked up by NMR?

19.4. In CSP experiments compound mixtures are often added for screening. How do you identify the binder in the mixture (if there is any)?

19.5. Describe the transfer-NOE experiment in simple terms.

19.6. NMR chemical shift mapping can be used to determine k_Ds from fits of the data to the theoretical binding isotherm. This, however, is very difficult if the binding affinity is very high (e.g., in the nM range). Can you think of a way to still measure high affinities by NMR?

19.7. For weak binders the line widths of the peaks become very broad for intermediate values complicating monitoring of peak positions. Explain why the lines become broad.

Further Reading

Zerbe, O. (ed.) (2003) *BioNMR in Drug Research*, Chapters 13–17, Wiley-VCH Verlag GmbH.

Stockman, B.J. and Dalvit, C. (2002) NMR screening techniques in drug discovery and drug design. *Prog. Nucl. Magn. Reson. Spectrosc.* **41**, 187–231.

Pellecchia, M., Bertini, I., Cowburn, D., Dalvit, C., Giralt, E., Jahnke, W., James, T.L., Homans, S.W., Kessler, H., Luchinat, C., Meyer, B., Oschkinat, H., Peng, J., Schwalbe, H., and Siegal, G. (2008) Perspectives on NMR in drug discovery: A technique comes of age. *Nat. Drug Discov.*, **7**, 738–745.

Part Five
Structure Determination of Natural Products by NMR

Introduction

So far we have learnt a lot about NMR theory and NMR experiments that should help us establish the chemical nature of compounds. Unfortunately, we do not really know well how to apply these techniques to a real-world problem. In this part of the book we will go through some classes of natural products and teach you a selection of experiments that are particularly helpful for those compounds as well as a strategy for their assignments. In almost all these classes of natural products it is extremely important to follow a certain strategy during assignments – things will be much faster then and the result (hopefully!) unambiguous. We will also try to teach you the most important facts about the particular class of natural products. If you know all of that already, then just concentrate on the NMR part. Despite the fact that sugars, peptides, nucleic acids or steroids look very different, they share some common properties and some of the NMR strategy is therefore similar. We also need to develop a common language to describe assignments so that we can easily compare results. The intention of the first short introductory chapter is to establish knowledge of how to combine information from different 2D spectra in an efficient manner. The following chapters will then build upon this strategy and describe how to apply it to a particular class of natural products. There are of course many more types of natural products. We have just picked a few that are particularly suitable for NMR and that require the correct approach for successful structure identification. If your favorable class of molecules is not amongst our selection, you will certainly be able to adopt the described methods to them!

The Strategy of Compound Identification

The first data to look at will usually be the 1D spectra. First, they will tell you about the purity of your isolate. If your compound is not sufficiently pure, interpretation of the spectra becomes very complicated, and sometimes it is difficult to recog-

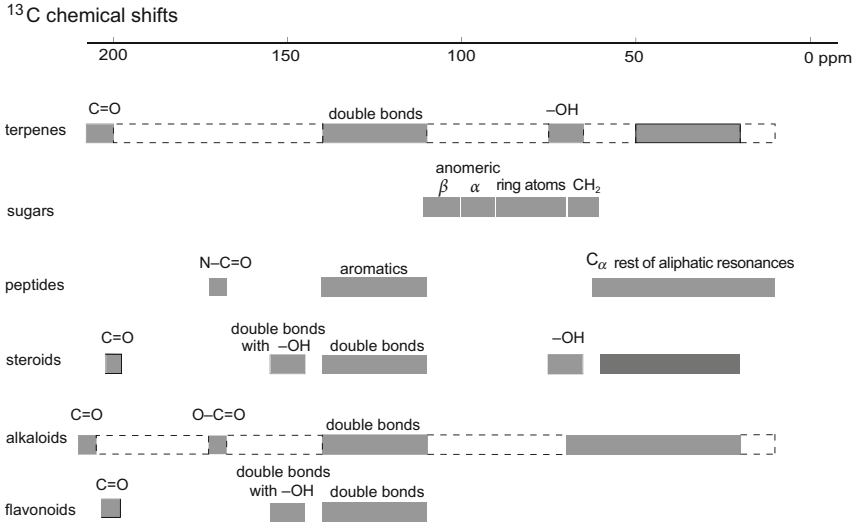

Figure 1 ^{13}C chemical shift ranges in selected natural product classes.

nize impurities. This is particularly true for 2D spectra with a wide dynamic range. NOESY spectra for example may contain weak peaks because the corresponding distances are large or because the peak is from a less abundant impurity. Distinguishing the two cases is very tricky – and it is much better to start with pure compounds right away! The other reason why simple 1D spectra are so important is that you will have a good idea about the chemical nature of your compound from the range of observed signals. Proton NMR spectra will reveal the presence of methyl groups, double bonds, aromatic moieties, and so on. It is even easier to recognize them from ^{13}C NMR spectra, but you might have to use indirect-detection methods such as HSQC-type experiments if you have insufficient quantities for direct detection. Figure 1 provides you with an overview of which ^{13}C chemical shift ranges are occupied by signals for some natural product classes.

It is more difficult to sketch such an overview for proton signals because of the solvent dependence of the signals. Nevertheless, we have added a few spectra from natural products and you can try to find out which spectrum belongs to which class (Figure 2).

Often we can already guess what class of natural product our compound belongs to. However, highly functionalized compounds often produce completely different spectra. So, be cautious.

A Short Example

In the following we will go through the spectra of a fairly simple compound to demonstrate the procedure. The mass as obtained from the mass spectrometry (MS) spectrum is 324. In this case it is crucial to have an MS spectrum as we will

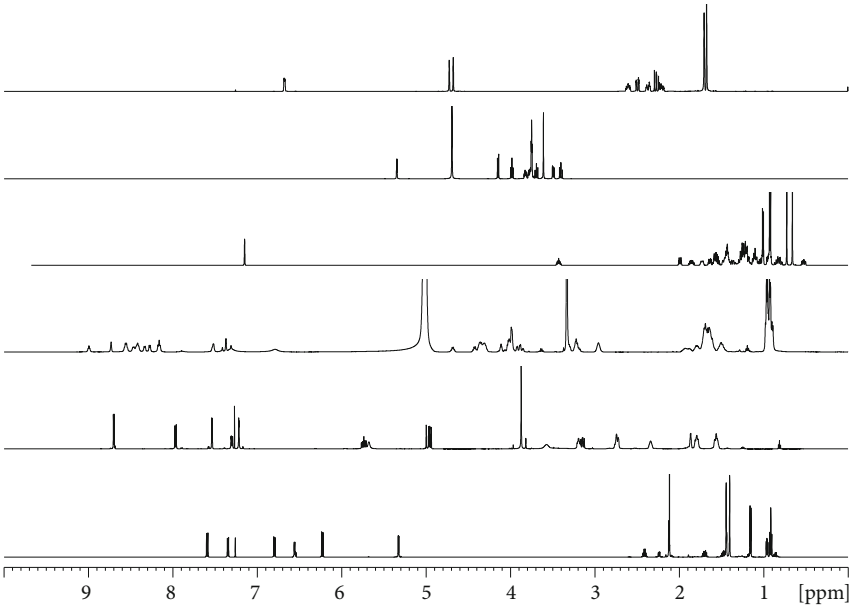

Figure 2 One-dimensional proton NMR spectra from the following classes of natural products: carbohydrates, steroids, peptides, flavonoids, alkaloids, and terpenes. Can you guess which spectrum belongs to which class?

not be able to derive the correct solution without! Only in simple cases are NMR data sufficient because many atoms are NMR-invisible (e.g., O, (N), Cl, Br).

To find a common language in the spectral analysis, it is important to be able to number signals so that we are sure we are talking about the same resonances and correlations. Numbering signals in proton NMR spectra is difficult due to the multiplet nature of the signals and their high overlap. In contrast, signals in carbon NMR spectra are singlets, and overlap occurs very rarely. For the moment we assume that we have been able to record a 1D ^{13}C NMR spectrum (see Figure 3).

We will start numbering the ^{13}C resonances from the right to the left (with increasing chemical shift). The carbon NMR spectrum reveals the presence of 20 signals. We observe a lot of signals in the range coding for aromatic carbons. Some of those signals are downfield shifted – either a heteroaromatic system or a substituted aromatic system. The signal at approximately 101 ppm might stem from an olefinic moiety. This is supported by the presence of a methylene carbon at 115 ppm (see the DEPT 135 NMR spectrum) – maybe this is a terminal double bond. We find a number of carbon signals in the aliphatic range and a methyl carbon at 55 ppm, likely a methoxy group.

The proton NMR spectrum confirms the presence of an aromatic system and the methoxy group (the singlet at 3.9 ppm) (see Figures 4 and 7).

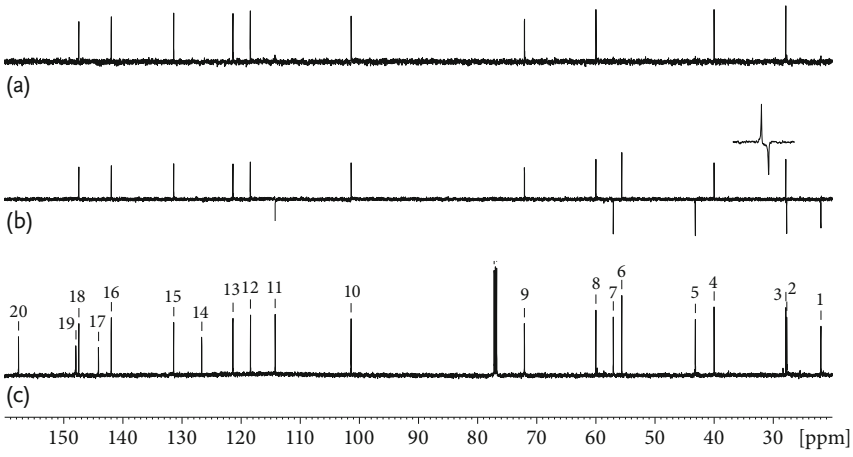

Figure 3 ^{13}C (c), DEPT-135 (b), and DEPT-90 (a) NMR spectra.

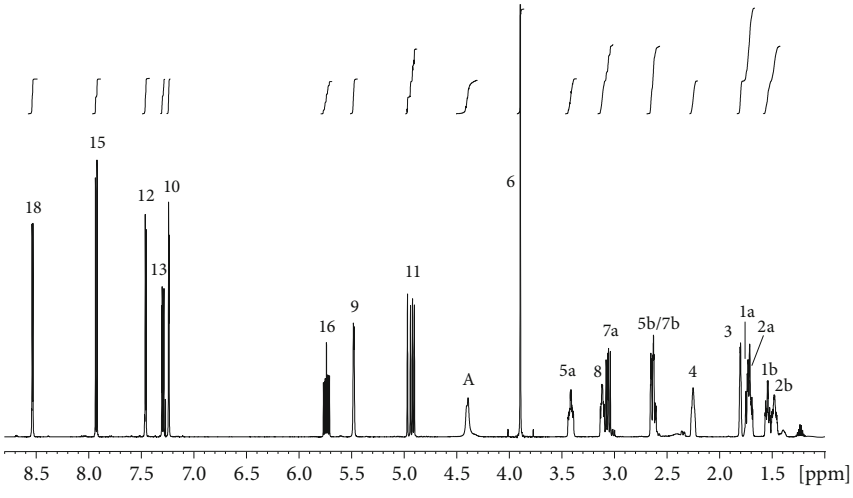

Figure 4 A 600 MHz proton NMR spectrum.

The proton NMR spectrum even more clearly than the carbon NMR spectrum reveals the presence of a double bond. The next step is to correlate carbon nuclei to the directly bonded protons.

With the help of the [^{13}C,^{1}H] HSQC spectrum (Figure 5) we can rapidly number the signals in the proton NMR spectrum. Again we would like to emphasize that diastereotopic methylene protons can be easily recognized as such since two proton signals correlate to a unique carbon signal. Another important feature is that we can recognize protons *not* bound to a carbon because they do not display a corresponding cross peak in that spectrum. We find such a signal and annotate it with "A" (Figure 4).

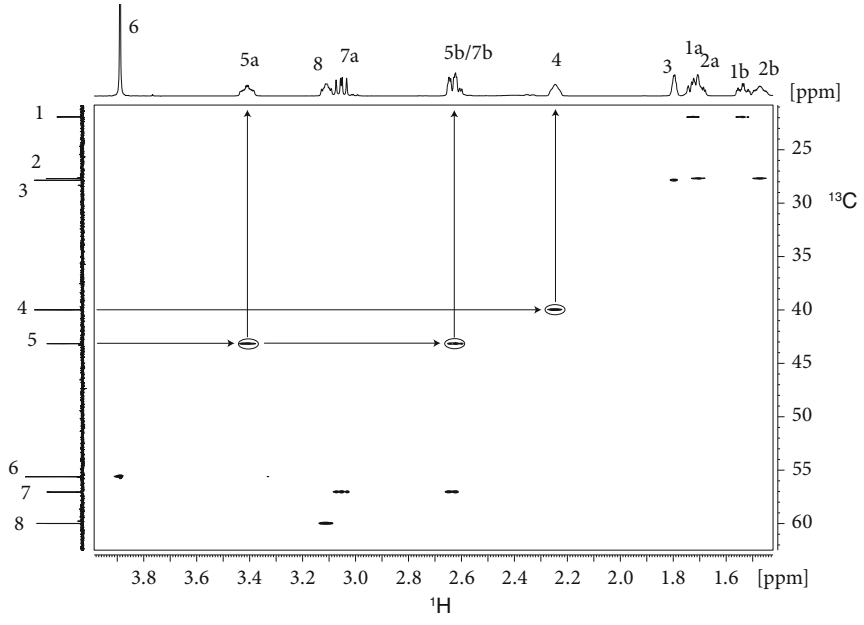

Figure 5 [^{13}C,^{1}H] heteronuclear single-quantum coherence (HSQC) spectrum: Expansion of the aliphatic region.

Now we can start to have a closer look at the COSY spectrum (Figure 6). Remember, COSY correlates protons that are scalarly coupled, usually via either two (geminal) or three (vicinal) bonds.

Particularly helpful are the vicinal couplings because they report on the protons at neighboring carbons. Let us start at H(C9). It is coupled to proton A, a proton that is not carbon bound, and H(C8). It is then straightforward to step from H(C8) to H(C1) and to H(C3). H(C3) is further coupled to both H(C2) and H(C4), apparently a branching point in the chain. From H(C4) we can go to H(C16), an olefinic proton, or to H(C7). From H(C7) we find no further correlations. H(C16) is coupled to H(C11). The other branch from H(C3) continues to H(C2) and H(C5), from which we also fail to observe further correlations. Similarly, we can develop two aromatic fragments, one containing C12–C18, the other containing C13–C15, which displays a long-range coupling to C10. In the COSY spectrum the latter fragment cannot be deduced unambiguously because we cannot be sure which correlations are from vicinal and which are from long-range couplings in the aromatic spin systems. In that case the best thing to do is to look at the 1D spectrum (Figure 7): H(C15) is a doublet, H(C13) is a doublet of doublets with a small and a large coupling, and H(C10), H(C12), and H(C18) display only small couplings.

The coupling between H(C12) and H(C18) is too large for a long-range coupling, but a bit small for a vicinal coupling. This is something to think about. Maybe you can already figure out a method to see whether these two protons are next to each

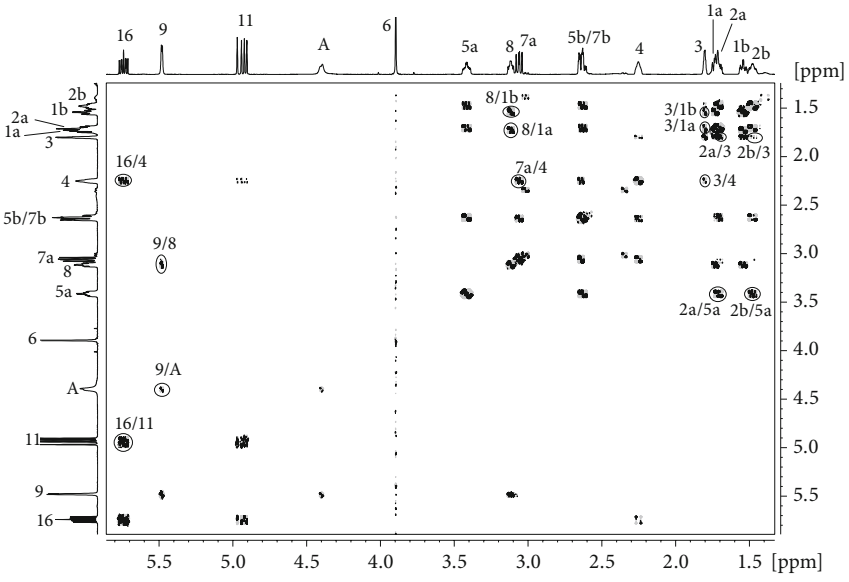

Figure 6 COSY spectrum.

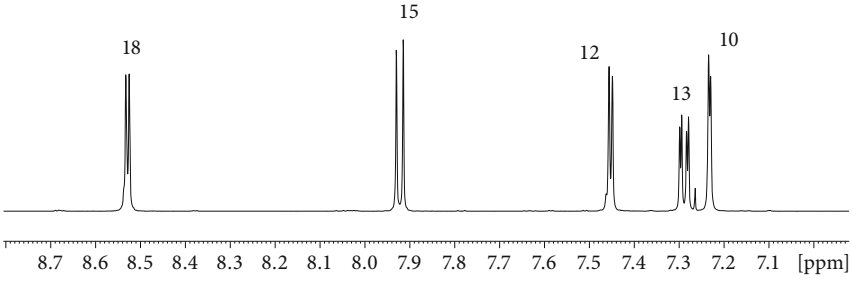

Figure 7 Spectral range of the proton NMR spectrum displaying aromatic resonances.

other on the ring or not. For completeness we also show the expansion of the COSY spectrum in the range of aromatic signals (Figure 8).

We simply write down the three fragments that we have developed so far with the help of the COSY spectrum (see Figure 9). The positioning of C12 and C18 is a bit speculative at the moment, and we should keep this in mind.

There are no further correlations in the COSY spectrum. To connect the fragments we will therefore need to use experiments that are capable of making connections across quaternary centers, and those are the heteronuclear multiple-quantum coherence (HMBC)-type experiments, which transfer magnetization along the long-range proton–carbon couplings. Alternatively we might use NOEs, but since NOEs are always a bit ambiguous, we will usually start with the [^{13}C,^{1}H] HMBC spectrum first. The HMBC spectrum of the compound is depicted in Figure 10.

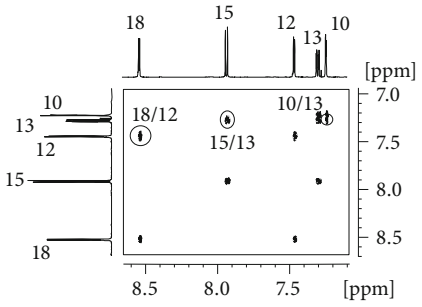

Figure 8 Expansion of the aromatic region of the COSY spectrum.

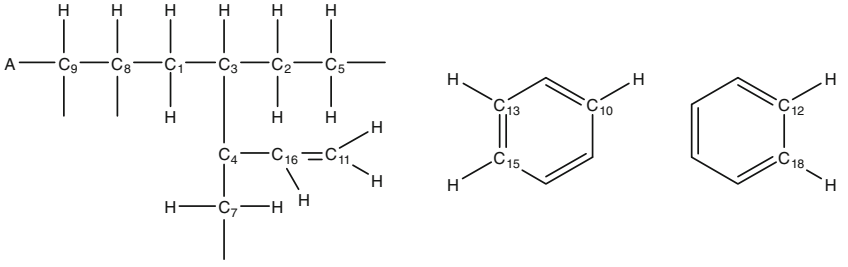

Figure 9 Fragments from COSY correlations.

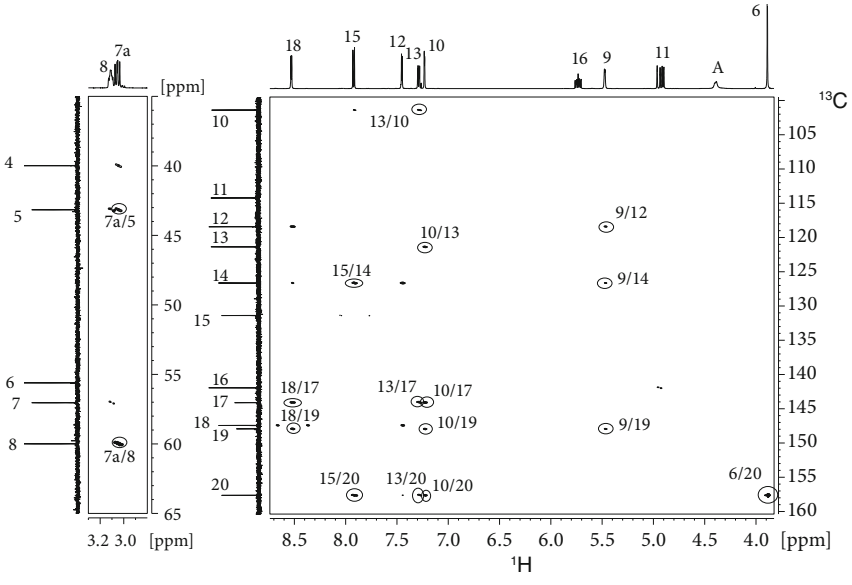

Figure 10 HMBC spectrum.

A very strong correlation exists from the methoxy proton to C20. That leaves us with two more quaternary carbons on one of the aromatic systems; maybe the

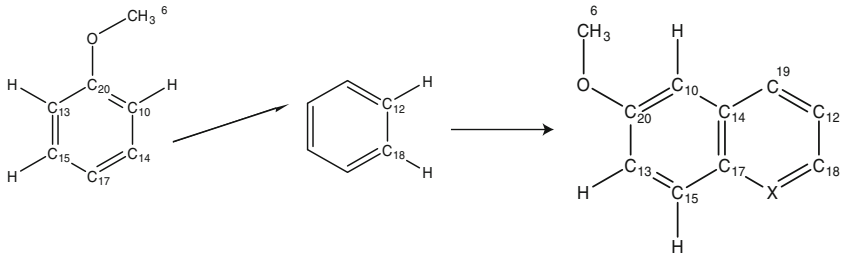

Figure 11 Fragment II comprising the aromatic moiety.

aromatic rings are simply attached to each other. If this is true, we need to see a correlation from H(C10) or H(C15) to the other ring. But before we look at that, we need to find out which of the carbon nuclei are part of the same ring as the methoxy group. H(C13) is a good spy, because it is too far away for a long-range coupling to carbons of other rings. The DEPT spectra reveal that C20, C19, C17, and C14 are quaternary carbons. C20 is the anchoring point for the methoxy group. A strong HMBC correlation is seen from H(C15) to C14 and to C20, and from H(C13) to C17, C10, and C20. H(C10) is correlated to C19, C17, C20, and C13 and H(C18) is correlated to C19 and C17. This allows us to join the two aromatic rings as depicted in Figure 11. Maybe you wonder why we do not see the correlation between H(C10) and C14. Often, in aromatic systems ^{2}J(C,H) correlations are not observed. However, this is certainly something we should worry about a bit.

We have now combined two fragments into one, but we still need to add the third one. It could be connected via A (A could be part of an NH moiety), or via C7, C8, C9, or C5. The easiest way to find this out is to look for HMBC correlations from H(C7), H(C5), H(C8), H(C9), or A to aromatic carbons. There is a clear candidate: H(C9) displays correlations to C12, C14, and C19, while we do not find any correlations from the other protons. This allows us to unambiguously join the two fragments (Figure 12).

At the moment we do not know what the X stands for, and to which other atoms C8, C7, and C5 are connected.

At this point let us consider the MS spectrum for a second. The mass was 324. The fragment that we have developed so far is $C_{20}H_{22}O$, which corresponds to a mass of 278. That means we are missing quite a bit, a mass of 46 to be precise. The X in the second aromatic ring could be "O" or "N"; from the carbon chemical shifts of C17 and C18 it is likely an "N" (we need to confirm this later!). This leaves us with a mass of 30, maybe "N" plus "O." We have three carbon positions with still open valencies, and we could connect them to each other by inserting an "N" in between. Then the A would be an OH group. If we decided that A is NH_2, then we would end up with the problem of how to connect the remaining three valencies, and at least the chemical shift of C5 is wrong for an oxygen attachment. We end up with molecule shown in Figure 13.

The HMBC correlations from H(C7) to C8 and C5 confirm that linkage.

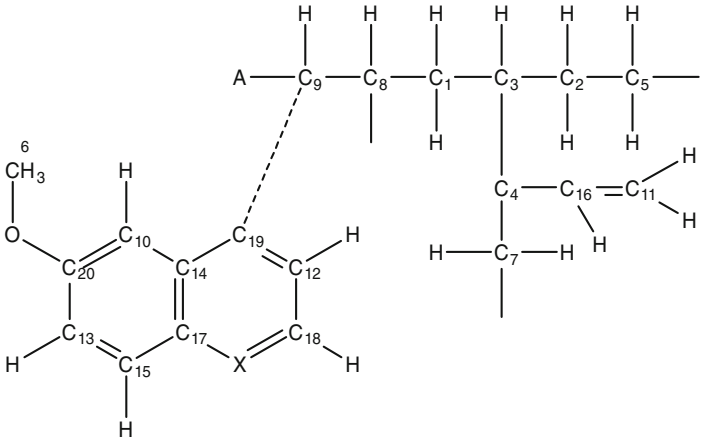

Figure 12 In fragment III most connections have been made.

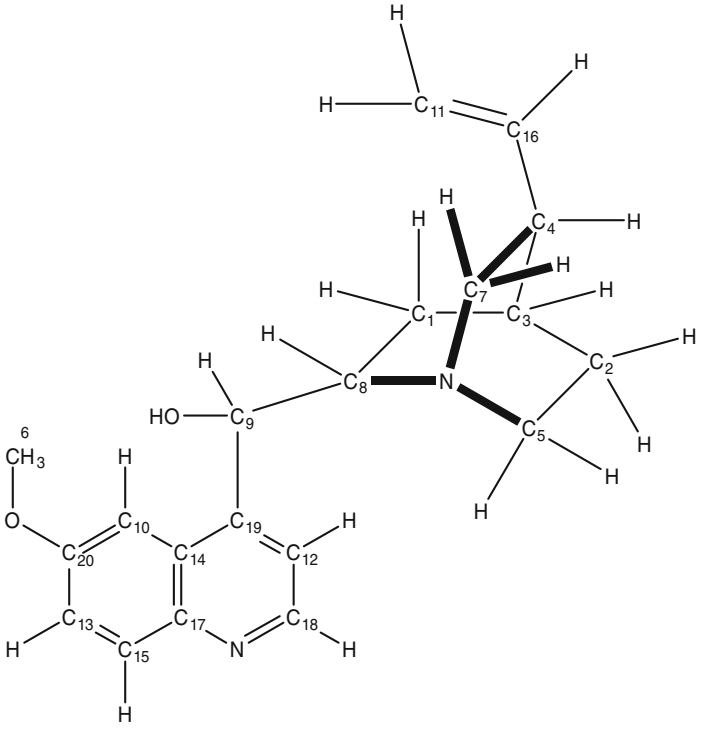

Figure 13 Joining all the fragments together reveals the covalent structure.

We need to figure out the stereochemistry from the ROESY spectrum (Figure 14). What needs to be determined is the stereochemistry at C8, which can be nicely fixed based on the ROE between H(C8) and H(C7) as well as from H(C9) to Ha(C5).

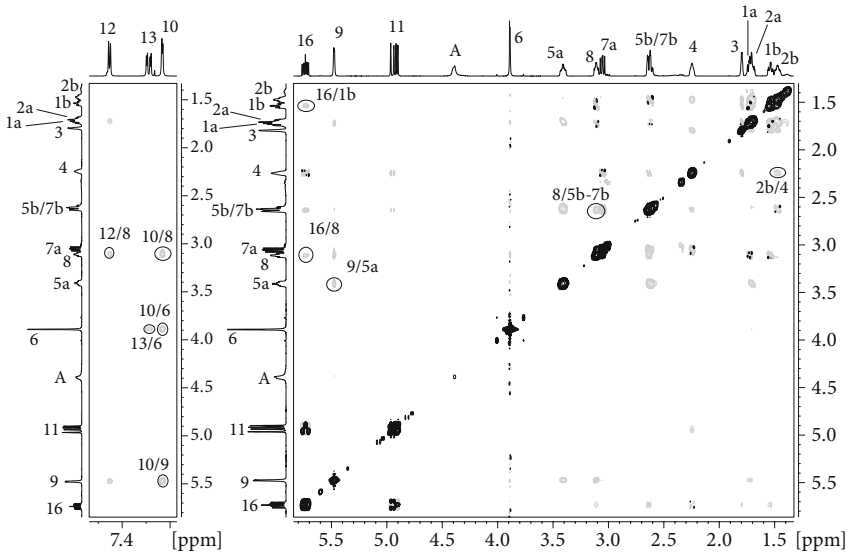

Figure 14 ROESY spectrum.

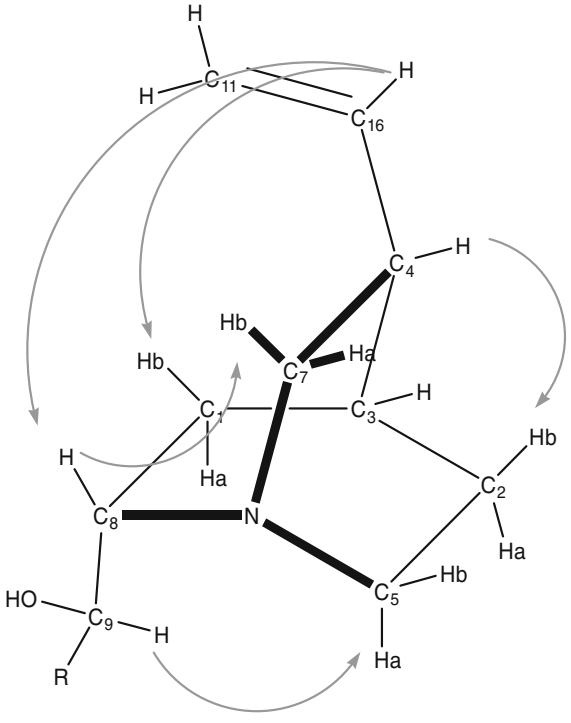

Figure 15 Important ROESY correlations for determining the stereochemistry at C8 and C4. For the total structure compare with Figure 13.

The rest is useful to complete the assignment but not required to determine the stereochemistry. The compound is depicted in Figure 15; it is an alkaloid called chinin. Once you have made all these connections, it is important to check whether the proposed structure is compatible with all the NMR data. We had tentatively inserted an X=N into the second aromatic ring. Of course, C18 could also be directly connected to C17 to form a five-membered ring instead. If this were the case, we would need to observe an ROE between H(C18) and H(C17), which we fail to see! And the mass of our molecule would not match with the value from the MS spectrum.

The important message of this example is twofold: first, use scalar couplings to build fragments, and join them by using HMBC (or NOE/ROE) connectivities; second, it is allowed (even advised) to use your chemical intuition to join fragments, but then you will need to confirm all the connections with unambiguous spectroscopic evidence! However, a good suggestion can be rapidly confirmed with a few strategically chosen HMBCs/ROEs, and you know which correlations you need to look for! Use Ockham's razor principle: before constructing something terribly complicated, start with the simple solutions first. And ask yourself whether the structure you have proposed is the only one that is compatible with the NMR data. Include MS and any other additional information that you might have.

In the remainder of this part of the book we will go through a few selected classes of natural products and apply similar methods for their identification.

20
Carbohydrates

Polysaccharides form an important group of biomacromolecules. Sugar units play a structural role and constitute important components of membranes. Sugars are part of DNA and RNA, molecules that are used to store and transfer genetic information. Sugars are also an important area of active synthetic work for organic chemists. As we will see very soon, polysaccharide analytics can be much more demanding than polypeptide analytics. NMR spectroscopy has always been an important method for determining the chemical identity of carbohydrates. In fact NMR spectroscopy method development was driven for some time by the requirements of sugar chemists, and the first 3D spectra were recorded on oligosaccharides and not on proteins. Similarly to proteins, polysaccharides are built from simple units that are connected through covalent bonds. Although the number of different building blocks is probably not much greater than the number of different amino acids, the fact that two hexose sugars can be linked in six different ways results in a much larger variety/uncertainty of isomers. Moreover, because the different building blocks often differ only in the stereochemistry of hydroxyl groups, they are much more chemically similar than the 20 amino acids are with respect to each other. As a consequence, chemical shift dispersion is comparably small, and it may often be necessary to resort to instruments at the highest available field to work through the spectra. To make things even more complicated, different conformations, for example, about the glycosidic bond may exist, and interconversion may take place on an unfavorable timescale, leading to significant line broadening. To summarize, NMR spectroscopy of carbohydrates is certainly interesting but may be technically very demanding. Similarly to NMR spectroscopy of proteins, it is important to use the appropriate set of NMR experiments and start assignment from strategically well chosen entities.

20.1
The Chemical Nature of Carbohydrates

Carbohydrates are mostly but not exclusively composed of the elements carbon, hydrogen, and oxygen, as the name implies. Their general formula is therefore $C_n(H_2O)_n$. Biologically (and mostly chemically) relevant is the series of C6 sugars

Applied NMR Spectroscopy for Chemists and Life Scientists, First Edition. Oliver Zerbe and Simon Jurt.
©2014 WILEY-VCH Verlag GmbH & Co. KGaA. Published 2014 by WILEY-VCH Verlag GmbH & Co. KGaA.

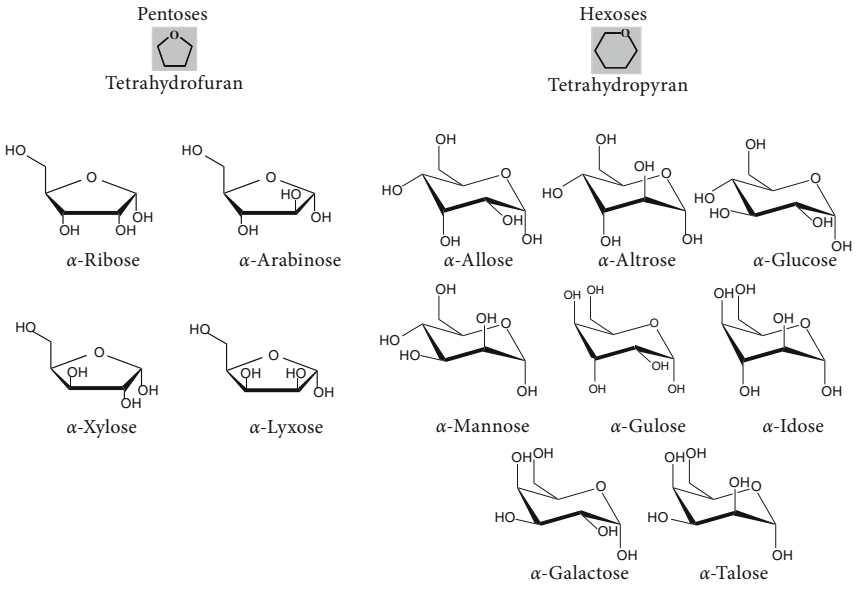

Figure 20.1 Chemical formula of the D-form of important monosaccharides. Furanoses are depicted in the Haworth presentation, pyranoses in the chair conformation.

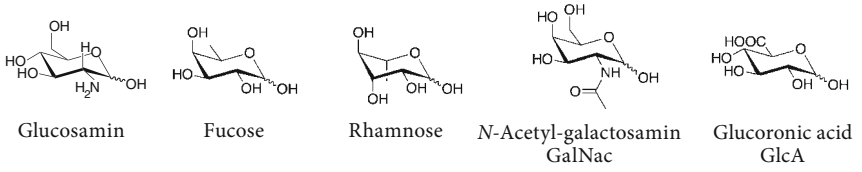

Figure 20.2 Chemical modifications of sugars.

(hexoses), derived from tetrahydropyran, and C5 sugars (pentoses), derived from tetrahydrofuran (Figure 20.1).

Some modifications of sugars often occur in nature, for example, removal of a hydroxyl group (deoxy sugars), replacement of a hydroxyl function with an amino group (amino sugars, *N*-acetylamino groups), and oxidation of a CH_2OH group to a carboxyl group (Figure 20.2).

Pentoses play an important role in nucleic acids as the ribose and deoxyribose, whereas hexoses are abundant in other natural products and are involved in many biologically relevant processes. Monosaccharide units can be covalently coupled and the newly formed bond is called a glycosidic bond. Often (but not exclusively found) linkages are 1,2, 1,4, and 1,6 linkages. Prominent examples are sucrose, maltose, and lactose, for which the structures are depicted in Figure 20.3. Monosaccharide units can also be linked to longer polymers, such as cellulose, raffinose, amylose, and amylopectin. The longer oligosaccharides often play a structural role in biology.

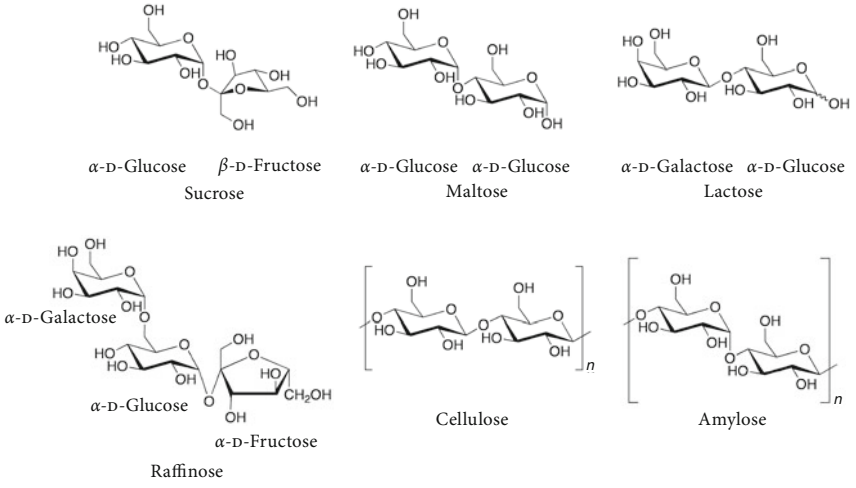

Figure 20.3 Chemical structures of oligosaccharides.

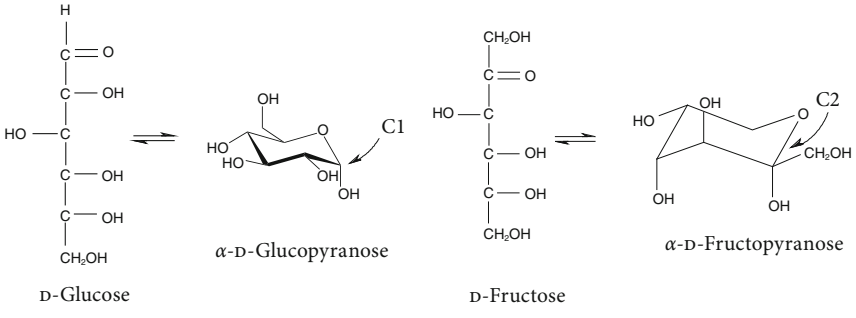

Figure 20.4 Equilibria of open-chain and cyclic sugars in aldoses and ketoses. Note that for both sugars, the pyranose forms are shown.

Carbohydrates in solution exist in an equilibrium mixture of acyclic aldehydes or ketones and cyclic hemiacetals and hemiketals. The equilibrium in solution is mainly shifted toward the cyclic form. Depending on which hydroxyl group reacts with the aldehyde/ketone group, five- or six-membered rings are formed. The five-membered rings are called *furanoses* and the six-membered *pyranoses*. Carbons are numbered from the anomeric center on, which denotes the aldehyde/ketone carbon of the acyclic form. Equilibration via the open-chain form and rotation about the C1–C2 bond results in scrambling of stereochemistry at the anomeric center (*mutarotation*). This is only possible for the hemiketals/hemiacetals; formation of the glycosides (formation of full acetals) results in stereochemical fixation.

For the pyranoses, the stereochemistry of hydroxyl groups determines the type of sugar (Figure 20.4). As we will see in more detail later, pyranoses mostly populate chair-type conformations. For glucose (a pyranose), all the sterically more demanding hydroxyl groups can be placed equatorially in one particular conformation. This

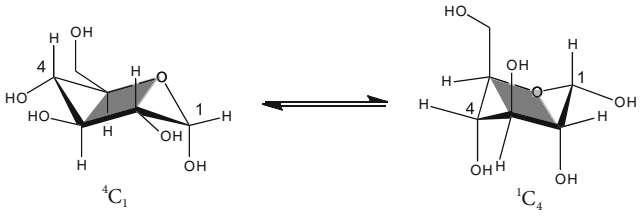

Figure 20.5 Chair ring conformations of pyranoses.

form is denoted as $^4C_1$ because when atoms C2, C3, C5, and O are drawn in one plane, C4 is placed above that plane (hence the superscript) and C1 below. A flip of the chair transforms it into $^1C_4$, which is energetically much more unfavorable (Figure 20.5):

Note that in the L series of the sugars, equatorial and axial positions of the hydroxyl groups are exchanged. To convert D-glucose into L-glucose, you need to transfer all hydroxyl groups, which are in equatorial positions, to the axial positions. If you do that, of course, the $^4C_1$ conformation will be of high energy, and you need to invert the ring to the $^1C_4$ conformation, after which all hydroxyl groups are equatorial again. Accordingly, the proton at the anomeric center is axial in both D-β-glucose and L-β-glucose. Considering the importance of D carbohydrates over L carbohydrates, we will for the remainder of this chapter only describe properties of the L series.

The two possible stereochemical conformations at the anomeric center are denoted as the α and β forms of glucose. In the low-energy $^1C_4$ conformation the hydroxyl group at C1 is axial in the α form and equatorial in the β form of the same sugar.

So what are the tasks we need to accomplish to unambiguously identify the type of sugar? To summarize, we need to

- identify the nature of the monosaccharide subunits (aldose or ketose; pyranose or furanose; derivatized sugar?)
- establish whether the individual monosaccharide units belong to the α and β forms
- establish the linkages of the sugars.

20.1.1 Conformations of Monosaccharides

Depending on whether the monosaccharides belong to the class of pyranoses or furanoses they will adopt conformations of six- or five-membered rings, respectively. Six-membered rings may adopt chair-like, boat-like, or twisted-boat-like conformations (Figure 20.6). Glucose adopts the classic chair-type conformation. In principle, the more hydroxyl groups are forced to occupy axial positions, the more likely the chair is to be distorted.

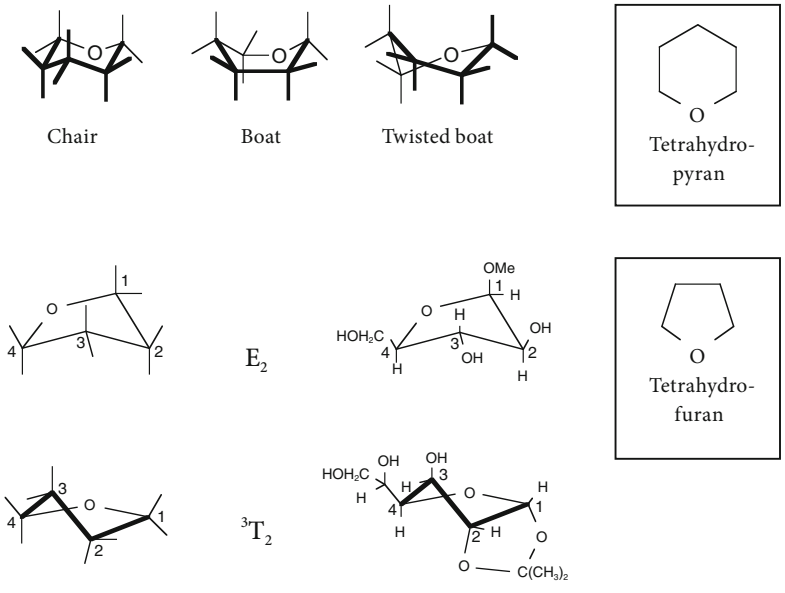

Figure 20.6 Important ring conformations of pyranoses and furanoses.

For the furanoses, envelope-type or twisted-envelope-type conformations are encountered. Which type of conformation is present is sometimes hard to predict, and therefore conformational analysis of furanoses can be tricky.

20.2
NMR Spectroscopy of Carbohydrates

20.2.1
Chemical Shift Ranges

The most important task at the beginning of course it to recognize that the compounds of interest is a sugar. If the saccharides has not been extensively modified, this task is actually not too difficult. Proton and carbon chemical shifts are observed in characteristic, narrow ranges (Figure 20.7). Note that the values presented serve only as a rule of thumb, and that compounds may fall outside the specified ranges. Nevertheless, such rules are helpful when assigning structures. For unmodified carbohydrates (not of the deoxy type, not methyl esters, etc.) almost all ring protons resonate between 3 and 4.7 ppm, while the anomeric protons are observed at low field between 4.5 and 5.7 ppm. No resonances are found below 3 ppm or above 6 ppm. Since most other natural products will display signals in those ranges, carbohydrates can be quickly recognized. In addition, modification of natural products such as peptides and steroids by carbohydrates can also be easily seen from the appearance of signals in those ranges. In ^{13}C NMR spectra all ring carbons are found in the 60–90 ppm range, and anomeric carbons will resonate between 90 and

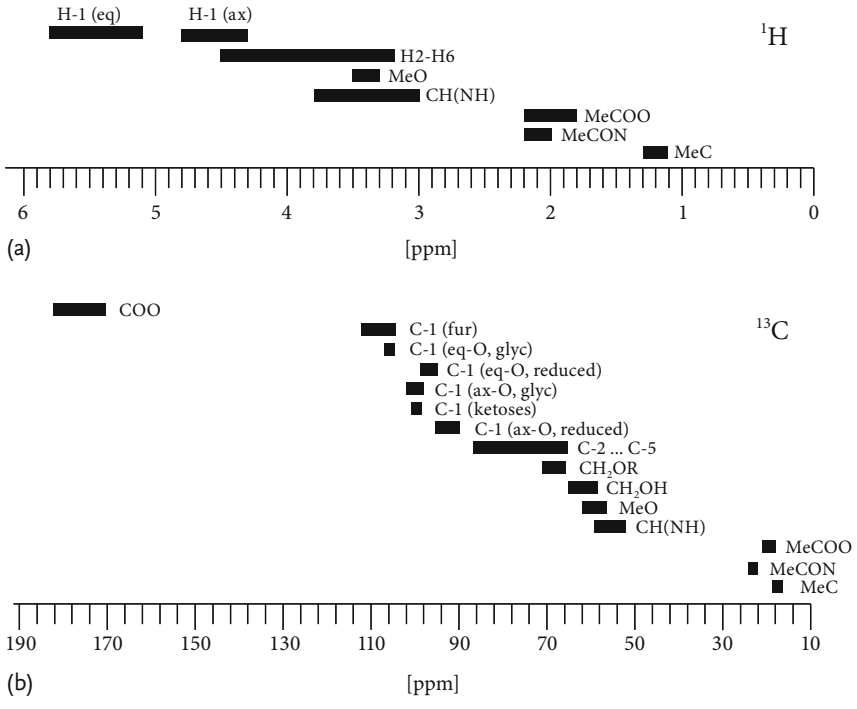

Figure 20.7 ^{1}H (a) and ^{13}C (b) shift ranges for saccharides. Consult carbohydrate NMR review articles for more specific information.

120 ppm. In particular no other signals are observed in the range of anomeric carbons, allowing one to recognize sugars in ^{13}C NMR spectra. To summarize, sugars can often be easily recognized from 1D proton or carbon NMR spectra.

Of course, modifications of the saccharide units will lead to signals in other regions of the spectrum. For example, a desoxy sugar will display carbon signals more upfield, and the same is true for amino sugars. In general, the type of monosaccharide unit gives rise to a particular ^{13}C NMR spectrum. Often, however, the monosaccharide units need to be established from first principles.

20.2.2
Systematic Identification by NMR Spectroscopy

We will briefly outline the procedure to establish monosaccharide units from first principles in the following.

20.2.2.1 How Many Monosaccharide Units Are Contained in the Sugar?

How many monosaccharide units are contained in the sugar is most easily seen from the ^{13}C NMR spectrum. For nonsubstituted pure carbohydrates, this can be deduced from the number of signals in the ^{13}C NMR spectrum, since the total number should be dividable by a combination of 5 and 6 mostly. More easily it

is seen from the number of signals in the anomeric region. While both proton and carbon NMR spectra can serve for that purpose, signal overlap in the proton NMR spectra may complicate that task. Therefore we recommend extracting this information from the [^{1}H,^{13}C] HSQC correlation. Cross peaks corresponding to anomeric carbons should be in the range above 90 ppm, and ^{1}H chemical shifts are usually higher than 4.5 ppm.

20.2.2.2 How Many of the Monosaccharide Units Are Aldoses or Ketoses?

If the sugar units are hexoses, a ketose will contain two methylene carbons, whereas aldoses will only contain a single methylene carbon. Accordingly, possibly with the help of a DEPT spectrum for each ketose, two CH_2 moieties occur in the 60–70 ppm range, one for each aldose.

20.2.2.3 Stereochemistry at the Anomeric Center

There are a number of parameter suitable for distinguishing α and β forms of the monosaccharide building blocks, such as the proton or carbon chemical shift, the $^3J(^1\mathrm{H},^1\mathrm{H})$ scalar coupling constant, and the $^1J(^{13}\mathrm{C},^1\mathrm{H})$ coupling constant. They are summarized in the Table 20.1.

Glycosylation will change the chemical shifts of proton and carbon frequencies at the anomeric center and vicinal to that side. Proton shifts will decrease by 0.2–0.6 ppm at the anomeric center and by 0.03–0.31 ppm at the adjacent center. Carbon shifts will increase by 4–10 ppm at the anomeric center and decrease by 1 ppm at the adjacent carbon.

20.2.2.4 Identification of the Different Spin Systems

The anomeric protons are low field shifted relative to the other ring protons, and connecting these to others can often be rather complicated. Knowledge of what proton and carbon frequencies belong to a common spin system, however, is of crucial importance when the individual monosaccharide units are to be identified.

It is important to realize that each monosaccharide unit is a separate spin system, since scalar couplings do not connect protons from different sugar units across the glycosidic bond. Considering that resolution is best in the region of anomeric protons/carbons, a strategy that tries to connect from there is most promising. The most suitable NMR experiment to achieve that is a TOCSY experiment. Correlations from the individual anomeric protons, in principle, should reveal which pro-

Table 20.1 Characteristic data for the α and β anomers.

	α form	**β form**
Proton chemical shift (H-1)	4.8–5.8 ppm	4.3–4.8 ppm
Carbon chemical shift (C-1)	98–103 ppm	103–106 ppm
$^3J(^1\mathrm{H},^1\mathrm{H})$ scalar coupling constant	1–4 Hz	6–8 Hz
$^1J(^{13}\mathrm{C},^1\mathrm{H})$ coupling constants	170 Hz	160 Hz

tons belong to the same unit. We should, however, add that often, in particular in furanoses, not all correlations are seen because scalar couplings can sometimes be fairly small. Whenever the complete spin systems cannot be traced through in the TOCSY spectrum, it may be necessary to additionally use heteronuclear multiple-bond correlation (HMBC) data and work one's way through the spin systems.

While the TOCSY experiment will reveal which protons belong to the same spin system, it fails to unambiguously distinguish between vicinal and long-range correlations. This can only be accomplished by a COSY experiment. Unfortunately, in a COSY spectrum cross peaks between resonances with similar chemical shifts will be very close to the diagonal, and will therefore often be very difficult to see. A very valuable alternative for that task is to use a 2D HSQC-TOCSY experiment, which allow one to separate the H–H correlations along the carbon dimension. Since signal dispersion in the carbon spectra is usually good, overlap is usually not an issue in these spectra. At the end of this procedure, the proton and carbon chemical shifts of each position in each monosaccharide units should be known.

20.2.2.5 Identification of the Monosaccharide Units Based on the Stereochemistry of the Hydroxyl Groups

Two parameter are suitable to distinguish the stereochemistry of the hydroxyl groups: nuclear Overhauser effects (NOEs) and ^{3}J scalar couplings. NOEs allow one to probe for proximity of protons. We wish to reemphasize that 1,2 NOEs (NOEs between vicinal protons) are of limited analytical value because those NOEs are mostly observed. Moreover, additional relaxation sources may change the intensity of NOEs, so their absolute value may be misleading. Considering that monosaccharides adopt five- or six-membered rings, it is much safer to use long-range correlations, in particular 1,3 correlations. For example, in glucose all nonanomeric protons adopt axial positions. Therefore, 1,3-diaxial NOEs establish the stereochemistry at two different centers simultaneously with great confidence. A summary of meaningful NOEs is depicted for the pyranoses in Figure 20.8.

Usage of the vicinal couplings presents a valuable alternative. Although at first glance this sounds complicated, it may actually simplify analysis tremendously. As predicted from the Karplus relationship, the three-bond scalar coupling depends on the magnitude of the dihedral angle involved. Diaxial (ϕ is approximately 180°) couplings are large (7–9 Hz), while equatorial–equatorial and axial–equatorial (both approximately 60°) couplings are much smaller (2–4 Hz). Let us consider an example, and we will see how easy it is to distinguish glucose from mannose and galactose on the basis of scalar couplings (Figures 20.9 and 20.10).

Let us assume that we have used a protic solvent so that all hydroxyl protons have exchanged and hence disappeared from the spectrum. The signal of the proton at C3 will be a triplet in the case of the glucose (two large, diaxial couplings), and a doublet of doublets in the case of mannose and galactose (one diaxial and one axial–equatorial coupling each). For H at C2, it will be a triplet for mannose (two equatorial–equatorial couplings) and a doublet of doublets for galactose (one diaxial and one axial–equatorial coupling). You see, it is straightforward to distinguish these three cases.

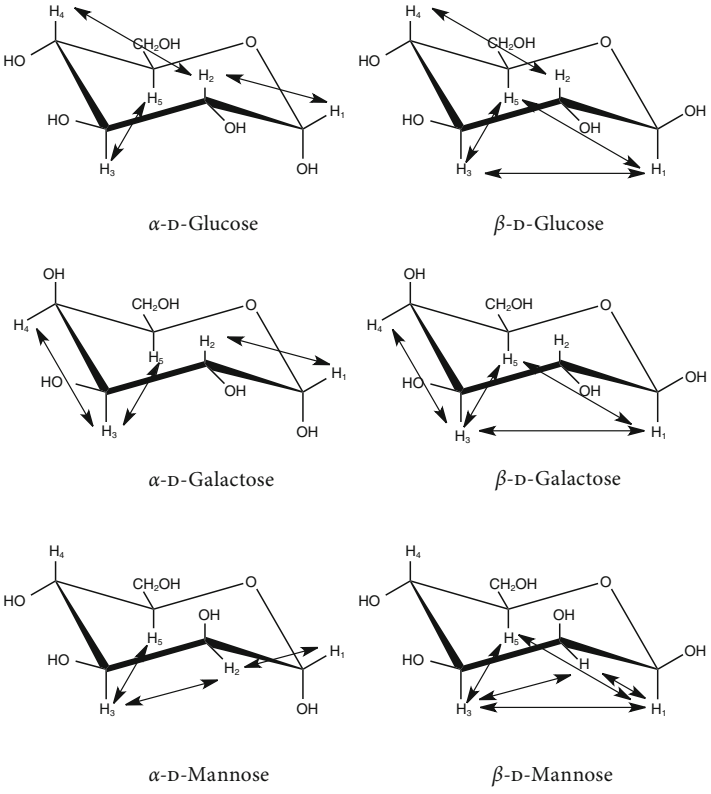

Figure 20.8 Nuclear Overhauser effects (NOEs) important for identification of monosaccharides.

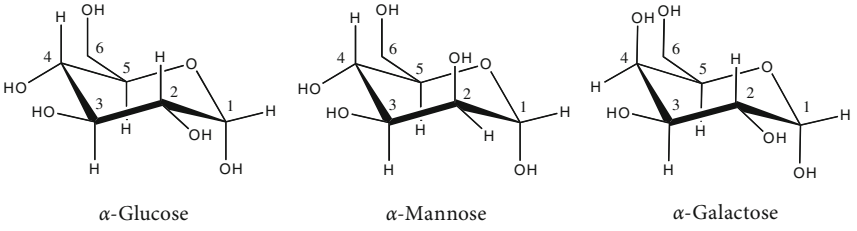

Figure 20.9 Chemical formulas of α-glucose, α-mannose, and α-galactose.

Of course the usage of couplings will not help us a lot if the signals are overlapping with others, and so the individual couplings cannot be extracted. Unfortunately, this is usually the case because the ring protons are highly overlapped since they all cluster between 3 and 4.5 ppm. But there is a convenient fix: extract the couplings from cross peaks in 2D COSY spectra. This bypasses the overlap problem, because now potentially overlapping signals are dispersed in two orthogonal

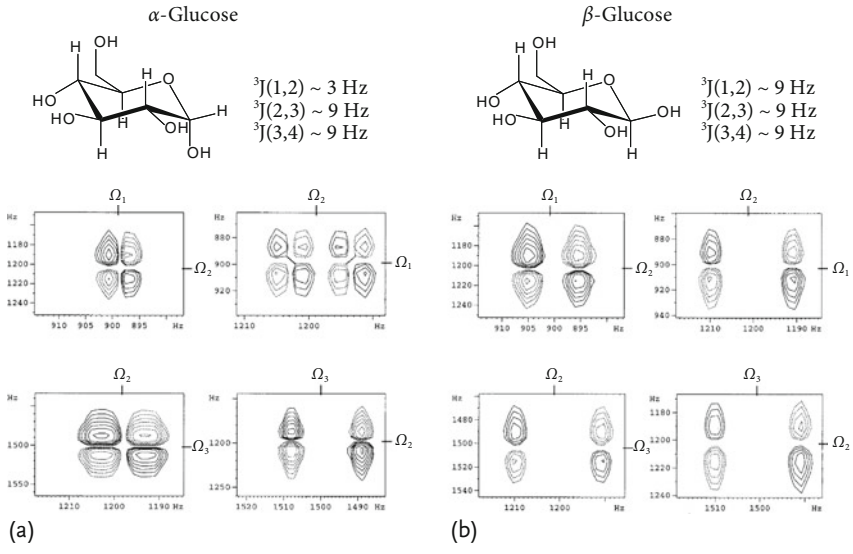

Figure 20.10 Correlation spectroscopy (COSY) cross peak patterns for α-glucose (a) and β-glucose (b) (see the text).

dimensions. How this works is demonstrated in Figure 20.10 for α-glucose and β-glucose.

Cross peaks between H–(C1) and H–(C2) (top two cross peaks) and H–(C2) and H–(C3) (bottom two cross peaks) are shown. For the H1–H2 cross peak, the H1–H2 coupling is the active coupling. In the frequency dimension of H1, no other coupling occurs, while in the dimension of H2, the coupling to H3 will show up as passive coupling. In the indirect (vertical) dimension the resolution is so poor that the additional couplings are not resolved. So, if we have a look at the H2(F2)–H1(F1) cross peak of α-glucose, a doublet of doublets is seen in F2, with the small coupling being the active one (the H2–H1 coupling), which must therefore be an equatorial–equatorial or an equatorial–axial coupling. The passive coupling is large; hence, H3 and H2 must both be axial. We can conclude that H2 and H3 are axial and H1 is equatorial. If we look at the same cross peak for β-glucose we see only two components in F2. This is the case because both the active and the passive couplings are large. But because the active coupling is in antiphase and the passive one is in phase, the center components of the triplet do not add up as in the 1D spectrum but mutually cancels each other. Such a cross peak unambiguously immediately reveals that H1, H2, and H3 are all axial. If we look at the corresponding cross peaks for the H3–H2 coupling, we again see a very large splitting with a missing center component (this time for both α-glucose and β-glucose), indicating that H2, H3, and H4 are all axial. The beauty is that we do not even have to measure all the couplings, and just the fact whether we see large or small couplings allows us to reveal the stereochemistry at a number of positions from a single cross peak!

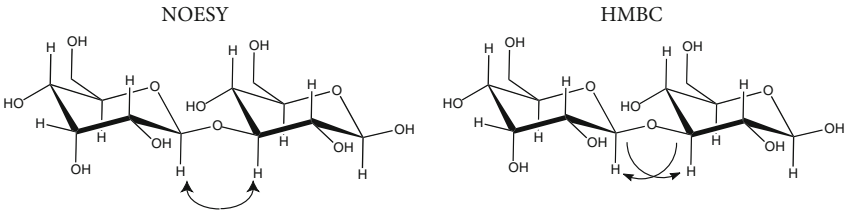

Figure 20.11 Important NOEs and heteronuclear multiple-bond correlations (HMBCs) for establishing linkages between sugar units. NOESY – nuclear Overhauser effect spectroscopy.

20.2.2.6 **Establishing the Linkage Sides**

Establishing the linkage side (e.g., are the two monosaccharide units 1,2 1,3, 1,4, or 1,6 linked?) can be achieved usually fairly easily. The linkage side can be seen either from an NOE between two protons that are part of different sugar units or via HMBCs between a carbon at one end of the glycosidic bond and the proton of the covalently bound sugar at the other end of the bridging oxygen (Figure 20.11). Both methods work equally well.

20.2.3 **Practical Tips: The Choice of Solvent**

A number of solvents are capable of dissolving carbohydrates, such as dimethyl sulfoxide, pyridine, methanol, and water. When choosing the correct solvent, the first question is whether a protic or a nonprotic solvent is to be used. In protic solvents all exchangeable protons, in particular the hydroxyl protons, will disappear from the spectra. However, hydroxyl signals will mostly be broadened in aprotic solvents as well, due to the exchange with water that is usually contained in the solvents. Hence, solvents should be carefully dried, or dried solvents from ampules should be used when recording spectra in these solvents. Recording carbohydrate spectra in protic solvents seems to be undesirable at first glance because we lose hydroxyl protons as structural probes. However, if we know the stereochemistry at the CH(OH) moiety for the proton, we also know the stereochemistry for the hydroxyl group, since the two are complementary. Using protic solvents, however, has the great advantage of clearing up spectra and removing a lot of signals from spectra that are crowded in any case. Moreover, signal patterns are simplified and scalar couplings are easier to extract.

Often, conformational exchange processes in carbohydrates result in severe line broadening. High-temperature NMR experiments may be a good way to remove some of this line broadening, and thereby improve the quality of the spectra. The choice of solvent may therefore also be based on whether it can be used for variable-temperature NMR experiments. Table 20.2 summarizes the most important properties of the standard solvents.

Table 20.2 Solvents used in carbohydrate NMR experiments.

Solvent	CH	OH	NH	Boiling point (°C)	Melting point (°C)
Dimethyl sulfoxide	+	+	+	190	18
Pyridine	+	+	+	114	−42
Methanol	+	−	−	65	−98
D_2O	+	−	−	101	4
90% H_2O/D_2O	+	−	+/−	101	4

20.3 Quick Identification

- *Typical ^{13}C range*: no signals below 60 ppm (for the typical carbohydrate skeleton! (exceptions are deoxy sugars and amino sugars).
- All ^{13}C signals in the range 60–110 ppm. The number of ^{13}C signals in the range 60–110 ppm can often be divided by 6 (or a combination of 5 and 6, but other signals due to added functional groups may be found in this region).
- Labile protons in the region between 3.5 and 5.0 ppm (Proof: Add D_2O, be careful when recording spectra in D_2O or MeOD!).
- One anomeric proton/carbon per sugar unit in a characteristic chemical shift range (^1H: 4.3–6.0 ppm; ^{13}C: 90–110 ppm).
- Usually no double bonds or aromatic carbons.
- Soluble in H_2O, dimethyl sulfoxide, MeOH, and pyridine.

The tools to characterize carbohydrates are summarized in Figure 20.12.

20.4 A Worked Example: Sucrose

In the following we will go through the spectra of sucrose, a typical disaccharide, and demonstrate how to identify and assign this sugar. Let us start with the 1D proton and carbon NMR spectra first (Figure 20.13). The proton NMR spectrum displays the typical spectral range for an unmodified saccharide, for example, resonances between 3 and 6 ppm exclusively. Note that the proton NMR spectrum was recorded in deuterated water, and therefore all signals from hydroxyl groups have disappeared. The signal at about 4.8 ppm is due to the residual HDO solvent line. The number of signals in the proton NMR spectrum already indicates that more than a single monosaccharide unit is present. The carbon NMR spectrum displays 12 resonances, and hence most likely two hexoses are present. This fact is also corroborated by the fact that two signals appears in the spectral range between 90 and 110 ppm, the range of the anomeric carbon signals. A brief glance at the DEPT-135 spectrum indicates the presence of *three* CH_2 carbons, so most likely one of

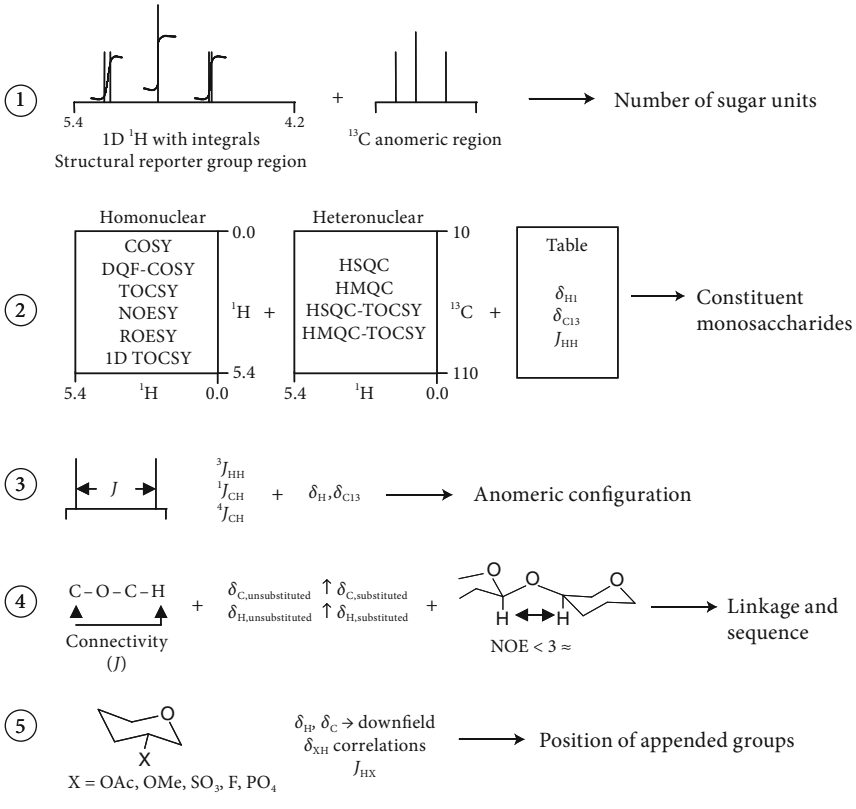

Figure 20.12 Summary of important NMR spectroscopic parameters for identifying saccharides. DQF – double quantum filtered, TOCSY – total correlation spectroscopy, ROESY – rotating-frame NOESY, HSQC – heteronuclear single-quantum coherence, HMQC – heteronuclear multiple-quantum coherence. Reproduced with kind permission from Duus *et al.* (2000) *Chem. Rev.*, **100**, 4589.

the monosaccharide units is an aldose and the other one a ketose. The DEPT-135 spectrum also indicates that the signal at approximately 107 ppm is a quaternary carbon. Otherwise all lines in the carbon NMR spectrum are nicely resolved, but much overlap is observed in the proton NMR spectrum.

Although a bit difficult to see from the spectrum, the coupling on the signal at approximately 5.4 ppm is rather small (in fact it is 3.9 Hz), which together with the typical low-field shift at 5.4 ppm indicates that the corresponding anomeric center has the α configuration. Interestingly, we do not observe another anomeric proton, and the corresponding carbon signal is from a quaternary carbon. Considering that one of the two subunits was a ketose, we can speculate at this point that the furanose (a hexose–ketose must be a furanose and cannot be a pyranose) is linked by its anomeric center to the second saccharide unit.

In the following we number all carbon signals with increasing chemical shift from 1 to 12 and use the HSQC spectrum (Figure 20.14) to annotate the proton

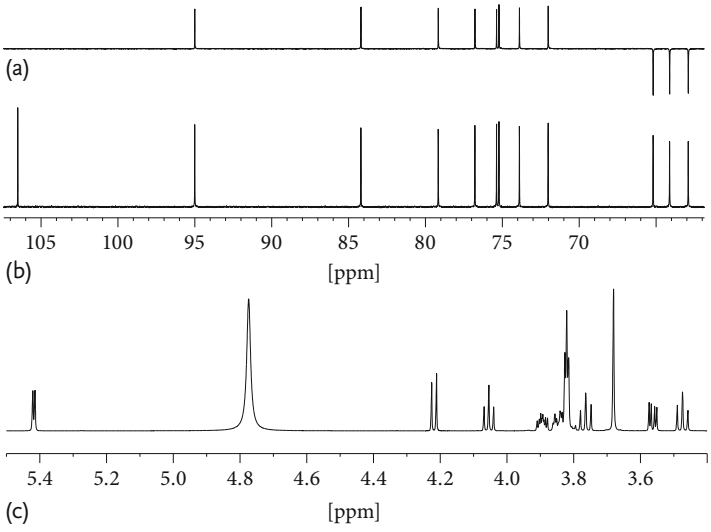

Figure 20.13 Proton (c), ^{13}C (b), and DEPT135 (a) NMR spectra of a disaccharide.

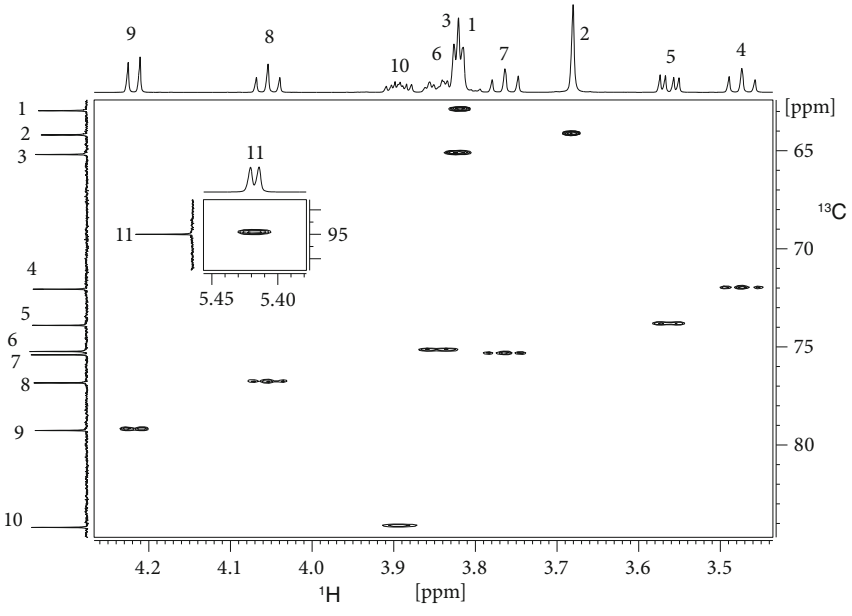

Figure 20.14 [^{13}C,^{1}H] HSQC spectrum.

NMR spectrum correspondingly. This is done quickly. One thing that we may notice at this stage is that two of the three methylene groups form an overlapping signal, a pseudotriplet, whereas the third one is a broad singlet. The pseudotriplet may be due to either overlap of two triplets or overlap of two doublets. If we look carefully at the position of the cross peaks, we notice that the two peaks are slightly

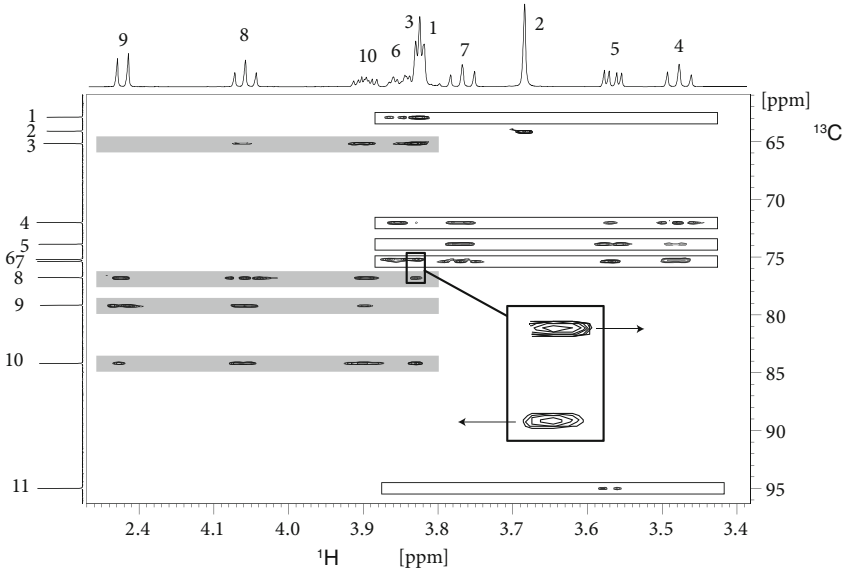

Figure 20.15 [^{13}C,^{1}H] HSQC-TOCSY spectrum. To guide the eye, resonances associated with the two different monosaccharide units are either shaded or boxed.

shifted in the proton dimension with respect to each other, and we conclude that two doublets are hidden under the pseudotriplet. At this stage we may speculate again that the singlet methylene is due to the methylene group next to the anomeric center in the furanose unit, but we need to verify this later.

Let us try to find out which protons/carbons belong to the two different monosaccharide subunits. There is a lot of overlap in the region from 3.7 to 3.9 ppm, and therefore we may not be able to trace everything through unambiguously with the COSY spectrum, and therefore we had better resort to some TOCSY-type spectrum. Actually, we will show here the HSQC-TOCSY spectrum, because this spectrum nicely resolves the proton signals along the (well-resolved) carbon spectrum (Figure 20.15):

This spectrum immediately reveals that protons 10, 9, 8, and 3 belong to one unit, and protons 11, 6, 7 (this is a bit difficult to see because the carbon signals are so close to each other, but we do not see any correlations to signals higher than 3.9 ppm), 5, 4, and 1 belong to the other unit. The methylene group 2 does not display any TOCSY-type correlations, and this is expected from the singlet nature of the signal. We will need to use either HMBCs or NOESY-type correlations to find out to which moiety this methylene group is attached.

Now, let us start to trace through the COSY spectrum (Figure 20.16). It is important to realize that the HSQC-TOCSY spectrum has told us already which signals belong to which subunit, so we can also work through regions of overlap! If we start from H11, we can trace through to H5 then to H7, from there to H4 and H6. H6 is next to H1, but we cannot really see the cross peak because H6 and H1 are

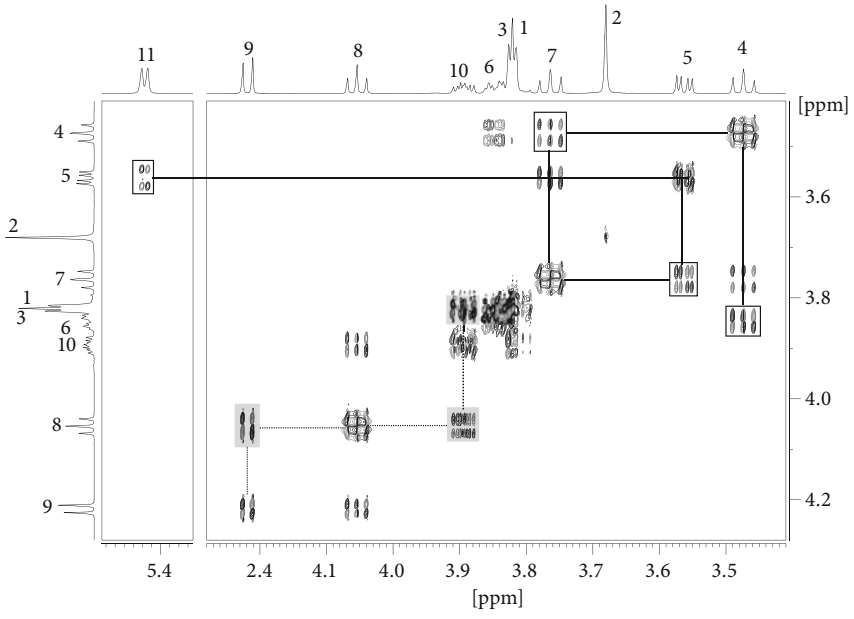

Figure 20.16 DQF-COSY spectrum.

very close to each other, so the cross peak will be almost on the diagonal and hence cannot be recognized as such. However, if we look at the HSQC-TOCSY spectrum again, we can easily see that the boxed spin system comprises either H3 or H1, but which of the two is difficult to see. We could try to find out by going straight to the computer and making an expansion of the spectrum. The inset in the HSQC-TOCSY spectrum reveals that the correlation from spins of the shaded system is to the low-field fraction of the signal 1/3, so it is H3 that is part of that spin system.

Similarly we can trace through the second spin system indicated by the shaded squares and we end up with three fragments from the analysis of the COSY and HSQC-TOCSY spectra (Figure 20.17).

We should also realize that one of the fragments already contains six correlations, indicating that one subunit is complete. Before we turn back to the COSY spectrum for a look at the magnitude of the scalar couplings to identify the stereochemistry, let us first assemble the covalent structure. Since we cannot find proper linkages

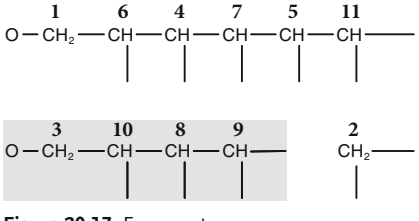

Figure 20.17 Fragments.

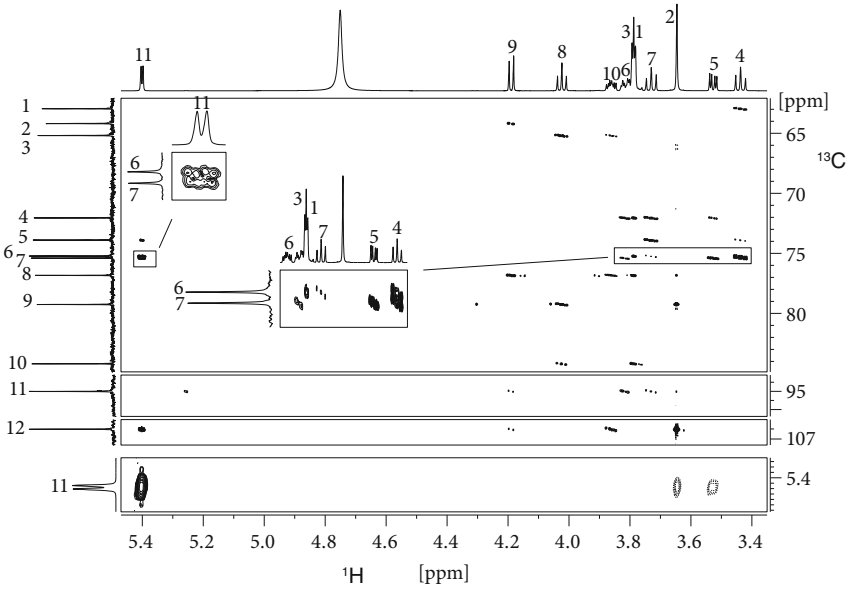

Figure 20.18 [^{13}C,^{1}H] HMBC spectrum.

for H2 from COSY or TOCSY spectra, we will have a look at possible correlations in the HMBC (Figure 20.18) or NOESY/ROESY spectra (Figure 20.16).

The HMBC spectrum displays two strong correlations from H2 to C9 and C12. C12 is an anomeric carbon, likely part of the same ring as C9. From the fact that both C2 and C3 are methylene carbons, we already know that this fragment constitutes a ketose. Hence, we need to build a five-membered ring with C12, the anomeric carbon, next to the ring oxygen. Because of this, C2 must be exocyclic. We can confirm this from the HMBC from H10 to C12. You may try to look up other HMBCs to confirm our covalent structure proposal (Figure 20.19),

Somewhat unusually, the ROESY spectrum does not help us establish the glycosidic linkage, but this is because one anomeric center does not bear a hydrogen. But the HMBCs help to establish the connectivity of H11 to C12 unambiguously.

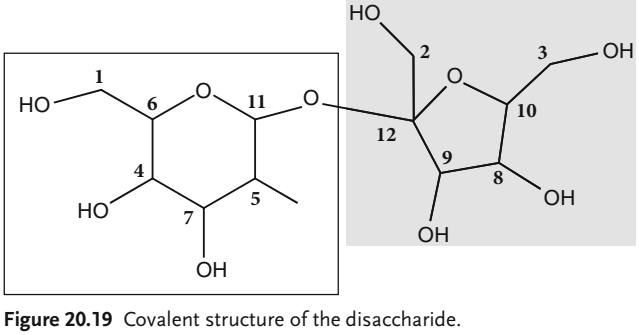

Figure 20.19 Covalent structure of the disaccharide.

Although it seems we are almost done, we still need to find out the stereochemistry at each carbon center, because at the moment we do not know which sugars are connected. Let us first turn to the easier part, the six-membered ring. In this case it is really easy. We see the two triplets of H4 and H7 with large couplings in the 1D spectrum, and we also find these large couplings in the corresponding cross peaks in the COSY spectrum. A large coupling defines the stereochemistry at that carbon plus at the two adjacent carbons as axial, because only then do we observe large couplings. We do not even need to look at the signal of H6 because the triplet of H4 tells us that it must be axial. The signal for H5 is actually a doublet of doublets with a small and a large coupling. We already know from the chemical shift of the anomeric proton at C11 that the stereochemistry is such that we observe the α anomer, and this is confirmed by the small coupling to H5. The pyranose is therefore identified as α-glucose. This is confirmed by the presence of 1,3-diaxial NOEs from H5 to H4, and from H7 to H6.

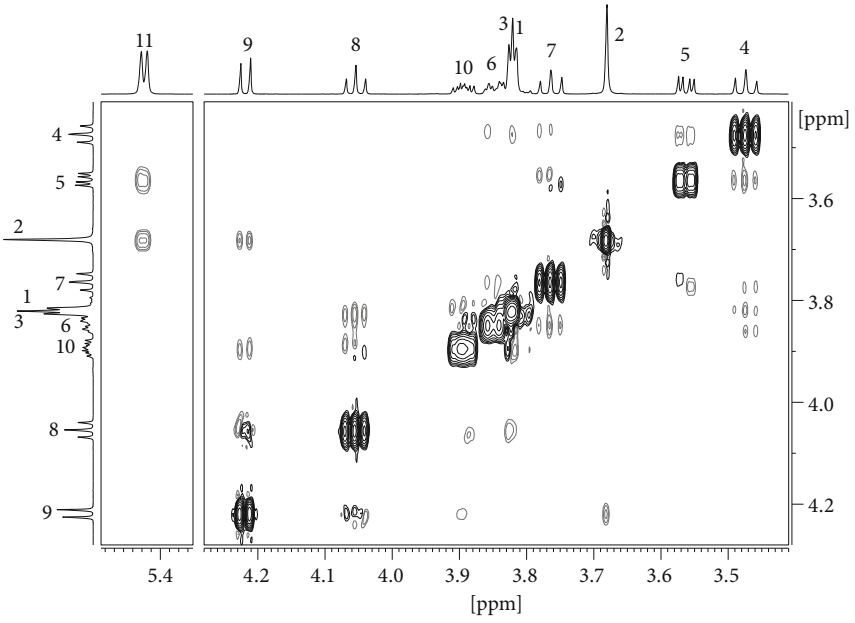

Figure 20.20 ROESY spectrum.

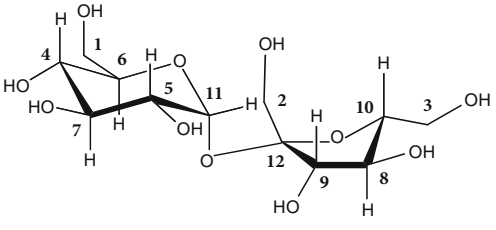

Figure 20.21 Chemical formula of the disaccharide (sucrose).

The five-membered ring in this case is also not difficult to identify. The triplet of H8 defines the protons at the adjacent two carbons as axial.

The ROESY spectrum displays NOEs from H2 to H9 and H11 (Figure 20.20). Hence, the stereochemistry shown in Figure 20.21has been established from first principles.

Further Reading

Duus, J., Gotfredsen, C.H., and Bock, K. (2000) Carbohydrate structural determination by NMR spectroscopy: modern methods and limitations. *Chem. Rev.*, **100**, 4589–4614.

Roberts, G.C.K. (ed.) (1993) *NMR of Macromolecules*, Chapter 9, IRL Press.

Jimenez-Barbero, J. and Peters, T. (eds) (2003) *NMR Spectroscopy of Glycoconjugates*, Wiley-VCH Verlag GmbH, Weinheim.

21
Steroids

21.1
Introduction

Steroids are an important class of natural and synthetic products. They are found in nature, for example, as hormones, with the male and female sex hormones testosterone and progesterone being well-known examples. Estrone, the first sex hormone discovered, was described in the literature in 1929. Imagine how complicated the structure determination of these molecules was in the early days in the absence of modern spectroscopic methods, in particular without NMR spectroscopy! Another well-known steroid is cortisone, which is synthesized in the human adrenal cortex, and is frequently used as a drug nowadays. Vitamin D_2 is a natural product that results from metabolism of the steroid ergosterol. Lack of vitamin D_2 leads to poor bone growth. Digitoxin is a cardiac glycoside that has been used to treat heart failure. Cholesterol is an important component of mammalian cell membranes. Contraceptives are synthetic steroids and are produced on a large scale.

Although the chemical nature of steroids is fairly diverse, a few modifications are found much more often than others. For example, the presence of angular methyl groups (at positions 18 and 19) is rather the norm than the exception. Ring A is often modified by an oxygen function (either a hydroxyl group or a ketone) at C3, as is the case, for example, in cholesterol. In the class of saponins, a glycosidic moiety is attached to the oxygen at C3. In many steroids, ring A is also aromatic, as in the synthetic contraceptive ethynylestradiol. Moreover, double bonds within rings A or B occur very frequently. Position 17 very often carries a (long) side chain. Figure 21.1 displays a few representative compounds from this class of natural products. We also wish to mention that most of the assignment strategy described below can be used in general for isoprenoids and is not limited to steroids.

Applied NMR Spectroscopy for Chemists and Life Scientists, First Edition. Oliver Zerbe and Simon Jurt.
©2014 WILEY-VCH Verlag GmbH & Co. KGaA. Published 2014 by WILEY-VCH Verlag GmbH & Co. KGaA.

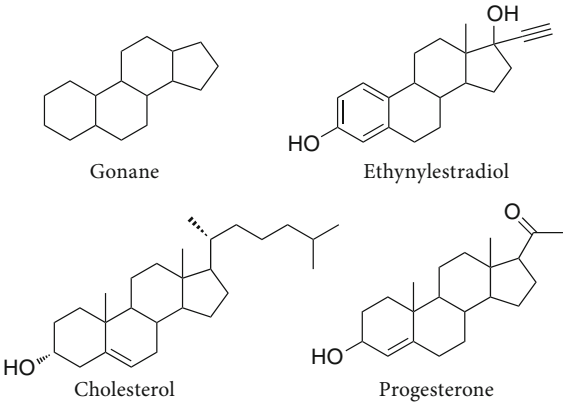

Figure 21.1 Chemical structures of some representative steroids.

21.1.1 The Chemical Nature

The steroids are characterized by a system of annealed rings. The parent compound gonane, in which three six-membered rings and one five-membered ring are fused to each other, is depicted as its C18,C19 dimethyl derivative in Figure 21.2 (note that in gonane itself the angular methyl groups are missing!).

Often methyl groups are attached at the ring-junction positions, and they are referred to as angular methyl groups. The four rings are labeled by capital letters (rings A to D). Numbering follows a somewhat confusing route, and it is advisable to check that you number your positions as indicated in Figure 21.2 in publications on those compounds.

The planar nature of the skeleton from the fused rings, particularly when rings A and B are fused trans, creates a rather flat surface. Substituents above that plane are on the α face, and those below are on the β face, as depicted in Figure 21.3.

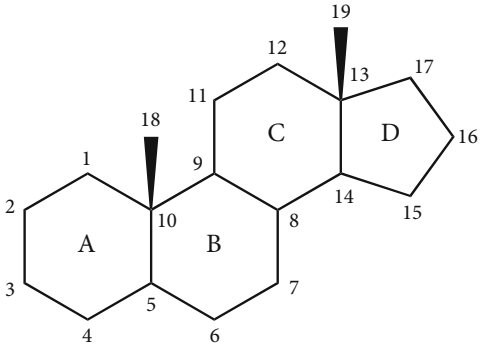

Figure 21.2 Numbering scheme in steroids. Capital letters are used to annotate the rings.

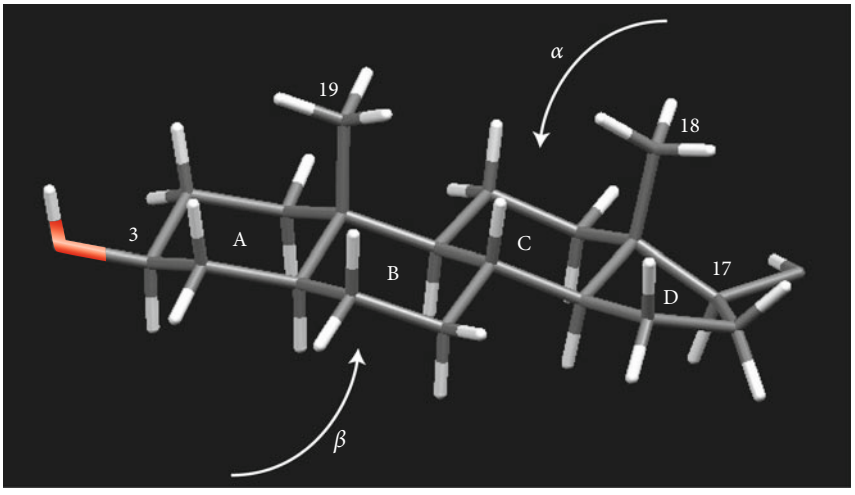

Figure 21.3 Conformation of the all-trans conformer. α and β faces are indicated by arrows.

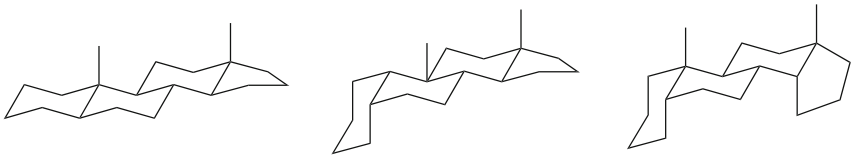

Figure 21.4 Possible ring junctions of the steroid skeleton.

Rings A and B can be fused cis or trans. Rings B and C are always fused trans, and for rings C and D again cis or trans is possible (see Figure 21.4)

21.1.2 Proton NMR Spectra of Steroids

Proton NMR spectra of steroids look very complicated. In particular, the nonfunctionalized steroids display little signal dispersion, and almost all signals are found between 0.5 and 2.5 ppm. This was a particular challenge in the 1960s, when a lot of these compounds were synthesized for their potential usage as contraceptives, and when 60 MHz spectrometers were often the highest-field spectrometers available. The region between 0.5 and 2.5 ppm observed in the spectra is often referred to as the steroid hump for obvious reasons, with often more than 30 protons found in that shift range. The occurrence of signals in different regions, for example, in the region around 7 ppm or around 5–6 ppm, indicates the presence of aromatic rings or double bonds, respectively. Similarly, signals at 4 ppm indicate the presence of hydroxyl groups. This information helps to quickly identify to which class of steroids the compound belongs. Because of the missing signal dispersion, it is highly recommended to record spectra at the highest available field. With lower-

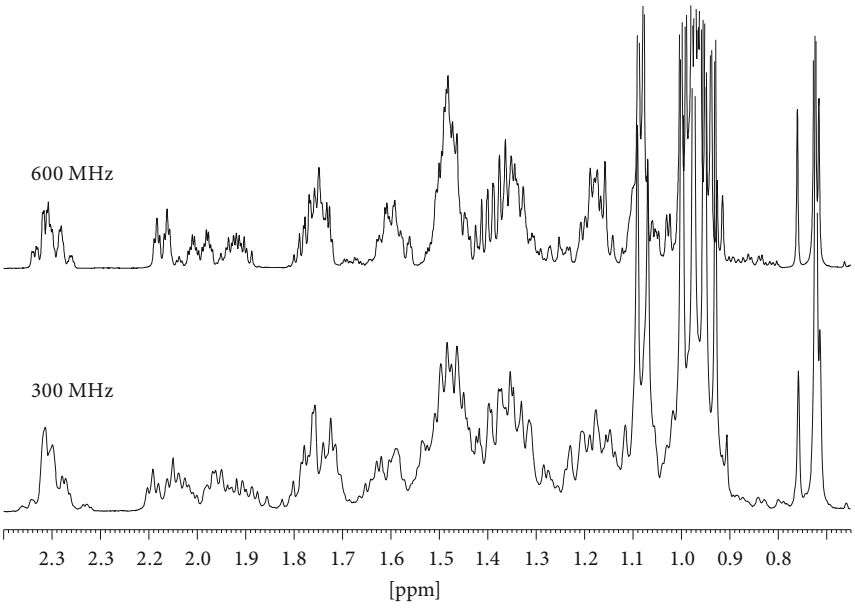

Figure 21.5 Proton spectra of β-sitosterol recorded at 300 and 600 MHz.

field instruments, second-order effects (if $\Delta\delta/J \leq 3$) will additionally complicate the analysis. Figure 21.5 displays the proton NMR spectra of β-sitosterol recorded at 300 and 600 MHz. The much better signal dispersion at higher field is obvious. For example, separate signals (and their coupling patterns) are observable between 1.87 and 2.12 ppm at 600 MHz, while the same region looks much less clear at 300 MHz.

If the signal dispersion at higher field is still poor, spectra may be recorded in different solvents. Usually, the chemical shifts are considerably influenced by the choice of solvent. In Figure 21.6 the spectra of 4-cholesten-3-one in acetone, benzene, and chloroform are displayed. The most frequently used solvent for steroids with little functionalization is chloroform; highly oxygenated compounds can also be measured in methanol. Often, a few drops of benzene are added to improve signal dispersion (aromatic solvent-induced shift effect). Another possibility to achieve better signal dispersion is addition of a *lanthanide shift reagent*, for example, Eu(fod)$_3$, Pr(fod)$_3$, or Yb(fod)$_3$ (see also Section 3.2.4). Substantial data have been accumulated for steroids, and an article by Kirk *et al*. serves as a good reference, containing data for more than 160 steroids. One of the general trends observed is that the equatorial protons are low field shifted with respect to the axial protons for diastereotopic methylene protons.

One of the initial issues (apart from recognizing that the compound of interest represents a steroid) is to identify the type of functionalization. No functionalization will result in featureless spectra, in which all proton signals occur between 0.5 and 2.5 ppm. The carbon NMR spectra will be of much more value because the

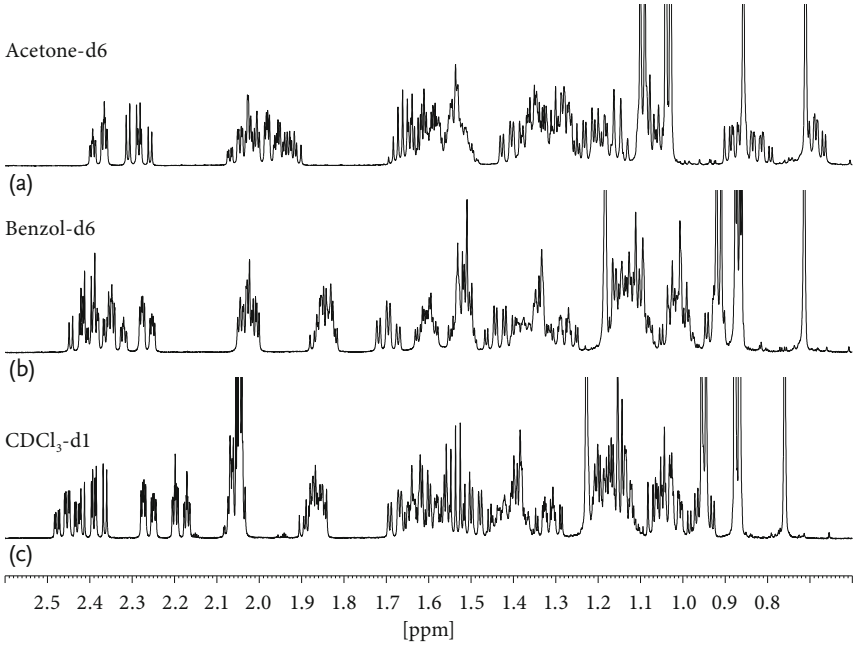

Figure 21.6 Solvent dependence of steroid ^{1}H NMR spectra. ^{1}H NMR spectra of 4-cholesten-3-one in acetone (a), benzene (b), and chloroform (c).

number of signals plus their resonance frequencies will reveal a lot. Figure 21.7 depicts proton NMR spectra of four different steroids. Unfortunately, the structures are attached to the wrong spectra. Maybe you can try to fix this?

21.1.3 Carbon Chemical Shifts

Carbon NMR spectra of steroids are much simpler than their proton counterparts because of the better signal dispersion and the lack of homonuclear couplings.

Figure 21.16 displays DEPT-90 and DEPT-135 NMR spectra of the steroid *prednisone*. Even if the proton NMR spectrum of this steroid is severly overlapped, unique carbon resonances are observed for each atom. In this particular case the combination of DEPT-135 and DEPT-90 is useful (and required!). Surprisingly, as demonstrated in the case of cholestane, carbon signals may be found as low as 50 ppm even in the absence of functional groups. The chemical shift of the angular methyl group C19 is between 11 and 19 ppm in the case of the 5α form and about 24 ppm in the case of the 5β form. A few examples are presented in Figure 21.8.

The chemical shift of 155.7 ppm, observed for C3 in estrone, is typical for an aromatized A ring to which a hydroxyl group has been attached. The double-bond carbon C5 in progesterone or testosterone is found at 170 ppm, which may be erroneously interpreted as a carbonyl carbon (ester, amide) part of some side-chain

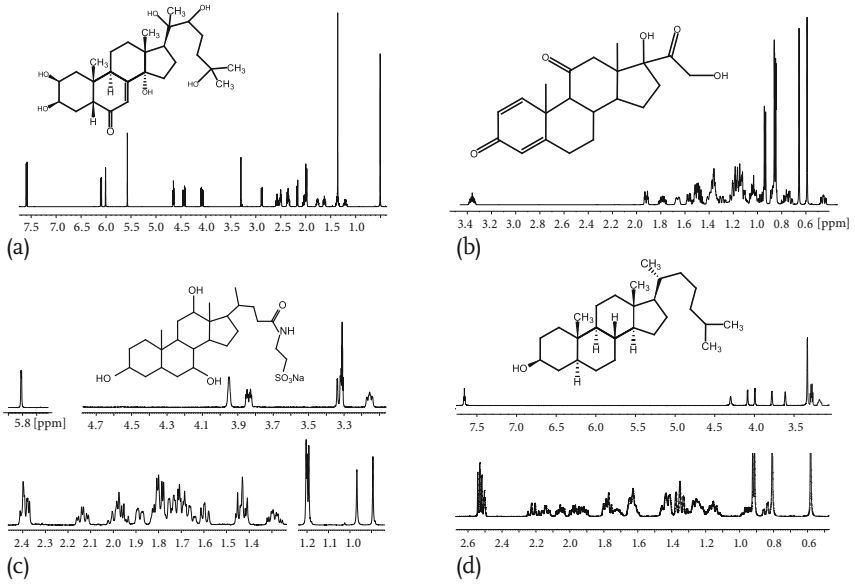

Figure 21.7 ^{1}H NMR spectra of a few steroids. The chemical structures are attached to the wrong spectra![1)]

functionality attached to C17. Carbon chemical shifts may be calculated quite accurately with the help of the increment system starting from known values of similar compounds.

21.1.4
Assignment Strategies

Assignment and hence identification of steroids is hampered by little signal dispersion. We will see in this section what experiments can used to assign compounds from this class. As for proteins and nuclei acids, it will be extremely important to use a clever strategy, and to start the assignment process from the correct position. In particular, the latter will speed up the assignment process tremendously.

Similarly to the situation for proteins, nucleic acids, or carbohydrates (biological macromolecules), signal overlap in proton NMR spectra is very strong, and any successful strategy must take advantage of the much better dispersion of carbon NMR spectra. A solution to the overlap problem may be to exploit higher-dimensionality NMR spectra (2D NMR spectra), and in particular to use ^{13}C-resolved spectroscopy. In contrast to the situation for biomacromolecules, smaller steroids do not necessarily contain smaller spin systems. In fact, the complete steroid skeleton may constitute a single spin system, and the TOCSY spectrum may reveal correlation throughout the whole molecule as shown in Figure 21.9.

1) If the structures are left at the original places the correct order of spectra is (from top left to bottom right) c, a, d, b.

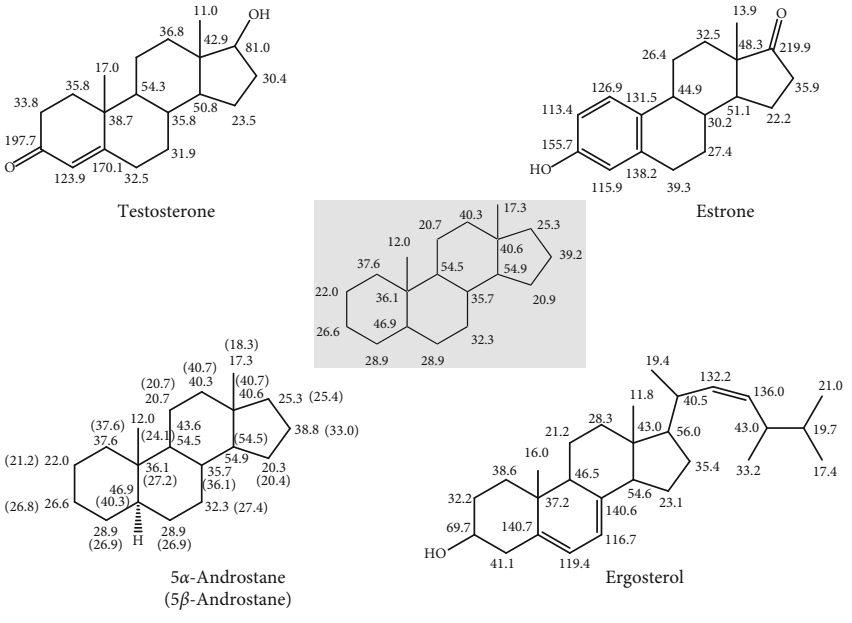

Figure 21.8 ^{13}C NMR data of selected steroids.

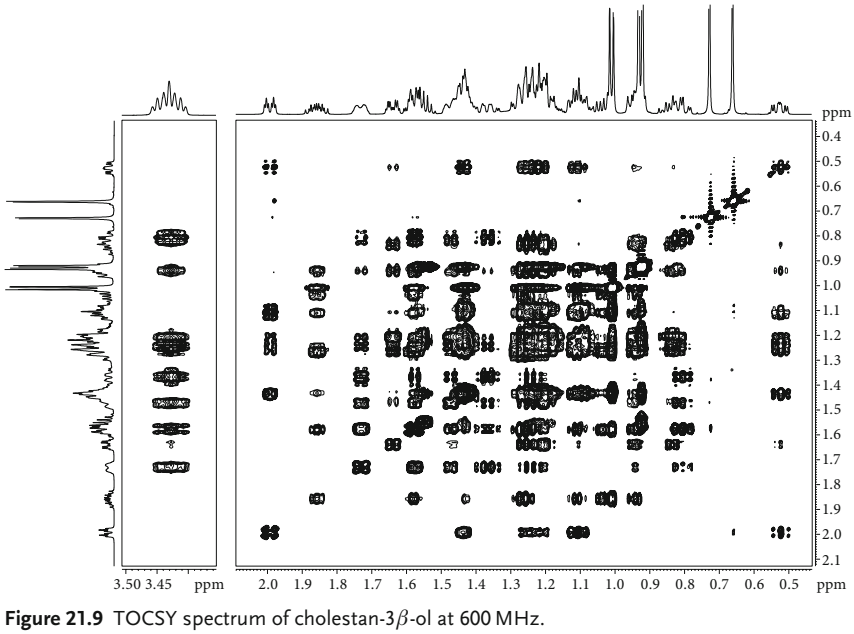

Figure 21.9 TOCSY spectrum of cholestan-3β-ol at 600 MHz.

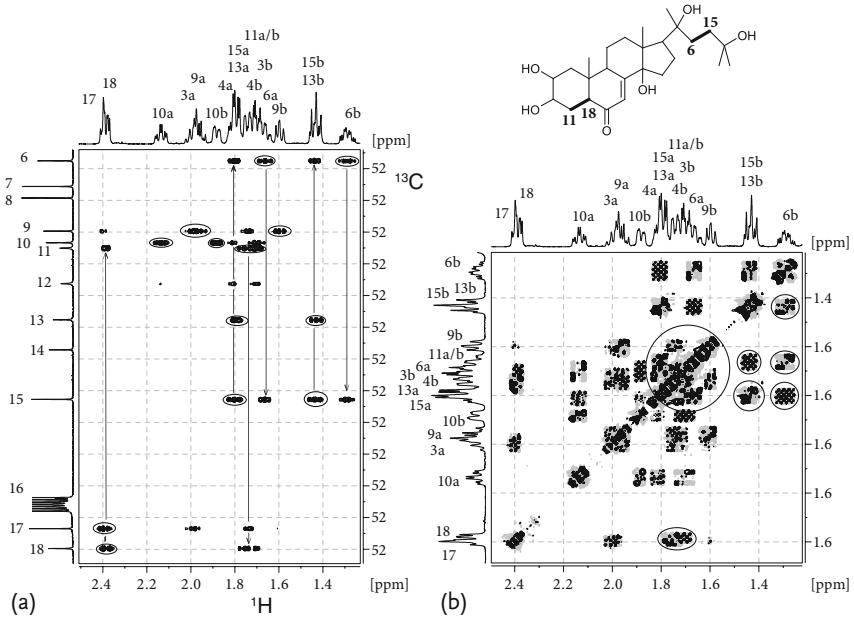

Figure 21.10 Comparison of (a) HSQC-TOCSY and (b) COSY spectra of β-ecdysone.

Constructing the molecule using sequential relationships from COSY spectra is often but not always possible, in particular when chemcial shift dispersion is small and cross peaks tend to be close to the diagonal. In that case HSQC-TOCSY spectra may be very helpful, as demonstrated in Figure 21.10.

Connectivities 11 to 18 lead to a clearly separated cross peak in the COSY spectrum, but because of overlap in that region, the assignment to H11 is ambiguous. Protons 6 and 15 have a similar chemical shift, and hence the cross peak is not clearly visible. Both cases can be easily recognized in the HSQC-TOCSY spectrum.

As is true for all macromolecules, the proper choice of the start is crucial. For steroids that contain angular methyl groups (and this is the vast majority of steroids), entry via the angular methyl groups in the HMBC spectrum is the trick! The angular methyl groups are singlet signals in the proton NMR spectrum that are usually immediately recognized, and can in most cases be distinguished from signals due to other methyl groups. Each methyl proton displays four *strong* correlations in the HMBC experiment, as depicted in Figure 21.11.

At least one correlation is to a quaternary carbon (C10 or C13). These correlations result in nice fragments that help to quickly build up the steroid skeleton using further COSY or HSQC-TOCSY correlations. We will see in the case of progesterone how this is done in Section 21.2.

The side chain, usually attached to C17, is identified and built up using standard techniques. For assignment of possible glycosidic attachments to O(C3), see Chapter 20.

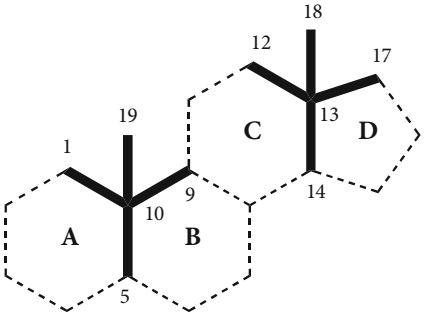

Figure 21.11 Important correlations from HMBC spectra starting from the two angular methyl groups.

21.1.5 Identification of the Stereochemistry

As for carbohydrates, stereochemistry of steroids can be established using either strategically chosen NOEs or vicinal scalar couplings. The type of ring fusion (trans–trans–trans, cis–trans–trans, or cis–trans–cis, see Section 21.1.1) is most conveniently investigated by NOEs. Figure 21.12 highlights useful NOEs that will very quickly help establish the type of stereochemistry at the ring junctions. All those distances are within the 2.5 Å range and hence give rise to strong NOEs. The presence of such NOEs unambiguously identifies the corresponding stereochemistry. Equally importantly, those distances will be so large in the alternative stereochemistry that they will not give rise to NOEs. These NOEs can be read out from 2D NOESY spectra. In principle, such information could possibly also be derived from scalar couplings, but the extraction of these couplings from the crowded spectra is difficult.

Of course the stereochemistry of any substituent can also be interrogated on the basis of NOEs. We strongly recommend the usage of 1,3-diaxial NOEs whenever possible.

Alternatively, scalar coupling constants can be used for that purpose, although similar arguments about the ease with which such couplings can be extracted apply as described above. The typical values for scalar couplings in steroids are

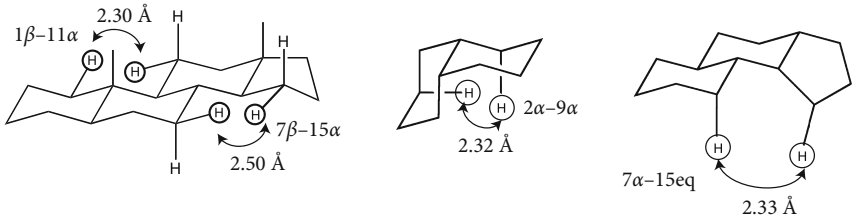

Figure 21.12 Important NOEs to determine ring junction stereochemistry.

- 12–14 Hz for geminal couplings
- 10.5–14 Hz for diaxial ^3J couplings
- 3.5–5 Hz for axial–equatorial ^3J couplings
- 2.5–4 Hz for equatorial–equatorial ^3J couplings
- less than 1 Hz for long-range couplings.

Steroids contain five- and six-membered rings. Figure 21.13 should briefly remind you of the type of ring conformations encountered in these rings.

Since steroid spectra are often so crowded that the couplings cannot be simply extracted from the 1D proton NMR spectra, *J*-resolved spectra are used. They were introduced in Chapter 17. To briefly remind you, these spectra provide the scalar couplings in the indirect dimension. The nice and really useful feature is that in the direct dimension homonuclear couplings are removed, and therefore peak overlap is substantially smaller. However, one should keep in mind that these experiments are significantly affected by strong couplings and therefore never look clean and nice as the other 2D spectra. The application is demonstrated in Figure 21.14. The highlighted signal is a doublet of doublet of doublets. Surprisingly the resolution in the indirect dimension is higher than in the simple proton NMR spectrum, and the apparent triplet is resolved as a doublet of doublets.

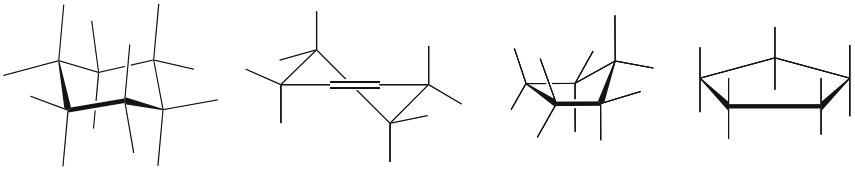

Figure 21.13 Ring conformations of six- and five-membered rings.

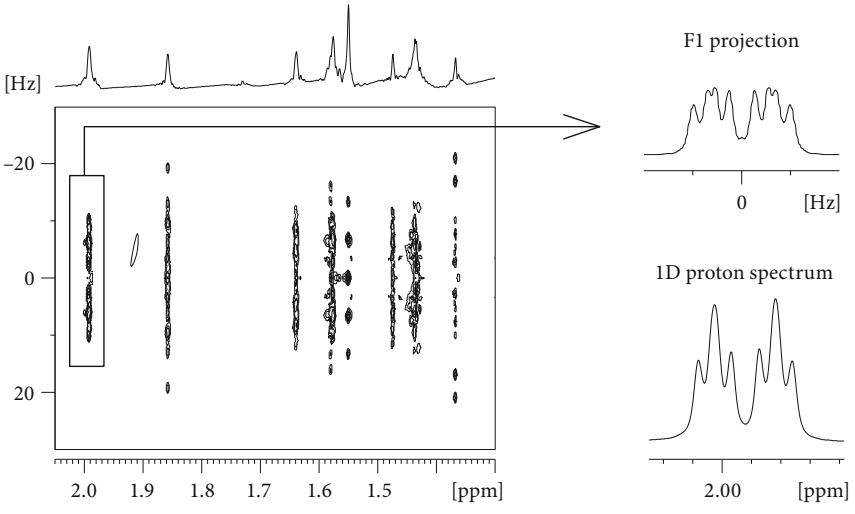

Figure 21.14 *J*-resolved spectrum of a steroide. A vertical slice is taken at 2.0 ppm (see box) and compared with the corresponding part of the 1D spectrum (right).

21.2
A Worked Example: Prednisone

As usual, let us have a first glance at the 1D proton and carbon NMR spectra in dimethyl sulfoxide as depicted in Figure 21.15. The proton NMR spectrum has a fairly unusual appearance for a steroid spectrum since signals are observed across almost the full spectral range. Our first guess when looking at the proton NMR spectrum would not necessarily be a steroid.

The carbon NMR spectrum shown in Figure 21.16 displays a lot of signals (21), and many resonances below 70 ppm. The carbon NMR spectrum at least suggests that we are looking at a fairly large molecule, and the low-field region (signals higher than 80 ppm) indicates that it is extensively functionalized. There is indication for a ketone (signals above 200 ppm, and possibly the signal at 186 ppm) as well as two double bonds, which are either close to a heteroatom or conjugated to

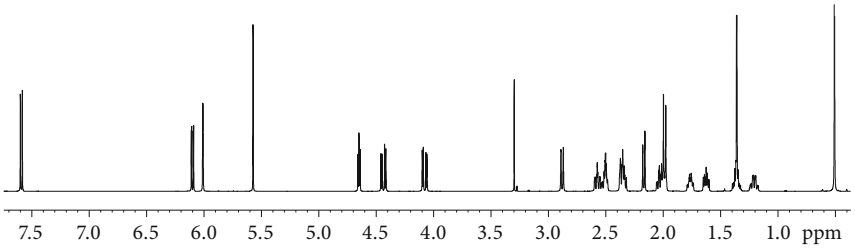

Figure 21.15 Proton NMR spectrum of prednisone.

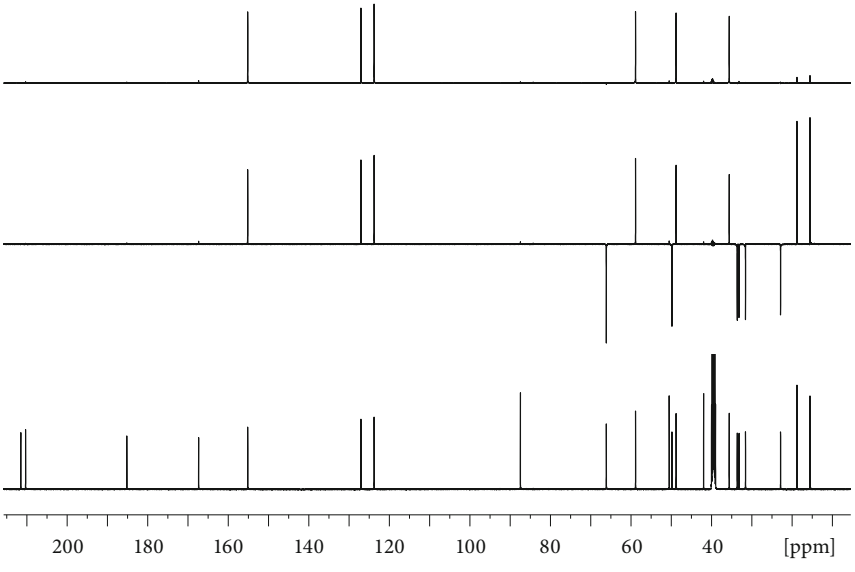

Figure 21.16 Proton-decoupled ^{13}C NMR spectrum of prednisone.

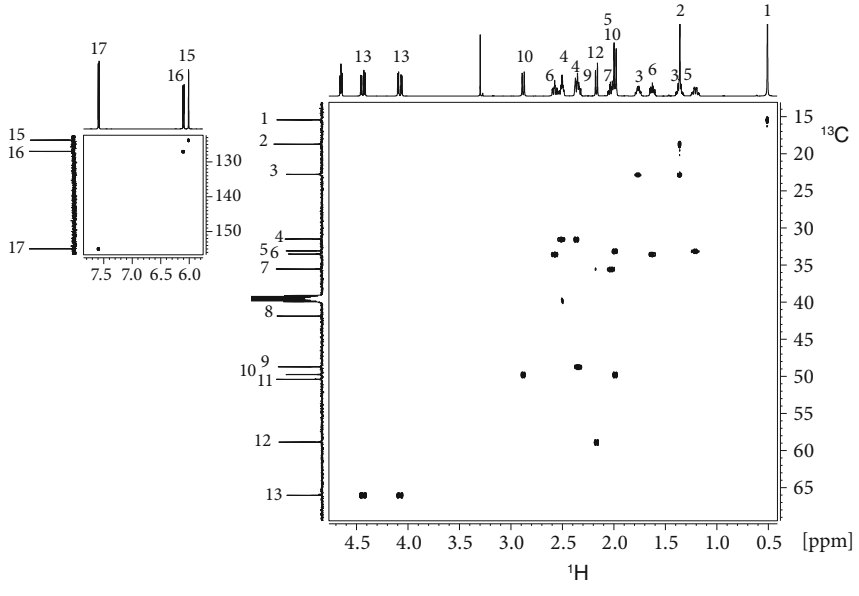

Figure 21.17 [^{13}C,^{1}H] HSQC spectrum of prednisone.

a carbonyl function. A bit unusual is also the signal at 88 ppm, a spectral range where we do not usually find signals. Now, if we go back to the proton NMR spectrum, we find indications for double bonds (signals between 5.5 and 6.5 ppm), as well as some functionalization (the signals at 4.0–4.7 ppm could be from protons attached to carbon that is next to oxygen). The doublet at 7.6 ppm falls in the aromatic range. Moreover, we observe two singlet methyl groups, and we suspect that these are angular methyl group for the moment.

We now enumerate the carbon NMR spectrum and transfer the numbering scheme to the proton NMR spectrum using the [^{13}C,^{1}H] HSQC data (see Figure 21.17). One thing we should remember later is that the low-field proton signals all correlate to low-field carbon resonances. Another nice feature from the HSQC spectrum is that in some cases we can recognize methylene protons, for example, the two proton signals at 4.0 and 4.3 ppm. We also realize that the singlet signals at 4.6 and 5.6 ppm do not correspond to CH protons, and are most likely protons attached to a heteroatom (e.g., a hydroxyl group?).

Inspection of the proton NMR spectrum indicates that two angular methyl groups are contained in the molecule. For successful assignment it is *very* important to start from their HMBCs. The corresponding HMBC spectrum is displayed in Figure 21.18.

The proton signals are highlighted by a gray box, and the strong HMBCs are indicated by small arrows. The high-field methyl group correlates to two aliphatic carbons and the signal at 88 ppm, and the other methyl group correlates to carbon signals at 42, 59, 155, and 168 ppm. The latter are clearly double-bond carbons. We end up with two fragments as shown in Figure 21.19.

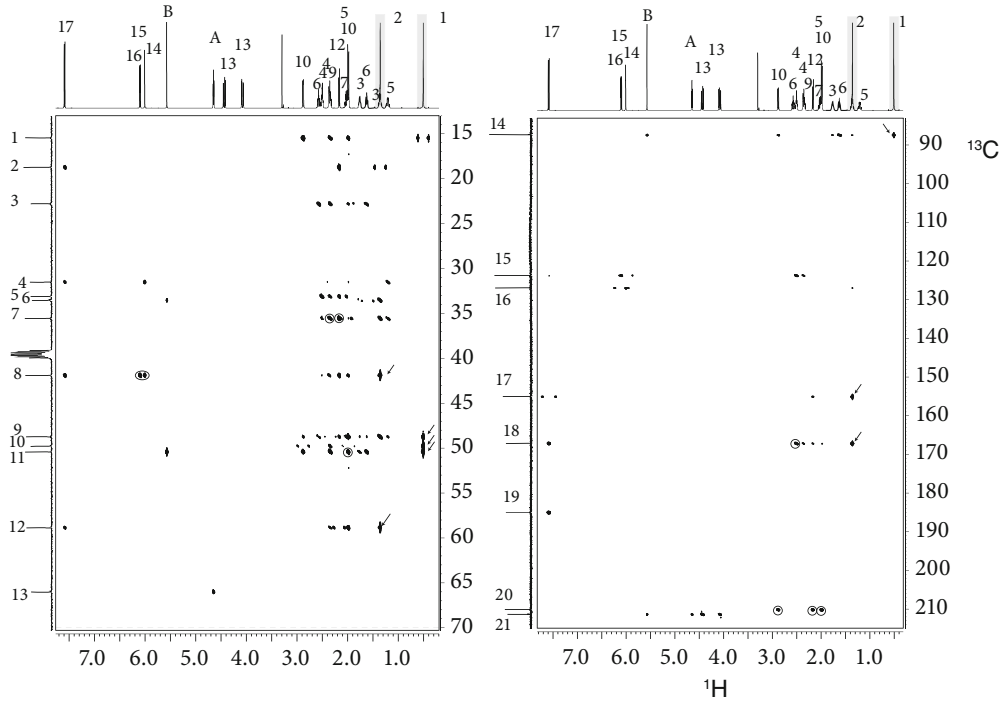

Figure 21.18 Expansions of the [^{13}C,^{1}H] HMBC spectrum of prednisone. Important correlations from the angular methyl groups are indicated by arrows.

In the case of the fragment on the right in Figure 21.19, we can decide which is the center carbon because only one carbon is a quaternary aliphatic carbon. In the case of the other fragment, both C11 or C14 could correspond to that position.

In the next step we will use experiments based on correlations via scalar couplings to link further fragments. This can be done using the COSY experiment (Figure 21.20) or the HSQC-TOCSY data (Figure 21.21). Examples for linking the C6–C3–C9–C7 fragment are indicated in the COSY spectrum, and a similar fragment comprising C12–C7–C5–C4 is outlined in the HSQC-TOCSY spectrum.

HMBCs from C7 to H9 and H12 help to link the two fragments that were derived from the angular methyl groups. We have encircled those correlations in the

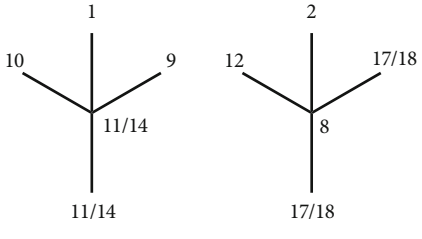

Figure 21.19 Fragments identified from the HMBCs to the angular methyl groups.

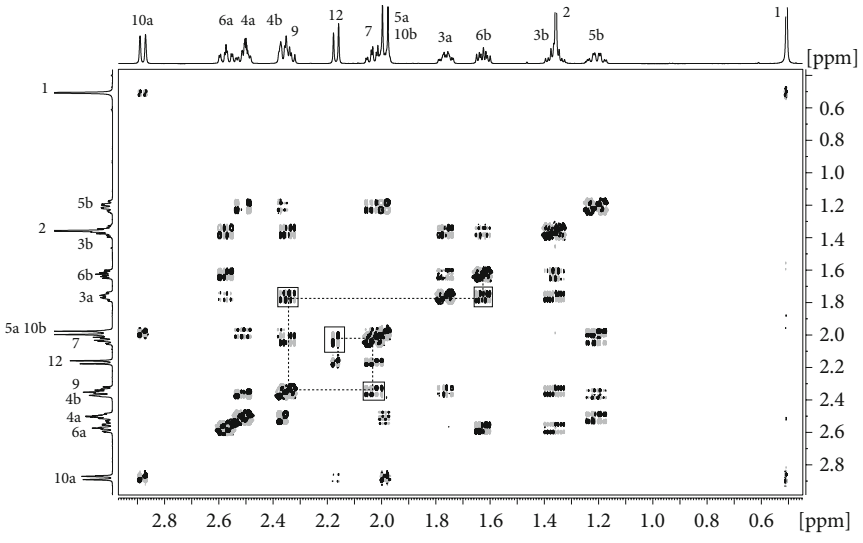

Figure 21.20 COSY spectrum of prednisone.

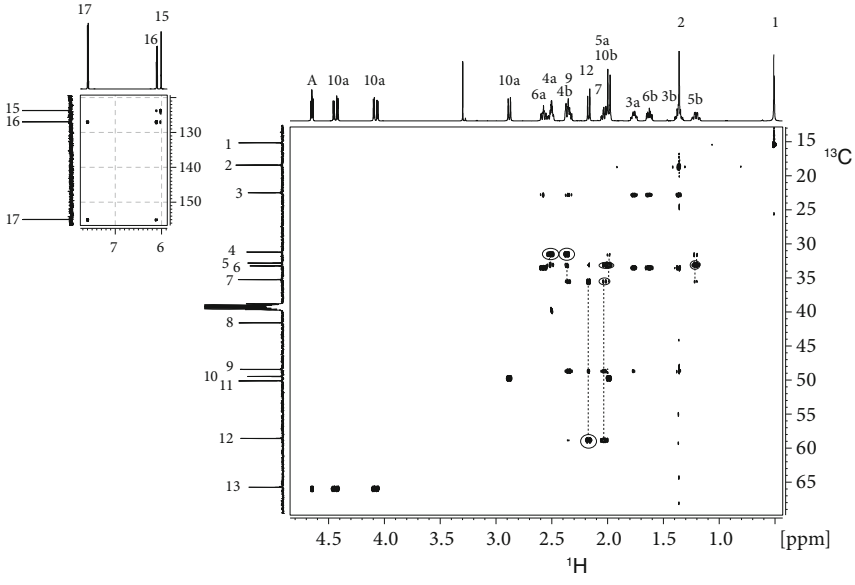

Figure 21.21 HSQC-TOCSY spectrum of prednisone.

HMBC spectrum. (The reader is encouraged to download the spectrum from the webpage www.chem.uzh.ch/static/nmrbook so that he or she can look at the expanded spectrum more clearly). Similarly, the correlation from C8 to the olefinic protons helps extend this fragment further. We can see that with the use of a few HMBCs we have already built up the core of the steroid skeleton (Figure 21.22)!

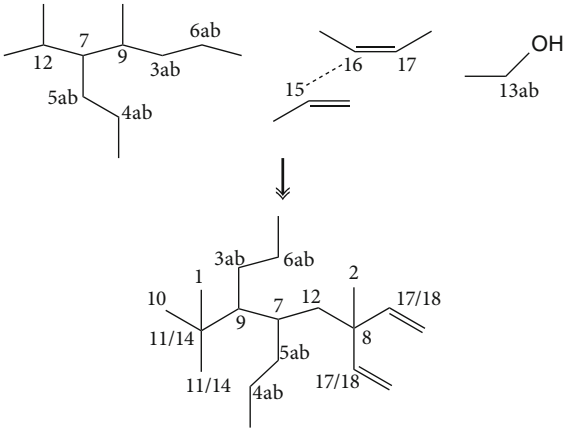

Figure 21.22 Fragments additionally identified from scalar couplings.

We can now speculate that the two double bonds are part of ring A, because it is this ring that is usually aromatized or carries multiple double bonds. But we need to verify this. We wish to emphasize again that in the end the structure needs to be firmly established on the basis of unambiguous correlations and not on chemical intuition! But let us finish the job first. H17 displays strong HMBCs to C19 and C18, indicating that the two double bonds are bridged by a carbonyl moiety. The conjugation of the ketone function is responsible for its high-field shifted position. After we have joined the fragments to form ring A, the next step must be to close ring B. C18 is a quaternary carbon, and may therefore be common to both rings. To find the important linkage, we therefore search for HMBCs of C18, and indeed the HMBC to H4 is the key correlation, which helps us to close ring B! It is important here to consider for a moment which type of correlation would help us the most, and then look at the spectra and search for it!

C12 must be the connecting point we are looking for; we already know that from the HMBC fragments that were derived from the angular methyl groups. The proton signal for H12 is nicely isolated in the spectrum, and it is a doublet. This is somewhat unusual, because we already have a scalar coupling from H7, so we would expect more. The obvious reason is that no protons are attached to the carbon connecting to C12. It could be a substituted double bond or a carbonyl moiety. Since we have three carbonyl functions in the molecule, let us quickly check that in the HMBC spectrum. C19 is already used in ring A, but H12 displays a strong correlation to C20, indicating that we should place the carbonyl in ring C next to C12! C20 displays further strong HMBCs to H10, which is part of the remaining HMBC fragment from the angular methyl group. With that information we can close ring C and we are almost done (Figure 21.23).

Unfortunately, we still do not know to which carbon the second angular methyl group is attached because both C11 and C14 are quaternary carbons. Let us look for a moment at the potential structure and try to find a strategically chosen HMBC that can be seen to only one of the two carbons! HMBCs from atoms of ring D

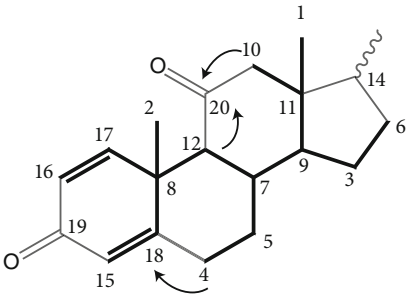

Figure 21.23 Linking the fragments by HMBCs.

will always be ambiguous, and therefore are not a good choice, but H7 could be a possibility. We need to look carefully at the spectra because H7 is close to protons 5 and 10. In fact there is a correlation from H7 to C11 but clearly not to C14, and we can close ring D. Phew, let us rest for a moment. Our advice for putting the skeleton together is to use the angular methyl groups as a start, and then use knowledge of the covalent nature of steroids to get a good idea for what to look for. Again, we need to prove our structure proposal from the correlations in the spectra; chemical intuition can *never* replace that step!

The rest is fairly easy. The H13 protons couple to signal A, which likely represents a hydroxyl group considering the low-field positions of H13 and C13. The remaining carbonyl C21 correlates to H13, B, and A. B displays a strong HMBC to C11. Considering that C6 and C3 are both methylene carbons, and hence cannot carry more substituents, we need to place both B and the carbonyl fragment on C14, thereby deriving the full covalent structure (Figure 21.24)!

Finally, we need to determine the stereochemistry (Figure 21.25). Let us first look at the ring junctions. The angular methyl group H2 displays a strong NOE to H4a, and similarly H5b displays a strong NOE to H12 and H9. The H5–H9 NOE is a bit doubtful, because H5b and H9 overlap and one needs to zoom in a lot to see what is going on. Moreover, we find NOEs from H7 to the other angular methyl group (H1), and from H1 to H6a and H3b. The stereochemistry at C14 can be decided on

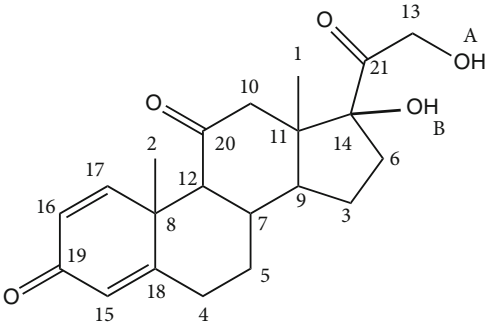

Figure 21.24 Resonance assignments of prednisone.

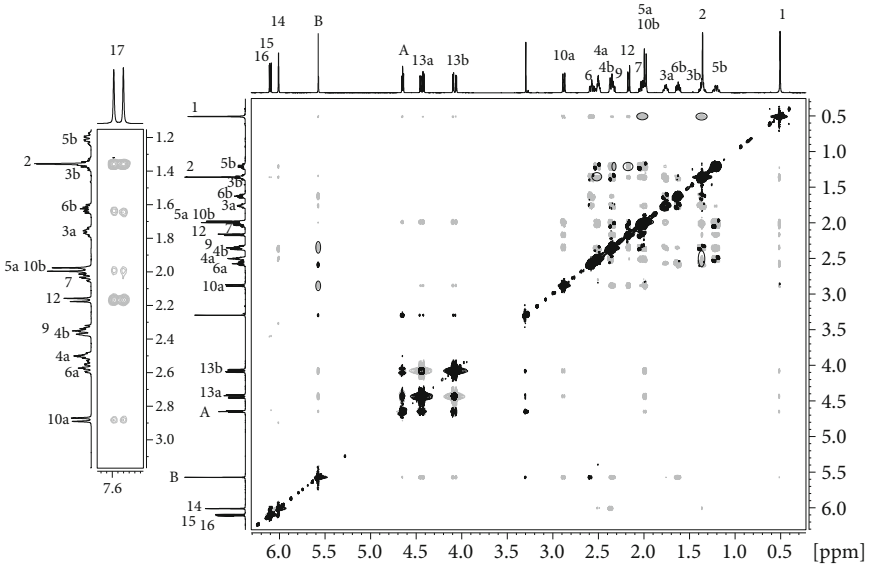

Figure 21.25 ROESY spectrum of prednisone. Correlations from the downfield signal at 7.6 ppm are depicted in the expansion on the left.

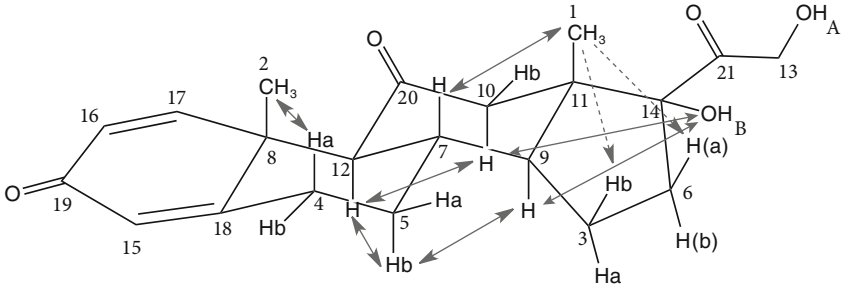

Figure 21.26 Important ROEs to determine the stereochemistry of prednisone.

the basis of the NOEs from the OH proton B (which gives rise to a sharp signal, often hydroxyl protons are broad signals and cannot be used for NOEs) to H9 and H10a.

The NOEs used are summarized in Figure 21.26, and have helped to fully establish the structure of prednisone. We have made extensive use of HMBC in this particular example. There may be many other ways to establish the assignments, but when using most of them we would have needed considerably more time to establish the structure and complete the assignments!

Further Reading

Croasmun, W.R. and Carlson, R.M.K. (eds) (1994) *Two-Dimensional NMR Spectroscopy*, Chapter 9, 2nd edn, Wiley-VCH Verlag GmbH.

Kirk, D.N., Toms, H.C., Douglas, C., White, K.A., Smith, K.E., Latif, S., and Hubbard, R.W.P. (1990) A survey of the high-field ^{1}H NMR spectra of the steroid hormones, their hydroxylated derivatives, and related compounds. *J. Chem. Soc. Perkin Trans.*, **2**, 1567.

22
Peptides and Proteins

22.1
Introduction

Peptides and proteins together with nucleic acids form the essential building blocks of life. They are part of tissues, interfere with signaling, and take part in almost all other biochemical processes. Enzymes can catalyze biochemical reactions that in their absence would be far too slow or would even never happen. Each protein has a distinct 3D structure which enables it to carry out its biological function. In the case of enzymes, this is because functional groups in their active center are presented in the optimum spatial arrangement, and side reactions are prevented from occurring because the substrate is shielded. Because of their mode of action, the structure of proteins is of pivotal importance for their function. Chemists have tried very hard to mimic the efficiency of enzymes, but most of them would agree that there is still a long way to go. Peptides and proteins have evolved in their function over millions or even billions of years, subjected to the pressure of evolutionary selection.

NMR spectroscopy has played an important role in biochemistry right from the beginning. So-called BioNMR is one of the driving forces for technical developments in the NMR field, and the largest magnets are mostly used for biochemical applications. Protein structure determination by NMR experiments has certainly helped to attract the interest of many scientists from diverse fields in this technique, and method development in that field has been honored by Nobel prizes in chemistry to Richard Ernst (in 1991) and Kurt Wüthrich (in 2002). Of course, competition from X-ray crystallography has always been fierce, and the latter technique is certainly the method of choice for very large proteins and assemblies. On the other hand, NMR spectroscopy is unique in its capability to characterize partially unfolded proteins and study their dynamics in solution. Its role in studying the question of structure, metabolism, and dynamics is ever increasing.

BioNMR is special in that its role is less in identifying the covalent structure of peptides in proteins. We will see that, while this is hardly possible for small peptides, it is a completely unrealistic task for proteins. Much better ways to establish the primary structure of proteins are available, with chemical degradation or DNA

Applied NMR Spectroscopy for Chemists and Life Scientists, First Edition. Oliver Zerbe and Simon Jurt.
©2014 WILEY-VCH Verlag GmbH & Co. KGaA. Published 2014 by WILEY-VCH Verlag GmbH & Co. KGaA.

sequencing providing much faster and reliable access to the sequence. Even when the amino acid sequence of a protein is known, resonance assignment is still a formidable task! Without sequence information this is impossible!

In this chapter we will briefly discuss the primary features of secondary structure of peptides and proteins. As is the case for all biomacromolecules, choosing the right strategy for assignment is crucial, and for proteins this is particularly the case. We will also very briefly show which method is used to assign isotopically labeled proteins, and what input is required for structure elucidation.

22.2
The Structure of Peptides and Proteins

Peptides and proteins are built from amino acids. Twenty *proteinogenic amino acids* are frequently encountered (Figure 22.1) (there are a few more that we will not consider here). Common to all amino acids except glycine is that they contain a chiral center at the C_α atom. All chiral amino acids other than cysteine are of the *S* type. The amino acids differ in their side chains attached to the C_α atoms and are classified as belonging to the class of hydrophobic residues (leucine, isoleucine, proline, phenylalanine, valine, and alanine), hydrophilic residues (arginine, lysine,

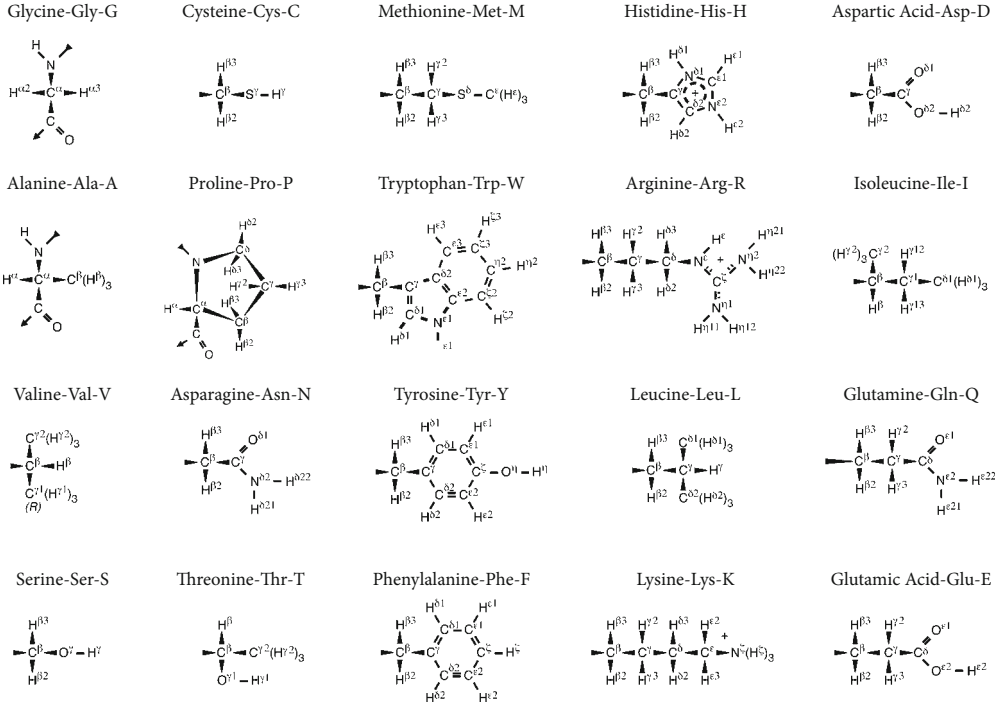

Figure 22.1 Structure and nomenclature of side chains of the 20 proteinogenic amino acids. Reproduced from Markley *et al.* (1998) *Eur. J. Biochem.*, **256**, 1–15.

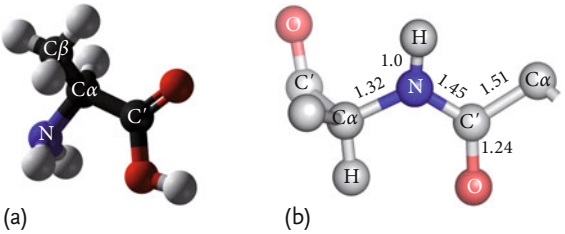

(a) (b)

Figure 22.2 Covalent structure of the amino acid alanine (a), and interatomic distances in angstroms (b).

aspartic acid, glutamic acid, serine, threonine, cysteine, asparagine, glutamine, and histidine), and amphipathic residues (tyrosine, methionine, and tryptophan). Figure 22.2a displays a 3D model of alanine. The backbone atoms comprise the amide proton and nitrogen and the α and carbonyl carbon atoms. Side chain heavy atoms are called C_β, $_\gamma$, $_\delta$, and so on. For branched side chains this can become rather complicated.

Amino acids are connected to each other via an amide bond, also called a *peptide bond*. The geometrical properties of the peptide bond are depicted in Figure 22.2b. Importantly, the N–C′ bond has partial double bond character. The peptide bond can be cis or trans, with trans usually favored for steric reasons (0° or 180° for the C_α–N–C′–C_α dihedral angle). The dihedral angles of the backbone determine the structure to a large extent. The backbone dihedral angles are called ϕ for the N–C_α bond, ψ for the C_α–C′ bond, and ω for the peptide bond. By simply rotating about backbone dihedral angles, we can alter the structure of the backbone. We will see later that this is exactly what structure calculation programs nowadays do when they try to compute the conformations on the basis of experimental constraints.

Not all combinations of dihedral angles are sterically allowed; in fact most of them lead to steric clashes. The *Ramachandran plot* displays the allowed combinations of ϕ, ψ dihedral angles for all amino acids other than glycine. Usually, in high-quality protein structures, dihedral angles are exclusively observed in the allowed regions of the Ramachandran plot (Figure 22.3).

Protein structures often contain stretches in which dihedral angles occupy similar values for consecutive residues. These stretches are called elements of regular *secondary structure*, and they are usually stabilized by *hydrogen bonds*. To a first approximation the peptide backbone can be either wound or straight. The first class is called the helical domain, with the α helix being its most prominent member. Further examples, though less common, are the 3_{10} helix and the π helix. The different types of helices are characterized by a different pitch and diameter. Figure 22.4 depicts a helical protein, the engrailed homeodomain, as well as schematic pictures of the backbone trace and the location of hydrogen bonds in helices.

Stretches occupying extended conformations are called β strands. Such strands form interstrand hydrogen bonds, giving rise to parallel or antiparallel β sheets (Figure 22.5).

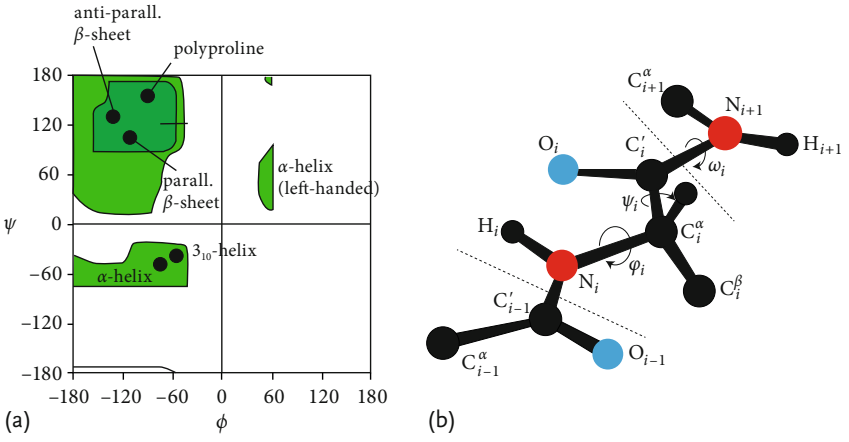

Figure 22.3 Ramachandran plot (a), and definition of dihedral angles (b).

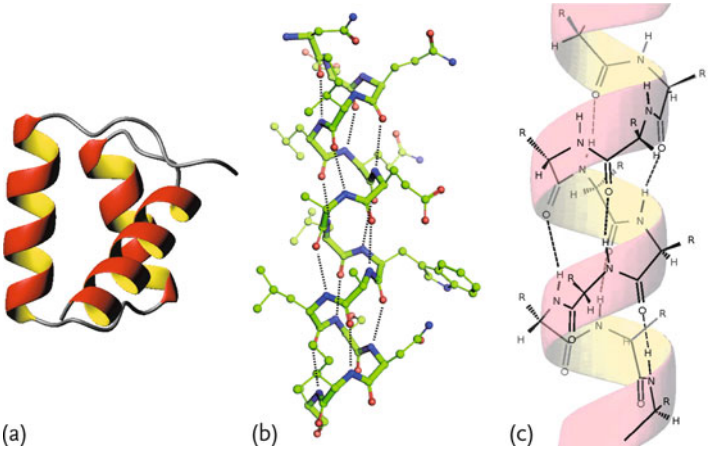

Figure 22.4 Structure of a small helical protein, the engrailed homeodomain (a), location of backbone hydrogen bonds in a helix (b), and schematic representation of helices (c).

Note that the side chains on the same strand alternatively point in opposite directions, and that side chains across the strand are on the same face and hence close in space. Figure 22.6 summarizes a few examples of helical structures, for example, peptide YY and the human prion protein, as archetypical examples of helical peptides/proteins, a member of the immunoglobulin fold, and an example of *Escherichia coli* outer-membrane proteins as β-strand proteins. Finally, thioredoxin as an α/β protein is shown.

Other regular elements are turns that reverse the overall direction of the polypeptide chain. Accordingly, β and the tighter γ turns are often found at the surface of proteins.

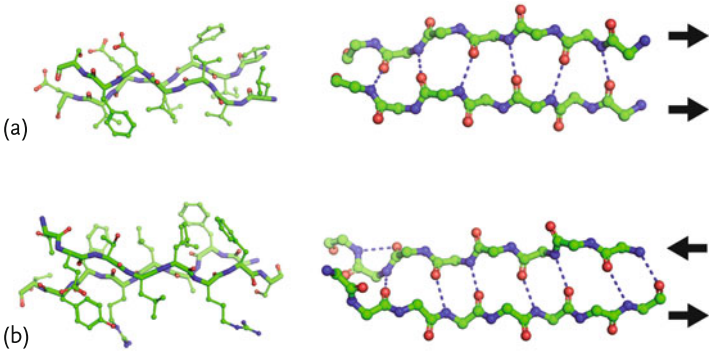

Figure 22.5 Parallel (a) and antiparallel (b) β strands.

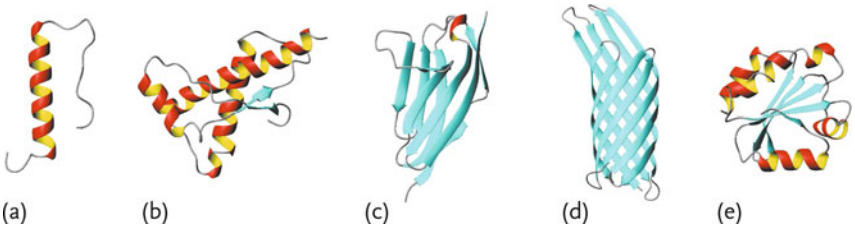

Figure 22.6 Schematic structures of peptide YY (a), the human prion protein (b), the immunoglobulin fold (c), an outer-membrane protein (d), and thioredoxin (e).

Natural or synthetic peptides often display cyclic structures, and often this is achieved by forming a peptide bond between the N-terminus and the C-terminus of the peptide chain. NMR spectroscopy has played a particularly important role in deciphering the structures of these peptides. Moreover, a lot of cyclic peptides are natural products, and some of them have gained tremendous therapeutic importance, for example, cyclosporin, which was a blockbuster immunosuppressant.

22.3 NMR of Peptides and Proteins

22.3.1 ^{1}H NMR

The 1D proton NMR spectrum of thioredoxin, a 105-residue protein, is depicted in Figure 22.7. We wish to discuss a few typical features.

Most prominent is the strong peak in the center that stems from the residual, nonsuppressed solvent (water) signal. Otherwise, the signals cover almost the complete spectral range from 0 to 10 ppm, with a noticeable exception of a small window around 6 ppm. Methyl groups are found at the right (high-field) end of the spectrum, and backbone amide protons are found at the left end. The spectrum

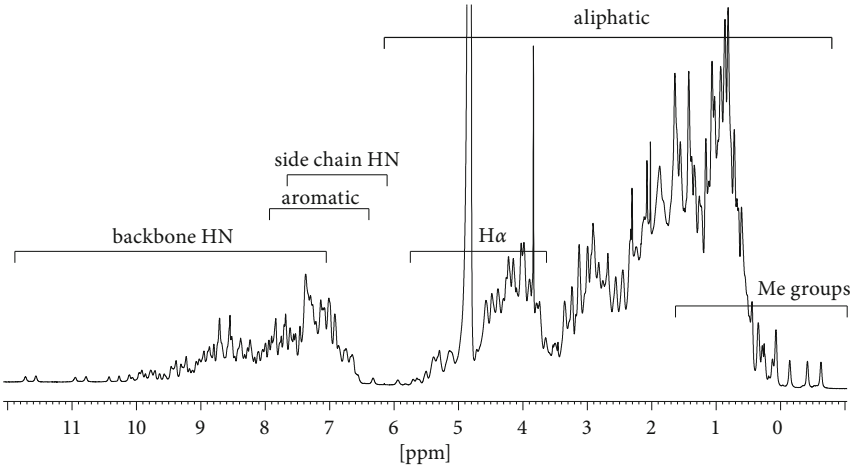

Figure 22.7 One-dimensional proton NMR spectrum of thioredoxin recorded at 700 MHz. The location of typical moities is indicated.

of thioredoxin displays characteristics of a folded protein. Unfolded peptides or proteins display reduced signal dispersion, and the spectral range above 8.5 ppm is largely devoid of signal, except for the indole protons from tryptophan residues that occur at low field (around 10 ppm). Much of the proton signal is due to labile protons, for example, protons that can exchange with the water. Backbone amide protons, side chain amide and amino protons, and hydroxyl and carboxyl protons belong to the class of labile protons. If the peptide or protein is dissolved in fully deuterated water, most of these signals will disappear. In folded proteins this may actually take some time, in particular for solvent-protected amide protons or for protons that are involved in the formation of stable hydrogen bonds. Hydroxyl protons are not usually observed in proton NMR spectra, even not in the typically used 90% normal water/10% deuterated water mixture.

Exchange of labile protons is mostly acid and base catalyzed, and the exchange rate is a minimum at a certain pH. The exchange rates in unprotected sites are depicted in Figure 22.8. As seen for backbone amide protons, exchange is slowest around pH 3.0. The gray shaded part indicates the range of exchange rates that would result in observable resonances. Each additional pH unit accelerates exchange by an order of magnitude. Smaller peptides which are unstructured, and in which amides are therefore not protected from solvent exchange, are therefore usually measured at pH 3–6. A few things can be seen very clearly in Figure 22.8. The free amino group at the N terminus will never be observable, and hydroxyl groups, except for the very rare cases when they are involved in very stable hydrogen bonds, are also not visible. For an unprotected amide, changing the pH from 3 to 7 will result in an almost complete disappearance of the amide proton signals. It should be emphasized however, that a stably folded protein can be perfectly investigated at pH 7.5, for example (it is actually much commoner to perform measurements in physiological conditions close to neutral pH).

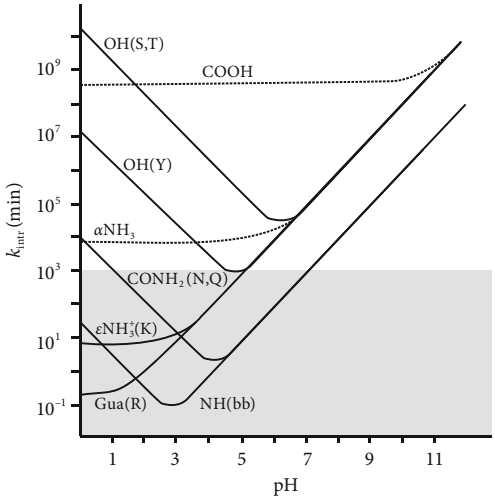

Figure 22.8 Exchange rates of unprotected protons in proteins. Note that the scale on the y axis is logarithmic.

In principle aprotic solvents such as dimethyl sulfoxide (DMSO) could also be used to avoid issues with solvent exchange. However, since DMSO is largely denaturing, and NMR spectroscopy is often used for structural purposes, DMSO is generally not a good choice. Sometimes highly hydrophobic peptides are measured in chloroform or in methanol/chloroform mixtures.

Signal dispersion of proton NMR spectra is a good indicator for whether a peptide/protein is folded or not. The anisotropic effects from the carbonyl group or in particular the aromatic side chains lead to large changes in signal dispersion. In unfolded proteins or unstructured peptides, all backbone amide resonances occur in the narrow spectral window between 8 and 8.5 ppm. If tryptophan residues are present, then additional signals will be observed around 10 ppm. In folded proteins, backbone amides will additionally be found in the range between 8.5 and 12 ppm. A similar observation can be made for the methyl resonances. In unfolded peptides and proteins, no methyl resonances are observed below 0.5 ppm, while in folded proteins, signals can be found as low as –1.0 ppm. A demonstration of the differences in signal dispersion is depicted in Figure 22.9, which displays both the low-field region and the high-field region of the proton NMR spectrum of thioredoxin and of a largely unfolded peptide pheromone. Since proton NMR spectra do not require isotope labeling, inspection of the 1D proton NMR spectrum is a convenient tool.

The *random coil proton chemical shifts* of amino acids are summarized in Table 22.1. They denote the signal location in unstructured peptides and proteins. Large differences from those values, in particular for amide protons, are observed in structured proteins.

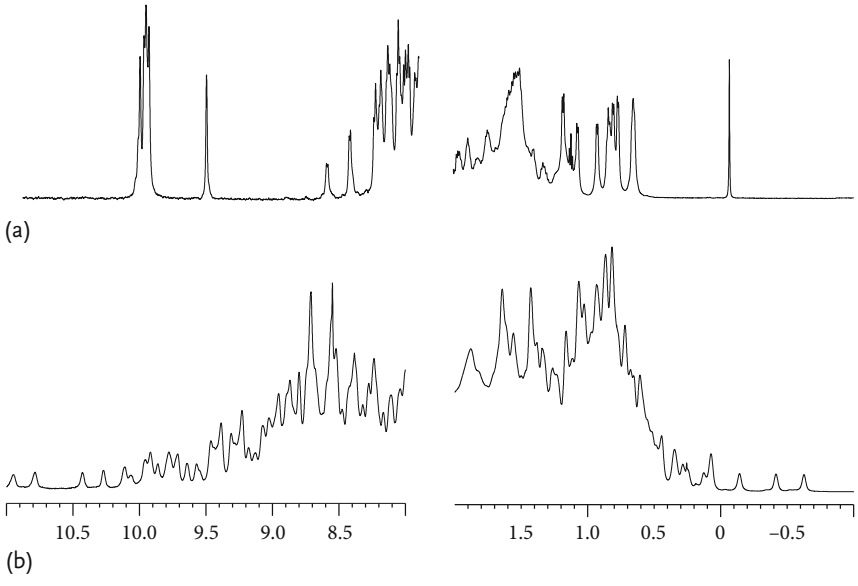

Figure 22.9 Typical expansions of proton NMR spectra of unfolded (a; peptide pheromone) and folded (b; thioredoxin) proteins.

22.3.2 ^{13}C NMR

Carbon signals of peptides and proteins are found at distinct places. Most of the resonances, including the aliphatic resonances, occur below 70 ppm. Another set of resonances at lower field is due to the aromatic ring systems (120–140 ppm) and the carbonyl resonances (around 176 ppm). Note that in the 1D ^{13}C NMR spectrum shown in Figure 22.10, the comparably large C–C couplings complicate the spectrum, which is because the thioredoxin used was ^{13}C labeled.

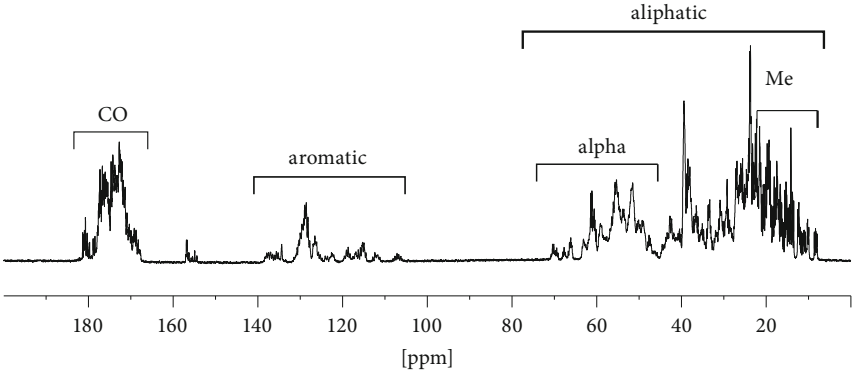

Figure 22.10 One-dimensional ^{13}C NMR spectrum of thioredoxin.

Table 22.1 Random coil proton chemical shifts for the 20 proteinogenic amino acids.

	HN	H_α	$H_\beta 2$	$H_\beta 3$	H_γ	H_δ	H_ε	
Ala	8.25	4.35	1.39					
Asp	8.1	4.76	2.84	2.75				
Asn	8.75	4.75	2.83	2.75	7.59, 6.91 (NH_2)			
Arg	8.27	4.38	1.89	1.79	1.7, 1.7	3.32	7.17, 6.62 (sc NH)	
Cys	8.31	4.69	3.28	2.96				
Gln	8.41	4.37	2.13	2.01	2.38, 2.38	6.87, 7.59 (sc NH_2)		
Glu	8.37	4.29	2.09	1.97	2.31, 2.28			
Gly	8.39	3.97						
His	8.41	4.63	3.26	3.26		8.12 (H2), 7.14 (H4)		
Ile	8.19	4.23	1.9		1.48, 1.19	0.95, 0.89		
Leu	8.42	4.38	1.65		1.64, 1.64	0.94, 0.9		
Lys	8.41	4.36	1.85	1.76	1.45, 1.45	1.7, 1.7	3.02, 3.02	7.52 (sc NH_3)
Met	8.42	4.52	2.15	2.01	2.64, 2.64		2.13	
Phe	8.23	4.66	3.22	2.99		7.30 (H2, H6), 7.39 (H3,H5), 7.34 (H4)		
Pro	–	4.44	2.28	2.02	2.03, 2.03	3.68, 3.65		
Ser	8.38	4.5	3.88	3.88				
Thr	8.24	4.35	4.22		1.23			
Trp	8.09	4.7	3.32	3.19	7.24 (H2), 7.65 (H4), 7.17 (H5), 7.24 (H6), 7.50 (H7), 10.22 (indole)			
Tyr	8.18	4.6	3.13	2.92		7.15 (H2,H6), 6.86 (H3,H5)		
Val	8.44	4.18	2.13	2.13	0.97, 0.94			

Note: sc – side chain.

When synthetic peptides or proteins isolated from nature are investigated, the sensitivity will often not permit ^{13}C NMR spectra to be measured within a reasonable time. Modern cryoprobes now enable measurements of 2–3 mM solutions of natural abundance ^{13}C within a few hours. However, such high concentrations can often not be obtained due to limited sample amounts or solubility issues. This is why protein NMR spectroscopy is mostly done using ^{13}C-labeled proteins, in which the ^{13}C content is enriched above 98%, and carbon NMR spectra can be measured in less than 15 min. As we will see later, assignment of peptide and protein resonances will usually require that the amino acid sequence is known. If this is not the case, ^{13}C NMR experiments and in particular $^{13}C,^{1}H$ correlation experiments are crucial for success. Unfortunately, this will only (if at all) work for small peptides, usually with 20 amino acids or fewer.

A typical [$^{13}C,^{1}H$] HSQC spectrum is depicted in Figure 22.11. Regions where groups of certain signals usually resonate are marked by boxes.

Some regions of the proton–carbon correlation map are very crowded, for example, the range of the C_α–H_α correlations. The C_β resonances of serine and threonine residues are well separated. The leucine C_β resonances are also observed in

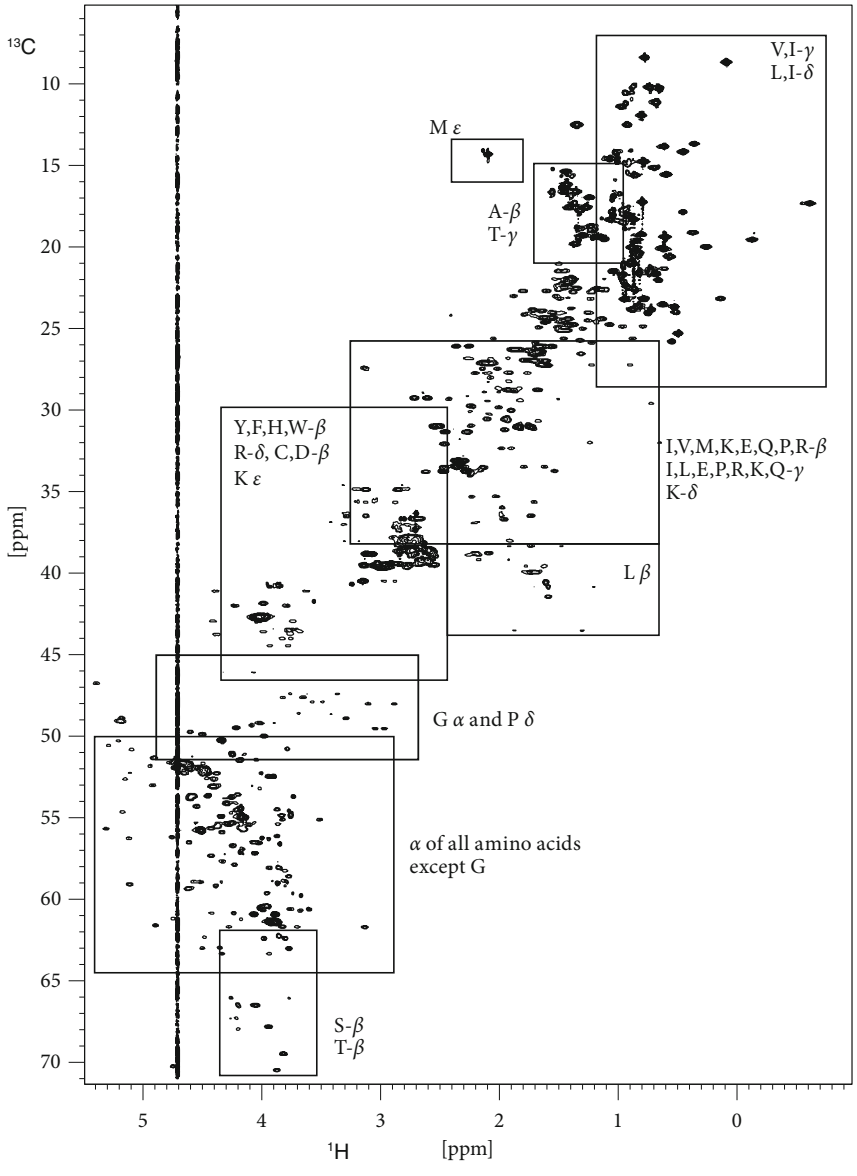

Figure 22.11 [^{13}C,^{1}H] HSQC spectrum of thioredoxin. The locations of resonances are indicated.

a distinct spectral window. Finally, the methyl groups mostly display good signal dispersion.

22.3.3
^{15}N NMR

^{15}N is a nucleus that is usually far too insensitive to be directly observed due to its low natural abundance. However, in indirect detection experiments of the HSQC-type or in ^{15}N-labeled proteins these nuclei become of much interest (see also Section 4.2). Indeed [^{15}N,^{1}H] HSQC experiments are one of the most sensitive experiments, and such experiments are usually the starting point from which resonance assignment proceeds. Alternatively, the spectra are used to decide whether a protein is amenable for detailed NMR analysis, so to say to find out whether it is well behaved or not. An [^{15}N,^{1}H] HSQC spectrum of thioredoxin is displayed in Figure 22.12.

For each amide moiety one cross peak is expected. If you remember, the N-terminal amino group cannot be detected because exchange with the water is too fast. The total number of peaks for a protein of N residues is therefore $N - 1 - x$, where x denotes the number of proline residues. However, we do see cross peaks due to side chain amides from glutamine and asparagine residues, as well as peaks due to guanidinium (arginine) moieties. Those resonances are folded when the ^{15}N spectral width is set to the usually chosen 30–40 ppm, and can be recognized because their position changes when the spectrum is recorded again with a slightly different spectral width or offset in the ^{15}N dimension.

^{15}N chemical shifts are largely determined by residue type and sequence, and much less by structure. The backbone ^{15}N chemical shifts are summarized in Table 22.2. Two features help us discriminate peaks: correlations from serine, threonine, and in particular, glycine residues are found in the upper part (low values of the ^{15}N chemical shift) of the [^{15}N,^{1}H] HSQC spectrum; side chain correlations

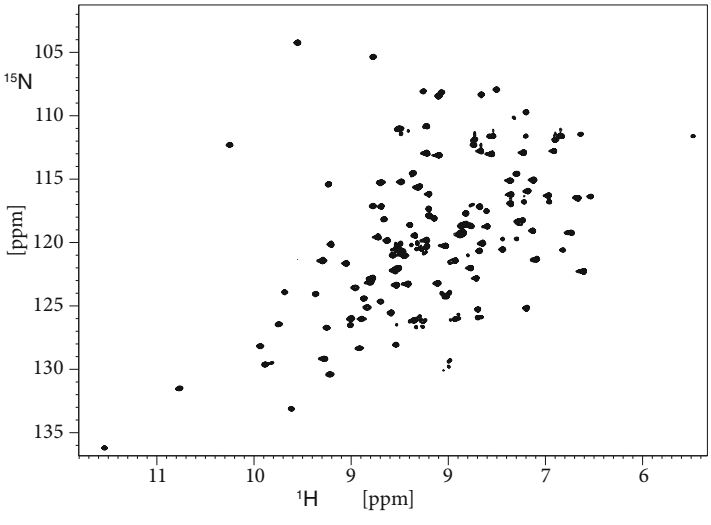

Figure 22.12 [^{15}N,^{1}H] HSQC spectrum of thioredoxin

Table 22.2 Random coil ^{13}C and ^{15}N chemical shifts.

	^{15}N	C′	C_α	C_β	C_γ	C_δ	C_ε	CO(sc)	aromatic
Ala	125.04	175.8	50.8	17.7					
Arg	121.22	175	54.6	28.8	25.7	41.7			
Asn	119.02	173.1	51.5	37.7				175.6	
Asp	119.07	174.2	52.7	39.8				178.4	
Cys	118.84	175.7	57.9	26					
Gln	120.46	174	54.1	28.1	32.2			179	
Glu	120.23	174.8	54.9	28.9	34.6			182.8	
Gly	107.47	172.7	43.5						
His	118.09	172.6	53.7	28					135.2(C2), 118.7 (C4), 130.3 (C5)
Ile	120.35	174.8	59.6	36.9	25.4, 15.7	11.3			
Leu	122.37	175.9	53.6	40.5	25.2	23.1, 21.6			
Lys	121.56	174.7	54.4	27.5	23.1	31.8			
Met	120.29	175	53.9	31	30.7		15.0		
Phe	120.69	176	57.4	37					136.2 (C1), 130.3 (C2/C6), 130.3 (C3/C5), 128.6 (C4)
Pro		175.2	61.6	30.6	25.5	48.2			
Ser	115.54	172.6	56.6	62.3					
Thr	111.9	172.7	60.2	68.3	20				
Trp	122.08	176.7	56.7	27.4					108.4 (C3), 112.8 (C7), 137.3 (C8), 127.5 (C9), 128.0 (C1), 130.0 (C2/C6), 117.0 (C3/C5), 156.0 (C4)
Tyr	120.87	176	57.4	37					
Val	119.31	174.9	60.7	30.8					

usually appear in the upper-right quadrant of the spectrum, although this part may also contain signals from the backbone. Figure 22.13 shows an expansion of the region of side chain amide moieties from a protein. Side chain amides can be recognized by the fact that *two* correlations are found on a horizontal line (the two amide protons must correlate to the same nitrogen frequency). Moreover, side chain amide peaks often show a second, small peak on top, which looks a little bit like a "flame." These additional peaks stem from the fact that measurements are performed in 90% H_2O/10% D_2O. On an NH_2 moiety, 10% will in fact be NHD, and the presence of deuterium will result in an isotope effect that shifts the nitrogen frequency to lower values.

In the spectrum, the three encircled peaks are not due to NH_2 moieties and can be easily recognized as such.

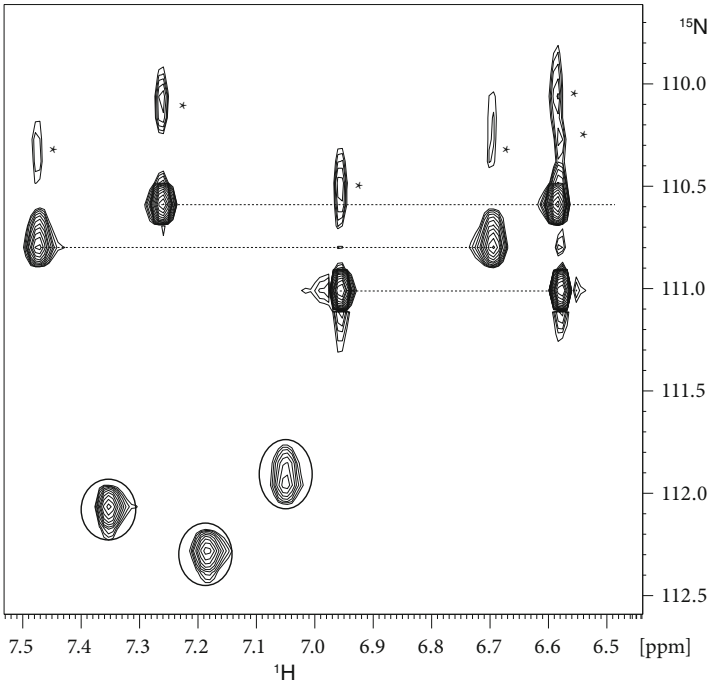

Figure 22.13 Expansion of the side chain region of an [^{15}N,^{1}H] HSQC spectrum. Signals from NHD species are labeled with a star. Signals from backbone resonances are encircled.

The random coil ^{13}C and ^{15}N chemical shifts of proteins are summarized in Table 22.2.

22.4
Assignment of Peptide and Protein Resonances

Assignment of peptide resonances is a prerequisite for determining the structure of a peptide or protein. Without the assignments, the measured nuclear Overhauser effects (NOEs) cannot be converted into distance limits because it is not known which two spins are correlated. The methods for assignment of resonances of proteins and peptides are very different. Small polypeptides and proteins can be assigned using unlabeled peptides and classic 2D homonuclear NMR experiments. For proteins this method fails for two reasons: the first is the increasing complexity of the spectra, which leads to much signal overlap, so tracing through spectra unambiguously becomes impossible; the other, and even more important, point is that larger proteins have broader lines, which reduces the sensitivity of homonuclear correlation experiments, which exploit the comparably small ^{3}J scalar couplings. We will describe the methods for both labeled and unlabeled peptides and proteins separately in what follows.

22.4.1 Peptides

Peptides will usually be either derived from chemical peptide synthesis or isolated from natural sources, and therefore be unlabeled. We have seen a 1D NMR spectrum of thioredoxin in Figure 22.7 already. But how do we know which proton belongs to which position in the polypeptide? It is of prime importance here to follow a clever protocol for assignment, otherwise we will never accomplish this task or it will take ages.

The procedure that is mostly used nowadays is called the sequence-specific sequential resonance assignment, and was developed in the 1970s by a few groups, in particular in the laboratory of Wüthrich. The procedure consists of the following basic steps:

- Recognizing and classifying the individual spin systems on the basis of through-bond couplings.
- Linking the spin systems in sequential order by through-space couplings to produce longer fragments
- Mapping the identified fragment onto the sequence and closing the gaps in between.

Assigning the spin systems in peptides is similar to assigning the spin systems in oligosaccharides. In the latter, the individual sugar rings form separate spin systems that need to be linked via NOEs or via heteronuclear multiple-bond correlations (HMBCs). In the case of peptides, the individual spin systems are the amino acids just like the monosaccharide units present the individual spin systems in oligosaccharides. In the case of carbohydrates, we used the anomeric protons as the signals with the least resonance overlap, and tried to identify the rest of the rings from TOCSY correlations starting from these. In the case of peptides, the spectral region with the least overlap is the range where the backbone amide signals occur (roughly 7–10 ppm). We will therefore zoom into a region of the TOCSY spectrum that in one dimension contains the amide protons and in the other dimension the full aliphatic range (0–5 ppm). This is schematically depicted in Figure 22.14.

This part of the spectrum helps us identify the type of spin system to which that particular amide moiety belongs. Rarely it allows us to directly recognize the particular amino acid type. In Figure 22.14 we see four spin systems, and on the right we see the structures of the four amino acids that form these spin systems. The system on the left, labeled as 1, contains two signals in the methyl region, and therefore must be valine, leucine, or isoleucine. From the number of peaks it is most likely that it is a valine residue. However, we need to emphasize that not always all correlations are seen in the TOCSY spectrum. The spin system labeled as 2 has the unusual feature that two signals occur in the α region, and no signals occur outside. This is clearly a serine residue (the β protons are downfield shifted due to the presence of the hydroxyl group). In principle this is also the case for threonine, but then we should find another signal in the methyl range. Spin system 3 could, in principle, be at least seven different amino acids, and we just assign it to a group

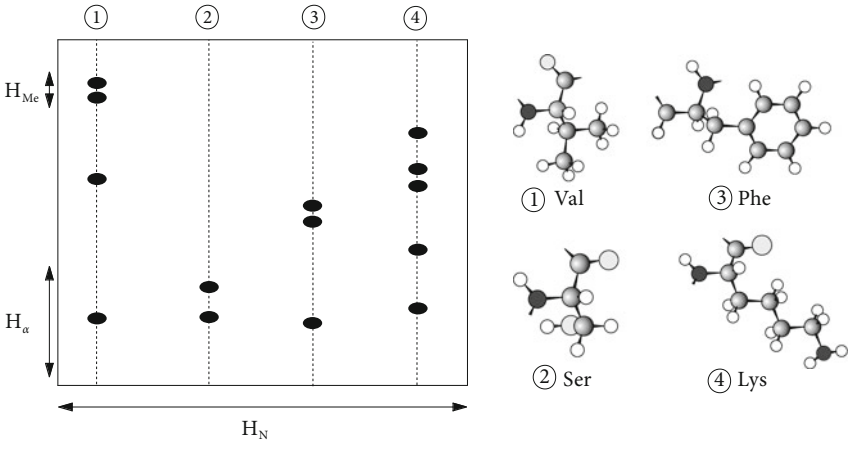

Figure 22.14 Typical appearance of valine, phenylalanine, serine, and lysine spin systems in the TOCSY spectrum.

composed of these. Spin system 4 contains a longer side chain. From the number of correlations, it could be any of the long side chains of leucine, isoleucine, methionine, arginine, or lysine. But the additional correlation at lower field indicates it is either lysine or arginine. If this were just a pentapeptide (remember we do not see the first residue because solvent exchange broadens the amino signal beyond detection), in this case we could assign them sequence specifically right away. But if this were part of a longer peptide, we would not know the exact assignments at this point, but rather the principal nature of the side chains (a long side chain, a side chain with a methyl, a short side chain, etc.) Figure 22.15 summarizes the principal appearance of the side chains in TOCSY spectra in this region of the spectrum. They are assigned to certain classes. Side chains within one class cannot be distinguished, but side chains from different classes can be. Note that the proline side chain is also depicted for completeness, but no correlations are observed in that part of the spectrum due to the absence of an amide proton in proline.

The next step is to link the spin systems in sequential order. We have seen that any experiment that transfers magnetization across scalar couplings does not help transfer the magnetization across the peptide bond, and so we need to use NOEs for that purpose. Which NOEs are useful depends on the type of secondary structure present in the segment of interest. In extended chains (this is β strands but also unstructured regions) we preferably use NOEs between the amide protons and the α protons. As indicated in Figure 22.16, an α proton is close to its own amide proton and to the amide proton of the *preceding* residue (but *not* to the amide proton of the following residue!). To see these correlations we need to zoom into the spectral region, which in one dimension displays the amide region and in the other the α proton region. We will see at least two strong correlations for each amide signal in this range. Moving along horizontal lines (that means keeping the α frequency

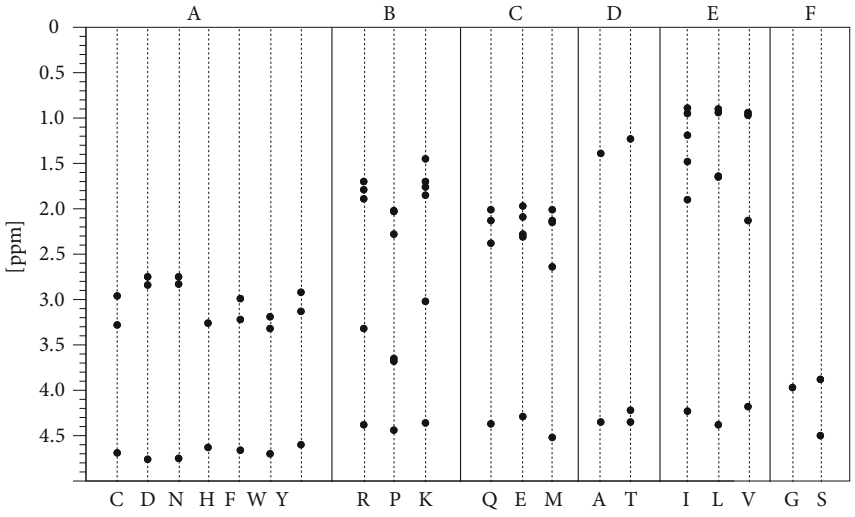

Figure 22.15 Typical appearance of TOCSY lanes displaying all side chain resonances as computed from the random coil chemical shifts.

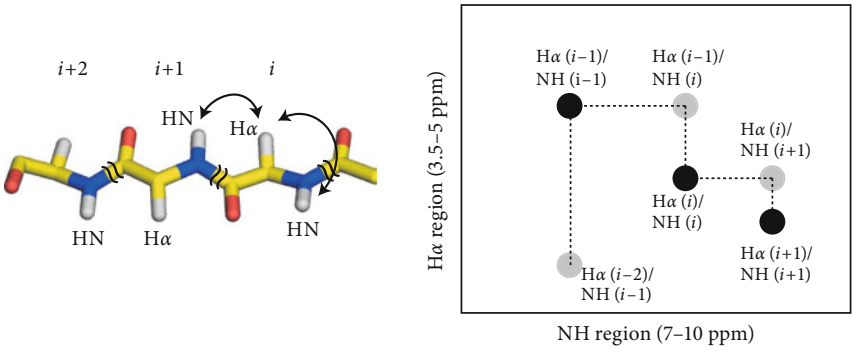

Figure 22.16 Assignment procedure for strands or unstructured parts displaying the connectivities between α and amide protons.

the same) will allow us to hop onto the next amide proton, which is the preceding one in the sequence. By this "*NOESY walk*" we can trace through the sequence.

If the amide proton of interest is part of a helical stretch, it is more convenient to use another set of correlations. As depicted in Figure 22.17, every amide proton in a helix is close to the sequentially neighboring amide protons (note that in this case we see correlations in both directions in the sequence). To find these correlations we need to zoom into a spectral region that contains amide signals in both dimensions, and then we can walk through the sequence. In the absence of resonance overlap this works very nicely!

Once we have linked the spin systems, we posses information such as "a long spin system is followed by one with a methyl group, which is followed by a short

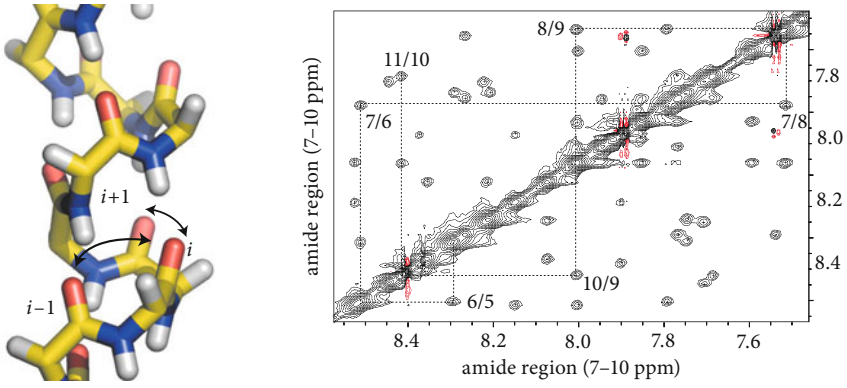

Figure 22.17 Assignments in helical stretches.

spin system, which in turn is followed by a serine residue." Once the fragments are long enough, we can unambiguously map fragments onto the amino acid sequence and make real (sequence-specific) assignments!

We still need to fully assign the side chains, which can be tricky sometimes. In principle we know from the TOCSY experiments which resonances belong to the same spin system, but we do not know which of the correlations are the β, γ, or δ protons. For that purpose we need to use the COSY experiment, because in this experiment we observe correlations between only vicinal protons, for example, from H_α to H_β but not to H_γ or H_δ. Another important issue is linking the aromatic ring spin systems onto the rest of the side chain. This again needs to be done by NOEs. In the case of phenylalanine, NOEs from the β protons to the closest ring protons (H_δ) are used, and these are usually strong enough. For histidine, tryptophan, and tyrosine, similar NOEs starting from the β protons can be used.

22.4.2 Proteins

Experiments which transfer magnetization along homonuclear scalar couplings do not work well on proteins. Instead a battery of 3D triple-resonance NMR experiments (see also Sections 17.5 and 13.8) are used in which magnetization is transferred along the much larger one-bond couplings. This requires full ^{13}C and ^{15}N labeling, and therefore proteins must be obtained from recombinant sources via protein expression. Mostly this is done using *Escherichia coli* as the expression host and labeled minimal medium (containing ^{13}C-glucose and ^{15}N-NH_4Cl as the sole carbon and nitrogen sources) as the growth medium. Figure 22.18 compares the transfer in a COSY experiment (70 ms) with the transfer in an HCCH-TOCSY experiment (21 ms), highlighting the much higher efficiency of the heteronuclear path. Moreover, the transfer is independent of the dihedral angle. For a small peptide a coupling of 7 Hz is okay for transfer, but for a protein with a 20 Hz line width all magnetization will be lost due to relaxation (remember to transfer magneti-

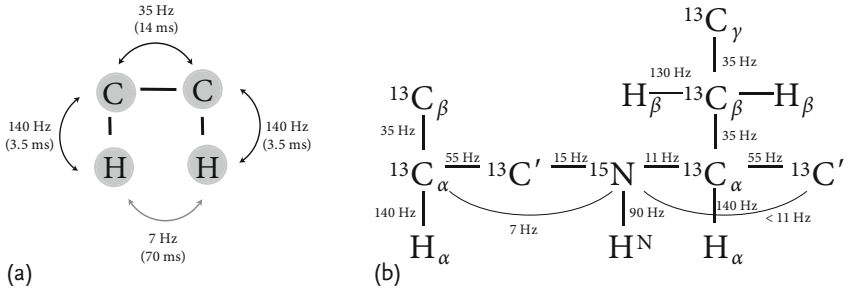

Figure 22.18 Transfer pathway in unlabelled (gray) and labelled (black) HCCH fragments (a). Typical scalar coupling constants for ^1J couplings in labeled proteins (b).

zation efficiently using a certain scalar coupling, the line width must not exceed that coupling). Figure 22.18 also specifies the various one-bond couplings, most of which are large. The larger the couplings, the more efficient such a coupling can be used for magnetization transfer. Note that the transfer efficiency additionally heavily depends on the transverse relaxation times of the nuclei involved.

Resonance assignment using triple-resonance methods comprises two parts: backbone and side chain assignment. Figure 22.19 displays the most frequently used experiments for obtaining backbone assignments. The nomenclature of these experiments is straightforward. An HNCO experiment correlates the amide proton and nitrogen with the carbonyl carbon of the preceding residue. An HN(CA)CO[1)] experiment is a similar experiment, but because it uses the C_α nucleus as a relay, it correlates with the carbonyl of its own residue. The combination of the two experiments will display the correlations to its own and the preceding carbonyl and thereby link fragments. Similarly the HNCACB experiment correlates the amide moiety with the C_α and C_β nuclei of its own and its preceding residue, while the HN(CO)CACB experiment does the same but this time exclusively with the C_α and C_β nuclei of the preceding residue. The combination of the four experiments helps link fragments via common C_α and C_β or C′ frequencies.

Side chains are mostly assigned using HCCH-TOCSY-type experiments. For details of this work, the reader is referred to reviews in that field or special monographs.

Excursus 22.1: Structure Calculations from NMR Data

The input for structure calculations are upper distance limits and dihedral angle restraints. Distance restraints are usually derived from NOEs, and dihedral angle restraints are usually derived from scalar couplings and NOEs. NOESY spectra are integrated and the NOE peaks are assigned. The volume of the cross peak between two protons is proportional to d^{-6}, where d is the distance be-

1) A nucleus in parentheses indicates that it is used for transfer but that its chemical shift is not recorded during the experiment.

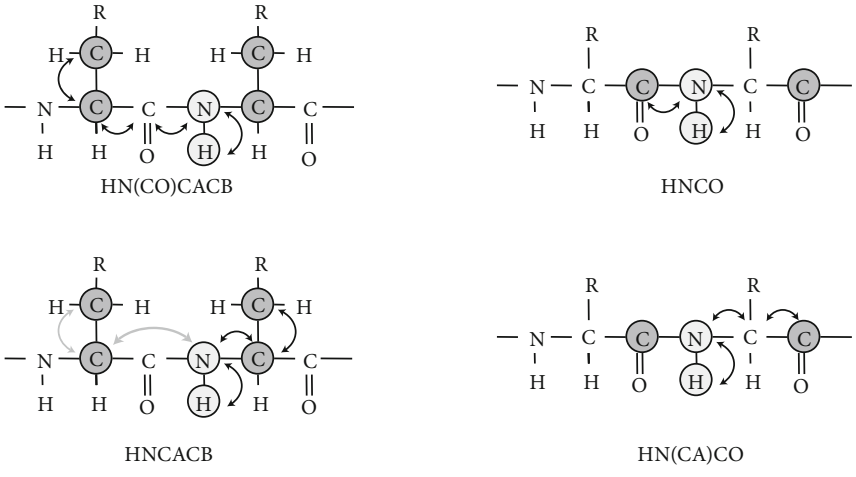

Figure 22.19 Transfer pathways in triple-resonance experiments most commonly used for backbone assignments.

tween them. The presence of a certain NOE puts an upper limit on the distance between the two protons, because if the distance were larger, the NOE would not have been detected or would not be so strong. No explicit lower limits are used but the sum of the van der Waals radii of the two protons. Astonishingly, although the distance limits used are fairly imprecise, the structures are well defined in the end, and this is true mainly because the system is so overdetermined (each proton position is defined by a large number of NOEs, sometimes more than 20 restraints per residue).

The structure calculation programs initially start with random conformers, and perform energy minimizations on those, usually using restrained molecular dynamics (see Figure 22.20). In the molecular dynamics runs a simplified force field is used (one that does not treat electrostatics very well but can be computed quickly). To account for the NMR restraints, additional potentials reflecting the upper distance limits and the dihedral angle restraints are introduced. Since the molecular dynamics algorithm tries to minimize the energy of the system in the end, it will change the positions of atoms at each step such that not only van der Waals contacts and other classical force field parameters are optimized, but also the upper distance limits are fulfilled. A big danger of such an algorithm is that it will fall into the nearest local minimum instead of into the global one. To circumvent this problem, a large number of structures are computed. To do this a random number generator is used to produce, for example, 100 different random conformers which all have the correct amino acid sequence and the correct local geometry in terms of bond distances and bond angles, but for which dihedral angles are chosen arbitrarily. For each of these 100 conformers, a separate restrained molecular dynamics calculation is per-

formed. The 20 lowest-energy conformers of the 100 conformers are selected. For analysis they are usually fitted for best superposition of backbone atoms.

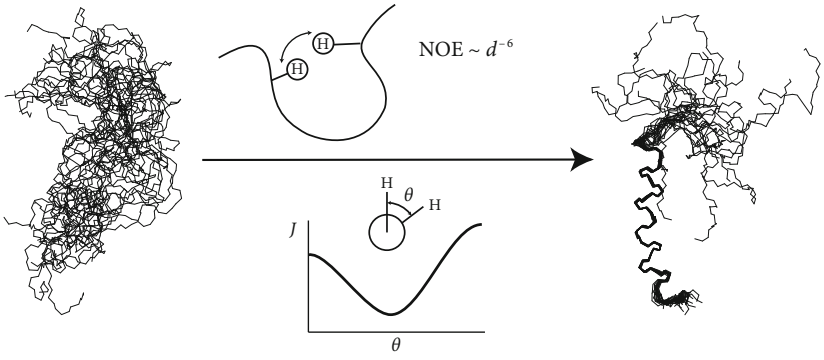

Figure 22.20 The structure calculation converts an ensemble of random confomers into (hopefully) correctly folded conformers when distance (top) and torsion angle (bottom) restraints are applied during the structure calculation.

The assignment procedure comprises a lot of manual wok, but much improvement has been seen recently in trying to use computers for that task. In particular, when assignments are known, NOESY spectra can be annotated automatically nowadays. This may sound like a trivial task, but in fact it is not, because even if the resonance frequencies of all protons are known in large proteins there will be many assignment possibilities for each NOESY cross peak because of resonance overlap. Clever algorithms decide on the basis of preliminary structures in an iterative fashion what the correct assignments are.

22.5
A Worked Example: The Pentapeptide TP5

In this section we will look at a small pentapeptide as an example. The peptide is called TP5, and is part of the larger protein thymopoietin. It has some interesting pharmacological effects, but for us it will serve to demonstrate how peptides are assigned from homonuclear data. TP5 is a textbook example for which assignments can be derived easily and quickly. Longer peptides will be much more complicated, but it is useful to understand how the whole procedure works. We will see that it is rather different from the way we looked at other compounds, because in this case we know the covalent structure already.

An important difference is that we usually have no access to ^{13}C NMR data (although in this case it would have been possible), and no HSQC or HMBC spectra. But let us start now and see how we proceed best. The sequence of TP5 is Arg-Lys-Asp-Val-Tyr. Because of rapid exchange of the N-terminal amino group, we expect

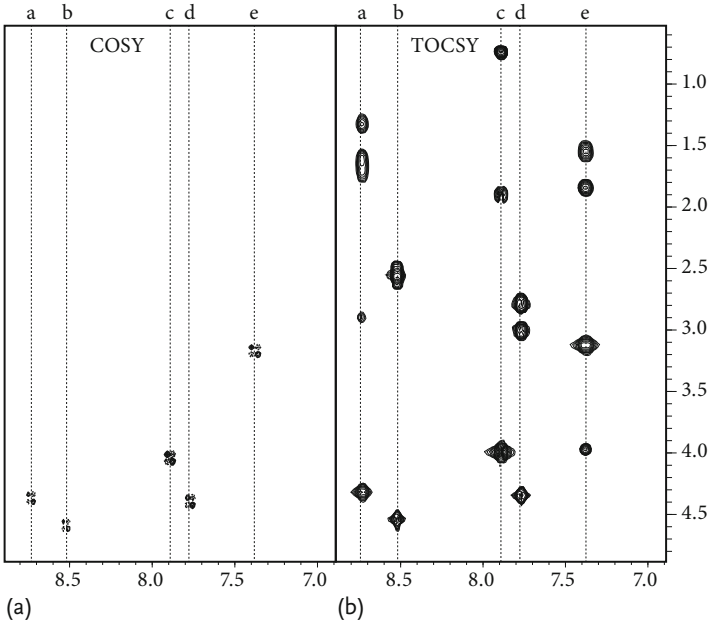

Figure 22.21 COSY (a) and TOCSY (b) expansions of spectral regions important for identifying spin systems.

to see four spin systems in the TOCSY amide region. Figure 22.21 displays side-by-side the TOCSY and COSY spectra of TP5 in that spectral window. Apparently, we can recognize five instead of four spin systems, which is a bit puzzling, and we will need to find an explanation for this later. At this point we notice that this is unusual.

Among the five spin systems we recognize two short ones (labeled as b and d), which most likely comprise an α proton and two β protons. Additionally we find a spin system (labeled as *c*) which contains a methyl group (a cross peak at approximately 0.8 ppm in the ^{1}H dimension). And we see two longer spin systems (labeled as *a* and *e*), both of which contain cross peaks around 3 ppm. If we look at our primary sequence, it becomes clear that spin system *c* must be Val-4 (this is the only amino acid in the sequence that contains a methyl group). The two long spin systems *a* and *e* are Arg-1 and Lys-2, and the short ones must be Asp-3 and Tyr-5.

Let us come back to the puzzling observation that we see five spin systems although we should only be able to observe four. Obviously we can see Arg-1, and the reason is that we can observe this spin system because arginine has a side chain NH from the guanidinium group (the H_ε), which is visible (see Figure 22.21). If we look at the COSY expansion, we realize that it is not the peak at 4.0 ppm from the TOCSY lane that we observe in the COSY spectrum but the peak at 3.1 ppm instead. This is the case because the scalar coupling from H_ε leads to H_δ and not to H_α. Because of this, spin system *a* is likely to be Lys-2 and spin system *e* is likely to be Arg-1.

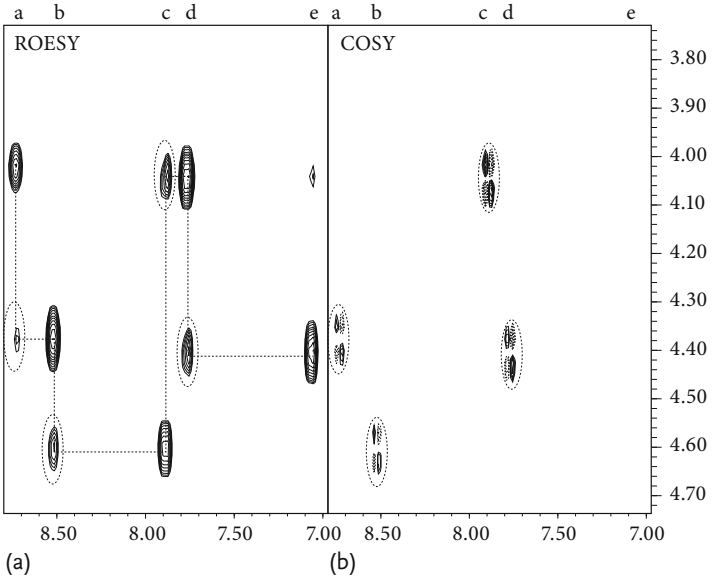

Figure 22.22 ROESY (a) and COSY (b) expansions of the fingerprint region used for sequential assignments.

After identifying the spin systems in the molecule, we need to link them in sequential order. TP5 is an unstructured peptide, and therefore we should look at the fingerprint (HN–H_α) region of the ROESY spectrum. To be able to distinguish intraresidual from sequential NOEs, we have plotted the COSY spectrum next to the ROESY spectrum. We could start with lane *c*, which we have identified as Val-4. The encircled peak is also observed in the COSY spectrum and therefore represents the HN(4)–H_α(4) cross peak. Moving horizontally from this resonance to the right (keeping the H_α frequency constant) leads to a correlation to system *d*. Since we see $H_\alpha(i)$–HN($i + 1$) correlations, this must be Tyr-5. If we move down vertically, we end up on the cross peaks that we also observe in the COSY spectrum, the H_α(5)–HN(5) peak. Again we can walk horizontally to the right and end up on HN of residue 6. Oops! There is no residue 6 in our molecule! So what NOEs do we observe there? If we look more closely at the TOCSY spectrum in Figure 22.21, we realize that there is no spin system at about 7.1 ppm! Obviously, this is not an amide proton! The important lesson to learn here is not to automatically proceed without critically reflecting (generally good advice in science). Anyhow, we can connect the beginning of the peptide sequence to Val-4 by moving to the left from the H_α(4)–HN(4) cross peak. By the way, it is pure coincidence that spin systems in this case line up from the left to the right in sequential order. The path we follow is indicated by the dotted lines in Figure 22.22.

In the next step we need to connect the aromatic ring of Tyr-5 to the aliphatic side chain. This is most conveniently done from the ROESY spectrum. Figure 22.23 displays an expansion of the required ROESY region. The signal at 7.1 ppm displays

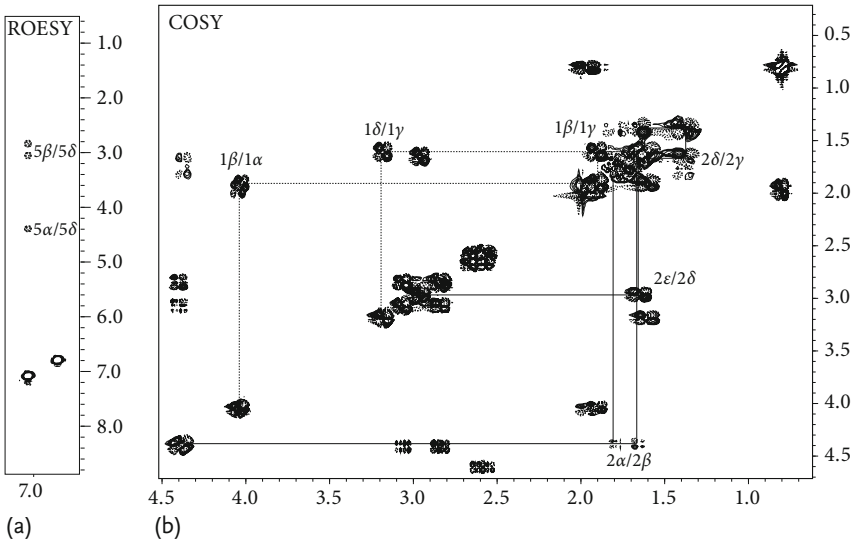

Figure 22.23 (a) ROESY correlations used for linking the aromatic spin systems to the rest of the side chain. (b) COSY correlations used to assign the aliphatic side chains.

rather strong NOEs to one α proton and two β protons, which are from Tyr-5. The cross peak to the α proton was the one that we misleadingly interpreted as the correlation to the mysterious residue 6 in the sequential assignment.

The next step is to use the COSY spectrum to trace through the aliphatic side chains. Residues Tyr-5 and Asp-3 can be readily assigned from the TOCSY spectrum because they only posses β protons, and therefore the assignment is unambiguous. This is not the case for Arg-1 and Lys-2. For both of these longer spin systems it is difficult to trace through from one end of the chain to the other because there are always regions with much peak overlap in between. Therefore, it is advisable to start from both ends of the chain. While the α proton is usually readily recognized from the chemical shift, for these two residues also the other end of the spin system can be spotted because the protons are next to a nitrogen and are therefore low field shifted (see also Figure 22.20) This means that we can start from the α and δ protons of Arg-1 and from the α and ε protons of Lys-2. The required correlations are depicted in Figure 22.23. When stepping through the spin systems, one should always cross check against the TOCSY spectrum to see whether the particular resonance is really part of the spin system of that residue. Due to peak overlap, one could easily cross over to another spin system by accident.

Once we have completed this task, all protons are (hopefully) assigned. If we wished to determine the structure, we would now need to integrate all the cross peaks in the ROESY spectrum, assign each of them and use this information to generate distance restraints that will be used in the structure calculation program. However, since this peptide is unstructured, we will refrain from doing that.

Further Reading

Roberts, G.C.K. (ed.) (1993) *NMR of Macromolecules*, IRL Press.

Croasmun, W.R. and Carlson, R.M.K. (eds) (1994) *Two-Dimensional NMR Spectroscopy*, Chapter 5, 2nd edn, Wiley-VCH Verlag GmbH.

Lian, L.-Y. and Roberts, G. (eds) (2011) *Protein NMR Spectroscopy: Principal Techniques and Applications*, John Wiley & Sons, Inc.

Wüthrich, K. (1986) *NMR of Proteins and Nucleic Acids*, John Wiley & Sons, Inc.

Cavanagh, J., Fairbrother, W.J., Palmer III, A.G., Rance, M., and Skelton, N.J. (2007) *Protein NMR Spectroscopy*, 2nd edn, Academic Press.

Bertini, I., McGreevy, K.S., and Parigi, G. (eds) (2012) *NMR of Biomolecules*, Wiley-VCH Verlag GmbH.

Rule, G.S. and Hitchens, T.K. (2006) *Fundamentals of Protein NMR Spectroscopy*, Springer.

23
Nucleic Acids

23.1
Introduction

The biopolymers deoxyribonucleic acid (DNA) and ribonucleic acid (RNA) are the two principal units in which genetic information is stored (DNA) or used to translate it in protein biosynthesis (RNA). Each cell, whatever its function or tissue origin, contains a full copy of the genetic information in the form of DNA, and hence in principle a single cell is sufficient for transferring that information onto later generations. The alphabet of life uses four different "letters" to encode the 20 common amino acids. Only a few articles have captured as much attention as the seminal paper of Watson and Crick on the structure of the DNA double helix, in which they stated that the base-complementary structure indicates a mechanism for replication of genetic information with high fidelity. Besides the important role for storage of genetic information, nucleic acids are additionally involved in catalysis of biological processes, as structural components, and for regulatory or control processes.

The introduction of recombinant technology has revolutionized biology during the last 30 years. With the help of the polymerase chain reaction, long stretches of DNA can be synthesized quickly. Sequencing techniques help to confirm the chemical nature of the material synthesized, culminating in the deciphering of the human genome at the beginning of the last decade. Importantly for the purpose of NMR experiments, recombinant work allows DNA or RNA to be produced in an isotopically labeled fashion, or site-specific mutations to be introduced in order to elucidate the role of a particular nucleic acid.

DNA and RNA are important not only in general biology, but have also important in the pharmaceutical industry in the form of antisense DNA or RNA. In particular, RNA interference has been used extensively to explore signaling pathways, and its potential for influencing signaling for use as drugs is presently being investigated. There are many reasons why it is interesting to learn about nucleic acids. We will show in the following how NMR can be exploited to help our understanding of these important biomolecules.

Applied NMR Spectroscopy for Chemists and Life Scientists, First Edition. Oliver Zerbe and Simon Jurt.
©2014 WILEY-VCH Verlag GmbH & Co. KGaA. Published 2014 by WILEY-VCH Verlag GmbH & Co. KGaA.

NMR spectroscopy has always played a pivotal role in the structural biology of nucleic acids, for example, in the pharmaceutical industry for the study of drug–DNA or drug–RNA complexes or for understanding interactions of proteins with nucleic acids that occur, for example, in transcription factors.

The NMR method applied to isotopically labeled DNA or RNA is distinctly different from that applied to DNA or RNA at natural abundance of ^{13}C or ^{15}N. Assignment of resonances of nucleic acids that exceed approximately 30 nucleotides is only possible when labeled nucleic acids are used. Presently, 50–60 nucleotides is the upper size limit, and the largest constructs that have been structurally characterized are about 100 nucleotides long.

23.2 The Structure of DNA and RNA

DNA and RNA are biopolymers that, similarly to proteins, are assembled in a linear fashion from a few building blocks. The building blocks are called nucleotides, and consist of a furanose sugar, which is deoxyribose in the case of DNA and ribose in the case of RNA. The sugars form a glycosidic bond with a base that is derived from either purine or pyrimidine. The single nucleotides are linked via a phosphate ester through the hydroxyl groups at C3′ and C5′ of the furanoses (see Figure 23.1).

The conformation about the glycosidic bond can be either syn or anti depending on whether the base is centered over the furanose or flipped out. The boxed example in Figure 23.1 displays a nucleotide in the anti conformation. For pyrimidines only the anti conformation exists for obvious steric reasons. In Z-DNA the syn conformation is found for purine bases.

We learned in Chapter 20 that furanoses can adopt a number of different ring puckering conformations (see Figure 23.2).

In the case of ribose or deoxyribose, envelope-type conformations are observed in which either C2′ or C3′ is moved out of the plane formed by the other four ring atoms. If the atom that is flipped out of the plane resides on the same face as the base, the conformation is called endo, otherwise it is called exo. Sometimes also the “south” and “north” nomenclature is used, because the pucker is similar in shape to an *S* or an *N*. The C2′-endo conformation occurs in B-DNA, and C3′-endo occurs in Z-DNA and RNA. The sugar conformation may deviate slightly from the classic C2′-endo or C3′-endo type, and is described by the pseudorotation phase angle and pucker amplitude. Moreover, the conformation may be in thermodynamic equilibrium between N- and S-type conformations.

Whether the sugar is C2′ or C3′ endo puckered has consequences for the overall structure of the polymer chain. As shown in Figure 23.3, the distance between sequential phosphorous atoms changes by more than 1 Å between the two forms.

DNA mostly exists in the form of a double-stranded helix. The phosphate-sugar backbone runs on a helical path along the outside, while the bases of the two strands form hydrogen bonds with each other in the center. The regular types of

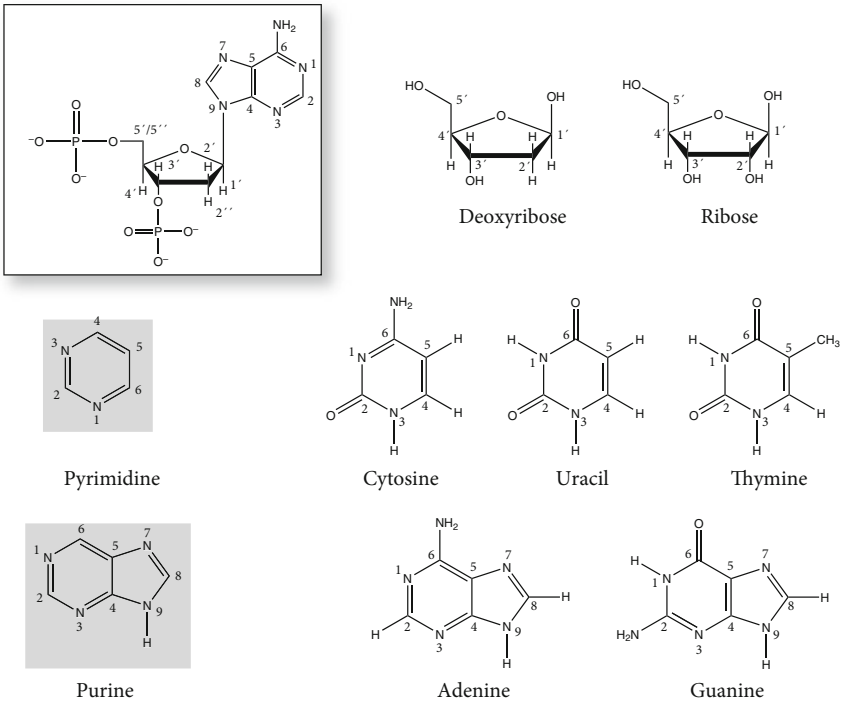

Figure 23.1 Chemical structures of nucleotides: The corresponding part from a DNA strand is depicted in the box.

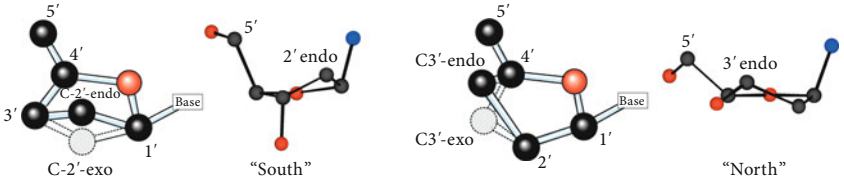

Figure 23.2 Sugar ring puckering.

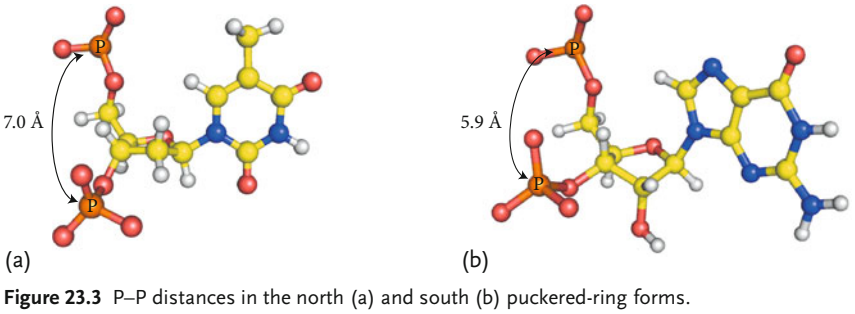

Figure 23.3 P–P distances in the north (a) and south (b) puckered-ring forms.

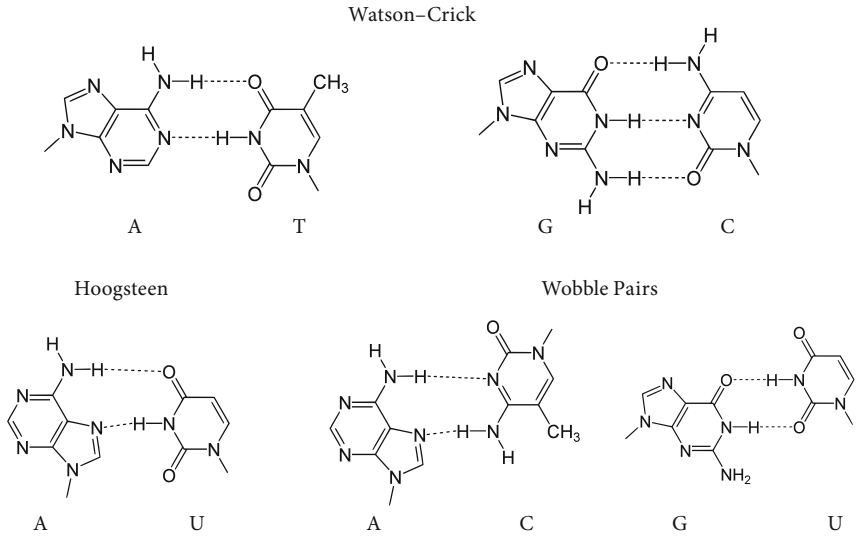

Figure 23.4 Types of base pairing in multiple-stranded nucleic acids.

hydrogen bonds are called Watson–Crick hydrogen bonds, but also Hoogsteen base pairs (e.g., in triple helices) or wobble pairs occur (see Figure 23.4).

The major forms of the helices are known as the B form (the predominant type of DNA at physiological conditions), the A form (mostly observed in RNA), and the Z form (Z-DNA). Regular B-DNA forms a deep and a small cleft, known as the major and minor grooves (Figure 23.5). The distance between the plane formed by the bases is approximately 3.4 Å. Distortion of the regular structure may occur when the two bases are rotated out of plane relative to each other (roll), when they rotated out of the regular position within the helix axis (twist), or when sequential pairs are rotated out of coplanarity (tilt).

In B-DNA the center of the bases coaligns with the helix axis (Figure 23.6). The major and minor grooves are similar in depth, but the major groove is much wider. Usually, C2′-endo sugar puckering is observed. Bases in the major groove are accessible, for example, to DNA-binding proteins.

A-DNA is formed in dehydrated DNA or when guanine-rich regions occur. The center of the hydrogen bond is placed away from the helix center owing to significant tilt of the bases. In contrast to B-DNA, the minor and major grooves have very different depth, with the minor groove being very shallow. In Z-DNA the phosphate backbone forms a zigzag path (hence its name). Z-DNA is tall and thin, and is favored by alternating pyrimidine–purine sequences.

The properties of the different forms of DNA are summarized in Table 23.1.

Other often encountered multimeric forms of DNA are the so-called *DNA quadruplexes* or *DNA triplexes* that may form with certain sequences (Figure 23.7).

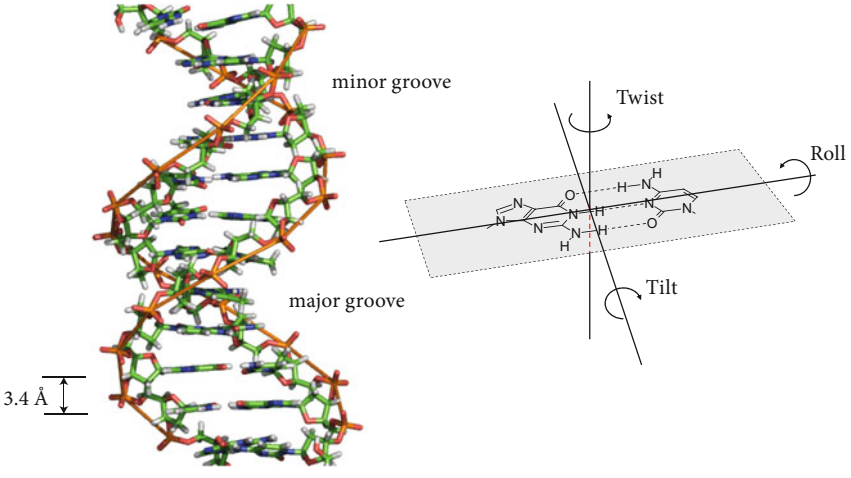

Figure 23.5 Typical geometric features of double-stranded DNA.

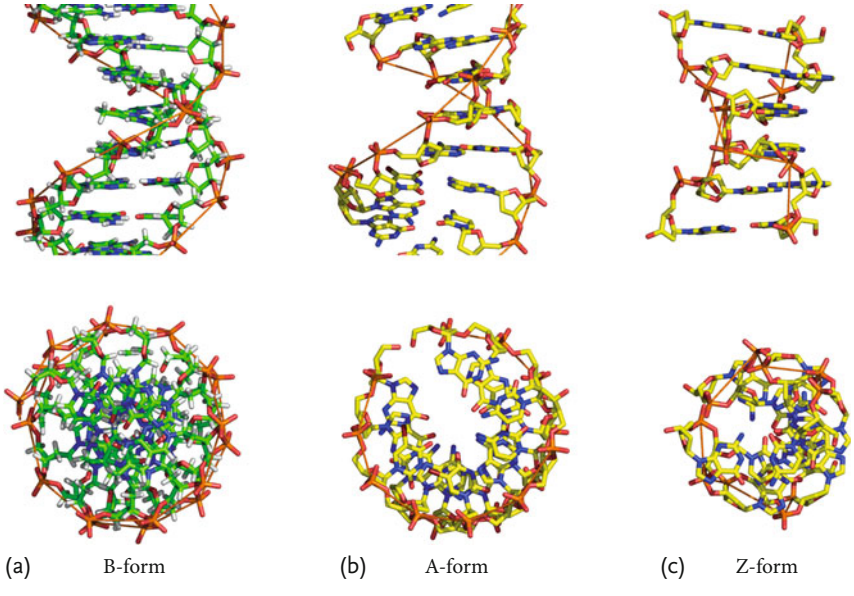

Figure 23.6 Structures of B-DNA (a), A-DNA (b), and Z-DNA (c) viewed perpendicular to (top) or along (bottom) the long axis.

RNA secondary structures include single-stranded regions, hairpins, duplexes, internal loops and bulges, junctions, and pseudoknots, all within a single polymer chain (Figure 23.8). In bulges and junctions, one or more nucleotides are not involved in hydrogen-bond formation.

Table 23.1 Important features of A-DNA, B-DNA, and Z-DNA.

Parameter	A-DNA	B-DNA	Z-DNA
Sense	Right-handed	Right-handed	Left-handed
Base pairs/turn	11	10.4	12
Rise per base pair (Å)	2.3	3.3	3.7
Pitch (Å)	25.4	34	45
Tilt (°)	19	0	–9
Glycosidic angle	Anti	Anti	Anti at C, C3′ syn at G
Pucker	C3′ endo	C2′ endo	C2′ endo at C, C3′ endo at G
Diameter (Å)	25	20	18
Major groove	Narrow and deep	Wide and deep	Flattened
Minor groove	Wide and shallow	Narrow and deep	Narrow and deep

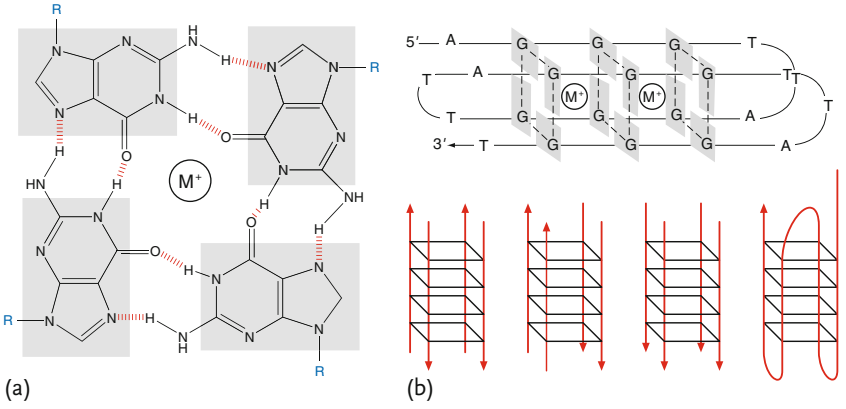

Figure 23.7 DNA quadruplexes (a). These can stack to assemble into i-motifs (b, top) or in various other ways (b, bottom).

23.3 NMR of DNA and RNA

23.3.1 ^{1}H NMR

DNA and RNA are composed of sugar units (deoxyribose or ribose) that are connected at the anomeric center to bases. Accordingly, we will find the characteristic signature of the pentoses in the proton NMR spectra (see Chapter 20). In the case of RNA, all ring protons (2′, 3′, 4′, and 5′) other than the anomeric 1′ protons will be observed in the range between 3.5 and 5 ppm. The anomeric protons are low field shifted (5.3–6.2 ppm). In DNA, the 2′ position contains no hydroxyl group and hence the 2′ and 2″ protons are upfield shifted (1.5–3 ppm).

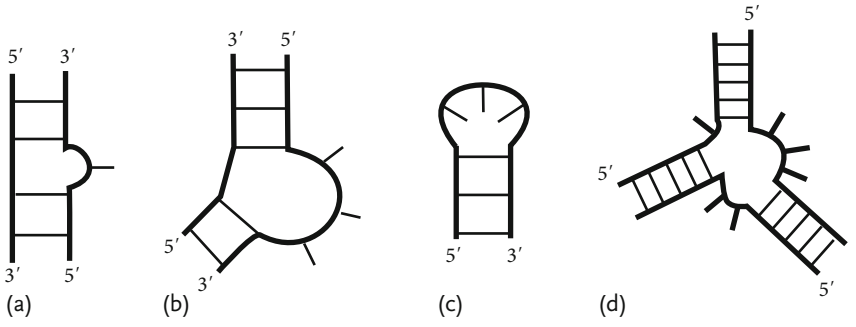

Figure 23.8 Typical elements of RNA secondary structure: single-nucleotide bulge (a), three-nucleotide bulge (b), hairpin loop (c) and junction (d).

The signals of the bases are characteristically low field shifted. The amino and imino protons will be observable only in duplexes when their exchange rate is reduced because of hydrogen bonding or sometimes in loops. Imino protons occur in a characteristic window around 11 ppm in loops, between approximately 12 and 14 ppm in duplexes, or between 15 and 16 ppm in triplexes, a window in which usually no other resonances are found. The amino protons are located in the range between 7 and 8.5 ppm. Aromatic protons of the bases occur in the range 7–8.5 ppm or 5.3–6.8 ppm. Figures 23.9 and 23.10 display proton NMR spectra of correspond-

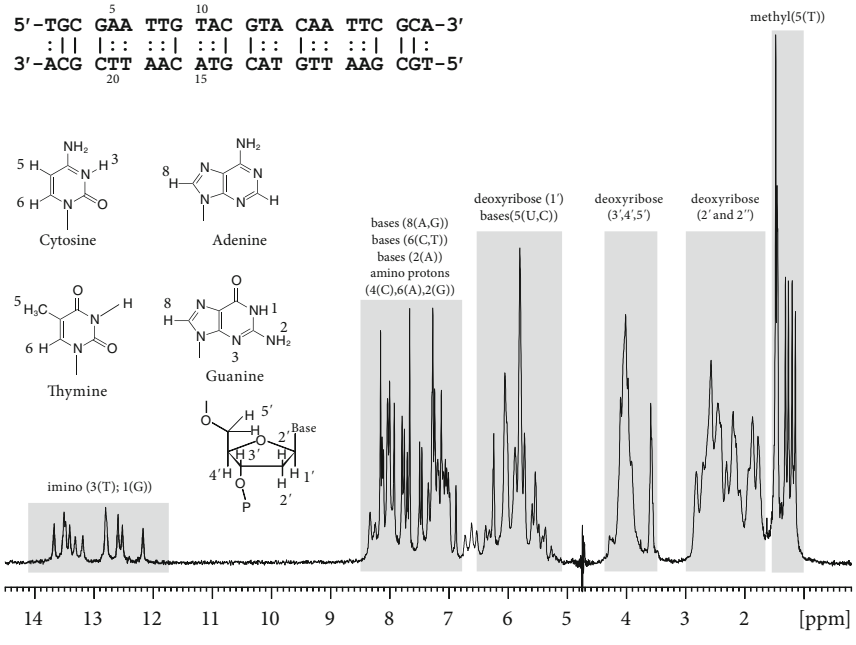

Figure 23.9 Proton NMR spectrum of a double-stranded DNA. Typical regions for protons are indicated in gray.

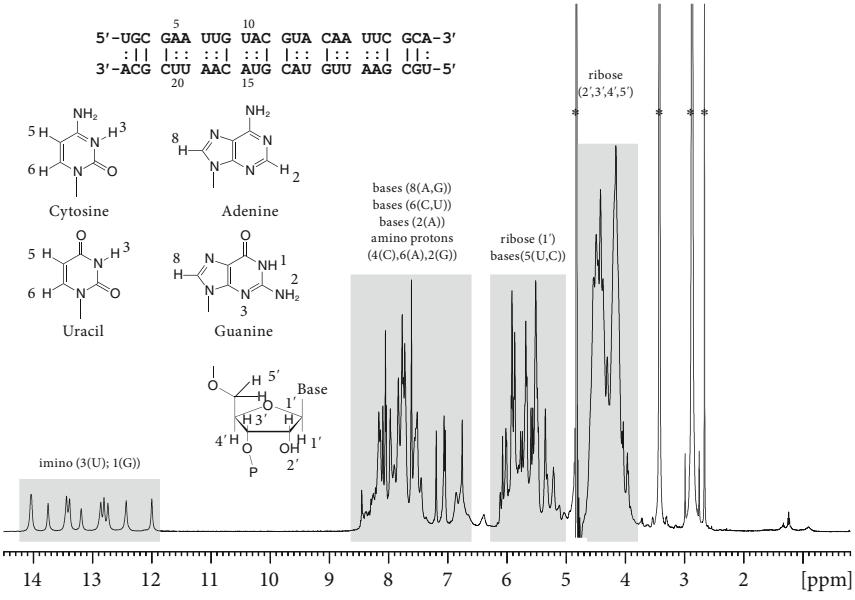

Figure 23.10 Proton NMR spectrum of a double-stranded RNA. Typical regions for protons are indicated in gray.

ing DNA and RNA duplex strands in 90% H_2O/10% D_2O. In DNA, the methyl groups of thymine give rise to sharp singlets in the 1–1.5 ppm range.

In protein–DNA (or protein–RNA) complexes, most of the DNA/RNA signals overlap with protein signals. However, the imino protons are usually clearly visible since they resonate at far low field with respect to protein signals.

DNA or RNA contains a number of exchangeable protons, for example, imino, amino, and hydroxyl protons. A plot of the exchange rate versus pH as depicted in Figure 23.11 clearly reveals that non-hydrogen-bonded imino protons cannot be observed. Amino protons will be observable at pH around 7 but are likely to display rather broad signals. Hydroxyl protons are almost never observed except when they are involved in stable hydrogen bonds, for example, in hairpin loops.

We have seen similar plots for the exchange rates of labile protons in proteins (see Section 22.3.1). Exchange rates of these protons have a dramatic effect on line widths, and this feature can be nicely used to detect hydrogen bonding or duplex formation. An example for RNA is presented in Figure 23.12, in which the proton NMR spectra of two complementary single-stranded RNA oligonucleotides and the proton NMR spectrum of the 1 : 1 mixture are shown. In the case of the single-stranded nucleotides, no signals are seen in the 12–14 ppm range, not even an indication that a (broad) signal may be in that region. In addition, the nucleotide in the top spectrum in Figure 23.12 also displays broad signals for some of the sugar and base protons. In contrast, the mixture of the two nucleotides reveals a set of rather sharp signals in the imino regions (shaded in gray) as well as generally sharper lines for the sugar and base protons.

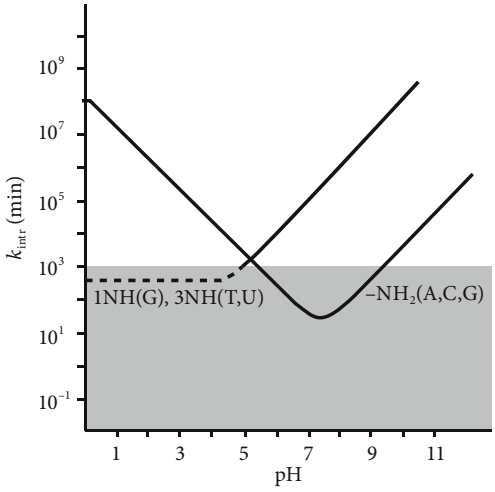

Figure 23.11 Exchange rates for unprotected labile base protons.

23.3.2 ^{13}C NMR

Similarly to the proton NMR spectra, carbon NMR spectra of DNA or RNA display features from carbohydrate spectra such as characteristically low field shifted C1′ carbon positions (see Chapter 3.2.4). The aromatic or carbonyl base carbons occur at values larger than 130 ppm. The general features are summarized in Figure 23.13: easily recognizable are the methyl carbons of thymine (about 20 ppm) and the C2′ carbons of DNA (about 35 ppm).

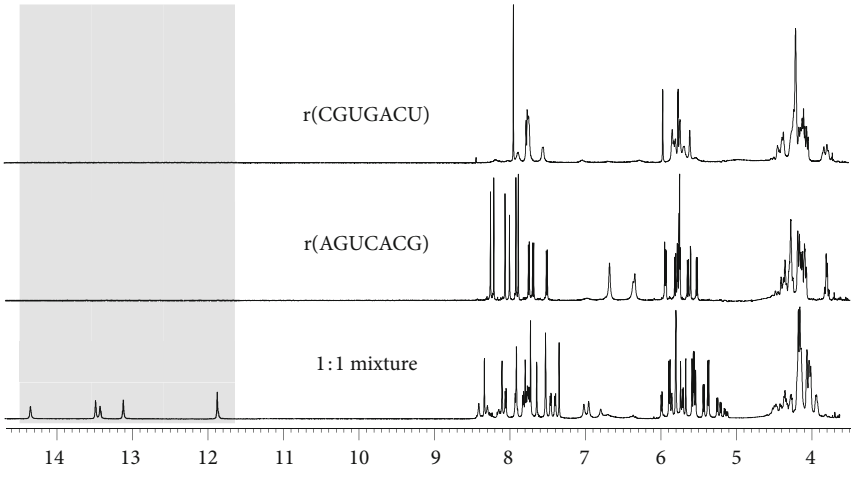

Figure 23.12 Comparison of proton NMR spectra of single-stranded and double-stranded RNA. The gray box denotes the region of the imino protons.

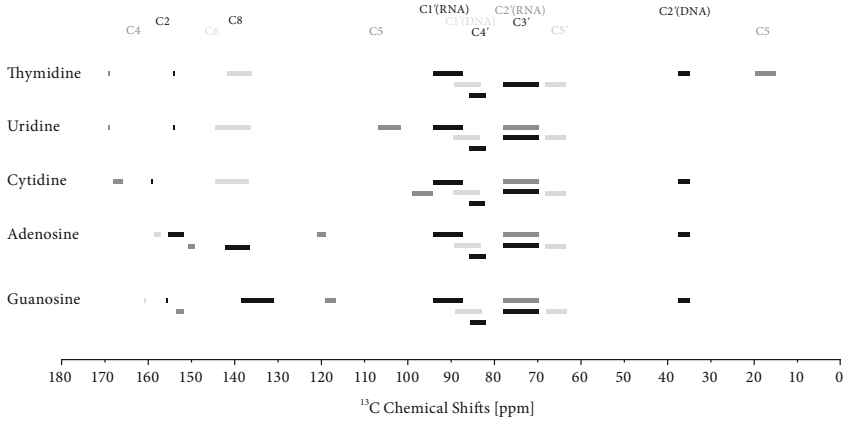

Figure 23.13 Typical carbon chemical shift ranges in DNA or RNA.

Figure 23.14 displays the [^{13}C,^{1}H] heteronuclear single-quantum coherence (HSQC) spectrum of a 14mer RNA. Clearly, the ribose anomeric ring atoms are low field shifted in both the proton (H1′) and the carbon (C1′) dimension. At the high-field end, there are 5′ carbon and proton signals. Moreover, they can be easily spotted because two correlations are always observed for each carbon due to the methylene nature of these moieties. C4′ carbons are observed in a well-separated region, while C2′ and C3′ moieties overlap.

23.3.3
^{15}N NMR

As for proteins, [^{15}N,^{1}H] HSQC spectra are very helpful for assignment purposes. Nevertheless, measurements even when using cryoprobes usually require ^{15}N enrichment. An overview of the chemical shifts is presented in Figure 23.15. Clearly the ^{15}N chemical shifts of amino nitrogens are different from the others. Moreover, cytosine, adenine, and guanine amino groups are located in distinct, well-separated regions, allowing one to distinguish them unambiguously.

Figure 23.16 depicts the [^{15}N,^{1}H] HSQC spectrum of a 14mer RNA fragment. Separation of imino and amino groups according to the base is obvious. Moreover, this spectrum is also very helpful to distinguish signals of aromatic protons from signals of amino protons in the 6–8 ppm range.

23.3.4
^{31}P NMR

^{31}P is an $I = 1/2$ nucleus, and therefore seems to be very promising for use in high-resolution NMR spectroscopy. Unfortunately transverse relaxation of ^{31}P is accelerated considerably by chemical shift anisotropy, and often 400 MHz is the best compromise between sensitivity and line broadening induced by chemical

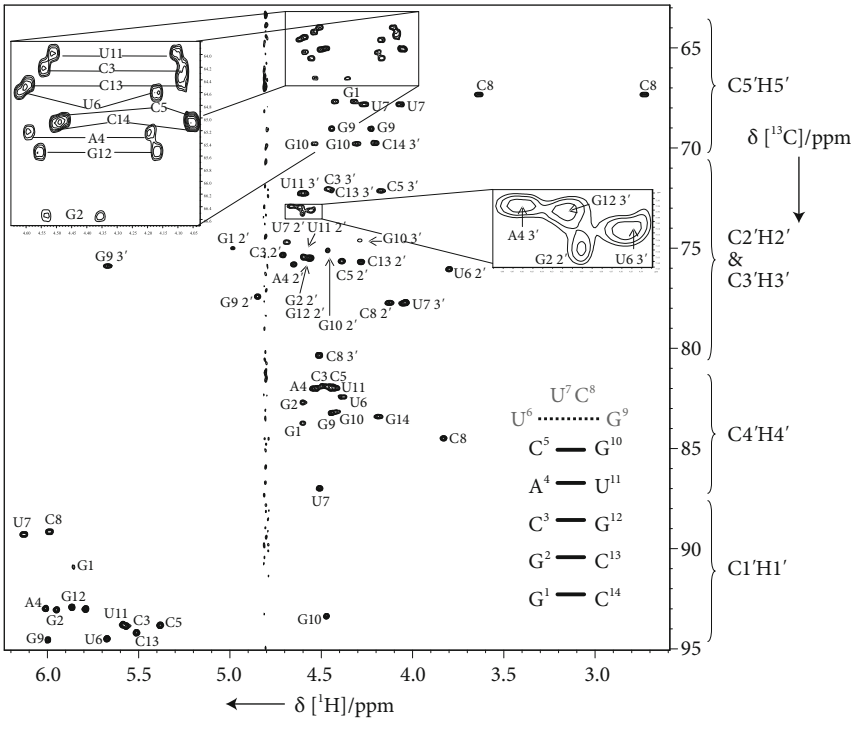

Figure 23.14 [^{13}C,^{1}H] heteronuclear single-quantum coherence (HSQC) spectrum of a 14mer RNA. Reproduced with permission from Fürtig *et al.* (2003) *ChemBioChem*, **4**, 936–962.

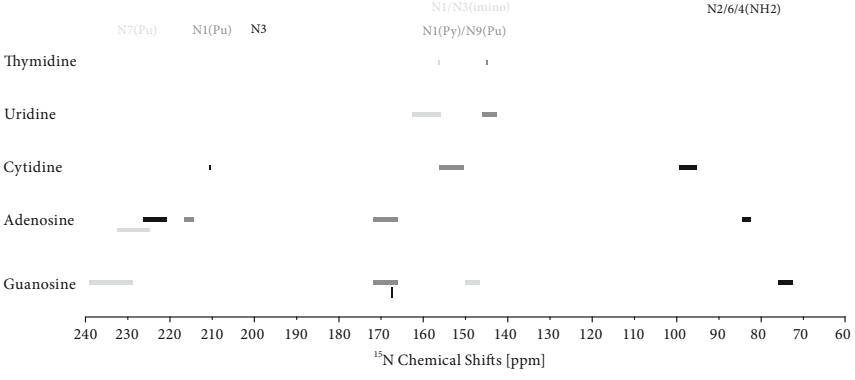

Figure 23.15 Typical ^{15}N chemical shift ranges for bases in DNA or RNA.

shift anisotropy. Nevertheless, the ^{31}P chemical shift may serve as a valuable tool to detect the presence of Z-DNA or changes in torsion angles involving phosphate (e.g., in loops). The ^{3}J(P,H) scalar coupling constants report on sugar or backbone conformations.

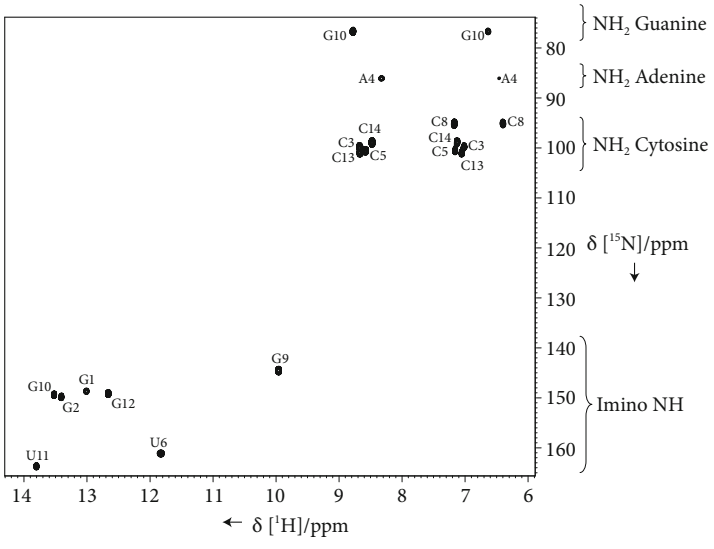

Figure 23.16 [^{15}N,^{1}H] HSQC spectrum of a 14mer RNA fragment. Reproduced with permission from Fürtig *et al.* (2003) *ChemBioChem*, **4**, 936–962.

23.4
Assignment of DNA and RNA Resonances

23.4.1
Unlabeled DNA/RNA

Oligonucleotides are built from individual nucleotides, each of which forms separate spin systems. The assignment procedure therefore is somewhat similar to the one used for proteins, in which the individual amino acids also form separate spin systems. Roughly speaking, the assignment comprises two steps: (i) assignment of the individual nucleotides, in particular of the ribose/deoxyribose units, and (ii) linkage of the individual nucleotides via internucleotide nuclear Overhauser effects (NOEs).

Although, in principle, scalar couplings between the H5′ and H5″ protons and the phosphorous may be used, in practice this rarely works because of short T2 relaxations times of the ^{31}P nuclei and poor signal dispersion of the latter. Therefore, sequential assignments must usually be based on internucleotide NOEs. The spin systems of nucleotides can be linked by connecting along the strand (5′ → 3′) in a "*sequential walk*" using NOEs between the base proton H6 or H8 and the sugar protons H1′. The same procedure is also possible using H2′(RNA) or H2′/H2″ (DNA) instead, thereby helping to confirm or even complete the sequential assignment (see Figure 23.17).

A typical NOESY spectrum in D_2O displaying the expansion of the region comprising the H1′ to base proton NOEs from the 14mer duplex RNA (CGUGACU):(AGUCACG) is depicted in Figure 23.18. The sequential assignments very

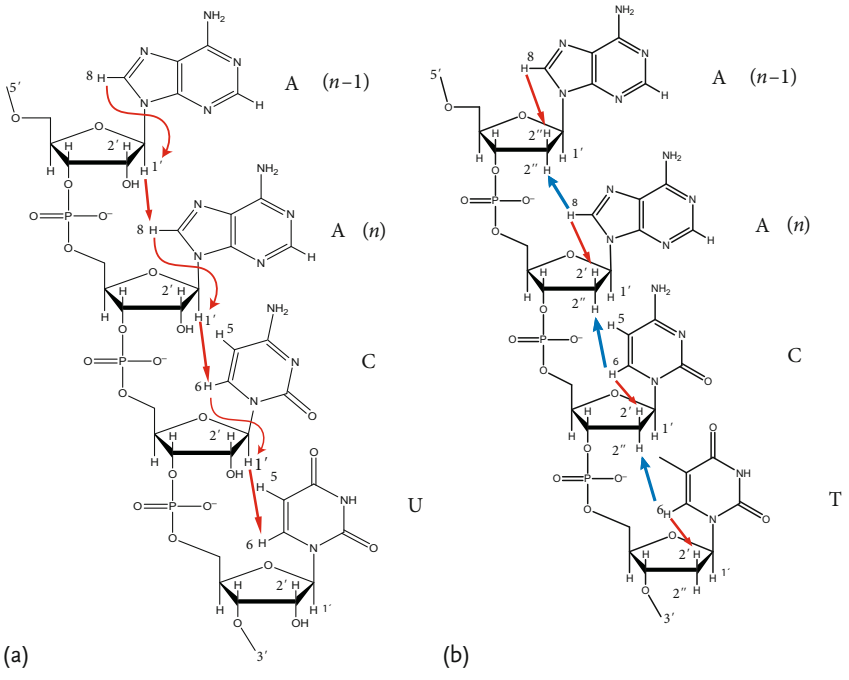

Figure 23.17 Sequential assignment in RNA (a) or DNA (b).

much remind us of a similar procedure used for assignment of peptide resonances (see Chapter 22). Each moiety, in this case each base proton, experiences an NOE to a sugar proton from its own nucleotide and from the preceding one. The sequential walk region comprising the H1′ to base correlations is also shown in Figure 23.18. Two correlations are present for each base proton at least, one corresponding to the intranucleotide and one corresponding to the preceding nucleotide. The base protons from which these correlations originate are usually H6 from cytosine or uracil and H8 from adenine or guanine. Additional base protons occurring in this chemical shift range are the H2 protons of adenine. In the case of cytosine and uracil, H6 is scalarly coupled to H5, and therefore appears as a doublet in spectra with reasonably sharp lines. Since the H5 base proton of uracil and cytosine also falls in the chemical shift range of sugar protons, very intense NOEs are observed for the H6–H5 correlations of uracil and cytosine. These intense NOEs as well as the doublet appearance of cross peaks are helpful in recognizing uracil and cytosine. These correlations are highlighted by squares in Figure 23.18. No correlation between U7 and A8 is visible, because the two strands are separated at this position. No imino or amino protons can be seen as this spectrum was recorded in D_2O.

Alternatively, cross-strand NOEs in duplex DNA or RNA can be used by looking at the amino and imino protons in NOESY spectra recorded in H_2O. Typically observed NOEs in Watson–Crick base pairs as well as in Hoogsteen or wobble base pairs are summarized in Figure 23.19.

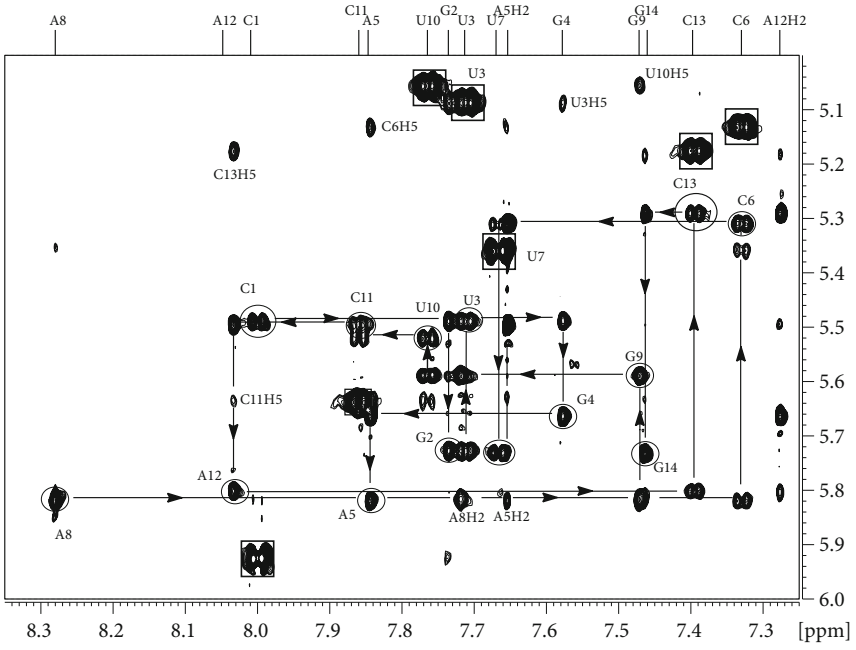

Figure 23.18 NOESY spectrum of duplex RNA displaying the region for the NOESY walk.

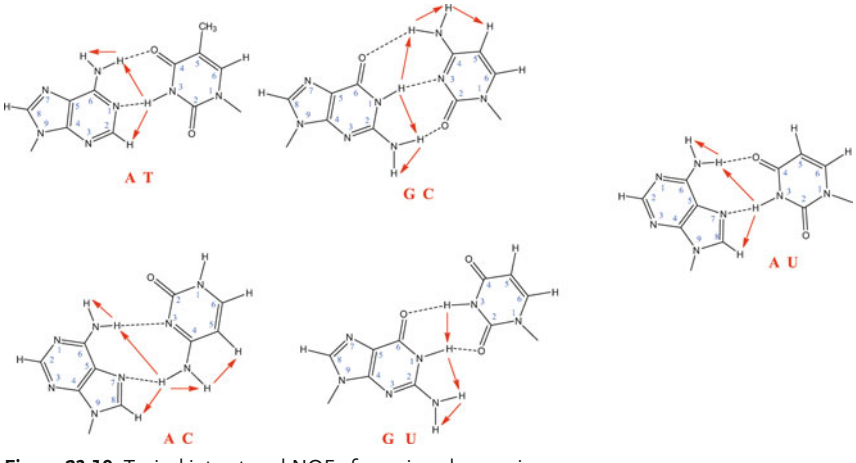

Figure 23.19 Typical interstrand NOEs for various base pairs.

An example taken from duplex RNA displaying the cross-strand imino–imino NOEs as well as other helpful NOEs of imino protons to amino, H2, H6/H8, or ribose protons is shown in Figure 23.20. The $^{15}N,^{1}H$ correlation is plotted at the bottom of Figure 23.20 because it conveniently allows us to distinguish guanine and uracil bases by their ^{15}N chemical shifts:

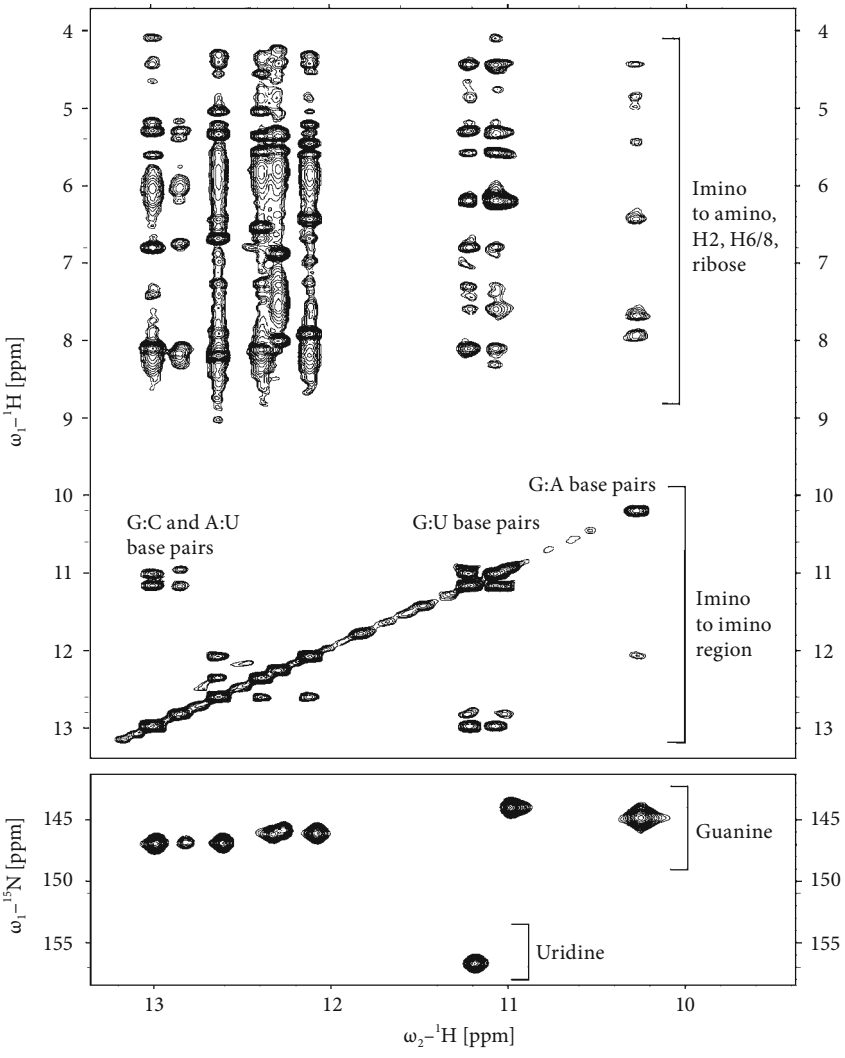

Figure 23.20 NOESY spectrum of duplex RNA displaying important correlations from imino protons. Reproduced with permission from Flinders *et al.* (2006) *Progr. NMR Spectrosc.*, **48**, 137–159.

Once the anomeric sugar protons have been identified, the carbohydrate spin systems need to be fully assigned. This procedure is similar to the one used for peptides, and relies on using total correlation spectroscopy (TOCSY) and correlation spectroscopy (COSY) spectra, this time mostly recorded in D_2O. Significant resonance overlap is encountered for all the nonanomeric ring protons in RNA and hence it is best to start from the anomeric protons, and use the TOCSY correlations to identify common spins within one ribose unit. In the case of DNA, the

2′ and 2″ protons may also be used as starting points. Note that $J(1', 2')$ is approximately 0 Hz for C3′-endo sugars in RNA, so those correlations will not be seen. Similarly, COSY spectra are used to connect H5 with H6 of cytosine or uracil and H6 with the methyl group of thymines (provided that the line widths are not too large). Unfortunately, signal dispersion for carbohydrates is worse than for amino acid side chains, and hence resonance overlap tends to be a serious issue.

23.4.2 Labeled DNA/RNA

Isotope-labeled DNA or RNA is important when trying to tackle structures of larger DNA or RNA, and usually will speed up the resonance assignment process significantly by removing the detrimental effects from resonance overlap, at least to some extent. Labeled RNA is conveniently produced using enzymatic *in vitro* transcription with RNA polymerases such as the T7 RNA polymerase that transcribes the RNA from a DNA template. Labeled nucleoside 5′-triphosphates as substrates are then required, and are commercially available. Usually, labeled RNA is easier to make in larger quantities and the production is also cheaper than for DNA. This is due to the fact that DNA oligomers are usually chemically synthesized because the DNA levels in the cell are too low to make a biosynthetic procedure for production of nucleoside 5′-triphosphates practical.

Similarly to the protein field, isotope-labeled DNA or RNA facilitates assignment using sensitive multidimensional through-bond correlation experiments. For example, sugar moieties are assigned on the basis of TOCSY/COSY data for unla-

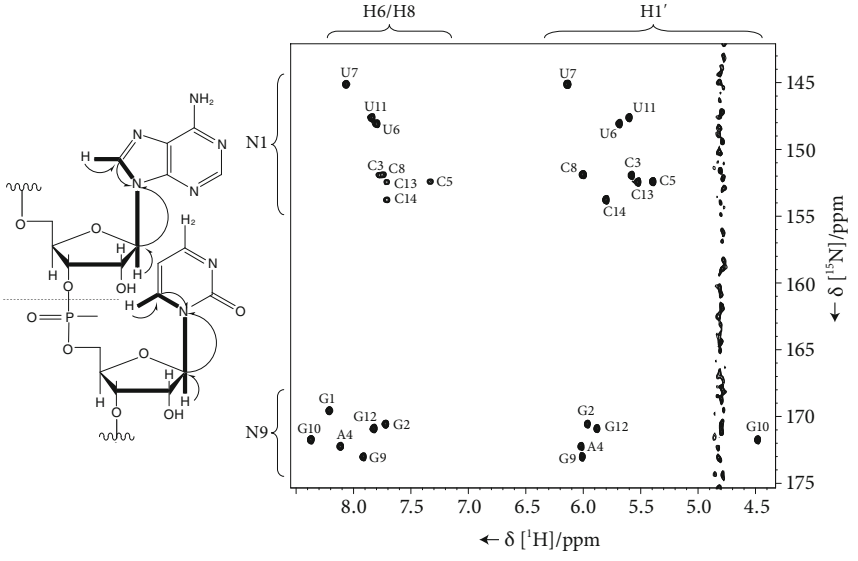

Figure 23.21 HCN correlations in an RNA oligomer. Reproduced with permission from Fürtig *et al.* (2003) *ChemBioChem*, **4**, 936–962.

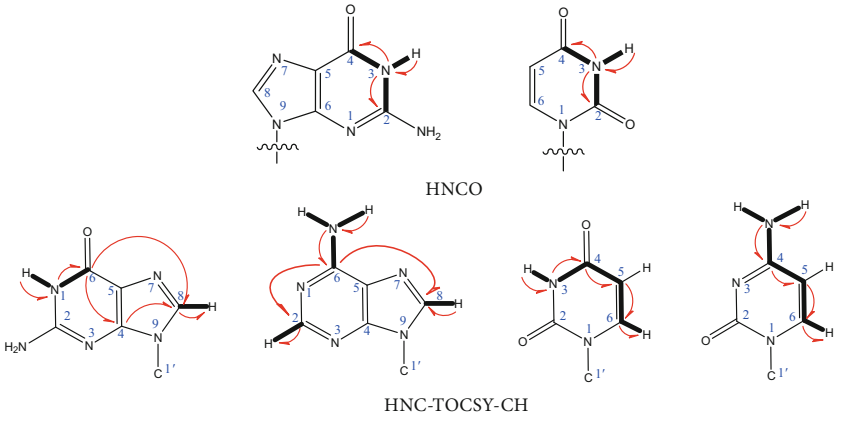

Figure 23.22 Important through-bond triple-resonance experiments for assignment of base resonances. Reproduced with permission from Fürtig *et al.* (2003) *ChemBioChem*, **4**, 936–962.

beled nucleotides, while for labeled nucleotides HCCH-type experiments can be used. These are not only much more sensitive but also offer the advantage of separating signals along the carbon frequencies, thereby removing signal overlap.

The sugar moieties are assigned from HCCH-TOCSY data. Linkage of the bases to the sugar units is achieved using NOEs as described in the previous section. Alternatively, an HCN experiment directly links the anomeric protons with the connected nitrogen nuclei of the base (Figure 23.21).

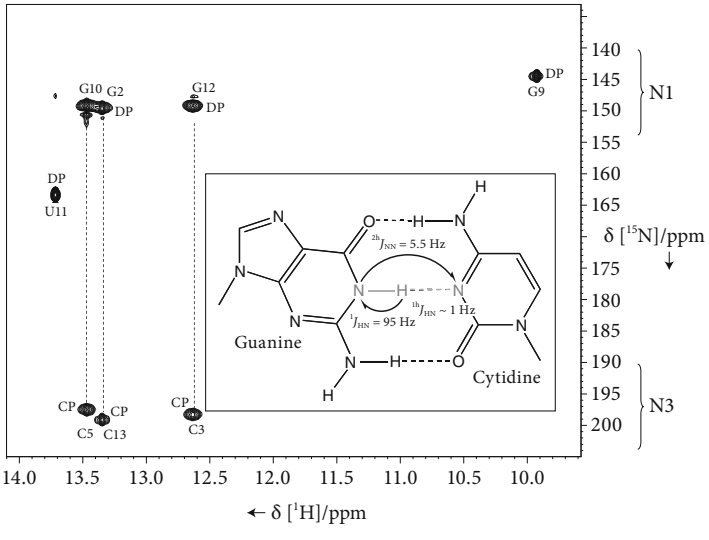

Figure 23.23 HNN-COSY spectrum to detect scalar couplings across hydrogen bonds. Reproduced with permission from Fürtig *et al.* (2003) *ChemBioChem*, **4**, 936–962.

For assignments within the bases, experiments that correlate labile protons with nonlabile protons have been successfully used, a selection of them being depicted in Figure 23.22. As an example, experiments that start on exchangeable protons and correlate them with CH protons are depicted. The HNCO experiment is already known from protein NMR spectroscopy, where it is one of the most sensitive experiments.

Moreover, experiments that correlate cross-strand nucleotides have been designed in which magnetization is transferred through scalar couplings across the hydrogen bonds. In contrast to proteins, those couplings are reasonably large and make possible such experiments provided that the molecular weight of the oligonucleotides does not resulting in lines that are too broad. Figure 23.23 depicts such an HNN-COSY spectrum which is used to conveniently identify and assign base-paired nucleotides.

In general the proton density in nucleic acids is lower than in proteins, and hence the exclusive use of NOEs is often not sufficient. Many experiments to determine scalar couplings have been developed to be able to also introduce dihedral angle restraints into the structure calculations. For more information, the interested reader is referred to reviews on this topic.

Further Reading

Roberts, G.C.K. (ed.) (1993) *NMR of Macromoleules*, Chapter 8, IRL Press.

Wüthrich, K. (1986) *NMR of Proteins and Nuclei Acids*, John Wiley & Sons, Inc.

Fürtig, B., Richter, C., Wöhnert, J., and Schwalbe, H. (2003) NMR spectroscopy of RNA. *ChemBioChem*, **4**, 936–962.

Wijmenga, S.S. and van Buuren, B.N.M. (1998) The use of NMR methods for conformational studies of nculei acids. *Prog. NMR Spectrosc.*, **32**, 287–387.

Flinders, J. and Dieckmann, T. (2006) NMR spectroscopy of ribonucleic acids. *Prog. NMR Spectrosc.*, **48**, 137–159.

Lam, S.L. and Chi, L.M. (2010) Use of chemical shifts for strucutral studies of nucleic acids. *Prog. NMR Spectrosc.*, **56**, 289–310.

Appendix

A.1
The Magnetic *H* and *B* Fields

The magnetic field is described by means of two related quantities, the H field and the B field. Both are vector quantities, having magnitude and direction. The H field, also referred to as the magnetic field strength or the auxiliary field, describes the magnetic field with respect to its source, a moving charge. A conducting loop of diameter d and current I produces in its center an H field of I/d amperes per meter ($\mathrm{A\,m^{-1}}$) (Figure A.1).

The B field (magnetic flux density or magnetic induction) is defined via the force which a magnetic field exerts on a magnetic object, and is specified in units of tesla (T) ($\mathrm{kg\,s^{-2}\,A^{-1}}$ or $\mathrm{N\,m^{-1}\,A^{-1}}$). It is the field that we can sense when we bring an iron stick close to a magnet, and it takes into account the magnetic properties of the medium. For the B field produced by a conducting loop it therefore makes a difference whether the loop is surrounded by air, water, or a vacuum. In contrast, it does not matter for the H field, which only depends on the actual current and the geometry of the loop, regardless of the surrounding medium. The B field and the H field are related to each other by

$$B = \mu_r \mu_0 H \tag{A1}$$

with μ_r being the relative *permeability* of the medium, and μ_0 the permeability of free space (vacuum), $\mu_0 = 4\pi \times 10^{-7}\,\mathrm{N\,A^{-2}}$. Depending on whether a medium is magnetically isotropic or anisotropic, the relative permeability is a dimensionless

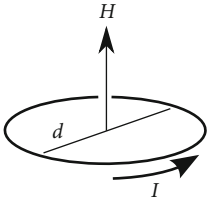

Figure A.1 The H field produced by a circular current.

Applied NMR Spectroscopy for Chemists and Life Scientists, First Edition. Oliver Zerbe and Simon Jurt.
©2014 WILEY-VCH Verlag GmbH & Co. KGaA. Published 2014 by WILEY-VCH Verlag GmbH & Co. KGaA.

scalar or a second rank tensor, respectively. For a vacuum, $\mu_r = 1$. Diamagnetic substances have a relative permeability less than 1, and paramagnetic substances have a relative permeability greater than 1. Relative permeability and *magnetic susceptibility* are related by

$$\mu_r = \chi + 1 \tag{A2}$$

and thus

$$B = \mu_0 H + \mu_0 \chi H$$

The value of μ_0 is indirectly given via the definition of the current, which states that 1 A corresponds to the amount of current when two parallel wires of infinite length and at a distance of 1 m are attracted by a force of 2×10^{-7} N/m.

A.2
Magnetic Dipole Moment and Magnetization

The magnetic dipole moment of an object (e.g., a tiny bar magnet) determines how strongly the dipole is attracted to coalign with the magnetic field. A prototype of a magnetic dipole is a circular loop of current. The magnetic dipole moment μ of such a current loop of area A and current I is $\mu = IA$ (A m^2). Thereby, μ is a vector pointing perpendicular to the plane of the loop as depicted in Figure A.2a.

When the loop is subjected to an uniform magnetic field B as shown in Figure A.2b, a force will act to align the magnetic dipole moment with the direction of the magnetic field, according to $F = \ell^{-1} \mu B \sin(\theta)$, in which ℓ can be thought of as a virtual lever arm. Thus, for a magnetic dipole moment of 1 A m^2 orthogonally positioned in a magnetic field of 1 T, we would need a force of 1 N using a lever arm of 1 m to maintain the dipole in its orthogonal position. Alternatively, we can specify the dipole moment by the torque acting to align it in a magnetic field of strength B:

$$\boldsymbol{\tau} = \boldsymbol{\mu} \times \boldsymbol{B} \tag{A3}$$

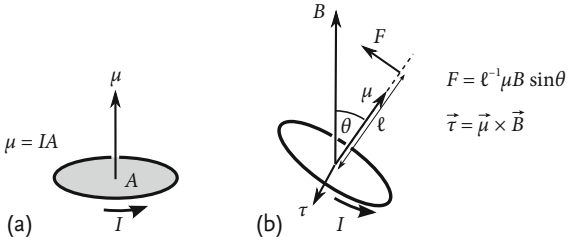

Figure A.2 Magnetic dipole moment of a current loop (a) and its attraction to align with an external magnetic field B (b). If the direction of the current were the other way around, μ would point in the opposite direction.

If we add up all microscopic dipole moments of an object we arrive at the macroscopic dipole moment m. This quantity is usually specified relative to the volume of the object as the magnetic moment per unit volume, the so-called *magnetization* M. With the dimension of ampere square meters ($\mathrm{A\,m^2}$) for the magnetic moment and cubic meters ($\mathrm{m^3}$) for the volume, magnetization has the dimension amperes per meter, and hence the same unit as the H field (see (5.1)).

A.3 Scalars, Vectors, and Tensors

A *scalar* is a quantity that has no direction associated with it (e.g., the mass). A *vector* is a quantity with an associated direction, for example, the force (Figure A.3).

Usually for quantities that act in 3D space, the components along the Cartesian axes, for example, F_x, F_y, and F_z are used:

$$\boldsymbol{F} = \begin{bmatrix} F_x \\ F_y \\ F_z \end{bmatrix}$$

When two vectors interact, the result can be a scalar or a vector. The former is described by taking the scalar product (inner product) between two vectors

$$\boldsymbol{A} \bullet \boldsymbol{B} = A_x B_x + A_y B_y + A_z B_z = |A||B|\cos(\alpha)$$

in which α is the angle between the two vectors. Scalar products are invariant under rotations. An example of a scalar product between two vectors is scalar coupling (hence its name). It is a scalar quantity, meaning that its magnitude is independent of the orientation of the coupled spins with respect to the external field.

Two vectors $\boldsymbol{A}$ and $\boldsymbol{B}$ can also be multiplied by the vector product (outer product). The result is a vector again ($\boldsymbol{C}$), whose direction is perpendicular to the plane formed between A and B (Figure A.4).

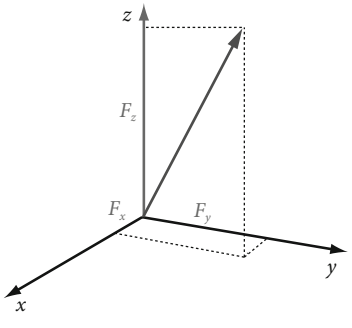

Figure A.3 Definition of a vector in terms of its *x*, *y*, and *z* coordinates.

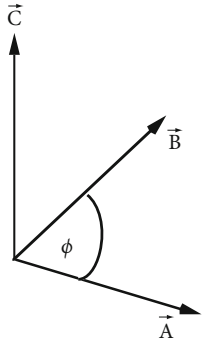

Figure A.4 Definition of the vector product between two vectors $\boldsymbol{A}$ and $\boldsymbol{B}$.

Therefore, the components of the vector $\boldsymbol{C}$ formed are

$$\boldsymbol{A} \times \boldsymbol{B} = (A_y B_z - A_z B_y)\hat{x} + (A_z B_x - A_x B_z)\hat{y} + (A_x B_y - A_y B_x)\hat{z}$$

so the individual components of the new vector $\boldsymbol{C}$ are

$$\begin{aligned} \boldsymbol{A} \times \boldsymbol{B} &= \boldsymbol{C} \\ C_x &= (A_y B_z - A_z B_y) \\ C_y &= (A_z B_x - A_x B_z) \\ C_z &= (A_x B_y - A_y B_x) \end{aligned}$$

and the magnitude of the vector C calculates as $|C| = |A||B|\sin(\phi)$. An example important in the context of NMR is the derivation of the Bloch equations describing the fate of magnetization:

$$\frac{\partial \boldsymbol{M}}{\partial t} = \gamma(\boldsymbol{M} \times \boldsymbol{B})$$

In the absence of an additional RF field, $B_z = B_0$, $B_x = B_y = 0$. Thereby,

$$\frac{\partial \boldsymbol{M_x}}{\partial t} = \gamma(\boldsymbol{M} \times \boldsymbol{B})_x = \gamma(M_y B_z - M_z B_y) = \gamma M_y B_0$$

Scalar products therefore express the extent of collinearity of two vectors, and result in a scalar quantity, whereas the vector product measures the extent of orthogonality, and results in a new vector, which is orthogonal to the existing ones.

Tensors are important to describe how vectors are transformed into each others. An example is given by the chemical shielding tensor. It is used to transform the vector B_0 describing the static magnetic field into a new vector B_{ind} that describes the induced magnetic field as

$$\boldsymbol{B}_{\text{ind}} = \sigma \cdot B_0$$

For vectors connected to the three Cartesian coordinates, a 3×3 matrix (a "second rank tensor") is required to describe the transformation. In matrix notation, the

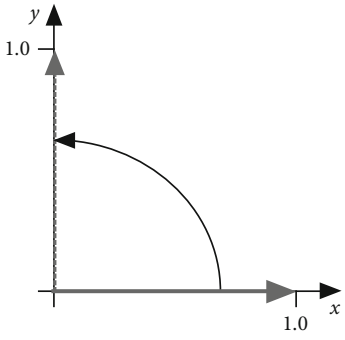

Figure A.5 Rotation of a vector from the *x* axis onto the *y* axis.

equation given above can be expressed as

$$\begin{bmatrix} B_{\mathrm{ind},x} \\ B_{\mathrm{ind},y} \\ B_{\mathrm{ind},z} \end{bmatrix} = \begin{bmatrix} \sigma_{xx} & \sigma_{xy} & \sigma_{xz} \\ \sigma_{yx} & \sigma_{yy} & \sigma_{yz} \\ \sigma_{zx} & \sigma_{zy} & \sigma_{zz} \end{bmatrix} \cdot \begin{bmatrix} 0 \\ 0 \\ B_0 \end{bmatrix}$$

A special case frequently encountered in quantum mechanics and in NMR is the transformation of two vectors into each other by a pure rotation. Since the magnitude (the "length," also called the "norm") is not changed by this transformation, it is called a "unitary transformation." Such a transformation may describe the rotation of spin vectors due to precession under the influence of the external field. Such unitary transformations are additionally used to transform vectors from one coordinate system into another. The example in Figure A.5 shows the transformation of a vector aligned along the x axis into one that is aligned along the y axis.

This transformation can be described by the following equation:

$$\begin{bmatrix} 0 \\ 1 \\ 0 \end{bmatrix} = \begin{bmatrix} 0 & -1 & 0 \\ 1 & 0 & 0 \\ 0 & 0 & 1 \end{bmatrix} \cdot \begin{bmatrix} 1 \\ 0 \\ 0 \end{bmatrix}$$

The rotation matrix describes the rotation of the coordinate system (in principle it is not relevant whether we rotate the vector or the coordinate system). The element $\sigma_{zz} = 1$ means that the z axis in the new coordinate system is the old z axis. $\sigma_{yx} = 1$ means that the old x axis becomes the new y axis and $\sigma_{xy} = -1$ means that the old y axis becomes the $-x$ axis. The length of the vector has not been changed through the operation.

A matrix that has special importance is the one where all nondiagonal elements are zero. In that case the diagonal elements point in the directions of the *principal axis system* and the elements σ_{xx}, σ_{yy}, and σ_{zz} are called the principal components of the tensor σ. In the case of the chemical shift tensor, the principal z axis points along the direction of the largest chemical shift anisotropy and in the case of the dipolar coupling tensor it points in the direction of the vector that connects the

dipolar coupled nuclei. The trace $\mathrm{Tr}(\sigma)$ is defined as $\mathrm{Tr}(\sigma) = \sigma_{xx} + \sigma_{yy} + \sigma_{zz}$. The quantity $1/3\,\mathrm{Tr}(\sigma)$ represents the isotropic average of the tensor quantity. The trace is invariant under rotations. All nondiagonal elements will average to zero under rapid rotation. Therefore, traceless tensors (the sum of all diagonal elements is zero) such as the dipolar coupling tensor will average to zero in solution.

A.3.1
Properties of Matrices

A matrix is an array:

$$\boldsymbol{M} = \begin{pmatrix} a_{11} & a_{12} & a_{13} & \cdots & a_{1n} \\ a_{21} & a_{22} & a_{23} & \cdots & a_{2n} \\ a_{31} & a_{32} & a_{33} & \cdots & a_{3n} \\ \vdots & \vdots & \vdots & \vdots & \vdots \\ a_{m1} & a_{m2} & a_{m3} & \cdots & a_{mn} \end{pmatrix}$$

Special matrices are the *unity matrix*

$$\boldsymbol{M} = \begin{pmatrix} 1 & 0 & 0 \\ 0 & 1 & 0 \\ 0 & 0 & 1 \end{pmatrix} \quad (1;\, E)$$

the *inverse matrix* $\boldsymbol{M}^{-1}$, with $\boldsymbol{M} \cdot \boldsymbol{M}^{-1} = 1$, and the transpose matrix

$$\begin{pmatrix} a & b & c \\ d & e & f \\ g & h & i \end{pmatrix} \rightarrow \begin{pmatrix} a & d & g \\ b & e & h \\ c & f & i \end{pmatrix}$$

Multiplication by a scalar gives

$$A \cdot \boldsymbol{M} = \begin{pmatrix} Aa_{11} & Aa_{12} & Aa_{13} \\ Aa_{21} & Aa_{22} & Aa_{23} \\ Aa_{31} & Aa_{32} & Aa_{33} \end{pmatrix}$$

Multiplication by another matrix is possible by forming the *inner product*, sometimes also called the *matrix product*,

$$\boldsymbol{A} \cdot \boldsymbol{B} = \overrightarrow{\begin{pmatrix} a_{11} & a_{12} & a_{13} \\ a_{21} & a_{22} & a_{23} \\ a_{31} & a_{32} & a_{33} \end{pmatrix}} \cdot \begin{pmatrix} b_{11} & b_{12} & b_{13} \\ b_{21} & b_{22} & b_{23} \\ b_{31} & b_{32} & b_{33} \end{pmatrix} = \begin{pmatrix} \boxed{c_{11}} & c_{12} & \cdot \\ c_{21} & \cdot & \cdot \\ c_{31} & \cdot & \cdot \end{pmatrix}$$

$$\begin{aligned} c_{11} &= a_{11}b_{11} + a_{12}b_{21} + a_{13}b_{31} \\ c_{21} &= a_{21}b_{11} + a_{22}b_{21} + a_{23}b_{31} \\ c_{31} &= a_{31}b_{11} + a_{32}b_{21} + a_{33}b_{31} \\ c_{12} &= a_{11}b_{12} + a_{12}b_{22} + a_{13}b_{32} \end{aligned}$$

or the *outer (direct) product*:

$$\boldsymbol{A} \otimes \boldsymbol{B} = \begin{pmatrix} (a_{11}B) & (a_{12}B) \\ (a_{21}B) & (a_{22}B) \end{pmatrix} = \begin{pmatrix} a_{11}b_{11} & a_{11}b_{12} & a_{12}b_{11} & a_{12}b_{12} \\ a_{11}b_{21} & a_{11}b_{22} & a_{12}b_{21} & a_{12}b_{22} \\ a_{21}b_{11} & a_{21}b_{12} & a_{22}b_{11} & a_{22}b_{12} \\ a_{21}b_{21} & a_{21}b_{22} & a_{22}b_{21} & a_{22}b_{22} \end{pmatrix}$$

with $\boldsymbol{B} = \begin{pmatrix} b_{11} & b_{12} \\ b_{21} & b_{22} \end{pmatrix}$

Solutions

Chapter 2: Basics of 1D NMR

2.1
The resultant energy level diagrams are depicted below:

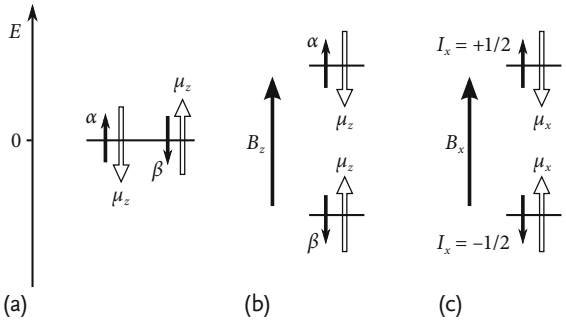

2.2
Regardless of the sign of the gyromagnetic ratio the thermal equilibrium magnetization points along the positive z direction. (a) In the case of a positive gamma it is the α state that is higher populated whereas (b) in the case of a negative gamma it is the β state that is higher populated.

2.3
Spin precession can be seen as a consequence of the conservation of angular momentum. In the case of the nuclear spin it is the intrinsic spin angular momentum that is conserved. A classical analogue would be the precessional motion of a spinning top or a gyroscope.

Applied NMR Spectroscopy for Chemists and Life Scientists, First Edition. Oliver Zerbe and Simon Jurt.
©2014 WILEY-VCH Verlag GmbH & Co. KGaA. Published 2014 by WILEY-VCH Verlag GmbH & Co. KGaA.

2.4
Transverse (xy) magnetization is measured during acquisition of the FID.

2.5
We create transverse magnetization by temporarily applying a radio-frequency field orthogonal to the B_0 field, a so-called RF pulse.

2.6
This is due to the chemical shift which has its source in the varying electron densities around the nuclei.

2.7
The definition of the chemical shift in ppm is such that it is independent of the strength of the external magnetic field. Therefore, the shift difference of two nuclei remains constant regardless of the magnetic field strength. However, a shift difference of 0.03 ppm on a 300-MHz spectrometer corresponds to a frequency difference of 9 Hz, and a shift difference of 0.01 ppm at 900 MHz also corresponds to a frequency separation of 9 Hz. Remembering that the scalar coupling in Hz does not alter with the strength of the external magnetic field, the two resonance lines are likely the two components of a doublet due to scalar coupling.

2.8
Longitudinal (T1) relaxation reestablishes equilibrium z magnetization. Transverse (T2) relaxation causes the decay of transverse xy magnetization.

2.9
To measure isomer B in order to obtain NMR spectra with a comparable signal-to-noise ratio you need nine more scans.

Chapter 3: 1H NMR

3.1

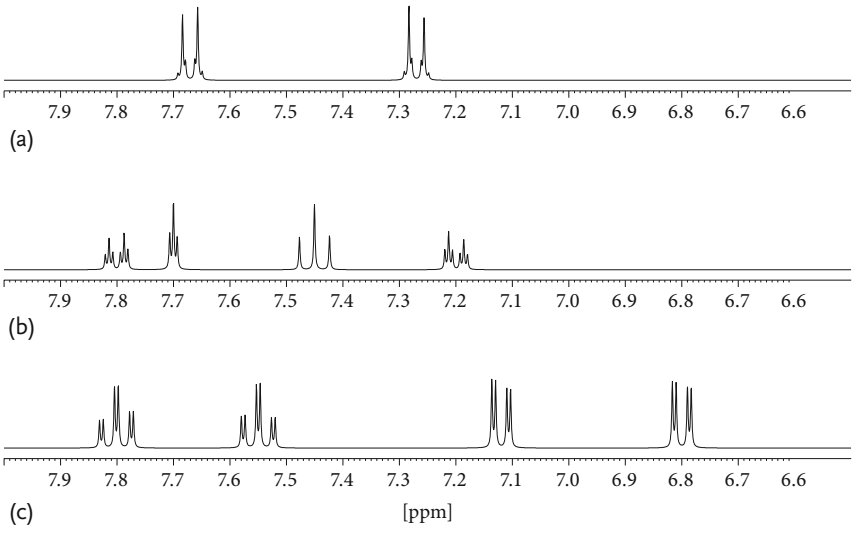

The spectra are assigned as follows: (a) para-disubstituted aromatic ring; (b) meta-disubstituted aromatic ring; (c) ortho-disubstituted aromatic ring.

3.2

The effect is referred to as the *roof effect* and it starts to occur when the chemical shift difference between two nuclei becomes smaller than ten times their mutual scalar coupling constant.

3.3

The spins are magnetically nonequivalent. Spin systems of magnetically nonequivalent spins give rise to higher-order spectra. The aromatic protons of a para disubstituted benzene ring form an AA′BB′ system.

3.4

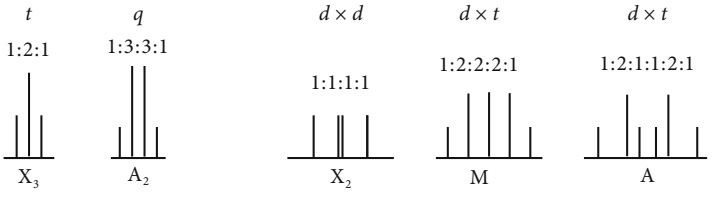

3.5

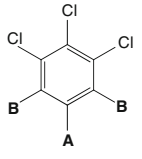

(a) AB_2

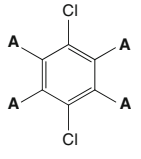

(b) A_4

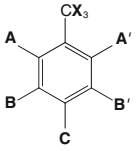

(c) $AA'BB'CX_3$

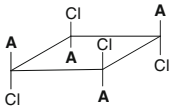

(d) A_4

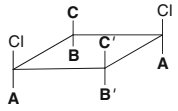

(e) $A_2BB'CC'$

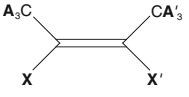

(f) $A_3A'_3XX'$

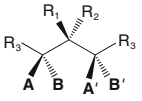

(g) $AA'BB'$

3.6

Use of chiral solvents, chiral shift reagents, or derivatization with a chiral compound. All these methods rely on the fact that in a chiral environment the two enantiotopic protons become diastereotopic, for which different chemical shifts are observed.

Chapter 4: NMR of ^{13}C and Other Heteronuclei

4.1

The sensitivity depends on its abundance. ^{3}H is very sensitive as such, but its natural abundance is extremely low. The sensitivity of this nucleus therefore largely depends on the enrichment level. The most sensitive nucleus on this list is ^{31}P (high freqency, 100% natural abundance). ^{29}Si is $I = 1/2$, natural abundance is moderate (4.7%), frequency is also fairly high, therefore this is a moderately sensitive nucleus. ^{57}Fe is a low-γ $I = 1/2$ nucleus, therefore insensitive. ^{2}H has a quadrupolar moment, but the latter is small. When highly enriched (there is no safety issue other than with ^{3}H), it is fairly sensitive. ^{10}B is a low-γ quadrupolar nucleus, therefore insensitive, and the same is true for ^{14}N. ^{16}O, ^{28}Si, and ^{32}S are NMR-inactive.

4.2

(from left to right): 1, 4, 2, 4, 6

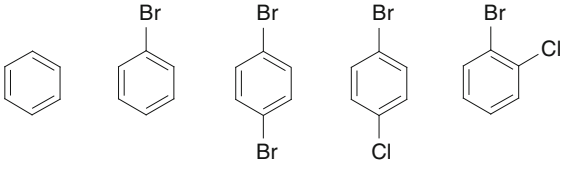

4.3

(from left to right) 5; 7; 2; 7

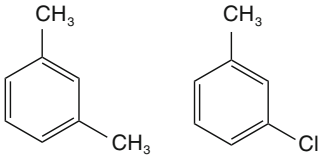

4.4

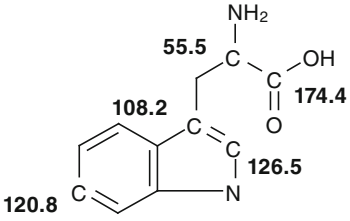

4.5

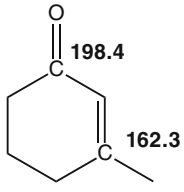

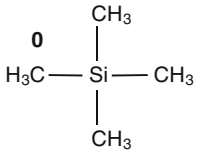

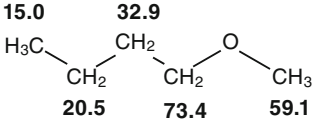

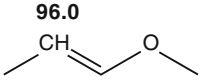

Chapter 5: Nuclear Magnetism – A Microscopic View

5.1

The nucleus must have spin different from zero so that it can be observed by NMR.

5.2

No. A simple rule states that if the proton and neutron numbers of an isotope are both even, the nucleus will have spin quantum number zero (I=0). Thus, ^{40}Ca is not an NMR-active isotope.

5.3
There are four Zeeman energy levels for a spin 3/2 nucleus ($m = -3/2, -1/2, +1/2, +3/2$).

5.4
Nuclear magnetism is a paramagnetic effect, irrespective of the sign of gamma.

5.5
(a) 200 MHz ; (b) 200 and 100 MHz

Chapter 6: Magnetization – A Macroscopic View

6.1
The population difference is related to the gyromagnetic ratio and the magnetic field strength in the following way: $\Delta N \propto \gamma B_0$

6.2
The amount of magnetization varies by a factor of four ($M \propto \gamma^2$).

6.3
Populations describe spin alignment along the z axis, whereas coherences describe spin alignment in the transverse plane.

6.4
No. The Bloch equations only apply to noninteracting spins and do not account for spin–spin couplings.

6.5
(longitudinal relaxation, spin–lattice relaxation, T1 relaxation)/(transverse relaxation, spin–spin relaxation, T2 relaxation)

6.6
The decay in the FID is fast. Accordingly the signal in the spectrum will be broad.

6.7
No. The line width depends also on the homogeneity of the B_0 field. In addition signals may also be broadened due to the presence of exchange phenomena.

6.8
The reference frequency is usually chosen to be the frequency of the RF pulse. This is usually the frequency at the center of the spectral range.

6.9
On-resonant magnetization is rotated into the xy plane. If the RF pulse is not on-resonant, only part of the magnetization is rotated to the transverse plane.

Chapter 7: Chemical Shift, Scalar and Dipolar Coupling

7.1
Nucleus B will have a higher precession frequency than nucleus A. The signal of nucleus B will appear to the left of signal A in the spectrum.

7.2
Also 200 ppm. Chemical shielding effects scale linearly with the strength of the applied external magnetic field.

7.3
In the case of the ^{1}H–^{13}C coupling both nuclei have a positive gyromagnetic ratio γ. Therefore, a parallel alignment of the spins z components (e.g., $I_z = 1/2$, $S_z = 1/2$) is equivalent to a parallel alignment of the spins dipole moments, which is energetically unfavorable, giving rise to a positive coupling constant (the states $\uparrow\uparrow$ and $\downarrow\downarrow$ are higher in energy than the $\uparrow\downarrow$ and $\downarrow\uparrow$ states). In contrast, because ^{15}N has a negative gamma, a parallel spin alignment of the proton and nitrogen spins results in an antiparallel alignment of the spin dipole moments. Consequently the $\uparrow\uparrow$ and $\downarrow\downarrow$ spin states are energetically favorable when compared to the $\uparrow\downarrow$ and $\downarrow\uparrow$ states, and therefore the coupling constant is negative.

7.4
Because of fast isotropic reorientation of the molecules in liquids, the direct dipole–dipole couplings are usually averaged to zero (in isotropic media).

7.5
The sign and magnitude of the direct spin–spin coupling depends on the relative orientation of the spins. As the molecules tumbles, the sign and the magnitude of the direct dipole–dipole interaction alters and the coupling becomes averaged to zero. In contrast, the indirect spin–spin coupling depends on the alignment of the spins but not on the relative spatial orientation of the nuclei. As the orientation of a spin does not alter upon rotation of the molecule, the scalar coupling is conserved.

7.6
Quadrupole nuclei interact with electric field gradients. Depending on the asymmetry of the ligand field, this interaction often results in very fast relaxation and therefore in severe line broadening.

Chapter 10: The Components of an NMR Spectrometer

10.1
The shim system is used to adjust the homogeneity of the external magnetic field within the sample volume.

10.2
By spinning the sample along its vertical axis the field inhomogeneities in the transverse plane are averaged.

10.3
RF coils are an integral part of the probehead.

10.4
One reason for the attenuated resonance signals is that the RF circuit is probably not properly tuned and matched.

10.5
The deuterium lock circuit is used to compensate for (a) magnetic field instabilities.

10.6
Room-temperature instabilities influence electronic components, and hence may result in frequency or phase shifts. They also influence the lock frequency, and thereby can introduce noise into the spectra.

Chapter 11: Acquisition and Processing

11.1
The Fourier transformation is not an approximation, but (in the limit of computational precession) an exact representation of the discrete time domain signal (inclusive noise) by a series of sines and cosines of various frequencies and amplitudes.

11.2
The term "complex" means that in order to distinguish between negative and positive frequencies relative to the carrier signal, the x and the y components of the magnetization must be detected. These two components are usually represented using complex numbers and the complex Fourier transform will then give the correct frequencies. Therefore, the answer is (c).

11.3
Doubling the spectral width means that the dwell time will be reduced by a factor of two. So to keep the acquisition time of the FID constant, the number of time domain points must also be doubled.

11.4
You may possibly have forgotten to also increase the number of calculated points (the size) of the spectrum. This means that the spectral point-to-point resolution now may be too poor to adequately cover the line shapes of the signals. Therefore, process the FID with a four times larger spectral size.

11.5
The spectrum will likely show some wiggles to the left and the right of the main component of the resonance signal – the so-called truncation artifacts. These can be reduced by multiplying the FID with a window function that smoothly drives the tail of the FID to zero (e.g., exponential or sine multiplication). This is at the expense of spectral resolution. Alternatively, the FID can be prolonged by linear prediction, which, provided the signal-to-noise ratio is good, even enhances the spectral resolution.

11.6
The correct order is: window multiplication/zero filling/Fourier transform/phase correction/baseline correction

11.7
Exponential multiplication is the window function most often applied to ^{13}C data. This improves the inherent low signal-to-noise ratio of ^{13}C spectra.

Chapter 12: Experimental Techniques

12.1
The pulse widths are 50 µs for the 90° pulse and 100 µs for the 180° pulse (the B_1 field strength is the inverse of the 360° pulse width).

12.2
The two alternative classes of RF pulse shapes with an improved inversion profile when compared to a simple rectangular 180° pulse are: 180° composite pulse; adiabatic 180° pulse

12.3
The gyromagnetic ratio of the ^1H spins is four times as large as the gamma of the ^{13}C spins. Accordingly, the ^1H spins encounter a four times larger phase change during a gradient pulse than the ^{13}C spins. Therefore, a four times weaker gradient

pulse must be applied to affect the magnetization on the ^{1}H spins by the same phase angle by which the ^{13}C spins were affected by the first gradient pulse. In addition, because the magnetization should be rephased, the polarity (the sign) of the gradient must be inverted. Thus we have: (a) −2.5 G/cm; (b) −5 G/cm.

12.4
Yes. If the gammas of the two nuclei would be of opposite sign, the polarity of the second gradient would have to be positive.

12.5
The phase cycling scheme of a one-pulse experiment [pulse phase: $X\ -X\ -Y\ Y$; receiver phase: $-Y\ X\ Y\ -X$] has (b) half signal intensity.

12.6
The delay τ is tuned to the scalar coupling constant ($\tau = 1/4\,J_{HX}$).

Chapter 13: The Art of Pulse Experiments

13.1
The HSQC essentially consists of two INEPT blocks separated by the X-nucleus evolution period. Magnetization is shuffled from the sensitive ^{1}H nucleus via the one-bond coupling to the X-nucleus in the first INEPT. After labeling of the X-nucleus chemical shift magnetization is again transferred to the sensitive ^{1}H nucleus for detection.

13.2
(a) A 180° pulse is missing in the center on the S-channel and (b) the phase of the second 90° proton pulse must be *y* and not *x*.

13.3
The HETCOR contains a single INEPT transfer (from the ^{1}H nucleus to the X-nucleus), the X-nucleus is detected. The HSQC experiment contains two INEPT transfers (^{1}H magnetization is detected).

13.4
The total difference in coherence levels (Δp) is 4. Therefore, we need a phase increment of $360/4 = 90°$ in the phase cycle and a four-step phase cycle.

13.5
You need to add a 180° pulse and a delay of the same duration as the gradient pulse to refocus chemical shift evolution during the gradient pulse. Otherwise you need a very large first-order phase correction in the indirect dimension.

13.6
If the sensitivity of the standard (phase-cycled) HSQC is set to 1, the corresponding experiment with gradient coherence selection during t_1 is $1/\sqrt{2}$ (one of the two coherence pathways is destroyed by the gradient), the sensitivity-enhanced experiments (both with and without gradients in t_1) are $\sqrt{2}$.

13.7
The TOCSY spin-lock serves to suppress chemical shift evolution during the mixing period. It is therefore composed of offset-compensated 180° pulses similar (although not always identical) to the ones used for decoupling.

13.8
In the phase-cycled experiments most of the signal is subtracted in consecutive scans to eliminate magnetization from protons bound to ^{12}C. Any instrument instability between consecutive scans will result in incomplete cancelation of these magnetization and thereby will result in t_1 noise.

Chapter 14: Relaxation

14.1
The most important relaxation mechanisms for the respective spins are (a) dipolar relaxation, (b) scalar relaxation of the second kind, and (c) chemical shift anisotropy

14.2
T1 leads to a change of enthalpy (the α and β states are associated with different energies). T2 is entropic in nature (the order of the system decreases when phase coherence is lost).

14.3
T2 effects result in differences in line width (short T2s result in broad lines, long T2s in sharp lines). T1 effects result in changes in peak intensities, if the relaxation delay is not sufficiently long.

14.4
You measure T1 relaxation times using inversion recovery and T2 relaxation times using Spin-Echo (Carr–Purcell–Meiboom–Gill (CPMG) sequence).

14.5
No, because the dipolar coupling depends not only on the distance but also on the gyromagnetic ratios of the two involved spins. Since the γ of ^{15}N is about 1/10th of the value of the proton, the dipolar interaction is *much* weaker.

14.6
An S^2 of 0.8 corresponds to an amide moiety in a rigidly structured part of a protein, a value of 0.3 to an amide moiety in a fairly flexible (although not entirely flexible) loop.

14.7
In the low-molecular weight range, both T1 and T2 decrease with increasing molecular weight (extreme narrowing regime). After going through a minimum (the cross-over point to the spin-diffusion regime) the T1 curve rises again, while T2 keeps decreasing all the time.

14.8
TROSY is most suitable for nuclei with nonspherical electron distribution, because it depends on the presence of CSA (e.g., ^{15}N or sp^2-hybridized ^{13}C). For ^{15}N the optimum magnetic field strength is close to 1 GHz. TROSY works best if the proteins are deuterated so that no additional pathways for ^{1}H,^{1}H dipolar coupling exist.

Chapter 15: The NOE

15.1
After saturation the population of the levels of α and β states of the corresponding spin are the same, and after inversion the population levels interconvert. As a result the signal vanishes after saturation and becomes negative after inversion.

15.2
The curves correspond to saturation curves. However, in the steady-state curves the signal reaches a plateau value, whereas in the curves corresponding to the transient NOE the level will fall off after reaching its maximum (due to T1 relaxation; for the shape of the curve see Figure 15.7).

15.3
(a) Close to T1 (about 1 s for protons) and (b) very short (tens of ms) to avoid spin diffusion.

15.4
See Figure 13.4. You can change temperature (to alter tumbling) or solvent (to change viscosity and again tumbling). Of course, you can also record a ROESY spectrum instead!

15.5
The buildup curve for a spin-diffusion NOE peak is characterized by a sigmoidal shape (no linear increase for very short mixing times; for the shape of the curve see Figure 15.8).

15.6
The negative heteronuclear NOE that results from the negative γ (the NOE arises due to decoupling) will decrease signal intensity otherwise. In the worst case the signal may completely disappear.

15.7
The NOE buildup is more efficient for larger molecules, and hence the NOE can be observed for larger distances.

15.8
The number of other protons in the vicinity of the proton that is perturbed (the presence of relaxation sinks).

15.9
You can use long mixing times when measuring spectra on perdeuterated proteins because spin-diffusion effects cannot occur (most protons, that serve as relay nuclei for the NOE, are replaced by deuterons).

Chapter 16: Chemical and Conformational Exchange

16.1
Slow exchange: $k_{ex} \ll \Delta\omega \rightarrow 2$ signals; fast exchange: $k_{ex} \gg \Delta\omega \rightarrow 1$ signal at the appropriately population weighted average frequency.

16.2
They rapidly exchange with the water signal. Because of the very much larger abundance of the water protons the population-weighted average frequency will fall on the water resonance.

16.3
Look at the solvent or the TMS signal. If these signals are sharp it is exchange, if these lines are broad as well, the problem is bad shims or paramagnetic impurities and so on.

16.4
Yes, because the coalescence temperature depends on the frequency separation of the two lines. If the two corresponding signals are very close to each other they will have a different coalescence temperature than if the two lines are separated by a large frequency difference.

16.5
(a) Measure the coalescence temperature or (b) measure NMR spectra at different temperatures and (from line-shape simulations) derive the exchange rates. Plot the exchange rate vs. $1/T$ in an Arrhenius-type plot.

16.6
Water protons can exchange with labile protons, for example with amide protons. If the water signal is suppressed by preirradiation of the water resonance, saturated protons that originated from the water line will exchange with amide protons, so that these are fully or at least partially suppressed in the end.

16.7
To determine exchange rates from EXSY spectra record a series of EXSY spectra with different mixing times. From the ratio of cross peak to diagonal peak vs. mixing time you can compute the exchange rate (see Eq. (16.9)).

Chapter 17: Two-Dimensional NMR

17.1
The names of the four blocks in the correct order are: Excitation (or preparation), evolution, mixing, and detection.

17.2
You determine the spectral width in the indirect dimension by choosing the correct t_1 increment. $\Delta t_1 = 1/\mathrm{SW}$ (Hz).

17.3
You determine the resolution in the indirect dimension by both, the spectral width in F1 and the number of t_1 increments that you record.

17.4
The measuring time will double.

17.5
You start with the aldehyde proton at 9.75 ppm, and work your way through the COSY to obtain all resonances from butanal (9.75; 2.4; 1.65; 0.9 ppm).

17.6
For most low-molecular weight compounds the combination of a [^{13}C,^{1}H]-HSQC (to record ^{13}C chemical shifts of protonated carbons) and the [^{13}C,^{1}H]-HMBC (for the quaternary carbons, carbonyls etc.) is sufficient. This, however, will not work if the molecule contains too few hydrogen atoms.

17.7
In order of decreasing sensitivity the 2D NMR experiments should be arranged as follows: COSY → HSQC → HMBC → INADEQUATE

17.8
The active couplings are the ones that lead to the cross peak, passive couplings are all other couplings that involve the two correlated spins. Active and passive couplings can be extracted from the multiplet fine structure of COSY cross peaks. The active couplings are antiphase (the multiplet components have different sign), passive couplings are in-phase.

17.9
t_1 noise is due to instrumental instabilities. It is random noise, and hence forms noise bands along a vertical line through (mostly intense) peaks. Axial peaks are due to magnetization that has recovered along z before the mixing pulse. Depending on the quadrature detection scheme, axial peaks are found either along a horizontal line through the center of the spectrum, or (more often) at the bottom edge of the spectrum.

17.10
Most 2D pulse sequences make use of phase cycling for selection of the desired signal. For proper suppression of the unwanted coherences, the number of scans per t_1 increment must then correspond to an integer multiple of the basic phase cycling scheme.

17.11
Double-quantum coherences are formed from antiphase magnetization. The antiphase magnetization builds up during t_1. In the first increments the t_1 delay is so short that almost no antiphase magnetization has been formed, and therefore nothing passes the double-quantum filter.

Chapter 18: Solid-State NMR

18.1
The following *additional* interactions become visible in solid-state NMR spectra compared to solution data: Dipolar couplings, effects from chemical shift anisotropy, and, if present, quadrupolar interactions.

18.2
You get rid of the interactions by rapid spinning at the magic angle (MAS).

18.3
Powder patterns describe the envelope of the signal from a single resonance. In the powder all orientations are possible and, due to CSA, chemical shifts are different in these. Powder patterns allow insight into the symmetry of the ligand field.

18.4
Recoupling allows one to reintroduce dipolar couplings into experiments recorded under MAS conditions. This is mostly achieved via rotor-synchronized RF pulses.

18.5
The REDOR experiment or a rotational resonance experiment will do. The important point is that a series of experiments is recorded in which the dipolar coupling is reintroduced during different amounts of time so that the signal intensity is modulated by the dipolar coupling.

18.6
In solution polarization transfer is achieved via INEPT elements (employing the scalar couplings). In SS-NMR this is mostly done via heteronuclear Hartman–Hahn cross-polarization (employing the dipolar couplings). This involved pulse trains on both RF channels.

Chapter 19: Detection of Intermolecular Interactions

19.1
Target-observe techniques usually use a labeled target and monitor binding via chemical shift mapping. In the ligand-observe techniques vastly different relaxation or diffusion properties of the bound ligand are exploited (no labeling required).

19.2
One measures a spectrum in absence of the ligand. Then you add the ligand and measure the spectrum again. A shift of peaks indicates binding. To distinguish ligand and target resonances the target is usually labeled and heteronuclear NMR experiments are used. Artifacts are mostly due to changes in conditions of the sample, for example a drift in pH, changes in buffer composition after addition of the ligand, decomposition of target etc., but also temperature changes. Complications may arise when the ligand is not soluble in the same buffer as the target, it reacts, is unstable, precipitates and so on.

19.3
Changes in T2 lead to considerable line broadening, the cross-relaxation (NOE) alters, and there are reduced diffusion rates upon binding. In addition chemical shifts from residues in the binding site change.

19.4
You de-convolute the mixture into mixtures consisting of less compounds until you have identified the binder.

19.5
The transfer NOE is an experiment to describe the conformation of a ligand *weakly* binding to a large target. Ideally, the ligand has little or no NOE itself, and the NOE exclusively builds up when bound. The NOE is detected using a normal NOESY experiment on the free state of the ligand, but the detected NOEs correspond to the bound state.

19.6
Perform a competition experiment, in which a weak binder competes with the strong binder.

19.7
This is due to exchange broadening. Weak binders are always in the fast exchange regime. At about 30% of bound ligand exchange contributions to line broadening are at maximum.

Index

Symbols
2,2-dimethyl-2-silapentane-5-sulfonic acid, 26
3-(trimethylsilyl)propionic acid sodium salt, 26
B_1 field, 117
J-resolved experiments, 368
^{1}H chemical shifts
– hydrogen bonding, 37
– pH effects, 37
– solvent effects, 37
– temperature effects, 37
^{1}H NMR
– anisotropy effects, 35
– chemical shifts, 34
– coupling constants, 50
– geminal coupling constants, 50
– general aspects, 33
– H,C coupling constants, 52
– H,F coupling constants, 53
– H,P coupling constants, 54
– influence of electronegativity on chemical shifts, 35
– shielding effects, 35
^{13}C, 329
^{15}N, 329
^{19}F, 329
^{31}P, 329

A
acquisition time
– and digital resolution, 217
activation energy
– measurement of, 346
analog-to-digital converter, 16
anisotropy, 133
Arrhenius plot, 347
asymmetry, 133
audio filter, 215
autocorrelation function, 308
autorelaxation, 315
axiality, 133

B
baseline correction
– in 2D spectra, 381
binding affinity, 400
Biot–Savart law, 127
Boltzmann distribution, 14, 293

C
carbohydrates, 419
– establishing linkages, 429
– identification by NMR, 424
– identification of stereochemistry, 426
– quick identification, 430
– solvent choice, 429
– structure, 419
carbon-13, 59
chemical shift, 16
– diamagnetic contribution, 17
– electric field effects, 62
– heavy atom effects, 63
– hybridization effects, 61
– increment systems, 64
– isotropic, 133, 384
– mesomeric effects, 63
– neighbor anisotropy effects, 63
– paramagnetic compounds, 131
– steric effects, 62
– substituent effects, 61
chemical shift anisotropy, 128
– ^{15}N, 129
chemical shift mapping, 395
chemical shift perturbation, 395, 397
coalescence, 337
coalescence temperature, 340
coherence, 108
– multiple quantum, 109

Applied NMR Spectroscopy for Chemists and Life Scientists, First Edition. Oliver Zerbe and Simon Jurt.
©2014 WILEY-VCH Verlag GmbH & Co. KGaA. Published 2014 by WILEY-VCH Verlag GmbH & Co. KGaA.

coherence selection, 287
coherence transfer, 271
complex, 401
composite pulse decoupling, 256
constant time, 279, 280
correlation function, 302
correlation time, 300
COSY, 358
– double quantum filtered, 284, 358
– multiplet pattern, 427
– triple quantum filtered, 285, 358
coupling
– geminal, 136
– heteronuclear, 44, 284
– homonuclear, 18, 44, 279
– scalar, 134
cross-relaxation, 315
cross-relaxation rate, 319, 320
CYCLOPS, 286

D
decoupling
– sidebands, 244
delay, 272
– relaxation, 273
density matrix, 172
DEPT, 276
detection, 355
diastereotopic, 40, 42, 43
diffusion, 403
diffusion coefficient, 403
digital filter, 215
digital resolution, 217
digitizer
– dynamic range, 214
dipolar coupling
– solid state, 386
DIPSI-2
– composite pulse decoupling, 256
direct dipolar relaxation rate, 320
direct spin–spin coupling, 141
DNA quadruplexes, 484
downfield, 17
dwell time, 196

E
eigenstate, 156
eigenvalue, 156
electric field effect, 130
enantiotopic, 42
equivalence
– magnetic, 39
exchange, 335, 398, 402
– chemical, 335
– conformational, 336
– examples, 342
– fast, 336, 338
– intermediate, 336, 340
– slow, 336, 340
– two state, 336
exchange rates
– measurement, 344
excitation sculpting, 274
expectation value, 157
EXSY, 345
extreme narrowing, 320, 322

F
Fermi contact, 131, 135
Fermi contact interaction, 37
field
– effective, 384
field gradients, 247
field-frequency lock, 192
FLOPSY, 257
folding, 204
Fourier transformation, 16
– discrete, 203
free induction decay, 15, 195
furanoses, 421

G
GARP, 256
Gaussian pulses, 236
gradient spin echo, 403
gyromagnetic ratio, 95

H
Hamilton operator, 169
Hartmann–Hahn condition, 360
HETCOR, 280
heteronuclear cross-polarization, 276
heteronuclear nuclear Overhauser effect, 329
high-temperature approximation, 107
Hilbert space, 158
HMQC, 276, 280, 364
HN(CO)CACB, 283
HNCA, 284
HNCACB, 283
HOESY, 329
homotopic, 42
HSQC, 280, 364
hydrodynamic radius, 403
hydrogen bonds, 130

I
INADEQUATE, 367
indirect detection, 59
induced field, 132

inductive effect, 65
INEPT, 275, 279, 283
inhomogeneous broadening, 114
initial-rate approximation, 346
interaction
– dipolar, 304
inverse detection
– transition metals, 79
inverse gated, 69
inversion, 315
inversion recovery, 282, 306
irradiation, 274
isochronous, 39
isotope shift, 76

J
jump return, 275

K
Karplus relationship, 51, 137, 426

L
Lamb shift, 127
line broadening
– exchange, 339
linear approximation, 325
linear prediction, 219, 378, 379
Liouville space, 175
Liouville–von Neumann equation, 174
Lipari–Szabo, 307
lock, 192, 333
longitudinal relaxation
– ^{13}C nuclei, 68
Lorentzian line shape, 199
– integral of, 201
– phase of, 201
lowering operator, 164
lowest unoccupied molecular orbital, 128

M
magic-angle spinning, 387
magnet, 181
magnetic anisotropy, 36
magnetic dipole moment, 13
magnetic quantum number, 95
magnetic susceptibility, 130
magnetism, 87
magnetization
– longitudinal, 106
– transverse, 106
magnetization transfer
– by isotropic mixing, 257
main group elements, 70
– ^{15}N, 71
– ^{19}F, 72
– ^{31}P, 73
matching, 190
mixing, 288
mixing time, 324, 333
MLEV
– composite pulse decoupling, 256
model-free approach, 307
Mosher's reagent, 43
multiplet structure, 47

N
neighbor anisotropy effect, 129
NMR
– basic phenomena, 13
NMR timescale, 336
NOESY, 278, 325, 345, 401
– isotope edited, 400
– isotope filtered, 400
nuclear Overhauser effect, 315, 400
– enhancements, 323
– intermolecular, 396, 400
– kinetics of, 324
– multispin systems, 325
– rotating frame, 327
– steady state, 318, 321
– transient, 318, 324
– use in stereochemical analysis, 330
nuclear quadrupole coupling constant, 141
nuclear spin, 94
– properties of heteronuclei, 57
nucleic acids, 481
– ^{13}C NMR, 489
– ^{31}P NMR, 490
– assignments, 492
– labeling, 496
– sequential walk, 492
– structure, 482
– triple-resonance experiments, 496
nutation, 119
nutation frequency, 235
Nyquist theorem, 204

O
offset frequency, 116
order parameter, 308
out and back, 284
oversampling, 215

P
paramagnetic, 333
paramagnetic spin–orbit, 135
parts per million scale, 17
Pascal's triangle, 46

Pauli principle, 135
Pauli spin matrices, 165
peak shape
– E.COSY, 362
peaks
– autocorrelation peaks, 352
peptide bond, 459
peptides, 457
– β strands, 459
– ^{1}H NMR, 461
– ^{13}C NMR, 464
– ^{15}N NMR, 467
– assignments, 469
– hydrogen bonds, 459
– NMR of, 461
– NOESY walk, 472
– nomenclature, 459
– random coil chemical shifts, 463, 469
– secondary structure, 459
– structure, 458
– structure calculation, 474
– triple-resonance experiments, 473
phase coherence, 20, 108
phase correction, 227, 381
phase cycle, 284
– number of steps in, 379
phase modulation, 371
Pirkle's reagent, 44
polarization operators, 164
polarization transfer, 275
– INEPT, 266
power spectra, 229
presaturation, 258
prescan delay, 228
principal axis system, 133
processing
– two-dimensional spectra, 380
protein dynamics, 306
proton spectra
– solvent dependence, 441
pseudocontact shift, 37, 131
pulse, 272
– calibration, 244
– width, 234
pulse experiments, 271
pulse program, 285
pulsed field gradients, 247, 272, 286

Q

quadrature detection, 286, 370
quadrupolar nuclei
– transition metals, 81
quadrupolar relaxation, 141
– metals, 57
quadrupole moment, 140
quench, 184
quintet, 46

R

radiation damping, 115
radio frequency coils, 189
radio frequency field
– inhomogeneity, 243
– power dissipation, 242
radio frequency pulses, 15, 117
– frequency shifted, 242
– hard, 235
– off-resonance effects, 243
– soft or selective, 236
Ramachandran plot, 459
receiver phase, 210, 252, 285
Redfield trick, 211
reduced coupling, 136
reference frequency, 115
referencing, 25
– direct, 25
relaxation, 293
– chemical shift anisotropy, 297
– longitudinal, 399
– mechanism, 303
– paramagnetic, 299
– spin–spin rotation, 299
– transverse, 398
relaxation delay, 333
relaxation dispersion, 310
relaxation interference, 309
relaxation reagent, 367
resolution, 216
– in 2D spectra, 377
resolution enhancement
– by apodization, 221
resonance frequency, 99
rhombicity, 133
ring current, 36
ring-current effect, 129
rising operator, 164
ROESY, 278, 327, 363
– artifacts in, 363
rotating frame experiments, 363
rotor, 383

S

salt, 24
sample spinning, 23, 187
sampling
– sequential, 211
sampling rate, 204

saturation, 315
saturation transfer, 274, 344
saturation transfer difference, 323, 344, 402
scalar coupling constants, 18, 474
scalar couplings
– active, 353
– geminal, 18
– X,^{13}C couplings, 64
scalar relaxation
– of the second kind, 141
screening, 395
self-decoupling, 339
sensitivity enhancement, 288
– by apodization, 221
septet, 46
sextet, 46
shaped pulses, 236
shift reagents, 37
– chiral, 44
– lanthanide, 44
Shigemi tubes, 367
shimming, 184
shims, 23
– room temperature shims, 183, 184
signal dispersion, 17
signal-to-noise ratio, 27
solid-state NMR, 383
Solomon equations, 318
solvent effect, 130
solvent exchange, 33
solvent suppression, 257
spectral density, 305
spectral width, 196
spin angular momentum, 88
– quantization of, 90
spin diffusion, 320, 322, 363
spin ensemble, 105
spin lock, 275, 327
spin precession
– right-hand rule, 99
spin quantum number, 94
spinning sidebands
– in liquid state, 187
spin–dipolar, 135
state vector, 158
Stern–Gerlach experiment, 93
steroids, 439
– ^{13}C spectra, 443
– assignments, 444
– conformation, 440
– nomenclature, 440
Stokes–Einstein, 403
strong coupling, 135
superposition, 108
superposition state, 157

T

T1 noise, 332, 363
T1 relaxation, 293
temperature calibration, 333
tensor
– chemical shift, 384
– shielding, 132
– trace, 384
three-dimensional NMR, 370
time domain signal, 195
time-proportional phase incrementation, 212
TOCSY, 278, 329
transferred nuclear Overhauser effect, 401
transition metal NMR, 78
transitions
– double quantum, 140
– multiple quantum, 140
– single quantum, 140
– zero quantum, 140
triple-resonance experiments, 283
triplet, 45
TROSY, 280
tumbling, 399
two-dimensional experiments
– heteronuclear, 279
– homonuclear, 278, 351
– setup of, 379
two-dimensional NMR
– building blocks, 354
– diagonal peaks, 355
– indirect dimension, 354

U

upfield, 17

V

variable-temperature NMR, 335
viscosity, 403

W

WALTZ
– composite pulse decoupling, 256
– isotropic mixing, 257
weak coupling, 135
window multiplication
– Lorentz-to-Gauss transformation, 225

Z

zero-quantum artifacts, 326
zero-quantum interference peaks, 362
zigzag arrangement, 52